TU Delft

Delft University of Technology

Document Version
Final published version

Licence
CC BY-NC

Citation (APA)
Carzana, L. (2026). *Sailing on Sunlight in Earth's Embrace: Dynamical Modeling and Maneuvering Capabilities of Earth-bound Solar Sails*. [Dissertation (TU Delft), Delft University of Technology]. https://doi.org/10.4233/uuid:d43cbab9-9f65-497f-acaa-b57dcb324d04

Important note
To cite this publication, please use the final published version (if applicable).
Please check the document version above.

Copyright
In case the licence states “Dutch Copyright Act (Article 25fa)”, this publication was made available Green Open Access via the TU Delft Institutional Repository pursuant to Dutch Copyright Act (Article 25fa, the Taverne amendment). This provision does not affect copyright ownership.
Unless copyright is transferred by contract or statute, it remains with the copyright holder.

Sharing and reuse
Other than for strictly personal use, it is not permitted to download, forward or distribute the text or part of it, without the consent of the author(s) and/or copyright holder(s), unless the work is under an open content license such as Creative Commons.

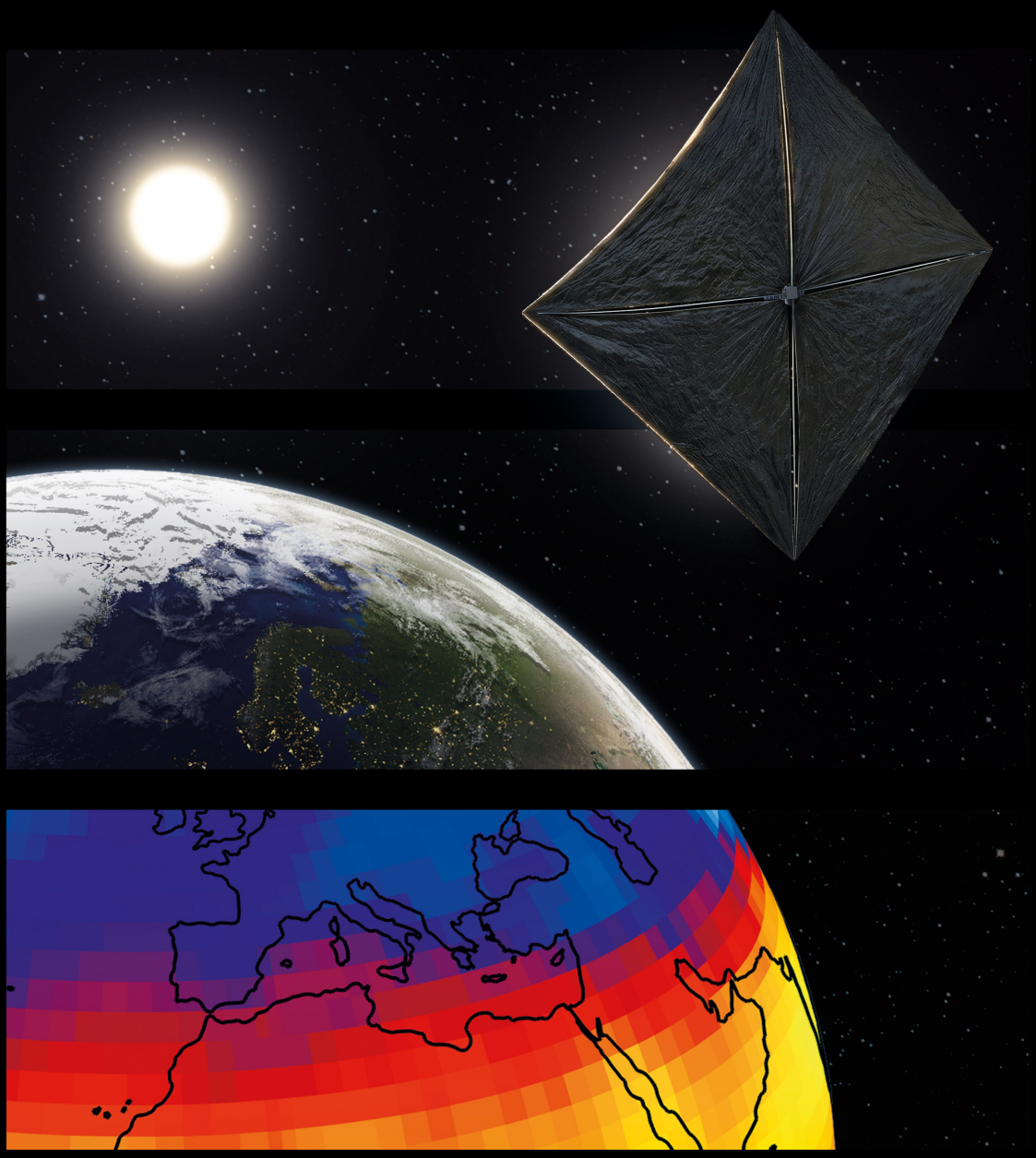
Takedown policy
Please contact us and provide details if you believe this document breaches copyrights.
We will remove access to the work immediately and investigate your claim.

This work is downloaded from Delft University of Technology.

Livio Carzana

Sailing on Sunlight in Earth's Embrace

Dynamical Modeling and Maneuvering Capabilities of Earth-bound Solar Sails



Sailing on Sunlight in Earth's Embrace

Dynamical Modeling and Maneuvering Capabilities of Earth-bound Solar Sails

SAILING ON SUNLIGHT IN EARTH'S EMBRACE

DYNAMICAL MODELING AND MANEUVERING CAPABILITIES OF EARTH-BOUND SOLAR SAILS

Dissertation

for the purpose of obtaining the degree of doctor
at Delft University of Technology
by the authority of the Rector Magnificus,
Prof. dr. ir. H. Bijl,
chair of the Board for Doctorates
to be defended publicly on
Friday 6 November 2026 at 10:00

by

Livio CARZANA

This dissertation has been approved by the (co)promotors.

Composition of the doctoral committee:

Rector Magnificus,	*chairperson*
Prof. dr. ir. P.N.A.M. Visser,	Delft University of Technology, *promotor*
Dr. ir. M.J. Heiligers,	Delft University of Technology, *copromotor*
Independent members:	
Prof. dr. L.L.A. Vermeersen	Delft University of Technology
Prof. dr. C. Colombo	Politecnico di Milano, Italy
Prof. dr. C.R. McInnes	University of Glasgow, Scotland, United Kingdom
Prof. dr. G. Mengali	Università di Pisa, Italy
Dr. W.K. Wilkie	Retired from NASA, United States of America
Prof. dr. M. Kotsonis	Delft University of Technology, *reserve member*



Keywords: Solar sailing, low-Earth orbit, dynamical modeling, planetary radiation, aerodynamic drag, maneuvering capabilities, orbit raising, inclination changing, ACS3 mission, calibration

Printed by: Ipskamp

Cover by: Vincenzo Bortone

Front: Artistic illustration of an Earth-orbiting solar sailcraft illuminated by sunlight, in a three-panel layout. The middle panel shows a realistic view of the Earth, while the bottom panel displays a map of the outgoing longwave radiation flux of the planet, generated by the ANGARA numerical model.

Back: Artistic illustration of the trajectory of a solar sailcraft passing over Delft, the Netherlands, in the top panel, and Naples, Italy, in the bottom panel.

Copyright © 2026 by L. Carzana

ISBN 978-94-6563-022-9

An electronic version of this dissertation is available at:
http://repository.tudelft.nl/

Ad Aurora

Abbiamo bisogno del vento in faccia
per vederle, le cose,
da un'altra angolazione.

Fabrica

CONTENTS

Summary xvii

Samenvatting xxi

Abbreviations xxv

1 Introduction 1
- 1.1 Heritage . . . 3
  - 1.1.1 Chasing the Heavenly Breezes . . . 3
  - 1.1.2 Solar Radiation as a Source of Thrust . . . 4
  - 1.1.3 First Solar-sail Concepts . . . 6
  - 1.1.4 Real-life Solar Sailing . . . 7
- 1.2 State of the Art . . . 11
  - 1.2.1 Technology Status Overview . . . 11
  - 1.2.2 Direction of Technological Progress . . . 14
  - 1.2.3 Research Status Overview . . . 16
- 1.3 Future Challenges . . . 18
- 1.4 Research Questions . . . 19

2 Mathematical Framework 23
- 2.1 Orbital Configurations of Interest . . . 25
- 2.2 Accelerations of Interest . . . 27
  - 2.2.1 Gravitational Accelerations . . . 27
    - 2.2.1.1 Non-spherical Gravity of the Earth . . . 27
    - 2.2.1.2 Third-body gravity . . . 29
    - 2.2.1.3 Gravity Induced by Earth tides . . . 29
    - 2.2.1.4 Relativistic corrections . . . 30
  - 2.2.2 Attitude-dependent Accelerations . . . 30
  - 2.2.3 Equations of Motion . . . 31
- 2.3 Sailcraft Characteristics . . . 31
  - 2.3.1 Sail Shape . . . 33
  - 2.3.2 Sail Optical Properties . . . 36
- 2.4 Near-Earth Environment . . . 37
  - 2.4.1 Gravitational Potential of the Earth . . . 37
  - 2.4.2 Atmosphere of the Earth . . . 38
    - 2.4.2.1 Atmospheric Density . . . 38
    - 2.4.2.2 Atmospheric Circulation . . . 40
  - 2.4.3 Solar Radiation . . . 41
    - 2.4.3.1 Total Solar Irradiance . . . 41
    - 2.4.3.2 Solar Flux . . . 43

2.4.3.3 Eclipses . . . 43
2.4.4 Planetary Radiation . . . 45
2.5 Modeling of the Sailcraft Accelerations . . . 48
2.5.1 Gravitational Acceleration . . . 48
2.5.2 Aerodynamic Acceleration . . . 51
2.5.2.1 General Formulation . . . 51
2.5.2.2 Gas-Surface Interaction . . . 53
2.5.3 Tensor Formulation of Radiation Pressure Acceleration . . . 56
2.5.3.1 Angular Moments of Radiative Specific Intensity . . . 56
2.5.3.2 Acceleration for Optical Sails . . . 57
2.5.3.3 Acceleration for Ideal Sails . . . 59
2.5.4 Solar Radiation Pressure Acceleration . . . 61
2.5.4.1 Ideal Model . . . 61
2.5.4.2 Optical Model . . . 62
2.5.5 Planetary Radiation Pressure Acceleration . . . 63
2.6 Trajectory Optimization . . . 66

3 A New Model for the Planetary Radiation Pressure Acceleration for Solar Sails 69
3.1 Introduction . . . 71
3.2 Dynamical Model . . . 72
3.2.1 Solar Radiation Pressure Acceleration . . . 73
3.2.2 Aerodynamic Acceleration . . . 74
3.2.3 J_2 Gravitational Acceleration . . . 74
3.2.4 Planetary Radiation Pressure Acceleration . . . 74
3.2.4.1 Blackbody Flux Model . . . 78
3.2.4.2 Albedo Flux Model . . . 79
3.3 Analysis of the Blackbody Radiation Pressure Acceleration . . . 82
3.4 Analysis of the Albedo Radiation Pressure Acceleration . . . 84
3.5 Comparison with the State of the Art . . . 87
3.5.1 Comparison with Finite-disk Radiation Source Model . . . 87
3.5.1.1 Blackbody Radiation Pressure Acceleration . . . 87
3.5.1.2 Albedo Radiation Pressure Acceleration . . . 88
3.5.2 Parametric Analyses . . . 90
3.5.2.1 Variation in Accuracy with the LTAN . . . 91
3.5.2.2 Variation in Accuracy with Altitude . . . 94
3.5.2.3 Variation in Accuracy with Inclination . . . 96
3.6 ACS3 Mission Analysis . . . 98
3.7 Conclusions . . . 101

4 Extending the Spherical Planetary Radiation Pressure Acceleration Model to Optical Solar Sails 103
4.1 Introduction . . . 105
4.2 Dynamical Model . . . 106
4.2.1 Solar Radiation Pressure Acceleration . . . 106
4.2.2 Planetary Radiation Pressure Acceleration . . . 107
4.2.2.1 Normal Specular Geometrical Factors . . . 112

4.2.2.2 Normal Diffuse Geometrical Factors . . . 113
4.2.2.3 Transversal Geometrical Factors . . . 113
4.3 Comparison with State of the Art . . . 114
4.3.1 Sailcraft Dynamics and Control . . . 114
4.3.2 Reference Mission Scenario . . . 115
4.3.3 Accuracy Metric . . . 116
4.3.4 Variation in Accuracy with the LTAN . . . 116
4.3.5 Variation in Accuracy with Altitude and Inclination . . . 118
4.4 Conclusions . . . 121

5 Steering Laws to Calibrate the Accelerations of NASA's Advanced Composite Solar Sail System 123
5.1 Introduction . . . 125
5.2 Dynamical Model . . . 126
5.2.1 Gravitational Acceleration . . . 126
5.2.2 Solar Radiation Pressure Acceleration . . . 127
5.2.3 Planetary Radiation Pressure Acceleration . . . 130
5.2.4 Aerodynamic Acceleration . . . 132
5.3 Calibration Steering Laws . . . 132
5.3.1 Calibration of the Maximum Accelerations . . . 133
5.3.2 Calibration of the Acceleration Envelopes . . . 135
5.3.2.1 Solar Radiation Pressure Acceleration . . . 135
5.3.2.2 Planetary Radiation Pressure Acceleration . . . 135
5.3.2.3 Aerodynamic Acceleration . . . 136
5.3.3 Calibration of Residual Accelerations . . . 136
5.4 Operational Challenges and Constraints . . . 136
5.5 Preliminary Analysis . . . 138
5.5.1 Setup . . . 138
5.5.2 Results and Discussion . . . 139
5.6 Revision of the Analysis Framework . . . 141
5.6.1 Revision of the Calibration Steering Laws . . . 142
5.6.2 Revision of the Operational Challenges . . . 143
5.7 Post-Launch Analysis . . . 146
5.7.1 Setup . . . 146
5.7.1.1 Year-long Propagation . . . 147
5.7.1.2 Week-long Propagations . . . 147
5.7.2 Results and Discussion . . . 147
5.8 Conclusions . . . 151

6 Locally Optimal Control Laws for Earth-bound Solar Sailing with Atmospheric Drag 153
6.1 Introduction . . . 155
6.2 Dynamical Model . . . 156
6.2.1 Reference Frames and Coordinate Systems . . . 156
6.2.1.1 Earth-centered Inertial Reference Frame . . . 156
6.2.1.2 Sunlight Reference Frame . . . 156

6.2.1.3 Aerodynamic Reference Frame . . . 157
6.2.1.4 Optimization Reference Frame . . . 158
6.2.2 Equations of Motion . . . 159
6.2.2.1 Solar Radiation Pressure Acceleration . . . 159
6.2.2.2 Aerodynamic Acceleration . . . 160
6.2.2.3 J_2 Gravitational Acceleration . . . 162
6.3 Optimal Control Problem . . . 162
6.3.1 Optimization based on Solar Radiation Pressure . . . 163
6.3.2 Aerodynamic-based Optimization . . . 164
6.3.3 Full-dynamics Optimization . . . 166
6.3.3.1 Numerical Approaches to the Optimization Problem . . . 166
6.3.3.2 Pre-run Optimization Phase . . . 168
6.3.3.3 In-run Interpolation Phase . . . 169
6.4 Validation and Testing . . . 171
6.4.1 Tuning of the Atmospheric Density Model . . . 172
6.4.2 Validation of Full-dynamics POINT Optimization . . . 175
6.4.2.1 Orbit Raising . . . 176
6.4.2.2 Inclination Increase . . . 176
6.4.3 Tuning of the Pre-run Optimization Grid . . . 178
6.4.3.1 Orbit Raising . . . 179
6.4.3.2 Inclination Increase . . . 179
6.4.4 Tuning of the Boundaries of the Acceleration Ratio . . . 180
6.4.4.1 Orbit Raising . . . 180
6.4.4.2 Inclination Increase . . . 181
6.5 Results and Analysis . . . 181
6.5.1 Orbit Raising . . . 183
6.5.2 Inclination Increase . . . 186
6.6 Conclusions . . . 187

7 High-fidelity Characterization of the Maneuvering Capabilities of Earth-bound Solar Sails 189
7.1 Introduction . . . 191
7.2 Dynamical Model . . . 193
7.2.1 J_2 Gravitational Acceleration . . . 193
7.2.2 Solar Radiation Pressure Acceleration . . . 194
7.2.3 Planetary Radiation Pressure Acceleration . . . 195
7.2.4 Aerodynamic Acceleration . . . 196
7.2.5 Reference Sailcraft Specifics . . . 197
7.3 Optimal Control Problem . . . 197
7.3.1 Characterization . . . 198
7.3.2 Optimization Algorithm . . . 201
7.3.3 Deorbit-safe Inclination-changing Steering Law . . . 205
7.3.4 Optimization Algorithm Tuning . . . 207

7.4 Near-Earth Dynamical Regimes . . . 211
7.5 Characterization of Solar-sail Maneuvering Capabilities . . . 213
7.5.1 Reference Scenario . . . 216
7.5.2 Analysis of the Effect of Planetary Radiation Pressure . . . 217
7.5.3 Analysis of the Effect of Solar Activity . . . 219
7.5.4 Analysis of the Effect of Characteristic Acceleration . . . 220
7.5.5 Analysis of the Effect of Orbital Inclination . . . 222
7.5.6 Analysis of the Effect of Solar Declination . . . 223
7.6 Conclusions . . . 225

8 Conclusions and Recommendations 227
8.1 Earth-bound Solar-sail Dynamical Modeling . . . 229
8.1.1 Research Findings . . . 229
8.1.2 Recommendations . . . 234
8.2 Earth-bound Solar-sail Maneuvering Capabilities . . . 236
8.2.1 Research Findings . . . 237
8.2.2 Recommendations . . . 238

A Derivation of Ideal Radiation Pressure Acceleration from Tensor Formulation 241

B Derivation of the Geometrical Factors 245
B.1 Geometry of the Problem . . . 245
B.2 Normal Specular Geometrical Factors . . . 250
B.2.1 Sail Plane Not Intersecting the Earth . . . 251
B.2.2 Sail Plane Intersecting the Earth . . . 252
B.2.2.1 Geometrical Factor of the Inward Side of the Sail . . . 252
B.2.2.2 Geometrical Factor of the Outward Side of the Sail . . . 256
B.2.3 Reduced Form for Ideal Sails . . . 258
B.3 Transversal Geometrical Factors . . . 258
B.3.1 Sail Plane Not Intersecting the Earth . . . 258
B.3.2 Sail Plane Intersecting the Earth . . . 259
B.3.2.1 Geometrical Factor of the Inward Side of the Sail . . . 259
B.3.2.2 Geometrical Factor of the Outward Side of the Sail . . . 259

C Derivation of the Latitudinal Factor 261
C.1 Geometry of the Problem . . . 261
C.2 Integral Formulation . . . 263
C.3 Analytical Evaluation . . . 264

D Derivation of the Albedo Phase Function 267
D.1 Geometry of the Problem . . . 267
D.2 Integral Formulation . . . 269
D.3 Analytical Evaluation . . . 270
D.3.1 Visible Surface Completely Illuminated . . . 270
D.3.2 Visible Surface Predominantly Illuminated . . . 271
D.3.3 Visible Surface Predominantly Dark . . . 273

List of Publications **311**

Curriculum Vitæ **313**

Acknowledgments **315**

SUMMARY

When sunlight illuminates an object in space, a faint pressure is exerted onto its surface. Although nearly imperceptible, this tiny pressure can generate a meaningful acceleration over the course of time, provided that the illuminated object is lightweight enough and has a large surface area exposed to radiation. This principle forms the foundation of solar sailing: a satellite propulsion method that takes advantage of thin, lightweight sails coated in highly reflective material and illuminated by sunlight to generate thrust.

While the idea of exploiting the "push" of solar radiation to travel the cosmos was first proposed by Johannes Kepler in the 1600s and then touched upon by other pioneers of solar sailing like Konstantin Tsiolkovsky and Friedrich Tsander at the beginning of the 20th century, the idea of using this propulsion method in real missions gained momentum only in the second half of the 20th century. Even then, the practical technological advancements required to build, launch, and deploy solar sails were achieved only relatively recently, around the turn of the new millennium. The solar-sail mission IKAROS launched by the Japan Aerospace Exploration Agency in 2010 became the first successful of its kind and, since then, several others have followed, with the primary aim to demonstrate the potential of solar sailing as a valid alternative to fuel-based propulsion systems. The primary motivation driving these technology demonstrations – and research on solar sailing as a whole – has been the mission-enabling potential that solar sailing holds, particularly thanks to its propellantless nature. Indeed, leveraging the infinite amount of energy provided by the Sun through sunlight, sailcraft may be able to travel across space for long periods of time, with an enhanced ability to maneuver at closer distances to the Sun.

Despite being suited for interplanetary missions and, particularly, for missions within the inner region of the Solar System, at the time of writing, solar sails have been launched mostly in low Earth orbit. The near-Earth environment has so far been viewed primarily as a testbed for demonstrating solar sailing, and only rarely as a region wherein solar sails could effectively be employed for Earth-bound mission applications. The reason underlying this view is the presence of different sources of perturbing accelerations in the near-Earth environment that are absent in interplanetary space, which render maneuvering and operational use of solar sails considerably more challenging. Notable examples of such accelerations include the aerodynamic acceleration caused by the interaction of the sailcraft with the atmosphere, as well as the planetary radiation pressure acceleration, which, similar to the acceleration produced by sunlight, arises by "Earthlight" coming from our planet and incident on the sail. Despite the above view, dedicated studies on the extent to which these accelerations actually perturb the motion and maneuverability of solar sails in proximity of the Earth have been conducted to a very preliminary, first-order extent. Similarly, and crucially, even less attention has been devoted to investigating whether these accelerations may be exploited to facilitate maneuvering, rather than viewing them as uncontrollable sources of perturbations.

The purpose of this dissertation is to challenge the aforementioned view of the near-Earth space as an unattractive region for solar sailing by characterizing the near-Earth dynamical environment, developing models of the governing accelerations, devising steering strategies to exploit these accelerations for maneuvering, and assessing the resulting maneuvering capabilities achievable by solar sails around the Earth. The characterization of the dynamics governing the motion of Earth-bound solar sails is performed by first determining the accelerations that dominate the dynamics and then reviewing the models available in the literature to represent said accelerations. In this way, the subsequent selection of the most appropriate acceleration models to employ in the investigation is performed. Furthermore, the discussion highlights the acceleration models that ought to be improved in their fidelity to accurately assess solar-sail maneuverability. Thereafter, motivated by the insights acquired, novel models for the planetary radiation pressure acceleration are formulated and presented, discussing their accuracy compared to state-of-the-art models. To further deepen understanding of the Earth-bound solar-sail dynamics, steering laws to facilitate the calibration of the solar-sail accelerations are also developed. By amplifying the in-orbit accelerations experienced by the sailcraft, these steering laws enable the calibration of said accelerations and highlight discrepancies between real and modeled dynamics, thereby providing a means to improve currently available solar-sail dynamical models. Finally, the acceleration models selected and developed are leveraged to devise steering-law optimization techniques which, in turn, enable optimal exploitation of the solar-sail accelerations to increase the orbital altitude and inclination. In this way, these steering laws are finally employed to assess how much sailcraft can maneuver in proximity of the Earth, considering broad ranges of orbital scenarios, sailcraft specifics, and characteristics of the near-Earth environment.

The results of the investigation highlight different important aspects concerning the dynamical modeling and maneuvering capabilities of Earth-orbiting sailcraft. The errors in the planetary radiation pressure acceleration arising from mismodeling of the Earth's radiative environment and the sail's optical properties can be reduced through the novel planetary radiation pressure acceleration models developed in this dissertation. Indeed, these models achieve a fidelity comparable to high-fidelity numerical models, with relative differences in the predicted maneuvering capabilities of solar sails consistently below 1%, while requiring approximately 30 times less computational effort. The developed models also highlight the significant effect planetary radiation pressure acceleration has on the sailcraft dynamics, as it can be even in the order of 30% of the solar radiation pressure acceleration in low Earth orbit. Accordingly, neglecting the planetary radiation pressure acceleration yields large errors in the predicted solar-sail maneuvering capabilities, which may differ by more than 50% from those obtained when accounting for this acceleration. Furthermore, actively exploiting this acceleration can increase maneuvering performance by up to 6% compared to the case in which planetary radiation pressure is considered but not leveraged for maneuvering. Planetary radiation pressure becomes increasingly exploitable at higher altitudes, as atmospheric density – and, therefore, aerodynamic drag – rapidly decrease. At altitudes below 650 km, on the other hand, the deorbiting effect induced by drag makes maneuvering highly challenging, if not completely unfeasible. Although less critically, eclipses also influence maneuverability by reducing the time solar radiation can be used as a source of thrust, thereby decreasing

the maneuvering capabilities by approximately 20-40% compared to non-eclipsing orbits. Importantly, the maneuverability of Earth-orbiting sailcraft scales approximately linearly with the acceleration capability of the sail. Therefore, the findings presented in this dissertation can be extended from present to futuristic sailcraft performance levels, thereby allowing to inform the design of both near-future and long-term Earth-bound solar-sail missions. Finally, analysis of the calibration capacity and ease of implementation of different calibration steering laws for NASA's ACS3 mission indicates that the calibration steering laws maintaining a fixed, Sun-facing orientation are preferable. These steering laws not only facilitate the calibration of the solar radiation pressure acceleration – which is of primary interest for solar sailing – but also ensure continuous power generation from the solar arrays and frequent communication with the ground stations, fulfilling two of the most critical operational requirements for Earth-bound solar-sail missions.

The investigation motivates further research directions and recommendations for future work. Given the large margins of uncertainty surrounding the near-Earth solar-sail dynamics, future work on the dynamical modeling and characterization of the maneuverability of Earth-orbiting sailcraft could be performed adopting a probabilistic approach. Accordingly, the development of solar-sail control laws could be pursued including information on the dynamics of probabilistic nature, building on the theory of robust optimal control. To reduce some of the aforementioned uncertainties, availability of data from real-life solar-sail missions is paramount. This data can be used both to refine existing acceleration models and, crucially, to assess the in-orbit thrust performance of solar sails. For this reason, using the calibration steering laws would be highly beneficial, and the inclusion of a dedicated calibration phase in the mission is recommended. Although the novel models for planetary radiation pressure acceleration presented in this dissertation have been developed to investigate Earth-bound solar sailing, these models may effectively be employed also for other purposes. Specifically, they could be used for the analysis and design of solar-sail missions in proximity of other celestial bodies, or be extended to enable analysis of the planetary radiation pressure acceleration exerted on satellites with more complex shapes than a flat sail. As the research conducted in this dissertation focuses exclusively on orbit-raising and inclination-changing maneuvers, future work may also explore other types of maneuvers to further broaden the investigation of Earth-bound solar-sail maneuverability. Among these, notable examples are near-Earth solar-sail orbital rendezvoused, as their successful execution would enable a range of applications, notably, in-orbit servicing and active debris removal. Finally, to bridge the gap between theoretical understanding and practical operational feasibility, the development of reliable, high-performance sailcraft attitude-control systems is paramount and, therefore, it should be prioritized to advance solar sailing toward operational readiness.

SAMENVATTING

Wanneer zonlicht een object verlicht, wordt er een zwakke druk op de oppervlakte uitgeoefend. Hoewel deze druk nagenoeg onmerkbaar is, kan deze in de ruimte een aanzienlijke versnelling genereren in de loop van de tijd, mits het verlichte object licht genoeg is en een grote oppervlakte heeft die aan de zonnestraling is blootgesteld. Dit principe vormt de basis van zonnezeilen: een methode voor satellietvoortstuwing die gebruikmaakt van dunne, lichtgewicht zeilen, bedekt met een sterk reflecterend materiaal en verlicht door zonlicht om stuwkracht te genereren.

Hoewel het idee om de “duwkracht” van zonnestraling te benutten om door de kosmos te reizen voor het eerst werd geopperd door Johannes Kepler in de 17e eeuw en vervolgens werd aangestipt door andere pioniers van zonnezeilen zoals Konstantin Tsiolkovsky en Friedrich Tsander aan het begin van de 20e eeuw, kreeg het idee om deze voortstuwingsmethode daadwerkelijk in missies te gebruiken pas in de tweede helft van de 20e eeuw echt momentum. Zelfs toen werden de praktische technologische vooruitgangen die nodig waren om zonnezeilen te bouwen, te lanceren en in te zetten pas relatief recent bereikt, rond de eeuwwisseling. De zonnezeilmissie IKAROS, gelanceerd door de Japan Aerospace Exploration Agency (JAXA) in 2010, was de eerste succesvolle in zijn soort en sindsdien zijn er verschillende andere geweest, met als primair doel het potentieel van zonnezeilen aan te tonen als een geldig alternatief voor op brandstof gebaseerde aandrijfsystemen. De belangrijkste drijfveer achter deze technologische demonstraties – en onderzoek naar zonnezeilen in het algemeen – is het missie-ondersteunende potentieel dat zonnezeilen biedt, met name dankzij het feit dat er geen brandstof nodig is. Door gebruik te maken van de oneindige hoeveelheid energie die de zon via zonlicht levert, zouden zeilvaartuigen in staat kunnen zijn om lange tijd door de ruimte te reizen, met een verbeterd vermogen om te manoeuvreren op kleinere afstand van de zon.

Ondanks dat zonnezeilen geschikt zijn voor interplanetaire missies en met name voor missies in het binnenste deel van het zonnestelsel, zijn ze op het moment van schrijven voornamelijk in een lage baan om de aarde (LEO) gelanceerd. De omgeving nabij de aarde werd tot nu toe vooral beschouwd als een testomgeving voor het demonstreren van zonnezeilen, en slechts zelden als een gebied waar zonnezeilen effectief ingezet zouden kunnen worden voor missies op aarde. De reden hiervoor is de aanwezigheid van verschillende bronnen van verstorende versnellingen in de omgeving nabij de aarde die afwezig zijn in de interplanetaire ruimte, waardoor manoeuvreren en operationeel gebruik van zonnezeilen aanzienlijk lastiger zijn. Opvallende voorbeelden van dergelijke versnellingen zijn de aerodynamische versnelling die wordt veroorzaakt door de interactie van het zeilvaartuig met de atmosfeer, evenals de versnelling door planetaire stralingsdruk, die, vergelijkbaar met de versnelling die door zonlicht wordt geproduceerd, ontstaat doordat äardlicht"van onze planeet op het zeil valt. Ondanks bovenstaande opvatting zijn er slechts zeer beperkte, eerste-orde studies verricht naar de mate waarin deze versnellingen daadwerkelijk de beweging en manoeuvreerbaarheid van zonnezeilen in

de nabijheid van de aarde beïnvloeden. Evenzo, en cruciaal, is er nog minder aandacht besteed aan de vraag of deze versnellingen kunnen worden benut om manoeuvreren te vergemakkelijken, in plaats van ze te beschouwen als oncontroleerbare bronnen van verstoring.

Het doel van dit proefschrift is om de bovengenoemde opvatting dat de ruimte nabij de aarde een onaantrekkelijk gebied is voor zonnezeilen te weerleggen door de dynamische omgeving nabij de aarde te karakteriseren, modellen te ontwikkelen van de bepalende versnellingen, stuurstrategieën te bedenken om deze versnellingen te benutten voor manoeuvreren, en de resulterende manoeuvreermogelijkheden van zonnezeilen rond de aarde te beoordelen. De karakterisering van de dynamiek die de beweging van zonnezeilen nabij de aarde bepaalt, wordt uitgevoerd door eerst de versnellingen te bepalen die de dynamiek domineren en vervolgens de in de literatuur beschikbare modellen te bekijken die deze versnellingen representeren. Op deze manier wordt de selectie van de meest geschikte versnellingsmodellen voor het onderzoek uitgevoerd. Verder belicht de discussie de versnellingsmodellen die verbeterd zouden moeten worden om de manoeuvreerbaarheid van zonnezeilen nauwkeurig te kunnen inschatten. Vervolgens worden, gemotiveerd door de verkregen inzichten, nieuwe modellen voor de versnelling door planetaire stralingsdruk geformuleerd en gepresenteerd, waarbij hun nauwkeurigheid wordt besproken in vergelijking met de huidige modellen. Om de kennis van de dynamiek van zonnezeilen op aarde verder te verdiepen, worden ook stuurwetten ontwikkeld die de kalibratie van de versnellingen van zonnezeilen vergemakkelijken. Door de versnellingen die het zeilschip in een baan om de aarde ondervindt te versterken, maken deze stuurwetten de kalibratie van de versnellingen mogelijk en brengen ze discrepanties tussen de werkelijke en gemodelleerde dynamiek aan het licht, waardoor een middel wordt geboden om de huidige dynamische modellen van zonnezeilen te verbeteren. Ten slotte worden de geselecteerde en ontwikkelde versnellingsmodellen gebruikt om optimalisatietechnieken voor stuurwetten te ontwikkelen. Deze technieken maken vervolgens een optimale benutting van de versnellingen van het zonnezeil mogelijk om de baan-hoogte en -inclinatie te verhogen. Op deze manier worden deze stuurwetten uiteindelijk gebruikt om de manoeuvreerbaarheid van ruimtevaartuigen in de buurt van de aarde te beoordelen, rekening houdend met een breed scala aan orbitale scenario's, specifieke kenmerken van het zeilvaartuig en eigenschappen van de nabije aardse omgeving.

De resultaten van het onderzoek belichten verschillende belangrijke aspecten met betrekking tot de dynamische modellering en manoeuvreermogelijkheden van een in een aardbaan draaiende zonnezeilvaartuigen. De fouten in de versnelling van de planetaire stralingsdruk, die voortkomen uit onjuiste modellering van de stralingsomgeving van de aarde en de optische eigenschappen van het zeil, kunnen worden gereduceerd door de nieuwe versnellingsmodellen voor planetaire stralingsdruk die in dit proefschrift zijn ontwikkeld. Deze modellen bereiken een nauwkeurigheid die vergelijkbaar is met zeer nauwkeurige numerieke modellen, met relatieve verschillen in de voorspelde manoeuvreermogelijkheden van zonnezeilen die consistent onder de 1% liggen, terwijl ze ongeveer 30 keer minder rekenkracht vereisen. De ontwikkelde modellen benadrukken ook het significante effect dat de versnelling door planetaire stralingsdruk heeft op de dynamiek van het zonnezeil, aangezien deze zelfs tot 30% van de versnelling door zonnestralingsdruk in een lage aardbaan kan bedragen. Het negeren van de versnelling door

planetaire stralingsdruk leidt dan ook tot grote fouten in de voorspelde manoeuvreermogelijkheden van het zonnezeil, die meer dan 50% kunnen afwijken van de resultaten die worden verkregen wanneer rekening wordt gehouden met deze versnelling. Bovendien kan het actief benutten van deze versnelling de manoeuvreerprestaties met maximaal 6% verbeteren ten opzichte van het geval waarin rekening wordt gehouden met planetaire stralingsdruk, maar deze niet wordt benut voor manoeuvreerdoeleinden. Planetaire stralingsdruk is steeds beter te benutten op grotere hoogten, omdat de atmosferische dichtheid – en daarmee de aerodynamische weerstand – snel afneemt. Op hoogten onder de 650 km maakt het deorbitatie-effect veroorzaakt door de weerstand manoeuvreren daarentegen zeer moeilijk, zo niet volledig onmogelijk. Hoewel minder cruciaal, beïnvloeden eclipsen ook de manoeuvreerbaarheid door de tijd te verkorten dat zonnestraling als stuwkrachtbron kan worden gebruikt, waardoor de manoeuvreermogelijkheden met ongeveer 20-40% afnemen in vergelijking met banen zonder eclips. Belangrijk is dat de manoeuvreerbaarheid van zeilschepen in een baan om de aarde ongeveer lineair schaalt met het acceleratievermogen van het zeil. Daarom kunnen de bevindingen in dit proefschrift worden uitgebreid van de huidige naar toekomstige prestatieniveaus van zeilschepen, waardoor ze van belang kunnen zijn voor het ontwerp van zowel nabije als lange termijn zonnezeilmissies op aarde. Ten slotte wijst een analyse van de kalibratiecapaciteit en de implementatiegemakkelijkheid van verschillende kalibratiestuurwetten voor NASA's ACS3-missie uit dat kalibratiestuurwetten die een vaste, naar de zon gerichte oriëntatie handhaven, de voorkeur verdienen. Deze stuurwetten vergemakkelijken niet alleen de kalibratie van de versnelling door de zonnestralingsdruk – wat van primair belang is voor zonnezeilen – maar zorgen ook voor continue energieopwekking door de zonnepanelen en frequente communicatie met de grondstations, waarmee wordt voldaan aan twee van de meest cruciale operationele vereisten voor zonnezeilmissies op aarde.

Het onderzoek geeft aanleiding tot verder onderzoek en aanbevelingen voor toekomstig werk. Gezien de grote onzekerheidsmarges rond de dynamiek van zonnezeilen in de buurt van de aarde, zou toekomstig onderzoek naar de dynamische modellering en karakterisering van de manoeuvreerbaarheid van zonnezeilvaartuigen in een baan om de aarde een probabilistische benadering moeten hanteren. Daarom zou de ontwikkeling van besturingswetten voor zonnezeilen kunnen worden voortgezet met informatie over de dynamiek van probabilistische aard, voortbouwend op de theorie van robuuste optimale besturing. Om een deel van de bovengenoemde onzekerheden te verminderen, is de beschikbaarheid van gegevens van daadwerkelijke zonnezeilmissies van cruciaal belang. Deze gegevens kunnen worden gebruikt om bestaande versnellingsmodellen te verfijnen en, belangrijker nog, om de stuwkrachtprestaties van zonnezeilen in een baan om de aarde te beoordelen. Om deze reden zou het gebruik van de kalibratiebesturingswetten zeer nuttig zijn en wordt de opname van een speciale kalibratiefase in de missie aanbevolen. Hoewel de nieuwe modellen voor planetaire stralingsdrukversnelling die in dit proefschrift worden gepresenteerd, zijn ontwikkeld om zonnezeilen in een baan om de aarde te onderzoeken, kunnen deze modellen ook effectief voor andere doeleinden worden gebruikt. Concreet zouden ze gebruikt kunnen worden voor de analyse en het ontwerp van zonnezeilmissies in de nabijheid van andere hemellichamen, of uitgebreid kunnen worden om de versnelling van de planetaire stralingsdruk te analyseren die wordt uitgeoefend op satellieten met complexere vormen dan een plat zeil. Aangezien het

onderzoek in dit proefschrift zich uitsluitend richt op manoeuvres die de orbitale hoogte en inclinatie veranderen, zou toekomstig onderzoek ook andere soorten manoeuvres kunnen verkennen om de studie naar de manoeuvreerbaarheid van zonnezeilen op aarde verder uit te breiden. Opvallende voorbeelden zijn rendezvous in een baan dicht bij de aarde, aangezien de succesvolle uitvoering ervan een reeks toepassingen voor zonnezeilen mogelijk zou maken, met name op het gebied van ruimteonderhoud en actieve verwijdering van ruimteafval. Ten slotte is de ontwikkeling van betrouwbare, hoogwaardige houdingsregelsystemen voor zonnezeilvaartuigen van cruciaal belang om de kloof tussen theoretisch begrip en praktische operationele haalbaarheid te overbruggen en moet dit daarom prioriteit krijgen om zonnezeilen operationeel gereed te maken.

ABBREVIATIONS

3U	3-unit
6U	6-unit
12U	12-unit
ACRIM	Active Cavity Radiometer Irradiance Monitors
ACS3	Advanced Composite Solar Sail System
ADCS	Attitude determination and control system
AE	Acceleration envelope
ANGARA	Analysis of Non-Gravitational Acceleration due to Radiation and Aerodynamics
ARP	Albedo radiation pressure
BBRP	Blackbody radiation pressure
CERES	Clouds and the Earth's Radiant Energy System
CFRP	Carbon-fiber-reinforced plastic
CHAMP	CHAllenging Minisatellite Payload
CLL	Cercignani-Lampis-Lord
CP1™	Colorless Polyimide 1
CSL	Calibration steering law
DLR	Deutsches Zentrum für Luft- und Raumfahrt
DRIA	Diffuse reflection with incomplete accommodation
DTM	Drag Temperature Model
ECEF	Earth-centered, Earth-fixed
ECI	Earth-centered inertial
EGM	Earth Gravitational Model
EoM	Equations of motion
ERBE	Earth Radiation Budget Experiment
ESA	European Space Agency
FD	Finite disk
GEO	Geostationary orbit
GMST	Greenwich mean sidereal time

GNSS	Global navigation satellite system
GOCE	Gravity field and steady-state Ocean Circulation Explorer
GRACE	Gravity Recovery And Climate Experiment
GSI	Gas-surface interaction
IDW	Inverse distance weighting
IKAROS	Interplanetary Kite-craft Accelerated by Radiation Of the Sun
ISS	International Space Station
JAXA	Japan Aerospace Exploration Agency
JB2008	Jacchia-Bowman 2008
JGM	Joint Gravity Model
KNMI	Koninklijk Nederlands Meteorologisch Instituut
LAGEOS	LAser GEOdynamics Satellite
LEO	Low Earth orbit
LTAN	Local time of the ascending node
MACHO	Memory-based Adaptive Coordinate-searcH Optimization
MISSE	Materials International Space Station Experiment
MSFC	Marshall Space Flight Center
MSIS	Mass Spectrometer and Incoherent Scatter
NASA	National Aeronautics and Space Administration
NEA	Near-Earth asteroid
NRTDM	Near Real-Time Density Model
PET	Polyethylene terephthalate
POINT	Pre-run Optimization and in-run INTerpolation
PPA	Planetary pitch angle
PRP	Planetary radiation pressure
RAAN	Right ascension of the ascending node
RMS	Root mean square
SMA	Semi-major axis
SRP	Solar radiation pressure
SSUJ	Solar Sail Union of Japan
TLE	Two-line element
TSI	Total solar irradiance
TU Delft	Technische Universiteit Delft / Delft University of Technology

U3P Union pour la Promotion de la Propulsion Photonique

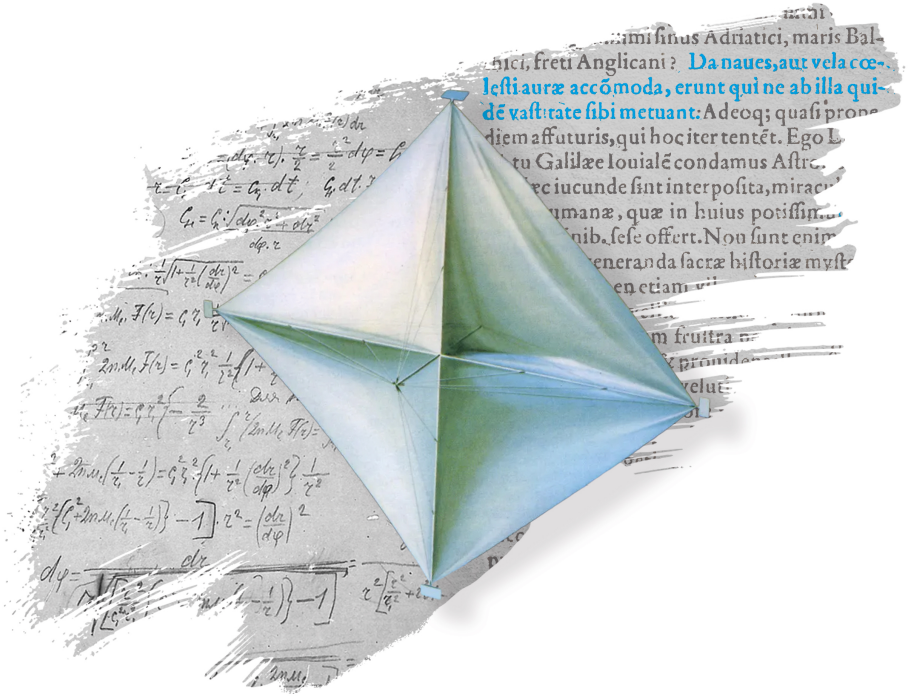
UHF Ultra-high frequency

UV Ultraviolet

WSF World Space Foundation

1

Introduction



ABSTRACT

Solar sailing is a propulsion system that makes use of large lightweight sails illuminated by sunlight to accelerate spacecraft through space. The acceleration is caused by the faint pressure exerted onto the sail by the incoming photons, which exchange momentum with the sail upon striking its highly reflective surface. As a result, this type of propulsion does not require propellant and gives spacecraft access to an inexhaustible source of energy: solar radiation. Thanks to this unique feature, solar sailing holds the potential to enable missions with much longer lifetimes than those allowed by conventional, fuel-based propulsion systems. Furthermore, as the thrust performance of a solar sail is strongly enhanced when reducing its distance from the Sun, sailcraft offer an increased flexibility in mission design particularly for – but not limited to – missions to the inner Solar System, potentially enabling mission applications unattainable to date.

Drawn by its prospects, the scientific community has been investigating solar sailing with increasing effort over the past decades. Starting from purely theoretical mission concepts, research and technological advancements have gradually increased the level of maturity of solar-sail technology, which now stands at the stage of technology demonstration. Although a number of sailcraft have been launched and successfully demonstrated the feasibility of the technology, further advancements are still required to reach the status of operationally mature propulsion system. Among the major challenges to be addressed are the need for accurate dynamical models and an improved understanding of sailcraft maneuvering capabilities, both of which are essential for the precise design of future solar-sail missions. These areas of research are particularly relevant for the design of missions around the Earth, which include the vast majority of those flown to date and planned for the near-future. Indeed, in proximity of the Earth, the motion of sailcraft is influenced by many sources of acceleration of complex, rapidly varying nature, which therefore complicate the accurate assessment of solar-sail maneuverability and render the design of Earth-bound missions particularly challenging. Despite their relevance, these fields of research stand mostly unexplored to this date, therefore motivating the research presented in this dissertation.

This chapter discusses the achieved advancements, current challenges, and gaps of knowledge characterizing solar-sail technology, providing context for the research presented in the remainder of the dissertation. First, a comprehensive overview of the history of solar sailing is provided, from its conceptual origins to the most recent mission successes. Next, the state of the art in solar sailing is reviewed, highlighting the current technology and operational readiness levels, and discussing advances in theoretical research, with a focus on solar-sail mission analysis and trajectory design. The discussion naturally leads to the main challenges characterizing solar sailing at present, and the experimental and research efforts required to overcome them. Finally, building on these challenges, the research questions addressed in this dissertation are outlined.

Cover graphic by Vincenzo Bortone. The illustration shows (from left to right): an excerpt from unpublished notes by Konstantin E. Tsiolkovsky [1], wherein the use of solar radiation pressure as a practical method for spacecraft propulsion was proposed; an artistic illustration of the square solar-sail concept for NASA's Comet Halley rendezvous mission [2]; and an excerpt from Johannes Kepler's letter to Galileo Galilei "Dissertatio cum Nuncio Sidereo" [3], containing the famous passage (translated) "*Provide ships or sails adapted to the heavenly breezes, and there will be some who will brave even that void.*"

1.1. HERITAGE

This section outlines the historical development of solar sailing, from early concepts to recent mission successes. This historical context prepares the ground for the next sections, which discuss the current readiness level of the technology, recent research advances, and open challenges.

1.1.1. CHASING THE HEAVENLY BREEZES

In the early 1600s, Johannes Kepler published his renowned "Astronomiæ Pars Optica" [4], a book that marked the first systematic investigation of the properties of light and their use in explaining astronomical phenomena [5]. In his work, Kepler was the first to notice that "*the beard of comets always are spread on the side opposite the Sun*"[1], exhibiting a peculiar curvature. Unable to find a sound explanation for his observations, he finally stated that "*if one cannot be found, this phenomenon must be left among the mysteries of nature.*"[2] Many centuries after Kepler wrote those words, we know that that "mystery of nature" was in fact the effect of solar radiation pressure acting on a comet's dust tail, making the work by Kepler the earliest known documented observation of this phenomenon.

While it took centuries to theoretically and experimentally demonstrate the existence of radiation pressure, the idea that (solar) radiation could exert a force when shining over the surface of a body arose to Kepler soon after publishing "Astronomiæ Pars Optica". Indeed, fascinated by his unexplained finding, Kepler dedicated himself to observing comets between approximately 1607 to 1615, eventually publishing his results in the collection of books "De Cometis Libelli Tres" [6]. It was during this time that he first speculated about the existence of radiation pressure, even envisioning ways of exploiting it for cosmic exploration. This led to his famous letter "Dissertatio cum Nuncio Sidereo", written in 1610 to Galileo Galilei [3], where Kepler wrote "*Provide ships or sails adapted to the heavenly breezes, and there will be some who will brave even that void.*"[3]

Kepler's ideas pointed in the right direction. Yet, they were unsupported by any mathematical theory or experimental evidence. The first to move a step towards a mathematical explanation of radiation pressure was Euler, in 1746. Building on Kepler's astronomical observations, the work by d'Alembert on the wave theory [7], and his own belief that light could propagate as a wave, Euler mathematically demonstrated that any longitudinal wave impinging on a surface would produce a force in the direction of propagation [8]. Shortly thereafter, De Mairan and Du Fay became the first to attempt an experimental demonstration of the existence of radiation pressure. To this aim, they independently conducted a number of tests in 1754 and 1756, respectively, which, however, proved unsuccessful [9–11]. In the decades that followed, different physicists embarked on the same experimental challenge, most notably, Bennet in 1789 and Fresnel in 1825 [10, 12–14], but once again, their efforts proved inconclusive.

The next step forward in understanding the nature of radiation pressure came only in 1873, thanks to the theory of electromagnetism developed by James Clark Maxwell [15]. He was the first to theoretically prove that light propagates as a wave – as hypothesized

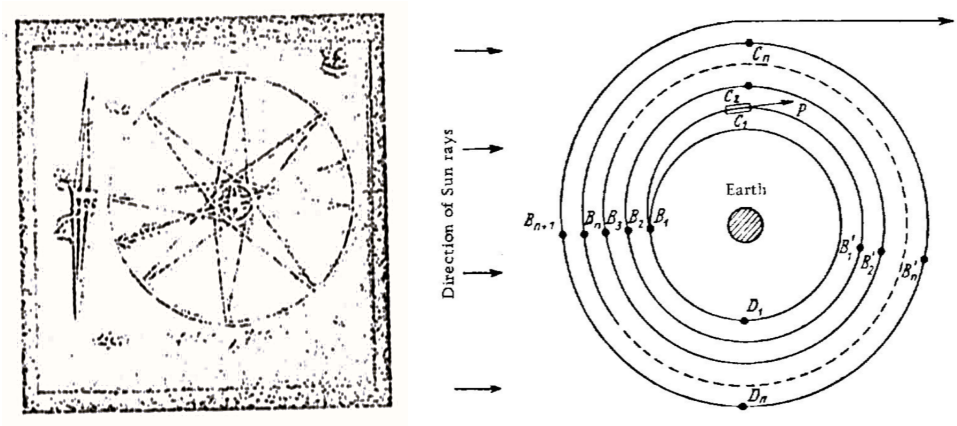
[1] Original text: "*Deprehenso, cometarum barbas semper in plagam à Sole contraria spargi nisi Soli oppositi.*"
[2] Original text: "*Alia curvitatis huius occasio quaerenda est, aut si nequit inveniri, reliquendum hoc phaenomenon inter arcana Naturæ.*"
[3] Original text: "*Da naves aut vela coelesti aurae accommoda, erunt qui ne ab illa quidem vastitate sibi metuant.*"

by Euler – and carries momentum which is transferred to an object upon impact with its surface, thereby resulting in a tiny pressure. Almost at the same time and independently from Maxwell, Bartoli also theoretically proved the existence of radiation pressure, in 1876. Unlike Maxwell, however, he reached this conclusion building on the second law of thermodynamics [16].

The studies of those years on radiation pressure – culminated in Maxwell and Bertoli's results – gave rise to renewed interest in the subject, both in the scientific community and the general public. It is no coincidence that, in 1865, Jules Verne wrote "De la Terre à la Lune" [17], becoming the first to dream of ships sailing through space pushed by sunlight – an idea closely resembling what we would now describe as solar sailing. Similarly, in 1889, Le Faure and de Graffigny envisioned the concept of solar reflectors in their series of science fiction novels "Les Aventures Extraordinaires d'un Savant Russe" [18], wherein reflecting dishes were used to direct sunlight towards space ships in order to propel them. Alongside science fiction, the second half of the 19th century was also characterized by an increasing number of theoretical studies conducted by other physicists of Maxwell and Bertoli's time, most importantly, Boltzmann, Galitzine, Guillaume, Heaviside, Fitzgerald, Lebedew, and Hull [10]. At the same time, this period also witnessed several efforts to experimentally detect radiation pressure. Of note is the experiment by Crooks in 1873, who incorrectly thought he observed radiation pressure while studying the radiometric effect [19]. While his theory got tested and disproved soon after by Arthur Schuster in 1876 and Osborne Reynolds in 1879 [10, 20, 21], it prompted other physicists to take on the experimental challenge. This led to the experiments by Zöllner, who "scored a near miss" [22], and Lebedew, who became the first to successfully confirm the theoretical findings by Maxwell and Bertoli, in 1899 [23, 24]. Finally, the results by Lebedew got further verified and were improved in accuracy by Nichols and Hull [10], who managed to reach a discrepancy of only approximately 10% between experimental and the theoretical (expected) results [25]. For further information on radiometry and related experiments conducted in those years, the reader is referred to the extensive bibliography given in Ref. [26].

1.1.2. SOLAR RADIATION AS A SOURCE OF THRUST

Building on Maxwell's theory of electromagnetism and the insight from experimental radiometry, the practical use of radiation as source of thrust was conceived at the beginning of the 20th century. The first to propose the idea in relation to spaceflight was Tsiolkovsky. In his unpublished notes from 1921 [1], he presented a number of propulsion methods that he thought could, one day, be used for propelling spacecraft through space, including "the pressure of light rays". Despite his vision, his successive research efforts focused mostly on conventional chemical engines, culminating in his well-known theory of rocketry still in use in modern days [27]. Drawing on the works of Tsiolkovsky, his colleague Friedrich Tsander investigated the feasibility of radiation-based propulsion from an engineering perspective, introducing a precursor to the modern concept of a solar sail [28]. In particular, conscious of the very minor intensity of radiation pressure, he proposed to use "tremendous mirrors of very thin sheets to utilize the pressure of sunlight to attain cosmic velocities" [2, 29]. In his studies of 1924 [30], Tsander investigated the material, thickness, and size of these mirrored sheets, the achievable magnitude of the ra-



(a) (b)

Figure 1.1: Illustrations taken from the works by Tsander of a) the design of a "spaceship with mirrors" [29], and b) the trajectory of a spacecraft leveraging radiation pressure for orbit raising [30].

diation pressure exerted onto them, the orbital changes radiation pressure would enable, and the flight times for different types of transfers. Sketches from his works are shown in Fig. 1.1. Inspired by the works of Tsiolkovsky and Tsander, some years later authors like Haldane, Bernal, and Stapledon also pictured the use of sailcraft to travel within and out of the Solar System [31–33], even suggesting that a sail could tack near the Sun to perform a solar photonic assist [32]. Nevertheless, these works were more conceptual than mathematical in nature, and therefore carried limited scientific value.

Further advances in solar sailing research came only decades later, in the 1950s, primarily thanks to the contributions by Carl Wiley and Richard Garwin. In his short story "Clipper Ships of Space" of 1951 [34], Wiley described possible sailcraft designs, approaches to build solar sails, and strategies to perform orbit raising, also considering the technical aspects of those challenges, to some extent. His work bears historical significance for its optimistic view of solar sailing – which Wiley considered more advantageous than rocket propulsion – as well as for anticipating later technical work in the field [2]. In 1958, Garwin coined the term "solar sailing" in the first known scientific article published on the topic [35], where he addressed the challenges presented by Wiley with a greater technical depth [2]. Indeed, Garwin discussed the main aspects affecting sailcraft performance (sail area, mass, reflectivity, and distance from the Sun), the challenges related to sail deployment, and torques generated by radiation pressure. Furthermore, he provided preliminary analyses on sailcraft maneuverability, considering both Earth-bound and interplanetary mission scenarios. Similar to Wiley, he concluded that solar sailing "*is perhaps more powerful than many competing schemes*", that is, chemical engines [35].

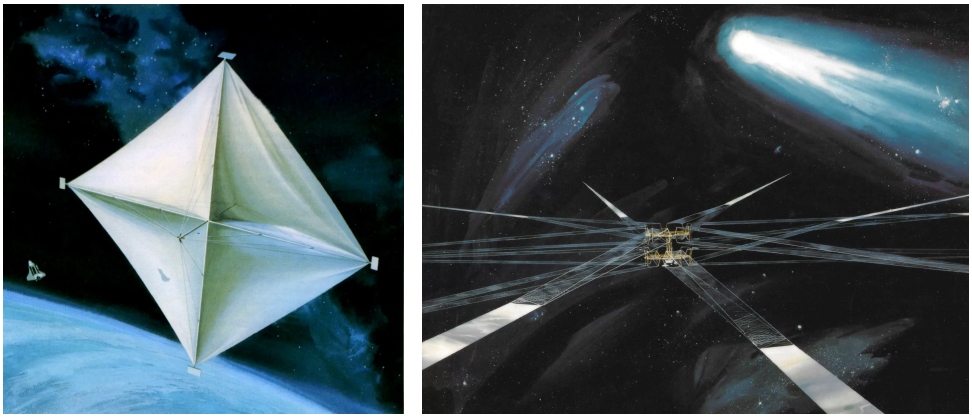
In the years that followed, the space race between the USA and USSR caused space research to focus mainly on rocketry [36]. Nevertheless, studies on solar-sail mission analysis, trajectory design, and optimization began to emerge, increasingly highlighting the potential benefits of solar sailing over conventional chemical propulsion, particularly

for interplanetary missions and even interstellar exploration, where sustained propulsion over prolonged periods is especially advantageous [37–50].

1.1.3. FIRST SOLAR-SAIL CONCEPTS

The research on solar sailing conducted up to the late 1960s often assumed the use of large sailcraft without accounting for limitations that could preclude their practical use, e.g., those related to manufacturing, stowing, and deploying sails, maintaining structural rigidity, and maneuvering under the effect of perturbations. The first studies covering these aspects and laying out detailed engineering designs emerged in the late 1960s and early 1970 [51–55]. Of particular importance were the works by MacNeal and Hedgepath [56–59], who introduced the heliogyro – an innovative solar-sail concept that gained considerable attention in the years that followed and is described later in this section. In 1974, the National Aeronautics and Space Administration (NASA) became the first space agency to fund a feasibility study to assess the potential of solar sailing for real-life mission scenarios. The research was led by Jerome Wright and produced promising results [60], thus encouraging NASA to investigate the topic further [61]. During this second phase of the investigation, Wright identified a trajectory that would allow a sailcraft to rendezvous with Halley's Comet in 1986, at its perihelion [62]. Such a mission would have required a time of flight of only four years – a significantly shorter time compared to the seven to eight years required by solar-electric ion propulsion. Therefore, encouraged by this finding, NASA formally initiated the design study of a Comet Halley rendezvous mission using solar sailing in 1976. Initial efforts focused on an 800x800 m^2 square solar sail. However, because of the high risks posed by the sail deployment, this option was discarded as early as 1977. In its place, MacNeal and Hedgepath's heliogyro was considered as a more viable alternative, owing to its simple deployment mechanism. Indeed, the proposed heliogyro design featured twelve sail strips – each 8-meter wide and 7.5-kilometer long – which could be unrolled from the satellite bus simply by spinning. To support this design, analyses of the heliogyro's structural dynamics and control were conducted, and candidate sail materials were manufactured and tested [59, 63]. Despite these efforts, eventually also the heliogyro mission concept was abandoned because of the high technological risks involved with it. Finally, the investigation turned to the use of solar-electric propulsion – an option that had been investigated in parallel to the solar-sail concepts. However, also this option was soon discarded due to the rapidly increasing cost estimates of such a mission [2, 64]. Artistic illustrations of the square solar-sail and heliogyro concept designs studied for the Comet Halley rendezvous mission are presented in Figure 1.2.

The Comet Halley rendezvous mission brought worldwide attention to solar sailing. This, in turn, led to an increasing number of solar-sail initiatives and studies. Between 1981 and 1982, a solar-sail race to the Moon was proposed by the World Space Foundation (WSF), the Union pour la Promotion de la Propulsion Photonique (U3P), and the Solar Sail Union of Japan (SSUJ) [36, 65–67]. Similarly, the US Columbus Quincentennial Jubilee commission proposed a solar-sail race to Mars in 1992 [2, 68, 69]. Those years were also characterized by significant advancements in solar-sail theory, design, and development. As discussed in Ref. [36], this progress resulted in the publication of the first treatises on solar sailing, most notably, Refs. [70–73].



(a) (b)

Figure 1.2: Artistic illustrations of the a) square solar-sail and b) heliogyro concepts for NASA's Comet Halley rendezvous mission [2].

1.1.4. REAL-LIFE SOLAR SAILING

During the 1990s and 2000s, research focused on experimentally validating solar sailing, leading to the first real-life demonstrations of the technology, presented hereinafter. Note that the ground tests and launched missions discussed in this section are also summarized in Tables 1.1 and 1.2, in order to support the technology status overview of solar sailing provided later in Section 1.2.1.

The year 1992 saw the launch of Znamya 2: a Russian satellite featuring a 20-meter wide solar reflector deployed through spin motion, similarly to the heliogyro. Although technically not a solar sail, this mission marked the first successful deployment of a reflective, thin film in orbit, hence validating the feasibility of deploying sails in space [74].

The years that followed were characterized by ground tests, primarily conducted by the Deutsches Zentrum für Luft- und Raumfahrt (DLR) – the German Aerospace Center – and NASA. Following a collaborative system study with NASA and the European Space Agency (ESA), DLR manufactured and deployed a 20x20 m^2 square solar sail in 1999. The ground test validated both the structural integrity and deployment functionality of ultra-lightweight Carbon-Fiber-Reinforced Plastic (CFRP) booms, thereby demonstrating the feasibility of the square solar-sail design [75, 76]. In 2005, NASA too started a project to build and deploy a 20x20 m^2 sail system on ground [77]. The project led to two independent designs developed by the companies ATK and L'Garde Inc.: the former proposed a sailcraft structure featuring coilable masts [78–82], whereas the latter relied on inflatable boom technology [83–87].

Around the same time as NASA's ground tests, The Planetary Society attempted the first orbital launch of a solar sail with their Cosmos 1 mission [88]. The sailcraft comprised eight 15-meter-long triangular sails to be deployed by spinning and, similar to the design by L'Garde Inc., it should have used inflatable booms as sail support. However, the sailcraft failed to reach orbit due to a malfunction (and subsequent explosion) of its Volna launcher only 82 s after launch [88]. With the failure of Cosmos 1, the first sailcraft to

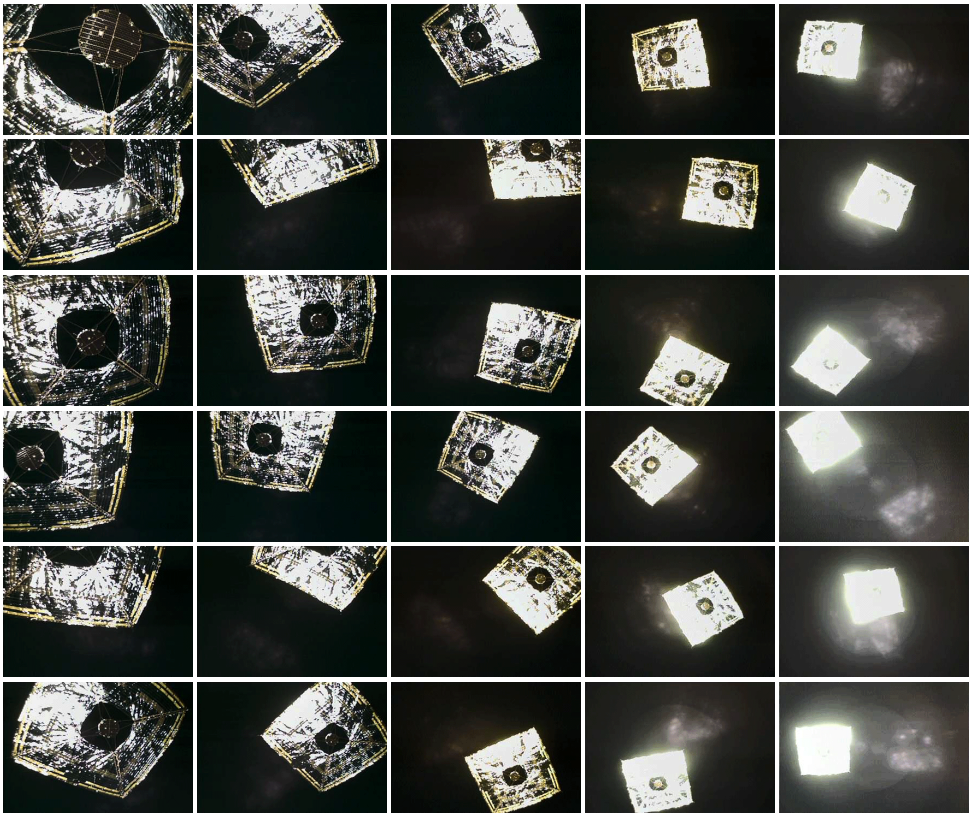


Figure 1.3: Photographs of IKAROS taken by one of its ejectable cameras after deployment [92, 93]. The photographs are arranged in chronological order from top to bottom in each column and moving left to right across columns.

successfully reach orbit, deploy its sail, and demonstrate solar-sail technology became IKAROS (Interplanetary Kite-craft Accelerated by Radiation Of the Sun), launched by the Japan Aerospace Exploration Agency (JAXA) in 2010 [89, 90]. The sailcraft had a total mass of 310 kg and featured a square sail with a side length of 14 m, deployed through spin motion. Unlike any other solar-sail mission that followed, IKAROS managed to perform solar sailing over several months in interplanetary space, demonstrating the presence of solar radiation pressure (SRP) acceleration and the feasibility of SRP-based attitude control [91]. Figure 1.3 shows multiple photographs of IKAROS with its sail deployed in deep space [92].

The IKAROS mission became a major milestone for solar-sail technology, stimulating further research and the development of new missions. In 2009, DLR launched the Gossamer Roadmap project in collaboration with ESA, with the objective to send three solar-sail demonstrators – namely, Gossamer-1, 2, and 3 – into orbit between 2013 and 2015 [94]. To test the scalability of solar sails, an incremental approach was used: Gossamer-1, 2 and 3 were designed to feature sails of 5, 20, and 50 m^2, respectively, and

be used for increasingly longer missions, either in low Earth orbit (LEO) (Gossamer-1 and 2) or interplanetary space (Gossamer 3). Although discontinued in the early 2010s during the Gossamer-1 development phase, the project led to extensive ground testing, resulting in an increased mechanical understanding of the sailcraft structure and deployment sequence [95–98].

The first fully developed solar sailcraft by NASA also came in those years with their NanoSail-D project [99, 100]. Following the loss of the sailcraft in 2008 due to a launcher failure, its ground spare, NanoSail-D2, successfully reached orbit and deployed in early 2011, unfurling its 10 m^2 sail. The sailcraft reentered the atmosphere after 240 days of operation, demonstrating the feasibility of solar- and drag-sail technology for CubeSats in LEO [101–103].

After NanoSail-D2, NASA began exploring the use of much larger solar sails through the Sunjammer mission in 2013, following an incremental approach similar to DLR's Gossamer Roadmap. Named after the popular 1964 story by Arthur C. Clarke [104], Sunjammer was supposed to feature the largest solar sail ever developed to date, with a surface area of 1208 m^2 and a total sailcraft mass of only 32 kg, corresponding to excellent thrust performance [105, 106]. The project provided large amounts of ground-test data but, unfortunately, was discontinued in 2014 due to key integration issues, increased schedule risk, and the inability of the contractor (L'Garde Inc.) to meet delivery requirements [107].

After their Cosmos 1 failure in 2005, The Planetary Society achieved success with the LightSail 1 and 2 CubeSat missions, launched in 2015 and 2019, respectively [108–110]. While LightSail 1 served as a brief LEO orbit test to validate the sail packaging and deployment mechanism used later on by LightSail 2, LightSail 2 achieved a much more ambitious goal: demonstrating controlled solar-sail maneuvering in LEO for the first time. To this end, the sailcraft performed orbit raising through its 32 m^2 sail over an extended period of time (approximately three years and a half), before reentering the atmosphere [111]. Notably, however, the mission also highlighted the detrimental impact of large uncertainties in sailcraft attitude knowledge and control, which strongly limited the orbit-raising capabilities. Indeed, these uncertainties posed major operational challenges that only allowed the sailcraft to perform rudimentary on-off steering, hindering the execution of more optimal maneuvers [111]. Figure 1.4 shows LightSail 2 during its sail deployment sequence [112, 113].

Another CubeSat solar-sail mission design was CubeSail, designed by the Surrey Space Center and planned for launch in 2015 [114]. With its 25 m^2 sail, the sailcraft aimed to demonstrate solar sailing and drag sailing in LEO by performing inclination-changing and orbit-lowering (deorbit) maneuvers, respectively. Despite completing the mission design, sailcraft design and ground-deployment testing phases, the mission has never been launched nor officially discontinued [114]. Nevertheless, the knowledge and technological advancement achieved through the CubeSail mission supported the development of later gossamer-sail projects at the University of Surrey, most notably the DeorbitSail drag-sail mission [115–117].

Sharing the same name as Surrey Space Center's mission, the CubeSail mission by the University of Illinois and CU Aerospace was launched in 2018 and was meant to serve as a low-cost demonstrator for the UltraSail mission concept developed by the same team [118,

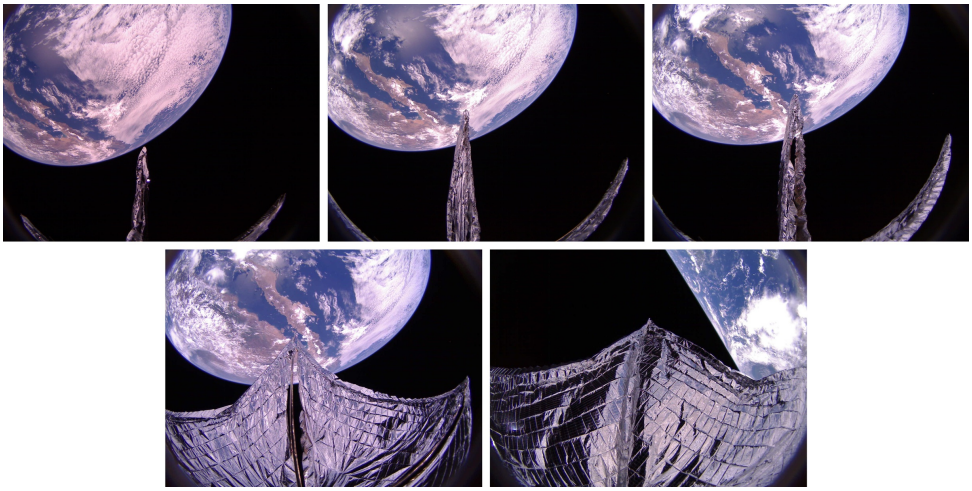


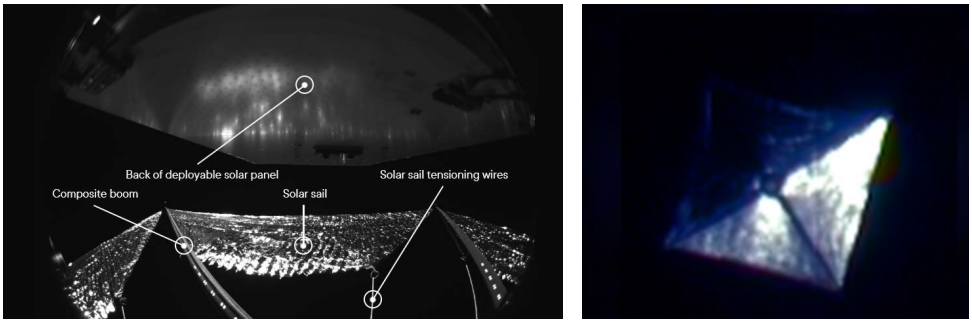
Figure 1.4: Photographs showing the sail deployment sequence of LightSail 2, taken from its central bus [112, 113]. The photographs are arranged in chronological order from left to right and top to bottom.

119]. CubeSail considered two identical CubeSats designed to deploy a 250-meter-long sail blade between them [120]. Nevertheless, communication issues caused the mission to fail prematurely, even before sail deployment.

A similar fate was faced by NASA's NEA (Near-Earth Asteroid) Scout mission, launched in 2022 [121, 122]. The 6-unit (6U) interplanetary CubeSat was supposed to deploy a solar sail of 83 m^2 to fly by the asteroid 2020 GE and demonstrate the feasibility of solar-sail enabled, low-cost reconnaissance of asteroids [123]. However, contact with the satellite could never be established and the mission failed soon after launch.

Among the most recent solar-sail missions is Gama Alpha, developed by the company Gama and launched in January 2023 [124, 125]. As many other missions, Gama Alpha was a CubeSat solar-sail technology demonstrator orbiting in LEO whose primary objective was to test the deployment and control of the sailcraft. However, soon after orbit insertion, technical issues related to the release of the sailcraft's actuators prevented it from deploying the sail, causing the mission to fail [126].

Finally, the most recent successful solar-sail mission is the Advanced Composite Solar Sail System (ACS3), developed by NASA and launched in April 2024. The mission's primary objectives were to demonstrate in-orbit deployment of its sail and characterize the sailcraft composite-boom technology, thereby increasing NASA's technology readiness level in the field [127, 128]. By deploying its 80 m^2 solar sail in late August 2024 and downlinking data on the sailcraft structural integrity and shape over the course of more than a year, ACS3 fulfilled both objectives, resulting in mission success [129]. In addition to the above, a secondary objective of ACS3 was to demonstrate active sailcraft control in LEO [129]. To accomplish this, the mission is planned to implement so-called calibration steering laws, that is, attitude control laws designed to facilitate the estimation of parameters governing the sailcraft accelerations. These steering laws were devised within the framework of this dissertation and are the result of a long-standing collaboration between NASA and Delft



(a) (b)

Figure 1.5: Photographs of a) one of ACS3's deployed sail quadrants, taken from the central bus [129, 130], and b) the entire sailcraft, taken by Maxar's WorldView-2 satellite [129]; credits to Maxar.

University of Technology (TU Delft). In light of their particular relevance to this work, ACS3 and the calibration steering laws will be discussed separately and in greater depth in Chapter 5. Figure 1.5 shows photographs of ACS3 taken after sail deployment from its central bus and by Maxar's WorldView-2 satellite [129, 130].

1.2. STATE OF THE ART

Section 1.1 discussed the historical progress in solar sailing, from scientific discoveries and mission concepts to ground tests and flown missions. Building on that timeline, the present section aims to provide an overview of the technology readiness level of solar sailing and delineate the direction of technological advancement, particularly in relation to sailcraft design, performance, and mission objectives. Furthermore, an overview of the theoretical research conducted thus far on solar-sail mission design is also presented. In this way, the state of the art and future prospects of the technology will be discussed, paving the way to the introduction of the research objectives of this dissertation, presented in Section 1.4.

1.2.1. TECHNOLOGY STATUS OVERVIEW

Tables 1.1 and 1.2 provide relevant information and specifics of all sailcraft presented in Section 1.1.4 that have flown and were ground tested to date. In this way – by disregarding theoretical mission concepts – the discussion will focus solely on advancements demonstrated in real-life applications.

To this date, solar sailing has always only been pursued in the context of technology demonstration, in order to assess its practical feasibility as propulsion system. The reason for this lies in the inherent challenges characterizing solar sailing that have not yet been fully resolved, which primarily stem from the strong dependence of the propulsion capabilities on the mass, sail area, structural integrity, and attitude control capabilities of the sailcraft. Consequently, in order for the technology to achieve operational maturity, the need for large sails made of lightweight – yet durable – materials that can be folded into small volumes, deployed in orbit, and effectively oriented in space arises. As research

Table 1.1: Information on solar-sail ground tests and launched missions to date. White, red, and green rows indicate ground tests, failed missions, and successful missions, respectively. Data taken from Refs. [131] (demonstration goals) and Refs. [76, 77, 90, 97, 100, 105, 109, 110, 120, 123, 125–127, 132, 133] (orbital regimes, bus types, and sail shapes).

Year	Project	Demonstration objective	LEO	Cubesat	Sail shape
1999	DLR/ESA Gr. Test	Ground deploy	–	✗	Square
2005	ATK Gr. Test	Ground deploy	–	✗	Square
2005	L'Garde Gr. Test	Ground deploy	–	✗	Square
2005	Cosmos 1	Active maneuvering	✓	✗	Windmill
2008	NanoSail-D	Deploy & deorbit	✓	3U	Square
2009	Gossamer-1	Ground deploy	–	✗	Square
2010	IKAROS	Attitude control	✗	✗	Square (spin)
2010	NanoSail-D2	Deploy & deorbit	✓	3U	Square
2013	Sunjammer	Ground deploy	–	✗	Square
2015	CubeSail (UK)	Active maneuvering	✓	3U	Square
2015	LightSail 1	Deploy	✓	3U	Square
2018	CubeSail (USA)	Deploy	✓	2x1.5U	Single blade
2019	LightSail 2	Active maneuvering	✓	3U	Square
2022	NEA Scout	Active maneuvering	✗	6U	Square
2023	Gama Alpha	Attitude control	✓	6U	Square (spin)
2024	ACS3	Deploy	✓	12U	Square

Note: ✓ indicates that the sailcraft was launched in LEO.
✗ indicates that the sailcraft was not launched in LEO, or that it is not a CubeSat.

in this field has progressed, boom-deployed square sailcraft have been identified as the optimal design option compared to its competitor designs. These designs include the heliogyro (which has never been adopted in real-life missions), the spin-deployed square sail (used by IKAROS and Gama Alpha), and the non-square boom-deployed sail (only used by Cosmos 1), see Table 1.1. Compared to these competitor designs, boom-deployable square sailcraft allow for easier ground testing while providing increased structural integrity and attitude control capabilities. However, they also involve more elaborate sail folding, stowing, and deployment procedures. This holds especially true for CubeSat satellites, which have become increasingly favored over large satellite buses over the last decades, see again Table 1.1. To address these challenges, a number of ground tests and solar-sail missions have been carried out over the years to characterize sail deployment. Given the limited technology readiness level, the majority of these

Table 1.2: Specifics of sailcraft employed in ground tests and launched missions to date. White, red, and green rows indicate ground tests, failed missions, and successful missions, respectively. Data taken from Refs. [76, 131, 134–136] (sail areas, sailcraft masses, and loading parameters), Refs. [75, 77, 80, 86, 90, 99, 105, 109, 110, 120, 125–127, 133, 137–139] (boom materials), and Refs. [76, 97, 100, 109, 110, 118, 127, 132, 133, 136, 139–142] (sail materials).

Year	Project	m [kg]	A [m^2]	σ [g/m^2]	Materials	
					Booms	Sail†
1999	DLR/ESA Gr. Test	28.9*	330.4	87.5*	CFRP	(various‡)
2005	ATK Gr. Test	44.8	400	112	Composite	CP1+Al
2005	L'Garde Gr. Test	11.4*	380.25	30*	Composite	Mylar+Al+Cr
2005	Cosmos 1	100	600	167	Plastic	Mylar+Al
2008	NanoSail-D	4	10	400	Elgiloy alloy	CP1+Al
2009	Gossamer-1	24	25	960	CFRP	Upilex-S+Al+Al
2010	IKAROS	310	196	1582	–	ISAS-TPI
2010	NanoSail-D2	4	10	400	Elgiloy alloy	CP1+Al
2013	Sunjammer	45	1200	38	Composite	Kapton+Al+Cr
2015	CubeSail (UK)	3	25	120	Be+Cu alloy	Kapton+Al+Al
2015	LightSail 1	5	32	156	Elgiloy alloy	Mylar+Al
2018	CubeSail (USA)	3	20	150	–	Mylar+Al
2019	LightSail 2	5	32	156	Elgiloy alloy	Mylar+Al
2022	NEA Scout	14	86	163	Elgiloy alloy	CP1+Al
2023	Gama Alpha	11	73	151	–	(not available)
2024	ACS3	16	80	200	CFRP	PEN+Al+Cr

Note: * Value considers only the sail assembly (no payload).
† Materials of the sail film + front coating (if present) + back coating (if present).
‡ Different combinations of polymer films and coatings were tested, namely, Mylar+Al, Kapton+Al+Al and PEN+Al+Al.

missions have been launched into Earth orbit, and only a subset of them have managed to successfully deploy their sail. Similarly, many sailcraft missions aiming at even more ambitious objectives – such as demonstrating feasibility of SRP-based attitude control and maneuvering – have failed, with the notable exceptions of IKAROS and LightSail 2.

Through ground testing and missions, advancements in solar-sail material technology have also been achieved. As shown in Table 1.2, while the first ground tests and missions considered a variety of materials for the sailcraft booms – ranging from plastics and metals to composites and polymers – subsequent missions have often employed metal alloys, particularly because of their structural strength which allows for more reliable deployments. In recent times, ACS3 has managed to demonstrate the practical feasibility of booms made of CFRP – a material that allows to stow and deploy larger sails, is more

lightweight, and less prone to thermal warping than metal alloys. These characteristics, in turn, allow to reduce the sailcraft moments of inertia, thus facilitating attitude control.

Solar sails have been built using a variety of sail films, particularly polyimide polymers (Kapton®, CP1™, Upilex-S®, and ISAS-TPI) and polyethylene polymers (Mylar® and PEN). Mylar® has often been employed as it is commercially available, strong, lightweight, and allows to be easily coated with reflective material (e.g., aluminum). However, it is not ideal for long-term use in space because of its low thermal stability and tendency to degrade under ultraviolet (UV) radiation [143]. Polyimide polymers, on the other hand, are characterized by a greater UV resistance and ability to withstand high temperatures, with Kapton being the most tensile resistant and NASA's Colorless Polyimide 1 (CP1™) having the best thermal properties [143, 144]. Notably, a range of materials have also been employed as sail coatings. While the front side of solar sails are usually coated with aluminum to ensure a high reflectivity, the back sides are either left uncoated or are coated in chromium, which enhances emissivity and, therefore, thermal control [2].

The use of different bus sizes, sail architectures, and materials has resulted in flown and tested sailcraft attaining sail areas, A, that span a wide range. In particular, while large-bus sailcraft could deploy sails extending over hundreds of meters squared, more recently flown 6U and 3-unit (3U) CubeSat sailcraft mounted sails with areas in the range of 73-86 m^2 and 10-32 m^2, respectively. This considerable reduction in sail area, however, has allowed for a substantial decrease in the complexity of the deployment subsystems and sailcraft mass, m, which is of 11-16 kg and 3-5 kg, again for 6U and 3U CubeSats, respectively. Appearing in Table 1.2 is also the sail loading parameter, σ, which represents the ratio of the sailcraft total mass (considering payload and sail assembly, unless otherwise stated) to the sail surface area. This parameter provides a measure of the sailcraft thrust performance, with smaller values indicating a better performance. As can be seen, among the successfully flown sailcraft, the ones attaining the best performance are the most recent CubeSat missions, with loading parameters in the range of $120 - 200$ g/m^2. Also, it is of note that larger sailcraft like Sunjammer may be able to achieve better performances by relying on the use of enormous sails. However, such designs have so far only been ground-tested and their employability in orbit is still to be demonstrated.

1.2.2. DIRECTION OF TECHNOLOGICAL PROGRESS

The way in which sailcraft characteristics have changed over time follows from a shift in development philosophy that has taken place, particularly over the last 10 to 15 years. As initial ground tests and missions involved the development of large-scale, high-complexity sailcraft, they exposed the considerable design and operational challenges posed by such sailcraft. Therefore, ambitions have scaled back over the last 10 to 15 years and a more gradual approach has been adopted to advance the readiness level of solar-sail technology. At present, missions aim to demonstrate the technology primarily through CubeSat sailcraft flown in LEO, whereas scaling the technology to larger sailcraft and enable more ambitious goals has become a longer-term objective.

The recognition of the challenges characterizing solar sailing and its effect on sailcraft development and research can be visually appreciated in Fig. 1.6. The figure shows the time progression of the sail area, A, and sailcraft loading parameter, σ, not only for the

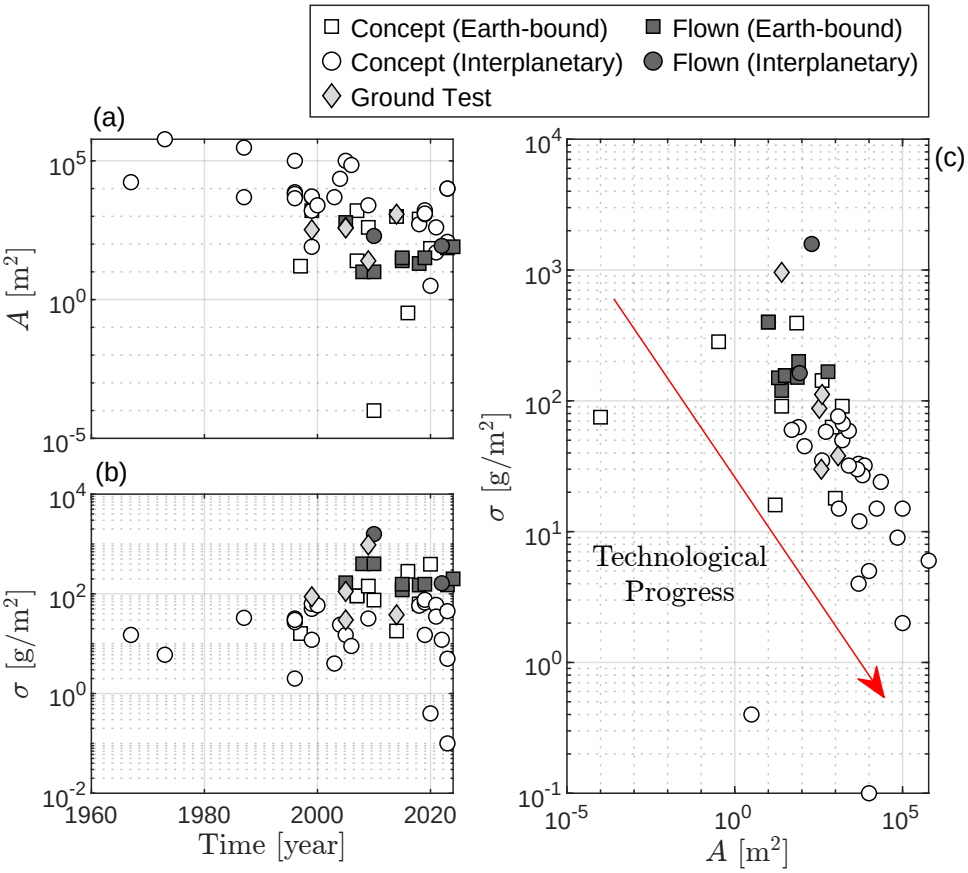


Figure 1.6: Sailcraft mass-to-area ratio – i.e., the loading parameter – and sail area of all solar-sail mission concepts and flown missions to date. Data taken from Ref. [131].

ground tests and flown missions discussed earlier in this section, but also for all missions conceptualized to date, taken from Ref. [131]. As can be seen in Figs. 1.6a and 1.6b, sail areas and loading parameters have been gradually decreasing and increasing over time, respectively, with the solar-sail missions flown thus far exhibiting some of the smallest and largest values of A and σ, respectively. This trend reflects the transition from idealistic, high-performance sailcraft to more realistic, limited-performance sailcraft. The graphs also show that, as the size and performance of the sailcraft considered decreased, the complexity and ambition of the mission scenarios considered also changed, gradually moving from only interplanetary scenarios to increasingly more Earth-bound scenarios. The correlation between sailcraft performance and applicable mission scenario can be even better appreciated in Fig. 1.6c, which shows the sail area and loading parameter plotted against each other. The graph highlights that the current state of solar-sail technology allows for missions primarily in proximity of the Earth. On the other hand, to enable interplanetary mission applications, scaling the technology and being able to

operate much larger, better-performing sails becomes a paramount requirement. This required change in sailcraft performance therefore identifies the direction of long-term technological progress, shown in Fig. 1.6c.

1.2.3. RESEARCH STATUS OVERVIEW

Alongside the advances achieved in solar-sail hardware and operational maturity through ground testing and real-life missions, extensive theoretical research on solar-sail mission analysis, trajectory design and optimization has been carried out over the past decades. The studies conducted, mission applications considered, and yet unexplored fields of research are briefly outlined hereinafter [107, 145, 146].

The majority of research on solar sailing has explored its use for interplanetary missions. Because radiation intensity – and therefore thrust performance – rapidly increase closer to the Sun, several studies have focused on trajectory optimization for missions to the inner Solar System. Such missions range from multi-planet tour and planetary sample-return missions [147–151] to more ambitious concepts like NASA's Solar Polar Imager mission [147, 152, 153], which envisioned a solar-sail transfer to a small-radius, high-inclination orbit over the ecliptic that would otherwise be unreachable using conventional propulsion. The idea of exploiting the large SRP available at close distance to the Sun for high-energy maneuvering has also been investigated in relation to solar-sail trajectories to the outer Solar System and beyond [154–160]. By spiraling towards the Sun, so-called solar photonic assists can be performed, allowing sailcraft to rapidly increase their orbital energy and escape the Sun's gravitational pull without the need for gravity assists. Solar sails also enable a range of non-Keplerian orbits, including pole-sitter orbits for continuous observation of planetary poles [161–163], displaced orbits for space-weather monitoring [164–166], and (quasi-)periodic orbits at artificial Sun-Earth libration points [167–172]. Furthermore, different works on the trajectory design for flybys and rendezvous missions to asteroids and comets have been carried out [173–179], particularly in recent years following the momentum created by the NEA Scout mission.

Closer to Earth, solar sailing has also been explored for missions in the cislunar environment. A number of studies have investigated the design of (quasi-)periodic orbits around the Earth-Moon libration points [180–184], as well as low-energy transfers between such orbits [185–187]. In addition, research has been conducted on the mission analysis and trajectory design for lunar observation missions [187–189], with a focus on the coverage of the Moon's poles [190–195]. Within the research on Earth-centered solar-sail applications, studies have primarily focused on the design of geocentric non-Keplerian orbits, including pole-sitter orbits [161, 196–198], displaced geocentric halo orbits [199], and highly elliptical, precessing orbits, as the one considered in the GeoSail mission concept to allow for prolonged observation times in the Earth's magnetotail [200, 201]. Furthermore, other works have explored the potential of solar sails for Earth escape [202–204], LEO-to-GEO transfers [205, 206], LEO-to-LEO transfers [207, 208], and station-keeping and debris removal in GEO [209–211].

The research outlined above addresses mission scenarios wherein the solar-sail dynamics are characterized only by SRP and gravitational accelerations. In close proximity to Earth, on the other hand, sailcraft are also subject to accelerations specific to the near-Earth environment – most notably, atmospheric drag, and the Earth's planetary

radiation pressure (PRP) acceleration – which render LEO solar-sail dynamics much more involved. While the use of solar sails for deorbiting has received particular attention thanks to its application for active debris removal [117, 212–217], only few studies on (non-deorbiting) solar-sail trajectory design have been conducted [218–221]. Similarly, the dynamics and trajectory design of solar sails under the influence of PRP have been explored only to a limited, preliminary extent [222, 223]. It is important to note that, in addition to its scarcity, the literature on Earth-bound solar sailing typically makes use of idealistic dynamical models. Indeed, sails are often approximated as flat, perfectly reflecting mirrors, thus neglecting the deformation, optical properties, and material degradation of the sail over time. At the same time, the studies that include the PRP or aerodynamic accelerations in the dynamics model these accelerations assuming perfect knowledge of the near-Earth radiative and aerodynamic environments. In reality, however, knowledge of these environments is limited and characterized by large margins of uncertainty that are seldom accounted for.

While the simplistic approach underlying the above dynamical models allows to greatly reduce complexity, it also limits the extent to which results obtained with such models can inform the design of real-life solar-sail missions. Indeed, research findings are characterized by a limited degree of fidelity that reduces their practical applicability, especially for mission applications requiring precise orbit control and maneuvering, such as active debris removal, in-orbit servicing, Earth observation, and formation-flying applications. Furthermore, relying on idealistic models also hinders the in-orbit estimation of the parameters governing the solar-sail accelerations [224], which forms an essential step to further develop understanding of the Earth-bound solar-sail dynamics.

The relatively small body of knowledge available on solar sailing in LEO reflects the long-standing view that this propulsion system is primarily suited to interplanetary and deep-space missions. Among the primary reasons underlying this view is the fact that, compared to deep space, sailcraft in LEO are governed by far more complex dynamics and, crucially, they are strongly affected by atmospheric drag. This force induces rapid orbital decay unless actively counteracted, and because any failure to do so can yield a premature end of life, the operational risks involved are inherently high. Therefore, deep-space solar sailing has always been deemed a more attractive and seemingly attainable objective than Earth-bound solar sailing. Nevertheless, the vast majority of solar-sail technology demonstrators – and, notably, all but one of those successful, see Table 1.1 – have been launched in Earth orbit. Furthermore, and crucially, Lightsail 2 successfully demonstrated orbit raising despite the presence of non-negligible aerodynamic drag, thus challenging the notion that the LEO region is unsuited for solar sailing [111].

The value of solar sails in LEO lies in their potential for mission applications that are impractical – or poorly suited – for conventional chemical thrusters. Specifically, the propellantless nature of solar sailing makes it particularly attractive for long-duration missions and for applications requiring continuous maneuvering. Among such applications, a notable one is multiple-target active debris removal. Assuming sufficient technological maturity and thrust performance, a single solar sail could deorbit multiple pieces of space debris in sequence. To this end, the sailcraft would perform a rendezvous to capture a piece of debris, lower the debris object's orbital altitude to induce atmospheric reentry, and then target the next piece of debris, allowing to repeat the sequence several times.

This approach therefore represents a paradigm shift from conventional missions constrained by finite propellant budgets, which restrict the number of debris objects that can be deorbited. Importantly, the same rationale applies to on-orbit servicing, where a solar sail could be used to rendezvous multiple target satellites sequentially. The continuous thrust provided by solar sails could also be leveraged for station-keeping operations and, in formation-flying missions, for continuous control of the along-track inter-satellite separation [131, 225]. Similarly, their continuous thrust make solar sails also suited for applications involving the gradual reshaping of the orbit, including scientific missions requiring to maintain a precise (repeated) ground track. When considering large-scale applications, solar sails could also be employed as orbital solar reflectors, that is, large mirrors redirecting sunlight to the dark hemisphere of the Earth, in order to lower terrestrial power demand or enable space-to-Earth power transmission [226–228]. In addition, it is of note that solar sails offer important advantages from the perspective of space sustainability. Indeed, while chemical propulsion requires part of the propellant budget to be reserved for end-of-life disposal, a solar sail can be reoriented into a maximum-drag configuration, effectively acting as a drag sail and enabling rapid deorbiting. This, in turn, provides greater flexibility in complying with end-of-life disposal requirements.

The LEO solar-sail applications described above require the ability to maneuver precisely and reliably. As discussed in the next section, fulfilling these requirements represents one of the most crucial challenges to render Earth-bound solar sailing practically viable.

1.3. FUTURE CHALLENGES

The previous section has highlighted that, to this date, solar-sail technology is still in its demonstration stage. Although in-orbit sail deployment remains among the most crucial phases of any solar-sail mission, its feasibility has been demonstrated multiple times. The next major milestone to achieve operational readiness is therefore demonstrating effective and reliable maneuvering. While LightSail 2 has made an important step in this direction by successfully performing orbit raising, this capability needs to be consolidated before solar-sail technology can advance from the demonstration stage to active employment in scientific and commercial missions.

It is also of note that, over the last two decades, a gradual shift in solar-sail design philosophy and testing has taken place, as evidenced in Fig. 1.6. This shift has led to Earth-bound solar sails of limited size and performance being increasingly favored over large, ambitious sailcraft for interplanetary applications. Consequently, most sailcraft missions launched to date have orbited in LEO. Nevertheless, the majority of research on solar-sail mission design has primarily focused on interplanetary applications, considering high-performance, futuristic sailcraft. Furthermore, the few studies investigating solar sailing in proximity of the Earth have been characterized by a limited knowledge of the solar-sail dynamics, often represented using overly simplistic models of the sailcraft, the near-Earth dynamical environment, and their interaction. This incomplete knowledge, in turn, hinders understanding of the maneuvering capabilities of sailcraft orbiting the Earth and, along with it, the ability to accurately design future Earth-bound missions.

The above considerations highlight a clear gap of knowledge in near-Earth sailcraft maneuverability from two complementary angles: operational readiness and theoretical

modeling of the solar-sail dynamics. To narrow this gap, progress may be pursued through sailcraft hardware and theoretical developments, respectively.

Hardware development should focus on further improving attitude-control systems, in order to achieve full and reliable sailcraft controllability. Due to their short orbital period, Earth-orbiting sailcraft require rapid changes of attitude to maneuver. Furthermore, such maneuvers ought to be executed far more frequently than for interplanetary sailcraft and throughout the mission lifetime, both to perform orbital transfers and to maintain orbital stability in the face of the perturbed near-Earth dynamical environment. In view of these reasons, the research and development of systems to control sailcraft accurately and reliably becomes particularly challenging and, at the same time, especially critical for Earth-bound applications more than interplanetary ones. Furthermore, adding to the problem's complexity is also the fact that miniaturized systems should be considered, in agreement with the increasingly preferred use of CubeSats over large buses.

Parallel to hardware development, high-fidelity modeling of the near-Earth solar-sail dynamics and subsequent investigation of the maneuvering capabilities of Earth-orbiting sailcraft should be conducted. Specifically, the dominant accelerations governing the near-Earth solar-sail dynamics should first be identified. Then, high-fidelity dynamical models for the selected accelerations should be developed, when necessary, giving priority to those accelerations for which currently available models only attain a limited fidelity. Finally, building on these improved dynamical models, the maneuverability of solar sails in proximity of the Earth should be characterized with the purpose of informing the design of a wide range of future Earth-bound solar-sail missions. To this end, a systematic investigation should therefore be conducted considering a broad variety of orbital scenarios, sailcraft characteristics spanning current to long-term performance levels, and varying conditions of the near-Earth environment.

Motivated by the considerations discussed in this section, this dissertation pursues the theoretical investigation outlined above into the dynamics and maneuvering capabilities of Earth-bound solar sails. The corresponding research questions structuring the research are detailed in the following section.

1.4. RESEARCH QUESTIONS

The objective of this dissertation is to characterize the maneuvering capabilities of solar sails in the near-Earth environment to a high degree of fidelity, thereby allowing to accurately inform the design of future solar-sail missions. Accordingly, the central research question addressed in this dissertation is:

What are the maneuvering capabilities of present-day and future solar sailcraft within the near-Earth dynamical environment?

Answering this question requires a range of subproblems to be addressed, corresponding to the research subquestions presented hereinafter.

First, the accelerations underlying the solar-sail dynamics in proximity of the Earth should be identified and accurately characterized. Because these accelerations may be represented with different degrees of fidelity, a preliminary assessment should be conducted to determine the most significant accelerations and appropriate models to describe them. Subsequently, the increases in model fidelity that are required to enable

accurate analysis of sailcraft maneuvering capabilities should be identified and implemented. The research subquestions accompanying this investigation are the following:

1. *How do the different accelerations characterizing the near-Earth environment contribute to the overall acceleration experienced by solar sails around the Earth?*

2. *How accurately do solar-sail acceleration models of varying fidelity describe the dynamics of Earth-bound solar sails?*

3. *Among existing solar-sail acceleration models, which are the least mature and require further development to support practical Earth-bound mission planning?*

4. *What higher-fidelity solar-sail acceleration models can be developed from the existing state of the art, and how do they improve upon available models?*

To answer these subquestions, Chapter 2 provides an overview of the accelerations underlying the dynamics of Earth-bound solar sails, including discussion on the nature and characteristic magnitudes of these accelerations, and a review of the acceleration models available in the literature. In this way, the chapter motivates the selection of the dynamical models adopted in the remainder of the dissertation. Furthermore, it highlights the need for the research presented in Chapters 3 and 4, wherein new models for the PRP acceleration for perfectly reflecting and optical solar sails are presented, respectively, and Chapter 5, which introduces the calibration steering laws used to enable in-orbit estimation of the solar-sail accelerations.

Building on the insights acquired from subquestions 1 to 4, the correlation between solar-sail accelerations, their perturbing effects, and potential for enhancing sailcraft maneuverability can be investigated. This objective is formalized through the following research subquestion:

5. *To what extent can accelerations specific to Earth-bound solar sails hinder or enhance the in-plane and out-of-plane maneuvering capabilities of sailcraft?*

This subquestion is addressed through a series of parametric analyses discussed in Chapters 3, 4, 6, and 7. To assess sailcraft maneuvering capabilities in a systematic manner, the analyses investigate in-plane and out-of-plane maneuverability separately by considering orbit-raising and inclination-changing control laws, respectively. Furthermore, the analyses differ in the types of accelerations considered, in the fidelity of their models, and in whether these accelerations are treated as controllable or uncontrollable accelerations. In this way, the benefit of leveraging these accelerations for maneuvering and, conversely, their detrimental effect when they are neglected, are clearly quantified. In particular, after presenting the PRP acceleration model for perfectly reflecting solar sails in Chapter 3, the model is used to assess the perturbing effect of uncontrolled PRP acceleration on Earth-bound solar sails. The analyses in Chapter 4 employ the PRP acceleration model for optical solar sails to more accurately characterize the perturbing effects of PRP acceleration. Finally, sailcraft maneuverability under the effect of controlled aerodynamic accelerations is explored in Chapter 6, whereas the combined effects of controlled aerodynamic and PRP accelerations are investigated in Chapter 7.

In addition to investigating how maneuvering capabilities relate to individual accelerations, it is also necessary to investigate how they vary across the near-Earth environment and with sailcraft performance. The former aspect is particularly important as it allows to fully characterize sailcraft maneuverability in its "phase space" around the Earth, that is, for virtually any Earth-bound orbital configuration. On the other hand, exploring the change in maneuvering capabilities with sailcraft performance allows to extend the insights obtained to inform the design not only of current, but also future Earth-bound solar-sail missions. The subquestions corresponding to these research needs are the following:

6. *How do solar-sail in-plane and out-of-plane maneuvering capabilities vary across the near-Earth environment?*

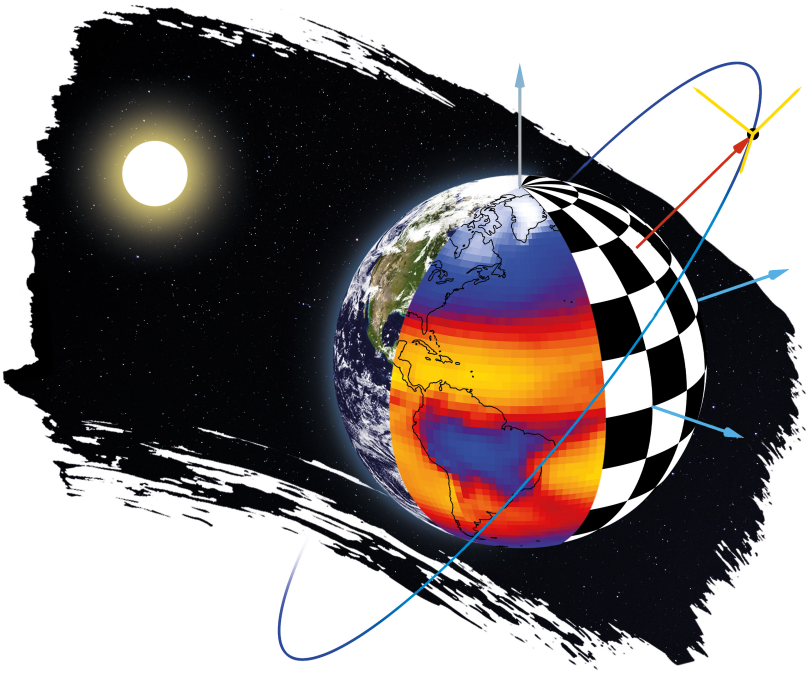
7. *How do solar-sail in-plane and out-of-plane maneuvering capabilities change with increasing sailcraft performance, from present-day to future levels?*

These subquestions will be addressed through the parametric analyses in Chapters 6 and 7, with the analyses in Chapter 7 offering greater depth by considering a wider variety of orbital configurations and a broader range of sailcraft performances.

Building on the research discussed in Chapters 2 through 7, Chapter 8 will finally present the conclusions of the work, formally answering the above research (sub-) questions, and providing recommendations for future research and developments in Earth-bound solar sailing.

2

Mathematical Framework



ABSTRACT

Solar sails orbit the Earth governed by several accelerations arising from the interaction of the sailcraft with the near-Earth environment. To describe this interaction, several models may be used, which differ in the ways the sailcraft and the near-Earth environment are represented, as well as their complexity and degree of fidelity. Consequently, the problem of selecting the models that are best suited for the investigation at hand arises. Similarly, the maneuvering capabilities of sailcraft may be assessed through a variety of control strategies, therefore rendering their selection paramount.

The aim of this chapter is to perform the above selections, thereby laying the foundation for the research conducted in the remainder of the dissertation. Establishing the most appropriate dynamical model to adopt requires a sequential approach. First, the orbital configurations that are of greatest interest for the investigation will be determined. In this way, the corresponding orbital regime of interest will be identified and, along with it, the accelerations that dominate the solar-sail dynamics in said regime. Thereafter, an overview of the models available in the literature to describe the sailcraft, the near-Earth environment, and their interaction will be presented. The proposed literature review will examine the fidelity of these models and the uncertainties characterizing them. On this basis, it will guide the subsequent selection of the acceleration models employed throughout the dissertation and identify where modeling fidelity may be improved to accurately assess solar-sail maneuverability. Finally, a review of the trajectory optimization methods most widely used in the literature will be provided, in order to lay out the trajectory optimization framework employed in the reminder of the dissertation to assess the maneuvering capabilities of sailcraft.

Cover graphic by Vincenzo Bortone. The illustration shows an Earth-orbiting satellite, reference frames used to describe its motion, and models to represent the Earth.

2.1. ORBITAL CONFIGURATIONS OF INTEREST

In order to comprehensively investigate the maneuverability of solar sails around the Earth, an extensive range of orbits spanning different altitudes, eccentricities and orientations ought to be considered. However, by assessing which orbits are of most interest for Earth-bound applications, and the insight these orbits would provide into near-Earth sailcraft maneuverability, a reduced set of orbital configurations can be considered. In this way, the investigation can be facilitated while retaining scientific relevance and applicability to future missions.

The near-Earth environment hosts a large number of satellites used for a variety of applications, from Earth observation and communication, to global navigation and positioning. The vast majority of these satellites reside in three regions, namely, the geostationary orbit (GEO) belt at an altitude of approximately 35800 km, the Global Navigation Satellite System (GNSS) region covering the altitude range between 19000 and 23000 km, and the low Earth orbit (LEO) region, corresponding to altitudes below 2000 km. The investigation discussed in the remainder of this dissertation will focus solely on the LEO region for two reasons. First, as mentioned in Section 1.3, most solar-sail missions launched to date have flown in LEO and, given the limited technology readiness level, this region is expected to be the target also of near-future solar-sail missions. Second, over 93%[1] of all currently active satellites around the Earth orbit in LEO. This highlights the significant relevance of this region for scientific and commercial applications, and, potentially in the longer term, also for solar sails.

To identify the orbital configurations that are most commonly considered in LEO and that, therefore, are particularly worth investigating, an analysis of the distributions of the orbital elements of LEO satellites was conducted. To this end, data from the CelesTrak database [229] was retrieved on December 1, 2025, and only active satellites were considered, that is, satellites that are either operational, partially operational, in spare, or standby mode. It should also be noted that the Starlink and OneWeb constellations have been factored out from the analysis, as they strongly skewed the distributions. Indeed, of the 13817 active satellites currently in orbit around the Earth (of which 12954 in LEO), these constellations alone account for 9685 satellites. Furthermore, the satellites of these constellations – which have all been launched from 2019 to present – fly in very specific altitude and inclination bands, thus hindering clear analysis of the distribution of the orbital elements for identifying different orbital configurations of interest.

Figure 2.1 displays the distributions of the altitude, h, inclination, i, and eccentricity, e, of active satellites in LEO. As can be observed in Fig. 2.1a, most satellites are found at altitudes below 1600 km, with a high density in the range 400-800 km, and a lesser presence in the range 800-1200 km and in proximity of 1500 km. The inclination distribution in Fig. 2.1b shows an even more skewed profile, with the vast majority of satellites having Sun-synchronous inclinations slightly below 100 deg, followed by inclinations of approximately 50 deg, and values in between. Figure 2.1c highlights that most satellites fly in almost-circular orbits, with eccentricities usually well below 0.003, corresponding to a difference in perigee and apogee radii of less than 50 km, but most often below 15 km. Finally, as a complementary view to the one-dimensional distributions in Figs. 2.1a

[1] 79% when disregarding the Starlink and OneWeb satellites.

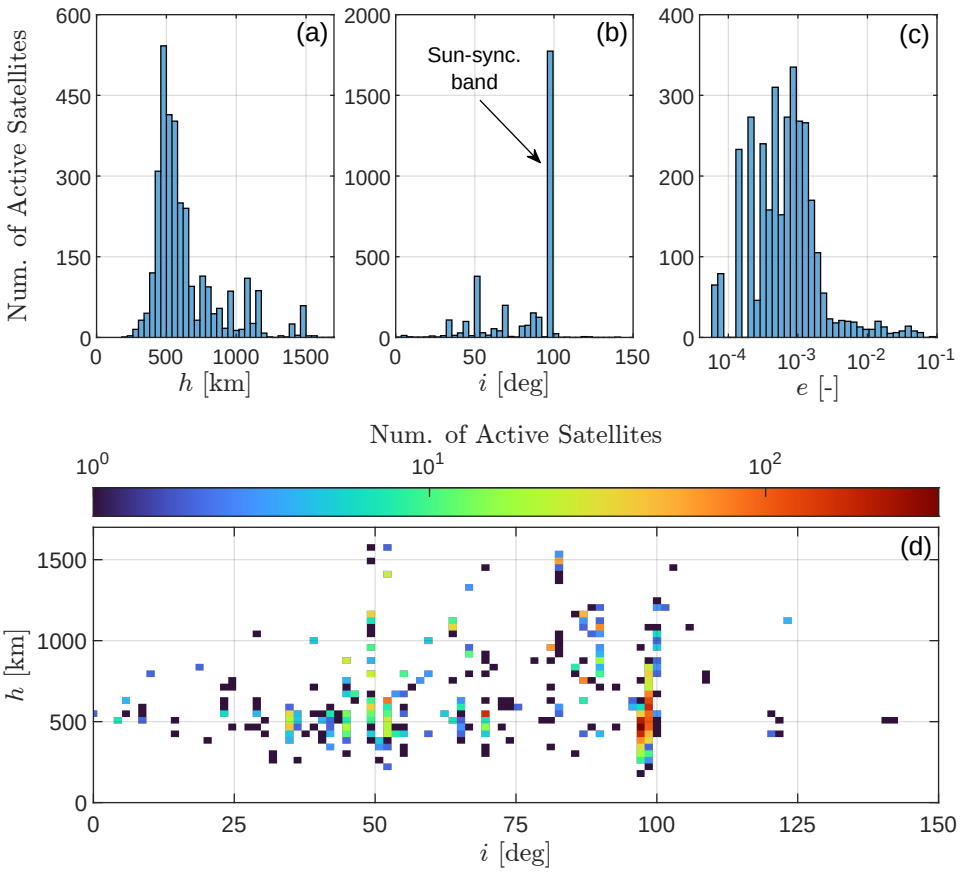


Figure 2.1: Distributions of the a) altitudes, b) inclinations, c) eccentricities, and d) altitudes and inclinations of all active satellites in LEO as of Dec 1, 2025. Note that the data disregards the Starlink and OneWeb constellations.

and 2.1b, Fig. 2.1d displays the two-dimensional distribution of altitude and inclination. The graph highlights the high-density region for $i \in [95, 100]$ deg and $h \in [400, 800]$ km, which hosts more than half of the entire population of LEO satellites.

To set up the investigation pursued in this dissertation, it is important not only to assess the most useful types of orbit for LEO mission applications, but also which of these orbital configurations are the most interesting to explore specifically for solar sailing. Sun-synchronous orbits are possibly the most attractive type of orbit to investigate. The reason for this stems from the fact that, by definition, these orbits gradually precess over time, maintaining a relatively stable orientation with respect to the Earth and Sun. This allows the amount of solar radiation reaching the sailcraft to remain stable as well, and the sailcraft control and ability to modify the orbit to be less dependent on the time of the year. Consequently, Sun-synchronous orbits are often the preferred choice in the design of solar-sail missions and should be given particular attention in the investigation. Another class of orbits deemed of particular relevance are those at altitudes below 1000 km. This

is commonly considered the upper limit of the thermosphere below which aerodynamics influence the motion of satellites. Furthermore, in this region, other accelerations affect the sailcraft dynamics in a significant manner, most notably, the planetary radiation pressure (PRP) acceleration. For this reason, at such low altitudes, retaining sailcraft controllability becomes much more critical to determine the feasibility of solar-sail missions than at higher altitudes. In view of this and the limited body of knowledge on solar sailing in this altitude range, investigating sailcraft maneuvering capabilities at these altitudes is deemed of paramount importance.

Based on the above considerations, discussion in the remainder of this dissertation will primarily focus on circular orbits, with altitudes of at most 1000 km. Sun-synchronous orbital inclinations will serve as baseline in the majority of analyses, whereas inclinations between 0 deg and the Sun-synchronous values will be considered only in a number of analyses to explore sailcraft maneuverability at lower inclinations. Finally, right ascensions of the ascending node (RAANs) will be considered taking values across the entire 360-degree span. In this way, it will be possible to study solar-sail maneuverability for orbits with different orientations with respect to the direction of sunlight, and therefore subject to different illumination conditions and presence or absence of eclipses.

2.2. ACCELERATIONS OF INTEREST

To accurately assess the maneuvering capabilities of sailcraft, it is crucial to identify the accelerations that most significantly affect the near-Earth solar-sail dynamics, as well as the nature and intensity of the orbital perturbations they induce. To this aim, this section presents the accelerations acting on the sailcraft and, for each of them, determines whether they should be accounted for in the investigation, based on their magnitude and effects on the orbit. Also, note that the mathematical description of the selected acceleration models will be provided in Section 2.5.

2.2.1. GRAVITATIONAL ACCELERATIONS

The main acceleration experienced by satellites in LEO is the central gravitational acceleration of the Earth, which allows spacecraft to remain Earth-bound. However, spacecraft are also affected by other gravitational accelerations with a smaller – but nonetheless significant – magnitude. These are discussed in the following.

2.2.1.1. NON-SPHERICAL GRAVITY OF THE EARTH

The Earth's gravity field is not exactly spherically symmetrical, but exhibits irregularities resulting from the non-spherical shape and uneven mass distribution of the Earth. These irregularities are commonly modeled using the theory of spherical harmonics, which allow to break down the gravity field into a (theoretically infinite, but in practice truncated) series of spherical-harmonic functions of different degree, n, and order, m, with $n \geq 2$ and $0 \leq m \leq n$. Each of these functions allow to represent the gravity field component of uneven mass distributions along lines of latitude, lines of longitude, or both. The corresponding spherical harmonics are referred to as zonal ($n \neq 0,\ m = 0$), sectorial ($n = m \neq 0$), and tesseral ($n \neq m \neq 0$) harmonics, see Fig. 2.2. In terms of notation, the multiplicative coefficients associated to the spherical harmonics are commonly denoted

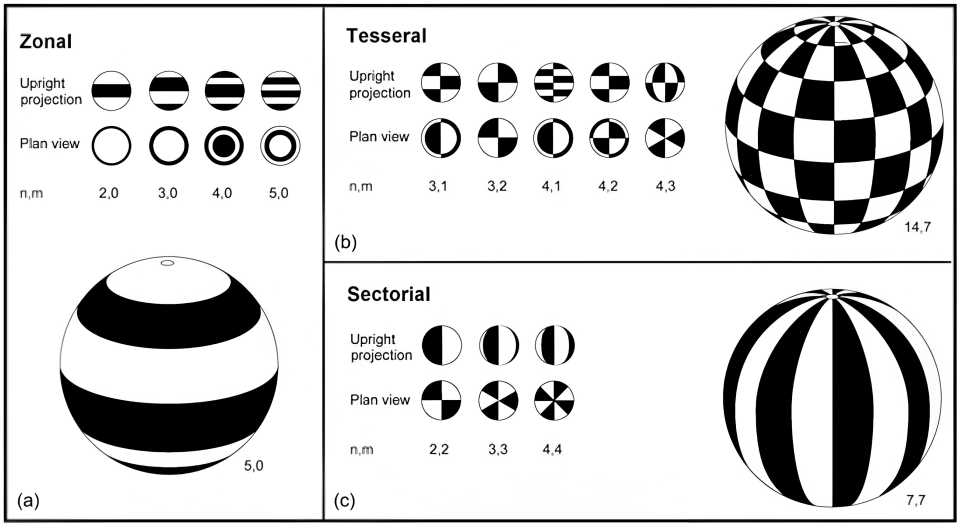


Figure 2.2: Representation of the a) zonal, b) tesseral, and c) sectorial spherical harmonics, taken from Fig. 12.6 in Ref. [230].

by $J_{n,m}$ for sectorial and tesseral harmonics, and $J_n \equiv J_{n,0}$ for zonal harmonics. Accordingly, the resulting acceleration terms are referred to as $J_{n,m}$ and J_n spherical-harmonic gravitational accelerations, respectively.

The J_2 acceleration is produced by the gravity field component associated with the equatorial bulge of the Earth, see Fig. 2.2a, and is by far the largest spherical-harmonic acceleration, in the order of 10^{-2} m/s^2 in LEO [231]. This acceleration induces short-period oscillations in all orbital elements, including the semi-major axis and inclination [232]. Because sailcraft maneuverability will be assessed through the orbit-raising and inclination-changing capabilities, these oscillations introduce significant noise in the results, rendering such assessment more challenging. On the other hand, the J_2 acceleration also yields secular variations in the mean anomaly, argument of pericenter and, most importantly, the RAAN [232]. The continuous change in RAAN results in the steady precession of the orbital plane, with effects on the sailcraft illumination conditions, and the presence and duration of eclipses. Furthermore, this precession is the fundamental mechanism enabling Sun-synchronous orbits, which are extensively considered in the investigation.

Similar to the J_2 acceleration, the accelerations caused by zonal harmonics of degree $n > 2$ also induce short-period oscillations in all orbital elements and secular variations in the mean anomaly, argument of pericenter, and RAAN [232]. However, these accelerations perturb the dynamics to a much lesser extent than the J_2 acceleration, as they are at least three orders of magnitude smaller [231].

Sectorial and tesseral harmonics not only induce short-term perturbations, but also long-term perturbations and, for specific orbits, resonant perturbations [232]. Nevertheless, also these gravitational accelerations are several orders of magnitude smaller than the J_2 acceleration.

In view of the above considerations, different spherical harmonic representations will be used in the remainder of the dissertation, depending on the application and corresponding degree of fidelity required. When tuning optimization parameters and assessing the accuracy of different PRP acceleration models, only Earth's central gravity will be considered in order to avoid introducing noise into the tuning process and the accuracy assessment. On the other hand, the J_2 gravitational acceleration will be considered in the analyses of the maneuvering capabilities of Earth-bound sailcraft to ensure the findings can be used inform real-life mission design. In these analyses – conducted across Chapters 3, 6, and 7 – the maneuvering capabilities will be assessed after filtering out the short-term oscillations in the semi-major axis and inclination from the results. To this aim, orbital changes will be evaluated at consecutive crossings of the equatorial plane and, specifically for the final high-fidelity analyses in Chapter 7, by previously converting the osculating orbital elements to J_2-mean orbital elements [233]. Finally, the J_2 gravitational acceleration will also be considered for the preliminary analysis of the Advanced Composite Solar Sail System (ACS3) mission presented in Chapter 5 and, together with all spherical harmonics up to degree and order 32, for the in-depth, post-launch mission analysis conducted in the same chapter. This choice is motivated by the need for high accuracy in these analyses – and especially in the post-launch analysis – as they were performed to investigate the calibration capabilities of ACS3 with a view toward actual operational use.

2.2.1.2. THIRD-BODY GRAVITY

The dynamics of satellites in LEO are also affected by the gravitational attraction of celestial bodies other than the Earth. Among these, the bodies that exert the largest gravitational accelerations are the Sun and the Moon, due to their large mass and proximity to Earth, respectively. While these accelerations determine short- and long-term periodic oscillations in all orbital elements, they also induce secular changes of similar nature to those produced by the Earth's J_2 gravitational acceleration. Indeed, the luni-solar attraction generates an external torque on the orbit that causes the orbital angular momentum vector to rotate, and the orbit to precess [234]. However, since in LEO the J_2 acceleration is approximately 10^4 larger than the lunar and solar gravitational accelerations [231], the secular variations in RAAN and argument of pericenter produced by luni-solar attraction are extremely small and are dominated by those induced by the Earth J_2 acceleration [234]. For this reason, these accelerations will be neglected.

2.2.1.3. GRAVITY INDUCED BY EARTH TIDES

Apart from exerting a gravitational attraction on satellites, the Moon and the Sun also exert a gravitational attraction on the Earth. These forces give rise to structural deformations in the entire Earth, while simultaneously inducing variations in sea levels across the globe. These so-called solid-Earth and ocean tides, respectively, therefore represent local, time-dependent variations in the mass distribution of the Earth, which in turn exerts a gravitational acceleration on LEO satellites. This acceleration, however, is approximately 10^4-10^5 times smaller than the J_2 acceleration and only of interest for applications involving geodesy and precise orbit determination [231]. For this reason, tide-induced gravitational accelerations will not be taken into account.

2.2.1.4. RELATIVISTIC CORRECTIONS

The gravitational accelerations discussed thus far are founded on the Newtonian theory of gravity. To account for relativistic effects, so-called relativistic post-Newtonian acceleration corrections can be considered. The most significant of these corrections are the Schwarzschild and Lense-Thirring acceleration terms, which are in the order of 10^{-8} and 10^{-10} m/s^2 for LEO satellites, respectively, and thus several orders of magnitude smaller than all other aforediscussed accelerations [231, 235, 236]. In view of this, relativistic corrections will not be considered.

2.2.2. ATTITUDE-DEPENDENT ACCELERATIONS

Gravitational accelerations only depend on the mass distribution, orientation, and position of celestial bodies relative to a satellite. As such, these accelerations are independent of the type of spacecraft considered. Other accelerations, on the other hand, do depend on the properties of the spacecraft, as they originate from its interaction with the space environment. Notable examples are the solar radiation pressure (SRP), PRP, and aerodynamic accelerations, which are produced by the impact of solar photons, photons emitted and reflected by the Earth, and atmospheric particles, respectively, on the surfaces of a spacecraft. The magnitudes of these accelerations strongly depend on the area-to-mass ratio of a satellite, its shape, and properties of its surface materials – that is, those characteristics that most differentiate solar sails from conventional satellites. Consequently, the SRP, PRP, and aerodynamic accelerations acting on sailcraft can be relatively large and affect the solar-sail dynamics to a significant extent. For example, while CubeSats with blunt shapes experience SRP accelerations in the order of at most 10^{-8} m/s^2, present-day solar sails like ACS3 can achieve SRP acceleration magnitudes of 10^{-5} m/s^2 [231]. The PRP acceleration – usually between 10% to 30% of the SRP acceleration, in LEO [222, 231, 237] – also undergoes an up-scaling of three orders of magnitude when considering sailcraft instead of conventional satellites. Lastly, the magnitude of the aerodynamic acceleration depends heavily not only on a satellite's characteristics, but also the atmospheric density, which varies with altitude and the intensity of solar activity. As a consequence, conventional CubeSats can be subject to a wide range of intensities of aerodynamic acceleration, in the order of 10^{-8}-10^{-5} m/s^2 at 500 km, and of 10^{-10}-10^{-8} m/s^2 at 1000 km [231, 238–240]. In comparison, ACS3-like solar (and drag) sails experience aerodynamic accelerations approximately 100 to 1000 times larger.

It should be noted that, even for solar sails, the SRP, PRP, and aerodynamic accelerations can still be smaller in magnitude than some gravitational accelerations. However, their relevance for the investigation lies in the fact that they can be actively controlled through the sail attitude. Indeed, by modifying the orientation of the sail with respect to the incoming solar and planetary radiation, and atmospheric wind, the magnitudes and directions of these accelerations can be changed, allowing a sailcraft to maneuver. Due to their central relevance to sailcraft maneuverability, these accelerations will all be included in the dynamics and the most appropriate models to represent them will be discussed later in this Chapter.

Finally, other solar-sail attitude-dependent accelerations also exist, although their magnitudes are extremely small. The acceleration from the Poynting-Robertson effect – which is caused by the relativistic aberration of sunlight and acts against the direction of

motion – has a magnitude in the order of 10^5 times smaller than the SRP acceleration [241, 242]. Similarly, the acceleration due to the pressure of solar-wind protons impacting onto the sail is approximately 10^4 times less than the SRP acceleration [2], whereas the Lorentz acceleration caused by the interaction of the sail's static charge with the Earth's magnetic field reaches even smaller magnitudes [243–245]. Therefore, these accelerations will all be neglected.

2.2.3. EQUATIONS OF MOTION

In the previous section, the gravitational, SRP, aerodynamic, and PRP accelerations were identified as the main accelerations to consider in the investigation. The corresponding solar-sail dynamics can be defined within an Earth-centered inertial (ECI) reference frame, $O_I(\hat{\boldsymbol{x}}, \hat{\boldsymbol{y}}, \hat{\boldsymbol{z}})$, with the $\hat{\boldsymbol{x}}$-axis direction pointing towards the mean vernal equinox at January 1$^{\text{st}}$, 2000, the $\hat{\boldsymbol{z}}$-axis direction perpendicular to the mean equatorial plane of that same epoch and pointing towards the North Pole, and the $\hat{\boldsymbol{y}}$-axis direction completing the right-handed frame. Within this frame, the dynamics can then be expressed through the following equations of motion in vectorial form:

$$\ddot{\boldsymbol{r}} = \boldsymbol{\nabla} U + \boldsymbol{a}_{SRP} + \boldsymbol{a}_{Aero} + \boldsymbol{a}_{PRP} \tag{2.1}$$

where $\boldsymbol{r}$ is the satellite position vector, U is the Earth gravitational potential, the dot notation indicates differentiation with respect to time, $\boldsymbol{\nabla}$ indicates vector differentiation with respect to spatial coordinates – i.e., the gradient operator – and $\boldsymbol{\nabla} U$, $\boldsymbol{a}_{SRP}$, $\boldsymbol{a}_{Aero}$, and $\boldsymbol{a}_{PRP}$ represent the Earth gravitational, SRP, aerodynamic, and PRP accelerations, respectively. Note that, at times, the PRP acceleration will also be expressed through its constituent parts as $\boldsymbol{a}_{PRP} = \boldsymbol{a}_{BBRP} + \boldsymbol{a}_{ARP}$, with $\boldsymbol{a}_{BBRP}$ and $\boldsymbol{a}_{ARP}$ denoting the blackbody radiation pressure (BBRP) and albedo radiation pressure (ARP) accelerations discussed in Section 2.4.4.

The expressions for the aforementioned accelerations depend on the way the sailcraft and near-Earth environment are described, and, crucially, on how the interaction between the two is modeled. These aspects will be thoroughly discussed in the following sections, in order to inform the selection of the most appropriate models for the investigation and help identify necessary improvements in modeling fidelity. To illustrate the strongly coupled nature of these physical dependencies, Fig. 2.3 provides a conceptual diagram linking the near-Earth environment and sailcraft characteristics to the resulting accelerations. The reader is invited to use this figure as a visual reference map for the discussion on sailcraft and environmental modeling conducted in the following sections.

2.3. SAILCRAFT CHARACTERISTICS

The models used to represent a sailcraft play a central role in the definition of the SRP, aerodynamic, and PRP accelerations. These models are discussed in the following subsections, focusing first on the sail shape and the structural uncertainties associated with it, and subsequently on the optical properties of the sail materials and their inherent variability.

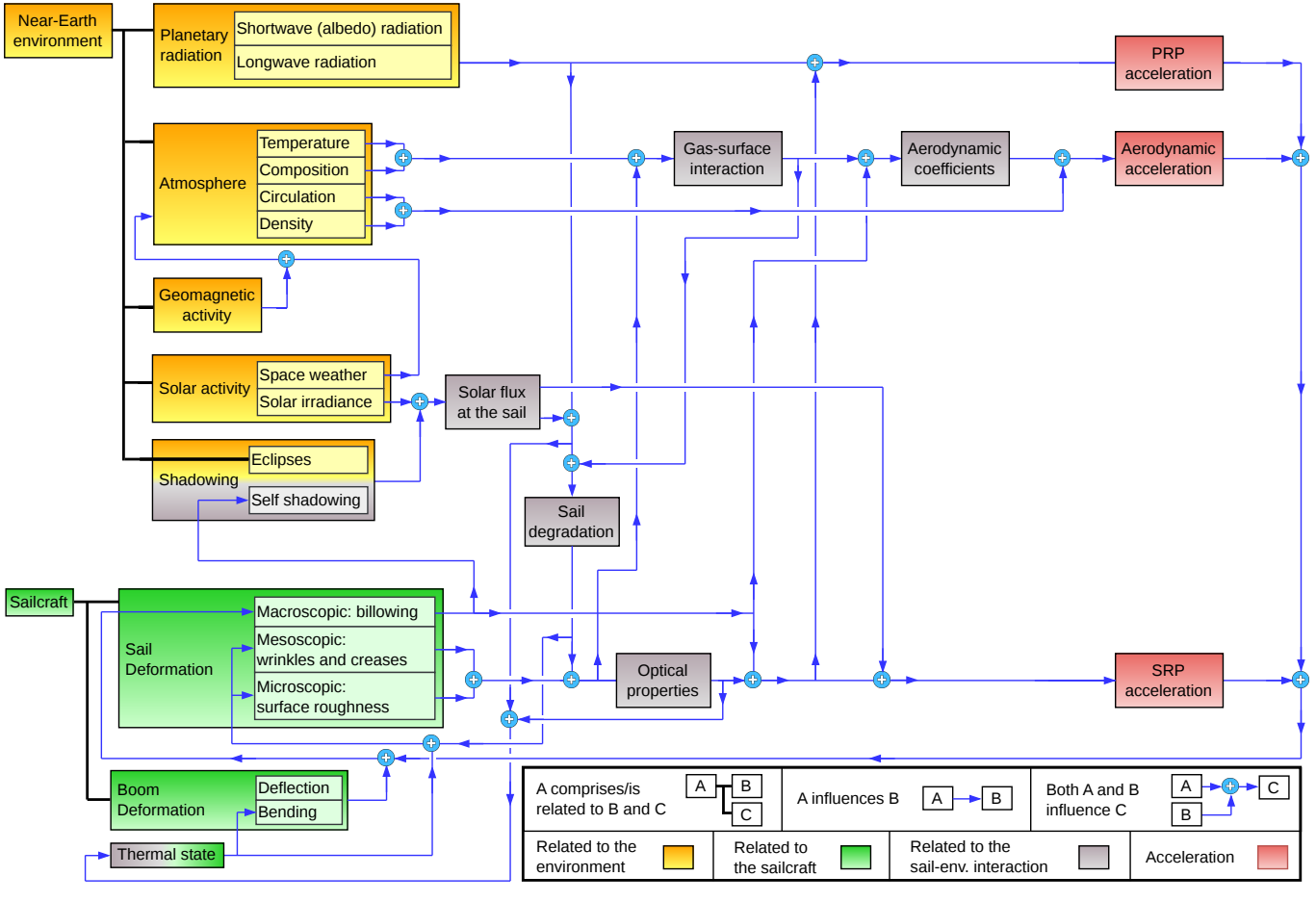


Figure 2.3: Diagram illustrating the dependencies of the attitude-dependent solar-sail accelerations on sailcraft characteristics and the near-Earth environment.

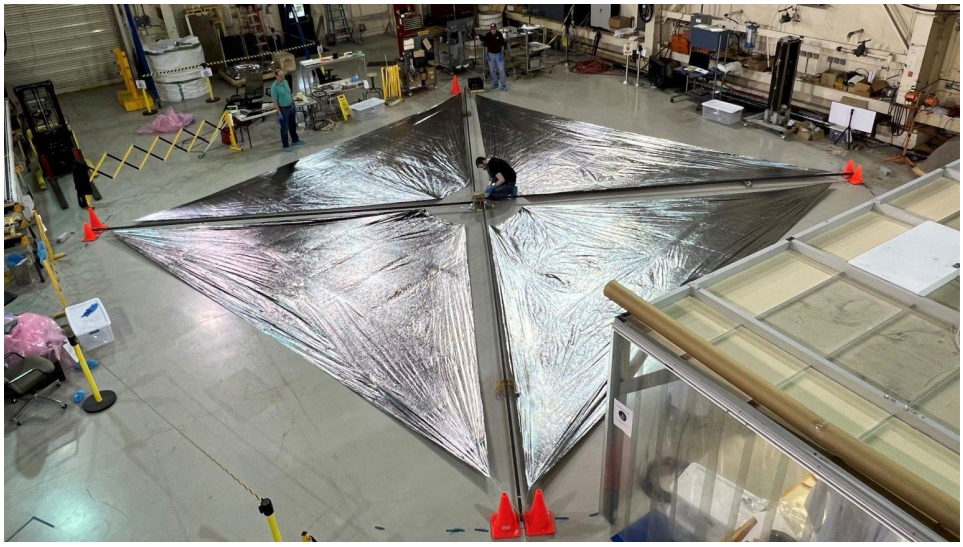


Figure 2.4: Ground deployment test of ACS3 at the NASA Langley Research Center, Hampton, Virginia, USA, on May 2022.

2.3.1. SAIL SHAPE

This dissertation focuses exclusively on boom-deployed square solar sails because this design has been identified as the most effective and operations-ready among competing options, see Section 1.2.1. The square design usually entails four booms deployed from a central bus, acting as masts to support a sail comprising four quadrants. An example is the ACS3 sailcraft, shown in Fig. 2.4 after ground deployment [128]. In this configuration, the corners of the sail quadrants are tied to the boom tips and the central bus by tensioning cables. Because the booms possess a finite stiffness and are subject to thermal gradients from uneven solar heating, they can bend, resulting in the sail quadrants deforming, especially in the out-of-sail-plane direction [246, 247]. Furthermore, the quadrants can billow also due to external forces, as well as the inertial loads generated by sailcraft re-orientation, e.g., for maneuvering [145].

Investigation of the structural dynamics and deformation of solar sails is an active field of research, with implications both on the orbital dynamics and attitude control [145, 146, 248–250]. Recent works have shown that, by accounting only for thermal gradients, sails with a side length of 20 to 40 m can deform from a few centimeters to 15 – 20 cm, respectively [246, 251]. These deformations give rise to complex sail shapes, like the ones shown in Fig. 2.5 for the National Aeronautics and Space Administration (NASA)'s Solar Cruiser sailcraft. On the other hand, when factoring in also possible deviations in the boom deployment procedure, sail deformations of even larger magnitudes can arise. This is the case for ACS3, which is currently in orbit in a slightly pyramidal configuration, with its boom tips vertically displaced by approximately 0.5-1 m, corresponding to a deflection angle from the nominal sail plane (where the bus lies) of 4-7 deg [129].

To account for these types of deformation and their effects in the sailcraft dynamics,

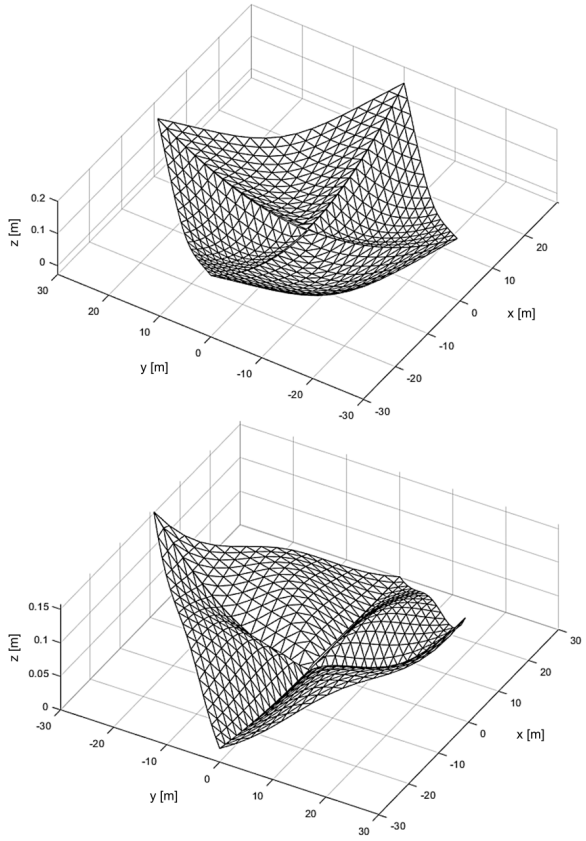


Figure 2.5: Example shapes of the sail of NASA's Solar Cruiser under different thermal loadings. Note that the scales of the vertical axes have been magnified to better visualize deformations. Image taken from Fig. 3 in Ref. [251].

different methods can be used. Finite element methods achieve the highest fidelity. They require the sail surface to be discretized into a large number of facets – see Fig. 2.5 – whose individual accelerations are computed and then summed to yield the overall sailcraft acceleration [249, 250, 252]. The discretization theoretically allows to represent any sail shape, potentially with time-varying shapes and variable optical characteristics across the surface. However, such methods are extremely computationally expensive, thus rendering their use impractical for mission analysis. Analytical models have also been developed which allow to compute the accelerations of curved sails, most notably, the generalized sail model by Rios-Reyes and Scheeres [253]. This model defines the sail surface as a bi-dimensional function and, crucially, in computing the SRP acceleration, it allows to decouple the contribution of the sail shape from the incidence angle of incoming sunlight. In this way, by defining the sail surface as a bi-dimensional function, this model allows to express the solar-sail SRP acceleration by means of algebraic tensors that only depend on the sail surface function and not on the direction of incoming sunlight. Therefore,

these tensors can be computed offline for any given sail shape, and can then be used to compute the SRP acceleration for specific sunlight incidence angles during propagation of the dynamics. While initially devised to compute the SRP acceleration, it is of note that a recent study has also applied this model to determine the aerodynamic forces on a curved (drag) sail [254]. The generalized sail model requires the surface shape to be constant, always with the same side illuminated by sunlight, and without any self-shadowing. Finally, the most widely used sail-shape model is the flat-sail model, which represents the sail as a rigid flat plate, neglecting any deformation. This assumption allows sailcraft accelerations to be formulated analytically in a very simple manner, making the model particularly easy to implement and computationally inexpensive, though sacrificing fidelity.

In this dissertation, the flat-sail model will be employed for all analyses. The reason for this choice is twofold. First, although other models can theoretically attain a higher fidelity, their use requires precise knowledge of the actual shape assumed by a solar sail throughout its flight, and its evolution over time. Such information is generally difficult to obtain and, even when available, it is subject to significant uncertainty. Because attempting to account for this uncertainty using approximate data would compromise the validity of the results and limit any meaningful improvement over the flat-sail model, the latter was selected and the aforementioned sail-shape uncertainties will not be considered. Second, the type and extent of the deformation undergone by the sail are dependent on factors that are sailcraft- and orbit-specific, such as the temperature of the sailcraft booms and sail, their materials, and the properties of the aerodynamic and radiation environments for the considered orbital scenario. Therefore, the use of any model accounting for the sail deformation would limit generalization of the results of the investigation.

It is important to note that, although the significant uncertainty surrounding the in-orbit shape of a sailcraft justifies the use of a flat sail model, deviations from a perfectly flat configuration have a considerable impact on acceleration. Indeed, preliminary research indicates that sail deformation affects solar-sail thrust performance [255–258], with realistic deformations inducing variations in achievable SRP acceleration in the order of 10% or more. Similarly, studies have shown that even slight billowing can produce extremely large errors in aerodynamic coefficients, of up to 100% [259–261], although under ground-based rather than in-orbit aerodynamic conditions. Therefore, while these results cannot be directly transposed to the free-molecular flow regimes characteristic of LEO sailcraft, see Section 2.5.2.2, errors in the aerodynamic accelerations of a similar magnitude can be expected.

Notably, the above discussion focused on the *macroscopic* modeling of the sail surface. On a smaller scale, the sail also exhibits deformations in the form of creases and wrinkles [262–265], which influence the overall thrusting performance of the sailcraft. Nevertheless, such deformations are by definition highly irregular, time-varying, and difficult to predict. Therefore, their representation and inclusion in the dynamics would require a probabilistic framework [266, 267], involving significant modeling effort. Furthermore, similar to macroscopic deformations, any improvement in accuracy gained from modeling these effects would remain secondary to the influence of other, more intense and uncertain perturbations. Consequently, this level of detail lies beyond the scope of this dissertation and such small-scale sail deformations will be neglected.

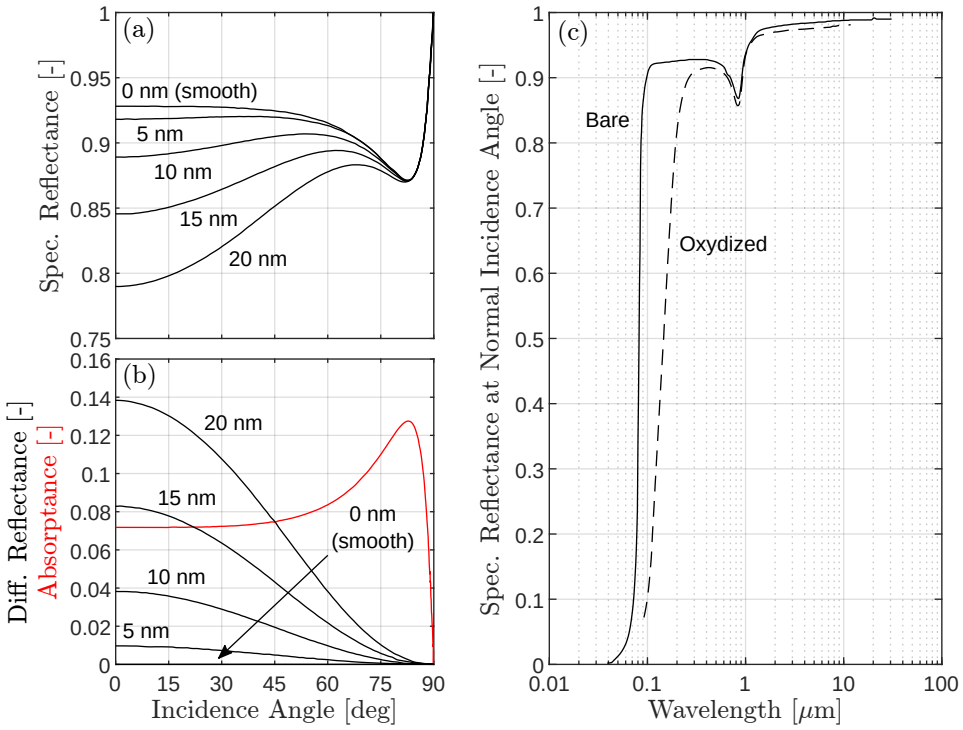


Figure 2.6: a) Specular and b) diffuse reflectance and absorption of thin aluminum films as a function of the radiation incidence angle and surface roughness (indicated by its root mean square). Reflectance is averaged over the 0.275-4 μm wavelength range, considering the solar blackbody spectrum at 5778 K. c) Specular reflectance of optically smooth, evaporated aluminum film at an incidence angle of 0 deg as a function of wavelength for bare aluminum and partially oxidized aluminum. Data taken from Refs. [268, 269].

2.3.2. SAIL OPTICAL PROPERTIES

Solar sails are coated in highly reflective materials to enhance reflectivity and, therefore, thrusting performance. However, their reflection properties and overall optical characteristics are not uniform, but vary across the sail surface, over time, and with the wavelength and incidence angle of the radiation. These effects may be captured or neglected depending on the level of fidelity required, corresponding to different models.

The simplest reflection model is the so-called ideal model [2]. This model approximates the sail as a perfect reflector, that is, a mirror-like surface reflecting all incident radiation specularly, causing the radiation pressure acceleration to always point normal to the sail plane. This model stems from the idea that sail coating materials like aluminum attain a high specular reflectivity in the visible spectrum, which, to a first approximation, can be assumed equal to one. Nevertheless, such an approximation introduces considerable acceleration errors, even in the order of 10% for the SRP acceleration [2, 255–257]. To date, the ideal model is the most widely used reflection model because it is extremely simple to implement and, despite its limited fidelity, it provides informative results for

preliminary solar-sail mission analysis and trajectory design. To more accurately represent the optical characteristics of the sail, the optical sail model devised by McInnes may be used [2]. This model accounts for the optical properties of the sail through a set of coefficients that describe its specular reflectivity, diffuse reflectivity, absorptivity, and emissivity. Importantly, by removing the assumption of perfect reflection used in the ideal model, the resulting radiation pressure acceleration achieves a smaller magnitude and does not necessarily point normal to the sail surface. In the vast majority of studies, the optical coefficients are assumed constant, despite changes in reflectivity and absorptivity with the incidence angle of radiation can be significant, as visualized in Fig. 2.6a-b. Similarly, the dependence of emissivity on sail temperature is seldom taken into account [270], while changes in reflectivity with radiation wavelength and those induced by sail material imperfections, such as aluminum oxidation, are also usually neglected, despite their potentially significant impact, see Fig. 2.6c [269]. On the other hand, time variations in the optical properties induced by sail material degradation have been investigated to a somewhat greater extent [271–276]. The studies on the topic employ the sail degradation model presented by Dachwald et al. [271] and its recent update by Klein et al. [276], which assume that the the sail reflection coefficients decay exponentially either as a function of the cumulative radiation flux or cumulative proton flux over the sail surface, respectively. Importantly, these studies show that errors in the order of 10% in acceleration magnitude and tens of degrees in acceleration direction are obtained when neglecting radiation-induced sail material degradation, although on long time scales spanning months to years. Finally, it should be noted that the optical sail model also assumes that the optical properties are uniform across the surface of the sail. This limit can be overcome by using the generalized sail model [253], which allows to treat variations in the optical coefficients across the sail surface analytically. However, as discussed in the Section 2.3.1, this model will not be considered in this work.

In the remainder of the dissertation, both the ideal and optical sail models will be considered. The former will be employed in Chapters 3 and 6, where a new PRP acceleration model is presented and preliminary analyses on sailcraft maneuverability are discussed, respectively. Chapters 4 and 7, on the other hand, will employ the optical sail model to increase fidelity, as they present the optical adaptation of the PRP acceleration model discussed in Chapter 3 and the final, high-fidelity analyses on sailcraft maneuverability, respectively. Finally, Chapter 5 will employ both the ideal and optical models for the preliminary and in-depth analyses of ACS3's calibration steering laws, respectively.

2.4. NEAR-EARTH ENVIRONMENT

This section aims to characterize the near-Earth environment, discussing the properties of the gravitational potential, atmosphere, and radiative output of the Earth, as well as the solar radiation environment.

2.4.1. GRAVITATIONAL POTENTIAL OF THE EARTH

As mentioned in Section 2.2.1.1, the gravitational potential of the Earth can be expressed as a spherical-harmonic series expansion. Using this approach, several geopotential models have been developed to this date. Examples include the Joint Gravity Models (JGMs)

2 and 3, developed in the 1990s from data obtained by TOPEX/Poseidon mission [277, 278], and the Earth Gravitational Model (EGM) of 2008, built on data from the GRACE (Gravity Recovery And Climate Experiment) mission [279]. Furthermore, among the most recent and accurate models are combined gravity models like EIGEN-6C4 and GOCO05c, which incorporate data from multiple sources, primarily the missions LAGEOS (Laser Geodynamics Satellite), GRACE, and GOCE (Gravity field and steady-state Ocean Circulation Explorer) [280, 281]. The above models differ in the values used for the mean radius and gravitational parameter of the Earth, and, most importantly, for the coefficients, maximum order, and maximum degree of the series expansion, which influence the model's accuracy. Differences in accuracy, however, are observable in practice only when considering a large number of harmonics and a high level of accuracy is required, e.g., for applications involving precise orbit determination, high-fidelity mission analysis, or operations. For this reason, in this dissertation, the JGM 2 model will be employed in Chapters 3, 4, 6, and 7, wherein harmonics at most up to the J_2 term are considered. On the other hand, the GOCO05c model will be employed with maximum degree and order up to 32 in Chapter 5, where detailed design of the ACS3 mission and the calibration steering laws are discussed.

2.4.2. ATMOSPHERE OF THE EARTH

The atmosphere of the Earth is characterized primarily by its density and circulation patterns. These aspects are discussed in the following sections.

2.4.2.1. ATMOSPHERIC DENSITY

The thermosphere represents the layer of the atmosphere extending from altitudes of approximately 80 km to approximately 500 to 1000 km. In this region – which corresponds to the altitudes of interest of this dissertation – atmospheric dynamics are strongly influenced by different physical processes. As a result, atmospheric density exhibits considerable variability with latitude, longitude, and altitude, and its modeling can be particularly challenging [282].

Thermospheric density is primarily influenced by the influx of energy from solar irradiance at specific frequency bands, namely, the Lyman-α, and X-ray, extreme, and far ultraviolet bands [282]. Incoming radiation heats the lower layer of the thermosphere, causing it to expand and, consequently, increase density at higher altitudes. This phenomenon results in the Sun-facing side of the atmosphere achieving much larger densities than the night side, even in the order of five times larger in the upper thermosphere [283]. Because the intensity of solar irradiance varies with the solar cycle, see Section 2.4.3.1, variations in density with a period of 11 years also occur [282]. An example visualization of this periodic variation is shown in Fig. 2.7, which highlights the substantial difference in density between solar minimum and maximum conditions. Finally, another source of disturbance in thermospheric density is the interaction of the Earth's magnetic field with the solar wind and, in particular, with its components originating from coronal mass ejections and coronal holes [282, 284, 285]. Because appearance of these phenomena is more frequent when in solar maximum conditions, the variation in density they yield aligns with the 11-year solar-cycle periodic trend. Furthermore, coronal holes corotate with the Sun, creating a shorter, superimposed periodicity of 27 days [285].

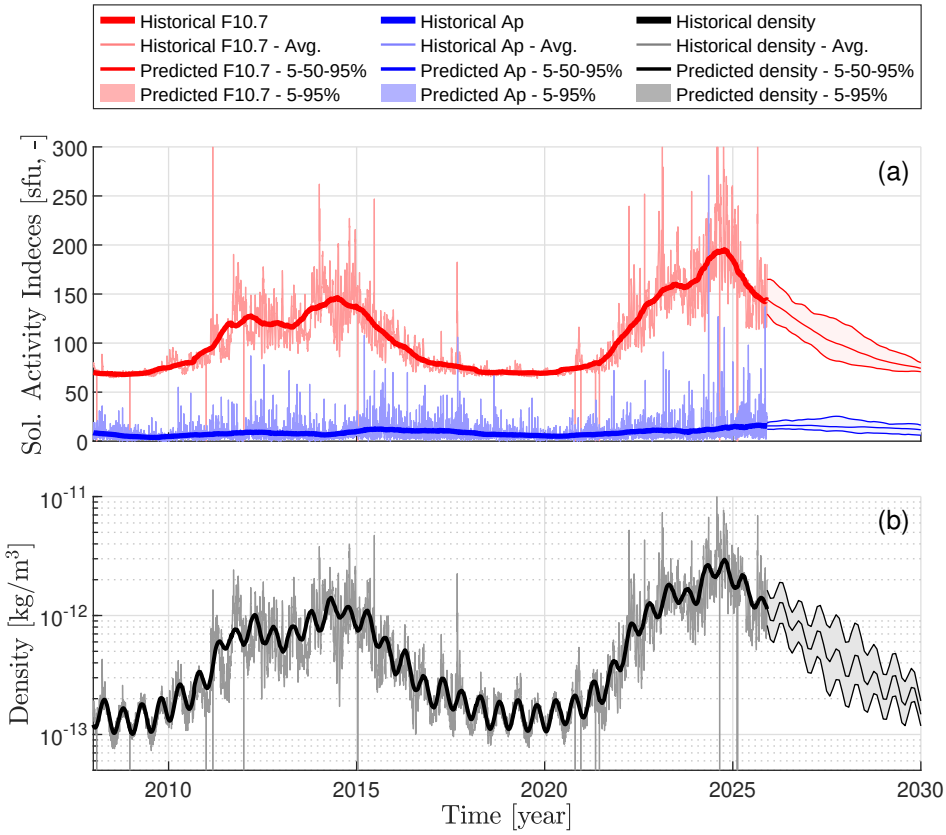


Figure 2.7: Temporal evolution of a) the F10.7 and Ap indices, and b) the atmospheric density at 500 km over Naples, Italy. Data prior to December 2025 correspond to historical daily values and one-year moving averages, whereas data after December 2025 represent predicted values for 5%, 50%, and 95% solar activity percentiles.

Because thermospheric density cannot be measured directly, the above physical phenomena are commonly examined instead, and then used to infer density. To this aim, coefficients have been defined over the years that measure the intensities of solar and geomagnetic activity. Solar activity is often described through measurements of the solar flux at a wavelength of 10.7 cm, F10.7, which represents a proxy for the irradiance of extreme ultraviolet radiation. Similar proxies include the solar flux at a wavelength of 30 cm, F30, and the M10, S10 and Y10 indices, which measure the influx of energy from different atmospheric species at various altitudes. Geomagnetic activity, on the other hand, is captured by indices such as the Kp, Ap, and Dst, which act as proxies that describe the heating of the upper thermosphere induced by the solar wind [282].

The solar and geomagnetic activity coefficients serve as inputs for several empirical density models, most notably, the models from the Jacchia, Drag Temperature Model (DTM), and Mass Spectrometer and Incoherent Scatter (MSIS) series. These models are formulated building on data from real-life LEO satellites and, to date, they are considered

the standard for prediction of atmospheric density [282, 286]. Nevertheless, they are also subject to limitations and non-negligible uncertainties. The most recent model of the DTM series, the DTM2020 model [287], was built using data from the Challenging Minisatellite Payload (CHAMP), GRACE, GOCE, and Swarm-A satellites. As these satellites orbited below 500 km, the accuracy of the model decreases swiftly for altitudes above this value [282]. Currently, the most popular model of the Jacchia family is the Jacchia-Bowman 2008 (JB2008) model [288], built by combining data from CHAMP and GRACE with data from the Air Force Space Command. While this model makes use of the indices M10, S10, Y10, and Dst to reduce uncertainties in density estimation, its performance also degrades rapidly for altitudes above 400-500 km [282]. Models from the MSIS family, like the popular NRLMSISE-00 model [289] and its recent update, NRLMSIS 2.0 [290], account for the presence of "anomalous oxygen" in the upper thermosphere to improve fidelity. Although some studies reported good agreement with density estimates up to 630 km [291, 292], above this altitude rapid loss in accuracy is again found [291]. In general, the literature shows that the above state-of-the-art models achieve relative errors in density estimates up to 15-20% for altitudes at 300 km, which rise to 30-50% at 500 km, and increase even more for higher altitudes [282, 286, 293].

The above considerations make evident that selecting a model to accurately represent atmospheric density across altitudes below 1000 km presents significant challenges. On the other hand, because all the above-discussed models share similar uncertainties and provide representative density values of comparable accuracy, any of them can be reasonably used [286]. Consequently, given its public availability and extensive use in the literature, the NRLMSISE-00 model will be adopted. Since the analyses involve future propagation dates, forecasted values of the F10.7 and Ap indices required by the model will be used. These will be retrieved from the archived forecast database of NASA's Marshall Space Flight Center (MSFC) [294], considering a percentile of 50% to avoid being under- or over-conservative. Finally, it should be noted that the NRLMSISE-00 model will be used as the inner core of a newly devised averaged density model. This model will be presented in Chapter 6, where it is also demonstrated that the averaging procedure yields negligible errors while reducing computational effort by approximately a factor of 10.

2.4.2.2. ATMOSPHERIC CIRCULATION

Defining the motion of the atmosphere is crucial to determine the relative velocity of satellites with respect to it and, therefore, the aerodynamic forces satellites experience.

At very low altitudes, approximately below 150 km, atmospheric density and viscosity are so high that the atmosphere can be considered to co-rotate with Earth [295–297]. At higher altitudes, on the other hand, density decreases and, with it, also the interaction between atmospheric particles. Consequently, atmospheric velocities can vary substantially from those of an Earth-fixed atmosphere. At altitudes between 200 km and 400 km, the complex interplay of solar heating and atmospheric waves gives rise to super-rotation effects, with studies indicating that the atmosphere can rotate even up to 40% faster than the Earth [298, 299]. The atmosphere's rotation rate then steadily decreases for higher altitudes up to 650 km, becoming smaller than the Earth's rotation rate by approximately 20% [298, 299]. It should be noted that the estimation of these rotation rates is characterized by strong uncertainty stemming from the scarce availability of satellite data. For this same reason, knowledge of atmospheric wind dynamics at altitudes above 650 km is

still very limited to date [299, 300]. Accordingly, current state-of-the-art numerical wind models are designed for altitudes below 500-600 km [301, 302], and their extension to higher altitudes represents an active area of research [303].

In view of the above, this dissertation will consider the atmosphere as either inertially fixed or Earth-fixed. Chapters 3 and 6, along with the preliminary analyses of ACS3's calibration steering laws in Chapter 5, consider an inertial atmosphere because the work they present was conducted chronologically earlier than the other chapters. At the time, this choice was adopted for the sake of simplicity and because the error introduced by assuming an inertially fixed atmosphere was deemed negligible. Indeed, for Sun-synchronous inclinations – that is, the inclination values most frequently considered in this dissertation – this assumption introduces errors in direction and magnitude of the relative velocity with respect to the atmosphere of at most 3.5 deg and 1.2%, respectively, for altitudes below 1000 km. For the higher-fidelity analyses in Chapters 5 and 7, on the other hand, the atmosphere will be considered to co-rotate with Earth – an assumption used in the majority of research on LEO satellite dynamics.

Mathematically, the velocity of the atmosphere at the sailcraft's location for an Earth-fixed or inertially fixed atmosphere can be expressed as follows:

$$\boldsymbol{v}_{atm} = \boldsymbol{\omega}_{\oplus} \times \boldsymbol{r} \qquad \text{where} \qquad \begin{cases} \boldsymbol{\omega}_{\oplus} = \dfrac{2\pi}{T_{sid}} \hat{\boldsymbol{z}}_{\oplus} & \text{for Earth-fixed atmosphere} \\ \boldsymbol{\omega}_{\oplus} = \boldsymbol{0} & \text{for inertially fixed atmosphere} \end{cases} \tag{2.2}$$

with $\boldsymbol{\omega}_{\oplus}$ the Earth angular momentum vector, $\hat{\boldsymbol{z}}_{\oplus}$ the direction of the Earth rotation axis – formally defined in Section 2.5.1 and assumed coincident with the $\hat{\boldsymbol{z}}$-axis direction of frame $\mathcal{O}_I$ – and $T_{sid} = 86164.091$ s the duration of the mean sidereal day [232]. As discussed in Section 2.5.2, the local velocity of the atmosphere allows to determine the relative velocity of atmospheric particle impinging on the sail and the resulting aerodynamic acceleration.

2.4.3. SOLAR RADIATION

To model the intensity of the solar radiation reaching the sail, it is necessary to define the radiative output of the Sun and the conditions in which eclipses occur. These aspects are discussed in the following subsections.

2.4.3.1. TOTAL SOLAR IRRADIANCE

The Total Solar Irradiance (TSI) represents the solar radiative power per unit of surface at 1 AU from the Sun. Due to the complex thermodynamics of the Sun, the TSI varies over time on different time scales. This variability is illustrated in Fig. 2.8, which shows the TSI and variation in the number of sunspots measured by different missions over the years [304]. First and foremost, the TSI follows a characteristic 11-year periodic trend that is marked by the solar cycle, which determines variations with amplitude in the order of 0.1%. Second, it evolves in a seemingly stochastic manner on much shorter time scales, with periods in the order of 27 days, corresponding to the period of solar rotation. These variations – also in the order of 0.1% – are caused by the appearance and disappearance of sunspots (dark spots) and faculae (bright spots) on the surface of the Sun, whose numbers

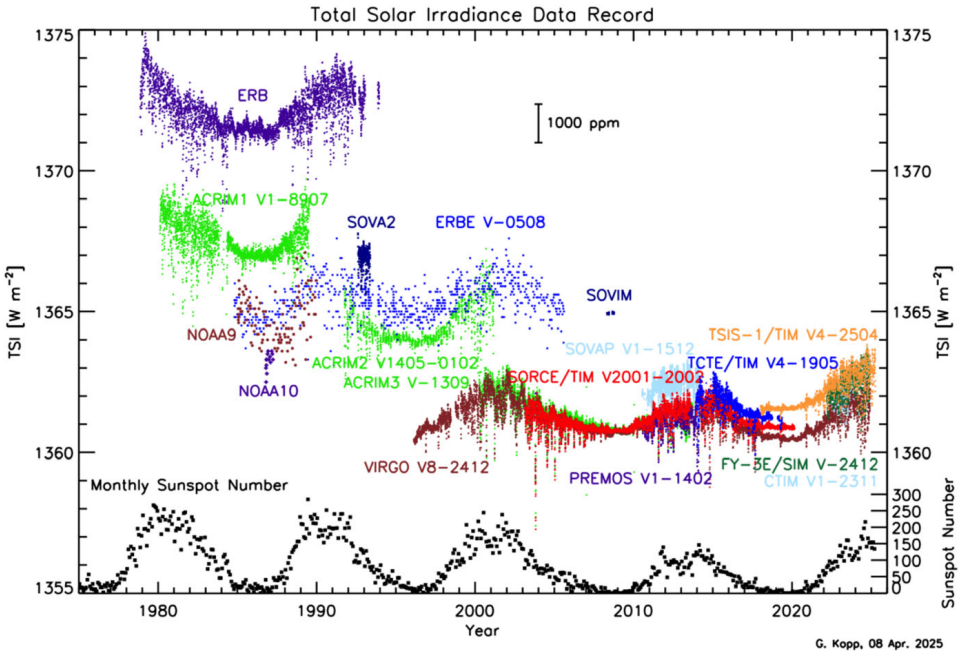


Figure 2.8: Space-born TSI data records relative from various instruments (colored dots) and sunspot number (black dots), taken from Fig. 6 in Ref. [304].

can only be forecasted to an approximate extent. Finally, on even shorter time scales of minutes to hours, the TSI also varies stochastically due to the presence of solar flares and other convection phenomena. These variations, however, are in the order of only 0.01% of the total TSI [304].

Figure 2.8 shows that, during the 1980s and 1990s, uncertainties in the aperture area of the instruments resulted in the measured TSI depending strongly on the mission considered, presenting evident biases [305, 306]. These biases managed to be eliminated almost entirely in later years, with TSI records converging to the range 1360-1363 W/m^2. It is also of note that the standard deviation associated with the measurements steadily decreased over time, from 0.2 W/m^2 to below 0.1 W/m^2 [304]. At present, consensus in the scientific community on the value of the TSI stands at 1361 ± 0.5 W/m^2 [304, 307].

As discussed above, the stochastic behavior of the TSI yields variations of its value in the order of 0.1%, that is, comparable to the variability induced by the solar cycle. Therefore, although the solar-cycle variations are – to some extent – predictable, the superimposed stochastic component constitutes a significant source of noise that precludes accurate forecast of the TSI. For these reasons, and given the limited error introduced, a constant mean TSI will be considered in the remainder of the work, equal to either 1367 W/m^2 or 1361 W/m^2. This differentiation stems from the fact that, at the beginning of the investigation, corresponding to the work in Chapters 3, 4, and 6, the employed TSI value of 1367 W/m^2 was taken from Ref. [308], which in turn was based on the measurements from the ACRIM (Active Cavity Radiometer Irradiance Monitors) 1 satellite, see

again Fig. 2.8. Then, for the analyses of ACS3's calibration steering laws in Chapter 5 and the high-fidelity parametric analyses in Chapter 7, an adjustment was carried out and the more accurate value of 1361 W/m^2 was adopted.

2.4.3.2. SOLAR FLUX

The solar flux at a satellite's location, S, depends not only on the radiative output of the Sun through the TSI, but also on the heliocentric distance. This dependence is expressed by the following relationship:

$$S = S_{TSI}\left(\frac{1\,\text{AU}}{r_\odot}\right)^2 \tag{2.3}$$

where $1\,\text{AU} = 1.49597870700 \cdot 10^8$ km [232] and $r_\odot$ is the Sun-to-sailcraft distance. This distance slightly varies throughout the year primarily because of the eccentricity of the orbit of the Earth around the Sun. Consequently, fluctuations in the perceived solar flux in the order of ±3.3% of the TSI are found. Nevertheless, these fluctuations will be neglected in this dissertation and a constant solar flux equal to the TSI will be considered, $S = S_{TSI}$. In this way, it will be possible to assess the solar-sail maneuvering capabilities in a way that is independent of the specific time of the year considered, therefore providing results of more general validity.

2.4.3.3. ECLIPSES

For particular orbit orientations, LEO satellites can experience eclipses, as the Earth hinders solar radiation from reaching the spacecraft. Depending on the geometrical representations of the Earth and Sun, different eclipse models can be defined. The most simple one, termed cylindrical shadow model, assumes the Earth to be spherical and the Sun to be an infinitely distant, point-like radiation source. As the model's name suggests, under these assumptions, the eclipse region assumes a cylindrical shape extending indefinitely behind the Earth as seen from the Sun. A more realistic and commonly used model is the so-called conical shadow model, sketched in Fig. 2.9 [231]. This model assumes both celestial bodies to be spherical, thereby resulting in the eclipse region being, indeed, conical. Unlike in the cylindrical model, when using the conical model, two sub-regions can be identified within the eclipse region, namely, the umbra and penumbra regions. These regions correspond to the regions wherein sunlight is completely and partially obstructed by the Earth, respectively. Importantly, in penumbra, the extent to which solar radiation is obstructed depends on how much the solar disk is visible from the satellite, see the insets in Fig. 2.9. To describe this occultation effect, a so-called shadow factor ν is used. Its value ranges from 0 to 1, with $\nu = 0$ corresponding to full eclipse (umbra), $\nu = 1$ corresponding to full illumination, and $0 < \nu < 1$ indicating partial eclipse (penumbra) conditions. Lastly, more advanced models also exist which consider the oblateness of the Earth [309–311] and, for applications requiring very high accuracy, even the effects of atmospheric refraction on the Sun's shape as seen from the satellite [312, 313] and of solar limb darkening [314].

For satellites orbiting at 1000 km that are not in a grazing orbit, eclipses can last approximately 33 min per orbit (corresponding to 32% of the orbital period) [308], whereas even larger values are found for satellites at lower altitudes. In comparison, transits in the penumbra region lasts in the order of 8-12 s, that is, approximately 0.5% and 0.16% of the

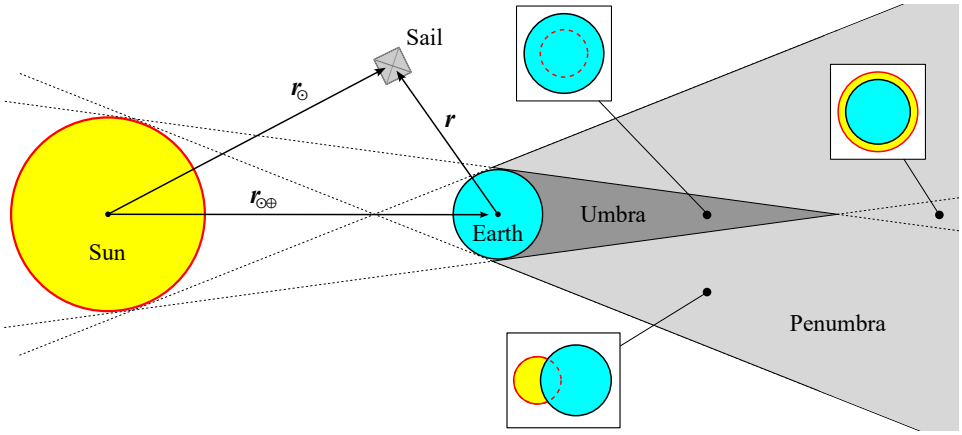


Figure 2.9: Geometry of the conical shadow model. The insets illustrate the view of the Sun as seen from the satellite.

total eclipse duration and orbital period, respectively. Therefore, while it is paramount to model full eclipses, inclusion of partial eclipses in the penumbra has a more limited effect on the dynamics. With this in mind, in this dissertation two eclipse models will be used. Chapters 3, 4, and 6 will consider a simplified variant of the conical shadow model discussed above, wherein penumbra is treated as umbra. This variant provides more conservative results than the standard conical model, and it was used in the first stages of the investigation for the sake of simplicity and computational efficiency. On the other hand, Chapters 5 and 7 will employ the standard conical model, for increased fidelity.

The standard and conservative conical shadow models are mathematically defined as follows. From the perspective of the sailcraft, the apparent angular radii of the Sun and the Earth, A and B, respectively, and the angular distance between the centers of the Sun and Earth, C, can be defined as:

$$A = \sin^{-1}\left(\frac{R_\odot}{r_\odot}\right) \qquad B = \sin^{-1}\left(\frac{R}{r}\right) \qquad C = \cos^{-1}\left(\frac{\boldsymbol{r}\cdot\boldsymbol{r}_\odot}{r\,r_\odot}\right) \tag{2.4}$$

where $R = 6378.1363$ km denotes the mean Earth radius, whose value corresponds to that of the gravitational models selected in Section 2.4.1 [277, 281], $R_\odot = 6.95508 \cdot 10^5$ km denotes the mean solar radius [232], $\boldsymbol{r}_\odot$ denotes the Sun-to-sailcraft vector, $r = \|\boldsymbol{r}\|$ and $r_\odot = \|\boldsymbol{r}_\odot\|$. When $C \geq A + B$, the Earth does not occult the Sun and $\nu = 1$, whereas, for $C < B - A$, the sailcraft is in the umbra region with the Earth totally obstructing sunlight, corresponding to $\nu = 0$, see Fig. 2.9. In all other cases, the sailcraft is in penumbra and partial eclipsing occurs. In these cases, the conservative conical shadow model prescribes $\nu = 0$. On the other hand, when using the standard conical shadow model, the shadow factor is given by:

$$\nu = 1 - \frac{\mathcal{A}}{\pi A^2} \tag{2.5}$$

with $\mathcal{A}$ denoting the fraction of the apparent solar disk that is covered by the Earth's disk,

defined as:

$$\mathcal{A} = \begin{cases} A^2 \cos^{-1}\left(\frac{X}{A}\right) + B^2 \cos^{-1}\left(\frac{C-X}{B}\right) - CY & \text{if } \left(|A-B| < C\right) \text{ and } \left(C < A+B\right), \\ \pi B^2 & \text{otherwise} \end{cases} \tag{2.6}$$

where the two conditions correspond to the cases in which the Earth's disk is not fully contained and is fully contained within the solar disk, respectively, see Fig. 2.9, and:

$$X = \frac{A^2 + C^2 - B^2}{2C} \qquad Y = \sqrt{A^2 - X^2} \tag{2.7}$$

It should be noted that computing the terms A and B in Eq. 2.4 requires knowledge of the instantaneous Sun-to-sailcraft vector, $\boldsymbol{r}_{\odot}$, in the ECI frame, O_I, consistent with the definition of $\boldsymbol{r}$ in the same frame. As shown in Fig. 2.9, the vector $\boldsymbol{r}_{\odot}$ can be found as:

$$\boldsymbol{r}_{\odot} = \boldsymbol{r}_{\odot\oplus} + \boldsymbol{r} \tag{2.8}$$

where $\boldsymbol{r}_{\odot\oplus}$ is the Sun-to-Earth position vector, expressible in the ECI frame as:

$$\boldsymbol{r}_{\odot\oplus}\big|_{O_I} = R_{O_{Ecl}\to O_I}\, \boldsymbol{r}_{\odot\oplus}\big|_{O_{Ecl}} = \begin{bmatrix} 1 & 0 & 0 \\ 0 & \cos\varepsilon_{obl} & -\sin\varepsilon_{obl} \\ 0 & \sin\varepsilon_{obl} & \cos\varepsilon_{obl} \end{bmatrix} \boldsymbol{r}_{\odot\oplus}\big|_{O_{Ecl}} \tag{2.9}$$

where the subscripts O_I and O_{Ecl} indicate the frames in which the vector $\boldsymbol{r}_{\odot\oplus}$ is expressed, O_{Ecl} denotes the ecliptic frame, $R_{O_{Ecl}\to O_I}$ is the rotation matrix to pass from the ecliptic frame to the ECI frame, and ε_{obl} is the obliquity of the ecliptic. Determining the Earth's position vector in the ecliptic frame, $\boldsymbol{r}_{\odot\oplus}|_{O_{Ecl}}$, generally requires either numerical ephemerides – such as NASA's well-known SPICE ephemerides [315, 316] – or analytical approximations. In this dissertation, the analytical ephemerides provided in Ref. [317] will be employed. This choice allows to strongly reduce computational effort while impacting accuracy to a negligible extent, for the purpose of the research. Following this rationale, the time-dependent obliquity of the ecliptic, ε_{obl}, will also be expressed analytically, using the formulation detailed in p. B52 of the astronomical almanac for the year 2010 [318]. For further information on the definition and motion of the ecliptic reference frame relative to Earth, the reader is referred to Ref. [318].

2.4.4. PLANETARY RADIATION

Accurate representation of the radiation environment in proximity of the Earth is required to determine the influence of planetary radiation on the solar-sail dynamics. The radiation emitted by the Earth comprises two components, namely, albedo radiation and blackbody radiation. Albedo radiation corresponds to the fraction of solar radiation that is scattered back into space by the Earth's atmosphere and surface. As shown in Fig. 2.10, solar radiation is predominantly confined in the so-called shortwave range of the electromagnetic spectrum, which corresponds to wavelengths below approximately 4 μm. Consequently, albedo radiation is also defined in the shortwave spectral range. The blackbody radiation represents the radiation emitted directly by the Earth to maintain thermal balance and, in contrast to albedo radiation, it originates from the fraction of

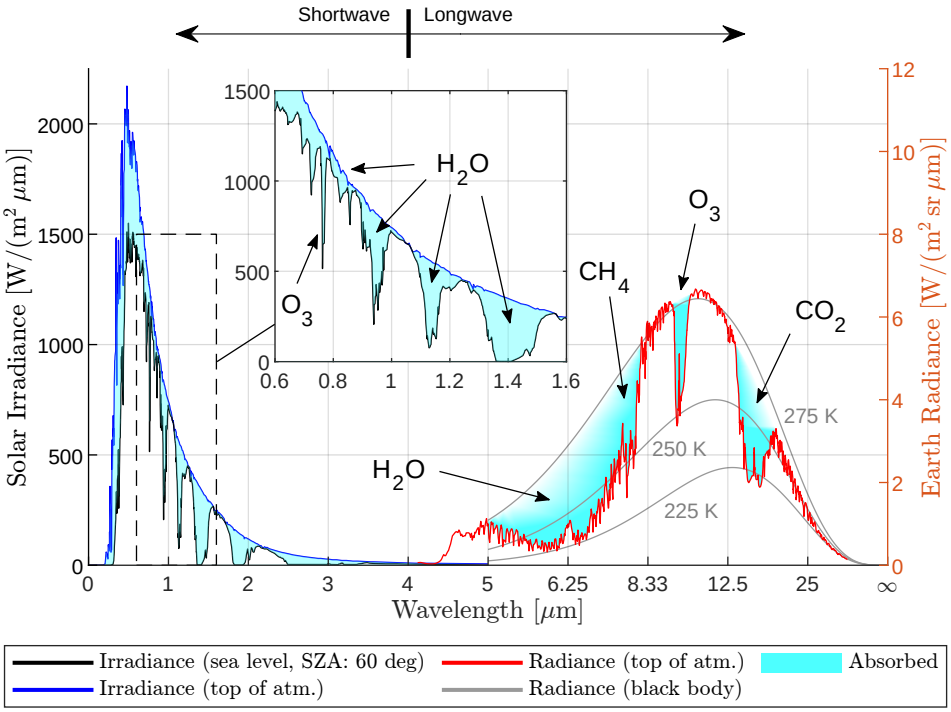


Figure 2.10: Spectrum of solar irradiance measured at sea level with solar zenith angle (SZA) of 60 deg and on top of the atmosphere, spectrum of Earth's longwave radiance on top of atmosphere, and radiances of ideal Planck's black bodies at different temperatures. The major atmospheric species that absorb radiation are also indicated. Data taken from Refs. [319, 320].

solar radiation that is absorbed by the Earth and its atmosphere. Figure 2.10 provides a visual representation of the fraction of solar irradiance that is absorbed by the atmosphere – corresponding to the difference between irradiance at the top of the atmosphere and at sea level – as well as some of the atmospheric species responsible for such absorption. This fraction of radiation, together with that absorbed by the Earth itself, are then re-radiated at infrared wavelengths above 4 μm, corresponding to the longwave region of the spectrum. The Earth's longwave radiation is also referred to as blackbody radiation in this dissertation because of the distribution of longwave radiance at the surface of the Earth, which approximately follows Planck's law for black bodies. However, it should be noted that by traveling through the atmosphere, part of this radiation gets absorbed or reflected back to the surface of the Earth by different atmospheric species, see Fig. 2.10. Consequently, radiance at the top of the atmosphere only loosely resembles an ideal blackbody distribution. The intensities of albedo and blackbody radiation vary geographically and temporally across the planet and, specifically for the albedo radiation, also with the incidence angle at which sunlight strikes the Earth. As a result, accurately characterizing (or predicting) the corresponding radiation flux is inherently challenging, and different models may be employed depending on the intended application and required level of

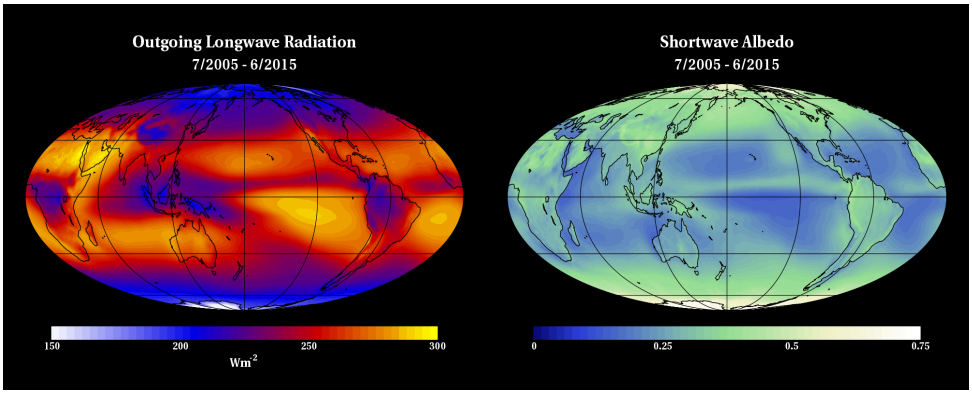


Figure 2.11: Global annual mean distributions of Earth's longwave radiation flux and albedo coefficient, obtained from NASA's CERES mission over the decade 2005-2015 [321].

fidelity.

Numerical models offer the most accurate representation of the distribution of Earth's radiative flux. They rely on discrete maps that capture the geographical and temporal variability of a number of properties of the Earth's radiation field, most importantly, the longwave and shortwave top-of-atmosphere radiative fluxes, and the albedo coefficient. Because these maps are built from satellite data, their spatial (i.e., longitudinal and latitudinal) and temporal resolutions depend on the specific mission considered and instrumentation on board the satellites. Notable examples of such missions include NASA's Earth Radiation Budget Experiment (ERBE) [322] and its successor, the Clouds and the Earth's Radiant Energy System (CERES) mission [323], whose data was used to generate the maps of the distributions of longwave radiative flux and albedo coefficient presented in Fig. 2.11 [321].

As a less computationally expensive alternative to numerical models, approximate analytical formulations have also been developed. In the most simple case, the blackbody radiation flux and albedo coefficient are assumed not to vary across the surface of the Earth, nor over time [324–327]. Despite their limited fidelity, such models are often considered for preliminary studies in view of their simplicity. More complex analytical models also exist that represent the distributions of the blackbody radiation flux and albedo coefficient using series expansions [328, 329], often in a similar fashion to spherical harmonics describing the geopotential field [330–336]. Although these formulations theoretically allow to achieve any desired level of precision, their practical use is often challenging. Indeed, the long series expansions that these formulations involve, together with the need to determine many coefficients, introduce substantial complexity that makes them often less attractive than numerical models. In addition, as discussed in Section 2.5.5, this complexity renders formulation and evaluation of the PRP acceleration very demanding, therefore discouraging their use even further.

In view of the significant computational effort required by numerical models and the complexity of series-expansion models, a newly devised analytical model will be presented in this dissertation, namely, the sinusoidal Earth radiation model. In this

model, the Earth's blackbody radiation flux and albedo coefficient are initially assumed to vary sinusoidally with latitude – equivalently to a zonal harmonic representation of degree two, see Fig. 2.2 – and are then locally averaged to approximate them as constant as seen from the sailcraft. The sinusoidal Earth radiation model has been developed in conjunction with the PRP acceleration model introduced in Chapter 3 and it will be employed in all subsequent chapters accounting for PRP. As a simpler alternative to the sinusoidal model, Chapter 3 will also introduce the so-called uniform Earth radiation model. This model – used in Chapter 5 for the preliminary analysis of ACS3's calibration steering laws – assumes constant blackbody radiation flux and albedo coefficient across the surface of the Earth, following the same approach of Refs. [324–327]. Finally, it should be noted that a numerical model will also be used in Chapter 3 for validation purposes. This model makes use of monthly averaged numerical maps from the Analysis of Non-Gravitational Acceleration due to Radiation and Aerodynamics (ANGARA) software, which in turn have been derived from the ERBE mission's satellite data.

2.5. MODELING OF THE SAILCRAFT ACCELERATIONS

The accelerations characterizing the solar-sail dynamics presented in Section 2.2.3 originate from the interaction of the sailcraft with the near-Earth environment. In this section, an overview and selection of the most appropriate models to represent these interactions and the corresponding accelerations is given, focusing separately on gravitational, aerodynamic, SRP, and PRP accelerations. As discussed in the following sections, the aerodynamic, SRP, and PRP accelerations are formulated directly in the ECI frame, O_I, enabling their straightforward insertion into Eq. 2.1. In contrast, the gravitational acceleration may require a frame transformation before it can be expressed in frame O_I.

2.5.1. GRAVITATIONAL ACCELERATION

To define the gravitational potential of the Earth and the corresponding acceleration, it is convenient to consider an Earth-centered, Earth-fixed (ECEF) frame $O_\oplus(\hat{\boldsymbol{x}}_\oplus, \hat{\boldsymbol{y}}_\oplus, \hat{\boldsymbol{z}}_\oplus)$ with origin at the Earth's center of mass, the $\hat{\boldsymbol{z}}_\oplus$-axis direction pointing along the rotation axis of the Earth towards the North Pole, the $\hat{\boldsymbol{x}}_\oplus$-axis direction pointing to the intersection of the equatorial plane with the Greenwich meridian, and the $\hat{\boldsymbol{y}}_\oplus$-axis direction forming a right-handed frame, see Fig. 2.12. Within this frame, the sailcraft position can be defined through its orbital radius, r, geocentric latitude, ϕ, and geographic longitude, λ, as:

$$\begin{aligned} r &= \sqrt{x_\oplus^2 + y_\oplus^2 + z_\oplus^2} \\ \phi &= \sin^{-1}\left(\frac{z_\oplus}{r}\right) \\ \lambda &= \operatorname{atan}_2\left(y_\oplus, x_\oplus\right) \end{aligned} \tag{2.10}$$

with $x_\oplus$, $y_\oplus$, and $z_\oplus$ the Cartesian coordinates of the sailcraft in frame $O_\oplus$, and $\operatorname{atan}_2()$ denoting the two-argument arctangent function commonly available in computational programming languages [337] and expressible in analytical form as:

$$\operatorname{atan}_2(Y, X) = 2\tan^{-1}\left(\frac{\sqrt{X^2 + Y^2} - X}{Y}\right) \tag{2.11}$$

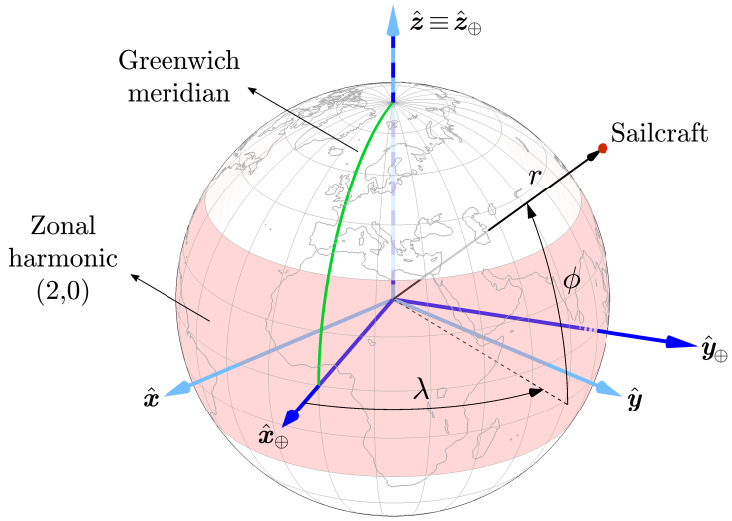


Figure 2.12: ECI frame, O_I, ECEF frame, $O_\oplus$, and spherical coordinates of the sailcraft position vector in frame $O_\oplus$.

The gravitational potential of the Earth can be defined using the theory of spherical harmonics as [338]:

$$U(r,\phi,\lambda) = \frac{\mu}{r}\sum_{n=0}^{\infty}\left(\frac{R}{r}\right)^n \sum_{m=0}^{n} \bar{P}_{n,m}\left(\sin\phi\right)\left[\bar{C}_{n,m}\cos(m\lambda) + \bar{S}_{n,m}\sin(m\lambda)\right] \tag{2.12}$$

where μ and R are the reference gravitational parameter and radius of the Earth of the geopotential model, $\bar{P}_{n,m}()$ are normalized associated Legendre functions of the first kind of degree n and order m, and $\bar{C}_{n,m}$ and $\bar{S}_{n,m}$ are normalized Stokes coefficients characterizing the series expansion. The corresponding acceleration exerted onto the sailcraft is then found as [338]:

$$\nabla U = \frac{\partial U}{\partial r}\frac{\partial r}{\partial \boldsymbol{r}_\oplus} + \frac{\partial U}{\partial \phi}\frac{\partial \phi}{\partial \boldsymbol{r}_\oplus} + \frac{\partial U}{\partial \lambda}\frac{\partial \lambda}{\partial \boldsymbol{r}_\oplus} \tag{2.13}$$

In Eq. 2.13, the partial derivatives with respect to $\boldsymbol{r}_\oplus$ correspond to the gradients of r, ϕ, and λ when expressed as functions of the Cartesian coordinates $x_\oplus$, $y_\oplus$, $z_\oplus$, see Eq. 2.10. Therefore [338]:

$$\begin{aligned}
\frac{\partial r}{\partial \boldsymbol{r}_\oplus} &= \frac{\boldsymbol{r}_\oplus}{r} = \frac{x_\oplus}{r}\hat{\boldsymbol{x}}_\oplus + \frac{y_\oplus}{r}\hat{\boldsymbol{y}}_\oplus + \frac{z_\oplus}{r}\hat{\boldsymbol{z}}_\oplus \\
\frac{\partial \phi}{\partial \boldsymbol{r}_\oplus} &= \frac{1}{\sqrt{x_\oplus^2 + y_\oplus^2}}\left[-\frac{x_\oplus z_\oplus}{r^2}\hat{\boldsymbol{x}}_\oplus - \frac{y_\oplus z_\oplus}{r^2}\hat{\boldsymbol{y}}_\oplus + \left(1 - \frac{z_\oplus^2}{r^2}\right)\hat{\boldsymbol{z}}_\oplus\right] \\
\frac{\partial \lambda}{\partial \boldsymbol{r}_\oplus} &= \frac{1}{x_\oplus^2 + y_\oplus^2}\left[-y_\oplus\hat{\boldsymbol{x}}_\oplus + x_\oplus\hat{\boldsymbol{y}}_\oplus\right]
\end{aligned} \tag{2.14}$$

The partial derivatives of the potential with respect to r, ϕ, and λ are instead found from direct differentiation of Eq. 2.12 [338]:

$$\begin{aligned}
\frac{\partial U}{\partial r} &= -\frac{\mu}{r^2}\sum_{n=0}^{\infty}\sum_{m=0}^{n}\left(\frac{R}{r}\right)^n (n+1)\bar{P}_{n,m}\left(\sin\phi\right)\left[\bar{C}_{n,m}\cos(m\lambda)+\bar{S}_{n,m}\sin(m\lambda)\right] \\
\frac{\partial U}{\partial \phi} &= \frac{\mu}{r}\sum_{n=0}^{\infty}\sum_{m=0}^{n}\left(\frac{R}{r}\right)^n \left[\bar{P}_{n,m+1}\left(\sin\phi\right)\Pi'_{n,m} - m\bar{P}_{n,m}\left(\sin\phi\right)\tan\phi\right]\cdot \\
&\qquad \cdot\left[\bar{C}_{n,m}\cos(m\lambda)+\bar{S}_{n,m}\sin(m\lambda)\right] \\
\frac{\partial U}{\partial \lambda} &= \frac{\mu}{r}\sum_{n=0}^{\infty}\sum_{m=0}^{n}\left(\frac{R}{r}\right)^n m\bar{P}_{n,m}\left(\sin\phi\right)\left[\bar{S}_{n,m}\cos(m\lambda)-\bar{C}_{n,m}\sin(m\lambda)\right]
\end{aligned} \tag{2.15}$$

where:

$$\Pi'_{n,m} = \sqrt{\frac{(n+m+1)(n-m)(2-\delta_{0m})}{2}} \tag{2.16}$$

with δ_{ij} denoting the Kronecker delta, for which $\delta_{0m} = 1$ only if $m = 0$ and $\delta_{0m} = 0$ otherwise.

Although the above series theoretically allow for an infinite number of terms, in practice, they are truncated to a maximum degree and order of choice. As discussed in Section 2.4.1, in this work, the GOCO05 model will be used with maximum degree and order of 32 – that is, neglecting harmonics corresponding to $n > 32$ and $m > 32$ – whereas the JGM 2 model will be employed with maximum degree of 0 or 2 and maximum order of 0. These geopotential models share the same reference gravitational parameter, $\mu = 398600.4415$ km/s^2, and Earth radius, $R = 6378.1363$ km [277, 281], whereas their normalized Stokes coefficients are provided in Ref. [339].

The gravitational acceleration for the GOCO05c model will be computed through Eqs. 2.13-2.16 and then transformed (rotated) from the Earth-fixed frame, $O_\oplus$, to the inertial frame, O_I, in order to be used in the equations of motion, see Eq. 2.1. In performing this frame transformation, this dissertation assumes that the $\hat{\boldsymbol{z}}_\oplus$ axis of frame $O_\oplus$ – that is, the Earth rotation axis – coincides with the $\hat{\boldsymbol{z}}$ axis of frame O_I, as illustrated in Fig. 2.12. Through this simplification, the effects of terrestrial precession, nutation, and polar motion are effectively ignored, introducing an angular error in the $\hat{\boldsymbol{z}}_\oplus$ direction of at most 0.15 deg, which was deemed negligible for the purpose of the research. The frame transformation therefore reduces to a rotation about the $\hat{\boldsymbol{z}}_\oplus$ axis, which allows to express the acceleration in the inertial frame, O_I, as:

$$\nabla U\big|_{O_I} = R_{O_\oplus \to O_I}\,\nabla U\big|_{O_\oplus} = \begin{bmatrix} \cos\lambda_\oplus(t) & -\sin\lambda_\oplus(t) & 0 \\ \sin\lambda_\oplus(t) & \cos\lambda_\oplus(t) & 0 \\ 0 & 0 & 1 \end{bmatrix} \nabla U\big|_{O_\oplus} \tag{2.17}$$

where the subscripts O_I and $O_\oplus$ indicate the frame in which the gravitational acceleration, ∇U, is expressed, $R_{O_\oplus \to O_I}$ is the rotation matrix to pass from frame $O_\oplus$ to frame O_I, and $\lambda_\oplus(t)$ is the time-varying rotation angle, given by [340]:

$$\lambda_\oplus(t) = \lambda_{GMST}(t_0) + \omega_\oplus(t - t_0) \tag{2.18}$$

where t is the current epoch, $\omega_\oplus = \|\boldsymbol{\omega}_\oplus\|$, and $\lambda_{GMST}(t_0)$ is the hour angle associated to the Greenwich Mean Sidereal Time (GMST) at an initial reference epoch t_0, that is, the angle measured between the axis directions $\hat{\boldsymbol{x}}$ and $\hat{\boldsymbol{x}}_\oplus$ at time t_0. For further information on the analytical definition of $\lambda_{GMST}(t)$, the reader is referred to Ref. [340] and p. B8 of Ref. [318].

The limited number of harmonics considered for the JGM 2 model allows to define an alternative expression for the gravitational acceleration that is equivalent, but significantly more compact, than Eqs. 2.13-2.16 used for the GOCO05c model. Indeed, by considering a maximum degree and order of 2 and 0, respectively, the series expansions in Eqs. 2.15 simplify greatly and Eq. 2.13 reduces to [232]:

$$\nabla U = \underbrace{-\frac{\mu}{r^3}\boldsymbol{r}_\oplus}_{\substack{\text{central}\\ \text{gravity}}} \underbrace{-\frac{3}{2}\frac{R^2}{r^5}\mu J_2\left[\left(x_\oplus\hat{\boldsymbol{x}}_\oplus + y_\oplus\hat{\boldsymbol{y}}_\oplus\right)\left(1-5\frac{z_\oplus^2}{r^2}\right)+z_\oplus\hat{\boldsymbol{z}}_\oplus\left(3-5\frac{z_\oplus^2}{r^2}\right)\right]}_{\substack{\text{J}_2\text{ gravity}\\ \text{(Earth oblateness)}}} \tag{2.19}$$

where the first and second terms on the right-hand side of Eq. 2.19 correspond to the central and J_2 gravitational acceleration terms, respectively, and the gravitational constant J_2 is found by denormalizing the Stokes coefficient $\bar{C}_{2,0} = -0.484165480\cdot10^{-3}$ [339] of the JGM 2 model as [338]:

$$J_2 = -\frac{\bar{C}_{2,0}}{\Pi_{2,0}} \tag{2.20}$$

through the following denormalization function:

$$\Pi_{n,m} = \sqrt{\frac{(n+m)!}{(n-m)!\,(2-\delta_{0m})\,(2n+1)}} \tag{2.21}$$

resulting in $J_2 = 1.082626925638815\cdot10^{-3}$ [308]. Finally, it should be noted that Eq. 2.19 only considers a zonal harmonic. This fact, along with the assumption that the $\hat{\boldsymbol{z}}_\oplus$ and $\hat{\boldsymbol{z}}$ axes coincide, allows Eq. 2.19 to be used not only in frame $O_\oplus$, but also in frame O_I. To this end, $\boldsymbol{r}_\oplus$, $\hat{\boldsymbol{x}}_\oplus$, $\hat{\boldsymbol{y}}_\oplus$, $x_\oplus$, and $y_\oplus$ must be replaced by $\boldsymbol{r}$, $\hat{\boldsymbol{x}}$, $\hat{\boldsymbol{y}}$, x, and y, respectively, while $\hat{\boldsymbol{z}} \equiv \hat{\boldsymbol{z}}_\oplus$ and $z = z_\oplus$. In this way, ∇U can be found directly in the inertial frame O_I, without warranting any frame transformation.

2.5.2. AERODYNAMIC ACCELERATION

Aerodynamic acceleration is influenced by several factors, including the properties of the sail surface, the atmosphere, and the interaction between the two. These aspects are discussed in detail in the following subsections, which outline the general formulation of the aerodynamic acceleration and the models used to determine the sailcraft aerodynamic coefficients.

2.5.2.1. GENERAL FORMULATION

The aerodynamic acceleration for a flat sail (plate) is given by [341]:

$$\boldsymbol{a}_{Aero} = \frac{1}{2}\frac{\rho v_{rel}^2}{\sigma}\left(C_D\hat{\boldsymbol{D}} + C_L\hat{\boldsymbol{L}}\right) \tag{2.22}$$

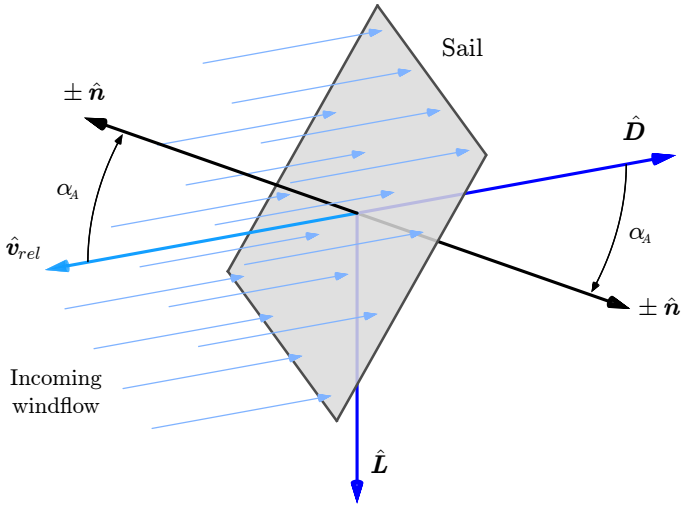


Figure 2.13: Aerodynamic pitch angle of a flat solar sail immersed in a windflow.

with σ the sailcraft loading parameter – that is, the sailcraft mass-to-sail area ratio – ρ the atmospheric density, modeled as per Section 2.4.2.1, and $v_{rel} = \|\boldsymbol{v}_{rel}\|$, where $\boldsymbol{v}_{rel}$ is the sailcraft relative velocity with respect to the atmosphere, assumed to be Earth- or inertially fixed, see Section 2.4.2.2. Furthermore, C_D and C_L denote the drag and lift coefficients, respectively, $\hat{\boldsymbol{D}}$ represents the drag direction pointing in the direction of the incoming windflow, and $\hat{\boldsymbol{L}}$ is the lift direction lying in the plane formed by $\hat{\boldsymbol{D}}$ and the sail normal direction, $\hat{\boldsymbol{n}}$, and pointing perpendicular to the former, see Fig. 2.13. Importantly, no side force appears in Eq. 2.22 because of the symmetry implied by the assumption of a flat sail. The sailcraft relative velocity, drag direction, and lift direction can be expressed mathematically as:

$$\boldsymbol{v}_{rel} = \boldsymbol{v} - \boldsymbol{v}_{atm} \tag{2.23}$$

$$\hat{\boldsymbol{D}} = -\hat{\boldsymbol{v}}_{rel} \tag{2.24}$$

$$\hat{\boldsymbol{L}} = \hat{\boldsymbol{D}} \times \frac{\hat{\boldsymbol{n}} \times \hat{\boldsymbol{D}}}{\left\|\hat{\boldsymbol{n}} \times \hat{\boldsymbol{D}}\right\|} \tag{2.25}$$

where $\boldsymbol{v} = \dot{\boldsymbol{r}}$ is the sailcraft inertial velocity vector, $\boldsymbol{v}_{atm}$ is the velocity of the atmosphere at the sailcraft's location defined in Eq. 2.2, and $\hat{\boldsymbol{v}}_{rel} = \boldsymbol{v}_{rel} / v_{rel}$. Note that, because in this dissertation $\hat{\boldsymbol{z}} \equiv \hat{\boldsymbol{z}}_{\oplus}$, see Section 2.5.1, Eq. 2.2 can be expressed directly in the ECI frame, O_I, as can Eqs. 2.23 and 2.24. Furthermore, by defining the sail normal direction, $\hat{\boldsymbol{n}}$, in frame O_I, Eq. 2.25 is also resolved in this frame. Consequently, the aerodynamic acceleration in Eq. 2.22 can be formulated entirely within the inertial frame O_I, enabling insertion in the equations of motion in Eq. 2.1 without warranting any frame transformation.

Equation 2.22 highlights that both the magnitude and direction of the aerodynamic acceleration are strongly influenced by the drag and lift coefficients, which capture the interaction between a body and the incident flow. Because this interaction depends on atmospheric composition, the thermal conditions of the flow, and the shape, surface

properties, and orientation of the body, these coefficients are intrinsically difficult to predict with accuracy. For this reason, a range of models have been developed over the years. These are reviewed in the following section, with a view to identifying the most appropriate one for the investigation.

2.5.2.2. GAS-SURFACE INTERACTION

Modeling the interaction between atmospheric particles and a satellite's surface – that is, the so-called Gas-Surface Interaction (GSI) – is fundamental to determine the drag and lift coefficients of spacecraft in LEO. This is an active field of research and one of the most challenging to investigate to date, owing to the inherent complexity in measuring (or inferring) such interaction from experimental tests and in-orbit satellite data [342]. GSI modeling for solar and drag sailing has been a research field explored to a very limited extent [254, 343]. Conversely, a well-established body of knowledge is available for GSI of conventional spacecraft, with different models developed over the years [342]. Although these models are valid only for bodies with rigid surfaces, which is not the case for solar sails, in first instance they may be used by approximating the sail as a flat plate. As discussed in the following, these models mostly differ in the flow regime of gas particles surrounding the satellite and the assumed nature of the interaction between said flow and the spacecraft's surfaces.

The flow regime of atmospheric particles depends on the Knudsen number, Kn, which represents the ratio of the average distance that particles travel before colliding with each other – that is, the length of the mean free path – to the characteristic length of the satellite. Its value indicates to what extent a gas behaves like a continuum or a collection of individual particles, corresponding to $Kn \ll 1$ and $Kn \gg 1$, respectively. In the latter case, the flow is said to be in free-molecular regime. Because the concentration of particles in the atmosphere decreases exponentially with altitude, see Fig. 2.14 [283], free-molecular conditions are satisfied already at altitudes of 200 km, with Knudsen numbers in the order of 10^3 for conventional satellites [344]. Within the free-molecular flow regime, a further differentiation between hyperthermal and non-hyperthermal conditions can be made through the adimensional parameter, S, representing the ratio of the spacecraft velocity to the most probable thermal velocity of the particles. In hyperthermal conditions, $S \gg 1$, indicating that the particles colliding with the spacecraft can be assumed as part of a streamlined, directed flow. In non-hyperthermal conditions, on the other hand, $S \ll 1$, meaning that the high temperature of the particles makes their motion appear more Brownian than streamlined from the spacecraft's perspective [344]. The speed ratio S depends strongly on the local translational temperature and molecular mass of the atmosphere, which, in turn, both vary with altitude. As a consequence, S decreases steadily with altitude, taking on values of approximately 7.4 and 3.7 at 300 and 700 km, respectively [344]. These example values show that perfect hyperthermal conditions – corresponding to $S = \infty$ – are hardly ever satisfied in reality, especially at the altitudes considered in this dissertation. Nevertheless, relatively small errors in the order of 2% to 7% are committed in the computation of the aerodynamic coefficients when assuming $S = \infty$, again for altitudes of 300 and 700 km, respectively [344].

When gas particles impact the surface of a satellite, they get reflected with modalities that depend on the surface properties and the type of particle considered. For example, atomic oxygen is particularly reactive and, therefore, prone to chemically interact with

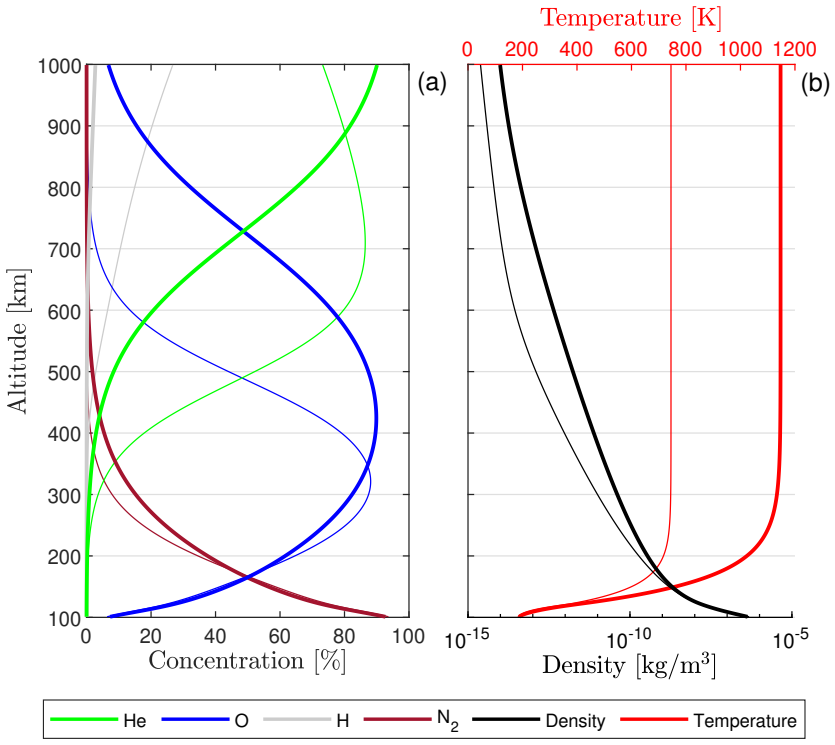


Figure 2.14: Variation with altitude and solar activity of a) the most abundant atmospheric species, and b) the atmospheric density and temperature. Thin and bold lines refer to December 3, 2019 and 2024, corresponding to solar minimum and maximum conditions, respectively. Data computed through the NRLMSISE-00 model over Naples, Italy.

the surface of satellites, giving rise to a process called chemisorption. At the same time, oxygen atoms also interact with a satellite's surface through weak intermolecular Van der Waals forces, in a process termed physisorption. Chemisorption and physisorption allow oxygen atoms to exchange part of their energy with the surface material, resulting in so-called particle energy accommodation [345]. When the energy accommodation between oxygen atoms and the surface is not total, these atoms are scattered in a non-specular, diffuse manner after striking the surface. Other species like Helium, on the other hand, are inert. Therefore, in these cases, energy accommodation hardly occurs, leading to an almost specular reflection [345]. In reality, spacecraft are subject to the impact of a variety of atomic and molecular species whose concentration varies with altitude and solar activity, see Fig. 2.14 [283]. Consequently, it is particularly challenging to describe such phenomena on a macroscopic scale using a single model. In view of this, a number of models have been developed over the years which assume different modalities of particle accommodation.

Although developed more than 60 years ago, the non-hyperthermal model by Sentman [346] is still used in many applications as it allows for closed-form expressions of

the aerodynamic coefficients of surfaces with simple shapes. This model assumes that the particles impinging on the surface reflect diffusely after complete accommodation, that is, leaving at the exact same temperature as the spacecraft surface [344, 346]. The Diffuse Reflection with Incomplete Accommodation (DRIA) model [347] also assumes purely diffused reflection, but unlike Sentman's model, it includes a variable accommodation coefficient to account for non-complete accommodation of gas particles [344, 347]. Among the most well-known models is also the one by Schaaf and Chambre [348], which also provides closed-form expressions of the aerodynamic coefficients [341, 349]. In contrast to the aforementioned models, this model allows for the possibility of non-diffuse reflection by means of two coefficients, namely, the normal and tangential momentum accommodation coefficients, σ_N and σ_T, respectively [344, 348]. Another model that also accounts for different types of reflection through accommodation coefficients is the Cercignani-Lampis-Lord (CLL) model [344, 350]. This model represents a popular choice for high-fidelity simulations of rarefied flow. However, in contrast to the model by Schaaf and Chambre, closed-form expressions for the aerodynamic coefficients may be much more challenging to find and often require the use of approximate relations or numerical simplifications [344]. It should be noted that, in addition to the above, several other GSI models exist, ranging from scattering kernel models to physical and molecular dynamics-informed models [342, 345]. These models, however, will not be discussed here as they can be considerably complex and are designed primarily for in-depth research on GSI.

The above models attain different accuracies depending on the altitude considered. As Sentman's model only accounts for diffuse reflection, it ought to be used only when accommodation is most likely to occur. This situation is found for altitudes approximately below 300 km, where diffusive reflection can account for up to 97% of total reflection [344]. For higher altitudes, on the other hand, particle accommodation occurs to a much lesser extent, making the model inappropriate above 500 km [344]. The DRIA model also accounts for diffuse reflection only. Therefore, its range of validity is also bounded to very low altitudes, similar to Sentman's model [345]. Because the model by Schaaf and Chambre and the CLL model are not constrained to diffuse reflection but also consider quasi- and purely specular reflection, they are more flexible than Sentman's and the DRIA models, and can be employed also for altitudes above 500 km [344]. Their fidelity, however, depends strongly on the knowledge of the accommodation coefficients at such altitudes, which remains largely uncertain to date. Indeed, although some works seem to indicate that particle reflection is more specular than diffusive above 500 km due to the relative abundance of Helium [351, 352], see Fig. 2.14 [283], the nature of GSI at these altitudes remains uncertain because clear evidence from satellite data is still lacking [344, 353]. This uncertainty translates into wide ranges of accommodation coefficients, with recent research indicating $\sigma_N \in [0.6, 0.8]$ and $\sigma_T \in [0.5, 0.9]$ [352]. In turn, the large uncertainty in the variation of the accommodation coefficients with altitude leads to large relative errors in the modeled aerodynamic coefficients, in the order of tens of percent [353, 354]. Furthermore, it should be noted that the above studies consider satellites with simple geometries and relatively smooth, rigid surfaces. Solar sails, on the other hand, are characterized by creases, wrinkles, and a generally time-varying shape. These characteristics therefore add to the uncertainty of the problem and, furthermore, they may make solar

sails reflect gas particles in a much more random, diffuse-like manner than conventional satellites in the same flow regime.

In view of the above, it is evident that the large amount of uncertainty surrounding GSI modeling makes selecting an appropriate model for sailcraft in LEO very challenging. For this reason, in the selection procedure, a limited priority is given to minimizing error margins, whereas computational effort, easiness of implementation and of comparison with other studies are given more priority. The solar sail will be approximated as a rigid flat plate for the sake of simplicity and because it enables analytical formulation of the aerodynamic coefficients. Although the altitudes considered in this dissertation correspond to non-hyperthermal conditions, the hyperthermal free-molecular flow will be considered. Employing this flow model simplifies the expressions for the sailcraft aerodynamic coefficients considerably, while the error committed – in the order of 5-10% [344] – is expected to be dominated by the errors stemming from uncertainty in particle accommodation dynamics. The GSI model by Schaaf and Chambre will be employed because of its ability to describe quasi-specular reflection through simple analytical expressions of the drag and lift coefficients, C_D and C_L, respectively, unlike the CLL model. These coefficients are defined as:

$$\begin{aligned} C_D &= 2\left[\sigma_T + \sigma_N V_R |\cos\alpha_A| + (2-\sigma_N-\sigma_T)\cos^2\alpha_A\right]|\cos\alpha_A| \\ C_L &= 2\left[\sigma_N V_R + (2-\sigma_N-\sigma_T)|\cos\alpha_A|\right]|\cos\alpha_A|\sin\alpha_A \end{aligned} \tag{2.26}$$

with V_R denoting the ratio of the average velocity of the atmospheric particles diffusively reflected by the sail and the sailcraft velocity relative to the atmosphere, and α_A representing the aerodynamic pitch angle between the direction of incoming windflow and the sail normal direction, $\hat{\boldsymbol{n}}$, see Fig. 2.13. Equations 2.26 will be employed with $\sigma_N = \sigma_T = 0.8$ and $V_R = 0.05$, based on Ref. [355]. This choice is motivated by the fact that these values of σ_N and σ_T lie within the suggested ranges indicated in [352] for satellites orbiting in the upper thermosphere, that is, the region of greatest interest for the investigation, wherein sailcraft can fly without deorbiting. Furthermore, these values for σ_N, σ_T, and V_R are also considered by other recent works on solar and drag sails in LEO [219, 220, 356–359], thus facilitating comparison with the results of this dissertation.

2.5.3. TENSOR FORMULATION OF RADIATION PRESSURE ACCELERATION

The general formulation of the radiation pressure acceleration exerted onto a flat sail in the presence of a spherical radiation source was developed by McInnes in Ref. [2]. This formulation is introduced in this section due to its relevance for modeling the SRP and PRP accelerations, discussed in Sections 2.5.4 and 2.5.5, respectively. As detailed in the following subsections, the formulation relies on two angular moments of radiative specific intensity to define different components of the acceleration, which in turn allow to express the total acceleration for both ideal and optical sail models.

2.5.3.1. ANGULAR MOMENTS OF RADIATIVE SPECIFIC INTENSITY

The first and second angular moments of radiative specific intensity are the radiation flux vector, $\boldsymbol{S}$, and radiation pressure tensor, $\underline{\underline{\boldsymbol{P}}}$, respectively, defined as [2]:

$$\boldsymbol{S} = \oint_{4\pi} I_*(\Omega)\,\hat{\boldsymbol{l}}\,d\Omega \tag{2.27}$$

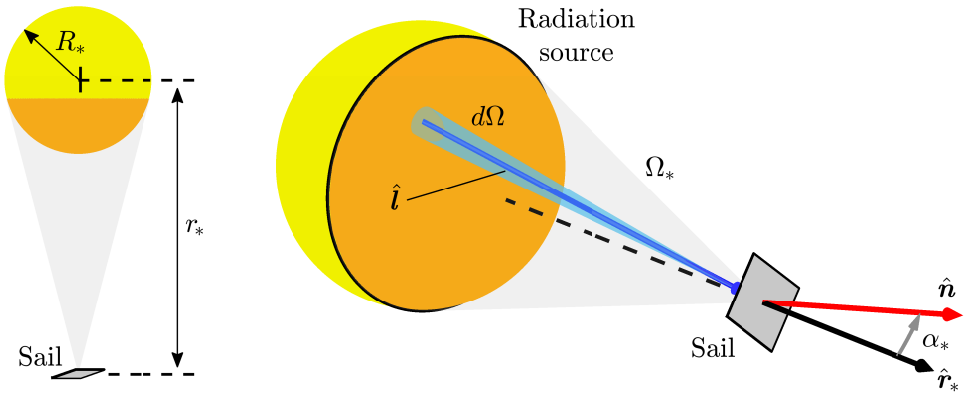


Figure 2.15: Geometry of a spherical radiation source illuminating a flat sail.

$$\underline{\underline{\boldsymbol{P}}} = \frac{1}{c} \oint_{4\pi} I_*(\Omega)\, \hat{\boldsymbol{l}} \otimes \hat{\boldsymbol{l}}\, d\Omega \tag{2.28}$$

where c is the speed of light in vacuum, I_* is the frequency-integrated specific intensity of the radiation source, $d\Omega$ is the solid angle subtending a differential element of surface of the source from the sailcraft's perspective, $\hat{\boldsymbol{l}}$ is the unit vector pointing from said surface element to the sailcraft, see Fig. 2.15, $\hat{\boldsymbol{l}} \otimes \hat{\boldsymbol{l}}$ is a dyadic tensor, and $\otimes$ denotes the tensor product. If the radiation source illuminates only one side of the sail and is fully visible from the sailcraft – that is, the sailcraft is not shadowed by a third, occulting body – then the radiation source subtends a conical solid angle Ω_* as seen from the illuminated side of the sail, see again Fig. 2.15. Also, if the radiation source behaves as a Lambertian, isotropic emitter, then its specific intensity, I_*, does not vary across the solid angle Ω_* and the radiation source appears as a uniformly bright finite disk. Under the above assumptions, Eqs. 2.27 and 2.28 can be rewritten as:

$$\boldsymbol{S} = I_* \int_{\Omega_*} \hat{\boldsymbol{l}}\, d\Omega \tag{2.29}$$

$$\underline{\underline{\boldsymbol{P}}} = \frac{I_*}{c} \int_{\Omega_*} \hat{\boldsymbol{l}} \otimes \hat{\boldsymbol{l}}\, d\Omega \tag{2.30}$$

The utility of the radiation flux vector and radiation pressure tensor lies in the fact that they fully capture the dependence of the radiative input to the sail and the resulting acceleration on the environmental factors, namely, the radiative properties of the source and its distance from the sailcraft. In this way, this formulation allows to decouple the impact of these environmental factors from the sailcraft orientation. This decoupling becomes evident when examining the accelerations for optical and ideal solar sails, discussed in the following subsections.

2.5.3.2. ACCELERATION FOR OPTICAL SAILS

As discussed in Section 2.3.2, the optical sail model accounts for the specular and diffuse reflection, absorption, and emission properties of the sail. When only the front of the sail

is illuminated – a prevalent assumption in the literature – these optical properties can be modeled through the following set of coefficients:

$$\boldsymbol{oc} = \left[\hat{r}_f,\ s_f,\ B_f,\ \varepsilon_f,\ \hat{r}_b,\ s_b,\ B_b,\ \varepsilon_b\right] \tag{2.31}$$

where $\hat{r}$, s, B, and ε represent the reflectivity, specular reflection coefficient, non-Lambertian reflection coefficient, and emissivity of the sail, respectively, with the subscripts "f" and "b" indicating whether the optical coefficient refers to the front or back of the sail.

The acceleration component originating from radiation absorbed by the sail is given by [2]:

$$\boldsymbol{a}_{*,abs} = \frac{1-\hat{r}_f}{\sigma}\underline{\underline{\boldsymbol{P}}} \cdot \hat{\boldsymbol{n}} \tag{2.32}$$

where $(1-\hat{r}_f)$ indicates the fraction of all photons reaching the sail that get absorbed, $\hat{\boldsymbol{n}}$ is the normal direction from the back of the sail, and $\cdot$ denotes tensor contraction. Notably, because radiation is assumed to reach the front of the sail, $\hat{\boldsymbol{n}}$ has a positive component along the radiation source-to-sailcraft direction, $\hat{\boldsymbol{r}}_*$, see Fig. 2.15. Furthermore, due to the symmetry of the tensor $\underline{\underline{\boldsymbol{P}}}$, see Eq. 2.30, $\boldsymbol{a}_{*,abs}$ always points along $\hat{\boldsymbol{r}}_*$.

Once absorbed, radiation is re-emitted from both sides of the sail to maintain thermal balance, producing the following acceleration component:

$$\boldsymbol{a}_{*,em} = \frac{1-\hat{r}_f}{\sigma}\frac{\varepsilon_f B_f - \varepsilon_b B_b}{\varepsilon_f + \varepsilon_b}\frac{\boldsymbol{S}\cdot\hat{\boldsymbol{n}}}{c}\hat{\boldsymbol{n}} \tag{2.33}$$

Equation 2.33 assumes that the sail irradiates uniformly on each side, so that the net change in momentum points parallel or antiparallel to the sail normal direction, $\hat{\boldsymbol{n}}$, depending on the optical properties of the front and back of the sail. Furthermore, it is of note that the term $\left(1-\hat{r}_f\right)(\boldsymbol{S}\cdot\hat{\boldsymbol{n}})$ captures the dependency of the acceleration on the intercepted flux of radiation absorbed by the sail before being reradiated.

The fraction of photons that are specularly reflected by the sail is given by $\hat{r}_f s_f$. These photons transfer an equal amount of momentum upon striking and reflecting from the surface, resulting in an acceleration that is directed along the sail normal direction, $\hat{\boldsymbol{n}}$. For this reason, the corresponding acceleration component assumes the following form involving double contraction of the radiation pressure tensor, $\underline{\underline{\boldsymbol{P}}}$, along the direction $\hat{\boldsymbol{n}}$:

$$\boldsymbol{a}_{*,spec} = 2\frac{\hat{r}_f s_f}{\sigma}\left(\hat{\boldsymbol{n}}\cdot\underline{\underline{\boldsymbol{P}}}\cdot\hat{\boldsymbol{n}}\right)\hat{\boldsymbol{n}} \tag{2.34}$$

The fraction of photons that are diffusively reflected is $\hat{r}_f(1-s_f)$. These photons also transfer momentum upon impact with the sail and when leaving its surface. Unlike specular reflection, however, the net acceleration resulting from these momentum transfers does not point along the normal direction. To account for this, the total acceleration is therefore divided into two sub-components:

$$\boldsymbol{a}_{*,diff} = \frac{\hat{r}_f(1-s_f)}{\sigma}\underline{\underline{\boldsymbol{P}}}\cdot\hat{\boldsymbol{n}} + \frac{\hat{r}_f(1-s_f)B_f}{\sigma}\frac{\boldsymbol{S}\cdot\hat{\boldsymbol{n}}}{c}\hat{\boldsymbol{n}} \tag{2.35}$$

The first and second terms on the right-hand side of the Eq. 2.35 indicate the acceleration caused by photons striking the sail and scattering diffusively from its surface, respectively.

Importantly, the term $B_f\,(\boldsymbol{S}\cdot\hat{\boldsymbol{n}})$ captures the dependency of the acceleration on the fraction of diffusively reflected radiation effectively converted into net normal acceleration, whose magnitude is driven solely by the radiation flux intercepted by the sail. Finally, summing the acceleration components from Eqs. 2.32-2.35, the total acceleration exerted on the sail is found:

$$\boldsymbol{a}_* = \frac{1}{\sigma}\left\{(1-\hat{r}_f s_f)\underline{\underline{\boldsymbol{P}}}\cdot\hat{\boldsymbol{n}} + 2\hat{r}_f s_f\left(\hat{\boldsymbol{n}}\cdot\underline{\underline{\boldsymbol{P}}}\cdot\hat{\boldsymbol{n}}\right)\hat{\boldsymbol{n}} + \left[\hat{r}_f(1-s_f)B_f + (1-\hat{r}_f)\frac{\varepsilon_f B_f - \varepsilon_b B_b}{\varepsilon_f+\varepsilon_b}\right]\frac{\boldsymbol{S}\cdot\hat{\boldsymbol{n}}}{c}\hat{\boldsymbol{n}}\right\} \tag{2.36}$$

As shown in Eq. 2.36, the radiation pressure tensor, $\underline{\underline{\boldsymbol{P}}}$, and flux vector, $\boldsymbol{S}$, provide a direct way to map any sail normal direction, $\hat{\boldsymbol{n}}$, to the corresponding radiation pressure acceleration. This mapping, however, requires solving the integrals arising from the contractions of the tensor $\underline{\underline{\boldsymbol{P}}}$ and vector $\boldsymbol{S}$ along the direction $\hat{\boldsymbol{n}}$. As discussed in the following sections, this process is often circumvented in the literature by assuming radiation to reach the sail in parallel rays, effectively treating the radiation source as infinitely distant.

2.5.3.3. ACCELERATION FOR IDEAL SAILS

The radiation pressure acceleration for an ideal sail can be found from the optical acceleration model in Eq. 2.36 assuming perfect specular reflection properties, that is, $\hat{r}_f = s_f = 1$. Substituting these optical coefficients, the following expression is found:

$$\boldsymbol{a}_* = \frac{2}{\sigma}\left(\hat{\boldsymbol{n}}\cdot\underline{\underline{\boldsymbol{P}}}\cdot\hat{\boldsymbol{n}}\right)\hat{\boldsymbol{n}} \tag{2.37}$$

When the sail is oriented with its normal along the source-to-sailcraft direction, $\hat{\boldsymbol{r}}_*$, the symmetry of the source-sailcraft geometry allows to reduce Eq. 2.37 to the following expression (derived in Appendix A):

$$\boldsymbol{a}_* = \frac{2}{\sigma}P_{FD}\hat{\boldsymbol{r}}_* \tag{2.38}$$

where

$$P_{FD} = \frac{2}{3}\frac{\pi I_*}{c}\left\{1-\left[1-\left(\frac{R_*}{r_*}\right)^2\right]^{\frac{3}{2}}\right\} \tag{2.39}$$

represents the so-called finite-disk radiation pressure acting on a perfectly absorbing sail, R_* is the radius of the radiation source, and r_* is the distance between the geometric center of the source and the sailcraft. Although Eq. 2.38 technically holds true only when the sail normal direction, $\hat{\boldsymbol{n}}$, points towards the radial direction $\hat{\boldsymbol{r}}_*$, this equation is often employed in the literature also when these directions form a non-zero pitch angle, α_*, see Fig. 2.15. In this case, the following adapted form of Eq. 2.38 is used:

$$\boldsymbol{a}_{*,FD} = \frac{2}{\sigma}P_{FD}\cos^2\alpha_*\,\hat{\boldsymbol{n}} \tag{2.40}$$

The $\cos^2\alpha_*$ scaling factor represents an engineering simplification to capture the dependency of the acceleration magnitude on the sailcraft orientation. The simplification stems from the fact that such a dependency on the pitch angle is achieved only when light rays

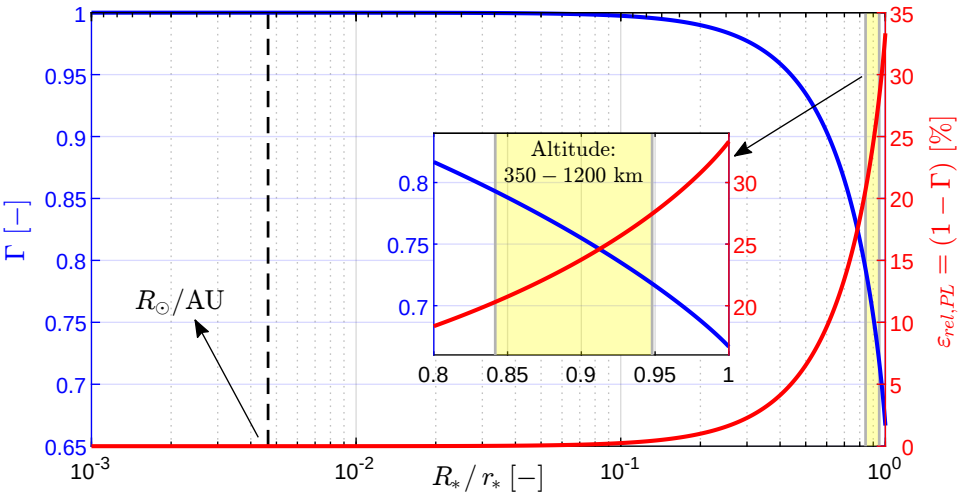


Figure 2.16: Variation of the finite-disk correction factor, Γ, and of the relative error, $\varepsilon_{rel,PL} = (1-\Gamma)$, with the adimensional inverse of the distance from the source, (R_*/r_*). Also indicated are the specific values for the average Sun-Earth distance and a range of LEO altitudes.

are perfectly aligned along $\hat{\boldsymbol{r}}_*$, that is, when the radiation source appears point-like rather than as a finite disk. Indeed, in this case, $(R_*/r_*) \to 0$ and Eq. 2.40 reduces to:

$$\boldsymbol{a}_{*,PL} = \frac{2}{\sigma} P_{PL} \cos^2\alpha_* \, \hat{\boldsymbol{n}} \tag{2.41}$$

with P_{PL} the point-like radiation pressure [2]:

$$P_{PL} = \frac{\pi I_*}{c} \left(\frac{R_*}{r_*}\right)^2 \tag{2.42}$$

It is important to note that the finite-disk and point-like radiation pressures and acceleration magnitudes for the ideal sail model can be related as follows [2]:

$$P_{FD} = \Gamma P_{PL} \tag{2.43}$$

$$\left\| \boldsymbol{a}_{*,FD} \right\| = \Gamma \left\| \boldsymbol{a}_{*,PL} \right\| \tag{2.44}$$

where the finite-disk correction factor Γ is given by:

$$\Gamma = \frac{P_{FD}}{P_{PL}} = \frac{2}{3} \left(\frac{r_*}{R_*}\right)^2 \left\{ 1 - \left[1 - \left(\frac{R_*}{r_*}\right)^2 \right]^{\frac{3}{2}} \right\} \tag{2.45}$$

This factor gives a measure of the "point-likeness" of the radiation source, as $\varepsilon_{rel,PL} = (1-\Gamma)$ represents the relative error (both in radiation pressure and corresponding acceleration magnitude) committed considering the point-like model instead of the finite-disk model. The variations in Γ and $\varepsilon_{rel,PL}$ with the distance from the source are displayed in Fig. 2.16.

As discussed in the following sections, the finite-disk and point-like acceleration models given in Eqs. 2.40 and 2.42 are commonly used to represent the SRP and PRP accelerations of sailcraft. However, the assumptions these models rely on introduce approximations which reduce accuracy, especially for the PRP acceleration.

2.5.4. SOLAR RADIATION PRESSURE ACCELERATION

The SRP acceleration depends on the type of reflection model considered for the sail. Because in this dissertation two models will be considered, namely, the ideal and optical models, see Section 2.3.2, the corresponding SRP accelerations will be discussed separately in the following subsections.

2.5.4.1. IDEAL MODEL

The SRP acceleration of an ideal, perfectly reflecting sail can be defined through the tensor formulation described in Section 2.5.3.3. At large Sun-sailcraft distances, $r_\odot$, the presence of sunspots, faculae and solar limb darkening can be reasonably neglected. This allows to approximate the Sun as an isotropic emitter with constant specific intensity equal to [2]:

$$I_\odot = \frac{S_{TSI}}{\pi}\left(\frac{1\,\text{AU}}{R_\odot}\right)^2 \tag{2.46}$$

where $R_\odot = 6.95508 \cdot 10^5$ km denotes the mean solar radius [232] and S_{TSI} is the TSI, assumed constant in this work, see Section 2.4.3.1. The point-like and finite-disk acceleration models described by Eqs. 2.39-2.42 can then be used by replacing I_* with $I_\odot$ in Eq. 2.46, and R_*, r_*, and α_* with $R_\odot$, $r_\odot$, and $\alpha_\odot$, respectively, where $\alpha_\odot$ denotes the SRP pitch angle between the Sun-to-sailcraft direction, $\hat{\boldsymbol{r}}_\odot = \boldsymbol{r}_\odot / \|\boldsymbol{r}_\odot\|$, and the sail normal direction with positive component along $\hat{\boldsymbol{r}}_\odot$, $\hat{\boldsymbol{n}}$. Furthermore, the shadow factor, ν, shall be included to account for eclipses, see Section 2.4.3.3. With the above in mind, the point-like SRP acceleration can be expressed as:

$$\boldsymbol{a}_{SRP} = \nu \frac{2}{\sigma} P_{PL} \cos^2\alpha_\odot \, \hat{\boldsymbol{n}} \tag{2.47}$$

where the point-like radiation pressure, P_{PL}, is related to the solar flux, S, by:

$$P_{PL} = \frac{S}{c} \tag{2.48}$$

Substituting Eq. 2.48 into Eq. 2.47 and assuming the solar flux is equal to the TSI, $S = S_{TSI}$, see Section 2.4.3.2, the SRP acceleration can then be rewritten as:

$$\boldsymbol{a}_{SRP} = \nu a_c \cos^2\alpha_\odot \, \hat{\boldsymbol{n}} \tag{2.49}$$

where

$$a_c = \frac{2 S_{TSI}}{c\sigma} \tag{2.50}$$

is the SRP characteristic acceleration, which represents the maximum SRP acceleration achievable by an ideal solar sail at 1 AU from the Sun and is commonly used as a measure

of sailcraft performance. Similar to Eq. 2.47 for the point-like case, the finite-disk SRP acceleration can be expressed as:

$$\boldsymbol{a}_{SRP} = \nu \frac{2}{\sigma} P_{FD} \cos^2\alpha_\odot \, \hat{\boldsymbol{n}} \tag{2.51}$$

where the finite-disk radiation pressure, P_{FD}, can be found from Eqs. 2.43 and 2.45 substituting $R_\odot$ and $r_\odot$ for R_* and r_*, respectively.

In Chapters 3, 5 and 6 of this dissertation – where ideal sails are considered – the SRP acceleration will be modeled through the point-like model in Eq. 2.49 for easiness of implementation and because, compared to the finite-disk acceleration model, it introduces negligible errors for the large Sun-sailcraft distances considered in the investigation. Indeed, the Sun attains an angular size of approximately 0.5 deg as seen from LEO. Therefore, it appears almost as a point source, justifying the cosine-squared approximation of the variation of the acceleration with the pitch angle, $\alpha_\odot$. Furthermore, as shown in Fig. 2.16, the relative error committed considering the point-like pressure instead of the finite-disk pressure, $\varepsilon_{rel,PL}$, is minimal. Indeed, for the average Earth-Sun distance, $r_\odot = 1\,\text{AU}$, this error is of only $5.4 \cdot 10^{-4}\%$.

It is of note that Eq. 2.49 can be resolved in the ECI frame, O_I, by defining the sail normal direction, $\hat{\boldsymbol{n}}$, in this frame, and by expressing the Sun-to-sailcraft vector and corresponding direction in frame O_I using the transformation described in Eqs. 2.8 and 2.9. In this way, the resulting SRP acceleration term, $\boldsymbol{a}_{SRP}$, can be inserted into the equations of motion given in Eq. 2.1.

2.5.4.2. OPTICAL MODEL

The model for the SRP acceleration of an optical sail was developed by McInnes in Ref. [2] and can be retrieved from the tensor formulation described in Section 2.5.3.2. Specifically, assuming that only the front of the sail is illuminated, the SRP acceleration can be defined as in Eq. 2.36, substituting $I_\odot$ for I_* in the definition of the radiation pressure tensor, $\underline{\underline{\boldsymbol{P}}}$, and flux vector, $\boldsymbol{S}$, see Eqs. 2.29 and 2.30. Further assuming that the Sun appears as a point-like radiation source and solving the integrals arising from the contractions of $\underline{\underline{\boldsymbol{P}}}$ and $\boldsymbol{S}$ along $\hat{\boldsymbol{n}}$, the following definition of the SRP acceleration is found [2]:

$$\boldsymbol{a}_{SRP} = \boldsymbol{a}_{SRP,n} + \boldsymbol{a}_{SRP,t} \tag{2.52}$$

where $\boldsymbol{a}_{SRP,n}$ and $\boldsymbol{a}_{SRP,t}$ are the components normal and tangential to the sail plane, respectively, defined as [2]:

$$\boldsymbol{a}_{SRP,n} = \nu \frac{a_c}{2} \left[\left(1+\hat{r}_f s_f\right) \cos^2\alpha_\odot + \left(1-s_f\right) \hat{r}_f B_f \cos\alpha_\odot + \left(1-\hat{r}_f\right) \frac{\varepsilon_f B_f - \varepsilon_b B_b}{\varepsilon_f + \varepsilon_b} \cos\alpha_\odot \right] \hat{\boldsymbol{n}} \tag{2.53}$$

$$\boldsymbol{a}_{SRP,t} = \nu \frac{a_c}{2} \left(1-\hat{r}_f s_f\right) \cos\alpha_\odot \sin\alpha_\odot \, \hat{\boldsymbol{t}} \tag{2.54}$$

with the tangential direction $\hat{\boldsymbol{t}}$ pointing along the intersection of the sail plane with the plane formed by $\hat{\boldsymbol{n}}$ and $\hat{\boldsymbol{r}}_\odot$, with a positive component along $\hat{\boldsymbol{r}}_\odot$, that is:

$$\hat{\boldsymbol{t}} = \hat{\boldsymbol{n}} \times \frac{\hat{\boldsymbol{r}}_\odot \times \hat{\boldsymbol{n}}}{\| \hat{\boldsymbol{r}}_\odot \times \hat{\boldsymbol{n}} \|} \tag{2.55}$$

The above SRP acceleration model will be employed in Chapters 4, 5, and 7, where optical solar sails are considered. It is important to note that although solar sails are commonly coated in highly reflective material only on their front side, in real-life missions the back of the sail may also get illuminated. Because the optical SRP acceleration model cannot account for this possibility, an extension of the model will be presented in Chapter 5. As will be discussed, this extended model incorporates information on the reflectivity and specular reflection coefficient of the back of the sail which are not required in McInnes' formulation of the model, due to the assumption of a constantly dark backside. In all chapters in the remainder of this dissertation except Chapter 5, the sailcraft attitude control is designed to explicitly forbid the back of the sail from being illuminated by solar radiation. Therefore, in these chapters, McInnes' model will be used without loss of generality.

Finally, it is of note that inserting the SRP acceleration term, $\boldsymbol{a}_{SRP}$, into the equations of motion, see Eq. 2.1, requires resolving Eqs. 2.52-2.55 in the ECI frame, O_I. Similar to the ideal case in Section 2.5.4.1, this can be achieved by expressing the sail normal direction, $\hat{\boldsymbol{n}}$, directly in the ECI frame, whereas the Sun-to-sailcraft direction can be expressed in frame O_I using Eqs. 2.8 and 2.9.

2.5.5. PLANETARY RADIATION PRESSURE ACCELERATION

To this date, research on the accelerations induced by planetary radiation and their impact on the orbital dynamics has been conducted mainly for conventional spacecraft of various geometries, rather than for solar sails. Historically, early studies on PRP-acceleration modeling were mostly analytical in nature, as they relied on the analytical representations of the Earth's radiation field discussed in Section 2.4.4. The resulting acceleration models – primarily developed within the framework of general perturbation methods – typically involved extensive derivations and series expansions, leading either to truncated-series representations of the PRP acceleration or to semi-analytical expressions requiring numerical evaluation [326, 328, 329, 334, 336]. In many cases, these works considered spherical satellites, with a view to providing preliminary results and simplifying the treatment [324, 326–328]. However, when considering a flat plate – which corresponds to a far more challenging geometry and the shape model adopted in this dissertation to represent solar sails, see Section 2.3.1 – no closed-form analytical expression of the PRP acceleration was found [334, 335]. Since the 1980s, advancements in computational power have made numerical PRP acceleration models increasingly more feasible and favored over analytical models [237, 360–363]. Nevertheless, they remain computationally expensive to this day. Consequently, they are mostly used only for specific applications requiring high accuracy – such as precise orbit determination – and remain impractical for mission analysis.

When focusing on research on PRP acceleration in the context of solar sailing, the available literature is extremely limited and relies totally on the use of simplistic models [222, 223]. These studies assume the Earth to have constant albedo and blackbody radiation flux, the sail to be perfectly reflecting (ideal), and, most importantly, they employ the finite-disk radiation pressure model presented in Section 2.5.3.3. In these works,

the PRP acceleration is therefore defined based on Eqs. 2.39 and 2.40 as:

$$\boldsymbol{a}_{PRP} = \frac{4}{3}\frac{\pi I_{\oplus}}{c\sigma}\left\{1-\left[1-\left(\frac{R}{r}\right)^2\right]^{\frac{3}{2}}\right\}\cos^2\alpha_{\oplus}\,\hat{\boldsymbol{n}} \tag{2.56}$$

where $I_{\oplus}$ is the frequency-integrated terrestrial specific intensity – which is determined based on the albedo and blackbody radiation flux – $\hat{\boldsymbol{n}}$ is the sail normal direction with positive component along $\hat{\boldsymbol{r}}$, and $\alpha_{\oplus}$ is the planetary pitch angle between $\hat{\boldsymbol{r}}$ and $\hat{\boldsymbol{n}}$.

The choice to adopt the finite-disk model instead of the point-like model is motivated by the large relative error associated with the latter, $\varepsilon_{rel,PL}$, which can exceed 20% for LEO altitudes, see Fig. 2.16. Nevertheless, despite its improved accuracy, the finite-disk model still relies on simplifying assumptions that limit its fidelity. In particular, the primary source of inaccuracy is the assumption that radiation reaches the sail in parallel rays, see Section 2.5.3.3. While this approximation is reasonable for the Sun, it becomes inappropriate for the Earth, which subtends an angle of 120 deg or even more as seen from a satellite in LEO. To preliminarily assess the corresponding error introduced in the model, the PRP acceleration can be formulated from the integral definition in Eq. 2.37, removing the assumption of parallelism of light rays and considering only relatively small planetary pitch angles, $\alpha_{\oplus}$, such that the Earth is fully visible from one side of the sail. Using this approach, the following expression (derived in Appendix A) is found:

$$\boldsymbol{a}_{PRP} = \frac{4}{3}\frac{\pi I_{\oplus}}{c\sigma}\left\{1-\left[1-\left(\frac{R}{r}\right)^2\right]^{\frac{3}{2}}\right\}\cos^2\alpha_{\oplus}\,\hat{\boldsymbol{n}} + \frac{2}{3}\frac{\pi I_{\oplus}}{c\sigma}\left\{2-\left[2+\left(\frac{R}{r}\right)^2\right]\sqrt{1-\left(\frac{R}{r}\right)^2}\right\}\sin^2\alpha_{\oplus}\,\hat{\boldsymbol{n}} \tag{2.57}$$

Comparison of Eqs. 2.56 and 2.57 makes evident that employing the parallel-rays assumption through the finite-disk model results in the second term on the right-hand side of Eq. 2.57 being neglected. As discussed in Section 2.5.3, this term is equal to zero when the sail normal is oriented radially with respect to the radiation source – that is, when $\hat{\boldsymbol{n}} = \hat{\boldsymbol{r}}$ and $\alpha_{\oplus} = 0$ – thus making Eq. 2.56 exact. Conversely, for increasing $\alpha_{\oplus}$, the magnitude of this term rises steeply. The relative error in acceleration magnitude committed by the finite-disk model is found as the ratio of the magnitudes of the two terms on the right-hand side of Eq. 2.57, namely:

$$\varepsilon_{rel,FD} = \frac{1}{2}\frac{2-\left[2+\left(\frac{R}{r}\right)^2\right]\sqrt{1-\left(\frac{R}{r}\right)^2}}{1-\left[1-\left(\frac{R}{r}\right)^2\right]^{\frac{3}{2}}}\tan^2\alpha_{\oplus} \tag{2.58}$$

The variation in relative error, $\varepsilon_{rel,FD}$, for different combinations of sailcraft altitudes, $h = r - R$, and planetary pitch angles, $\alpha_{\oplus}$, is illustrated in Fig. 2.17. As can be seen, relative errors of up to 10% can be found even for moderate $\alpha_{\oplus}$ below 30 deg, for the LEO altitudes considered in this dissertation. It is important to note that, for larger pitch angles, the sail receives planetary radiation on both sides. Because this effect is not captured by the finite-disk model, it constitutes an additional source of inaccuracy, and the errors may therefore become even larger as $\alpha_{\oplus}$ increases.

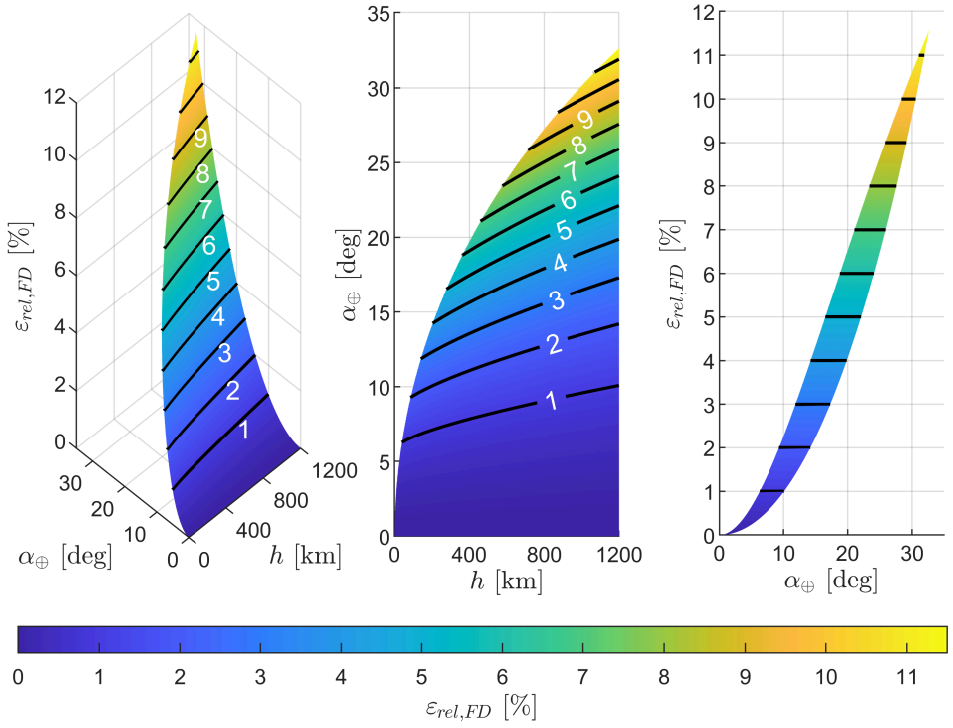


Figure 2.17: Relative errors on the magnitude of the PRP acceleration as found in the literature [222, 223] and based on the integral formulation by McInnes [2], for different combinations of sailcraft altitudes, h, and planetary pitch angles, $\alpha_\oplus$.

Another source of inaccuracy in the only known study that considers the effect of albedo radiation on the solar-sail dynamics [222] lies in the modeling of the variation of albedo radiative output across the Earth. Indeed, while in reality albedo radiation flux depends on the incidence angle of sunlight onto the Earth surface – that is, the Sun-*Earth surface*-sailcraft angle – the cited work approximates this angle with the Sun-*Earth center*-sailcraft angle. Similar to the finite-disk model, this approximation is increasingly more valid for larger distances from Earth. However, in LEO, it leads to inaccuracies.

Based on the above considerations and to minimize the sources of approximation introduced by the finite-disk PRP acceleration model, a new PRP acceleration model will be presented in this dissertation. The model will first be derived for ideal, perfectly reflecting sails in Chapter 3 and then extended to optical solar sails in Chapter 4. In addition to the large errors introduced by the finite-disk acceleration model, the choice of developing a new PRP acceleration model is motivated by preliminary studies indicating that PRP can reach values in the order of 20% of SRP [222]. As a consequence, the corresponding PRP acceleration is expected to have a significant impact on the sailcraft dynamics, therefore warranting its accurate representation.

Finally, consistent with the SRP and aerodynamic accelerations, the PRP acceleration will be expressed directly in the ECI frame, $\mathcal{O}_I$, to enable its insertion into the equations

of motion, see Eq. 2.1. As discussed in the next chapter and suggested by Eq. 2.57, this can be achieved by expressing both the sail normal direction, $\hat{\boldsymbol{n}}$, and radial direction, $\hat{\boldsymbol{r}}$, within this same frame.

2.6. TRAJECTORY OPTIMIZATION

As discussed in Chapter 1, to systematically assess the maneuverability of Earth-bound solar sails, the ability to modify their orbit both in the in-plane and out-of-plane directions will be investigated by means of orbit-raising and inclination-changing maneuvers, respectively. To enable such maneuvers, the corresponding solar-sail attitude control laws need to be determined. From an optimization standpoint, this problem corresponds to finding the evolution of the optimal control vector, $\boldsymbol{u}(t)$, over time, t, such that the following cost functional is minimized [364]:

$$J = \int_{t_0}^{t_f} \mathcal{L}(\boldsymbol{u}(t), \boldsymbol{x}(t), t)\, dt \tag{2.59}$$

where t_0 and t_f denote fixed initial and final times, $\boldsymbol{x}(t)$ represents the sailcraft state vector subject to the dynamics in Eq. 2.1 and with known initial condition $\boldsymbol{x}(t_0) = \boldsymbol{x}_0$, and $\mathcal{L}$ denotes the Lagrangian, defined as the negative rate of change of the orbital semi-major axis or inclination, that is, $(-da/dt)$ and $(-di/dt)$, for orbit-raising and inclination-changing maneuvers, respectively. It is important to note that solar sails may be controlled only by varying their orientation in space, which is uniquely identified by the sail normal direction, $\hat{\boldsymbol{n}}$. Therefore, in the above optimization problem, the time evolution of the control vector corresponds to the time evolution of the sail normal direction, $\boldsymbol{u}(t) = \hat{\boldsymbol{n}}(t)$, and, accordingly, the optimal control problem is solved by finding an optimal solar-sail attitude profile. The class of optimal control problems outlined above may be solved by means of different optimization methods, which are discussed hereinafter.

Indirect methods address the optimization problem analytically, reformulating it as a two-point boundary-value problem [365–367]. However, these methods require the dynamics to be sufficiently smooth to enable analytical treatment – a requirement that becomes challenging to satisfy when accounting for aerodynamics, since atmospheric density is computed through numerical models, see Section 2.4.2.1. The mathematical formulation can also become very involved when high-fidelity dynamics are considered and difficulties can arise if eclipses are present, as they introduce (quasi-) discontinuities in the sailcraft dynamics. Although the latter issue can be addressed by splitting the trajectory into arcs, enforcing continuity as constraints, and adopting a multiple-shooting approach, the other intrinsic difficulties of indirect methods remain nontrivial to solve.

A widely employed alternative to indirect methods is provided by direct transcription methods, which discretize the state and control histories, $\boldsymbol{x}(t)$ and $\boldsymbol{u}(t)$, to solve the resulting nonlinear programming optimization problem [368, 369]. Although generally more robust than indirect methods, direct methods can require substantial computational effort. Similar to direct transcription methods, pseudospectral methods also convert the continuous optimization problem into a set of algebraic equations, although discretizing the problem using high-order polynomials passing through collocation points [370–372]. Consequently, these methods can also lead to numerical difficulties when transitioning into or out of eclipse, as the dynamics exhibit (quasi-)discontinuities which are not

well captured by polynomial interpolants. More recently, differential dynamic programming [373–375] has been increasingly explored for low-thrust trajectory optimization showing promising results, primarily because the method models the dynamics and cost function locally in a quadratic fashion, thereby enabling rapid convergence and remaining computationally efficient as the problem dimension grows. Nevertheless, differential dynamic programming also requires the dynamics to be analytical and, crucially, it requires access to their second-order derivatives. While these derivatives can be approximated numerically via methods like finite differencing, such approaches demand considerable computational effort.

It should be noted that all the methods discussed above are *local* optimization methods and, as such, they require a sufficiently good initial guess to ensure convergence to the true optimal solution. To generate such an initial guess, global optimization methods can be employed. In the context of solar sailing, these global methods have often been implemented through evolutionary algorithms [376] in a variety of forms, e.g., combined with shape-based methods [377, 378] and pseudospectral methods [379], or employed for reinforcement-learning optimization [380]. By definition, global optimization methods can autonomously explore the solution space, therefore proving effective for virtually any orbital scenario. Their performance, however, depends strongly on the optimization settings, which need to be appropriately tuned for each such scenario.

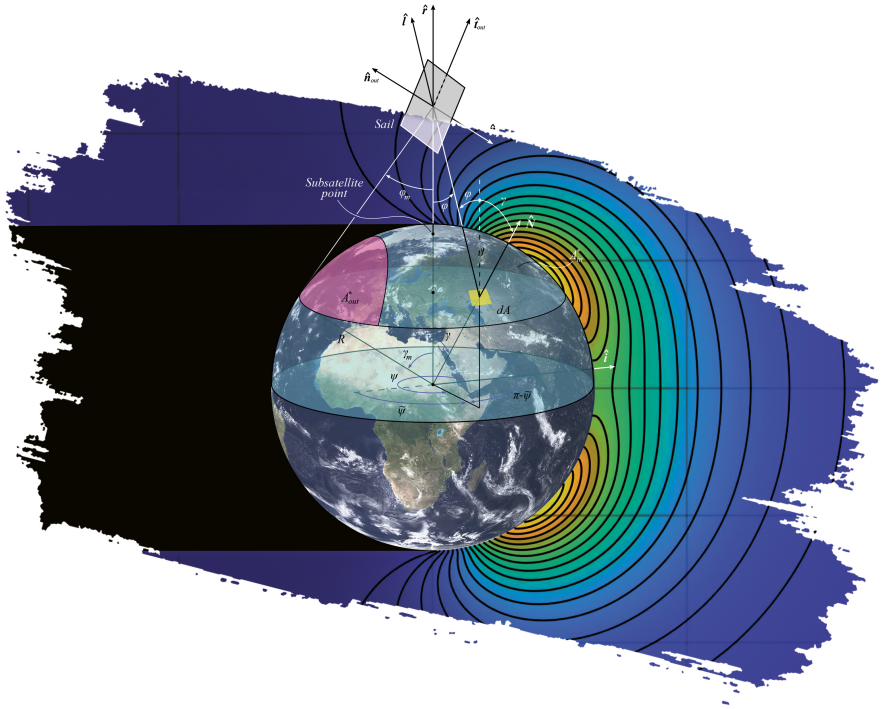
Finally, another popular strategy for the optimization of solar-sail trajectories is the formulation of locally optimal steering laws, based on the algorithm devised by McInnes [2]. These steering laws are defined by determining, at each time instant, the sailcraft attitude that maximizes the acceleration along a prescribed optimal thrust direction, which is typically derived analytically through the Lagrange planetary equations [2] or semi-analytically through other approaches [204, 206, 381, 382], depending on the application. As a result, the method is only locally optimal because the control at a given time is computed without leveraging information about the full trajectory [2]. Nevertheless, this method is particularly attractive because it does not require an initial guess, unlike many other locally optimal solvers. Furthermore, it is relatively easy to implement, does not require tuning of optimization settings, and is particularly robust to variations in the considered orbital scenarios. The locally optimal steering-law algorithm has been used extensively for maximizing the rate of change of orbital elements – similarly to the optimization problem introduced above – while employing solar-sail dynamics that include only gravity and ideal SRP [2, 203, 204, 382]. Notably, in this setting, the algorithm becomes fully analytical and typically yields solutions that are close to globally optimal [383], therefore making it particularly suited for the investigation at hand while requiring extremely low computational effort. It should be noted that, to the author's knowledge, the steering-law algorithm has never been employed for higher-fidelity dynamics that include additional attitude-dependent accelerations beyond the SRP acceleration.

In view of the above considerations, in this dissertation the locally optimal steering-law approach will be adopted to assess the in-plane and out-of-plane maneuverability of solar sails. This choice is driven primarily by the need for a computationally efficient method that can perform a large number of simulations covering a wide range of orbital conditions while retaining robustness. Depending on the analysis, the steering-law algorithm will be employed in its original form formulated by McInnes [2] for ideal

SRP acceleration, or it will be adapted to support other types of attitude-dependent accelerations. These extensions to McInnes' steering-law algorithm will be formulated in Chapters 6 and 7 through novel optimization frameworks. Specifically, Chapter 6 will present steering-law algorithms accounting for the aerodynamic acceleration and the combined effect of ideal SRP and aerodynamic accelerations, whereas, in Chapter 7, an algorithm considering the combined influence of the optical SRP, optical PRP, and aerodynamic accelerations will be developed.

3

A New Model for the Planetary Radiation Pressure Acceleration for Solar Sails



ABSTRACT

Solar sailing is a propellantless propulsion method that takes advantage of solar radiation pressure to generate thrust. The last decades have seen the launch of several solar-sail missions to demonstrate the technology's potential for space exploration and exploitation, the most recent being NASA's ACS3 and Gama's Alpha sailcraft, and even more missions are scheduled for launch in the near future. Most of these sailcraft have flown – or will fly – in low-Earth orbit, where the planetary radiation pressure is strong (up to approximately 20% of the solar radiation pressure). However, studies on the perturbing accelerations produced by the Earth's albedo and blackbody radiation have only been conducted to a very limited first-order extent. This chapter therefore provides a novel, detailed analytical model for these perturbing accelerations, valid for double-sided perfectly reflecting solar sails. The underlying assumptions of the model are presented and its full derivation is described. A thorough analysis of the blackbody and albedo radiation pressure accelerations is conducted for a variety of orbital conditions and Sun-Earth-sailcraft configurations. In order to validate the model and determine its accuracy, a comparison with the state of the art (the finite-disk radiation source model and a high-fidelity numerical model) is provided. Ultimately, a variety of analyses to quantify the effect of Earth's albedo and blackbody radiation on the maneuvering capabilities of solar sails is presented, using the orbit of the ACS3 mission as reference scenario. In these analyses, the planetary radiation pressure acceleration is uncontrolled and, therefore, it acts as a source of disturbance on the solar-sail maneuvering capabilities. The results show that, for an orbit-raising steering law, planetary radiation pressure can cause the achievable altitude gain to reduce to only 76% of that obtained in a hypothetical scenario where planetary radiation pressure is not accounted for. Similarly, for an inclination-changing steering law, the inclination gain can reduce to 80% of that achieved when planetary radiation pressure is not considered. These results highlight the non-negligible effect of uncontrolled planetary radiation pressure acceleration on the maneuvering capabilities of solar sails in LEO.

The content of this chapter has been published in the *Journal of Guidance, Control, and Dynamics*, see Ref. [384]: Livio Carzana, Pieter Visser, and Jeannette Heiligers. "A New Model for the Planetary Radiation Pressure Acceleration for Solar Sails". In: *Journal of Guidance, Control, and Dynamics* 47.8 (August 2024), pp.1674–1687. DOI: https://doi.org/10.2514/1.G007668

The dataset supporting the findings of this chapter is available in the *4TU Data Repository*, see Ref. [385]: Livio Carzana, Pieter Visser, and Jeannette Heiligers. *Data underlying the publication: "A New Model for the Planetary Radiation Pressure Acceleration for Solar Sails"*. 4TU.ResearchData, Dataset version 1, Apr. 2026. DOI: https://doi.org/10.4121/b87209ec-b247-428c-a62c-fb50fe218d5c.v1

Cover graphic by Vincenzo Bortone. The illustration shows the geometry used to determine the planetary radiation-pressure acceleration acting on a sailcraft and the maximum achievable acceleration due to albedo radiation pressure around the Earth.

3.1. INTRODUCTION

Solar sailing is a low-thrust propulsion method that has raised increasing interest over the last few decades, mainly because of its propellantless nature [2]. In light of its enabling potential for a wide variety of mission scenarios [107, 386], extensive research has been conducted on its dynamics and trajectory optimization. Although most of these studies focused on heliocentric flight regimes [154, 166, 381, 386, 387], the majority of solar-sail missions to date remained Earth-bound [99, 109, 110, 177, 388], including the recently launched Advanced Composite Solar Sail System (ACS3) [127–129] and Alpha [126] missions by NASA and Gama, respectively. Similarly, missions scheduled for the near future are also expected to fly in Earth orbit, e.g., Gama's upcoming Beta mission [125]. In close proximity of the Earth, the dynamics are much more complex than in interplanetary space because of the presence of eclipses, atmospheric drag, and planetary radiation pressure (PRP). While multiple studies on the effect of aerodynamic drag in low Earth orbit (LEO) have been conducted and showed the enabling capabilities of solar sails for deorbiting purposes [212–216], orbit raising [219], and inclination changing [218, 220], the accurate derivation of the PRP acceleration and the perturbing effect on the solar-sail dynamics have been investigated to a much lesser extent. Research on this topic has mainly focused on the first-order characterization of the blackbody radiation pressure (BBRP) and albedo radiation pressure (ARP) accelerations and the optimization of planetocentric solar-sail trajectories under these effects [222, 223]. In these studies, the models for the BBRP and ARP accelerations are based on the one devised by McInnes [2] and assume the radiating body to be a uniformly bright disk irradiating only in the planet-to-sailcraft direction. While this assumption correctly approximates the PRP acceleration experienced by sailcraft at large distances from Earth, at low altitudes a more realistic geometry of the problem and radiation properties of the Earth should be considered to achieve accurate results. Indeed, at low altitudes, the spherical shape of the Earth and the geographical variation of the albedo and blackbody radiation flux play an important role in the modeling of the PRP acceleration. To account for them, several acceleration models have been devised, differing in the formulation adopted (i.e., analytical or numerical), the model employed for the albedo and blackbody radiation flux distributions across the Earth, and the shape of the spacecraft considered. The first works on PRP-acceleration modeling focused mainly on the development of analytical models, particularly by means of approximations through series expansions in the frame of general perturbations methods [326–329, 334–336, 389]. The use of series expansions based on spherical harmonics increases the complexity of the acceleration equations significantly. As a result, the obtained acceleration formulas are difficult to employ and have limited applicability, especially when compared to currently available numerical models. In fact, these more recent models outperform analytical models in terms of accuracy, although requiring a considerably larger computational effort. These numerical methods are mostly used in software tools for geodetic parameter estimation and precise orbit determination, such as ARPA [362], NASA's GEODYN [361], ESA's NAPEOS [360], and Delft University of Technology's NRTDM [363]. To the best of the author's knowledge, no analytical model exists in the literature providing a closed-form, analytical solution for the PRP acceleration of a solar-sail that does not rely on series expansions, is easy to implement, and achieves a high accuracy. In light of this and the fact that the PRP

acceleration can reach a non-trivial magnitude in the order of 10-20% of the solar-sail characteristic acceleration [222], the need for formulating an accurate expression for the PRP acceleration in proximity of the Earth arises. Such an analytical acceleration model would provide a powerful tool to perform high-fidelity orbit analyses for solar-sail LEO missions. Furthermore, it would also lay the foundation for the accurate optimization of Earth-bound steering strategies through (semi-)analytical optimization methods accounting for both the solar radiation pressure (SRP) and PRP accelerations.

In light of the above, this chapter presents a novel closed-form, analytical model for the BBRP and ARP accelerations of solar sails, found through a sequential surface averaging approach. The model takes into account the complexity of the problem in its entirety as it considers the spherical shape of the emitting body (i.e., the Earth), accounts for the limited area of the radiating surface as seen from the sailcraft, the geographical dependencies of the albedo and blackbody radiation intensities, the illumination conditions of the radiating surface, and the possibility that both sides of the sail are exposed to the planetary radiation. This model – hereinafter referred to as the "spherical" model – forms an extension of the finite-disk (FD) radiation pressure acceleration model devised by McInnes [2], is valid at any altitude, and can be used for flat-shaped, two-sided reflective solar sails, i.e., solar sails with perfectly reflecting front and back sides. In the chapter, the assumptions and full derivation of the model are discussed and analyses are performed to quantify the magnitude of the BBRP and ARP accelerations for different altitudes, sail attitudes, and Sun-planet-sailcraft relative orientations. Then, the model is validated through a thorough error analysis with extensive comparisons against McInnes' FD model and the NRTDM numerical model. Finally, a variety of analyses are presented to assess the effect of the PRP accelerations on the maneuvering capabilities of real-life solar sails in Earth orbit. To this end, the solar-sail orbital dynamics are propagated with and without PRP acceleration using locally optimal orbit-raising and inclination-changing steering laws. In this way, the impact of the uncontrolled PRP acceleration on the maximum achievable altitude and inclination changes is quantified. The analyses are performed considering NASA's ACS3 mission as reference scenario [127]. This solar-sail mission was launched in April 2024 and reflects the currently available technology readiness level of solar-sail missions in LEO.

3.2. DYNAMICAL MODEL

The dynamics of a solar sail in proximity of the Earth are expressed in an inertial Earth-centered reference frame, $O_I(\hat{\boldsymbol{x}}, \hat{\boldsymbol{y}}, \hat{\boldsymbol{z}})$, with the $\hat{\boldsymbol{x}}$-axis direction pointing towards the mean vernal equinox at January 1$^{\text{st}}$, 2000, the $\hat{\boldsymbol{z}}$-axis direction perpendicular to the mean equatorial plane of that same epoch and pointing towards the North Pole, and the $\hat{\boldsymbol{y}}$-axis direction completing the right-handed frame. Within this frame the equations of motion of a solar sail can be expressed in vectorial form as:

$$\ddot{\boldsymbol{r}} + \frac{\mu}{r^3}\boldsymbol{r} = \boldsymbol{a}_{SRP} + \boldsymbol{a}_{Aero} + \boldsymbol{a}_{J2} + \boldsymbol{a}_{BBRP} + \boldsymbol{a}_{ARP} \tag{3.1}$$

where the dot notation indicates differentiation with respect to time, $\boldsymbol{r} = [x, y, z]^{\mathrm{T}}$ is the sailcraft position vector, x, y, and z are the Cartesian coordinates of the sailcraft in frame O_I, $r = \|\boldsymbol{r}\|$, $\mu = 398600.4415\ \mathrm{km^3 s^{-2}}$ is the Earth gravitational parameter of the

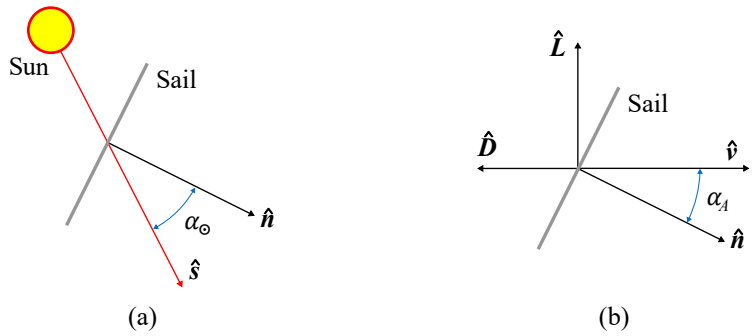


Figure 3.1: Solar-sail attitude angles to determine the SRP and aerodynamic accelerations.

geopotential Joint Gravity Model (JGM) 2 [277, 308], and $\boldsymbol{a}_{SRP}$, $\boldsymbol{a}_{Aero}$, $\boldsymbol{a}_{J2}$, $\boldsymbol{a}_{BBRP}$, and $\boldsymbol{a}_{ARP}$ are the SRP, aerodynamic, J_2 gravitational, BBRP, and ARP accelerations, respectively. These accelerations will be described in more detail in the following sections.

It should be noted that, in the analyses presented in the remainder of this chapter, only steering laws to increase the semi-major axis and inclination are considered. While the Earth's J_2 gravitational perturbation has no secular effect on these Keplerian elements [308], other gravitational perturbations with a secular effect on the inclination exist, such as the gravitational accelerations of the Moon and Sun. However, these are orders of magnitude smaller than the accelerations on the right-hand side of Eq. 3.1, for the orbits considered in this chapter [232]. As a consequence, they have not been considered in the equations of motion in order to avoid hampering a clear investigation into the effects of the BBRP and ARP accelerations on the solar-sail orbital dynamics.

3.2.1. SOLAR RADIATION PRESSURE ACCELERATION

The SRP acceleration is defined assuming a flat, perfectly reflecting sail as per the ideal sail model [2]:

$$\boldsymbol{a}_{SRP} = \nu\, a_c \cos^2\alpha_\odot\, \hat{\boldsymbol{n}} \tag{3.2}$$

where $\nu \in [0, 1]$ is the shadow factor and $\alpha_\odot \in [0, \pi/2]$ is the solar-sail cone angle measured between the direction of sunlight, $\hat{\boldsymbol{s}}$, and the sail normal direction with no component pointing towards the Sun, $\hat{\boldsymbol{n}}$, see Fig. 3.1a. The shadow factor ν accounts for the effect of eclipses and its value ranges from 0 (no sunlight reaches the sail) to 1 (sail completely illuminated). In this chapter, eclipses are modeled using the conical shadow model presented in Ref. [211, 231], with the only difference that $\nu = 0$ both when in umbra and penumbra. a_c represents the SRP characteristic acceleration, i.e., the maximum SRP acceleration (achieved for $\alpha_\odot = 0$) at a distance of 1 AU from the Sun [2]:

$$a_c = \frac{2 S_{TSI}}{c\,\sigma} \tag{3.3}$$

In Eq. 3.3, $S_{TSI} = 1367\ \mathrm{W\,m^{-2}}$ represents the solar flux at Earth [308], $c = 299792.458\ \mathrm{km\,s^{-1}}$ is the speed of light in vacuum [390], and σ is the sailcraft mass-to-sail area ratio.

3.2.2. AERODYNAMIC ACCELERATION

The sailcraft aerodynamics are modeled assuming the sail to be a flat plate orbiting at a velocity much larger than the thermal velocity of the atmospheric particles. Under these assumptions, the hyperthermal free-molecular flow model can be used to define the aerodynamic acceleration as [219, 220, 341, 349]:

$$\boldsymbol{a}_{Aero} = \frac{1}{2}\frac{\rho v^2}{\sigma}\left(C_D\hat{\boldsymbol{D}} + C_L\hat{\boldsymbol{L}}\right) \tag{3.4}$$

In Eq. 3.4, C_D and C_L are the drag and lift coefficients of the sail, v is the sailcraft inertial velocity, and ρ is the atmospheric density, which is modeled using an averaging technique based on the NRLMSISE-00 atmospheric model and presented in Chapter 6. The unit vectors $\hat{\boldsymbol{D}}$ and $\hat{\boldsymbol{L}}$ indicate the drag and lift directions, which lie in the same plane formed by the sail normal direction, $\hat{\boldsymbol{n}}$, and the sailcraft inertial velocity direction, $\hat{\boldsymbol{v}}$, and are anti-parallel and perpendicular to $\hat{\boldsymbol{v}}$, respectively, see Fig. 3.1b. The expressions for C_D and C_L are given by [219, 220, 341, 349]:

$$C_D = 2\left[\sigma_T + \sigma_N V_R\left|\cos\alpha_A\right| + (2-\sigma_N-\sigma_T)\cos^2\alpha_A\right]\left|\cos\alpha_A\right| \tag{3.5}$$

$$C_L = 2\left[\sigma_N V_R + (2-\sigma_N-\sigma_T)\left|\cos\alpha_A\right|\right]\left|\cos\alpha_A\right|\sin\alpha_A \tag{3.6}$$

where $\alpha_A \in [0, \pi/2]$ is the aerodynamic pitch angle corresponding to the complementary angle to the solar sail's angle of attack, see again Fig. 3.1b, σ_N and σ_T are the normal and tangential momentum accommodation coefficients, respectively, and V_R is the ratio of the atmospheric particle average thermal velocity to the sailcraft inertial velocity. Based on Refs. [219, 220, 355, 357–359], $\sigma_N = \sigma_T = 0.8$, $V_R = 0.05$.

3.2.3. J_2 GRAVITATIONAL ACCELERATION

The gravitational acceleration due to the Earth's J_2 effect in frame $O_I(\hat{\boldsymbol{x}}, \hat{\boldsymbol{y}}, \hat{\boldsymbol{z}})$ is given by [232]:

$$\boldsymbol{a}_{J2} = -\frac{3}{2}\frac{R^2}{r^5}\mu J_2\left[\left(x\hat{\boldsymbol{x}} + y\hat{\boldsymbol{y}}\right)\left(1-5\frac{z^2}{r^2}\right) + z\hat{\boldsymbol{z}}\left(3-5\frac{z^2}{r^2}\right)\right] \tag{3.7}$$

where $R = 6378.1363$ km is the Earth radius [308], and $J_2 = 1.082626925639\cdot10^{-3}$ is the Earth's J_2 gravitational field constant of the JGM 2 geopotential model [277, 308].

3.2.4. PLANETARY RADIATION PRESSURE ACCELERATION

In order to determine the PRP acceleration exerted on a solar sail, it is essential to first establish the amount of planetary radiation received by the sail, define its flux and finally the radiation pressure. If an elementary piece of Earth's surface dA is considered, see Fig. 3.2a, the amount of power irradiated in a generic direction $\hat{\boldsymbol{l}}$ and enclosed within an infinitesimal solid angle $d\Omega$ is represented by the second differential $d^2\mathcal{P}$ as [391]:

$$d^2\mathcal{P} = I_\oplus \cos\vartheta\, d\Omega\, dA \tag{3.8}$$

In Eq. 3.8, $I_\oplus$ represents the planetary radiation intensity (across the entire electromagnetic spectrum) along the normal direction to dA, $\hat{\boldsymbol{N}}$, and $\vartheta \in [0, \pi/2]$ is the angle between

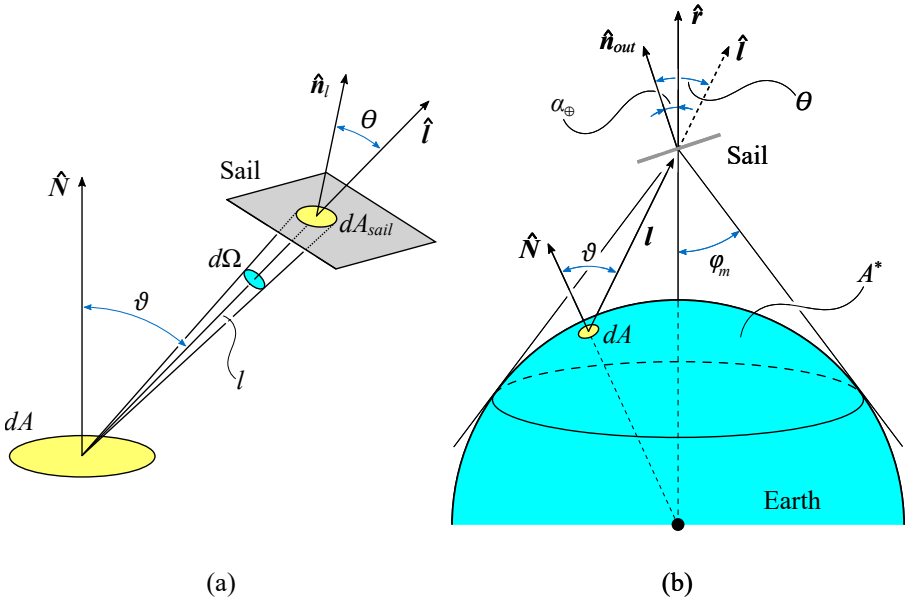


Figure 3.2: Geometry of the problem to determine the PRP acceleration exerted on a solar sail.

$\hat{\boldsymbol{N}}$ and $\hat{\boldsymbol{l}}$, see again Figs. 3.2a and 3.2b. Assuming the Earth's surface to be a Lambertian scatterer, the radiation intensity can be expressed as [392]:

$$I_\oplus = \frac{S}{\pi} \tag{3.9}$$

where S is the planetary radiation power flux (i.e., the emitted radiation power per unit area) at the surface element, dA. When only the radiation received by the solar sail is considered, $d\Omega$ represents the solid angle subtended by an infinitesimal piece of illuminated sail surface, dA_{sail}. In this case, $d\Omega$ is defined as [393]:

$$d\Omega = \frac{dA_{sail}\cos\theta}{l^2} \tag{3.10}$$

where l is the magnitude of the vector $\boldsymbol{l}$ pointing from dA to dA_{sail} and $\theta \in [0, \pi/2]$ is the angle between $\hat{\boldsymbol{l}}$ and the sail normal direction with positive component along $\hat{\boldsymbol{l}}$, $\hat{\boldsymbol{n}}_l$, see Fig. 3.2a. It should be noted that, depending on the relative orientation of the sail and the surface element dA, $\hat{\boldsymbol{n}}_l$ can either coincide with the sail normal direction pointing away from the Earth, $\hat{\boldsymbol{n}}_{out}$, as shown in Fig. 3.2b, or it can be anti-parallel to it. Mathematically, this corresponds to:

$$\hat{\boldsymbol{n}}_l = \mathrm{sgn}\left(\hat{\boldsymbol{l}} \cdot \hat{\boldsymbol{n}}_{out}\right) \hat{\boldsymbol{n}}_{out} \tag{3.11}$$

Making use of Eqs. 3.9 and 3.10, Eq. 3.8 can be rewritten as:

$$d^2\mathcal{P} = \frac{S}{\pi}\frac{\cos\vartheta\,\cos\theta}{l^2} dA_{sail}\, dA \tag{3.12}$$

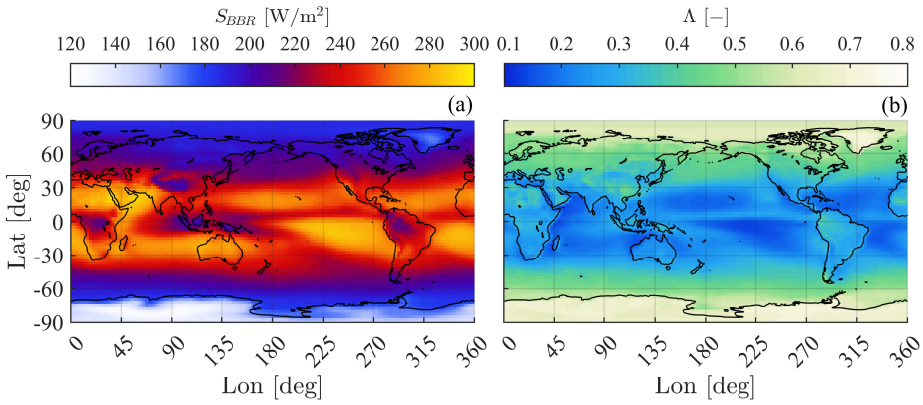


Figure 3.3: Yearly averaged maps of the blackbody radiation flux (a) and albedo coefficient (b) of the ANGARA model.

Since this chapter considers a flat-shaped solar sail whose dimensions are significantly smaller than l, θ and l can be assumed to be constant across the entire sail surface. This assumption allows to easily integrate Eq. 3.12 with respect to dA_{sail} over the entire sail surface, A_{sail}, thus yielding the radiation power $d\mathcal{P}$ received by the entire sail due to the radiation emitted by dA:

$$d\mathcal{P} = \frac{S}{\pi}\frac{\cos\vartheta\,\cos\theta}{l^2}A_{sail}\,dA \tag{3.13}$$

The power flux at the sail's location due to the radiation emitted by dA, dS_{sail}, is then found as:

$$dS_{sail} = \frac{d\mathcal{P}}{A_{sail}\cos\theta} = \frac{S}{\pi}\frac{\cos\vartheta}{l^2}dA \tag{3.14}$$

The corresponding radiation pressure dP is given by [2]:

$$dP = \frac{dS_{sail}}{c} = \frac{S}{\pi c}\frac{\cos\vartheta}{l^2}dA \tag{3.15}$$

and the acceleration of the sail is [2]:

$$d\boldsymbol{a}_{PRP} = 2\frac{dP}{\sigma}\cos^2\theta\,\hat{\boldsymbol{n}}_l = \frac{2S}{\pi c\sigma}\frac{\cos\vartheta\cos^2\theta}{l^2}dA\,\hat{\boldsymbol{n}}_l \tag{3.16}$$

Ultimately, in order to find the total acceleration exerted on the sailcraft, Eq. 3.16 needs to be integrated over the entire visible surface of the Earth as seen from the sailcraft, A^*, yielding:

$$\boldsymbol{a}_{PRP} = \frac{2}{\pi c\sigma}\int_{A^*}\left(S\frac{\cos\vartheta\cos^2\theta}{l^2}\hat{\boldsymbol{n}}_l\right)dA \tag{3.17}$$

The solution to the surface integral of Eq. 3.17 depends on the Earth-sail geometrical configuration and, most importantly, on the definition of the planetary radiation flux, S. Indeed, the planetary radiation flux quantifies the amount of radiation emitted by the

surface elements dA across A^* and its definition depends on whether the blackbody or albedo radiation is considered. In order to differentiate between the two, in the following the symbols S_{BBR} and S_{AR} will be used instead of S to refer to the blackbody and albedo radiation fluxes, respectively. Because the amount of radiation emitted by an elementary piece of Earth surface strongly depends on its geographical location, both S_{BBR} and S_{AR} vary across the surface of the Earth following a complex pattern. This renders the integral of Eq. 3.17 non-elementary, i.e., not solvable in terms of elementary functions. To solve this problem, two different approaches have been used in literature to find approximated solutions. The first is to approximate the integrand function of Eq. 3.17 using Legendre polynomials series expansions (particularly for the planetary flux term, S), so as to make the PRP acceleration integral solvable [334, 335]. The second is to approximate the PRP acceleration integral by a finite sum over a set of discretized surface elements of the Earth visible from the sailcraft. To apply this method, discrete maps of the geographical distribution of the blackbody radiation flux and albedo coefficient (formally defined later in this section) are required. As an example, Fig. 3.3 displays the yearly averaged maps of the blackbody radiation flux and albedo coefficient, based on the ANGARA (Analysis of Non-Gravitational Acceleration due to Radiation and Aerodynamics) numerical model developed by Hyperschall Technologie Göttingen GmbH [394] and used for different applications, spanning from precise orbit determination to parameter estimation [283, 363, 395]. Although such numerical approaches allow to achieve accurate results, this comes at the cost of a high computational effort. In order to derive a closed-form expression for the BBRP and ARP accelerations, this chapter uses an analytical approach instead. In particular, a closed-form solution to the integral of Eq. 3.17 has been found by approximating the planetary flux, S, with a surface-averaged flux $\bar{S}$, whose definition is given later in this section. By employing $\bar{S}$, the radiation emitted by the visible surface A^* is assumed to be irradiated isotropically, i.e., such that any elementary piece of the Earth's visible surface, dA, emits the same amount of radiation, regardless of its geographical location. Taking advantage of this simplification and using Eq. 3.11 to express $\hat{\boldsymbol{n}}_l$, an analytical solution to the integral of Eq. 3.17 can be found, leading to the following expression for the PRP acceleration:

$$\boldsymbol{a}_{PRP} = \frac{2\bar{S}}{\pi c \sigma} \int_{A^*} \left(\frac{\cos\vartheta \cos^2\theta}{l^2} \hat{\boldsymbol{n}}_l \right) dA = a_{c,PRP} G_F \, \hat{\boldsymbol{n}}_{out} \tag{3.18}$$

where $a_{c,PRP}$ is the PRP characteristic acceleration and $G_F \in [0,1]$ is the so-called geometrical factor. The geometrical factor correlates the Earth-sail geometrical configuration to the PRP acceleration and is defined as:

$$G_F = \frac{3}{2\pi} \int_{A^*} \left[\frac{\cos\vartheta \cos^2\theta}{l^2} \operatorname{sgn}\left(\hat{\boldsymbol{l}} \cdot \hat{\boldsymbol{n}}_{out} \right) \right] dA \tag{3.19}$$

The full analytical evaluation of the surface integral on the right-hand side of Eq. 3.19 is detailed in Appendix B and, in particular, in Sections B.1 and B.2. The resulting expression for the geometrical factor depends on the geometrical configuration of the sail with respect to the Earth, which is uniquely identified by the planetary pitch angle (PPA), $\alpha_\oplus \in [0, \pi/2]$, and maximum view angle, $\varphi_m \in (0, \pi/2)$, see Fig. 3.2b. The former is defined

as the angle between $\hat{\boldsymbol{n}}_{out}$ and the radial direction, $\hat{\boldsymbol{r}}$, while the latter is the angle between the direction pointing to the Earth's tangent as seen from the sailcraft and $-\hat{\boldsymbol{r}}$. Two possible configurations can then be defined:

a) If $\alpha_\oplus + \varphi_m \leq \pi/2$, the incoming radiation from the visible surface A^* illuminates only one side of the sail. In this case, the geometrical factor is equal to:

$$G_F(H, \alpha_\oplus) = 1 - \sqrt{1-H^2}\left[1 - H^2\left(1 - \frac{3}{2}\sin^2\alpha_\oplus\right)\right] \tag{3.20}$$

where $H = R/r$ is the adimensional inverse orbital radius introduced for conciseness.

b) If $\alpha_\oplus + \varphi_m > \pi/2$, the incoming radiation from the visible surface A^* illuminates both sides of the sail. In this case, each of the two sides of the double-sided reflecting sail provides an acceleration that points either along or opposite to $\hat{\boldsymbol{n}}_{out}$. Consequently, G_F assumes a more complex expression, given by:

$$\begin{aligned} G_F(H, \alpha_\oplus) = 1 - \frac{1}{\pi}\Bigg\{ & 2\sqrt{1-H^2}\left[1 - H^2\left(1 - \frac{3}{2}\sin^2\alpha_\oplus\right)\right]\sin^{-1}\mathcal{A} + 2\tan^{-1}\mathcal{B} \\ & -3\mathcal{B}^3\cos^4\alpha_\oplus - 2\mathcal{B}\cos^2\alpha_\oplus\left(1 - \frac{3}{2}\sin^2\alpha_\oplus\right)\Bigg\} \end{aligned} \tag{3.21}$$

where:

$$\mathcal{A} = \frac{\cos\alpha_\oplus}{\sin\alpha_\oplus}\sqrt{\frac{1}{H^2} - 1} \qquad \mathcal{B} = \sqrt{\frac{H^2}{\cos^2\alpha_\oplus} - 1} \tag{3.22}$$

The PRP characteristic acceleration is defined as:

$$a_{c,PRP} = \frac{4}{3}\frac{\bar{S}}{c\sigma} \tag{3.23}$$

Unlike the geometrical factor, the PRP characteristic acceleration depends on the type of radiation considered through the surface-averaged flux, $\bar{S}$. Its definition is provided in the following subsections for both the blackbody and albedo radiations. Note that hereinafter the symbols $\bar{S}_{BBR}$ and $\bar{S}_{AR}$ will be used instead of $\bar{S}$ to refer to the blackbody and albedo radiation fluxes, respectively. In a similar fashion, $a_{c,BBRP}$ and $a_{c,ARP}$ will be used instead of $a_{c,PRP}$ to indicate the BBRP and ARP characteristic accelerations, respectively.

3.2.4.1. BLACKBODY FLUX MODEL

As shown in Fig. 3.3a, the blackbody radiation flux, S_{BBR}, varies across the surface of the Earth following a complex trend. To a first-order level, this trend can be approximated assuming a sinusoidal variation with the latitude $\eta \in [-\pi/2, \pi/2]$:

$$S_{BBR} = S_{BBR,eq} - \left(S_{BBR,eq} - S_{BBR,pol}\right)\sin^2\eta \tag{3.24}$$

In the above equation, $S_{BBR,eq} = 264.609\ \mathrm{W m^{-2}}$ and $S_{BBR,pol} = 173.436\ \mathrm{W m^{-2}}$ are the reference blackbody radiation fluxes at the equator and the poles. These values have been found by a least-squares fit of the right-hand side of Eq. 3.24 to the numerical data of the

ANGARA yearly averaged flux map of Fig. 3.3a. Expressing S_{BBR} as in Eq. 3.24 allows to define the surface-averaged blackbody radiation flux, $\bar{S}_{BBR}$, analytically as follows:

$$\bar{S}_{BBR} = \frac{\int_{A^*} S_{BBR}\, dA}{\int_{A^*} dA} = S_{BBR,eq} - \left(S_{BBR,eq} - S_{BBR,pol}\right) L_F \tag{3.25}$$

where $L_F \in [0,1]$ is the so-called latitudinal factor defined as:

$$L_F = \frac{\int_{A^*} \sin^2\eta\, dA}{\int_{A^*} dA} \tag{3.26}$$

with analytical solution derived in Appendix C and given by:

$$L_F(H,\eta^*) = \frac{1}{3}\left(H^2 + H + 1\right) - \frac{1}{2} H\,(H+1)\cos^2\eta^* \tag{3.27}$$

where η^* is the latitude of the subsatellite point, defined as the angle between the Earth's equatorial plane and the sailcraft position vector, $\boldsymbol{r}$. Because S_{BBR} varies sinusoidally with latitude, hereinafter this model will be referred to as the "sinusoidal" blackbody flux model. As mentioned before, this model assumes the blackbody radiation to be emitted isotropically, i.e., with a constant flux $\bar{S}_{BBR}$ by the visible surface, A^*. However, the flux value depends on the size and location of A^* relative to the equator/poles through the factor L_F. It is worth noting that if $S_{BBR,eq} = S_{BBR,pol}$, the sinusoidal variation with latitude is lost, see Eqs. 3.24-3.25, and $S_{BBR,eq}$, $S_{BBR,pol}$, S_{BBR}, and $\bar{S}_{BBR}$ coincide. In this case a uniform (i.e., constant) flux distribution across the entire Earth's surface is obtained and the model is consequently referred to as the "uniform" blackbody flux model. In the reminder of this chapter, whenever the uniform flux model is employed, a flux of $S_{BBR} = 234.732\ \mathrm{W\,m^{-2}}$ is used. This value was found by performing a numerical surface average of the flux values of the ANGARA yearly averaged flux map given in Fig. 3.3a. Because $\bar{S}_{BBR}$ is constant, $a_{c,BBRP}$ is also constant and its value represents the maximum achievable BBRP acceleration, in a similar fashion to the "traditional" SRP characteristic acceleration, a_c. However, this situation occurs only for a nadir-pointing solar sail ($\hat{\boldsymbol{n}}_{out} = \hat{\boldsymbol{r}}$, $\alpha_\oplus = 0$) at zero altitude, as in this case $G_F = 1$, see Eq. 3.20, and $\|\boldsymbol{a}_{BBRP}\| = a_{c,BBRP}$. Finally, it is worth noting that $a_{c,BBRP}$ can also be expressed in terms of the SRP characteristic acceleration, a_c, by substituting Eq. 3.3 in Eq. 3.23:

$$a_{c,BBRP} = \frac{2}{3}\frac{\bar{S}_{BBR}}{S_{TSI}} a_c = 0.1145\, a_c \tag{3.28}$$

3.2.4.2. ALBEDO FLUX MODEL

The albedo radiation flux, S_{AR}, is defined as [396]:

$$S_{AR} = \Lambda\, S_{TSI} \max(0, \cos\chi) \tag{3.29}$$

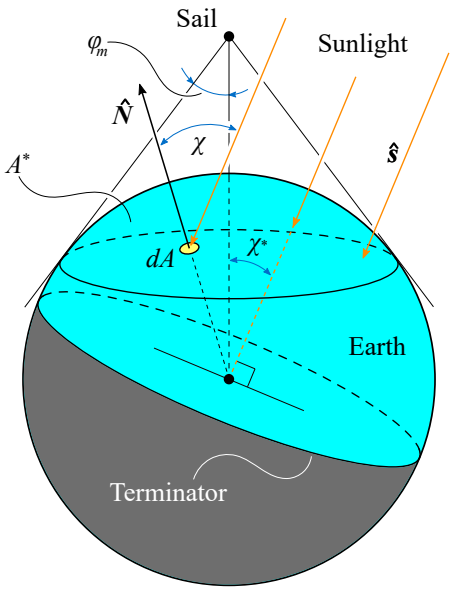


Figure 3.4: Geometry of the problem to determine the albedo radiation flux at the sail's location.

where Λ is the Earth's albedo coefficient, i.e., the average amount of solar radiation received by the Earth reflected into space [396], and χ is the sunlight incidence angle between the reverse sunlight direction, $-\hat{\boldsymbol{s}}$, and $\hat{\boldsymbol{N}}$, see Fig. 3.4. The albedo coefficient, Λ, provides the dependency of S_{AR} on the reflectivity properties of the Earth's surface, which vary following a complex trend, see Fig. 3.3b. At the same time, the sunlight incidence angle, χ, provides the dependency of S_{AR} on the illumination conditions of the visible surface A^*, determined by the relative positions of the Earth, Sun, and sailcraft. In light of this, any high-fidelity analytical expressions for S_{AR} assumes a highly nonlinear form, for which the corresponding surface-averaged flux, $\bar{S}_{AR}$, cannot be expressed in terms of elementary functions. To solve this issue, in this chapter different approximations are introduced to express $\bar{S}_{AR}$ in a closed, analytical form. Firstly, the albedo coefficient is approximated as a sinusoidal function of the latitude η, similar to S_{BBR} in Eq. 3.24:

$$\Lambda = \Lambda_{BBR,eq} + \left(\Lambda_{BBR,pol} - \Lambda_{BBR,eq}\right)\sin^2\eta \tag{3.30}$$

where $\Lambda_{BBR,eq} = 0.1854$ and $\Lambda_{BBR,pol} = 0.6149$ are the reference albedo coefficients at the equator and poles. Similar to $S_{BBR,eq}$ and $S_{BBR,pol}$, $\Lambda_{BBR,eq}$ and $\Lambda_{BBR,pol}$ have been found by a least-squares fit of the right-hand side of Eq. 3.30 to the numerical data of the ANGARA yearly averaged albedo map of Fig. 3.3b. Secondly, the effect of the albedo and sunlight incidence angle on the albedo radiation flux is uncoupled by approximating the surface-averaged albedo flux, $\bar{S}_{AR}$, with the product of the surface-averaged albedo, $\bar{\Lambda}$, and surface-averaged cosine of the sunlight incidence angle, Φ. In this way, $\bar{S}_{AR}$ can be

defined as:

$$\bar{S}_{AR} = \frac{\int_{A^*} S_{AR}\, dA}{\int_{A^*} dA} = S_{TSI}\, \bar{\Lambda}\, \Phi \tag{3.31}$$

where:

$$\bar{\Lambda} = \frac{\int_{A^*} \Lambda\, dA}{\int_{A^*} dA} = \Lambda_{BBR,eq} + \left(\Lambda_{BBR,pol} - \Lambda_{BBR,eq}\right) L_F \tag{3.32}$$

$$\Phi = \frac{\int_{A^*} \max\left(0, \cos\chi\right) dA}{\int_{A^*} dA} \tag{3.33}$$

In literature, $\Phi \in [0,1]$ is known as albedo phase function [392] and will be referred to as such in the remainder of the work. The phase function accounts for the illumination conditions of the visible surface of the Earth and its expression depends on whether the Earth's visible surface, A^*, is completely illuminated (if the sailcraft "sees" only the sunlit side of the Earth), partially illuminated (if the Earth's day-night terminator is visible from the sailcraft), or completely dark (if the sailcraft "sees" only the dark side of the Earth). These three cases can be identified through the maximum view angle, φ_m, and the phase angle, $\chi^* \in [0,\pi]$, i.e., the angle between $\hat{\boldsymbol{r}}$ and the opposite to the sunlight direction, $-\hat{\boldsymbol{s}}$, see Fig. 3.4. For each of these cases, the surface integrals appearing on the right-hand side of Eq. 3.33 can be solved analytically as detailed in Appendix D. The resulting expressions for the phase function, Φ, are the following:

a) If $\chi^* \leq \varphi_m$, the visible surface A^* is completely illuminated by the Sun. In this case, Φ is equal to:

$$\Phi\left(H, \chi^*\right) = \frac{1}{2}\left(1 + H\right)\cos\chi^* \tag{3.34}$$

b) If $\varphi_m < \chi^* < \pi - \varphi_m$, the visible surface A^* is partially illuminated by the Sun. In this case, Φ is given by:

$$\begin{aligned}\Phi\left(H, \chi^*\right) = \frac{1}{2\pi}\Bigg\{&\left(1 - H\right)^{-1}\left[\cos^{-1}\left(\frac{H}{\sin\chi^*}\right) - H\sqrt{\sin^2\chi^* - H^2}\right] \\ &+ \left(1 + H\right)\cos\chi^*\cos^{-1}\left(-\frac{H}{\sqrt{1 - H^2}}\frac{\cos\chi^*}{\sin\chi^*}\right)\Bigg\}\end{aligned} \tag{3.35}$$

c) If $\pi - \varphi_m \leq \chi^*$, the visible surface A^* is completely dark and $\Phi = 0$.

The introduction of $\bar{\Lambda}$ and Φ to separate the dependencies of Λ and χ – and therefore compute $\bar{S}_{AR}$ analytically – introduces two sources of approximation. Indeed, by employing $\bar{\Lambda}$ a constant albedo coefficient is considered across the entire visible surface A^*, despite the sinusoidal variation with latitude assumed in Eq. 3.30. Similar to $\bar{S}_{BBR}$ the value of $\bar{\Lambda}$ depends on the size and location of A^* relative to the equator/poles by

means of the latitudinal factor L_F. Secondly, the usage of the phase function, Φ, implies that all the albedo radiation is emitted isotropically (i.e., uniformly) by the entire visible surface A^*. As a result, the fact that in reality radiation is emitted unevenly and only by the illuminated part of A^* is not taken into account.

Similar as to the blackbody flux model, it is worth noting that if $\Lambda_{BBR,eq} = \Lambda_{BBR,pol}$, the sinusoidal variation of the albedo with latitude is lost, see Eqs. 3.30 and 3.32, and $\Lambda_{BBR,eq}$, $\Lambda_{BBR,pol}$, Λ, and $\bar{\Lambda}$ coincide. In this case a uniform (i.e., constant) albedo distribution across the entire Earth's surface is obtained and therefore the model is referred to as the "uniform" albedo model. Hereinafter, whenever the uniform albedo model is employed, an albedo coefficient of $\Lambda = 0.3259$ is used. This value was found by performing a numerical surface average of the albedo values of the ANGARA yearly averaged albedo map given in Fig. 3.3b. By assuming a constant albedo coefficient and substituting Eq. 3.3 in Eq. 3.23, $a_{c,ARP}$ can be expressed as a function of the phase function, Φ, and the SRP characteristic acceleration, a_c, as follows:

$$a_{c,ARP} = \frac{2\Lambda}{3}\Phi a_c = 0.2173\,\Phi a_c \tag{3.36}$$

In the next two sections, different analyses are presented which aim to characterize the BBRP and ARP accelerations achievable in close proximity of the Earth. Here, the discussion will focus mostly on the uniform blackbody flux model and uniform albedo model, unless stated otherwise, for the sake of clarity and easiness of the treatment. The higher-fidelity sinusoidal blackbody flux model and sinusoidal albedo model will be employed later on in the chapter, where the validation of the spherical BBRP and ARP acceleration models and the analyses of PRP-perturbed trajectories are discussed.

3.3. ANALYSIS OF THE BLACKBODY RADIATION PRESSURE ACCELERATION

Figure 3.5 shows the contour plots of the BBRP acceleration magnitude relative to the solar-sail characteristic acceleration, a_c, in the near-Earth environment, for altitudes up to $h = 34200$ km. Two different sail attitudes are considered, namely, a nadir-pointing solar sail (i.e., $\hat{\boldsymbol{n}}_{out} = \hat{\boldsymbol{r}}$) and inertial-pointing solar sail (chosen to point along the $\hat{\boldsymbol{x}}$ axis, $\hat{\boldsymbol{n}}_{out} = \pm\hat{\boldsymbol{x}}$, without loss of generality). As can be seen in Fig. 3.5a, for a nadir-pointing attitude, the BBRP acceleration magnitude, a_{BBRP}, depends solely on the orbital altitude, h, as the PPA is constantly equal to zero. This allows correlating a_{BBRP} and h, as shown in the legend of Fig. 3.5a. The contour plot shows the rapid decay of a_{BBRP}, especially at low altitudes. This is because each elementary piece of Earth's visible surface, dA, emits radiation whose power intensity, $d\mathcal{P}$, decreases as an inverse square law of the distance from the sail, l, see Fig. 3.2a and Eq. 3.13. Although increasing the altitude also extends the size of the visible surface of the Earth (that is, the size of the surface emitting radiation), A^*, the inverse-square-law decay of the radiation intensity remains dominant. As a result, a_{BBRP} declines swiftly, displaying a behavior similar to an inverse square law. Nevertheless, the contour plot shows that accelerations even up to 11% of a_c can be achieved for low altitudes, which is in agreement with Eq. 3.28 and in line with the results found in the literature [222]. Similar to Fig. 3.5a, Fig. 3.5b shows the iso-acceleration

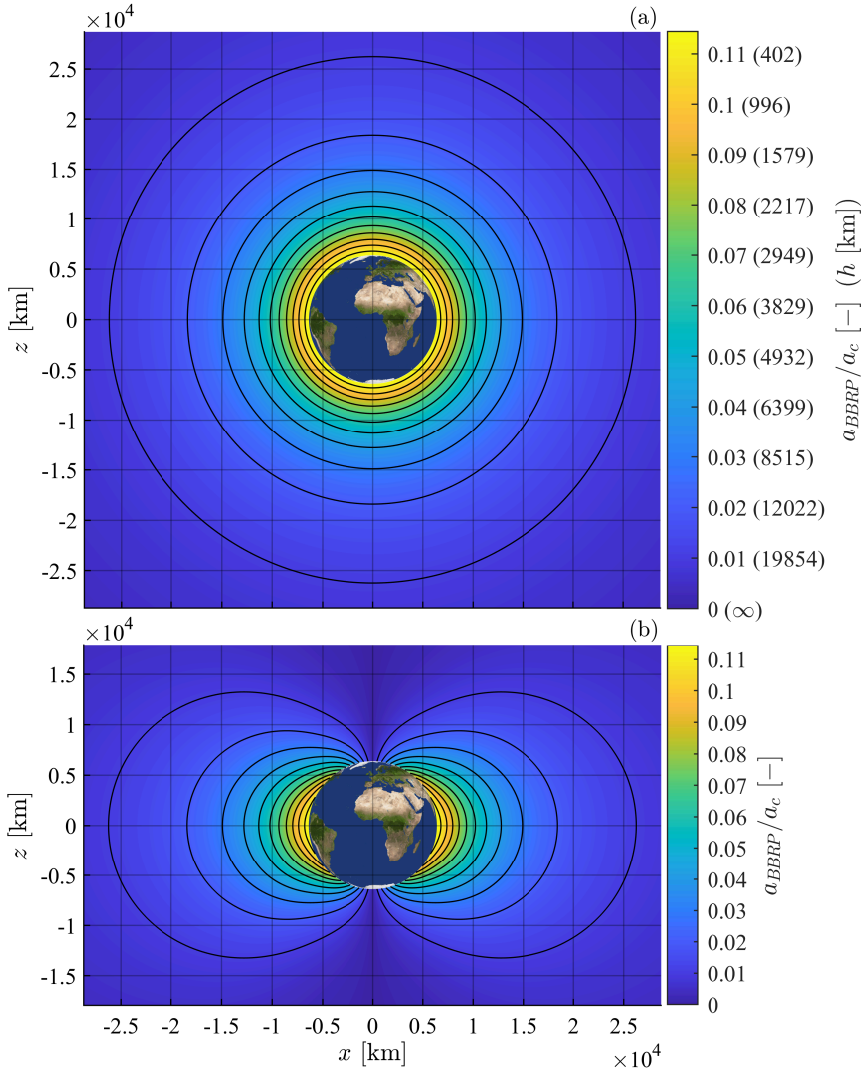


Figure 3.5: BBRP acceleration for a) nadir-pointing and b) inertially pointing solar sails, as per the spherical uniform model.

curves for an inertial-pointing solar sail, with the sail normal pointing along the $\hat{\boldsymbol{x}}$ axis. In this case, the acceleration varies less uniformly as the PPA is not constant. In particular, a_{BBRP} is equal to zero along the $\hat{\boldsymbol{z}}$ axis, that is, for $x = 0$: this is because the sail is oriented edgewise with respect to the radial direction ($\alpha_{\oplus} = \pi/2$), therefore causing the BBRP accelerations exerted on the sail's front and back sides to counteract each other. Also, it is worth noting that the acceleration profile is symmetric with respect to the $\hat{\boldsymbol{z}}$ axis, which is a consequence of the fact that a double-sided perfectly reflecting solar sail has been

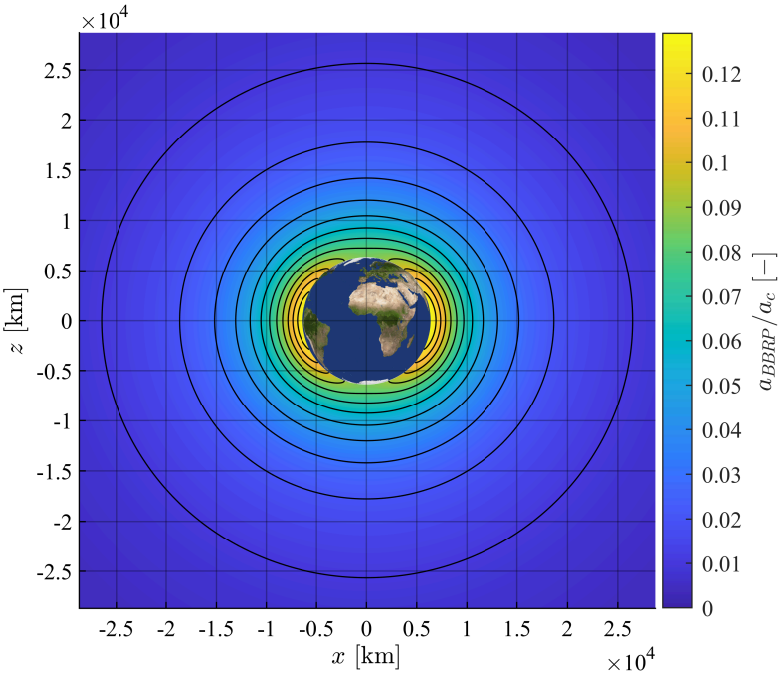


Figure 3.6: BBRP acceleration for a nadir-pointing solar sail, as per the spherical sinusoidal model.

considered. Indeed, for a solar sail with different optical properties on the front and back sides, no symmetry would be found.

The results presented above in this section considered a spherical uniform PRP acceleration model. In order to gain insights also on the spherical sinusoidal model, Fig. 3.6 displays the sinusoidal model's distribution of the BBRP acceleration magnitude around the Earth for a nadir-pointing solar sail, considering altitudes up to $h = 34200$ km. Unlike the uniform model's distribution of Fig. 3.5a, the sinusoidal model's distribution shows no spherical symmetry, only an axial symmetry along the Earth's polar axis. This is due to the latitudinal variation of the BBRP acceleration magnitude introduced by the latitudinal factor, L_F, see Eq. 3.27. The latitudinal variation of a_{BBRP} is especially evident at low altitudes as it creates an equatorial bulge in the acceleration magnitude distribution with a maximum value of almost 13% of a_c. On the other hand, a smaller acceleration magnitude is achieved at the poles, where a_{BBRP} reaches at most 8.4% of a_c. Finally, it is worth noting that for increasing altitudes the contour lines circularize, meaning that a spherical symmetry is found and the sinusoidal model tends to the uniform model.

3.4. ANALYSIS OF THE ALBEDO RADIATION PRESSURE ACCELERATION

Similar to Fig. 3.5 for the BBRP acceleration, Fig. 3.7 shows the variation of the ARP acceleration magnitude, a_{ARP}, relative to the characteristic acceleration, a_c, for a nadir-

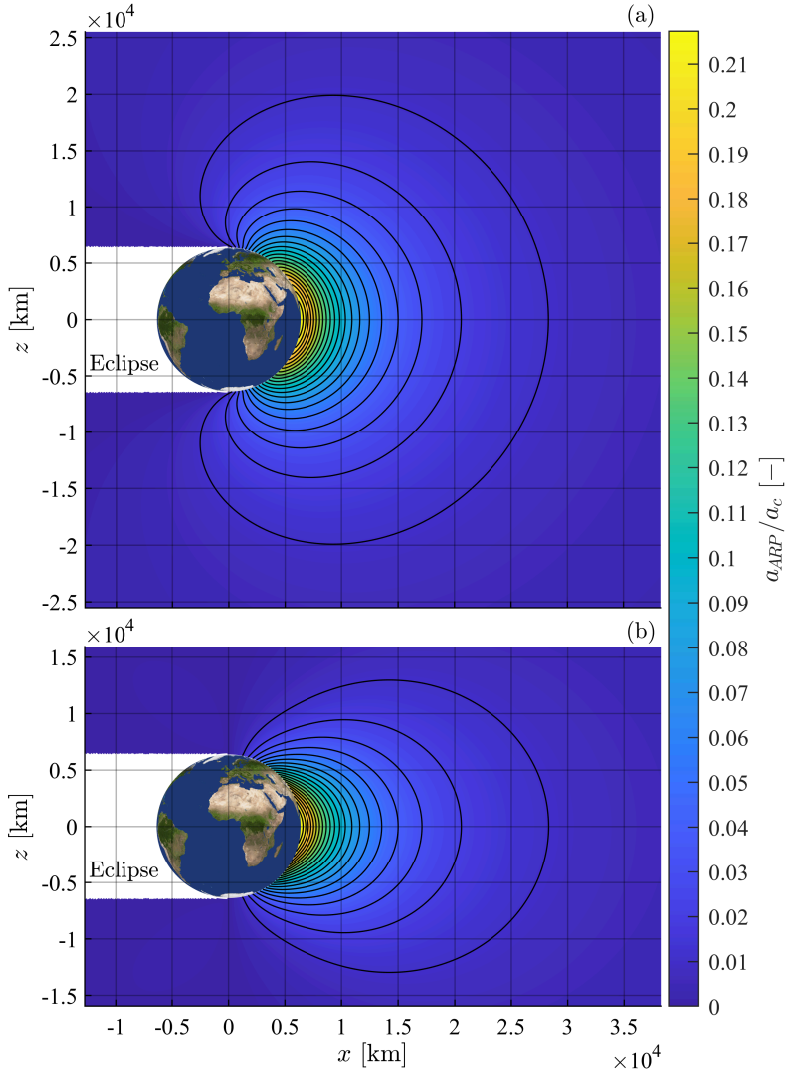


Figure 3.7: ARP acceleration for a) nadir-pointing and b) Sun-pointing solar sail, as per the spherical uniform model.

pointing and Sun-pointing solar sail, and for altitudes up to $h = 39600$ km. While for the BBRP acceleration the relative position of the Sun with respect to the sail was not of any importance, it is for the ARP acceleration. In both plots of Fig. 3.7, the Sun is placed along the positive $\hat{\boldsymbol{x}}$-axis direction and, therefore, the direction of sunlight is $\hat{\boldsymbol{s}} = -\hat{\boldsymbol{x}}$. Compared to the BBRP acceleration, the variation of the ARP acceleration around the Earth for a nadir-pointing sail displays a more complex pattern, due to the additional dependency of a_{ARP} on the phase angle, χ^*. Indeed, Fig. 3.7a shows that large ARP accelerations are

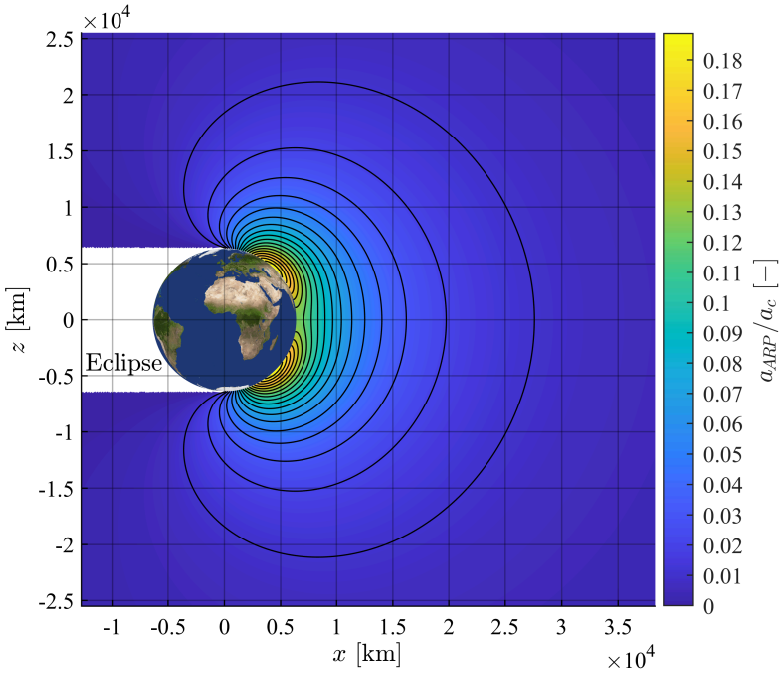


Figure 3.8: ARP acceleration for a nadir-pointing solar sail, as per the spherical sinusoidal model.

achieved when the sail is above the sunlit side of the Earth, reaching values up to 21% of the characteristic acceleration for low altitudes and $\chi^* = 0$ (sub-solar point, on the positive $\hat{\boldsymbol{x}}$-axis direction), in agreement with Eq. 3.36. The ARP acceleration decreases rapidly when moving towards the dark side of the Earth and, notably, the acceleration contour lines assume a high curvature in proximity in the terminator. This highlights that a_{ARP} does not decrease monotonically with altitude in this region, which is due to two counteracting effects: while for increasing altitudes the intensity of the radiation emitted by the Earth decreases, a higher altitude also allows the illuminated part of the Earth visible from the sailcraft to be larger, thus making the sail receive more albedo radiation. Since this latter effect is predominant at low altitudes, an increase in altitude initially yields a larger a_{ARP}. However, for even larger altitudes, the radiation intensity decreases rapidly and its effect becomes predominant, hence making a_{ARP} decrease as well. Similar to Fig. 3.5b, Fig. 3.7b displays the variation in ARP acceleration for a Sun-pointing solar sail. In this case, the region of high ARP acceleration shrinks, since moving towards the dark side of the Earth yields increasingly larger PPAs that negatively affect the ARP acceleration magnitude.

To gain insights in the ARP acceleration as per the spherical sinusoidal model, Fig. 3.8 displays the sinusoidal model's distribution of the ARP acceleration magnitude around the Earth, for altitudes up to $h = 39600$ km, for a nadir-pointing solar sail, and assuming the Sun to be in the equatorial plane (along the positive positive $\hat{\boldsymbol{x}}$-axis direction). Comparison of Figs. 3.7a and 3.8 shows that the accelerations of the uniform and sinusoidal

models vary similarly at large distances from the Earth, while differences arise at low altitudes. Indeed, the largest ARP acceleration magnitude in the sinusoidal model is about 19% of a_c and it is found at intermediate latitudes. The reason behind this peculiar acceleration magnitude distribution is twofold. On the one hand, the surface-averaged albedo radiation flux, $\bar{S}_{AR}$, tends to decrease when moving away from the sub-solar point, as the phase function, Φ, assumes increasingly lower values, see Eqs. 3.31 and 3.34. On the other hand, because in the sinusoidal model the albedo coefficient increases with latitude, the albedo radiation flux tends to increase when moving away from the equator, see Eqs. 3.31, 3.32 and 3.30. These two effects work in opposite directions, thereby resulting in an acceleration distribution with a maximum magnitude at mid-latitudes.

3.5. COMPARISON WITH THE STATE OF THE ART

This section presents several analyses that aim to measure the accuracy of the spherical PRP acceleration model compared to other models in the state of the art. In particular, Section 3.5.1 provides a comparison with the FD model devised by McInnes [2] and Section 3.5.2 presents different parametric analyses to validate the spherical model by measuring its accuracy relative to a high-fidelity numerical model.

3.5.1. COMPARISON WITH FINITE-DISK RADIATION SOURCE MODEL

The FD model has been widely applied in the literature [222, 223] and assumes that the emitting body (the Earth) appears as a uniformly bright disk whose radiation is collimated along the radial direction, $\hat{\boldsymbol{r}}$. As such, it does not take into account the angular distribution of the incoming radiation, nor the possibility of having both sides of the sail illuminated simultaneously. Similar to the spherical uniform model, the FD model also assumes a constant blackbody radiation flux and albedo coefficient. In light of this, in the following subsections the FD model will be compared against the spherical uniform model, rather than the spherical sinusoidal model. In this way, the differences arising from the different geometrical assumptions underlying the FD and spherical uniform models will be better highlighted.

3.5.1.1. BLACKBODY RADIATION PRESSURE ACCELERATION

When using the FD model, the BBRP acceleration, $\boldsymbol{a}_{BBRP,FD}$, can be expressed as [2, 222, 223]:

$$\boldsymbol{a}_{BBRP,FD} = a_{c,BBRP}\, G_{F,FD}\, \hat{\boldsymbol{n}}_{out} \tag{3.37}$$

where $G_{F,FD}$ represents the geometrical factor of the FD model:

$$G_{F,FD} = \left[1 - \left(1 - H^2\right)^{3/2}\right] \cos^2\alpha_{\oplus} \tag{3.38}$$

The only difference between the BBRP accelerations of the spherical uniform model and FD model is given by the definition of the geometrical factors, see Eqs. 3.18 and 3.37. For this reason, the comparison of the BBRP accelerations of these two models also provides direct insights in the difference between G_F and $G_{F,FD}$.

Figure 3.9 displays a comparison between the acceleration envelope curves of the spherical and FD models for a range of altitudes. These curves represent the set of all

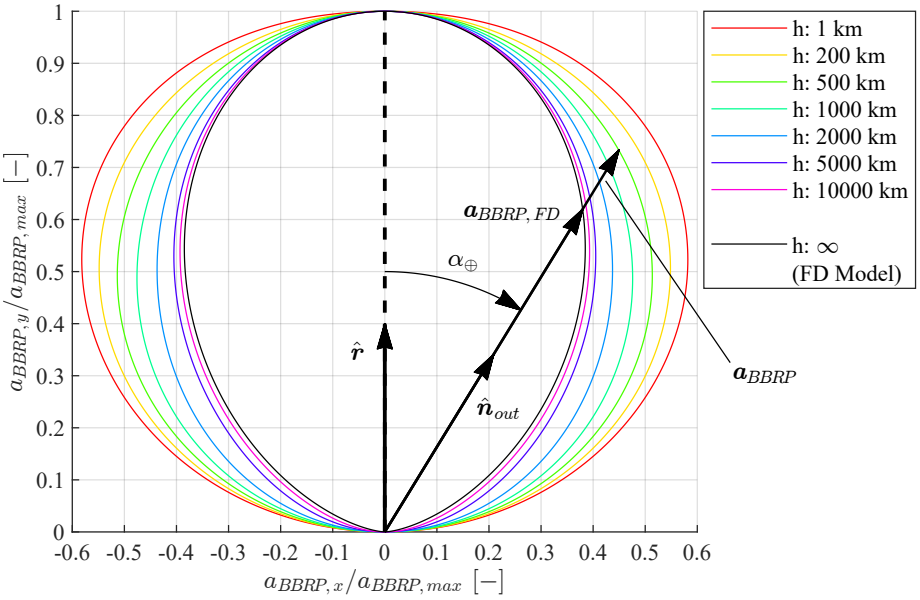


Figure 3.9: BBRP acceleration envelope curves of the FD and spherical models, and corresponding acceleration vectors for $h = 500$ km and generic PPA.

attainable BBRP accelerations achievable when changing the PPA. As can be seen, both models provide the same BBRP acceleration when $\alpha_\oplus = 0$. This is because, for $\alpha_\oplus = 0$, the spherical and FD models' geometrical factors are identical, see Eqs. 3.20 and 3.38. For increasing PPAs, discrepancies between the acceleration envelope curves arise, particularly in the transversal direction (i.e., perpendicular to $\hat{\boldsymbol{r}}$). These differences depend on the altitude considered, because for increasingly larger altitudes, the approximation introduced by considering the planet as a uniformly irradiating disk rather than a spherical radiation source reduces. Consequently, the spherical model's envelope curve converge to the FD model's envelope curve for $h \to \infty$. Because the spherical model's envelope curve depends on altitude and exhibits a larger transversal component compared to the FD model's envelope curve, the largest acceleration differences between the two models are found for low altitudes and intermediate values of the PPA ($45 - 75$ deg), reaching values even in the order of 3-4% of the characteristic acceleration, a_c.

3.5.1.2. ALBEDO RADIATION PRESSURE ACCELERATION

Similar to the analysis for the spherical BBRP acceleration model, the accuracy of the spherical uniform ARP acceleration model is quantified by comparing it against the FD ARP acceleration model. The ARP acceleration of the FD model can be expressed as [2]:

$$\boldsymbol{a}_{ARP,FD} = a_{c,ARP,FD}\, G_{F,FD}\, \hat{\boldsymbol{n}}_{out} \tag{3.39}$$

where $a_{c,ARP,FD}$ is the albedo characteristic acceleration of the FD model. Similar to Eq. 3.36 for the spherical uniform model, $a_{c,ARP,FD}$ can be defined in terms of the SRP

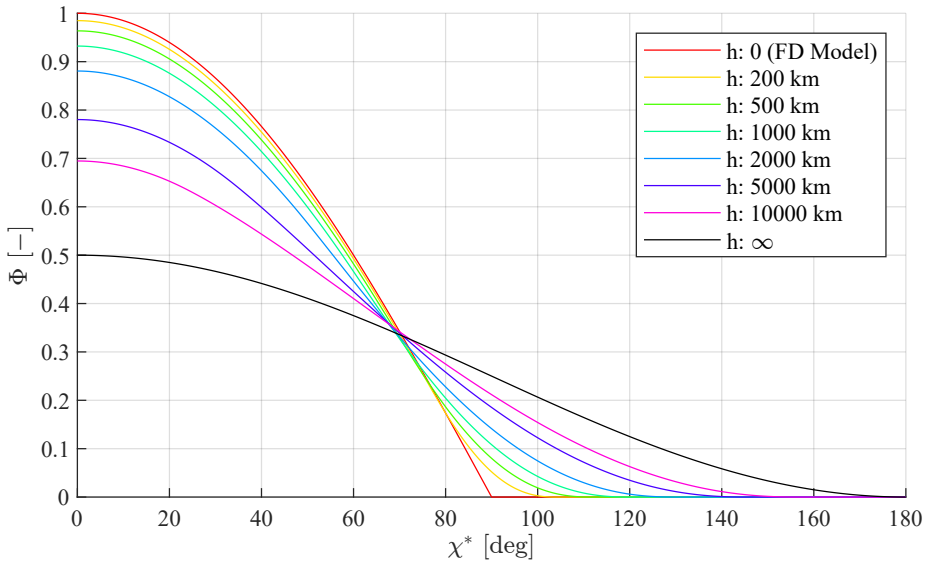


Figure 3.10: Albedo phase functions of the FD and spherical models.

characteristic acceleration, a_c, as:

$$a_{c,ARP,FD} = \frac{2\Lambda}{3}\Phi_{FD}\, a_c = 0.2173\,\Phi_{FD}\, a_c \tag{3.40}$$

where Φ_{FD} is the albedo phase function of the FD model, given by:

$$\Phi_{FD} = \max\left(0, \cos\chi^*\right) \tag{3.41}$$

The above definition of $a_{c,ARP,FD}$ is based on albedo flux models commonly used in the literature [222, 396] and differs from $a_{c,ARP}$ only for the use of Φ_{FD} instead of Φ, see Eqs. 3.36 and 3.40.

The different definitions of the geometrical factor and phase function of the spherical and FD models are at the core of the acceleration differences between the two models. Different geometrical factors determine different shapes of the ARP acceleration envelope curves, in a similar fashion to the BBRP acceleration envelope curves of Fig. 3.9. On the other hand, the albedo phase functions affect the maximum achievable ARP accelerations of the two models, so that different phase functions translate into different dimensions of the ARP acceleration envelope curves. To provide insights into this difference, Fig. 3.10 displays the albedo phase functions of the two models. As can be observed, the spherical model's phase function depends on altitude, unlike the FD model's phase function, in agreement with Eqs. 3.34, 3.35, and 3.41. Furthermore, it is interesting to note that while the geometrical factor of the spherical model converges to that of the FD model for increasing altitudes, see Fig. 3.9, the opposite is true for the phase function. Indeed, the spherical model's phase function, Φ, and FD model's phase function, Φ_{FD}, coincide for $h = 0$. Then, for increasing altitudes, the difference between Φ and Φ_{FD} (and, therefore,

between the sizes of the acceleration envelope curves) increases steadily, reaching values even in the order of 0.05 – 0.10 for altitudes in the range 500 – 1000 km and a maximum of 0.5 for $h \to \infty$.

3.5.2. PARAMETRIC ANALYSES

In this section, different parametric analyses are presented which aim to validate the spherical PRP acceleration model and quantify its accuracy compared to a high-fidelity numerical model. To achieve this, a wide variety of PRP-perturbed, Earth-bound orbits have been propagated using different PRP acceleration models. The equations of motion employed are given in Eq. 3.1, but with $\boldsymbol{a}_{Aero} = \boldsymbol{a}_{J2} = \mathbf{0}$, i.e., excluding the effect of aerodynamic drag and J_2 gravitational accelerations. These terms have been neglected as they would have introduced additional perturbations in the dynamics, thus making it more difficult to clearly determine the accuracy of the different PRP acceleration models. The PRP acceleration models considered are as follows:

a) The PRP acceleration model implemented in the software tool NRTDM (Near Real-Time Density Model), which computes the BBRP and ARP accelerations by approximating the acceleration integral of Eq. 3.17 with a finite sum. NRTDM is a software tool developed at the Delft University of Technology under ESA contract whose results have been used for different applications, including precise orbit determination, parameter estimation for the ERS and ENVISAT satellites, and processing of the GOCE and Swarm satellites' measurements [283, 363, 395]. In order to model the planetary flux distribution across the Earth, this model makes use of two monthly averaged maps, one for the blackbody radiation flux and one for the albedo coefficient, similar to the yearly averaged maps of Fig. 3.3. These maps have been obtained from the ANGARA software package developed by Hyperschall Technologie Göttingen GmbH [394] and they have been created based on the satellite data collected across the 1980s by the Earth Radiation Budget Experiment (ERBE) mission [363]. Thanks to the fine angular resolution of 2.5x2.5 deg^2 and the fact that a monthly variability is considered in the maps, this model allows to determine the BBRP and ARP accelerations to a very high accuracy, although requiring a large computational effort. For more information on NRTDM, the reader is referred to [363].

b) The spherical model with uniform blackbody radiation flux/albedo distributions, see Sections 3.2.4.1 and 3.2.4.2.

c) The spherical model with sinusoidal blackbody radiation flux/albedo distributions, see Sections 3.2.4.1 and 3.2.4.2.

d) The finite-disk model, see Section 3.5.1.

e) A model neglecting the PRP acceleration altogether, that is, $\boldsymbol{a}_{BBRP} = \boldsymbol{a}_{ARP} = \mathbf{0}$ at any time.

All analyses make use of the ACS3 mission orbit as baseline scenario, with a solar-sail characteristic acceleration of $a_c = 0.045\ \text{mm}\,\text{s}^{-2}$ and the following vector of initial orbital

elements defined in the inertial reference frame O_I:

$$\left[a_0,\ e_0,\ i_0,\ \text{LTAN}_0,\ \omega_0,\ f_0\right]^T = \left[7093.1363\ \text{km},\ 0,\ 98.2490\ \text{deg},\ \begin{Bmatrix} 0000\ \text{hrs} \\ 0030\ \text{hrs} \\ \vdots \\ 2330\ \text{hrs} \end{Bmatrix},\ 0\ \text{deg},\ 0\ \text{deg}\right]^T \tag{3.42}$$

where a is the semi-major axis, e the eccentricity, i the inclination, ω the argument of perigee, f the true anomaly, LTAN stands for local time of the ascending node, and the subscript "0" denotes the initial value of these variables[1]. These orbital elements represent a circular, Sun-synchronous orbit with initial altitude $h_0 = a_0 - R = 715$ km. In Eq. 3.42, several values of the LTAN are considered, spaced by 0.5 hours along the entire 24-hour time span. This parameter defines the orbit orientation in frame O_I and is equivalent to the right ascension of the ascending node, which, in a similar fashion, is spaced by 7.5 deg across the entire 360-degree angular span. The parametric analysis also considers 12 different simulation start times, corresponding to the 15$^{\text{th}}$ day of each month of 2023. For each initial orbit, the solar-sail dynamics are propagated while implementing locally optimal orbit-raising and inclination-changing steering laws. These steering laws are computed using an algorithm devised by McInnes [2], accounting only for SRP in the optimization process. Therefore, the BBRP and ARP accelerations are considered as uncontrolled perturbing accelerations affecting the orbit. For each initial orbit, each simulation start time and each steering law, five different propagations are performed in which the PRP acceleration is computed through the five models listed above. Then, the relative errors between the final altitude/inclination obtained by the NRTDM model (taken as the ground truth) and each of the analytical models, ε_{rel}, are computed. The parameter ε_{rel} is used as metric of the accuracy of the analytical models and it is defined as:

$$\varepsilon_{rel} = \frac{\left|\text{œ}_{NRTDM,f} - \text{œ}_{An,f}\right|}{\text{œ}_{NRTDM,f} - \text{œ}_0} \tag{3.43}$$

where œ_0 indicates the initial value of the steering law's target parameter (i.e., h or i) and $\text{œ}_{NRTDM,f}$ and $\text{œ}_{An,f}$ represent the final values of the target parameter found through the NRTDM and the analytical model under consideration, respectively. For each simulation, the dynamics have been propagated for 10 days, using Matlab®'s *ode45* integrator with absolute and relative tolerances of 10^{-12}. The above-presented analysis settings will be used as reference settings in the following subsections to investigate the accuracy of the spherical models and its variation with the initial LTAN, altitude, and inclination.

3.5.2.1. VARIATION IN ACCURACY WITH THE LOCAL TIME OF THE ASCENDING NODE

Fig. 3.11 shows the variation of the relative error with the LTAN for the orbit-raising steering law for all analytical models. For each model, a band is displayed which represents the range of relative errors obtained by considering simulation start times at different months. All the error bands follow a 12-hour periodic trend, approximately symmetric with respect

[1] ACS3 mission data taken from personal communication with W.K. Wilkie, Principal Investigator of the ACS3 mission, NASA Langley Research Center, February 2023.

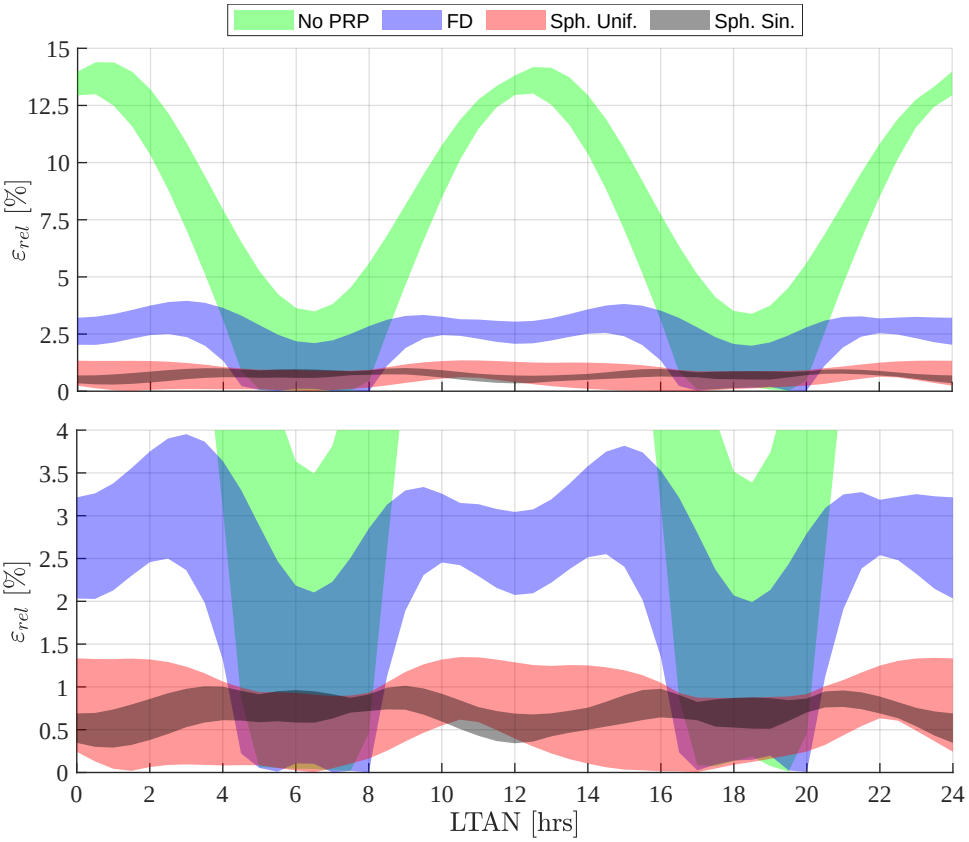


Figure 3.11: Relative error on the orbital altitude increase of different PRP acceleration analytical models with respect to the NRTDM model. Full plot on top and zoomed inset on the bottom.

to the LTAN at 1200 hrs. This is due to the relative orientations of the Sun-synchronous orbits with respect to the direction of sunlight, which can be similar even for different LTANs and therefore yield similar errors, ε_{rel}. When the PRP is neglected or the FD model is used, the relative errors approach a minimum for an LTAN at 0600/1800 hrs (corresponding to a dawn-dusk orbit). The reason for this is that the phase angle, χ^*, is always close to 90 deg and therefore a very small ARP acceleration is exerted on the sail, see Figs. 3.7 and 3.8. Furthermore, by implementing the orbit-raising steering law, the sail is constantly oriented almost edgewise with respect to the radial direction. This corresponds to a PPA, $\alpha_\oplus$, approximately equal to 90 deg at all times and thus a minor BBRP acceleration, see Figs. 3.5b and 3.9. When an LTAN at 0000/1200 hrs is considered (corresponding to a noon-midnight orbit), the BBRP and ARP accelerations are the largest and therefore the errors achieved by these two models, ε_{rel}, are maximum. This result is due to the fact that the sailcraft flies in the vicinity of the sub-solar point once per orbit, where the ARP acceleration is the largest. Also, in this case, the PPA, $\alpha_\oplus$, varies in a wide range, from 0 to 90 deg, thus yielding considerable BBRP accelerations. While these considerations hold

true also for the spherical models, their error bands exhibit a weaker dependency with the LTAN. This stems from the fact that the spherical models manage to approximate the ARP and BBRP accelerations better than the "No-PRP" and FD models, particularly for LTANs close to 0000/1200 hrs. Although the errors that the uniform and sinusoidal models produce are similar in magnitude, it is worth noting that the width of the uniform model's error band is larger than the sinusoidal model's error band. This is due to the higher level of approximation of the uniform model, which introduces a larger error uncertainty with respect to the simulation start time. The narrower error band displayed by the sinusoidal model also highlights its different trend compared to the other models, with a minimum for an LTAN at 0000/1200 hrs and a maximum for LTANs close to 0600/1800 hrs. This trend is determined by a second-order source of error, originating from a complex interplay between the sail orientation and the Sun-Earth-sailcraft relative geometry. Indeed, when the day-night terminator is visible from the sailcraft and for specific sail attitudes, the outward-facing side of the sail can receive more albedo radiation than its inward-facing side. This yields an ARP acceleration that points opposite to $\hat{\boldsymbol{n}}_{out}$. However, because of the simplifying assumption that the Earth irradiates isotropically, the sinusoidal model always provides ARP accelerations pointing towards $\hat{\boldsymbol{n}}_{out}$, see Eq. 3.18. This discrepancy affects the results particularly if the day-night terminator is often visible from the sailcraft, i.e., for an LTAN at 0600/1800 hrs, thus yielding a larger relative error, ε_{rel}. Conversely, for LTANs close to 0000/1200 hrs, the day-night terminator is visible only for short periods of time and, therefore, ε_{rel} is minimum.

As can be seen in the plots, neglecting the PRP acceleration in the dynamics yields large relative errors, even in the order of 14%. When employing the FD model, these errors are strongly reduced, reaching values of 4% at most. Due to their higher fidelity with respect to the FD model, the spherical models achieve even smaller errors, in the range 0-1.3% and 0.3-1% for the uniform and sinusoidal models, respectively.

Similar to Fig. 3.11 for the orbit-raising case, Fig. 3.12 displays the variation of ε_{rel} for the inclination-changing steering law, for different LTANs and PRP acceleration models. In this case, a 12-hour periodicity in the errors is again obtained, although the error bands appear skewed and asymmetric, unlike the ones observed in Fig. 3.11. This asymmetry is due to the complex, discontinuous nature of the inclination-changing steering law, for which orbits with similar orientations with respect to the sunlight direction still yield different increases in inclination [2]. Similar to the orbit-raising case, only a minor ARP acceleration perturbs the orbit for LTANs close to 0600/1800 hrs, as the phase angle is close to 90 deg at all times. This leads to small relative errors, ε_{rel}, particularly when the "No-PRP", FD, or uniform models are used. The errors achieved by these three models increase as the LTAN deviates from 0600/1800 hrs, reaching their maximum between 1100/2300 hrs and 1400/0200 hrs. In these cases, the sail flies in the vicinity of the sub-solar point once per orbit with a small PPA. This results in considerable ARP and BBRP accelerations, which yield larger errors for all models except the sinusoidal model. Indeed, for the same range of LTANs, the sinusoidal model achieves much smaller errors, even compared to the uniform model. This is due to the higher fidelity with which the blackbody and albedo radiation fluxes are modeled. As such, the error difference between the uniform and sinusoidal models provides direct insights into how the modeling of the blackbody and albedo radiation fluxes affects the accuracy. Comparing the error bands

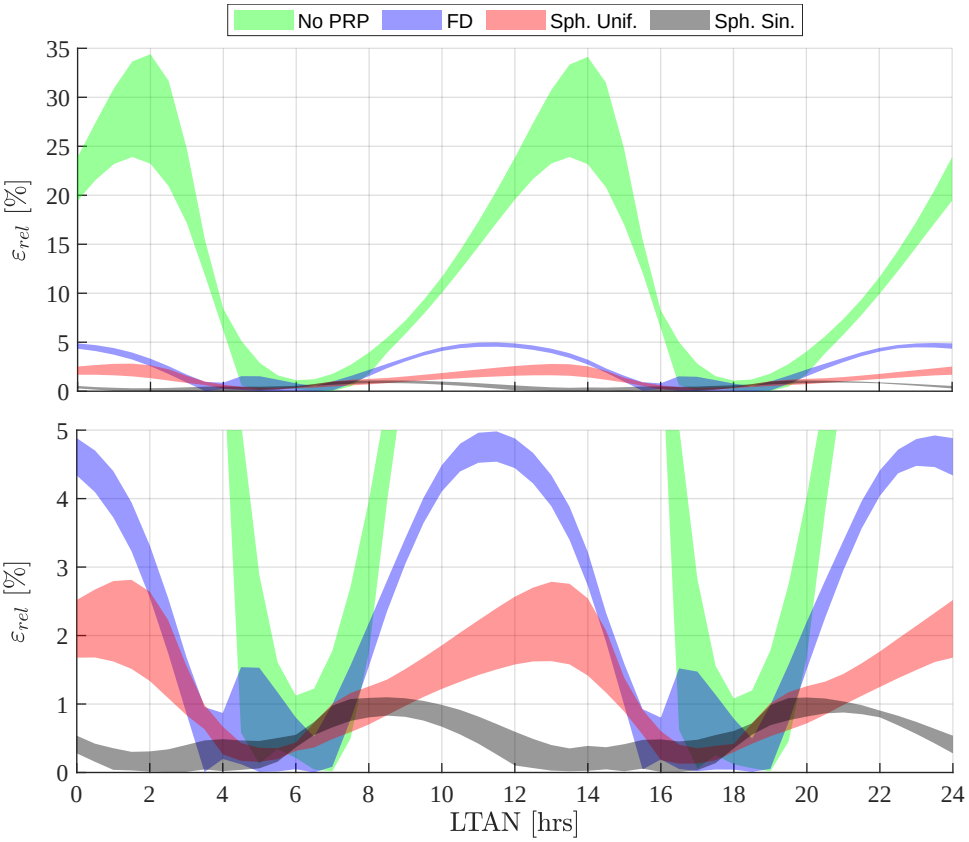


Figure 3.12: Relative error on the inclination increase of different PRP acceleration analytical models with respect to the NRTDM model. Full plot on top and zoomed inset on the bottom.

of the spherical sinusoidal and uniform models, it can be noted that the former exhibits a narrower spread than the latter. As for the orbit-raising case, this is due to the better level of approximation of the sinusoidal model, which yields a lower error uncertainty. The plots also show that the sinusoidal model achieves its maximum error for an LTAN at 0800/2000 hrs. Like in the orbit-raising case, this is due to the approximation that the Earth behaves as an isotropic radiator, which can lead to errors in the ARP acceleration direction when in proximity of the day-night terminator.

Fig. 3.12 shows that if the PRP is not accounted for in the dynamics, large errors are produced, reaching magnitudes even in the order of 34%. On the other hand, smaller errors are achieved when the FD, spherical uniform, and spherical sinusoidal models are employed, reaching values of at most 5.0%, 2.8% and 1.1%, respectively.

3.5.2.2. VARIATION IN ACCURACY WITH ALTITUDE

The parametric analysis discussed in Section 3.5.2.1 provided insights into the accuracy of the PRP acceleration models for a wide variety of LTANs and simulation start times.

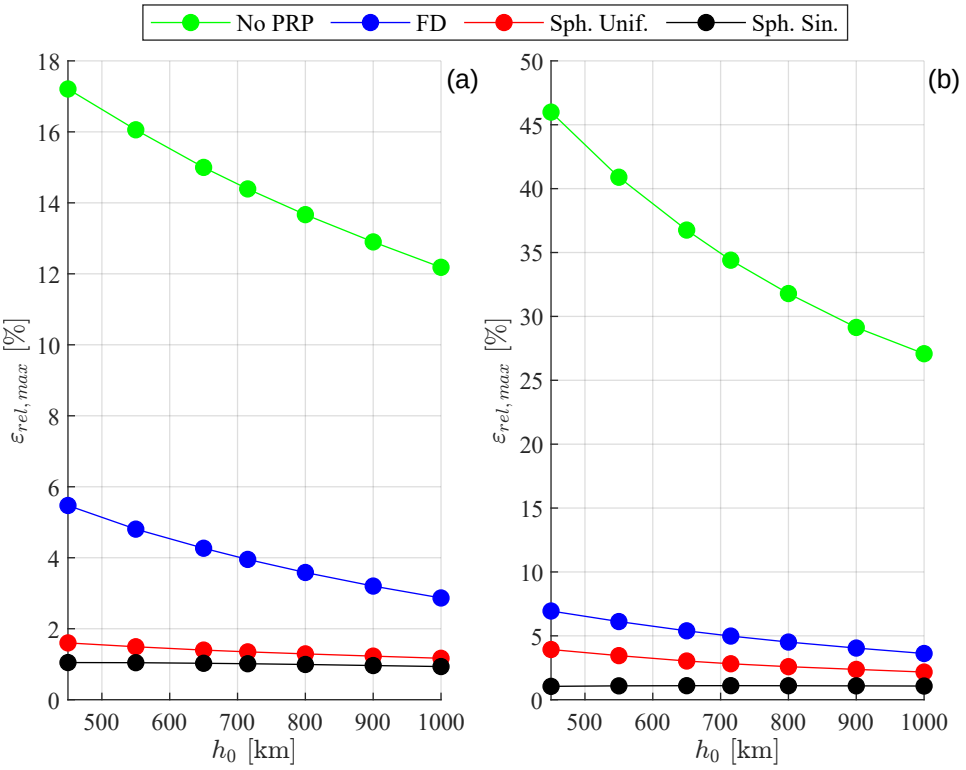


Figure 3.13: Maximum relative error on the a) altitude increase and b) inclination increase for different altitudes.

Nevertheless, the fidelity of the FD and spherical PRP acceleration models also depends on the orbital altitude considered, as highlighted in Section 3.5.1. In light of this, additional parametric analyses – similar to the ones presented above – have been conducted, in order to quantify the variation in the accuracy of the PRP acceleration models with altitude. More specifically, the same parametric analyses of Section 3.5.2.1 have been performed again multiple times, although considering the set of initial altitudes $h_0 = \{450, 550, 650, 715, 800, 900, 1000\}$ km and their corresponding Sun-synchronous inclinations, which range between $i_0 = 97.2139$ deg and $i_0 = 99.4790$ deg. It should be noted that the altitude lower bound of 450 km was chosen as this represents the lowest altitude for which solar sails can maneuver without deorbiting, despite the intense atmospheric, see Chapter 6. In order to conveniently summarize the results obtained, Fig. 3.13 displays the maximum relative error achieved over all LTANs and simulation start times, $\varepsilon_{rel,max}$, for each PRP acceleration model, steering law, and initial altitude.

Fig. 3.13a shows the variation of $\varepsilon_{rel,max}$ with the initial altitude for the orbit-raising steering law. As can be observed, $\varepsilon_{rel,max}$ increases for decreasing values of h_0, for all PRP acceleration models. This stems from the fact that, by lowering the altitude, the sail experiences larger PRP accelerations perturbing the orbit to a larger extent. The increase in $\varepsilon_{rel,max}$ for increasingly lower h_0 is especially visible when PRP is not considered,

as $\varepsilon_{rel,max}$ varies between 12.2% and 17.2%. Using the FD model yields better results, although maximum relative errors between 2.9% and 5.5% can still be achieved. The spherical PRP acceleration models also show a slight increase in error for decreasing altitudes, although much less pronounced than the FD and "No-PRP" models: $\varepsilon_{rel,max}$ always assumes values in the ranges 1.2-1.6% and 0.9-1.1% for the uniform and sinusoidal models, respectively. Fig. 3.13b shows the change of $\varepsilon_{rel,max}$ with the initial altitude for the inclination-changing steering law. Similar to the orbit-raising case, the results show that the "No-PRP", FD, and spherical uniform models perform less accurately for decreasing initial altitudes. Neglecting the PRP acceleration yields large maximum relative errors, particularly at low altitudes, where $\varepsilon_{rel,max}$ can even reach 45%. In contrast, the FD and uniform models perform considerably better than the "No-PRP" model, achieving $\varepsilon_{rel,max}$ in the ranges 3.6-6.9% and 2.2-3.9%, respectively. Ultimately, when the spherical sinusoidal model is employed, the error variation with altitude almost disappears, as $\varepsilon_{rel,max}$ remains between 1.05% and 1.10%.

3.5.2.3. VARIATION IN ACCURACY WITH INCLINATION

The parametric analyses discussed in Section 3.5.2.2 provided insights into the accuracy of the PRP acceleration models for a variety of orbital conditions, though only considering Sun-synchronous orbits. Therefore, in order to investigate also the impact of inclination on the accuracy of the different PRP acceleration models, additional parametric analyses have been conducted. In particular, the same parametric analyses of Section 3.5.2.1 have been performed again multiple times considering the inclinations $i_0 = \{0.5, 24, 50, 75, 90, 98.2490\}$ deg, where the last value corresponds to the Sun-synchronous inclination for $h_0 = 715$ km.

Fig. 3.14a shows the variation of $\varepsilon_{rel,max}$ with the initial inclination for the orbit-raising steering law. As can be seen, neglecting the PRP acceleration leads to considerable errors, with values of $\varepsilon_{rel,max}$ even in the order of 14% for (quasi-) polar orbits. For equatorial orbits, the FD model performs particularly well and, notably, it achieves $\varepsilon_{rel,max}$ even lower than the uniform model's. However, for increasing initial inclinations, the accuracy of the FD model reduces while that of the uniform model improves. This causes the error curve of the FD model to grow from 1.9% to a maximum of 4.2%, whereas for the uniform model $\varepsilon_{rel,max}$ reduces from 2.6% to 1.3%. The uniform model displays large errors for small inclinations because of its limited accuracy in predicting the planetary radiation flux near the equator. Because the sailcraft flies only on top of the equatorial region for an equatorial orbit, the error committed accumulates rapidly over time. On the other hand, for larger inclinations, the sailcraft's ground track covers a larger portion of the Earth's surface, thus alleviating the accumulation of error and lowering $\varepsilon_{rel,max}$. Ultimately, the sinusoidal model achieves the lowest errors for any initial inclination considered, with $\varepsilon_{rel,max}$ varying in the range 0.4-1.2%. Fig. 3.14b shows the change of $\varepsilon_{rel,max}$ with the initial inclination for the inclination-changing steering law. The error curves of the "No-PRP" model shows a weak dependency with the initial inclination, whereas the FD and uniform models display trends similar to those found in Fig. 3.14a. Compared to the orbit-raising case, however, the magnitude of the errors is amplified: $\varepsilon_{rel,max}$ reaches even 34.7% when PRP is neglected, while values in the ranges 4.2-5.0% and 2.7-5.5% are found for the FD and uniform models, respectively. Unlike Fig. 3.14a, the sinusoidal model performs worse for equatorial orbits than high-inclination orbits, as

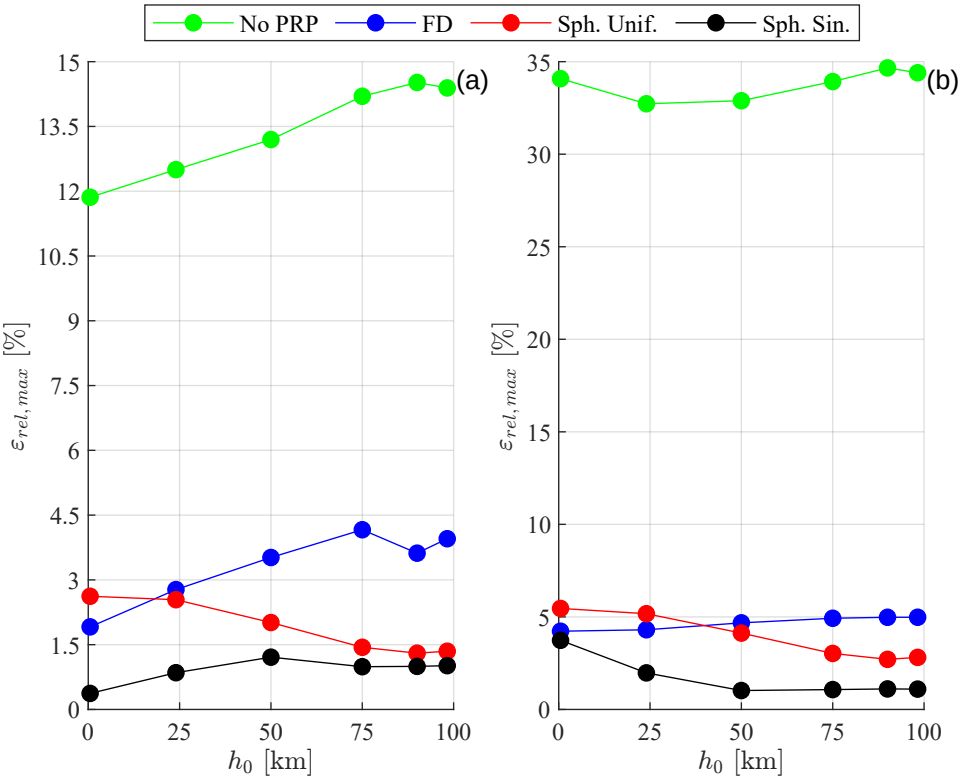


Figure 3.14: Maximum relative error on the a) altitude increase and b) inclination increase for different inclinations.

$\varepsilon_{rel,max} = 3.7\%$ is found for $i_0 = 0.5$ deg while smaller errors of at most of 1.1% are found for (quasi-) polar inclinations. Nonetheless, the sinusoidal model still performs the best among all models and for all inclinations considered.

The results presented in Figs. 3.13 and 3.14 highlight the limits of both the FD and "No-PRP" acceleration models to accurately represent the solar-sail dynamics, especially at low altitudes and for orbits with high inclination. On the other hand, the spherical uniform and sinusoidal models achieve much lower errors, with the sinusoidal model performing the best among all analytical models, as it achieves a consistent accuracy independent of altitude and only slightly dependent on inclination. Based on these results, therefore, the spherical uniform and sinusoidal models are deemed validated. In addition to their accuracy, it should also be noted that using the spherical uniform or sinusoidal models incurs only minor additional computational costs compared to the FD model. This is due to the fact that all these models are analytical. Therefore, they require a similar computational effort which is, however, substantially smaller than the computational effort required by numerical methods such as NRTDM. More specifically, by considering several orbital scenarios and computing the corresponding PRP accelerations through the aforementioned models, it was found that the spherical sinusoidal model requires

a runtime 1.02 and 2.73 times larger than that of the spherical uniform and FD models, respectively. In contrast, the runtime of the sinusoidal model was found to be 31.7 times shorter than the runtime of the NRTDM model.

3.6. ACS3 MISSION ANALYSIS

In this section, the effect of the BBRP and ARP accelerations on the orbit-raising and inclination-changing capabilities of different Earth-bound solar-sail orbits is analyzed. Similar to the last section, all analyses make use of the ACS3 mission as baseline scenario, with a simulation start time of June 1st, 2024 (i.e., the expected deployment date of the solar sail at the time of this study). The initial orbital elements are given in Eq. 3.42, although the initial LTAN values have been restricted to 0600 and 1200 hrs only. These identify two orbits in dawn-dusk and noon-midnight conditions, corresponding to right ascensions of the ascending node of 339.9554 and 69.9554 deg, respectively. Unlike Section 3.5 – where the dynamics considered only the SRP and PRP accelerations – in this section a more realistic full-dynamical model is employed, which accounts also for the aerodynamic and J_2 gravitational accelerations. In these dynamics, the PRP acceleration is modeled using the spherical sinusoidal model, because of its high accuracy and limited computational costs, as seen in Section 3.5. For each initial orbit, the solar-sail dynamics are propagated and locally optimal orbit-raising and inclination-changing steering laws are employed. These steering laws are computed using the algorithm presented in Chapter 6, which accounts for SRP, atmospheric drag, and the J_2 perturbation in the optimization process, but not for the PRP. Therefore, the BBRP and ARP accelerations are considered as uncontrolled perturbing accelerations affecting the orbit. To quantify the effect of these accelerations on the orbit-raising and inclination-changing capabilities of the ACS3 mission, the equations of motion presented in Eq. 3.1 are propagated with and without PRP acceleration on the right-hand side. In this way, the final increases in altitude and inclination for PRP-perturbed and PRP-unperturbed orbits can be compared and their difference assessed. Similar as in Section 3.5, for each scenario, the equations of motion are propagated for 10 days using Matlab®'s *ode45* integrator, with absolute and relative tolerances of 10^{-12}. More details on the optimization scheme as well as the settings used for the optimizer are provided in Chapter 6.

Figure 3.15 shows the variation of the SRP, aerodynamic, BBRP, and ARP accelerations over one orbital period, for the orbit-raising and inclination-changing steering laws (top and bottom plots, respectively) and LTANs at 0600 and 1200 hrs (left and right plots, respectively). It should be noted that although the J_2 gravitational acceleration has also been included in the dynamics, its magnitude is not displayed in Fig. 3.15. This is because the J_2 acceleration is significantly larger than the other accelerations considered, ranging between 206 and 459 times the characteristic acceleration, a_c. The large differences in the acceleration profiles for the four cases are due to the different sail attitude control profiles adopted. Indeed, as discussed in Chapter 6, the solar-sail attitude control is computed through the optimization process and strongly depends on the steering law and LTAN considered. As shown in the plots, most of the time the SRP acceleration is the dominant acceleration. However, the BBRP and ARP accelerations can get as large as 10-15% of the solar-sail characteristic acceleration and, for some cases and in some particular sections of the orbit, attain values even larger than the SRP acceleration. These large values of the

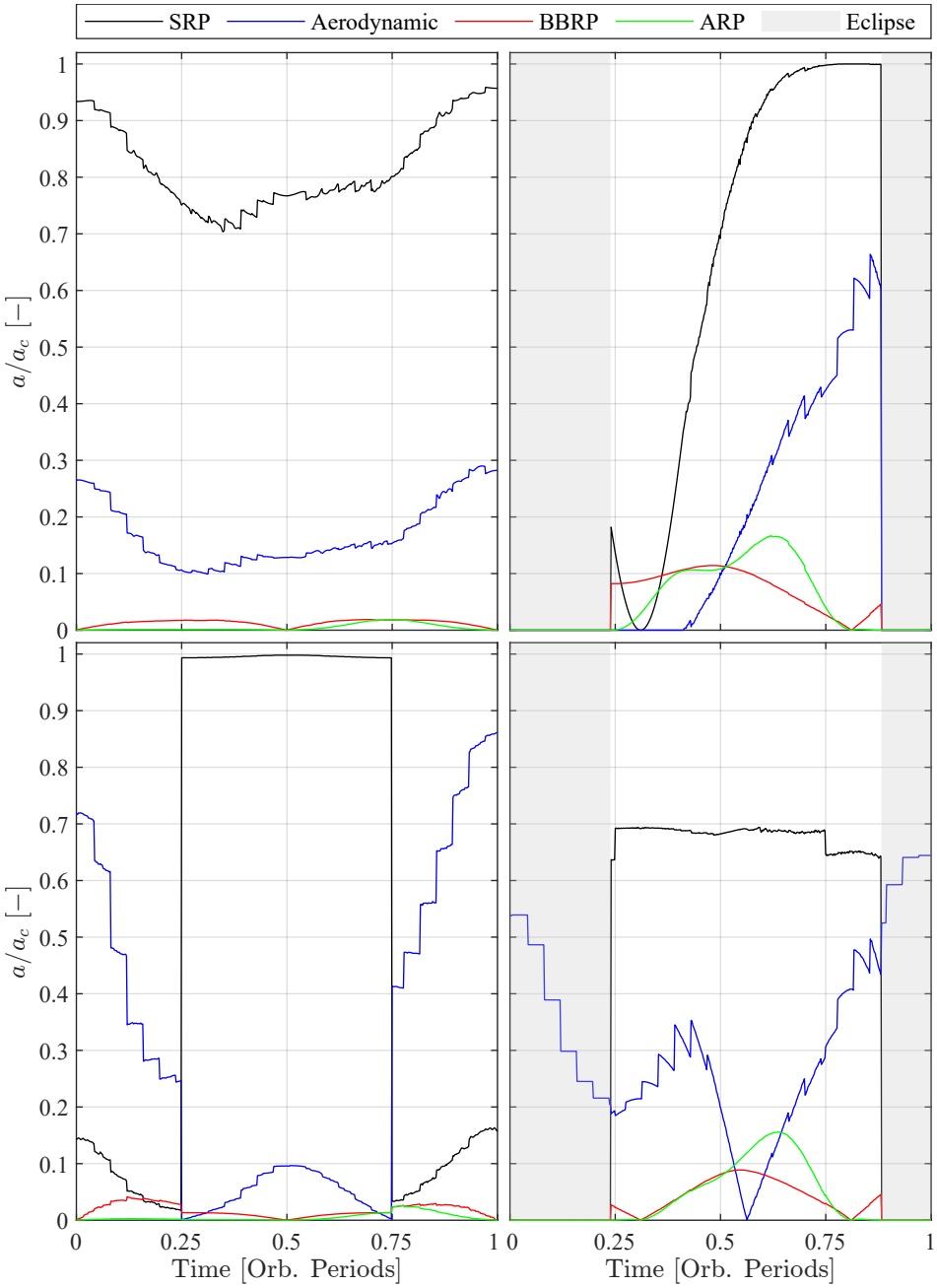


Figure 3.15: ACS3 acceleration profiles for the orbit-raising (top) and inclination-changing (bottom) steering laws with LTAN at 0600 hrs (left) and 1200 hrs (right).

Table 3.1: ACS3 simulation results for different steering laws and initial LTANs, with and without PRP.

Steering law	Orbit raising				Inclination changing			
LTAN	0600 hrs		1200 hrs		0600 hrs		1200 hrs	
PRP	✗	✓	✗	✓	✗	✓	✗	✓
$a_{BBRP,avg}/a_c$, %	N/A	1.31	N/A	4.57	N/A	2.59	N/A	2.88
$a_{ARP,avg}/a_c$, %	N/A	0.48	N/A	4.85	N/A	0.71	N/A	3.82
$\Delta\alpha$	19.581 km	19.445 km	12.834 km	10.332 km	$9.370\cdot10^{-2}$ deg	$9.347\cdot10^{-2}$ deg	$4.886\cdot10^{-2}$ deg	$4.085\cdot10^{-2}$ deg
$\varepsilon_{rel,f}$, %	0.701		24.21		0.246		19.61	

Note: ✓ indicates that the PRP is considered.
✗ indicates that the PRP is not considered.

BBRP and ARP accelerations are achieved when an initial LTAN of 1200 hrs is considered. As discussed in Section 3.5, this is due to the orbit orientation – which allows the sailcraft to fly in proximity of the sub-solar point – and the low PPA values encountered along the orbit. On the other hand, for an initial LTAN at 0600 hrs, the PPA and phase angle assume values close to 90 deg, thus yielding smaller BBRP and ARP accelerations equal to at most 4% of the characteristic acceleration. It is interesting to note that when an orbit-raising steering law is considered, no BBRP and ARP accelerations are produced during eclipses. Indeed, in this circumstance the normal vector of the sail is oriented perpendicular to the orbital plane. This translates into the sail being oriented parallel to the wind flow to prevent atmospheric drag while, at the same time, the BBRPs on the sail front and back sides counteract each other to produce a null net acceleration. In addition, because the sail is in eclipse, no solar radiation or albedo is present, thus making the total acceleration exerted on the sail reduce to the J_2 acceleration only. When an inclination-changing steering law is employed and the sail is in eclipse, a similar phenomenon takes place. Indeed, in this case the sail is oriented edgewise with respect to the radial direction, but with a non-zero angle of attack with respect to the wind flow. As a consequence, this sail attitude yields once again a null BBRP acceleration but also a nontrivial aerodynamic acceleration. This is visible in the bottom-right plot of Fig. 3.15 for the inclination-changing steering law with LTAN at 1200 hrs, which shows that the aerodynamic acceleration is the only non-zero acceleration (except for the J_2 acceleration, not displayed).

Table 3.1 displays the average BBRP and ARP accelerations experienced by the sail and the final altitude and inclination increases obtained after 10 days, for all orbit scenarios, with and without PRP in the dynamics. In the table, $\Delta\alpha$ is the total increase in the steering law's target parameter (i.e., h or i) after 10 days and $\varepsilon_{rel,f}$ is the relative error between the $\Delta\alpha$ found with and without PRP in the dynamics. It should be noted that although the J_2 acceleration is orders of magnitudes larger than the SRP, PRP, or aerodynamic accelerations, the results given in Table 3.1 are affected by the J_2 perturbation only to a limited extent. Indeed, the J_2 perturbation has no secular effect on the altitude and inclination, only a short-term periodic effect [308]. Consequently, accounting for the J_2 perturbation affects the investigation of the orbit-raising and inclination-changing

capabilities of solar sails only slightly. As observed also in Fig. 3.15, the average BBRP and ARP accelerations are considerably smaller for an LTAN at 0600 hrs than at 1200 hrs. Therefore, for an LTAN at 0600 hrs the effect of the PRP on the orbit-raising/inclination-changing capabilities of the sail is only minor. This translates into relative errors in the altitude/inclination change in the range 0.2-0.7% with respect to the case in which the PRP is not accounted for. Conversely, for an LTAN at 1200 hrs, larger BBRP and ARP accelerations are found and the orbit is perturbed significantly: neglecting the PRP in the dynamics yields relative errors of 24.21% and 19.61% for the orbit-raising and inclination-changing steering laws, respectively. It is interesting to note that the relative errors, $\varepsilon_{rel,f}$, given in Table 3.1 assume values close to the relative errors, ε_{rel}, displayed in Figs. 3.11 and 3.12, for the "No PRP" error band. This is due to the fact that $\varepsilon_{rel,f}$ is defined similar to Eq. 3.43, where the final altitude/inclination achieved by the NRTDM model, $\alpha_{NRTDM,f}$, is substituted with the final altitude/inclination of the spherical sinusoidal model. Since the difference between the final altitude/inclination achieved by these two models is minor, see again Figs. 3.11 and 3.12, ε_{rel} and $\varepsilon_{rel,f}$ assume similar values. More specifically, the values assumed by $\varepsilon_{rel,f}$ for the inclination-changing steering law are within or slightly below the error band of Fig. 3.12. On the other hand, the errors $\varepsilon_{rel,f}$ for the orbit-raising steering law are within the error band of Fig. 3.11 for an LTAN at 0600 hrs, but are far above the error band for an LTAN at 1200 hrs. Further investigations showed that this discrepancy is due to the presence of the aerodynamic drag, which strongly affects the achieved altitude increase. Consequently, accounting for it in this section but not in Section 3.5 produces larger relative errors compared to the those of Fig. 3.11.

The results provided in this section show that the PRP acceleration can achieve a non-negligible magnitude compared to the SRP and aerodynamic accelerations. When the PRP is uncontrolled, the orbit-raising and inclination-changing capabilities of solar sails can be affected negatively to a significant extent. Therefore, in future research, accounting for the PRP in the optimization procedure may prove beneficial. In this way, the detrimental effects observed in the above-presented analysis may be counteracted and, potentially, even larger altitude and inclination changes might be achieved than foreseen to date.

3.7. CONCLUSIONS

In this chapter, a novel analytical model for the planetary radiation pressure (PRP) accelerations of double-sided perfectly reflecting solar sails has been presented. The accuracy of this model, named spherical PRP acceleration model, has been measured by analyzing the orbit-raising and inclination-changing capabilities of NASA's ACS3 mission under the influence of PRP, for a wide variety of orbital scenarios. The results show the spherical model's superiority in terms of accuracy compared to another state-of-the-art analytical model, namely, the finite-disk radiation pressure acceleration model devised by McInnes [2]. Furthermore, when the spherical model is used assuming sinusoidal distributions of the Earth's blackbody radiation flux and albedo coefficient with latitude, it achieves a very high accuracy even compared to a high-fidelity numerical model, with errors at most in the order of 1% and 3% in the measured altitude and inclination gains, respectively. This accuracy is found consistently for all orbit scenarios analyzed, regardless of the orbit orientation, altitude, steering law, or time of the year considered. In

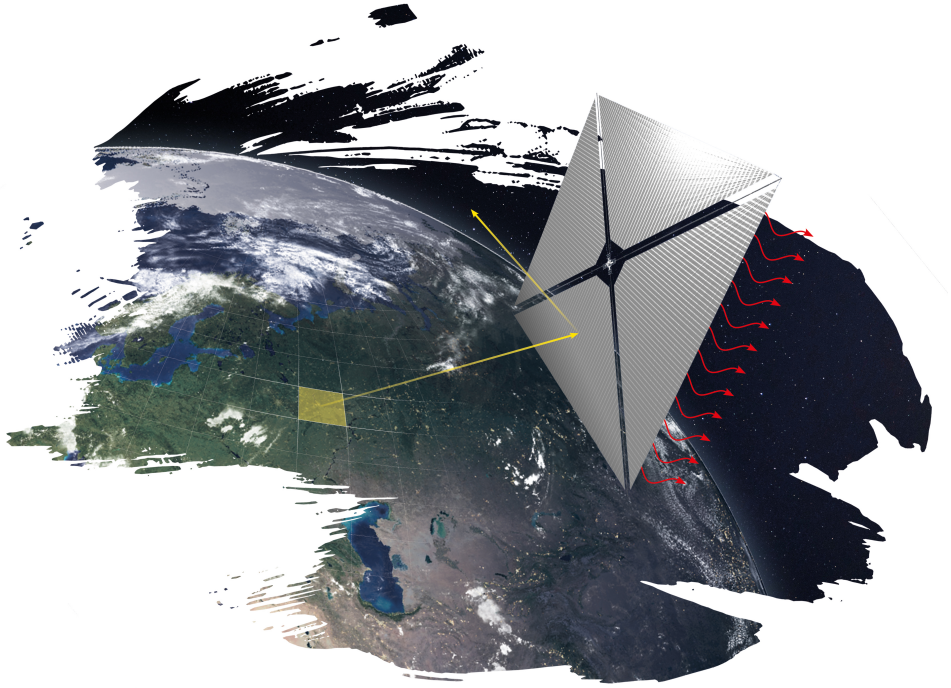
addition, the spherical model was also found to require 32 times less runtime than the above-mentioned numerical model. These results demonstrate the validity of the spherical model as a computationally efficient, yet accurate, alternative to numerical PRP acceleration models, particularly for planetocentric solar-sail mission design and analysis. Finally, the newly devised spherical model has also been used to determine the perturbing effect of the PRP acceleration on Earth-orbiting solar sails. Using the ACS3 mission as reference scenario, it was shown that neglecting the PRP acceleration in the dynamics can lead to large errors in the estimated orbit-raising and inclination-changing capabilities, even in the order of 20%. This result highlights the importance of accounting for the PRP acceleration in the solar-sail dynamics. Furthermore, since the PRP acceleration can reach magnitudes up to 10-20% of the solar-sail characteristic acceleration in proximity of the Earth, the results also suggest that the PRP acceleration may be exploited beneficially to enhance the maneuvering capabilities of solar sails.

ACKNOWLEDGEMENTS

Sincere thanks go to W. Keats Wilkie from NASA Langley Research Center and Andrew Heaton from NASA Marshall Space Flight Center for fruitful discussions on the ACS3 mission and valuable information shared. Gratitude is also extended to Dr. Christian Siemes and Natalia Hladczuk from Delft University of Technology and Dr. Eelco Doornbos from KNMI (Koninklijk Nederlands Meteorologisch Instituut) for sharing the software tool NRTDM and their knowledge of the ANGARA Earth radiation maps.

4

Extending the Spherical Planetary Radiation Pressure Acceleration Model to Optical Solar Sails



ABSTRACT

Solar sailing is a propulsion method that uses solar radiation pressure (SRP) as its primary source of thrust. Nevertheless, in proximity of the Earth – where the majority of solar sail missions have been launched to date – the dynamics of sailcraft are also influenced by significant perturbations, including eclipses, atmospheric drag and, notably, planetary radiation pressure (PRP). Although preliminary works have indicated that PRP acceleration can reach magnitudes even larger than 20% of the SRP acceleration around the Earth, the impact of PRP acceleration on the solar-sail dynamics has only been investigated to a first-order extent. Indeed, studies typically model the Earth as a finite disk of constant brightness and approximate the sail as an ideal, perfect reflector – simplifying assumptions that strongly limit the fidelity of the resulting dynamics. As a first step to address these limitations, Chapter 3 introduced the spherical PRP acceleration model, which represents the Earth's radiation environment in a more realistic manner than the finite-disk model. Nevertheless, it still assumed a perfectly reflecting sail. Therefore, to further improve fidelity, in this chapter the assumption of perfect reflection is no longer considered and an analytical extension to the spherical PRP acceleration model for optical (non-ideal) solar sails is presented. Analyses show that the proposed optical PRP acceleration model improves accuracy by a factor of approximately 4-5 compared to the ideal (perfectly reflecting) formulation. Furthermore, the optical PRP acceleration model achieves an accuracy comparable to a high-fidelity numerical counterpart, though requiring 31 times less computational effort.

The content of this chapter has been published in the *Journal of Guidance, Control, and Dynamics*, see Ref. [397]: Livio Carzana, Pieter Visser, and Jeannette Heiligers. "Extending the Spherical Planetary Radiation Pressure Acceleration Model to Optical Solar Sails". In: *Journal of Guidance, Control, and Dynamics* 48.7 (July 2025), pp.1662–1669. DOI: https://doi.org/10.2514/1.G008940

The dataset supporting the findings of this chapter is available in the *4TU Data Repository*, see Ref. [398]: Livio Carzana, Pieter Visser, and Jeannette Heiligers. *Data underlying the publication: "Extending the Spherical Planetary Radiation Pressure Acceleration Model to Optical Solar Sails"*. 4TU.ResearchData, Dataset version 1, Apr. 2026. DOI: https://doi.org/10.4121/8a606add-36f7-438a-85b4-31271d336c6a.v1

Cover graphic by Vincenzo Bortone. The illustration shows the interaction between planetary radiation and an optical solar sail in Earth orbit, including the specular reflection of photons incident from Earth and the thermal radiation emitted from the back of the sail to maintain thermal balance.

4.1. INTRODUCTION

Solar sailing is a propulsion method that makes use of solar radiation pressure (SRP) as primary source of thrust [2]. Due to its propellantless nature, solar sailing has drawn increasing attention in the scientific community in recent years, with several studies investigating its use particularly for heliocentric science missions and future space exploration [131, 399]. Although there is potential for such applications, most solar sails flown to date have only been used as technology demonstrators, from JAXA's IKAROS sailcraft [91] – the first to successfully demonstrate the technology – to the recently launched Advanced Composite Solar Sail System (ACS3) by NASA [127]. The vast majority of these demonstrators have flown around the Earth. As the technology matures, near-future solar-sail missions are also expected to remain Earth-bound, in order to further explore the feasibility of solar sailing for different applications [107, 146], such as in-orbit servicing and active debris removal [115, 211, 213, 215, 217, 358, 359, 400–402]. In addition to gravity and SRP, the solar-sail dynamics are affected by several sources of perturbations in proximity of the Earth, including eclipses, atmospheric drag [212, 218–220], and notably, planetary radiation pressure (PRP) [222, 223]. The PRP acceleration and its effect on the solar-sail dynamics and control have been investigated only to a first-order extent. In line with the results of Chapter 3, studies have shown that PRP acceleration can reach magnitudes in the order of – or even above – 20% of the SRP acceleration around the Earth [222]. Such a large perturbation warrants for the accurate modeling of the PRP acceleration, particularly for detailed mission design of future near-Earth missions. In these studies, the Earth planetary radiation is modeled using analytical models, specifically, the finite-disk radiation model by McInnes [222, 223] and the spherical radiation model developed in Chapter 3, which accounts for the spherical shape of the Earth and its varying brightness depending on the sail's altitude and location. However, both these models assume the sail to be ideal (i.e., perfectly reflecting), which introduces an approximation that limits the fidelity of the solar-sail dynamics. In addition to these analytical models, numerical models exist which allow for a higher fidelity [360–363, 394, 403], particularly in the way they model the geographical distribution of planetary radiation flux. This is done by representing the surface of the Earth as a set of facets, each with known radiation flux and its variation over time. The limitation of numerical models, however, is the significantly high computational cost they require especially compared to analytical models, which can be more than 30 times computationally faster, see Chapter 3. Furthermore, the numerical nature of these models can also pose limitations when using routines that require analytical knowledge of the PRP acceleration's derivatives. Among these are, for example, several (gradient-based) trajectory optimization algorithms [368], as well as precise orbit determination and estimation routines [231]. In light of the above, the need for an analytical model that can efficiently, yet accurately, determine the PRP acceleration arises. Such a model could be effectively used to perform detailed orbit analysis for Earth-bound (or planetocentric) solar-sail missions. The model would also enable the accurate optimization of Earth-bound solar-sail control laws, leveraging (semi-) analytical optimization methods to account for both the SRP and PRP accelerations. Finally, the model would provide a versatile tool also for orbit determination applications, including, but not limited to, the in-orbit estimation of solar-sail acceleration parameters for calibration purposes, as discussed in Chapter 5.

Building upon the spherical sinusoidal PRP acceleration model presented in Chapter 3 and valid for ideal sails, this chapter presents an extension to this model for optical solar sails that is analytical in nature. To determine the PRP acceleration, the model draws on the same theory of sail-radiation interaction used by McInnes to develop the optical SRP acceleration model [2], though considering a different radiation source: the Earth. First, the model's assumptions and full derivation are discussed. Then, using NASA's ACS3 mission as a baseline, a parametric analysis considering several orbital scenarios is conducted. The analysis aims to compare the newly devised model against other state-of-the-art models. The results highlight the new model's accuracy, which is found to be 4-5 times higher than that of the ideal PRP acceleration model of Chapter 3, and comparable to the accuracy of a high-fidelity numerical model, though requiring a fraction of the run time. Finally, the conclusions of the study and possible future expansions of the work are presented.

4.2. DYNAMICAL MODEL

The dynamics of an Earth-orbiting solar sail are described using an Earth-centered reference frame, $O_I(\hat{\boldsymbol{x}}, \hat{\boldsymbol{y}}, \hat{\boldsymbol{z}})$, with the $\hat{\boldsymbol{x}}$-axis direction towards the mean vernal equinox at January 1$^{\text{st}}$, 2000, the $\hat{\boldsymbol{z}}$-axis direction perpendicular to the mean equatorial plane of that same epoch and pointing towards the North Pole, and the $\hat{\boldsymbol{y}}$-axis direction completing the right-handed frame. Within this frame, the solar-sail dynamics can be expressed as:

$$\ddot{\boldsymbol{r}} + \frac{\mu}{r^3}\boldsymbol{r} = \boldsymbol{a}_{SRP} + \boldsymbol{a}_{BBRP} + \boldsymbol{a}_{ARP} \tag{4.1}$$

In Eq. 4.1, the dot notation indicates differentiation with respect to time, $\boldsymbol{r} = [x, y, z]^{\mathrm{T}}$ is the sailcraft position vector, with x, y, and z representing the Cartesian coordinates of the sailcraft, $\mu = 398600.4415\ \mathrm{km^3 s^{-2}}$ is the Earth gravitational parameter of the geopotential Joint Gravity Model (JGM) 2 [277, 308], $r = \|\boldsymbol{r}\|$, $\boldsymbol{a}_{SRP}$ represents the SRP acceleration, and $\boldsymbol{a}_{BBRP}$ and $\boldsymbol{a}_{ARP}$ denote the two possible types of PRP acceleration, i.e., the blackbody radiation pressure (BBRP) and albedo radiation pressure (ARP) accelerations, respectively. The full expressions of these accelerations are provided in the following sections. Note that, in the following, PRP will serve as a unifying term to refer to either BBRP or ARP.

4.2.1. SOLAR RADIATION PRESSURE ACCELERATION

The SRP acceleration is defined using the optical sail model devised by McInnes [2], valid for fully opaque (non-transmissive) solar sails. Contrary to the ideal sail model, which assumes the sail to behave as a perfect reflector [2], the optical sail model accounts for the non-ideal, optical properties of the sail through its optical coefficients, namely, the absorptivity, specular reflectivity, diffuse reflectivity, and emissivity. The corresponding optical SRP acceleration, $\boldsymbol{a}_{SRP}$, is found from the sum of its components normal to the sail, $\boldsymbol{a}_{SRP,n}$, and tangential to the sail, $\boldsymbol{a}_{SRP,t}$, namely:

$$\boldsymbol{a}_{SRP} = \boldsymbol{a}_{SRP,n} + \boldsymbol{a}_{SRP,t} \tag{4.2}$$

where:

$$\boldsymbol{a}_{SRP,n} = \nu \frac{P_\odot}{\sigma}\left[\left(1+\hat{r}_f s_f\right)\cos^2\alpha_\odot + \left(1-s_f\right)\hat{r}_f B_f \cos\alpha_\odot + \left(1-\hat{r}_f\right)\frac{\varepsilon_f B_f - \varepsilon_b B_b}{\varepsilon_f + \varepsilon_b}\cos\alpha_\odot\right]\hat{\boldsymbol{n}} \tag{4.3}$$

$$\boldsymbol{a}_{SRP,t} = \nu \frac{P_\odot}{\sigma} \left(1 - \hat{r}_f s_f\right) \cos\alpha_\odot \sin\alpha_\odot \, \hat{\boldsymbol{t}} \tag{4.4}$$

As illustrated in Fig. 4.1, $\hat{\boldsymbol{n}}$ represents the sail normal direction with positive component along the direction of sunlight, $\hat{\boldsymbol{s}}$, and $\hat{\boldsymbol{t}}$ is the transversal direction defined as:

$$\hat{\boldsymbol{t}} = \hat{\boldsymbol{n}} \times \frac{\hat{\boldsymbol{s}} \times \hat{\boldsymbol{n}}}{\|\hat{\boldsymbol{s}} \times \hat{\boldsymbol{n}}\|} \tag{4.5}$$

In Eqs. 4.3 and 4.4, σ is the sailcraft mass-to-sail area ratio, and $\nu \in [0,1]$ represents the shadow factor, which accounts for the effect of eclipses. Its value is computed using a conical shadow model similar to the one presented in Refs. [211, 231], though considering $\nu = 0$ not only in the umbra, but also in the penumbra. This means that no sunlight is assumed to reach the sailcraft when this is in partial eclipse, as the latter is conservatively treated as full eclipse. $P_\odot$ is the SRP at 1 AU from the Sun:

$$P_\odot = \frac{S_{TSI}}{c} \tag{4.6}$$

where $S_{TSI} = 1367\ \mathrm{W\,m^{-2}}$ is the solar flux at Earth [308] and $c = 299792.458\ \mathrm{km\,s^{-1}}$ is the speed of light in vacuum [390]. The solar-sail pitch angle is indicated by $\alpha_\odot \in [0, \pi/2]$ and is measured between $\hat{\boldsymbol{s}}$ and $\hat{\boldsymbol{n}}$, see Fig. 4.1. Finally, the optical properties of the sail are specified through the reflectivity $\hat{r}$, specular reflection coefficient s, non-Lambertian reflection coefficient B, and emissivity ε, with the subscripts "f" and "b" indicating whether the optical coefficient refers to the front or back of the sail, respectively. Note that the above coefficients are specific to the shortwave region of the electromagnetic spectrum, wherein solar and albedo radiation are primarily defined, see Fig. 2.10. In view of this, the values of these coefficients will be provided directly in the next section, where ARP acceleration is formally defined. It should also be noted that Eqs. 4.3 and 4.4 are based on the assumption that only the sail's front is exposed to sunlight and the back is never illuminated [2]. As a result, $\hat{\boldsymbol{n}}$ always points out of the back of the sail, see Fig. 4.1, and the normal and transversal components of the SRP acceleration do not depend on the reflectivity and specular reflection coefficient of the sail backside, $\hat{r}_b$ and s_b. Although in real-life solar-sail missions sunlight may illuminate also the back of the sail, the assumption in this chapter that only the front side is illuminated is in line with the analyses conducted in Section 4.3. Indeed, in that section, locally optimal steering laws developed under the same assumption will be considered. It should be noted that, unlike for sunlight, these steering laws do not prevent planetary radiation from illuminating the back of the sail. As discussed in the next section, this makes knowledge of $\hat{r}_b$ and s_b essential to compute the PRP acceleration, as opposed to the SRP acceleration.

4.2.2. PLANETARY RADIATION PRESSURE ACCELERATION

In this section, the PRP acceleration model for optical solar sails is derived. This model forms an extension of the spherical sinusoidal PRP acceleration model presented in Chapter 3, valid for double-sided perfectly reflecting (ideal) solar sails. Although these two PRP acceleration models represent the sail optical properties differently, they also share common characteristics, particularly the assumption that the sail is flat and the way the Earth's planetary radiation distribution is represented. Indeed, in both models

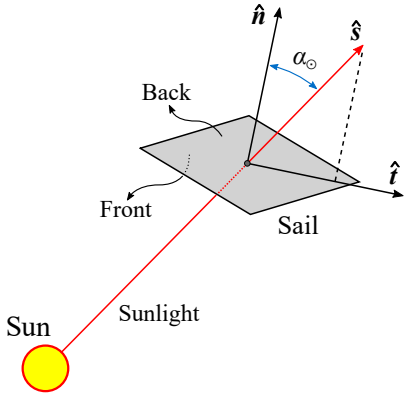


Figure 4.1: Geometry of the optical SRP acceleration model.

the Earth is assumed to be a spherical radiation source emitting blackbody and albedo radiation with varying intensity across its surface. The emitted blackbody radiation flux is assumed to vary sinusoidally with latitude, with a maximum at the equator. On the other hand, the emitted albedo radiation flux is computed assuming the Earth's albedo coefficient to vary sinusoidally (with maxima at the poles) and accounting for the illumination conditions of the Earth's surface through a so-called phase function. This function is maximum at the subsolar point and decreases moving towards the dark side of the Earth, where it attains a value of zero, indicating the complete absence of albedo radiation. Finally, the planetary radiation flux at the sail's location, S, is determined by assuming that the blackbody and albedo radiation fluxes found are uniformly spread over the visible surface of the Earth as seen from the sailcraft. In this way, the Earth is locally approximated as an isotropic radiation source, allowing the PRP acceleration to be expressed analytically. As discussed in Chapter 3, this approximation introduces an error, but its impact on sailcraft maneuverability is limited, as relative errors compared to a high-fidelity numerical model consistently in the order of 1% are found across several orbital scenarios. For more information on the derivation of the planetary flux, S, the reader is referred to Chapter 3. Throughout the remainder of this section, the value of S will be assumed to be known.

As defined in Eq. 3.15 of Chapter 3, the radiation pressure at the sail's location due to the radiation emitted by a differential element of Earth surface, dA, is:

$$dP = \frac{S}{\pi c}\frac{\cos\vartheta}{l^2}dA \tag{4.7}$$

where l is the distance between the surface element dA and the sail, and $\vartheta \in [0, \pi/2]$ is the angle between the normal direction to dA, $\hat{\boldsymbol{N}}$, and the direction from dA to the sail, $\hat{\boldsymbol{l}}$, see Fig. 4.1. The optical PRP acceleration given by the differential element of radiation pressure dP, $d\boldsymbol{a}_{PRP}$, can be found by adding the acceleration components normal to the sail, $d\boldsymbol{a}_{PRP,n}$, and tangential to the sail, $d\boldsymbol{a}_{PRP,t}$, similarly to the optical SRP acceleration given in Eqs. 4.2-4.4:

$$d\boldsymbol{a}_{PRP} = d\boldsymbol{a}_{PRP,n} + d\boldsymbol{a}_{PRP,t} \tag{4.8}$$

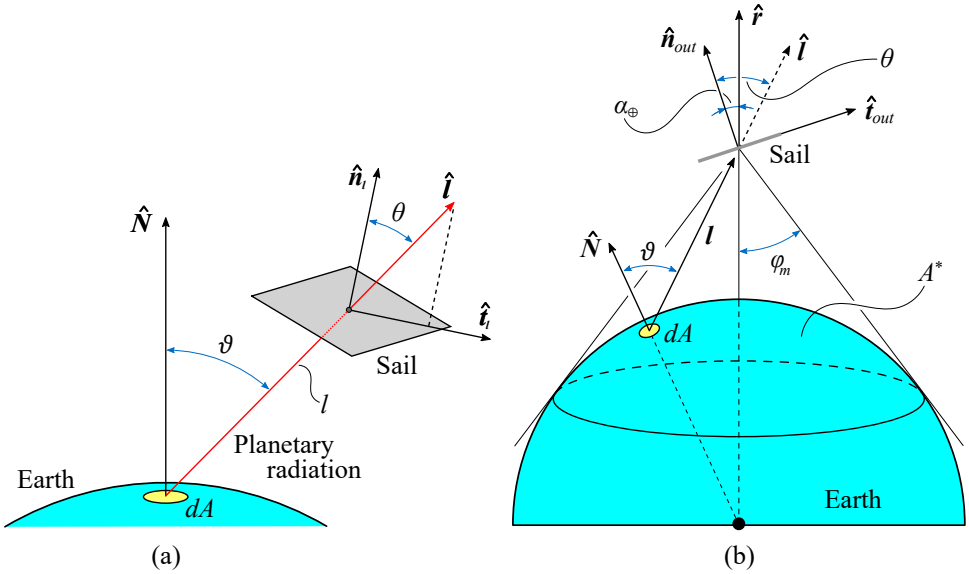


Figure 4.2: Geometry of the problem to determine the PRP acceleration exerted on an optical solar sail.

where:

$$d\boldsymbol{a}_{PRP,n} = \frac{dP}{\sigma}\left[\left(1+\hat{r}_{lit}\,s_{lit}\right)\cos^2\theta\,\hat{\boldsymbol{n}}_l + \left(1-s_{lit}\right)\hat{r}_{lit}\,B_{lit}\cos\theta\,\hat{\boldsymbol{n}}_l + \left(1-\hat{r}_{lit}\right)\frac{\varepsilon_f B_f - \varepsilon_b B_b}{\varepsilon_f + \varepsilon_b}\cos\theta\,\hat{\boldsymbol{n}}\right] \tag{4.9}$$

$$d\boldsymbol{a}_{PRP,t} = \frac{dP}{\sigma}\left(1-\hat{r}_{lit}\,s_{lit}\right)\cos\theta\sin\theta\,\hat{\boldsymbol{t}}_l \tag{4.10}$$

It should be noted that Eqs. 4.9 and 4.10 share the same structure as Eqs. 4.3 and 4.4 for the optical SRP acceleration because they describe the same physical phenomenon, i.e., the acceleration produced by radiation when interacting with a sail with given optical properties. This analogy is evidenced also by the sketches of Fig. 4.1 and Fig. 4.2a, which depict an equivalent geometry and differ only in the radiation source considered and the side of the sail exposed to the incoming radiation. Indeed, unlike sunlight, the radiation emitted by a surface element dA may also illuminate the back of the sail. An example is shown in Fig. 4.3, which illustrates how planetary radiation may impinge on either side of the sail, depending on the sail orientation and surface element dA considered. In view of this, the subscript "*lit*" is used in Eqs. 4.9 and 4.10 to specify the optical coefficients of the sail side illuminated by the radiation emitted by the surface element dA considered. Equations 4.9 and 4.10 also make use of the angle $\theta \in [0, \pi/2]$, which forms the equivalent of the SRP acceleration's pitch angle, $\alpha_\odot$, and is measured between $\hat{\boldsymbol{l}}$ and the sail normal direction with positive component along $\hat{\boldsymbol{l}}$, $\hat{\boldsymbol{n}}_l$, see Fig. 4.2a. Finally, $\hat{\boldsymbol{t}}_l$ represents the transversal direction relative to dA, which can be found from Eq. 4.5 by substituting $\hat{\boldsymbol{t}}_l$ for $\hat{\boldsymbol{t}}$ and $\hat{\boldsymbol{l}}$ for $\hat{\boldsymbol{s}}$.

Substitution of Eq. 4.7 in Eqs. 4.9 and 4.10 yields:

$$\begin{aligned} d\boldsymbol{a}_{PRP,n} = \frac{S}{\pi c\sigma}\Bigg[&\left(1+\hat{r}_{lit}s_{lit}\right)\frac{\cos\vartheta\cos^2\theta}{l^2}\,\hat{\boldsymbol{n}}_l + \\ &\left(1-s_{lit}\right)\hat{r}_{lit}B_{lit}\frac{\cos\vartheta\cos\theta}{l^2}\,\hat{\boldsymbol{n}}_l + \\ &\left(1-\hat{r}_{lit}\right)\frac{\varepsilon_f B_f-\varepsilon_b B_b}{\varepsilon_f+\varepsilon_b}\frac{\cos\vartheta\cos\theta}{l^2}\,\hat{\boldsymbol{n}}\Bigg]\,dA \end{aligned} \tag{4.11}$$

$$d\boldsymbol{a}_{PRP,t} = \frac{S}{\pi c\sigma}\left(1-\hat{r}_{lit}s_{lit}\right)\frac{\cos\vartheta\cos\theta\sin\theta}{l^2}\,\hat{\boldsymbol{t}}_l\,dA \tag{4.12}$$

Using the above expressions for $d\boldsymbol{a}_{PRP,n}$ and $d\boldsymbol{a}_{PRP,t}$, Eq. 4.8 can be integrated over the entire surface of the Earth visible from the sailcraft, A^*, see Fig. 4.2b. This yields the total PRP acceleration exerted on the solar sail:

$$\boldsymbol{a}_{PRP} = \int_{A^*} d\boldsymbol{a}_{PRP} = \int_{A^*}\left(d\boldsymbol{a}_{PRP,n} + d\boldsymbol{a}_{PRP,t}\right) \tag{4.13}$$

The PRP acceleration integral of Eq. 4.13 depends on the Earth-sail relative geometry and, most importantly, on the definition of the planetary radiation flux, S. Indeed, depending on how the planetary flux distribution across the surface A^* is modeled, a closed-form solution to the PRP acceleration integral may or may not exist. As mentioned at the beginning of this section, in this study the visible surface A^* is assumed to irradiate isotropically, i.e., with a constant radiation flux, S. With this assumption, the integral of Eq. 4.13 can be solved analytically, yielding the following expression for the optical PRP acceleration:

$$\begin{aligned} \boldsymbol{a}_{PRP} = \frac{S}{c\sigma}\Bigg\{&\frac{2}{3}\Big[\left(1+\hat{r}_{in}s_{in}\right)G_{FNS,in}-\left(1+\hat{r}_{out}s_{out}\right)G_{FNS,out}\Big]\,\hat{\boldsymbol{n}}_{out} + \\ &\Big[\left(1-s_{in}\right)\hat{r}_{in}B_{in}G_{FND,in}-\left(1-s_{out}\right)\hat{r}_{out}B_{out}G_{FND,out}\Big]\,\hat{\boldsymbol{n}}_{out} + \\ &\frac{\varepsilon_f B_f-\varepsilon_b B_b}{\varepsilon_f+\varepsilon_b}\Big[\left(1-\hat{r}_{in}\right)G_{FND,in}-\left(1-\hat{r}_{out}\right)G_{FND,out}\Big]\,\hat{\boldsymbol{n}} + \\ &\frac{2}{3\pi}\Big[\left(1-\hat{r}_{in}s_{in}\right)G_{FT,in}-\left(1-\hat{r}_{out}s_{out}\right)G_{FT,out}\Big]\,\hat{\boldsymbol{t}}_{out}\Bigg\} \end{aligned} \tag{4.14}$$

Since planetary radiation can illuminate both sides of the sail simultaneously, the subscripts "*in*" and "*out*" are used to refer to the inward and outward sides of the sail relative to the Earth, respectively, see Fig. 4.3. The outward-pointing sail normal and transversal directions, $\hat{\boldsymbol{n}}_{out}$ and $\hat{\boldsymbol{t}}_{out}$, respectively, are displayed in Fig. 4.2b. Recalling that the sail normal direction $\hat{\boldsymbol{n}}$, defined in Section 4.2.1, always points out from the back of the sail, $\hat{\boldsymbol{n}}_{out} = \text{sgn}(\hat{\boldsymbol{n}}\cdot\hat{\boldsymbol{r}})\,\hat{\boldsymbol{n}}$ while $\hat{\boldsymbol{t}}_{out}$ is found from Eq. 4.5 by substituting $\hat{\boldsymbol{t}}_{out}$ for $\hat{\boldsymbol{t}}$, $\hat{\boldsymbol{n}}_{out}$ for $\hat{\boldsymbol{n}}$, and the radial direction, $\hat{\boldsymbol{r}}$, for $\hat{\boldsymbol{s}}$. Finally, the optical coefficients of the inward, outward, front,

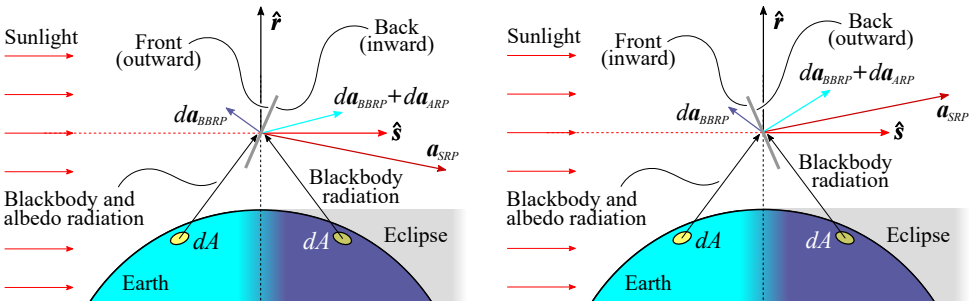


Figure 4.3: Example configurations of a solar sail illuminated by solar radiation on its front side and by planetary radiation on both sides, together with the corresponding radiation pressure accelerations, for the front side facing outward (left) and inward (right).

4

and back sides of the sail can be related as follows:

$$\left[\hat{r}_{in},\, s_{in},\, B_{in},\, e_{in},\, \hat{r}_{out},\, s_{out},\, B_{out},\, e_{out}\right] = \begin{cases} \left[\hat{r}_f,\, s_f,\, B_f,\, \varepsilon_f,\, \hat{r}_b,\, s_b,\, B_b,\, \varepsilon_b\right] & \text{if } \hat{\boldsymbol{r}} \cdot \hat{\boldsymbol{n}} \geq 0 \\ \left[\hat{r}_b,\, s_b,\, B_b,\, \varepsilon_b,\, \hat{r}_f,\, s_f,\, B_f,\, \varepsilon_f\right] & \text{otherwise} \end{cases} \tag{4.15}$$

It should be noted that, in Eq. 4.14 and the remainder of this chapter, $\boldsymbol{a}_{PRP}$ is used to indicate either the BBRP acceleration, $\boldsymbol{a}_{BBRP}$, or ARP acceleration, $\boldsymbol{a}_{ARP}$. For each of these accelerations, a specific radiation flux, S, and set of sail optical coefficients should be considered because the Earth's albedo and blackbody radiations can differ greatly in intensity and, notably, in wavelength. As discussed in Section 2.4.4 of Chapter 2, albedo and solar radiations are both emitted in the shortwave wavelength band, between 0.25 μm and 4 μm, see Fig. 2.10. Blackbody radiation, on the other hand, is emitted in the longwave infrared band, approximately between 4 and 30 μm, see again Fig. 2.10. Since the sail material responds differently to different wavelengths of the incoming radiation, wavelength-specific sets of optical coefficients should be considered. In the remainder of this chapter, the following sets of optical coefficients for the shortwave and longwave radiation, $\boldsymbol{oc}_{SW}$ and $\boldsymbol{oc}_{LW}$, respectively, will be used:

$$\boldsymbol{oc}_{SW} = \left[\hat{r}_f,\, s_f,\, B_f,\, \varepsilon_f,\, \hat{r}_b,\, s_b,\, B_b,\, \varepsilon_b\right] = \left[0.90,\, 0.82,\, 0.79,\, 0.03,\, 0.43,\, 0.53,\, 2/3,\, 0.60\right] \tag{4.16}$$

$$\boldsymbol{oc}_{LW} = \left[\hat{r}_f,\, s_f,\, B_f,\, \varepsilon_f,\, \hat{r}_b,\, s_b,\, B_b,\, \varepsilon_b\right] = \left[0.97,\, 0.82,\, 0.79,\, 0.03,\, 0.40,\, 0.53,\, 2/3,\, 0.60\right] \tag{4.17}$$

These optical coefficients refer to NASA's ACS3 solar sail[1], whose membrane is non-transmissive and consists of a polymer film (polyethelene nepthalate) with an aluminum coating on the front and chromium on the back [142].

In Eq. 4.14, G_{FNS}, G_{FND} and G_{FT} indicate the so-called normal specular, normal diffuse, and transversal geometrical factors, respectively. As their names suggest, the

[1] ACS3 optical coefficients taken from personal communication with J. Ho Kang, Advanced Materials and Processing Branch, NASA Langley Research Center, March 2024.

geometrical factors express the dependency of the optical PRP acceleration on the Earth-sail geometrical configuration and, similar to the optical coefficients, are specified for both the inward-facing and outward-facing sides of the sail. Denoting A^*_{in} and A^*_{out} as the regions of the surface A^* that are visible from the inward and outward sides of the sail, respectively, the geometrical factors can be defined as:

$$G_{FNS,\diamondsuit} = \frac{3}{2\pi}\int_{A^*_\diamondsuit} \frac{\cos\vartheta\cos^2\theta}{l^2}\,dA \tag{4.18}$$

$$G_{FND,\diamondsuit} = \frac{1}{\pi}\int_{A^*_\diamondsuit} \frac{\cos\vartheta\cos\theta}{l^2}\,dA \tag{4.19}$$

$$G_{FT,\diamondsuit} = \frac{3}{2}\int_{A^*_\diamondsuit} \frac{\cos\vartheta\cos\theta\sin\theta}{l^2}\cos\xi\,dA \tag{4.20}$$

where ξ represents the angle between $\hat{\boldsymbol{t}}_l$ and $\hat{\boldsymbol{t}}_{out}$, and "$\diamondsuit$" is used as placeholder to indicate either "*in*" or "*out*". The surface integrals appearing on the right-hand sides of Eqs. 3.33-4.20 can be solved as detailed in Appendix B. The resulting analytical expressions for the geometrical factors are provided in the following subsections. As will be shown, the geometrical factors depend only on the orbital radius, r, the planetary pitch angle, $\alpha_\oplus \in [0,\pi/2]$, measured between $\hat{\boldsymbol{n}}_{out}$ and $\hat{\boldsymbol{r}}$, and the maximum view angle between $-\hat{\boldsymbol{r}}$ and the direction from the sailcraft to the Earth's tangent, $\varphi_m \in (0,\pi/2)$, see Fig. 4.2b.

4.2.2.1. NORMAL SPECULAR GEOMETRICAL FACTORS

Sections B.1 and B.2 provide the full derivations of the normal specular geometrical factors. As discussed in these sections, depending on the sail orientation with respect to the Earth, two possible configurations can be identified:

a) If $\alpha_\oplus + \varphi_m \leq \pi/2$, the incoming radiation from the visible surface A^* illuminates only one side of the sail. In this case, the outward geometrical factor is $G_{FNS,out} = 0$, while the inward geometrical factor, $G_{FNS,in}$, is given by:

$$G_{FNS,in}(H,\alpha_\oplus) = 1 - \sqrt{1-H^2}\left[1 - H^2\left(1 - \frac{3}{2}\sin^2\alpha_\oplus\right)\right] \tag{4.21}$$

where the adimensional inverse orbital radius, $H = R/r$, was introduced for conciseness, with $R = 6378.1363$ km the Earth radius [308].

b) If $\alpha_\oplus + \varphi_m > \pi/2$, both the inward and outward sides of the sail are illuminated, see Figs. 4.2b and 4.3. The corresponding geometrical factors are:

$$\begin{aligned} G_{FNS,in}(H,\alpha_\oplus) = 1 - \frac{1}{\pi}\Bigg\{&\frac{1}{2}\sqrt{1-H^2}\left[H^2\left(1-3\cos^2\alpha_\oplus\right)+2\right]\cos^{-1}(-\mathcal{A}) + \tan^{-1}\mathcal{B} \\ &-\frac{1}{2}\mathcal{B}\cos^2\alpha_\oplus\left[3\cos^2\alpha_\oplus\left(1+\mathcal{B}^2\right)-1\right]\Bigg\} \end{aligned} \tag{4.22}$$

$$G_{FNS,out}(H,\alpha_\oplus) = \frac{1}{\pi}\left\{-\frac{1}{2}\sqrt{1-H^2}\left[H^2\left(1-3\cos^2\alpha_\oplus\right)+2\right]\cos^{-1}\mathcal{A}+\tan^{-1}\mathcal{B}\right.$$
$$\left.-\frac{1}{2}\mathcal{B}\cos^2\alpha_\oplus\left[3\cos^2\alpha_\oplus\left(1+\mathcal{B}^2\right)-1\right]\right\} \tag{4.23}$$

where the following coefficients are used for conciseness:

$$\mathcal{A} = \frac{\cos\alpha_\oplus}{\sin\alpha_\oplus}\sqrt{\frac{1}{H^2}-1} \qquad \mathcal{B} = \sqrt{\frac{H^2}{\cos^2\alpha_\oplus}-1} \tag{4.24}$$

4.2.2.2. NORMAL DIFFUSE GEOMETRICAL FACTORS

The normal diffuse geometrical factors correspond to the view factors of the sail sides with respect to the Earth. Their expressions were found by F. G. Cunningham in Ref. [393] and are reported here for completeness:

a) If $\alpha_\oplus+\varphi_m \leq \pi/2$, $G_{FND,out}=0$ and $G_{FND,in}=0$ is:

$$G_{FND,in} = H^2\cos\alpha_\oplus \tag{4.25}$$

b) If $\alpha_\oplus+\varphi_m > \pi/2$, the $G_{FND,out}$ and $G_{FND,in}$ are given by:

$$G_{FND,in}(H,\alpha_\oplus) = \frac{1}{2}-\frac{1}{\pi}\left\{\sin^{-1}\left(\frac{\sqrt{1-H^2}}{\sin\alpha_\oplus}\right)+\mathcal{B}\cos\alpha_\oplus\sqrt{1-H^2}-H^2\cos\alpha_\oplus\cos^{-1}(-\mathcal{A})\right\} \tag{4.26}$$

$$G_{FND,out}(H,\alpha_\oplus) = \frac{1}{2}-\frac{1}{\pi}\left\{\sin^{-1}\left(\frac{\sqrt{1-H^2}}{\sin\alpha_\oplus}\right)+\mathcal{B}\cos\alpha_\oplus\sqrt{1-H^2}+H^2\cos\alpha_\oplus\cos^{-1}\mathcal{A}\right\} \tag{4.27}$$

4.2.2.3. TRANSVERSAL GEOMETRICAL FACTORS

The full derivations of the transversal geometrical factors are given in Sections B.1 and B.3. As discussed in these sections, the definitions of these geometrical factors – similar to the other geometrical factors – depend on whether one or both sides of the sail are illuminated, namely:

a) If $\alpha_\oplus+\varphi_m \leq \pi/2$, $G_{FT,out}=0$ and $G_{FT,in}=0$ is:

$$G_{FT,in} = \frac{3\pi}{4}H^2\sqrt{1-H^2}\sin(2\alpha_\oplus) \tag{4.28}$$

b) If $\alpha_\oplus+\varphi_m > \pi/2$, the $G_{FT,out}$ and $G_{FT,in}$ are given by:

$$G_{FT,in}(H,\alpha_\oplus) = \frac{1}{2}\left\{\mathcal{B}\left[2\sin\alpha_\oplus\cos^3\alpha_\oplus\left(\mathcal{B}^2+2+\frac{\cos^2\alpha_\oplus}{\sin^2\alpha_\oplus}\right)-\left(1+H^2\right)\frac{\cos^3\alpha_\oplus}{\sin\alpha_\oplus}\right]\right.$$
$$\left.+3H^2\sqrt{1-H^2}\sin\alpha_\oplus\cos\alpha_\oplus\cos^{-1}(-\mathcal{A})\right\} \tag{4.29}$$

$$G_{FT,out}(H,\alpha_\oplus) = \frac{1}{2}\left\{\mathcal{B}\sin\alpha_\oplus\cos^3\alpha\left[\mathcal{B}^2\left(2-\frac{\cos^2\alpha_\oplus}{\sin^2\alpha_\oplus}\right)+3\right]\right.$$
$$\left.-3H^2\sqrt{1-H^2}\sin\alpha_\oplus\cos\alpha_\oplus\cos^{-1}\mathcal{A}\right\} \tag{4.30}$$

4

4.3. COMPARISON WITH STATE OF THE ART

In this section, different parametric analyses are presented which aim to quantify the accuracy of the optical PRP acceleration model compared to other analytical models and a high-fidelity numerical model. To this end, several simulations are performed, considering different initial orbital altitudes, orbit orientations, simulation start times, and PRP acceleration models. The analysis settings, accuracy metric, and results are discussed in the following subsections.

4.3.1. SAILCRAFT DYNAMICS AND CONTROL

For each simulation in the parametric analyses, the dynamics presented in Section 4.2 are propagated using the following models for the PRP acceleration, $\boldsymbol{a}_{PRP}$:

a) Optical NRTDM model. In this model, the planetary radiation flux is computed numerically from discrete maps of the Earth's albedo coefficient and blackbody radiation flux obtained from the ANGARA (Analysis of Non-Gravitational Acceleration due to Radiation and Aerodynamics) software package developed by Hyperschall Technologie Göttingen GmbH [394]. This approach allows to compute the optical PRP acceleration integral of Eq. 4.13 as a finite sum. Although it is computationally expensive, this method enables a high accuracy and is therefore considered the ground truth against which the other PRP acceleration models will be compared. This algorithm is implemented in the software tool NRTDM (Near Real-Time Density Model) developed at Delft University of Technology [283, 363]. Finally, note that this model is employed considering the shortwave and longwave optical coefficients of ACS3 given in Eqs. 4.16 and 4.17.

b) Ideal NRTDM model. This model is equivalent to the optical NRTDM model, with the only difference that a double-sided, perfectly reflecting sail is considered, corresponding to the following sets of optical coefficients [2]:

$$\boldsymbol{oc}_{SW} = \boldsymbol{oc}_{LW} = \left[\hat{r}_f,\ s_f,\ B_f,\ \varepsilon_f,\ \hat{r}_b,\ s_b,\ B_b,\ \varepsilon_b\right] = \left[1,\ 1,\ 2/3,\ 0,\ 1,\ 1,\ 2/3,\ 0\right] \tag{4.31}$$

c) Optical sinusoidal PRP acceleration model presented in Section 4.2.2. The PRP acceleration is found through Eq. 4.14, with the planetary flux, S, determined analytically as per the sinusoidal model presented in Chapter 3. Similar to the optical NRTDM

Table 4.1: PRP acceleration models considered in Section 4.3.

Models			Optical coefficients	
PRP acceleration	Planetary flux	Solar sail	$\boldsymbol{oc}_{SW}$	$\boldsymbol{oc}_{LW}$
Optical NRTDM	Based on num. maps	Optical	$[0.90, 0.82, 0.79, 0.03, 0.43, 0.53, 2/3, 0.60]$	$[0.97, 0.82, 0.79, 0.03, 0.40, 0.53, 2/3, 0.60]$
Optical sinusoidal	Sinusoidal dependence on latitude	Optical	$[0.90, 0.82, 0.79, 0.03, 0.43, 0.53, 2/3, 0.60]$	$[0.97, 0.82, 0.79, 0.03, 0.40, 0.53, 2/3, 0.60]$
Ideal NRTDM	Based on num. maps	Ideal	$[1, 1, 2/3, 0, 1, 1, 2/3, 0]$	$[1, 1, 2/3, 0, 1, 1, 2/3, 0]$
Ideal sinusoidal	Sinusoidal dependence on latitude	Ideal	$[1, 1, 2/3, 0, 1, 1, 2/3, 0]$	$[1, 1, 2/3, 0, 1, 1, 2/3, 0]$
No PRP	(absent)	N/A	N/A	N/A

Note: Optical coefficients given as $[\hat{r}_f, s_f, B_f, \varepsilon_f, \hat{r}_b, s_b, B_b, \varepsilon_b]$.

model, the optical sinusoidal model also considers ACS3's shortwave and longwave optical coefficients, see Eqs. 4.16 and 4.17.

d) Ideal sinusoidal PRP acceleration model. This model corresponds to the spherical sinusoidal PRP acceleration model developed in Chapter 3 for ideal sails. Note that this model can be found from the optical sinusoidal model using the set of ideal optical coefficients in Eq. 4.31.

e) Model in which the PRP acceleration is neglected, i.e., $\boldsymbol{a}_{PRP} = \mathbf{0}$ at any time.

For the reader's convenience, the characteristics of the above models are summarized in Table 4.1. It should be noted that while the set of optical coefficients to compute the PRP acceleration depends on the specific PRP acceleration model considered, this is not the case for the SRP acceleration. Indeed, the SRP acceleration, $\boldsymbol{a}_{SRP}$, is computed through the optical model presented in Section 4.2.1, employing the set of coefficients in Eq. 4.16 for all analyses. In this way, differences in the analysis results originate only from the PRP acceleration modeling, allowing a clear assessment of the models' accuracy. For each simulation, the solar-sail dynamics are propagated for 10 days, using Matlab®'s *ode45* integrator with absolute and relative tolerances of 10^{-12}, while implementing locally optimal orbit-raising and inclination-changing steering laws. These steering laws are computed based on an algorithm similar to the one devised by McInnes for ideal sails [2], though adapted to the optical sail model presented in Section 4.2.1. It should be noted that because these steering laws account only for SRP in the optimization process, in the analyses, the PRP acceleration is considered as an uncontrolled perturbing acceleration affecting the orbit.

4.3.2. REFERENCE MISSION SCENARIO

The ACS3 mission is used as baseline scenario in all analyses, with a solar-sail characteristic acceleration of $0.045\ \mathrm{mm\,s^{-2}}$ (corresponding to $\sigma = 0.2027\ \mathrm{kg\,m^{-2}}$) and the following

vector of initial orbital elements defined in frame O_I:

$$\left[a_0,\ e_0,\ i_0,\ \text{LTAN}_0,\ \omega_0,\ f_0\right]^T = \left[7093.1363\ \text{km},\ 0,\ 98.2490\ \text{deg},\ \left\{\begin{matrix}0000\ \text{hrs}\\0030\ \text{hrs}\\\vdots\\2330\ \text{hrs}\end{matrix}\right\},\ 0\ \text{deg},\ 0\ \text{deg}\right]^T \tag{4.32}$$

where a is the semi-major axis, e the eccentricity, i the inclination, ω the argument of perigee, f the true anomaly, LTAN indicates the local time of the ascending node, and the subscript "0" denotes the initial value of these variables[2]. These orbital elements represent a circular, Sun-synchronous orbit with initial altitude $h_0 = a_0 - R = 715$ km, where the Earth radius, R, is given in Section 4.2.2.1. Although this altitude does not coincide with the actual altitude of ACS3 at launch [129, 404], it was chosen for consistency – and to facilitate comparison – with the analyses in Section 3.5.2 of Chapter 3. Indeed, these also examine the accuracy of different PRP acceleration models considering the initial orbital elements in Eq. 4.32, though using *ideal* orbit-raising and inclination-changing steering laws. In Eq. 4.32, several values of the LTAN are considered, spaced by 0.5 hours along the entire 24-hour time span. This parameter provides a measure of the relative orientation of the orbital plane with respect to the sunlight direction and it is correlated to the right ascension of the ascending node. Indeed, for a LTAN at 0000 hrs, the right ascension of the ascending node is uniquely determined by the position of the Sun, and each 0.5-hour increment in LTAN corresponds to a 7.5-degree increment in right ascension of the ascending node. Finally, the parametric analyses also consider 12 different simulation start times, corresponding to the 15$^{\text{th}}$ day of each month of 2024.

4.3.3. ACCURACY METRIC

To compare the accuracy of the four PRP acceleration models presented in Section 4.3.1, four propagations are performed for each combination of initial orbit, simulation start time, and steering law. Then, the relative errors between the final altitude/inclination obtained by the optical NRTDM model (as mentioned previously, considered the ground truth) and each one of the other models, ε_{rel}, are computed. The relative error ε_{rel} is defined as:

$$\varepsilon_{rel} = \frac{\left|\text{œ}_{ref,f} - \text{œ}_f\right|}{\text{œ}_{ref,f} - \text{œ}_0} \tag{4.33}$$

where œ_0 indicates the initial value of the steering law's target parameter (i.e., h or i), and $\text{œ}_{ref,f}$ and œ_f represent the final values of the target parameter found through the optical NRTDM (reference) model and the other models under consideration, respectively.

4.3.4. VARIATION IN ACCURACY WITH THE LOCAL TIME OF THE ASCENDING NODE

Figure 4.4 shows the variation of the relative error with the LTAN for the orbit-raising steering law, for the no-PRP, ideal sinusoidal, and optical sinusoidal acceleration models.

[2] ACS3 mission data taken from personal communication with W.K. Wilkie, Principal Investigator of the ACS3 mission, National Aeronautics and Space Administration (NASA) Langley Research Center, February 2024.

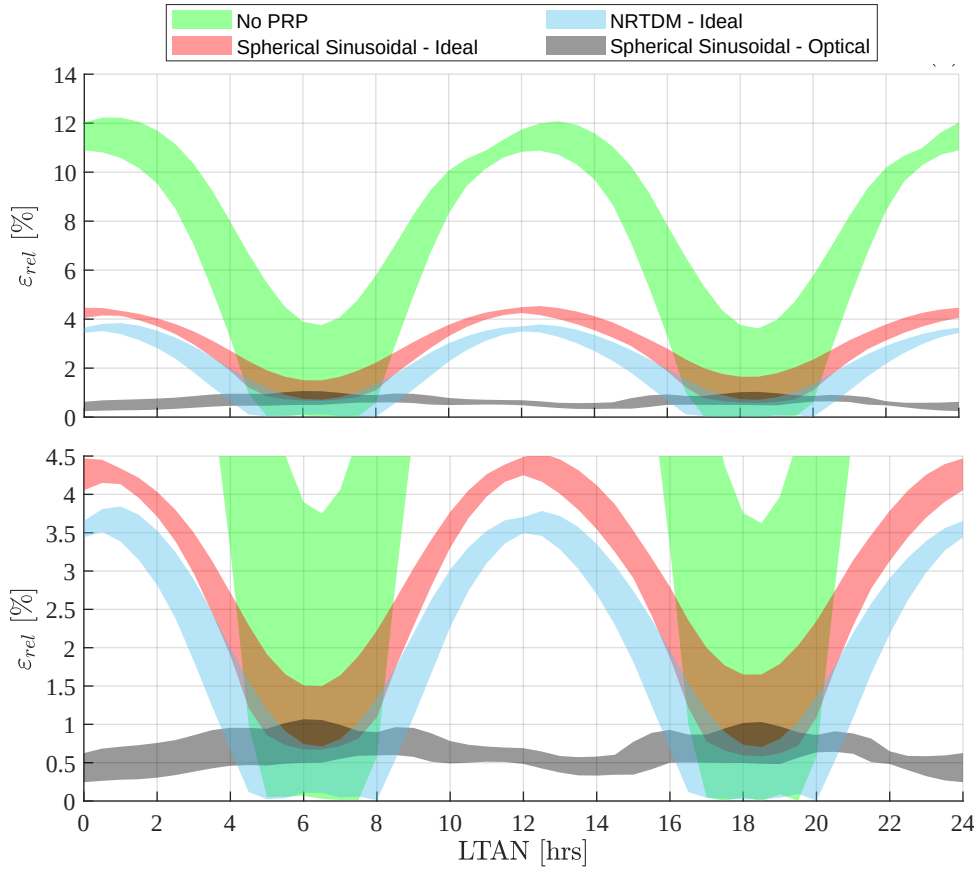


Figure 4.4: Relative error on the altitude increase of different PRP acceleration models with respect to the NRTDM optical model. Full plot on top and zoomed inset on the bottom.

For each model, a band is displayed which represents the range of relative errors obtained by considering the 12 simulation start times at each month of 2024. The plot illustrates that all error bands follow a 12-hour periodic trend, approximately symmetric with respect to the LTAN at 1200 hrs. This symmetry is due to the similar relative orientation of the orbital plane to the sunlight direction in Sun-synchronous orbits with a 12-hour LTAN difference, which therefore yields similar orbit-raising performances. The results show that the error of the optical sinusoidal model is only weakly dependent on the LTAN. On the other hand, the error bands of the no-PRP and ideal sinusoidal models exhibit a more pronounced trend, with larger errors found for LTANs around 0000/1200 hrs. This is because, for these LTANs, the sailcraft flies in the vicinity of the subsolar point once per orbital period, where albedo radiation is most intense. Therefore, the dynamics are more easily perturbed and errors resulting from mismodeling the ARP acceleration are amplified. Conversely, for a LTAN at 0600/1800 hrs, the sailcraft remains close to the day-night terminator throughout its orbit, thus resulting in a minor albedo radiation

intensity and smaller errors. It is also interesting to note that the error band of the optical sinusoidal model appears narrower than those of the no-PRP and ideal sinusoidal models. As the width of the error band represents the range of errors achieved when changing the simulation start date, this result highlights the superior accuracy of the optical sinusoidal model also with respect to the simulation start date. The plot shows that neglecting the PRP can induce errors in the altitude gain of up to 12.2%, in agreement with the results found in Chapter 3 for ideal solar-sail steering laws. Accounting for the PRP through the ideal or optical sinusoidal models strongly reduces the error to a maximum of 4.54% and 1.07%, respectively. It should be noted that these models consider the same planetary radiation distribution and only differ in the assumed optical properties of the sail. Consequently, the difference between the error bands of these two models provides a direct measure of the error introduced when assuming the sail to be a perfect reflector for planetary radiation. This result is also evidenced by the ideal NRTDM error band, whose trend and magnitude resembles the error difference between the ideal and optical sinusoidal models. Using the optical sinusoidal model yields minor relative errors oscillating between 0.24% and 1.07%. Similar to the results presented in Chapter 3 for the ideal sinusoidal model, this error originates from the approximation that the visible surface of the Earth irradiates isotropically, which can represent a source of error particularly for the ARP acceleration, when the day-night terminator is visible from the sailcraft.

Similar to Fig. 4.4, Fig. 4.5 displays the variation of for the inclination-changing steering law, for different LTAN values and PRP acceleration models. A 12-hour periodicity in the errors is again obtained, although the error bands appear skewed and asymmetric. This asymmetry is due to the complex nature of the inclination-changing steering law, for which orbits with similar orientations with respect to the sunlight direction still yield different increases in inclination. Similar to the orbit-raising case, small errors are achieved for LTANs around 0600/1800 hrs, due to the minor perturbing effect of the ARP acceleration on the dynamics. Also, the error band of the optical sinusoidal model exhibits a narrower spread compared to the other models, reflecting its lower error variation with the simulation start date. Neglecting the PRP in the dynamics yields large relative errors, even up to 47.5%. The errors of the ideal and optical sinusoidal models, on the other hand, induce smaller errors up to 14.9% and 2.35%, respectively.

4.3.5. VARIATION IN ACCURACY WITH ALTITUDE AND INCLINATION

To assess the accuracy of the optical sinusoidal model at different altitudes and inclinations, the parametric analysis presented in Section 4.3.4 is repeated firstly for initial altitudes $h_0 = \{450, 550, 650, 715, 800, 900, 1000\}$ km and their corresponding Sun-synchronous inclinations, and, secondly, assuming $h_0 = 715$ km and $i_0 = \{0.5, 24, 50, 75, 90, 98.2490\}$ deg, where the last value corresponds to the Sun-synchronous inclination at $h_0 = 715$ km. The results appear in Fig. 4.6, which displays the maximum relative error achieved over all LTANs and simulation start times, $\epsilon_{rel,max}$, for each PRP acceleration model, steering law, initial altitude and inclination. Notably, the optical sinusoidal model performs consistently better than the other models for all cases analyzed. When changing the initial altitude, it achieves values for $\epsilon_{rel,max}$ of at most 1.07% and 3.7% for the orbit-raising and inclination-changing steering laws, respectively, regardless of

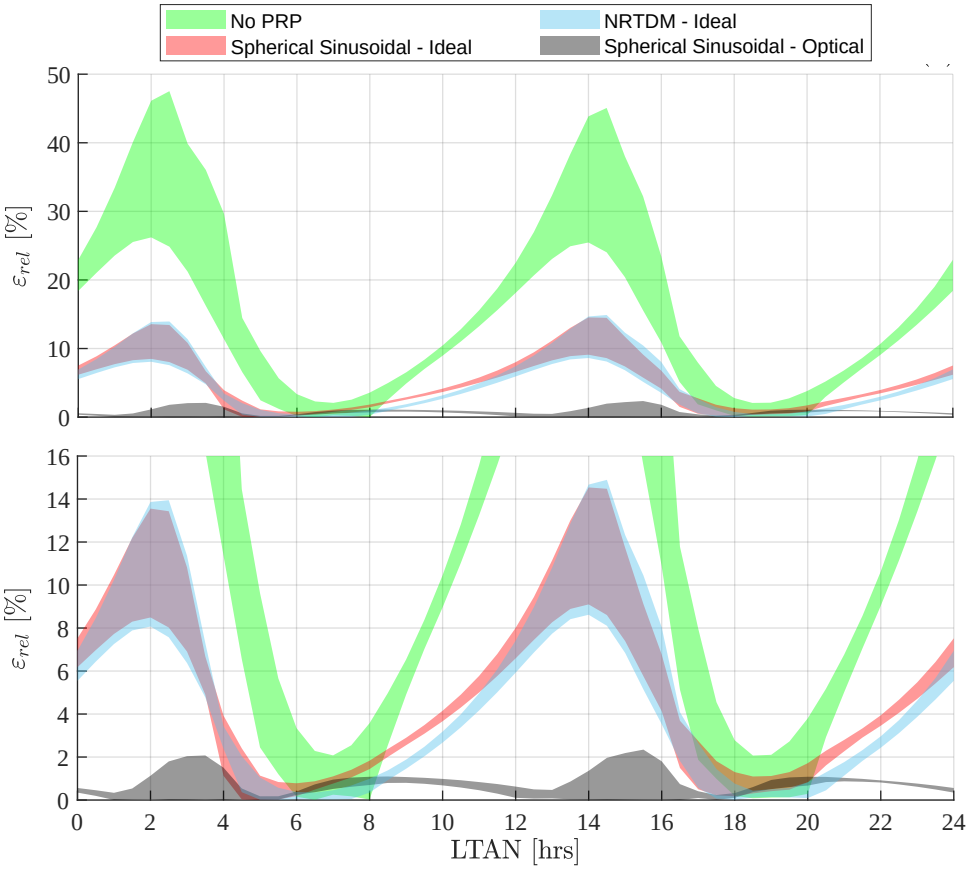


Figure 4.5: Relative error on the inclination increase of different PRP acceleration models with respect to the NRTDM optical model. Full plot on top and zoomed inset on the bottom.

the initial altitude, see Fig. 4.6a and 4.6b. Similarly, when varying the initial inclination, values for $\varepsilon_{rel,max}$ of 0.35-1.07% and 2.29-6.55% are found for the orbit-raising and inclination-changing steering laws, respectively, see Fig. 4.6c and 4.6d. In comparison, the ideal sinusoidal model achieves larger errors, attaining values within 3.23% and 5.00% for the orbit-raising steering law, see Fig. 4.6a and 4.6c, and within 9.37% and 22.7% for the inclination-changing steering law, see Fig. 4.6b and 4.6d. Neglecting the PRP induces even larger errors, consistently above 10% for all orbit-raising cases analyzed, see again Fig. 4.6a and 4.6c, and within and 30% and 90% for all the inclination-changing cases analyzed, see Fig. 4.6b and 4.6d. Finally, it is interesting to note that the error associated to the ideal NRTDM model is strongly correlated with the difference between the error curves of the ideal sinusoidal and optical sinusoidal models. Similarly as in Figs. 4.4 and 4.5, this highlights that the low errors achieved by the optical sinusoidal model stem primarily from modeling the sail optical properties more realistically and no longer assuming perfect reflection.

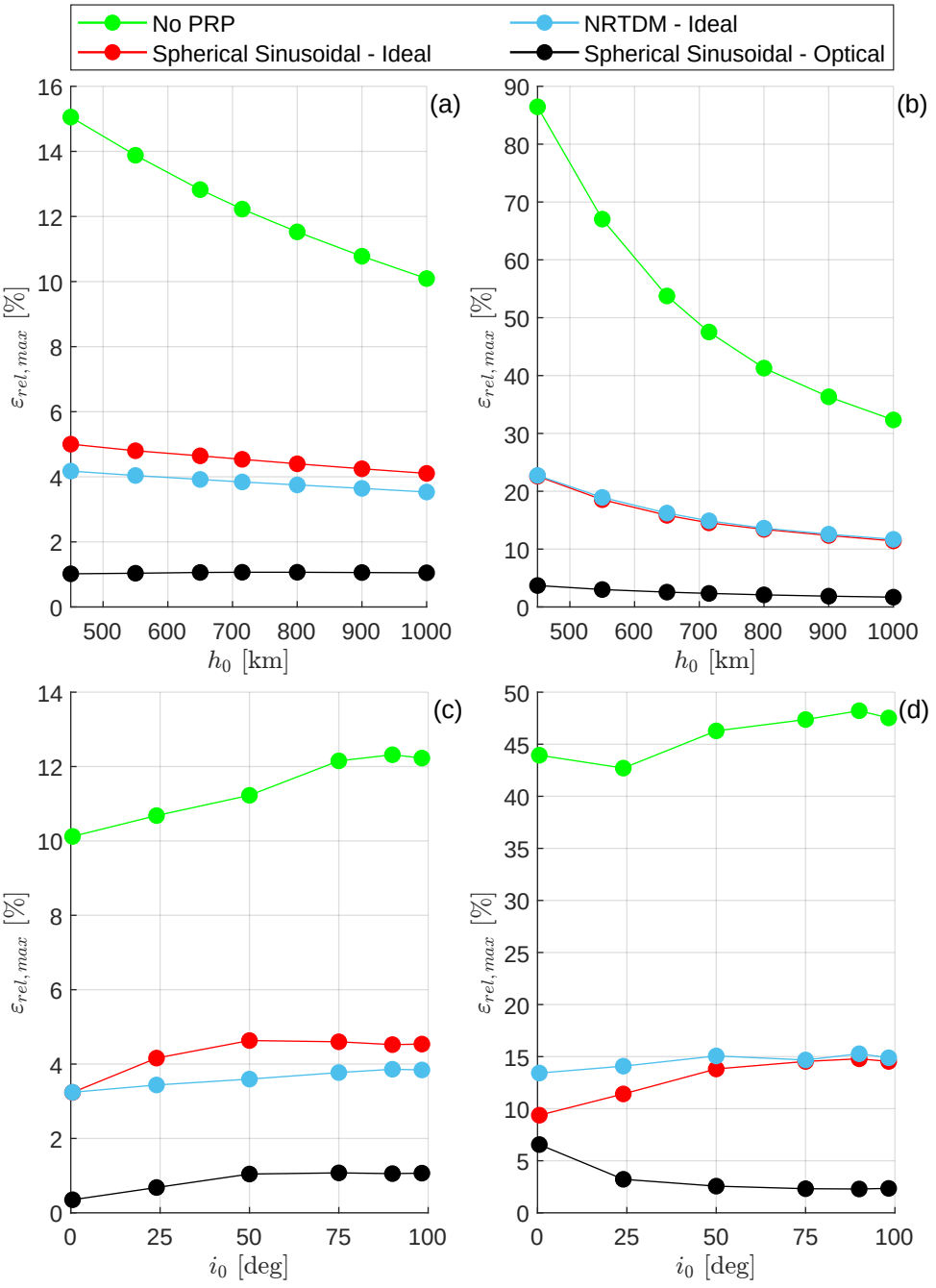


Figure 4.6: Maximum relative error on a, c) the altitude increase, and b, d) inclination increase, for different initial altitudes and inclinations.

The above-discussed results highlight that, despite its analytical nature, the optical sinusoidal model achieves a very high fidelity for a wide variety of orbital scenarios, even compared to its numerical counterpart. Finally, it is worth noting that the optical model reduces the computational effort compared to the numerical model by a factor 31. Since both these models are implemented in Matlab® R2020b, this value is independent of the computing hardware.

4.4. CONCLUSIONS

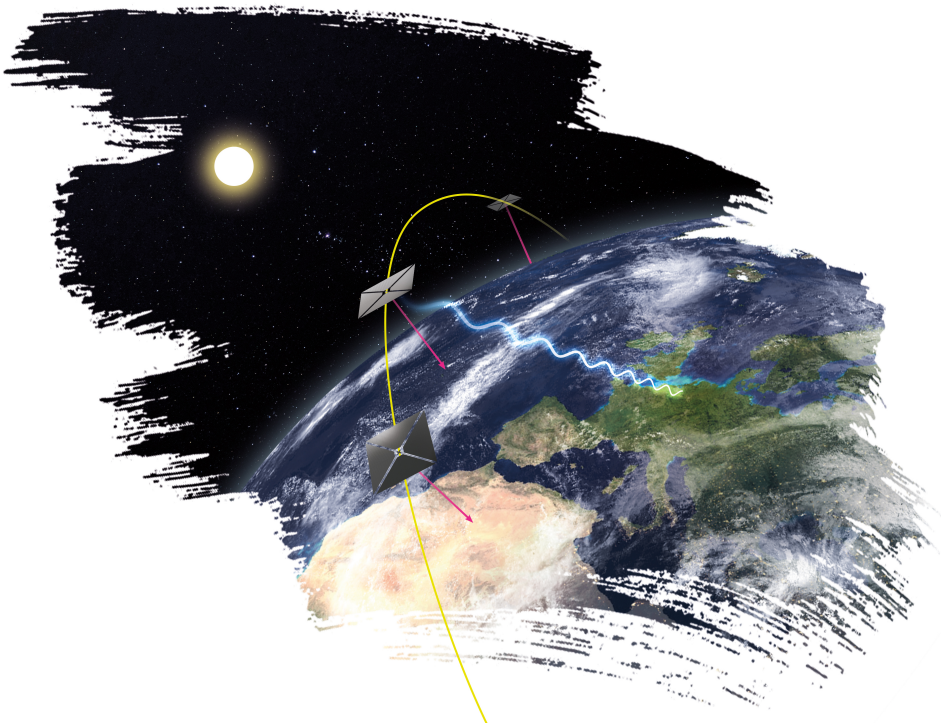
This chapter presented a new analytical model for the planetary radiation pressure (PRP) acceleration of optical solar sails, analytical in nature. The model was found to predict the orbit-raising and inclination-changing capabilities of NASA's ACS3 sailcraft with relative errors of at most 1% and 6%, respectively, compared to a high-fidelity numerical model. This accuracy marks a significant improvement with respect to the pre-existent ideal PRP acceleration model, for which errors up to 5% and 23% were found. The new model furthermore reduces the computational effort compared to its numerical counterpart by a factor 31. These results therefore demonstrate the effectiveness of the newly devised optical PRP acceleration model for accurately describing the PRP-perturbed solar-sail dynamics. The proposed optical PRP acceleration model may be used in the design of solar-sail steering laws that leverage PRP to enhance the sailcraft maneuverability. This in turn opens up avenues of research in the PRP-based trajectory optimization of Earth-orbiting sailcraft. Since the proposed model assumes the sail to be non-transmissive, future work may also focus on further extending the model to transmissive or refractive materials. In this way, the model could be applied to a broader range of solar-sail designs, widening its scope of applicability. Finally, while developed for solar sails, it should be noted that the optical PRP acceleration model is applicable to any flat surface illuminated by planetary radiation. Therefore, the model can also be used to compute the PRP acceleration of spacecraft with arbitrarily complex shape, when the latter is represented as a set of adjacent flat surfaces and only the faces exposed to planetary radiation are considered.

ACKNOWLEDGEMENTS

Special thanks go to W. Keats Wilkie and Jin Ho Kang from NASA Langley Research Center for sharing the ACS3 solar-sail optical properties and mission data. Furthermore, gratitude is extended to Dr. Christian Siemes and Natalia Hladczuk from Delft University of Technology and Dr. Eelco Doornbos from KNMI (Koninklijk Nederlands Meteorologisch Instituut) for sharing the software tool NRTDM and their knowledge of the ANGARA Earth radiation maps.

5

Steering Laws to Calibrate the Accelerations of NASA's Advanced Composite Solar Sail System



ABSTRACT

Solar sailing is a propulsion method which takes advantage of solar radiation pressure (SRP) as main source of thrust. However, around Earth, other sources also affect the solar-sail dynamics, including planetary radiation pressure (PRP) and atmospheric drag. In literature, the accelerations from SRP, PRP, and atmospheric drag are modeled using different theoretical and idealistic models, which make use of simplifying assumptions to describe the near-Earth dynamical environment, the geometry of the sail, and its aerodynamic and optical properties. Consequently, sailcraft in Earth orbit experience accelerations different from the theoretically predicted ones.

To help quantify the discrepancies between the real and modeled solar-sail dynamics, so-called calibration steering laws may be employed. Through careful design, these steering laws allow to amplify the SRP, PRP, and aerodynamic accelerations, either individually or in combination. This, in turn, facilitates subsequent estimation of these accelerations, their variation with the sailcraft attitude, and the sailcraft parameters that govern them.

This chapter presents the first definition of calibration steering laws for Earth-bound solar sails. To this end, the steering laws to calibrate different solar-sail accelerations are introduced, with a focus on the rationale driving the steering-law design. Then, to account for the operational feasibility of these steering laws in real-life missions, analyses are conducted taking NASA's ACS3 mission as baseline. Preliminary and in-depth analyses – performed before and after the launch of the mission, respectively – are presented which assess the severity of different operational challenges characterizing the steering laws, ranging from power-generation and ground-station communication capabilities, to altitude maintenance, sail material degradation, and required angular rates for attitude change. The results highlight the benefits and implementation challenges of each steering law, including discussion on the most convenient orbit orientations and times of the year for their adoption.

The content of this chapter was published in the following conference and journal publications, see Refs. [405, 406]:

Livio Carzana, W. Keats Wilkie, Andrew Heaton, Benjamin Diedrich, and Jeannette Heiligers. "Solar-sail Steering Laws to Calibrate the Accelerations from Solar Radiation Pressure, Planetary Radiation Pressure, and Aerodynamic Drag". In: *Proceedings of the 6th International Symposium on Space Sailing*. New York City College of Technology, New York, USA, June 2023, pp. 58–65.

Andrea Minervino Amodio, Livio Carzana, Dominic Dirkx, and Jeannette Heiligers. "Covariance-Based Estimation Performance for In-Flight Calibration of NASA's ACS3 Solar Sail". In: *Advances in Space Research* (2025). DOI: https://doi.org/10.1016/j.asr.2025.10.090

Cover graphic by Vincenzo Bortone. The illustration shows a solar sail in Earth orbit employing the backside nadir-pointing calibration steering law, which facilitates communication with the ground station.

5.1. INTRODUCTION

Solar sailing is a propulsion method using solar radiation pressure (SRP) as primary source of thrust [2]. Over the last years, solar sailing has drawn increasing attention in the scientific community particularly because of its propellantless nature and potential for a variety of mission applications, both in the near-Earth and interplanetary environments [107, 386]. In light of this, several solar sails have been launched in the recent past to increase the solar-sail technology readiness level and assess its potential for real-life mission applications. Most of these sailcraft have flown in close proximity of the Earth and, similarly, even more Earth-bound missions are planned for the near future. Among these are, for example, the recently launched Advanced Composite Solar Sail System (ACS3) and Alpha sailcraft by NASA and Gama [126–129], respectively, and Gama's upcoming Beta missions [125]. Orbiting about the Earth, the dynamics of these solar sails are affected by other sources of acceleration in addition to SRP. The main non-gravitational accelerations include the Earth's planetary radiation pressure (PRP) and atmospheric drag. Because the PRP and aerodynamic accelerations depend on the sail attitude and can perturb sailcraft orbits to a significant extent [218–223], accurately predicting their magnitudes is crucial for the design of Earth-bound solar-sail missions. In the literature, the accelerations from SRP, PRP, and atmospheric drag are modeled using different theoretical and idealistic models, most of which assume the sail to be a thin, flat surface with known optical properties [2, 388, 407]. These models therefore do not account for secondary effects, like the sail billowing, presence of wrinkles, degradation, and uncertainties in the sail's optical properties. Furthermore, these models make use of simplifying assumptions to describe the near-Earth dynamical environment, particularly with respect to the atmospheric density [219–221] and the intensity of the solar and planetary radiation [222, 223]. Because of these assumptions, real-life sailcraft generally experience accelerations that differ from the predicted ones. In order to quantify these differences, the calibration of the actual SRP, PRP, and aerodynamic accelerations experienced by sailcraft in orbit can be performed. In this way, these accelerations can be measured and compared to the predicted ones. The discrepancies found would then provide insights into the accuracy and fidelity of the available solar-sail dynamical models and, crucially, an opportunity to improve these models through estimation of the parameters that govern them. Calibration of the SRP, PRP, and aerodynamic accelerations requires the definition of steering laws designed ad hoc for this purpose. In addition, the implementation of these control strategies in real life can prove challenging for different reasons, including the presence of operational constraints, deorbiting effects on the sailcraft orbit, and degradation of the sail material.

In light of the above and the fact that studies on the design of such steering laws have never been conducted, this chapter presents a set of Calibration Steering Laws (CSLs) specific for Earth-bound solar sails. Furthermore, their operational feasibility is also explored, using NASA's ACS3 mission as a baseline. This specific mission is considered because, through frequent exchanges with the mission team over the years, the use of these steering laws to perform in-orbit calibration evolved from a conceptual idea to an increasingly realistic opportunity. Accordingly, preliminary and final, in-depth analyses of the steering-law operational feasibility were conducted before and after launching the mission, respectively, using the best available information on the mission at each stage.

The chapter is organized as follows. The sailcraft dynamics are presented in Sec-

tion 5.2, where an extension to the optical SRP acceleration model by McInnes [2] is introduced and the acceleration models employed for the preliminary and final analyses of the chapter are specified. Section 5.3 provides the general definitions of the CSLs for Earth-bound solar sails, designed to calibrate the SRP, PRP, aerodynamic, and residual accelerations. Thereafter, Section 5.4 introduces the operational challenges that, before launch of the ACS3 mission, were identified as most critical for implementing the CSLs. Section 5.5 discusses the preliminary analysis of the operational feasibility of the CSLs, conducted before the launch of ACS3. Building on this analysis and including information acquired by the ACS3 mission team after launch, revisions of the CSLs and operational challenges are discussed in Section 5.6, paving the way to the in-depth analysis of operational feasibility of Section 5.7. Finally, Section 5.8 presents the conclusions of the study.

5.2. DYNAMICAL MODEL

In this chapter, the equations of motion describing the dynamics of ACS3 are expressed in an inertial Earth-centered reference frame, $O_I(\hat{\boldsymbol{x}}, \hat{\boldsymbol{y}}, \hat{\boldsymbol{z}})$, with the $\hat{\boldsymbol{x}}$-axis direction towards the mean vernal equinox at January 1$^{\text{st}}$, 2000, the $\hat{\boldsymbol{z}}$-axis direction perpendicular to the mean equatorial plane of that same epoch and pointing towards the North Pole, and the $\hat{\boldsymbol{y}}$-axis direction completing the right-handed frame. Within this frame, the equations of motion of a solar sail subject to the Earth's gravitational, SRP, PRP, and aerodynamic accelerations can be expressed in vectorial form as:

$$\ddot{\boldsymbol{r}} = \nabla U + \boldsymbol{a}_{SRP} + \boldsymbol{a}_{Aero} + \boldsymbol{a}_{PRP} \tag{5.1}$$

where $\boldsymbol{r} = [x, y, z]^{\mathrm{T}}$ is the sailcraft position vector, x, y, and z are the Cartesian coordinates of the sailcraft in frame O_I, the dot notation and ∇ denote differentiation with respect to time and the Cartesian spatial coordinates, respectively, U is the Earth's gravitational potential, and ∇U, $\boldsymbol{a}_{SRP}$, $\boldsymbol{a}_{Aero}$, and $\boldsymbol{a}_{PRP}$ represent the gravitational, SRP, aerodynamic, and PRP accelerations, respectively. The full definition of these accelerations is provided in the following sections, specifying the modeling assumptions used for the preliminary and final analyses of the work.

5.2.1. GRAVITATIONAL ACCELERATION

The gravitational acceleration of the Earth is defined as the gradient of the gravitational potential, ∇U, with the potential U defined through the following spherical-harmonic representation [338]:

$$U = \frac{\mu}{r} \sum_{n=0}^{N} \left(\frac{R}{r}\right)^n \sum_{m=0}^{M} \bar{P}_{n,m}\left(\sin\phi\right)\left[\bar{C}_{n,m}\cos(m\lambda) + \bar{S}_{n,m}\sin(m\lambda)\right] \tag{5.2}$$

where μ and R are the gravitational parameter and mean equatorial radius of the Earth, respectively, $r = \|\boldsymbol{r}\|$, $\bar{P}_{n,m}(\,)$ denote the normalized associated Legendre function of the first kind of degree n and order m, ϕ is the geocentric latitude, λ is the geographic longitude, and $\bar{C}_{n,m}$ and $\bar{S}_{n,m}$ are normalized coefficients of the spherical-harmonic series expansion, which is truncated at a maximum degree N and order $M \leq N$. In this chapter, the $\bar{C}_{n,m}$ and $\bar{S}_{n,m}$ coefficients, and the values $\mu = 398600.4415$ km^3 s^{-2} and

$R = 6378.1363$ km are taken from the GOCO05c geopotential model, which was developed from data of the GRACE and GOCE missions, altimetry, and terrestrial measurements [281, 339]. Finally, depending on the level of accuracy required, different pairs of maximum degree N and order M will be considered. For the preliminary analysis in Section 5.5, $N = 2$ and $M = 0$, which corresponds to considering only the J_2 gravitational acceleration caused by the oblateness of the Earth. For the final analysis in Section 5.7, on the other hand, $N = M = 32$.

5.2.2. SOLAR RADIATION PRESSURE ACCELERATION

The SRP acceleration is modeled assuming the sail to be perfectly flat and to have optical characteristics constant across its surface. In the literature, the most widely used model accounting for these properties is the so-called optical SRP acceleration model devised by McInnes in Ref. [2]. This model, however, is also based on the assumption that sunlight always only reaches the front of the sail and never its back. Although desirable, this condition is not necessarily met in real-life missions and, as discussed in Section 5.3, this is indeed the case for different CSLs. Therefore, the need for an optical SRP acceleration model that also accounts for the back of the sail receiving solar radiation arises. In view of this, an extension to the optical model by McInnes which relaxes the condition of front-side illumination is presented hereinafter.

The SRP acceleration is defined as:

$$\boldsymbol{a}_{SRP} = \boldsymbol{a}_{SRP,n} + \boldsymbol{a}_{SRP,t} \tag{5.3}$$

where $\boldsymbol{a}_{SRP,n}$ and $\boldsymbol{a}_{SRP,t}$ represent the acceleration components normal and tangential to the sail plane, respectively, given by:

$$\boldsymbol{a}_{\mathrm{SRP},n} = \nu \frac{a_c}{2} \Bigg[\underbrace{\left(1+\hat{r}_{sl}s_{sl}\right)\cos^2\alpha_{sl}\,\hat{\boldsymbol{n}}_{sl}}_{\substack{\text{Specular reflection and} \\ \text{normal absorption}}} + \underbrace{\left(1-s_{sl}\right)\hat{r}_{sl}B_{sl}\cos\alpha_{sl}\,\hat{\boldsymbol{n}}_{sl}}_{\text{Diffuse reflection}} + \underbrace{\left(1-\hat{r}_{sl}\right)\frac{\varepsilon_f B_f - \varepsilon_b B_b}{\varepsilon_f + \varepsilon_b}\cos\alpha_{sl}\,\hat{\boldsymbol{n}}}_{\text{Emission}} \Bigg] \tag{5.4}$$

$$\boldsymbol{a}_{\mathrm{SRP},t} = \nu \frac{a_c}{2} \underbrace{\left(1-\hat{r}_{sl}s_{sl}\right)\cos\alpha_{sl}\sin\alpha_{sl}\,\hat{\boldsymbol{t}}}_{\text{Transversal absorption}} \tag{5.5}$$

In Eqs. 5.4 and 5.5, $\nu \in [0,1]$ represents the shadow factor computed using the conical shadow model presented in Ref. [231], which accounts both for partial eclipse (penumbra) and full eclipse (umbra). The solar-sail characteristic acceleration, a_c, is defined as:

$$a_c = \frac{2S_{TSI}}{c\sigma} \tag{5.6}$$

with $S_{TSI} = 1361\ \mathrm{W\,m^{-2}}$ the Total Solar Irradiance (TSI) [304], $c = 299792458$ m/s the speed of light in vacuum [390], and σ the mass-to-sail area ratio, also referred to as loading parameter. The directions $\hat{\boldsymbol{n}}$ and $\hat{\boldsymbol{n}}_{sl}$ indicate the sail normal directions pointing out of the back of the sail and having a positive component along the Sun-to-sailcraft direction, $\hat{\boldsymbol{s}}$, respectively. In the optical model originally devised by McInnes, the assumption that only

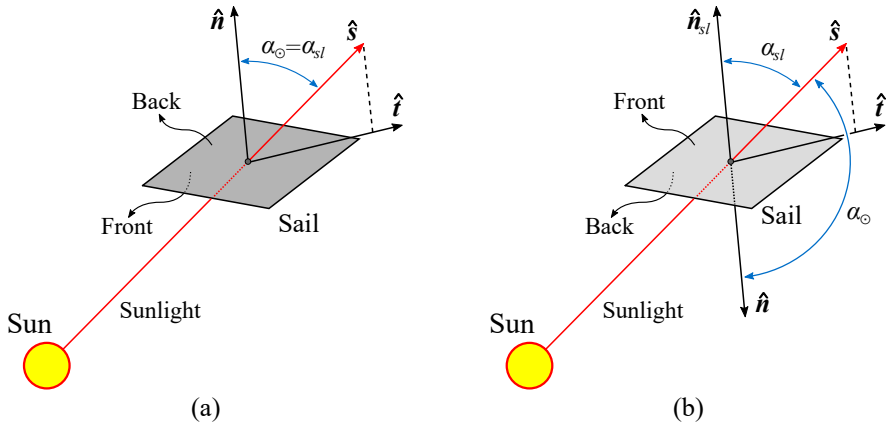


Figure 5.1: Geometry of the extended optical SRP acceleration model for sunlight illuminating a) the front of the sail and b) the back of the sail.

5

the front of the sail is illuminated implies that $\hat{\boldsymbol{n}} = \hat{\boldsymbol{n}}_{sl}$ always. Because this assumption is not valid in the proposed model, the sail normal directions are related differently as:

$$\hat{\boldsymbol{n}}_{sl} = \text{sgn}(\hat{\boldsymbol{s}} \cdot \hat{\boldsymbol{n}})\, \hat{\boldsymbol{n}} = \text{sgn}(\cos\alpha_\odot)\, \hat{\boldsymbol{n}} = \text{sgn}\left(\frac{\pi}{2} - \alpha_\odot\right) \hat{\boldsymbol{n}} \tag{5.7}$$

where $\alpha_\odot \in [0, \pi]$ is the solar-sail backside pitch angle, measured between $\hat{\boldsymbol{s}}$ and the sail backside normal direction, $\hat{\boldsymbol{n}}$. Similar to $\alpha_\odot$, the pitch angle of the sunlit side of the sail, $\alpha_{sl} \in [0, \pi/2]$, is measured between $\hat{\boldsymbol{s}}$ and $\hat{\boldsymbol{n}}_{sl}$. It is related to $\alpha_\odot$ by:

$$\alpha_{sl} = \frac{\pi}{2} - \left| \frac{\pi}{2} - \alpha_\odot \right| \tag{5.8}$$

so that $\alpha_{sl} = \alpha_\odot$ when the front side is illuminated, that is, for $\alpha_\odot \leq \pi/2$. The transversal direction, $\hat{\boldsymbol{t}}$, is defined as:

$$\hat{\boldsymbol{t}} = \hat{\boldsymbol{n}} \times \frac{\hat{\boldsymbol{s}} \times \hat{\boldsymbol{n}}}{\| \hat{\boldsymbol{s}} \times \hat{\boldsymbol{n}} \|} \tag{5.9}$$

where $\hat{\boldsymbol{n}}$ may also be substituted by $\hat{\boldsymbol{n}}_{sl}$ without loss of validity. Finally, the optical properties of the sail are specified through the reflectivity $\hat{r}$, specular reflection coefficient s, non-Lambertian reflection coefficient B, and emissivity ε, with the subscripts "f", "b", and "sl" indicating whether the optical coefficient refers to the front of the sail, the back of the sail, or the sunlit side of the sail, respectively. The optical coefficients of the sunlit side of the sail are related to those of front and back by the following relationship:

$$\left[\hat{r}_{sl},\ s_{sl},\ B_{sl}\right] = \begin{cases} \left[\hat{r}_f,\ s_f,\ B_f\right] & \text{if } \hat{\boldsymbol{s}} \cdot \hat{\boldsymbol{n}} \geq 0 \\ \left[\hat{r}_b,\ s_b,\ B_b\right] & \text{otherwise} \end{cases} \tag{5.10}$$

Comparison of Eqs. 5.4 and 5.5 with Eqs. 2.53 and 2.54 highlights the main differences between the extended and original optical SRP acceleration models. As can be observed,

Table 5.1: ACS3 sailcraft specifics.

Hardware	Mass	16 kg
	Area	80 m^2
	σ	0.2 kg/m^2
	a_c	$4.540 \cdot 10^{-2}$ mm/s^2
	$\dot{\varphi}_{max}$	0.5 $deg\,s^{-1}$
	Q_{max}	130 Wh
	$P_{in,max}$	70 W
Optical properties	$\boldsymbol{oc}_{SW}$	[0.90, 0.82, 0.79, 0.03, 0.43, 0.53, 2/3, 0.60]
	$\boldsymbol{oc}_{LW}$	[0.97, 0.82, 0.79, 0.03, 0.40, 0.53, 2/3, 0.60]
Aerodynamics	σ_N	0.8
	σ_T	0.8
	V_R	0.05

Notes: The data in the table was taken from personal communication with W.K. Wilkie, Principal Investigator of the ACS3 mission, NASA Langley Research Center, May 2025. The optical coefficients are given as $[\hat{r}_f, s_f, B_f, \varepsilon_f, \hat{r}_b, s_b, B_b, \varepsilon_b]$.

α_{sl} is employed instead of $\alpha_\odot$ in order to consider the effective incidence angle at which sunlight strikes the sail, regardless of whether its front or back is illuminated. For the same reason, the acceleration terms associated with specular reflection, normal absorption, and diffuse reflection, see Eq. 5.4, are directed along the normal direction $\hat{\boldsymbol{n}}_{sl}$ instead of $\hat{\boldsymbol{n}}$. Similarly, the optical coefficients of the sunlit side of the sail are always considered instead of the optical coefficients of the front side, with the only exception of the fractional term on the right-hand side of Eq. 5.4, indicated in orange. This exception stems from the fact that the fractional term contains information on the relative amounts of radiation emitted (in opposite directions) from the front and back of the sail to maintain thermal balance. Crucially, these relative amounts only depend on the sailcraft properties and are independent of the direction of incoming sunlight. Therefore, the fractional term does not present any reference to the optical coefficients of the sunlit side and, when multiplied by the sail backside normal direction, $\hat{\boldsymbol{n}}$, it determines whether the net acceleration caused by radiative emission will be directed out of the front or back of the sail. Finally, it is important to note that the extended optical model requires knowledge of the backside reflectivity, $\hat{r}_b$, and specular reflection coefficient, s_b, which, on the other hand, are not required by McInnes' optical model.

In this chapter, the extended optical model presented above will be used considering ACS3's loading parameter, σ, provided in Table 5.1, and different optical coefficients for the preliminary and final analyses of Sections 5.5 and 5.7, respectively. In particular, the final analysis will consider ACS3's optical coefficients for the shortwave wavelength band – that is, the wavelength band wherein solar radiation is primarily defined – denoted by $\boldsymbol{oc}_{SW}$ in Table 5.1. The preliminary analysis, on the other hand, will consider an ideal sail that is perfectly reflecting on both sides, corresponding to the following set of optical

coefficients:

$$\boldsymbol{oc}_{id} = \left[\hat{r}_f,\, s_f,\, B_f,\, \varepsilon_f,\, \hat{r}_b,\, s_b,\, B_b,\, \varepsilon_b\right] = \left[1,\, 1,\, 2/3,\, 0,\, 1,\, 1,\, 2/3,\, 0\right] \tag{5.11}$$

Note that, when employing the coefficients in Eq. 5.11, Eqs. 5.4 and 5.5 simplify greatly, resulting in the following final expression for the ideal SRP acceleration:

$$\boldsymbol{a}_{SRP} = \nu a_c \cos^2\alpha_{sl}\, \hat{\boldsymbol{n}}_{sl} \tag{5.12}$$

5.2.3. PLANETARY RADIATION PRESSURE ACCELERATION

To compute the PRP acceleration, the spherical optical model presented in Chapter 4 is employed. The model assumes the sail to be perfectly flat and builds on the same theory of sail-radiation interaction described in Section 5.2.2 for the optical SRP model. At the same time, the model assumes the Earth to be a spherical radiation source emitting two types of radiation, namely, the blackbody radiation and albedo radiation. Blackbody radiation is emitted directly by the Earth to maintain thermal balance and it is primarily defined in longwave, infrared band of the electromagnetic spectrum, see Section 2.4.4. Albedo radiation, on the other hand, corresponds to the fraction of solar radiation that, upon striking the upper layers of the atmosphere and the surface of the Earth, is scattered back into space. Therefore, this type of radiation is primarily emitted in the same wavelength band as solar radiation, that is, the shortwave band, see again Section 2.4.4. The intensities of both blackbody and albedo radiations vary across the surface of the Earth following complex distributions that depend on the geographical location considered, time, and – specifically for albedo radiation – the illumination conditions of the Earth as seen from the sailcraft. To capture these sources of variability in an analytical manner, the spherical PRP acceleration model introduces different approximations. The geographical distribution of the Earth's blackbody radiation flux, S_{BBR}, and albedo coefficient, Λ, are expressed analytically in one of two alternative ways, corresponding to the so-called uniform and sinusoidal variants of the spherical model. In the uniform variant of model, S_{BBR} and Λ are assumed constant across the entire surface of the Earth. On the other hand, the sinusoidal variant of the model assumes S_{BBR} and Λ to vary as sinusoidal functions of latitude, which are uniquely determined by the equatorial and polar values of the blackbody radiation flux and albedo coefficient, denoted as $S_{BBR,eq}$ and $S_{BBR,pol}$, and $\Lambda_{BBR,eq}$ and $\Lambda_{BBR,pol}$, respectively. The values of the uniform, equatorial, and polar blackbody radiation flux and albedo coefficient considered in this chapter are given in Table 5.2. These values are derived from least-squares fits of the numerical Earth radiation monthly maps of the ANGARA (Analysis of Non-Gravitational Acceleration due to Radiation and Aerodynamics) model [394]. Therefore, different fitted values of the blackbody flux and albedo coefficients can be considered at each month, allowing to capture the temporal variability of the Earth's radiation field. Leveraging the analytical formulation of the problem, averaging procedures are then performed with respect to the blackbody radiation flux, albedo coefficient, and illumination conditions of the visible surface of the Earth as seen from the sailcraft. In this way, the Earth is locally approximated as an isotropic emitter irradiating with constant blackbody and albedo radiation fluxes across its surface, though retaining the dependency of said fluxes on the sailcraft position with respect to the Sun and Earth. Through the above approximations, the PRP acceleration can be expressed analytically

Table 5.2: Coefficients of the uniform and sinusoidal Earth radiation models, derived from the numerical radiation maps of the ANGARA model [394].

Radiation model	Month	$S_{BBR,eq}$ $[\mathrm{Wm}^{-2}]$	$S_{BBR,pol}$ $[\mathrm{Wm}^{-2}]$	$\Lambda_{BBR,eq}$ $[-]$	$\Lambda_{BBR,pol}$ $[-]$
Sinusoidal	January	260.732	173.841	0.1917	0.6416
	February	262.209	170.302	0.1837	0.6252
	March	263.876	167.552	0.1745	0.6219
	April	264.737	170.334	0.1772	0.6116
	May	264.387	173.348	0.1889	0.6005
	June	265.350	179.492	0.2063	0.5535
	July	267.194	179.849	0.2122	0.5320
	August	268.654	176.797	0.1925	0.5700
	September	269.156	172.356	0.1762	0.6039
	October	266.892	169.200	0.1741	0.6272
	November	262.583	171.688	0.1879	0.6439
	December	259.544	176.469	0.1955	0.6250
Uniform	December	$S_{BBR} = 231.911\ \mathrm{Wm}^{-2}$		$\Lambda = 0.324$	

as a function only of the sailcraft altitude, the Sun-Earth-sailcraft angle, the latitude of the subsatellite point, and the planetary pitch angle, $\alpha_{\oplus}$, measured between the Earth radial direction, $\hat{\boldsymbol{r}}$, and the sail backside normal direction, $\hat{\boldsymbol{n}}$, see Fig. 5.2b. For more information on the derivation and formulation of the optical spherical PRP acceleration model, the reader is referred to Chapters 3 and 4.

In this chapter, the optical spherical PRP acceleration model will be used either in the uniform or sinusoidal variant and with different optical coefficients depending on whether the preliminary or final analyses are considered. In particular, in the final analysis in Section 5.7, the optical sinusoidal model will be used with values of the equatorial and polar blackbody flux and albedo coefficient fitted to the ANGARA model's monthly averaged radiation data, see Table 5.2. Furthermore, the albedo and blackbody radiation pressure components of the PRP acceleration will be computed using ACS3's optical coefficients for the shortwave and longwave wavelength bands, $\boldsymbol{oc}_{SW}$ and $\boldsymbol{oc}_{LW}$, respectively, see Table 5.1. Because the preliminary analysis in Section 5.5 will consider only one simulation start date in December, the uniform spherical model will be employed with values of the blackbody flux and albedo coefficient fitted to the ANGARA model's radiation data for December, see again Table 5.2. In agreement with Section 5.2.2, the preliminary analysis will also consider the ideal optical coefficients in Eq. 5.11. Notice that, in this way, the optical PRP acceleration model presented above and detailed in Chapter 4 effectively reduces to the ideal PRP acceleration model presented in Chapter 3.

5.2.4. AERODYNAMIC ACCELERATION

The aerodynamic acceleration is computed assuming the sail to behave as a perfectly flat plate in hyperthermal free-molecular flow conditions, that is, the sailcraft is assumed to orbit with a velocity much larger than the thermal velocity of the atmospheric particles [341]. Under these conditions, the aerodynamic acceleration is found as [219, 220]:

$$\boldsymbol{a}_{Aero} = \frac{1}{2}\frac{\rho v^2}{\sigma}\left(C_D\hat{\boldsymbol{D}} + C_L\hat{\boldsymbol{L}}\right) \tag{5.13}$$

In Eq. 5.13, v is the magnitude of the sailcraft relative velocity to the atmosphere and ρ is the atmospheric density, which is modeled using an averaging technique based on the NRLMSISE-00 atmospheric model, presented in Chapter 6. The underlying NRLMSISE-00 model is employed with solar radio flux at 10.7 cm and geomagnetic activity relative to the 50$^{\text{th}}$ percentile, retrieved from the space weather forecast data of the NASA Marshall Space Flight Center (MSFC) [294]. $\hat{\boldsymbol{D}}$ and $\hat{\boldsymbol{L}}$ represent the drag and lift directions pointing opposite and perpendicular to the relative velocity direction, $\hat{\boldsymbol{v}}$, respectively, see Fig. 5.2c. C_D and C_L are the drag and lift coefficients, respectively, given by [219, 220, 341, 349]:

$$C_D = 2\left[\sigma_T + \sigma_N V_R|\cos\alpha_A| + (2-\sigma_N-\sigma_T)\cos^2\alpha_A\right]|\cos\alpha_A| \tag{5.14}$$

$$C_L = 2\left[\sigma_N V_R + (2-\sigma_N-\sigma_T)|\cos\alpha_A|\right]|\cos\alpha_A|\sin\alpha_A \tag{5.15}$$

where V_R is the ratio of the atmospheric particle average thermal velocity to the sailcraft inertial velocity, σ_N and σ_T are the normal and tangential momentum accommodation coefficients, respectively, and α_A represents the aerodynamic pitch angle, that is, the complementary angle to the angle of attack, see again Fig. 5.2c. Based on Refs. [219, 220, 355], in this chapter $\sigma_N = \sigma_T = 0.8$ and $V_R = 0.05$.

The aerodynamic model presented above will be used in the preliminary analysis of Section 5.5 assuming the atmosphere fixed to the inertial frame, O_I, for simplicity. In this way, the relative velocity of the sailcraft with respect to the atmosphere effectively coincides with the inertial velocity of the sailcraft. Conversely, for the final analysis of Section 5.7, the atmosphere will be assumed to corotate with the Earth. Finally, the preliminary and final analyses will consider the MSFC forecast data of May 2023 and May 2025, respectively, corresponding to the time the analyses were performed.

5.3. CALIBRATION STEERING LAWS

In this section, the definition of a set of steering laws designed to calibrate the SRP, PRP, and aerodynamic accelerations of solar sails in Earth-bound, circular orbits is discussed. To this aim, it is essential to first define the concept of the acceleration envelope (AE): this is a curve representing the set of all possible accelerations achievable by a sailcraft when changing its attitude. Because the SRP, PRP, and aerodynamic accelerations change their magnitudes and directions with the sail attitude, an AE can be defined for each of them. For example, when the acceleration models presented in Section 5.2 and a perfectly reflecting sail are considered, these curves assume the shapes depicted in Fig. 5.2. As can be seen, all AEs are symmetric with respect to a different reference direction, namely, the sunlight direction, $\hat{\boldsymbol{s}}$, radial direction, $\hat{\boldsymbol{r}}$, and velocity direction, $\hat{\boldsymbol{v}}$, for the SRP, PRP, and aerodynamic AEs, respectively. The reference directions provide information

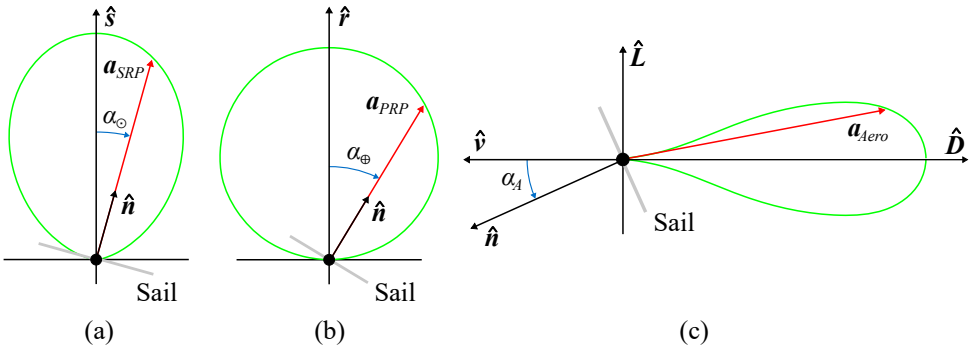


Figure 5.2: Directions, pitch angles, and envelope curves of the a) SRP acceleration, b) PRP acceleration, and c) aerodynamic acceleration.

on which attitudes maximize or minimize a particular acceleration. Indeed, if the sail normal direction, $\hat{\boldsymbol{n}}$, is directed along a reference direction or perpendicular to it, the corresponding acceleration is maximized or minimized, respectively. On the other hand, for arbitrary orientations of $\hat{\boldsymbol{n}}$, intermediate accelerations are obtained whose magnitude and direction are described by the AEs, see Fig. 5.2.

Given the notion of AE, the CSLs can be regarded as control strategies that solar sails can adopt to reconstruct the AEs based on the in-orbit accelerations experienced. The difficulty in designing CSLs for the SRP, PRP, and aerodynamic accelerations is the fact that all these accelerations depend on the sail attitude and are therefore coupled. Consequently, in most cases it is not possible to calibrate a single acceleration independently without experiencing a perturbing effect from the others. In addition, it is worth noting that the design of the CSLs also depends on the relative orientation of the orbit with respect to sunlight, as the presence of eclipses hinders the calibration of the SRP acceleration.

Hereinafter seven CSLs with different degrees of complexity are presented. In Section 5.3.1, steering laws to calibrate the maximum SRP, PRP, and aerodynamic accelerations are discussed. Afterwards, Section 5.3.2 presents other three CSLs to calibrate the entire SRP, PRP, and aerodynamic AEs. Finally, a steering law designed to calibrate the residual accelerations acting on solar sails in the absence of SRP, PRP, and aerodynamic accelerations is discussed in Section 5.3.3.

5.3.1. CALIBRATION OF THE MAXIMUM ACCELERATIONS

The steering laws discussed in this section aim to calibrate the maximum magnitudes of the SRP, PRP, and aerodynamic accelerations, therefore allowing to determine the characteristic dimensions of their AEs. To achieve this, for each of these acceleration a steering law can be designed in which the sail is constantly oriented with its normal parallel to the acceleration's reference direction, that is, $\hat{\boldsymbol{n}}$ points along $\hat{\boldsymbol{s}}$, $\hat{\boldsymbol{r}}$, and $\hat{\boldsymbol{v}}$ when calibrating the maximum SRP, PRP, and aerodynamic accelerations, respectively. For the sake of visualization, the implementation of these steering laws over one orbital period is displayed in Figs. 5.3a-c. The approach described above can be used to calibrate

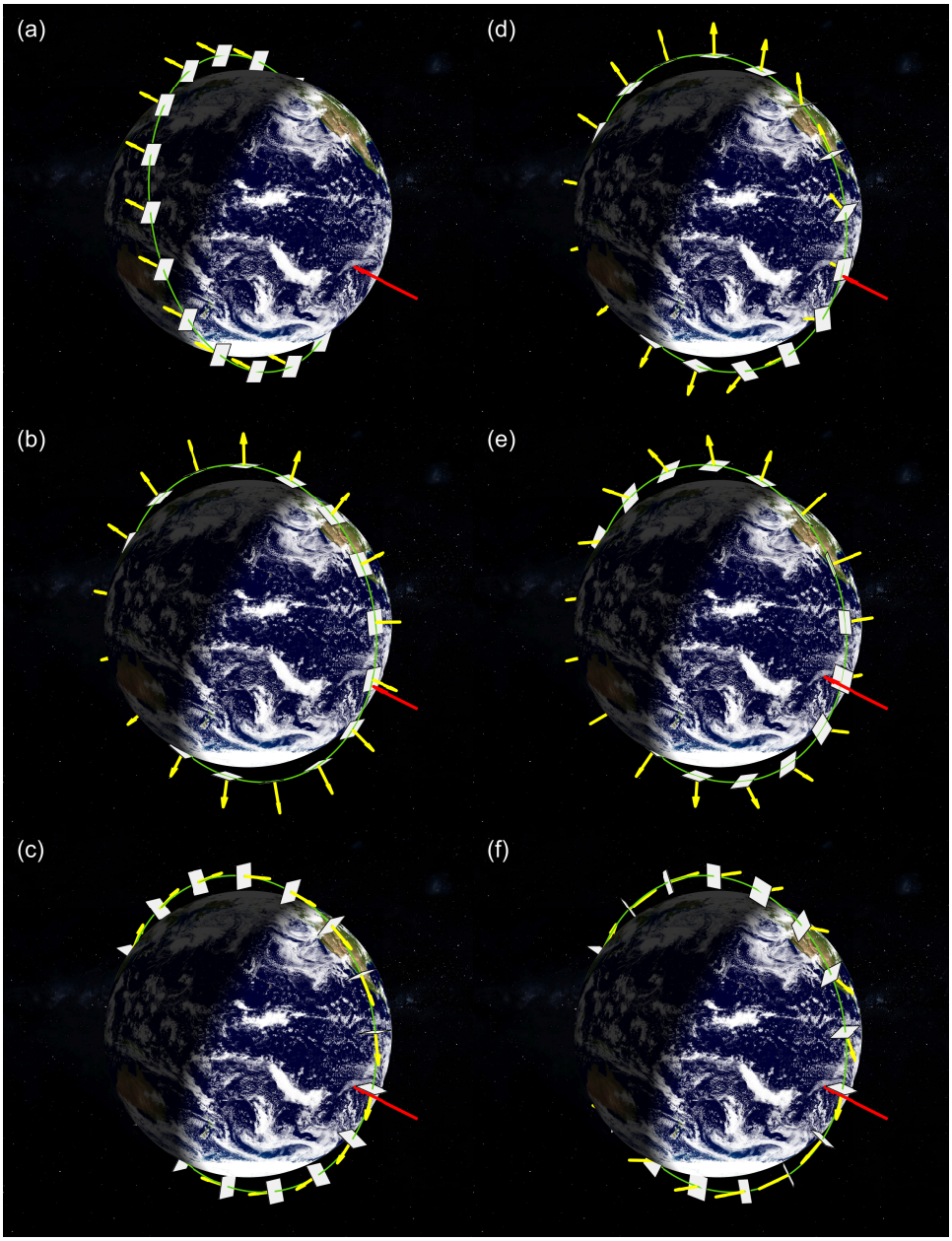


Figure 5.3: Steering laws to calibrate the maximum acceleration from a) SRP, b) PRP, and c) aerodynamic drag, and the envelope curves of the d) SRP, e) PRP, and f) aerodynamic accelerations. Sailcraft orbits in green. Directions of sunlight and sail backside normal directions in red and yellow, respectively.

the maximum PRP and aerodynamic accelerations at any point along the orbit and the maximum SRP acceleration only when the sailcraft is illuminated. Indeed, when the sailcraft is in eclipse conditions ($\nu = 0$), sunlight cannot reach the sailcraft and, therefore, the SRP acceleration cannot be measured. In this case, an alternative control strategy can be adopted: the sail is oriented edgewise with respect to the velocity direction, $\hat{\boldsymbol{v}}$, and with its normal pointing along the radial direction, $\hat{\boldsymbol{r}}$. This configuration minimizes drag, therefore preventing the sail from deorbiting. On the other hand, the PRP acceleration is maximized, hence potentially enabling its calibration. It should be noted that this variant of the CSL is only implemented when eclipses longer than a specified threshold duration, Δt_{ecl}, take place. The reason for this is that switching to this alternative control strategy requires a sudden reorientation of the sailcraft, which can prove demanding for real-life attitude control systems. As a consequence, it may be preferable not to implement this variant of the CSL when short eclipses are experienced, despite the perturbations PRP acceleration and drag may yield. In this chapter, a value of Δt_{ecl} equal to 1/5 of the orbital period is considered for all CSLs where applicable.

5.3.2. CALIBRATION OF THE ACCELERATION ENVELOPES

This section presents three CSLs that aim to calibrate the entire AEs of the SRP, PRP, and aerodynamic accelerations.

5.3.2.1. SOLAR RADIATION PRESSURE ACCELERATION

In order to calibrate the SRP AE, the sailcraft ought to change its attitude gradually, covering values of the pitch angle, $\alpha_{\odot}$, in the range 0-90 deg, see Fig. 5.2a. Depending on whether eclipses occur, two possible control strategies are adopted.

If the sailcraft is continuously illuminated along the entire orbit, the sail's normal direction, $\hat{\boldsymbol{n}}$, points along the sunlight direction, $\hat{\boldsymbol{s}}$, at the point in the orbit closest to the Sun. When moving away from this point, $\hat{\boldsymbol{n}}$ slowly changes its direction so as to increase the pitch angle, until becoming perpendicular to the direction of sunlight and parallel to the radial direction, $\hat{\boldsymbol{r}}$, after one quarter of the orbital period. Thereafter, the sail is gradually reoriented to make $\hat{\boldsymbol{n}}$ be once again parallel to $\hat{\boldsymbol{s}}$ after another quarter of the orbital period. Finally, the entire process is repeated also in the second half of the orbit, thus making the pitch angle span across the 0-90 deg range twice per orbital period.

If eclipses last longer than the specified threshold duration, Δt_{ecl}, the same eclipsing variant of the CSL presented in Section 5.3.1 for the calibration of the maximum SRP acceleration can be used. When this variant of the CSL is adopted, the pitch angle spans across the 0-90 deg range only once per orbital period. For the sake of visualization, this variant of the CSL is displayed in the Fig. 5.3d.

5.3.2.2. PLANETARY RADIATION PRESSURE ACCELERATION

When implementing the CSL for the PRP AE, the sailcraft gradually changes its attitude by translating its normal direction from $\hat{\boldsymbol{r}}$ to $\pm\hat{\boldsymbol{h}}$ (and vice versa) every quarter of the orbital period, with $\hat{\boldsymbol{h}} = (\hat{\boldsymbol{r}} \times \hat{\boldsymbol{v}}) / \|\hat{\boldsymbol{r}} \times \hat{\boldsymbol{v}}\|$ the orbital momentum direction. In this way, the planetary pitch angle measured between $\hat{\boldsymbol{n}}$ and $\hat{\boldsymbol{r}}$, $\alpha_{\oplus}$, see Fig. 5.2b, spans across the entire 0-90 deg range twice per orbit. Implementing this steering law does not yield any aerodynamic drag, thus preventing the sailcraft from deorbiting. On the other hand,

the SRP acceleration is present and acts as a perturbing acceleration. For the sake of visualization, this CSL is displayed in Fig. 5.3e.

5.3.2.3. AERODYNAMIC ACCELERATION

Similar to the CSL presented in the last subsection, the steering law to calibrate the aerodynamic AE considers a gradual variation of the sail normal direction between two reference directions: the velocity direction, $\hat{\boldsymbol{v}}$, and the orbital momentum direction, $\hat{\boldsymbol{h}}$. In particular, $\hat{\boldsymbol{n}}$, is continuously reoriented so as to point intermittently along $\hat{\boldsymbol{v}}$ and $\pm\hat{\boldsymbol{h}}$ every quarter of the orbital period. By doing so, the complementary angle to the angle of attack, α_A, spans across the entire 0-90 deg range twice per orbit. When employing this CSL, no PRP acceleration is experienced by the sailcraft, whereas the SRP acceleration acts as a perturbing acceleration. For the sake of visualization, this CSL is displayed in Fig. 5.3f.

5.3.3. CALIBRATION OF RESIDUAL ACCELERATIONS

The only sail orientation that does not produce any SRP, PRP, and aerodynamic accelerations corresponds to a sail normal direction, $\hat{\boldsymbol{n}}$, that is simultaneously perpendicular to the sunlight direction, $\hat{\boldsymbol{s}}$, radial direction, $\hat{\boldsymbol{r}}$, and velocity direction, $\hat{\boldsymbol{v}}$. The relative orientation of $\hat{\boldsymbol{s}}$, $\hat{\boldsymbol{r}}$, and $\hat{\boldsymbol{v}}$ therefore plays a central role in determining whether a zero-acceleration steering law can be designed. The only scenario in which all three accelerations can be simultaneously nullified is when $\hat{\boldsymbol{s}}$, $\hat{\boldsymbol{r}}$, and $\hat{\boldsymbol{v}}$ are coplanar, that is, for an orbit oriented parallel to the direction of sunlight. Then, the sail normal direction, $\hat{\boldsymbol{n}}$, can be directed perpendicular to the orbital plane, i.e., along $\pm\hat{\boldsymbol{h}}$. On the other hand, when the directions $\hat{\boldsymbol{s}}$, $\hat{\boldsymbol{r}}$, and $\hat{\boldsymbol{v}}$ do not lie in the same plane – that is, for the vast majority of orbital scenarios – at least one non-zero acceleration is always obtained, which therefore hinders calibration of the residual accelerations. In these cases, calibration may be performed only during eclipses, provided that these have a sufficiently large duration. To this end, the sailcraft should again be oriented such that $\hat{\boldsymbol{n}} = \pm\hat{\boldsymbol{h}}$, allowing the PRP and aerodynamic accelerations to vanish, while the SRP acceleration is inherently absent due to the eclipse.

5.4. OPERATIONAL CHALLENGES AND CONSTRAINTS

The CSLs introduced in the previous sections entail a number of operational difficulties that may hinder – or even prevent – their practical implementation. Therefore, investigating the operational feasibility of each CSL becomes paramount. Such an investigation will be performed through a large number of simulations in Sections 5.5 and 5.7, building on the operational challenges defined hereinafter.

Following consultation with the ACS3 mission team, five operational challenges were identified as especially critical. To quantify their degree of severity – and, therefore, determine which impose hard operational constraints to be met – the following five metrics were defined, listed hereinafter in decreasing order of criticality:

- **Attitude rate of change**. The CSLs require active change of the sailcraft's attitude over time. This may prove demanding to ACS3's attitude control system, which allows for a maximum attitude rate of change of $\dot{\varphi}_{max} = 0.5\ \mathrm{deg\,s^{-1}}$, see Table 5.1. In view of this hard operational constraint, the maximum angular rates of ACS3 is determined for

each simulation, with a view to comparing them with $\dot{\varphi}_{max}$ to assess the feasibility of implementation of the steering laws.

- **Power generation**. The solar panels of ACS3 are mounted parallel to the sail plane, in order to generate power when the front of the sail is illuminated. Conversely, no power is produced when the sailcraft is oriented edgewise or with its back exposed to sunlight. Some of the CSLs require ACS3's attitude to change considerably over time and, with it, also the exposure of the solar arrays to sunlight. As a consequence, prolonged periods of time during which power cannot be generated may occur, leading to potential power issues. In view of this, the exposure time of the front of the sail – and, with it, of the solar panels – to sunlight is considered as metric.

- **Altitude loss**. Implementation of a CSL for an extended period of time can induce the undesirable decay of the orbital altitude – primarily driven by atmospheric drag – thereby introducing a high operational risk. Therefore, the altitude rate of change is evaluated for each simulation performed.

- **Exposure of the back of the sail to sunlight**. ACS3's solar sail consists of a polyethylene terephthalate (PET) film coated with highly reflective aluminum on its front side to enhance its thrusting capabilities. The back of the sail, on the other hand, is coated in chromium to maximize the sail's emissivity for thermal control [142]. Exposure of the sail's back side to solar radiation – particularly its ultraviolet component – can cause the sail material to degrade rapidly, together with the sail's optical properties and performance. Because some of the CSLs lead to temporary exposure of the back of the sail to sunlight, the exposure time is considered as metric. Nevertheless, it should be noted that minimizing this exposure represents a soft operational requirement rather than a hard mission constraint.

- **Exposure of the sail's back side to the ram direction**. The Materials International Space Station Experiment (MISSE) is an ongoing series of experiments performed on board the International Space Station (ISS) that aim to characterize the long-term durability of different materials when exposed to the near-Earth space environment [408]. Among these materials, different samples of sail films coated in aluminum and chromium have also been considered. Preliminary results of the experiment analyzed by the ACS3 mission team showed that, in addition to sunlight, the materials on the back of the sail experienced rapid degradation also when exposed to the ram direction, i.e., the direction of motion [408]. The main cause for this accelerated degradation was believed to be atomic oxygen, which creates cracks in the chromium coating upon impact, thereby further allowing atomic oxygen to degrade the underlying sail film material. Although the dynamics employed in this chapter do not account for these degradation effects, see Section 5.2, the analyses presented in Section 5.5 will provide insights into the frequency with which the back of the sail is exposed to the ram direction, so as to quantify its potential effect on real-life sailcraft missions to a first-order extent. Similar to solar illumination, minimizing the exposure of the sail's back side to the ram direction constitutes a soft operational constraint. Note that, as with sunlight, limiting the exposure to the ram direction is considered a soft operational requirement.

5.5. PRELIMINARY ANALYSIS

The analysis discussed in this section was conducted in May 2023 – almost one year before the launch of ACS3 – and aimed at providing a preliminary assessment of the estimation capabilities of the CSLs, as well as their operational feasibility in the face of the challenges described in Section 5.4. The analysis setup will first be introduced, followed by the discussion of the results.

5.5.1. SETUP

The analysis makes use of NASA's ACS3 mission as baseline scenario, with hardware specifics provided in Table 5.1 and the following vector of initial orbital elements defined in frame O_I:

$$\left[a_0,\ e_0,\ i_0,\ \Omega_0,\ \omega_0,\ f_0\right]^T = \left[7093.1363\ \text{km},\ 0,\ 98.2490\ \text{deg},\ \begin{Bmatrix}157.328\ \text{deg}\\ 202.328\ \text{deg}\\ 247.328\ \text{deg}\end{Bmatrix},\ 0\ \text{deg},\ 0\ \text{deg}\right]^T \tag{5.16}$$

where a_0, e_0, i_0, Ω_0, ω_0, and f_0 represent the initial orbit's semi-major axis, eccentricity, inclination, right ascension of the ascending node (RAAN), argument of pericenter, and true anomaly, respectively[1]. The orbital elements in Eq. 5.16 identify a circular, Sun-synchronous orbit with an initial altitude of $h_0 = a_0 - R = 715$ km. Furthermore, the three initial values of the RAAN considered correspond to local times of the ascending node (LTANs) of 0600, 0900, and 1200 hrs, allowing to consider different orbit orientations with respect to sunlight and different eclipse conditions. In the analysis, the dynamics presented in Section 5.2 have been considered including the following simplifying assumptions:

- The Earth gravitational acceleration assumes a gravity potential field truncated at a spherical-harmonic degree and order of 2 and 0, respectively.
- The SRP and PRP accelerations models assume a perfectly reflecting (ideal) sail.
- The PRP acceleration is determined considering the uniform spherical radiation model of the Earth, assuming a constant blackbody radiation flux and albedo coefficient, see Table 5.2.
- The aerodynamic acceleration is computed assuming an inertially fixed atmosphere.

The above dynamics have been propagated using Matlab®'s *ode45* integrator, with absolute and relative tolerances set to 10^{-12}, for each of the initial orbits given in Eq. 5.16 and each CSL presented in Section 5.3. All trajectory propagations consider a simulation start date of December 1st, 2023 (i.e., the expected deployment date of the sail at the time of the study) and a simulation duration of 96 orbital periods, deemed the maximum amount of time to perform any given CSL by the ACS3 mission team. Finally, to account for realistic solar-sail attitude-change capabilities, the CSLs have been implemented considering ACS3's maximum attitude rate of change (RoC), $\dot{\varphi}_{max}$, equal to 0.5 deg s^{-1}, see Table 5.1.

[1] ACS3 orbital elements taken from personal communication with W.K. Wilkie, Principal Investigator of the ACS3 mission, NASA Langley Research Center, June 2023.

5.5.2. RESULTS AND DISCUSSION

Table 5.3 presents the results of the analyses for each combination of initial LTAN and CSL. In order to provide insights into the calibration of the target acceleration and perturbing effects of the other accelerations, the three columns on the left-hand side of the table specify the extent to which each AE is covered when employing a specific CSL. The acceleration to be calibrated (referred to as "calibration target") is displayed in bold, while the perturbing accelerations are given in brackets. Here, the terms "Max" and "Zero" indicate that a particular acceleration is constantly equal to its maximum achievable value or zero, respectively. Similarly, in the case a CSL covers a larger portion of the AE, the terms "Full", "Intermediate", and "Minor" are given, which indicate that the calibration target/perturbing AE is covered completely, partially, or only to a minor extent. The right-hand side of the table provides information on the operational difficulties introduced in Section 5.4. Here, the altitude loss per day experienced while implementing the CSLs is shown, as well as the maximum attitude RoC. To quantify the effect the CSLs have on the degradation of the sail, two columns are added which provide the percentage of orbital period during which the sail's back side is exposed to sunlight and the ram direction. In a similar fashion, to measure the effect each steering law has on the sailcraft power-generation capabilities, the percentage of orbital period during which the sail's front side is exposed to sunlight is given. Finally, to enable a qualitative overview of the benefits and drawbacks of each CSLs, a color code has been applied to the data of the table, with green representing benefits and yellow, orange, and red indicating potential issues of increasing degree of severity.

As can be seen in the table, calibration of the maximum SRP acceleration and its AE can prove challenging due to multiple reasons. To begin with, the sailcraft experiences increasingly large perturbations from the aerodynamic and PRP accelerations for increasing values of the initial LTAN, which lead to moderate decreases in altitude in the range 0.77-1.48 km day^{-1}. Furthermore, exposure of the back of the sail to the ram direction for long periods of time also occurs and large attitude RoC may also be required, driven by the sudden attitude changes executed when entering or exiting eclipse, see Section 5.3.2.1.

The CSLs for the maximum aerodynamic and PRP accelerations present common challenges due to the significant perturbation from SRP (especially for larger initial LTANs) and the prolonged exposure of the sail's backside to sunlight. Both these CSLs imply potential power issues, as the sail's front side is exposed to sunlight only for a limited time. This is particularly evident when calibrating the maximum PRP acceleration, as the sail has its front side constantly facing the Earth, therefore allowing little sunlight to illuminate it. The CSL for the maximum aerodynamic acceleration, on the other hand, presents another major disadvantage, that is, the deorbiting effect on the sailcraft. This happens because drag is maximized, therefore yielding a rapid loss in altitude in the order of 3.4-3.7 km day^{-1}. It should be noted that this large value is also due to the simulation start time considered. Indeed, because December 1st, 2023 falls within a period of high solar activity, the atmospheric density is also high and, therefore, aerodynamic drag is significant.

The steering laws to calibrate the PRP and aerodynamic AEs present potential problems similar to the CSLs for the maximum PRP and aerodynamic accelerations. Large perturbations by the SRP are experienced and, once again, the back of the sail is exposed

Table 5.3: Preliminary analysis of the calibration capabilities and operational challenges of the CSLs for different initial LTANs.

Calibration steering law	Initial LTAN [hrs]	**Calibration target** (Perturbation)			Altitude decay rate [km/day]	Max. attitude RoC [deg/s]	Backside Exposure [% orb. period]		Exposure of solar arrays to sunlight [% orb. period]
		SRP acceleration	PRP acceleration	Aerodynamic acceleration			Sunlight	Ram direction	
Max. SRP acc.	0600	**Max**	(Minor)	(Minor)	0.750	0	0	50	82.826
	0900	**Max**	(Intermediate)	(Intermediate)	0.979	0.5	0	36.027	68.301
	1200	**Max**	(Full)	(Full)	1.404	0.5	0	34.126	64.415
Max. PRP acc.	0600	(Minor)	**Max**	(Zero)	0	0.061	50	0	33.132
	0900	(Intermediate)	**Max**	(Zero)	0	0.061	50	0	18.399
	1200	(Full)	**Max**	(Zero)	0	0.061	50	0	14.473
Max. Aerodynamic acc.	0600	(Minor)	(Zero)	**Max**	3.556	0.061	41.117	0	41.262
	0900	(Intermediate)	(Zero)	**Max**	3.205	0.061	34.085	0	34.135
	1200	(Full)	(Zero)	**Max**	3.547	0.061	32.191	0	32.180
SRP AE curve	0600	**Full**	(Full)	(Intermediate)	0.913	0.061	0	50	82.770
	0900	**Full**	(Full)	(Intermediate)	0.844	0.061	0	25	68.305
	1200	**Full**	(Full)	(Full)	1.326	0.061	0	25	64.423
PRP AE curve	0600	(Full)	**Full**	(Zero)	0	0.086	50	0	33.003
	0900	(Intermediate)	**Full**	(Zero)	0	0.086	50	0	18.343
	1200	(Intermediate)	**Full**	(Zero)	0	0.086	48.253	0	16.169
Aerodynamic AE curve	0600	(Full)	(Zero)	**Full**	1.846	0.086	41.325	0	41.329
	0900	(Intermediate)	(Zero)	**Full**	1.700	0.086	34.166	0	34.123
	1200	(Intermediate)	(Zero)	**Full**	2.019	0.086	32.007	0	32.416
Residual	1200	**Zero**	**Zero**	**Zero**	0	0	0	0	0

to sunlight frequently. The CSL for the PRP AE also yields short time windows in which the solar arrays can generate power, whereas the CSL for the aerodynamic AE yields large altitude loss, in the order of 1.8-2.1 km day^{-1}. The results in Table 5.3 also highlight an interesting property of the PRP and aerodynamic accelerations, that is, their orthogonality. Indeed, because the analyses in this section consider circular initial orbits, the radial and velocity directions are roughly perpendicular at all times during the propagations. This implies that it is always possible to design CSLs for which the PRP or aerodynamic acceleration is varied while the other is left unchanged. Because of this, in Table 5.3, the steering laws to calibrate the aerodynamic acceleration show that PRP never perturbs the dynamics. In a similar fashion, for the CSLs for the PRP acceleration, aerodynamic drag is always equal to zero.

Finally, the CSL to quantify the residual accelerations only implies one major operational challenges, that is, the fact that sunlight never illuminates the sail's front side and no power can be generated. This is due to the particular attitude of the sail, which is constantly oriented edgewise with respect to sunlight. It is also worth noting that, to implement this CSL, the sail must be oriented edgewise also with respect to the velocity and the radial directions. As discussed in Section 5.3.3, these three conditions can be met only if the direction of sunlight is coplanar with the velocity and radial directions. As this is the case only for an initial LTAN at 1200 hrs, no simulation has been performed for this CSL for LTANs at 0600 hrs and 0900 hrs.

Although the operational challenges in Table 5.3 may render adoption of the CSLs more difficult, it should be noted that the severity of some of these challenges may be mitigated, while others may be endured for limited periods of time without necessarily compromising the mission. For example, the CSLs requiring a large attitude RoC of 0.5 deg s^{-1} may be implemented allowing for a slower reorientation of the sail when entering the eclipse region, so as to decrease the attitude RoC and, therefore, the effort required by the sailcraft attitude control system. Alternatively, the reorientation of the sail may be avoided altogether, although this would yield increased drag and, therefore, rate of altitude decay. Although exposure of the back of the sail to the ram direction and/or sunlight yields accelerated degradation of the sail material, such a circumstance may be endured without yielding critical consequences, especially if calibration of the solar-sail accelerations requires relatively short periods of time compared to the characteristic times over which degradation occurs.

In contrast to the above, some operational challenges deemed particularly critical are the altitude decay and inability to generate power. These challenges may be less severe for sailcraft at high altitudes – where the atmospheric drag and risk of deorbiting are lower – and sailcraft with sufficiently large energy storage capacities. Nevertheless, they remain critical drivers of the steering-law operational feasibility.

5.6. REVISION OF THE ANALYSIS FRAMEWORK

ACS3 was launched on April 23rd, 2024 and successfully deployed its sail on August 29th, 2024. Once operational, information on its orbit, its real-life attitude control capabilities, and the severity of the operational challenges characterizing the CSLs became more clearly understood. The information acquired enabled the downselection of the most

suitable CSLs to further explore, primarily driven by their ease of execution and operational risks they involved. Furthermore, the process led to the introduction of two additional CSLs. In a similar fashion, the set of operational challenges was also revisited, incorporating additional data offered by the ACS3 mission team.

This section presents the revised sets of CSLs and operational challenges of ACS3, paving the way to the final analysis of operational feasibility in Section 5.7.

5.6.1. REVISION OF THE CALIBRATION STEERING LAWS

Following the preliminary analysis discussed in Section 5.5, the steering law to calibrate the solar-sail residual accelerations was determined to be unfeasible. The decision was primarily driven by the low rate of exposure of the solar arrays to sunlight, which would have yielded a rapid decay in available power to operate the sailcraft, therefore posing the entire mission at risk. Furthermore, because of the orientation of its orbit, ACS3 experienced eclipses of very short duration. Therefore, the periods during which SRP, PRP, and aerodynamic accelerations could simultaneously be absent was very short, strongly reducing the ability to calibrate any residual acceleration.

Although the calibration of the SRP, PRP, and aerodynamic AEs had initially been deemed among the most scientifically interesting to pursue, the corresponding CSLs were associated with a high operational risk, rendering their practical implementation unfeasible. Specifically, the sequence of maneuvers that these steering laws involved required precise knowledge of the sailcraft state at each point in time and, crucially, precise timing for implementing the maneuvers, which was identified as a major challenge. Also, the onboard software required the data to perform the attitude rotations be uploaded from ground multiple times per orbital period. Since ACS3 relied on only one ground station to manage its operations, contacts with such a high frequency were, in practice, unattainable. Furthermore, as these CSLs required frequent attitude changes, they would have proven demanding on the attitude control system and facilitated saturation of the reaction wheels. Finally, losing control of the sailcraft while constantly changing the solar-sail orientation – as prescribed by these steering laws – would have caused the satellite to enter a tumbling state, with potentially critical consequences on the mission. In view of above reaons, the CSLs to calibrate the AEs were therefore discarded.

The steering laws considered the safest to implement were those requiring a fixed or – at most – slowly changing attitude, as they were deemed more easily executable by the onboard attitude control systems and ground control. Consequently, the steering laws to calibrate the maximum PRP and aerodynamic accelerations were retained, while the CSL for the maximum SRP acceleration was modified to keep the Sun-facing attitude even when in eclipse, thereby avoiding rapid attitude changes, see Table 5.3. In addition, two other steering laws requiring easily executable attitude changes were introduced, namely, the fixed in-plane pointing and backside nadir-pointing steering laws. The fixed in-plane pointing CSL prescribes the sail to be constantly oriented with its normal, $\hat{\boldsymbol{n}}$, pointing within the orbital plane, while forming the smallest possible angle with the direction of sunlight, $\hat{\boldsymbol{s}}$. This steering law was introduced because it was believed to provide relatively good calibration capabilities, while offering continuous exposure of the solar arrays to sunlight. Unlike the other steering laws, the backside nadir-pointing steering law was introduced not for its calibration capabilities, but to facilitate communication time with

the ground station. Indeed, this steering law prescribes the sail normal direction, $\hat{\boldsymbol{n}}$, to point toward nadir at all time, that is, opposite to the radial direction, $\hat{\boldsymbol{r}}$. In this way, the sailcraft is constantly oriented with its back, where the antennas are mounted, facing the Earth, thereby maximizing opportunities for communication with the ground station.

It should be noted that the steering laws to calibrate the maximum SRP, PRP, and aerodynamic accelerations, as well as the new CSLs introduced above, require the sail normal to point along a reference direction. With this in mind, the CSLs were renamed to include said direction in their name, in order to facilitate intuitive understanding of the corresponding sailcraft attitude. For the sake of clarity, the final list of CSLs considered in the rest of the chapter, including their brief description, is summarized hereinafter:

- **Sun-pointing**. The sail is oriented with its normal direction constantly pointing towards the direction of sunlight, that is, $\hat{\boldsymbol{n}} = \hat{\boldsymbol{s}}$. In this way, the front of the sail is oriented facing the Sun at all time, unless in eclipse. This CSL corresponds to the steering law to calibrate the maximum SRP acceleration, presented in Section 5.3.1.

- **Drag-pointing**. The sail is oriented with its normal direction constantly pointing antiparallel to the inertial velocity of the sailcraft, that is, $\hat{\boldsymbol{n}} = -\hat{\boldsymbol{v}}$. In this way, the front of the sail is oriented facing the incoming atmospheric particles at all time. This CSL corresponds to the steering law to calibrate the maximum aerodynamic acceleration, presented in Section 5.3.1.

- **Frontside nadir-pointing**. The sail is oriented with its normal direction constantly pointing parallel to the radial direction, that is, $\hat{\boldsymbol{n}} = \hat{\boldsymbol{r}}$. In this way, the front of the sail is oriented towards the Earth at all time. This CSL corresponds to the steering law to calibrate the maximum PRP acceleration, presented in Section 5.3.1.

- **Backside nadir-pointing**. The sail is oriented with its normal direction constantly pointing antiparallel to the radial direction, that is, $\hat{\boldsymbol{n}} = -\hat{\boldsymbol{r}}$. In this way, the back of the sail, where the antennas are mounted, is oriented towards the Earth at all time, facilitating communication with the ground station. Note that this CSL represents the nominal, standby attitude mode of ACS3, employed when no other CSL is being performed.

- **Fixed in-plane pointing**. The sail is oriented with its normal direction constantly pointing within the orbital plane while forming the smallest possible angle with the direction of sunlight, that is, $\hat{\boldsymbol{n}} = \hat{\boldsymbol{d}}$, where:

$$\hat{\boldsymbol{d}} = \hat{\boldsymbol{h}} \times \frac{\hat{\boldsymbol{s}} \times \hat{\boldsymbol{h}}}{\left\| \hat{\boldsymbol{s}} \times \hat{\boldsymbol{h}} \right\|} \tag{5.17}$$

5.6.2. REVISION OF THE OPERATIONAL CHALLENGES

As mentioned in Section 5.4, the MISSE experiment on board the ISS enhanced understanding of the causes and modalities in which sail film degradation occurs. Nevertheless, in the time between the preliminary and post-launch analyses of this chapter, additional tests were performed at the NASA Langley Research Center, with the aim to reproduce

the results obtained by the MISSE experiment. The tests showed that the erosion of the chromium coating and the underlying PET film on the back of the sail could not be clearly attributed to atomic oxygen, as its interaction with the materials did not result in any accelerated degradation. As a consequence, it was concluded that the experiment results observed on board the ISS had not been caused by atomic oxygen alone, but likely by its interplay with other drivers, possibly ultraviolet radiation. In light of these tests, it was agreed with the ACS3 mission team to not consider the exposure of the back of the sail to the ram direction a critical aspect to account for in the mission. Accordingly, the corresponding operational challenge was discarded.

The operational challenges concerning the altitude decay, attitude rate of change of the sailcraft, and exposure of its back to sunlight were retained, employing again the metrics presented in Section 5.4. On the other hand, although power generation was again regarded as an operational challenge, the associated metric was updated to incorporate additional data provided by the ACS3 mission team, which allowed to clearly assess the rates of battery charging and depletion. Furthermore, a new operational challenge was introduced to reflect the need for regular communication of the sailcraft with the ground station.

The above considerations led to the final list of operational challenges presented hereinafter alongside their corresponding metrics, which will be considered for the analysis of Section 5.7:

- **Attitude rate of change**. See definition in Section 5.4.
- **Power generation**. As discussed in Section 5.3, some of the CSLs require ACS3's attitude to change considerably over time and, with it, also the exposure of the solar arrays to sunlight. This circumstance can negatively impact the battery charging capabilities which, coupled with the energy consumption required for operating the sailcraft, may prevent implementation of the steering laws for prolonged periods of time. Therefore, knowledge of the battery charging and consumption rates over time becomes paramount.

  As presented in Table 5.1, ACS3 features a battery with total capacity of $Q_{max} = 130$ Wh and a set of four solar panels on the front side of the sailcraft that can collectively achieve a maximum power intake of $P_{in,max} = 70$ W. Such power intake is achieved only when the panels are oriented orthogonal to the direction of incoming sunlight. In all other cases, the effective power intake is:

$$P_{in} = \nu P_{in,max} \max(0, \cos\alpha_{\odot}) \tag{5.18}$$

  where ν and $\alpha_{\odot}$ are the shadow factor and sail backside pitch angle introduced in Section 5.2.2, and the "max" function is used to indicate that no charging occurs when sunlight illuminates the back of the sail (and of the solar arrays). Following input from the mission team, the overall average power required for operating the satellite is $P_{ops} = 14.2$ W. Based on the above values, the averaged battery charging/usage rate from time t_0 to time t_f relative to the total battery capacity, Q, can be formulated as:

$$\dot{Q}_{rel} = \frac{1}{Q_{max}} \frac{\int_{t_0}^{t_f} \left(P_{in}(t) - P_{ops}\right) dt}{t_f - t_0} \tag{5.19}$$

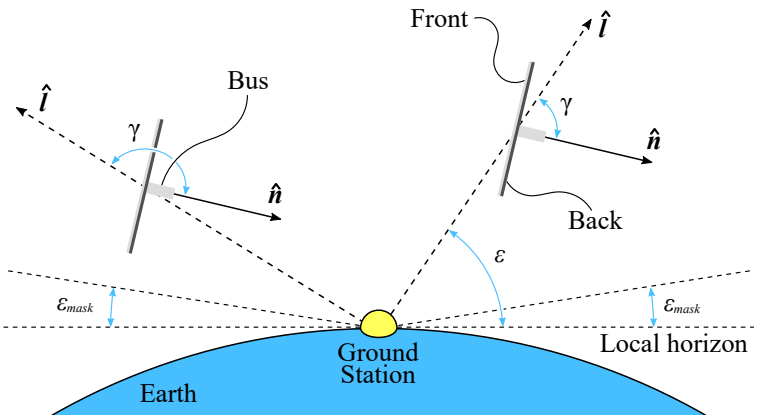


Figure 5.4: Geometry of ACS3's communication to its ground station.

When $(t_f - t_0)$ corresponds to an orbital period, $\dot{Q}_{rel}$ indicates the fraction of the battery capacity that is charged or expended to implement the steering law for said orbital period.

- **Contact time with the ground station**. ACS3 is equipped with two types of antennas, namely, ultra-high frequency (UHF) and S-band antennas. S-band antennas allow for much larger data transfer rates and reduced data latency than UHF antennas, rendering them the preferred means of communication with the ground station. However, while UHF antennas are omnidirectional, S-band antennas are directional and mounted on the back of the sailcraft. Therefore, S-band antennas enable communication only when the back of the sailcraft is visible from the ground station. Some CSLs prescribe the sailcraft to be oriented for extended periods of time with its back facing away from the Earth, thereby strongly reducing ACS3's communication capabilities. In view of this, assessing the available satellite-ground station contact time for each steering law becomes essential.

  To compute the available contact time between ACS3 and its ground station, the geometry depicted in Fig. 5.4 can be considered. As illustrated, contact between the sailcraft and ground station can take place only if the sailcraft is above the ground station's local horizon and attains an elevation, ε, larger than the ground station's elevation mask, ε_{mask}. Furthermore, when $\varepsilon > \varepsilon_{mask}$, communication is possible only if the bus (and antennas) are visible from the ground station. Geometrically, this correspond to $\gamma > 90$ deg, with γ the angle between the sail backside normal direction, $\hat{\boldsymbol{n}}$, and the direction pointing from the ground station to the sailcraft, $\hat{\boldsymbol{l}}$. When the above two conditions are simultaneously met, the sailcraft is assumed to be in contact with the ground station.

  ACS3's ground station is located in Santa Clara, California, USA, with geodetic latitude and longitude of 37.3541 deg and −121.9552 deg, respectively. Furthermore, in the absence of specific data on the elevation mask, a value of $\varepsilon_{mask} = 10$ deg was assumed. Because ACS3's orbit does not have a repeating ground track, the amount of contact

opportunities and their durations strongly depend on the duration of the time window considered. Therefore, as discussed in the following, to assess the communication capabilities in a reliable manner, seven-day long time windows have been considered. The average contact time over such windows is selected as metric.

- **Altitude loss**. See definition in Section 5.4.
- **Exposure of the back of the sail to sunlight**. See definition in Section 5.4.

5.7. POST-LAUNCH ANALYSIS

The updates to the CSLs and operational challenges discussed in the previous section, together with the precise knowledge of ACS3's orbital parameters and the availability of high-fidelity solar-sail dynamical models, paved the way to the in-depth analysis of the operational feasibility of the CSLs for the ACS3 mission. This analysis forms the primary focus of this section, with the analysis setup introduced in Section 5.7.1, followed by the discussion of the results in Section 5.7.2.

5.7.1. SETUP

The analysis presented in this section investigates the feasibility of the CSLs at different time instants over the course of one year. Motivating the study is the fact that the severity of the operational difficulties associated to the implementation of the CSLs strongly depend on the orientation of the orbital plane with respect to the Sun and Earth, which, for ACS3, was found to change appreciably over the course of its first year in orbit. More specifically, ACS3 was launched on April 23rd, 2024 in a quasi-circular orbit, with altitude and inclination of approximately 1007 km and 97.4 deg, respectively. However, at this altitude, Sun-synchronous conditions can only be achieved for an inclination of 99.5 deg. This slight deviation from the Sun-synchronous inclination therefore led ACS3's orbital plane to precess at a rate that made its orientation with respect to the Sun-Earth line gradually change over time. Accordingly, the LTAN changed as well, decreasing from 2251 hrs at the time of launch to 1729 hrs on May 22nd, 2025, that is, the time of the study. Furthermore, the obliquity of the ecliptic also represents an important source of variability in the Sun-Earth-orbit geometry, as it causes the apparent motion of the Sun as seen from Earth, with the solar declination varying sinusoidally with an amplitude of 23.44 deg over a period of one year.

The analysis comprised a year-long propagation to determine the evolution of the orientation of ACS3's orbital plane in time, followed by a series of week-long propagations to assess the feasibility of the CSLs at different times across the year. Both the year-long and week-long propagations were performed employing the dynamics presented in Section 5.2. Importantly, the following differences with the respect to the dynamics considered for the preliminary analysis were introduced, in order to obtain results that could better inform ACS3's mission operations:

- The Earth gravitational acceleration assumes a gravity potential field truncated at a spherical-harmonic degree and order of 32.
- The SRP and PRP accelerations models assume the optical sail model, with shortwave and longwave optical coefficients specified in Table 5.1.

- The PRP acceleration is determined considering the sinusoidal spherical radiation model of the Earth, assuming a monthly variation of the blackbody radiation flux and albedo coefficient at the equator and poles, as specified in Table 5.2.
- The aerodynamic acceleration is computed assuming the atmosphere to corotate with the Earth, that is, to be Earth-fixed.

Further details on the year-long and week-long propagations are provided in the following subsections.

5.7.1.1. YEAR-LONG PROPAGATION[2]

The starting epoch and initial orbital elements in frame O_I considered for the year-long propagation were derived from the latest available ACS3's two-line element (TLE) data at the time of the study. These are May 22$^{\text{nd}}$, 2022 at 13:17:38.9109 (UTC time) and:

$$\begin{aligned}&\left[a_0,\, e_0,\, i_0,\, \Omega_0,\, \omega_0,\, f_0\right]^T = \\ &\left[7355.6441\text{ km},\, 6.230\cdot10^{-3},\, 97.5656\text{ deg},\, 141.9933\text{ deg},\, 79.6341\text{ deg},\, 280.4770\text{ deg}\right]^T\end{aligned} \tag{5.20}$$

where the altitude corresponding to the semi-major axis is $h_0 = a_0 - R = 977.5078$ km. The sailcraft dynamics have been propagated for a total propagation time of one year, using an Adam-Bashforth-Moulton integration scheme with a fixed step size of three seconds. Also, the backside nadir-pointing steering law was adopted for the entire duration of the propagation, as this steering law corresponds to ACS3's standby pointing mode. Finally, to account for the sailcraft attitude-change capabilities, the maximum attitude RoC of $\dot{\varphi}_{max} = 0.5\,\text{deg}\,\text{s}^{-1}$ specified in Table 5.1 was considered.

5.7.1.2. WEEK-LONG PROPAGATIONS

The week-long propagations aimed to simulate the implementation of the CSLs at different times across the year, in order to assess how different orbit orientations influence operational feasibility of the CSLs. To this end, time instants spaced by 10 days from each other were considered across the one-year time span of the year-long propagation. Then, for each time instant, the corresponding state of the sailcraft from the year-long propagation was retrieved and used as initial state for a shorter propagation. Each such propagation lasted 96 orbital periods, corresponding to approximately one week and the maximum amount of time allocated by the ACS3 mission team to implement any CSL before returning to the standby (backside nadir-pointing) attitude mode. Finally, the states of the sailcraft during these week-long propagations were considered to compute the five metrics presented in Section 5.6.1. This approach allowed to assess the long-term evolution of the metrics in time with a meaningful resolution while capturing their local averaged trend.

5.7.2. RESULTS AND DISCUSSION

Figure 5.5 shows the evolution of the LTAN, solar declination, and all metrics except the maximum attitude rate of change over the one-year time span of the analysis. The maximum attitude rate of change was found to vary only minimally with time, rendering

[2]The work discussed in this section was conducted by A. Minervino Amodio; see Ref. [406] for more details.

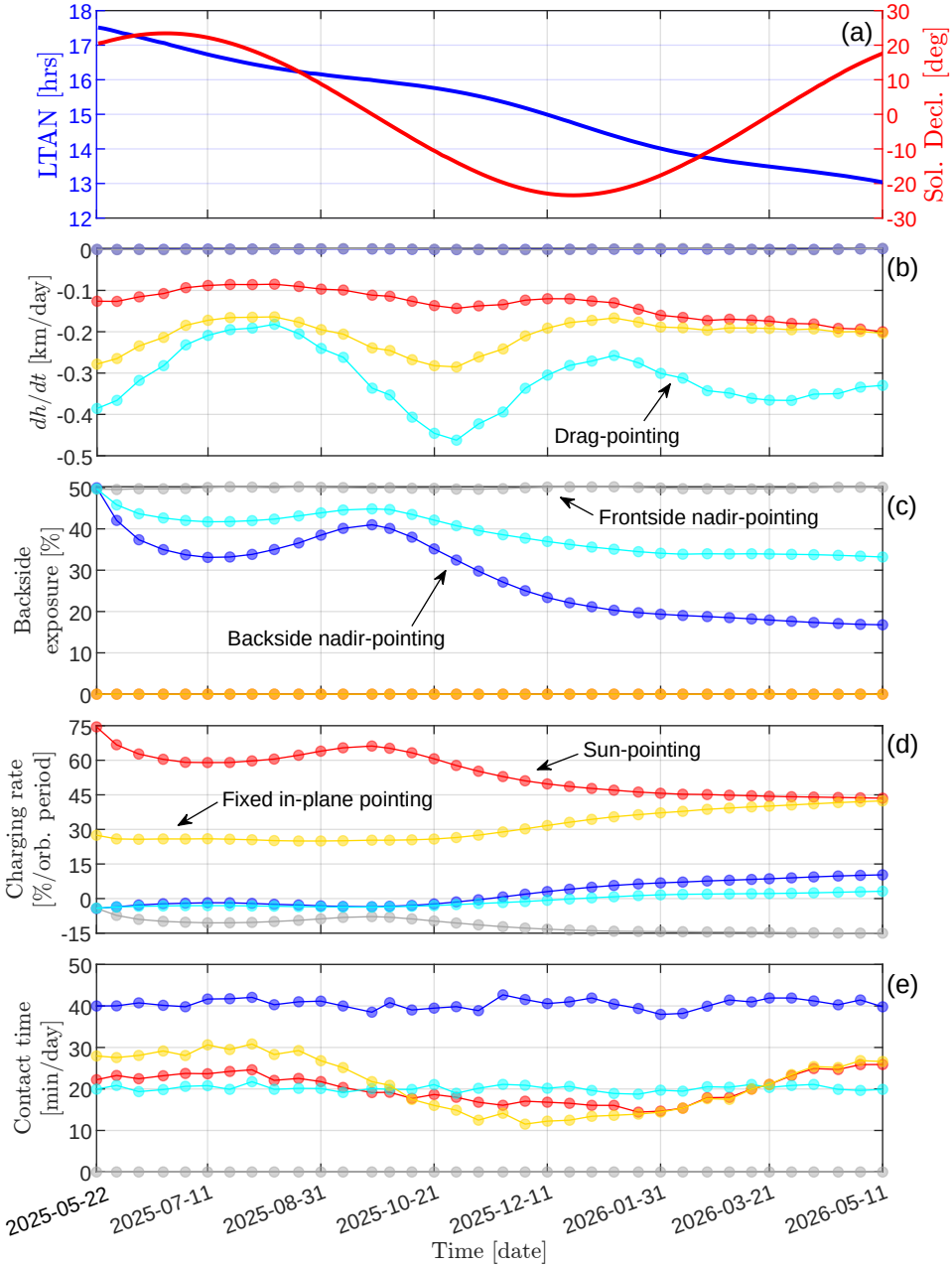


Figure 5.5: Time evolution of the a)[3] LTAN and solar declination, b) altitude rate of change, c) exposure of the back of the sail to sunlight, d) battery charging rate, and e) contact time with the ground station, for all calibration steering laws over one year.

[3]The results presented in this graph were generated by A. Minervino Amodio; see Ref. [406] for more details.

visualization of its time evolution unnecessary. The maximum attitude rate of change was found to be equal to approximately 0 $\mathrm{deg\,s^{-1}}$ for the Sun-pointing and fixed in-plane pointing steering laws, and 0.057 $\mathrm{deg\,s^{-1}}$ for the other steering laws. As these values are much smaller than the maximum limit of $\dot{\varphi}_{max} = 0.5\ \mathrm{deg\,s^{-1}}$, all calibration steering laws are deemed feasible in terms of attitude control requirements.

Figure 5.5b displays the average rate of altitude change, dh/dt. As can be seen, the nadir-pointing steering laws yield almost no altitude loss, as the sail is approximately oriented edgewise to the incoming airflow at all time, thus minimizing drag. The other steering laws, on the other hand, lead to altitude loss and show a similar trend in their time evolutions, though with different magnitudes. The observed time variation of the rate of altitude decay is due to the LTAN of ACS3 gradually changing from 1729 hrs to 1253 hrs over one year, see Fig. 5.5a. This change in orbital orientation affects the atmospheric density and, therefore, the drag experienced by the sailcraft, thus leading to the nonlinear time variations observed in the plot.

Figure 5.5c shows the average fraction of time the back of the sail is exposed to sunlight for all steering laws. Since the Sun-pointing and fixed in-plane pointing steering laws prescribe the sail front side to always be illuminated, these steering laws yield, by definition, no backside exposure. The plot also shows a substantial time variation in backside exposure when implementing the backside nadir pointing steering law, which is due to the change in LTAN undergone over one year. Specifically, at the beginning of the propagation, an approximate dawn-dusk orbital orientation is found, resulting in no eclipses. Therefore, for each orbit, the sailcraft's back side is exposed to sunlight exactly 50% of time. Conversely, at the end of the propagation, the sailcraft is in eclipse approximately 33% of each orbital period. Since the direction of sunlight points to the back of the sail only when flying over the dark side of the Earth, sunlight can actually illuminate the sail's back only briefly before entering and right after exiting eclipse. Therefore, the backside exposure to sunlight decreases from 50% to 18%, as can be observed in the plot. It is also interesting to note that, around the summer solstice, a considerable decrease in backside exposure occurs. This is due to the coupled effect of the high solar declination at that time of the year and the orbit inclination, which yield short eclipses in the vicinity of the South Pole and, therefore, a decreased backside exposure. Unlike the other steering laws, the frontside nadir pointing steering law shows almost no variation over time, with a backside exposure of approximately 50% at all time. This stems from the fact that the back of the sail is illuminated only when flying over the sunlit side of the Earth. Therefore, the change in LTAN and potential presence of eclipses do not affect the results. Lastly, the drag-pointing steering law shows a similar trend to the backside nadir-pointing steering law, although with a different magnitude. On the one hand, this follows from the fact that, when flying over the sunlit side of the Earth, the back of the sail is exposed to sunlight for half as long as the frontside nadir pointing steering law. On the other hand, when flying over the dark side of the Earth, the back of the sail is exposed to sunlight for half the time as the backside nadir pointing steering law. Consequently, the fraction of time the sail's back is exposed to sunlight in the drag-pointing case is exactly the average of those found for the two nadir-pointing steering laws. This result is highlighted in Fig. 5.5c, which shows that the curve pertaining to the drag-pointing steering law lies exactly between those found for the two nadir-pointing steering laws.

Figure 5.5d shows the fraction of battery capacity, Q_{max}, that is charged for each steering law, per orbital period. Note that the values displayed were computed using Eq. 5.19 with $(t_f - t_0) = 96$ orbital periods and are expressed as a percentage. The results show that, not surprisingly, the Sun-pointing steering law corresponds to the best, power-positive steering law, with values ranging from 44% to 74% for (in absence of eclipses). Interestingly, a local decrease in battery charging rate can be observed for simulation times around the summer solstice. As explained for the results in Fig. 5.5c, this is due to the presence of short eclipses in the vicinity of the South Pole at this specific time of the year. The fixed in-plane pointing steering law is the other only power-positive steering law across the entire year. In this case, however, the sail is slightly tilted with respect to the direction of sunlight, thereby resulting in overall smaller charging rates. Notably, the time evolution of these rates shows a positive trend. This results from the change in LTAN over the year, which makes the orbital plane increasingly more aligned with the direction of sunlight, thus tilting the solar arrays to face the incoming sunlight more directly. As shown in Fig. 5.5d, the backside nadir pointing and drag pointing steering laws achieve comparable results and, importantly, both of them are slightly power negative for approximately the first half of the year. During this period of time the sailcraft experience little to no eclipses, therefore making the sailcraft exposed to sunlight most of the time. However, because the orbital orientation is close to a dawn-dusk configuration, the incidence angle with which sunlight illuminates the solar arrays is large, hence resulting in a reduced battery charging capability and a *discharge* rate of as much as 4% per orbital period. For the second half of the year, the opposite argument holds: as LTANs closer to a noon-midnight configuration are achieved, smaller sunlight incidence angles with the solar panels are obtained. This yields slightly positive charging rates, of up to 3% and 10% per orbital period for the drag-pointing and backside nadir-pointing steering laws, respectively. Lastly, as Fig. 5.5d highlights, the frontside nadir-pointing steering law achieves the worst results among all steering laws, with discharge rates between 4% and 15% per orbital period. This result is due to the front side of the sailcraft always facing the Earth, thereby minimizing the amount of sunlight received by the solar arrays.

Finally, Fig. 5.5e displays the contact time with the ground station, expressed in minutes of available contact time per day. As shown, the best results are obtained by the backside nadir-pointing steering law, which maximises the opportunities for contact by orienting the back of the sailcraft, where the antennas are mounted, facing the Earth all the time. This results in contact times of approximately 40 min/day, regardless of the time of the year. In contrast, for the frontside nadir-pointing steering law, a diametrically opposed argument holds: in this case, the sailcraft is oriented with its antennas always facing away from the Earth, resulting in a contact time constantly equal to zero. Interestingly, the drag-pointing steering law achieves contact times consistently around half of those of the backside nadir-pointing case, that is, around 20 min/day. This result stems from the fact that, for each passage over the ground station, employing the drag-pointing steering law allows to make contact only in the second half of the passage, as in the first half $\gamma < 90$ deg and the antennas are not visible from the ground station, see Fig. 5.4. Finally, the Sun-pointing and fixed in-plane pointing steering laws are the only steering laws showing a noticeable performance variation over the year. It is interesting to note that, despite the substantially different LTANs at the beginning and the end of the propagation,

comparable contact times are achieved by both steering laws at these times of the year, with values in the range 22-30 min/day. On the other hand, for intermediate LTANs between the dawn-dusk and noon-midnight configurations, worse results are found for both steering laws. In this case, contact times as short as 11 min/day are achieved.

5.8. CONCLUSIONS

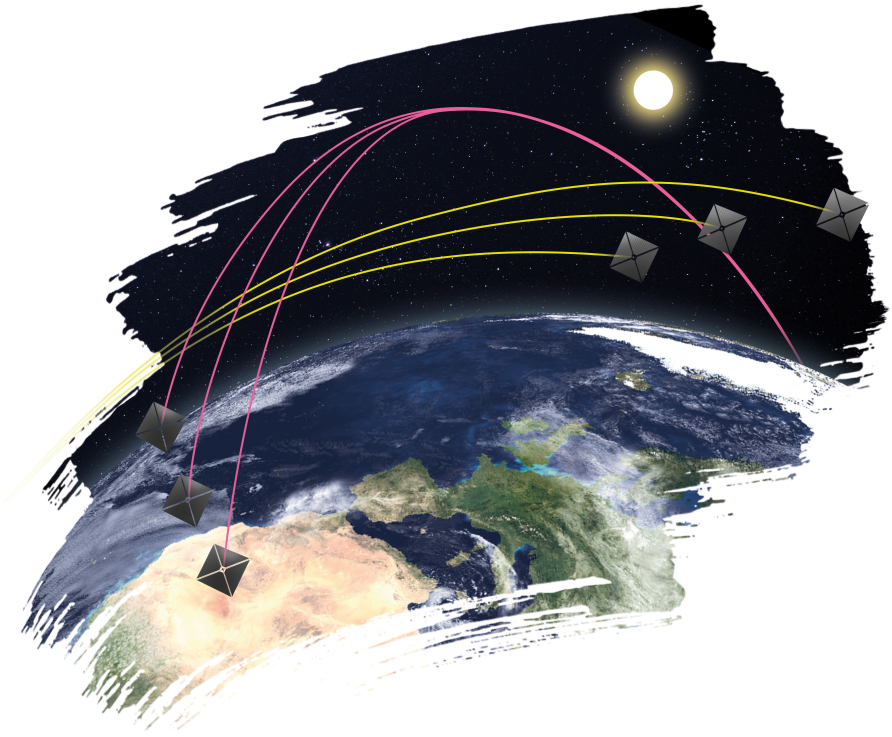
This chapter provided the first investigation on strategies to calibrate the accelerations experienced by real-life solar sails in Earth-bound orbits, with particular focus on the solar radiation pressure (SRP), planetary radiation pressure (PRP), and aerodynamic accelerations. To characterize the maximum magnitude of these accelerations and their variation with the sail attitude from orbit data, several calibration steering laws (CSLs) have been presented. Also, to assess the calibration capabilities of these steering laws and their real-life operational feasibility, analyses have been conducted using NASA's ACS3 mission as a baseline.

The analyses showed that the calibration of the SRP acceleration is more easily achieved for dawn-dusk Sun-synchronous orbits than for other Sun-synchronous orbits, as in the former case the PRP and aerodynamic accelerations affect the dynamics less severely. Indeed, for noon-midnight orbits, the PRP and aerodynamic accelerations produce larger perturbations which render the calibration process more challenging. Similarly, when the CSLs for the PRP and aerodynamic accelerations are employed, SRP represents a source of disturbance that hinders their calibration, regardless of the orientation of the orbit. The presence of unwanted accelerations affecting the calibration process is particularly relevant also for the calibration of the residual accelerations, which can be effectively performed only for perfectly noon-midnight orbits or when in eclipse, as only in these scenarios can all disturbing accelerations be nullified.

The analyses also highlighted that the attitude rates of change required by the CSLs are typically sustainable for ACS3-like sailcraft. Nevertheless, further consideration of the risks associated with the execution of complex, time-varying pointing modes suggests that control laws prescribing fixed pointing ought to be preferred. Among the practical implementation challenges of the CSLs, the most severe ones are the abilities to generate power through the solar arrays and guarantee enough contact time with the ground station. When accounting for these operational needs, the Sun-pointing and fixed in-plane pointing steering laws emerge as the only fully feasible CSLs, regardless of the orbit orientation. Conversely, the frontside nadir-pointing steering law proves generally unfeasible in every orbital scenario, while the backside nadir-pointing and drag-pointing steering laws may be employed only for local times of the ascending node close to noon/midnight values, that is, 1200/0000 hrs. Implementing the CSLs may yield a gradual decrease in altitude caused by the deorbiting effect of atmospheric drag. Consequently, this operational challenges should also be accounted for especially at low altitudes, whereas, for high-altitude orbits like that of ACS3, it assumes a much lower, noncritical degree of severity. Finally, although exposure of the back of the sail to sunlight accelerates degradation and should therefore be avoided, this operational concern is generally less critical than the others discussed above, unless calibration is performed over periods of time of several months to years. Even then, when this operational constraint is considered, the Sun-pointing and fixed in-plane pointing steering laws again emerge as the most viable CSLs.

6

Locally Optimal Control Laws for Earth-bound Solar Sailing with Atmospheric Drag



ABSTRACT

Solar sailing is a spacecraft propulsion method relying solely on solar radiation pressure to provide thrust and is therefore propellantless by nature. Although it represents a practical and promising propulsion system particularly suited for heliocentric flight regimes, the majority of sailcraft missions flown to date have remained Earth-bound and more Earth-bound missions are scheduled for the near future. However, the fundamental dynamics and trajectory optimization of a solar sail around the Earth have only been investigated to a limited extent, often neglecting the effect of non-negligible perturbations in the dynamics and the optimal control problem. Among these perturbations are the effect of eclipses, non-spherical gravity, and aerodynamic drag. Their magnitude can be comparable to, or even exceed that of solar radiation pressure and their effect on the solar-sail dynamics should be investigated to ensure the sailcraft's transfer capabilities and controllability. This chapter does so by including these perturbations in the dynamics and by considering aerodynamic drag in the optimal control problem. Using this formulation, it is shown that the optimal control problem is independent of the solar-sail loading parameter and that, by solving it, locally optimal steering laws can be derived to effectively change individual orbital elements. These newly derived steering laws form an extension to the laws found by McInnes for unperturbed solar-sail Earth-bound motion. By accounting for the perturbations in the derivation of the steering laws, it is possible to characterize how the perturbations affect the solar-sail maneuvering capabilities. This is quantified based on the established increase of the targeted orbital element. Furthermore, a range of different starting orbits will be considered to analyze the effects of perturbations in different orbital regimes. As demonstration of the real need for this investigation, NASA's Advanced Composite Solar Sail System (ACS3) mission will be considered as real-case scenario. This mission, originally scheduled for launch in mid-2022, could benefit from the steering laws derived in this chapter to demonstrate the maneuverability of solar sails in Earth orbit.

The content of this chapter has been published in *Aerospace Science and Technology*, see Ref. [409]:
Livio Carzana, Pieter Visser, and Jeannette Heiligers. "Locally Optimal Control Laws for Earth-bound Solar Sailing with Atmospheric Drag". In: *Aerospace Science and Technology* 127 (August 2022), p.107666. DOI: https://doi.org/10.1016/j.ast.2022.107666

The dataset supporting the findings of this chapter is available in the *4TU Data Repository*, see Ref. [410]:
Livio Carzana, Pieter Visser, and Jeannette Heiligers. *Data underlying the publication: "Locally Optimal Control Laws for Earth-bound Solar Sailing with Atmospheric Drag"*. 4TU.ResearchData, Dataset version 1, Apr. 2026. DOI: https://doi.org/10.4121/5c1d3263-3267-44c4-9560-50872e9c90b3.v1

Cover graphic by Vincenzo Bortone. The illustration shows a solar sail in Earth orbit performing orbit-raising maneuvers (yellow trajectories) and inclination-changing maneuvers (pink trajectories).

6.1. INTRODUCTION

The usage of solar sails as main propulsion system for spaceflight applications is an idea that was first investigated at the beginning of the last century and has since drawn increasingly more attention worldwide [2]. The research interest in solar sailing, initially within the scientific community and later also within space agencies, is mainly driven by its propellantless nature. In the last decades many studies on solar sailing demonstrated its applicability to a wide variety of mission scenarios, ranging from interplanetary and interstellar missions to planet-centered ones [107, 386]. Analyses of solar-sail interplanetary and deep-space trajectories have clearly shown the mission-enabling potential of solar sails and, in particular, the promising thrusting capabilities when approaching the inner Solar System, where solar radiation pressure (SRP) is particularly strong and an improved sailcraft maneuverability is achieved [154, 386]. While the majority of research works indeed focus on interplanetary solar-sail mission applications, most solar-sail missions launched to date have flown solely in low Earth orbit (LEO). Their purpose was to either show the feasibility of solar-sail de-orbiting (e.g., NASA's NanoSail-D2 mission [99, 388]), the successful control of SRP as propulsive means, or the advancements in sail manufacturing and deployment capabilities (e.g., The Planetary Society's LightSail 1 and LightSail 2 [109, 110]). In a similar fashion, other missions planned for the near future at the time of this research, including NASA's Advanced Composite Solar Sail System (ACS3) mission, were launched in LEO to act as sail technology and orbit control demonstrator [127].

Although solar-sail technology demonstrators have been flown mostly in LEO, thus far the research conducted on planetocentric solar-sail orbital dynamics and control is very limited. Several studies on the topic are based on the solar-sail control laws first devised by McInnes [2], valid for simplistic, perfectly-reflecting solar sails with either unperturbed two-body problem dynamics or gravitational perturbations only. Applications of such control laws range from the analysis of planetocentric solar-sail trajectories [200, 201, 382] to the study of Earth-escape strategies [202–204]. When considering also non-gravitational perturbations in the analysis of Earth-bound solar-sail trajectories an increased degree of complexity is achieved, which stems from the highly nonlinear dynamics to be considered. Indeed, perturbing accelerations such as the planetary radiation pressure and aerodynamic accelerations can achieve magnitudes comparable to – or even greater than – the SRP acceleration, therefore making the dynamics deviate substantially from the ones of the two-body problem with ideal SRP acceleration. As a consequence, results found with the latter dynamics have limited applicability in the analysis of high-fidelity solar-sail trajectories. Preliminary studies on perturbed, Earth-bound sailcraft trajectories have been proposed only in small numbers, with particular focus on the analysis of the coupled effects of SRP and planetary radiation pressure for Earth-centered orbits [222, 223], studies on SRP and aerodynamics-based optimal control laws for orbit raising and maneuvering [218–221], and the analysis of the drag-induced active debris removal and de-orbiting capabilities of solar sails [212–215]. The highly-nonlinear dynamical models considering the effects of planetary radiation pressure and/or aerodynamics significantly complicate the computation of optimal steering laws. Consequently, the methods and results proposed are valid only under simplifying assumptions (e.g., on the orbit shape and its orientation with respect to the Sun's position) and for orbit-raising and inclination-changing steering laws only.

As a first step towards a generic, high-fidelity solar-sail planetocentric optimal control solver, this chapter proposes a novel technique to efficiently and accurately optimize Earth-bound solar-sail trajectories in the presence of SRP, gravitational perturbations, and aerodynamic drag. Unlike all other methods employed to date to solve this optimization problem, the one proposed here can be used for any steering law and applied to any orbital regime. This first-of-its-kind technique is based on the idea of pre-solving the optimization problem for a wide set of conditions and to interpolate the optimal solutions found during the trajectory propagation. In this work, this optimization technique is described in its entirety, with focus on its accuracy and limited runtime. NASA's ACS3 mission is taken as a specific and realistic test case. At the time of this research, the ACS3 mission was planned for launch into a 715 km altitude Sun-synchronous orbit. The results in this chapter will demonstrate the sailcraft's ability to change its orbital altitude and inclination. However, also more generic analyses on applicable steering laws and orbital altitudes are provided, though limited to Sun-synchronous orbits. This class of orbits is selected to reduce the design space, justified by the fact that this class is often used for Earth-centered scientific missions. Nevertheless, the designed novel optimization method presented in this work is applicable to any steering law and orbital regime. Hence, this chapter significantly contributes to the body of knowledge on optimal solar-sail control laws in the near-Earth environment.

6.2. Dynamical Model

In this section the dynamical model used throughout this chapter is presented. First, different reference frames and coordinate systems are defined and subsequently the sailcraft equations of motion Equations of Motion (EoM) are provided.

6.2.1. Reference Frames and Coordinate Systems

In the following sections, different reference frames and coordinate systems are presented to conveniently express the sailcraft dynamics and optimization problem under investigation.

6.2.1.1. Earth-centered Inertial Reference Frame

The Earth-centered inertial reference frame is the frame in which the sailcraft EoM are propagated. This Cartesian frame is indicated by $O_I(\hat{\boldsymbol{x}}, \hat{\boldsymbol{y}}, \hat{\boldsymbol{z}})$ and is centered at the Earth's center of mass, with the $\hat{\boldsymbol{x}}$-axis direction pointing towards the mean vernal equinox at January 1$^{\text{st}}$, 2000, the $\hat{\boldsymbol{z}}$-axis direction pointing perpendicular to the mean equatorial plane at January 1$^{\text{st}}$, 2000 (towards the northern hemisphere), and the $\hat{\boldsymbol{y}}$-axis direction completes the right-handed frame.

6.2.1.2. Sunlight Reference Frame

The sunlight reference frame is a sailcraft-centered frame indicated by $O_S(\hat{\boldsymbol{x}}_S, \hat{\boldsymbol{y}}_S, \hat{\boldsymbol{z}}_S)$, see Fig. 6.1. The $\hat{\boldsymbol{x}}_S$-axis direction points in the Sun-to-sailcraft direction (i.e., parallel to the direction of sunlight), $\hat{\boldsymbol{s}}$, $\hat{\boldsymbol{y}}_S$ is found from the O_I frame's $\hat{\boldsymbol{z}}$-axis direction as $\hat{\boldsymbol{y}}_S = \hat{\boldsymbol{z}} \times \hat{\boldsymbol{s}} / \|\hat{\boldsymbol{z}} \times \hat{\boldsymbol{s}}\|$, and the $\hat{\boldsymbol{z}}_S$-axis direction completes the right-handed frame. Since a flat solar-sail model is considered in this work (see Section 6.2.2.1 for more details), the sailcraft orientation is uniquely determined by the sail normal direction, $\hat{\boldsymbol{n}}$. By making use of a spherical

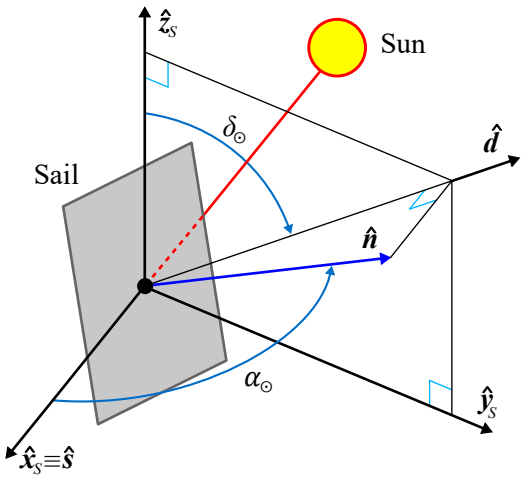


Figure 6.1: Sailcraft normal direction and attitude angles in the sunlight reference frame, $O_S(\hat{x}_S, \hat{y}_S, \hat{z}_S)$.

coordinate system, $\hat{n}$ can be defined by two attitude angles: the pitch angle $\alpha_\odot$, defined as the angle between the direction of sunlight, $\hat{s}$, and the sail normal direction, $\hat{n}$, and the clock angle $\delta_\odot$, measured from the $\hat{z}_S$ direction to the projection of the sail normal onto the $(\hat{y}_S, \hat{z}_S)$ plane, $\hat{d}$, see Fig. 6.1. Solar sails are commonly designed with only their front side coated in highly reflective material, as only that side is supposed to be exposed to sunlight. In view of this, in this chapter it is assumed that the sail normal has no component pointing towards the Sun, i.e., $\alpha_\odot \in [0, \pi/2]$ and $\delta_\odot \in [0, 2\pi]$. The sail normal expressed in the sunlight frame, $\hat{n}_S$, is then found as:

$$\hat{n}_S = \cos\alpha_\odot \, \hat{x}_S + \sin\alpha_\odot \sin\delta_\odot \, \hat{y}_S + \sin\alpha_\odot \cos\delta_\odot \, \hat{z}_S \tag{6.1}$$

6.2.1.3. AERODYNAMIC REFERENCE FRAME

The aerodynamic reference frame $O_A(\hat{x}_A, \hat{y}_A, \hat{z}_A)$, see Fig. 6.2, is centered at the sailcraft center of mass and has its $\hat{x}_A$-axis direction pointing along the direction of the inertial velocity, $\hat{v}$, the $\hat{z}_A$-axis direction parallel to the satellite's orbital momentum vector, $\hat{h}$, and the $\hat{y}_A$-axis direction forming a right-handed frame. By using a spherical coordinate system, the sail normal direction, $\hat{n}$, can be uniquely identified by the angles ξ, χ, and α_A, see Fig. 6.2, with:

$$\cos\alpha_A = \cos\xi \cos\chi \tag{6.2}$$

The range for each of these angles depends on the instantaneous position of the Sun with respect to the sailcraft, in agreement with the assumption that the sail normal has no component pointing towards the Sun. Using these angular coordinates and Eq. 6.2, the sail normal direction expressed in frame O_A, $\hat{n}_A$, is defined as:

$$\hat{n}_A = \cos\alpha_A \, \hat{x}_A + \cos\xi \sin\chi \, \hat{y}_A + \sin\chi \, \hat{z}_A \tag{6.3}$$

Figure 6.2 also illustrates the aerodynamic drag direction, $\hat{D}$, and lift direction, $\hat{L}$: the former is always opposite to $\hat{v}$ while the latter points either parallel or antiparallel to the

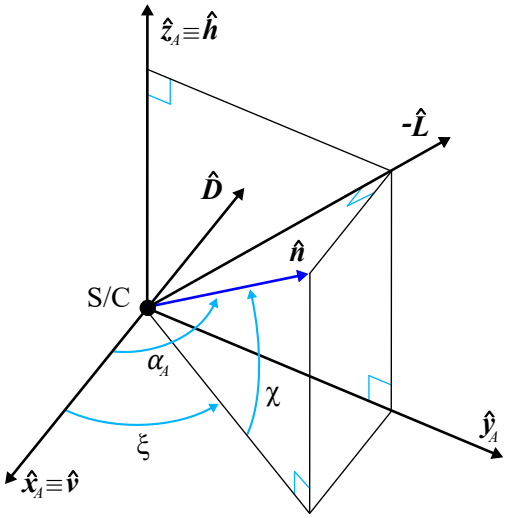


Figure 6.2: Sailcraft attitude angles and aerodynamic drag, lift, and sail normal directions in the aerodynamic reference frame, $O_A(\hat{x}_A, \hat{y}_A, \hat{z}_A)$.

projection of $\hat{\boldsymbol{n}}$ onto the $(\hat{x}_A, \hat{z}_A)$ plane, as expressed by the following relation:

$$\hat{\boldsymbol{L}} = -\text{sgn}(\cos\alpha_A)\,\frac{\sin\xi\cos\chi\;\hat{y}_A + \sin\chi\;\hat{z}_A}{\left\|\sin\xi\cos\chi\;\hat{y}_A + \sin\chi\;\hat{z}_A\right\|} \tag{6.4}$$

In Eq. 6.4 the minus sign guarantees that $\hat{\boldsymbol{n}}_A \cdot \hat{\boldsymbol{L}} \leq 0$ (which should always hold true for a flat sail), while the "sign" function takes into account the aerodynamic symmetry of the flat sail and ensures that the lift direction corresponding to the sail normal directions $\hat{\boldsymbol{n}}$ and $-\hat{\boldsymbol{n}}$ is the same. Ultimately, it is worth noting that due to the aerodynamic symmetry, the directions $\hat{\boldsymbol{v}}$, $\hat{\boldsymbol{n}}$, $\hat{\boldsymbol{L}}$, and $\hat{\boldsymbol{D}}$ all lie in the same plane.

6.2.1.4. OPTIMIZATION REFERENCE FRAME

The optimization reference frame $O_O(\hat{x}_O, \hat{y}_O, \hat{z}_O)$, see Fig. 6.3a, is centered at the center of mass of the sailcraft and defined such that its $\hat{\boldsymbol{x}}_O$-axis direction points along the drag direction, $\hat{\boldsymbol{D}}$, the $\hat{\boldsymbol{z}}_O$-axis direction is found as $\hat{\boldsymbol{z}}_O = \hat{\boldsymbol{D}} \times \hat{\boldsymbol{s}} / \left\|\hat{\boldsymbol{D}} \times \hat{\boldsymbol{s}}\right\|$, and the $\hat{\boldsymbol{y}}_O$-axis direction completes the right-handed frame. The angle $\eta \in [0, \pi]$ is measured from the drag direction to the direction of sunlight:

$$\eta = \cos^{-1}\left(\hat{\boldsymbol{D}} \times \hat{\boldsymbol{s}}\right) \tag{6.5}$$

Within frame O_O, the sail normal direction, $\hat{\boldsymbol{n}}_O$, can be expressed using two spherical coordinate angles: $\alpha_O = (\pi - \alpha_A)$ and δ_O, see Fig. 6.3b. Then, $\hat{\boldsymbol{n}}_O$ is defined in a similar fashion to Eq. 6.1 as:

$$\hat{\boldsymbol{n}}_O = \cos\alpha_O\;\hat{\boldsymbol{x}}_O + \sin\alpha_O\sin\delta_O\;\hat{\boldsymbol{y}}_O + \sin\alpha_O\cos\delta_O\;\hat{\boldsymbol{z}}_O \tag{6.6}$$

The other variables in Fig. 6.3 will be defined in Section 6.3.3.2.

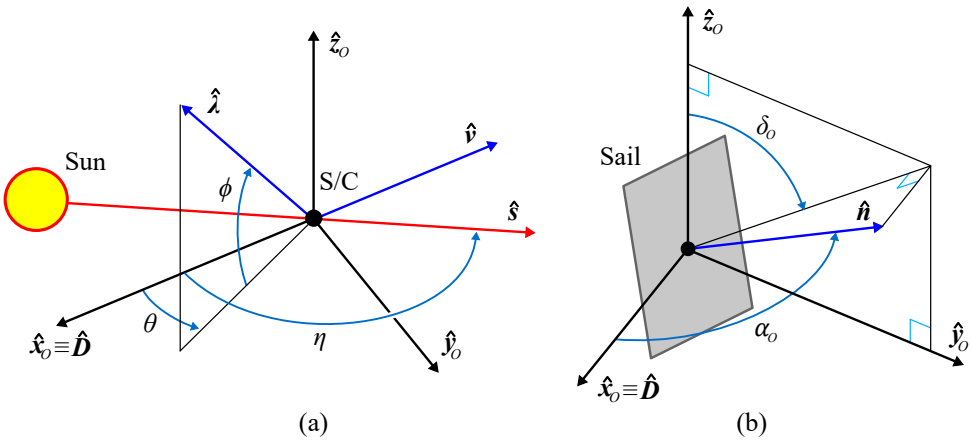


Figure 6.3: Angular coordinates of a) the direction of sunlight, optimal thrust directions, and b) the sail normal direction in the optimization reference frame, $O_O(\hat{\boldsymbol{x}}_O, \hat{\boldsymbol{y}}_O, \hat{\boldsymbol{z}}_O)$.

6.2.2. EQUATIONS OF MOTION

In this chapter, the solar sail is assumed to be Earth bound and its motion is determined by the SRP, aerodynamic, and gravitational accelerations. Its EoM are defined in frame O_I and take the following form:

$$\ddot{\boldsymbol{r}} + \frac{\mu}{r^3} = \boldsymbol{a}_{SRP}\big(\boldsymbol{u}(t)\big) + \boldsymbol{a}_{Aero}\big(\boldsymbol{u}(t)\big) + \boldsymbol{a}_{J2} \tag{6.7}$$

where the overhead dot notation is used to indicate differentiation with respect to time t and $\mu = 398600.4415\ \text{km}^3/\text{s}^2$ is the Earth's gravitational parameter of the geopotential Joint Gravity Model (JGM) 2 [277, 308]. The vectors $\boldsymbol{r}$ and $\boldsymbol{a}$ represent the sailcraft position and acceleration vectors in frame O_I, respectively, while $\boldsymbol{u}(t) = \hat{\boldsymbol{n}}_I(t)$ is the sailcraft control vector, with $\hat{\boldsymbol{n}}_I$ the sail normal direction in frame O_I. The subscripts "SRP" and "Aero" refer to the SRP and aerodynamic accelerations, respectively, while "J2" indicates the gravitational perturbing acceleration due to the non-spherical, oblate shape of the Earth, modeled through the J_2 spherical harmonics coefficient. These accelerations will be described in more detail in the following sections. By providing an initial time, t_0, an initial sailcraft state, $\boldsymbol{X}_0 = \big[\boldsymbol{r}(t_0)\ \dot{\boldsymbol{r}}(t_0)\big]$, and the control law $\boldsymbol{u}(t)$, Eq. 6.7 can be used to propagate the solar-sail state vector $\boldsymbol{X}(t)$ and find the sailcraft trajectory.

6.2.2.1. SOLAR RADIATION PRESSURE ACCELERATION

The SRP acceleration model used in this work assumes the solar sail to behave as a flat, perfectly reflecting surface. Therefore, this model is often referred to as "ideal" SRP acceleration model. Unlike other models that take into account the optical properties of the sail film material [2, 407, 411, 412] or more complex sail shapes [253, 413–415], the ideal SRP acceleration model allows for a straightforward definition of the SRP acceleration, which becomes a function of the sailcraft attitude only and can be conveniently expressed in the sail-fixed reference frame O_S as [2]:

$$\boldsymbol{a}_{SRP,S} = \nu a_c \cos^2\alpha_\odot\ \hat{\boldsymbol{n}}_S \tag{6.8}$$

where $\nu \in [0,1]$ is the shadow factor and a_c denotes the sailcraft characteristic acceleration defined as [2]:

$$a_c = \frac{2S_{TSI}}{c\sigma} \tag{6.9}$$

with $S_{TSI} = 1367$ W/m^2 equal to the solar flux at a distance of 1 AU from the Sun [308], $c = 299792458$ m/s representing the speed of light in vacuum [390], and σ the solar-sail loading parameter, equal to the ratio of the sailcraft total mass to its sail surface area. The shadow factor ν in Eq. 6.8 accounts for the effect of eclipses and its value ranges from 0 (no sunlight reaches the sail) to 1 (sail completely illuminated). In this chapter, eclipses are modeled with a conical shadow model similar to the one presented in Refs. [211, 231], with the only difference that penumbra is treated as umbra. This means that $\nu = 0$ not only when the sailcraft is in the Earth's umbra, but also when in penumbra, thus leading to more conservative results. The Earth radius considered for this conical shadow model is $R = 6378.1363$ km, consistent with the value used by the JGM 2 geopotential model (see Section 6.2.2.3) [277, 308].

Based on Eq. 6.8, the expression for the SRP acceleration in frame O_I is:

$$\boldsymbol{a}_{SRP,I} = \nu a_c \cos^2\alpha_\odot \, \hat{\boldsymbol{n}}_I \tag{6.10}$$

with

$$\hat{\boldsymbol{n}}_I = \underline{\underline{\boldsymbol{R}}}_{S\rightarrow I} \cdot \hat{\boldsymbol{n}}_S \tag{6.11}$$

with $\hat{\boldsymbol{n}}_S$ defined in Eq. 6.1 and $\underline{\underline{\boldsymbol{R}}}_{S\rightarrow I}$ the rotation matrix to transform vectors from the O_S frame to the O_I frame, which depends on time and the sailcraft instantaneous position.

6.2.2.2. Aerodynamic Acceleration

The aerodynamic acceleration is also modeled assuming the solar sail to be a flat plate. By making the additional assumption that the sailcraft velocity is much larger than the thermal velocity of the atmospheric particles, the hyperthermal free-molecular flow model presented in Ref. [341] can be used to describe the sail aerodynamics. This model has already been employed in Refs. [219, 220] to analyze solar-sail trajectories in the presence of atmospheric drag and is based on the following expression for the aerodynamic acceleration in frame O_A [220]:

$$\boldsymbol{a}_{Aero,A} = \boldsymbol{D} + \boldsymbol{L} = \frac{1}{2}\frac{\rho v^2}{\sigma}\left(C_D\hat{\boldsymbol{D}} + C_L\hat{\boldsymbol{L}}\right) \tag{6.12}$$

In Eq. 6.12, ρ represents the atmospheric density, v the magnitude of the sailcraft inertial velocity, and C_D and C_L the drag and lift coefficients defined as [220]:

$$C_D = 2\left[\sigma_T + \sigma_N V_R |\cos\alpha_A| + (2-\sigma_N-\sigma_T)\cos^2\alpha_A\right]|\cos\alpha_A| \tag{6.13}$$

$$C_L = 2\left[\sigma_N V_R + (2-\sigma_N-\sigma_T)|\cos\alpha_A|\right]|\cos\alpha_A|\sin\alpha_A \tag{6.14}$$

where σ_N and σ_T represent the normal and tangential momentum accommodation coefficients, respectively, and V_R is the ratio of the average velocity of the atmospheric particles diffusively reflected by the sail to the sailcraft velocity. Based on Ref. [355], this chapter uses: $\sigma_N = \sigma_T = 0.8$, $V_R = 0.05$.

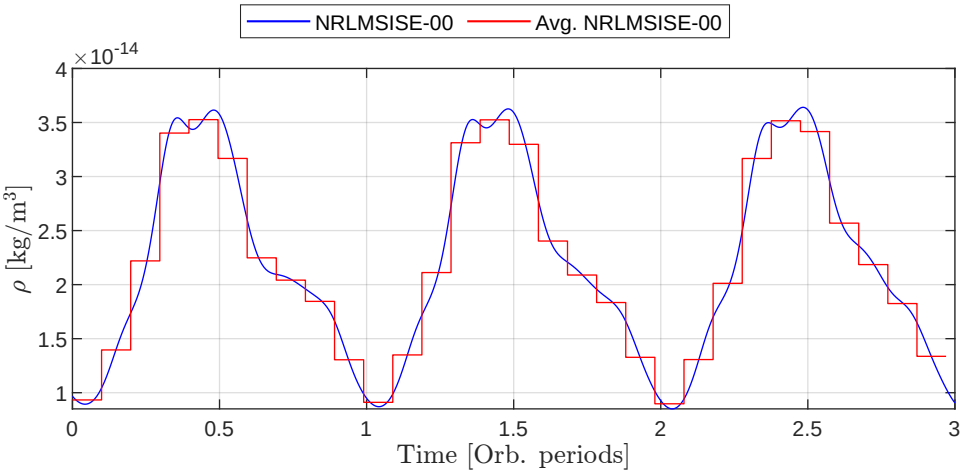


Figure 6.4: Example evolution of the atmospheric density as per the traditional and averaged NRLMSISE-00 models. Data computed by propagating the sailcraft state in Eq. 6.32 for three orbital periods with $ApO = NpA = 10$.

The atmospheric density ρ used in Eq. 6.12 is found through an averaging technique based on the NRLMSISE-00 model[1] available in Matlab® [289]. To aid visualization, an example of time evolution of densities as per the "traditional" and averaged NRLMSISE-00 model can be observed in Fig. 6.4. As will be discussed in Section 6.4.1, this density averaging process is adopted to decrease the simulation runtime at the cost of a slight reduction in the accuracy of the results. The routine is as follows:

a) Given the sailcraft state at time t_0, $\boldsymbol{X}_0 = \boldsymbol{X}(t_0)$, its osculating Keplerian orbit is found.

b) A time interval $[t_0, t_0 + \Delta t]$ is considered, with $\Delta t = P/ApO$, where P is the osculating orbit's period and ApO a user-provided parameter corresponding to the number of orbital arcs per orbit to consider for the averaging.

c) Across the time interval, a set of evenly spaced time nodes $\{t_0, t_1, \ldots, t_{(NpA-1)} = t_0 + \Delta t\}$ is defined and the corresponding states along the osculating orbit $\{\boldsymbol{X}_0, \boldsymbol{X}_1, \ldots, \boldsymbol{X}_{(NpA-1)}\}$ are found. Note that NpA is a user-provided parameter indicating the number of nodes per orbital arc used.

d) The atmospheric density is computed through the NRLMSISE-00 model for each state of the set $\{\boldsymbol{X}_0, \boldsymbol{X}_1, \ldots, \boldsymbol{X}_{(NpA-1)}\}$, hence resulting in a set of densities $\{\rho_0, \rho_1, \ldots, \rho_{(NpA-1)}\}$ which are averaged to give $\bar{\rho}$.

e) The averaged value $\bar{\rho}$ is used as constant atmospheric density to numerically propagate the perturbed dynamics from $\boldsymbol{X}(t_0)$ to $\boldsymbol{X}_{(NpA-1)}$.

[1] Throughout this chapter, the NRLMISE-00 model is used with the index of the solar radio flux at 10.7 cm and the index of planetary geomagnetic activity taken from the Marshall Space Flight Center's archived forecast of January 2021 [294], for a percentile value of 50.

f) The process is repeated until the end of the time interval, taking $t_{(NpA-1)}$ and $\boldsymbol{X}_{(NpA-1)}$ as t_0 and $\boldsymbol{X}_0$ of the next time interval.

Given $\boldsymbol{a}_{Aero,A}$, the expression for the aerodynamic acceleration in frame O_I becomes:

$$\boldsymbol{a}_{Aero} = \underline{\underline{\boldsymbol{R}}}_{A\to I} \cdot \boldsymbol{a}_{Aero,A} \tag{6.15}$$

where $\underline{\underline{\boldsymbol{R}}}_{A\to I}$ is the rotation matrix to transform vectors from the O_A frame to the O_I frame, which depends on the sailcraft instantaneous position and velocity.

6.2.2.3. J_2 Gravitational Acceleration

The gravitational acceleration due to the Earth's J_2 effect in frame O_I is given by [232]:

$$\boldsymbol{a}_{J2} = -\frac{3}{2}\frac{R^2}{r^5}\mu J_2 \left[(x\hat{\boldsymbol{x}} + y\hat{\boldsymbol{y}})\left(1 - 5\frac{z^2}{r^2}\right) + z\hat{\boldsymbol{z}}\left(3 - 5\frac{z^2}{r^2}\right)\right] \tag{6.16}$$

where $J_2 = 1.082626925639 \cdot 10^{-3}$ is the Earth J_2 gravitational field constant of the JGM 2 geopotential model [277, 308].

6.3. Optimal Control Problem

The optimal control problem considered in the present study builds on the one first investigated by McInnes in Ref. [2], where control laws to maximize the instantaneous rate of change of any given orbital element were found under unperturbed, ideal solar-sail dynamics. Hereinafter the same maximization problem will be considered, however also taking into account aerodynamic and gravitational perturbations in the equations of motion and control.

By referring to the generic orbital element as α, the optimization problem at hand can be defined as finding the optimal control vector $\boldsymbol{u}(t) = \hat{\boldsymbol{n}}(t)$ maximizing the cost function $J(\boldsymbol{u}(t)) = \alpha(\boldsymbol{u}(t))$ at any given time, subject to the dynamics described in Section 6.2. When the rate of change of a given orbital element is expressed through a Lagrange planetary equation, the cost function assumes the following form [2]:

$$J(\boldsymbol{u}(t)) = \dot{\alpha}(\boldsymbol{u}(t)) = \boldsymbol{\lambda} \cdot \boldsymbol{a}(\boldsymbol{u}(t)) \tag{6.17}$$

where $\boldsymbol{a}$ is the sum of the accelerations on the right-hand side of Eq. 6.17 and $\boldsymbol{\lambda}$ is the so-called primer vector, which points along the optimal thrusting direction $\hat{\boldsymbol{\lambda}}$ that maximizes the orbital element's rate of change. It is worth noting that although the J_2 acceleration, $\boldsymbol{a}_{J2}$, influences the orbital element rate of change (and therefore the cost function $J(\boldsymbol{u}(t))$, it does not explicitly depend on the control vector $\boldsymbol{u}$, as shown in Eq. 6.17. Consequently, the problem of maximizing $J(\boldsymbol{u}(t))$ at any time is independent of the J_2 acceleration. For this reason, hereinafter only the SRP and aerodynamic accelerations are considered in the control optimization process, whereas the J_2 acceleration is taken into account only in the propagation of the EoM.

To solve the optimization problem, three different approaches are employed, depending on the relative magnitude of the SRP and aerodynamic accelerations: an SRP-based optimization, an aerodynamic-based optimization, and a full-dynamics optimization. These optimization techniques are discussed in the following sections and can be applied

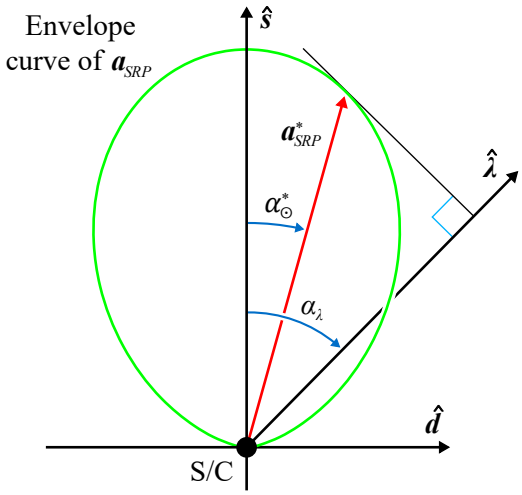


Figure 6.5: Envelope curve of the SRP acceleration in the $(\hat{s}, \hat{d})$ plane.

to find the optimal sail orientation at a specific instant in time. By applying such algorithms at each integration step during the sailcraft trajectory propagation, a sequence (history) of optimal sail normal directions representing the optimal steering law is obtained.

6.3.1. OPTIMIZATION BASED ON SOLAR RADIATION PRESSURE

The SRP-based optimization method is employed when the SRP acceleration is the predominant acceleration (e.g., for high-altitude orbits). In this case, the aerodynamic acceleration is considered in the propagation of the EoM but neglected in the optimization process, therefore largely simplifying the optimal control computation. Under this assumption, the optimal control history $\boldsymbol{u}^*(t)$ is found using the method devised by McInnes in Ref. [2], where an analytical formulation to compute locally optimal steering laws is presented. The method can be summarized as follows. Given the optimal thrust direction $\hat{\boldsymbol{\lambda}}$ in the O_S frame, its pitch and clock angles can be defined as $\alpha_\lambda \in [0, \pi]$ and $\delta_\lambda \in [0, 2\pi]$, respectively (note that α_λ can assume values greater than $\pi/2$ as no constraint on the direction $\hat{\boldsymbol{\lambda}}$ is applied, unlike the sail normal direction $\hat{\boldsymbol{n}}$). Then, the optimal pitch and clock angles of the sail normal, $\alpha^*_\odot$ and $\delta^*_\odot$, are found as [382]:

$$\alpha^*_\odot = \tan^{-1}\left(\frac{-3\cos\alpha_\lambda + \sqrt{9\cos^2\alpha_\lambda + 8\sin^2\alpha_\lambda}}{4\sin\alpha_\lambda}\right) \tag{6.18}$$

$$\delta^*_\odot = \delta_\lambda \tag{6.19}$$

These optimal attitude angles maximize the SRP acceleration component along the direction $\hat{\boldsymbol{\lambda}}$, see Fig. 6.5. This figure displays the SRP acceleration envelope (AE) curve in the plane formed by $\hat{\boldsymbol{s}}$ and $\hat{\boldsymbol{d}}$, where $\hat{\boldsymbol{d}}$ is the projection of $\hat{\boldsymbol{n}}$ onto the $(\hat{y}_S, \hat{z}_S)$ plane, see Fig. 6.1. With α^* and δ^* given by Eqs. 6.18-6.19, the optimal control vector, $\boldsymbol{u}^* = \hat{\boldsymbol{n}}^*_I$, can be found

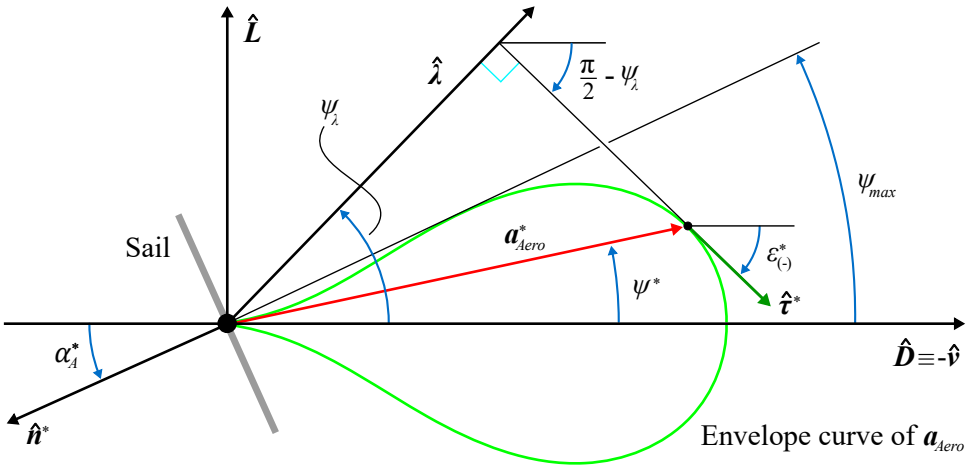


Figure 6.6: Envelope curve of the aerodynamic acceleration in the $(\hat{L}, \hat{D})$ plane and variables used to find the optimal aerodynamic acceleration.

using Eq. 6.1 and Eq. 6.11. It should be noted that, because of Eq. 6.19, the optimal sail normal direction found by the SRP-based optimization is always coplanar with $\hat{s}$, $\hat{d}$, and $\hat{\lambda}$.

6.3.2. AERODYNAMIC-BASED OPTIMIZATION

The aerodynamic-based optimization method is employed when the aerodynamic acceleration is the predominant acceleration (e.g., for low-altitude orbits or when in eclipse). In this case, the SRP acceleration is considered in the propagation of the EoM but neglected in the optimization process. Similar to the method described in Section 6.3.1, the optimal sail attitude is found by imposing that the aerodynamic acceleration component along $\hat{\lambda}$ is maximized. However, because of the complex expression of the aerodynamic AE surface, α^* and δ^* are found using a root-finding method. Since the aerodynamic AE surface is symmetric with respect to the $\hat{x}_A$-axis, the intersection of this surface with a plane passing through the $\hat{x}_A$-axis is considered, which results in an AE curve. An illustration of the aerodynamic AE curve in the $(\hat{L}, \hat{D})$ plane is given in Fig. 6.6, where the variables used to describe the optimization procedure are also shown.

By using Eq. 6.12, the angle ψ measured from the direction $\hat{D}$ to the acceleration vector a_{Aero} can be defined as:

$$\psi = \tan^{-1}\left(\frac{\|\hat{L}\|}{\|\hat{D}\|}\right) = \tan^{-1}\left(\frac{C_L}{C_D}\right) \tag{6.20}$$

As shown by Eq. 6.13-6.14, C_L and C_D are functions of α_A, and therefore so is ψ. Its maximum value, ψ_{max}, can then be found by imposing:

$$\frac{d\psi}{d\alpha_A} = 0 \iff \frac{d}{d\alpha_A}\left(\frac{C_L}{C_D}\right) = \frac{C'_L C_D - C_L C'_D}{C_D^2} = 0 \tag{6.21}$$

In Eq. 6.21, C'_D and C'_L are the derivatives of C_D and C_L with respect to α_A:

$$C'_D = -\left[2\sigma_N V_R + 3\left(2-\sigma_N-\sigma_T\right)\cos\alpha_A\right]\sin\left(2\alpha_A\right) - 2\sigma_T \sin\alpha_A \tag{6.22}$$

$$C'_L = \frac{3}{2}\left(2-\sigma_N-\sigma_T\right)\cos\left(3\alpha_A\right) + 2\sigma_N V_R \cos\left(2\alpha_A\right) + \frac{1}{2}\left(2-\sigma_N-\sigma_T\right)\cos\alpha_A \tag{6.23}$$

Equation 6.21 is solved using Matlab®'s root-finding function *fzero* with a tolerance of 10^{-10} rad.

The angle $\psi_\lambda \in [0,\pi]$ is measured from the direction $\hat{\boldsymbol{D}}$ to the direction $\hat{\boldsymbol{\lambda}}$ and based on its value two different scenarios can be defined. If $\psi_{max} \leq (\psi_\lambda - \pi/2)$, the aerodynamic acceleration vector with the largest component along $\hat{\boldsymbol{\lambda}}$ is a zero vector, i.e., the sail is oriented parallel to the wind flow with an optimal attitude angle of $\alpha_A^* = \pi/2$. Instead, if $\psi_{max} > (\psi_\lambda - \pi/2)$, a non-trivial solution for α_A^* exists, which can be found by imposing that the direction perpendicular to $\hat{\boldsymbol{\lambda}}$ and the tangent to the AE curve, $\hat{\boldsymbol{\tau}}$, are aligned, see Fig. 6.6. This condition is equivalent to:

$$\varepsilon - \left(\psi_\lambda - \frac{\pi}{2}\right) = 0 \tag{6.24}$$

where $\varepsilon \in [-\pi/2, \pi/2]$ is a function of α_A and is defined as the angle measured from the direction $\hat{\boldsymbol{D}}$ to the direction $\hat{\boldsymbol{\tau}}$:

$$\varepsilon = \tan^{-1}\left(\frac{C'_L}{C'_D}\right) \tag{6.25}$$

Note that ε is illustrated in Fig. 6.6 with the subscript "(-)" to indicate the direction in which this angle decreases. The non-trivial solution α_A^* can be found by solving Eq. 6.24 with a root-finding method (again, in the present work, Matlab®'s *fzero* function is used with a tolerance of 10^{-10} rad).

After computing the angle α_A^*, the optimal direction of the normal vector in frame O_I, $\hat{\boldsymbol{n}}_I^*$, can be found by considering the aerodynamic symmetry of the problem, for which $\hat{\boldsymbol{n}}$ always lies in the $\left(\hat{\boldsymbol{L}}, \hat{\boldsymbol{D}}\right)$ plane and is coplanar with $\hat{\boldsymbol{v}}$ and $\hat{\boldsymbol{\lambda}}$. Given the latter two directions expressed in frame O_I, $\hat{\boldsymbol{v}}_I$ and $\hat{\boldsymbol{\lambda}}_I$, it is possible to compute the optimal direction $\hat{\boldsymbol{n}}_I^*$ in the $\left(\hat{\boldsymbol{L}}, \hat{\boldsymbol{D}}\right)$ plane at an angular distance α_A^* from $\hat{\boldsymbol{v}}_I$ as:

$$\hat{\boldsymbol{n}}_I^* = \cos\alpha_A^* \, \hat{\boldsymbol{v}}_I + \sin\alpha_A^* \left[\frac{\hat{\boldsymbol{v}}_I \times \hat{\boldsymbol{p}}}{\left\|\hat{\boldsymbol{v}}_I \times \hat{\boldsymbol{p}}\right\|} \times \hat{\boldsymbol{v}}_I\right] \tag{6.26}$$

where $\hat{\boldsymbol{p}} = -\hat{\boldsymbol{\lambda}}_I$ if $\alpha_A^* \neq \pi/2$. If $\alpha_A^* = \pi/2$, no lift or drag is generated by the sail and any direction of $\hat{\boldsymbol{n}}$ perpendicular to $\hat{\boldsymbol{v}}$ is optimal. In this case, the optimal sail normal direction, $\hat{\boldsymbol{n}}_I^*$, is arbitrarily chosen to be the direction with the smallest possible angle with the sailcraft inertial position unit vector, $\hat{\boldsymbol{r}}$, such that $\hat{\boldsymbol{p}} = \hat{\boldsymbol{r}}$ in Eq. 6.26. The sail normal direction found through Eq. 6.26 does not take into account the direction of sunlight, $\hat{\boldsymbol{s}}$. As such, it is possible that $\hat{\boldsymbol{n}}_I^*$ has a component in the direction of the Sun, meaning that the pitch angle α is not defined and the SRP acceleration cannot be computed (see Sections 6.2.1.2 and 6.2.2.1). This issue can be solved by considering the aerodynamic symmetry of the sail, for which the same aerodynamic acceleration is found for both $\hat{\boldsymbol{n}}_I^*$ and $-\hat{\boldsymbol{n}}_I^*$. Based on this, a final check on the direction $\hat{\boldsymbol{n}}_I^*$ can be implemented. If $\hat{\boldsymbol{n}}_I^* \cdot \hat{\boldsymbol{s}} \geq 0$,

$\hat{\boldsymbol{n}}_I^*$ has no component in the direction of the Sun and therefore it can be taken as the final optimal sail normal direction. Conversely, if $\hat{\boldsymbol{n}}_I^* \cdot \hat{\boldsymbol{s}} < 0$, $-\hat{\boldsymbol{n}}_I^*$ is taken as the optimal sail normal vector.

6.3.3. Full-dynamics Optimization

The full-dynamics optimization technique is used when the aerodynamic and SRP accelerations are of comparable magnitudes. Similar to the procedures used in Sections 6.3.1 and 6.3.2, an AE surface is defined and the sail orientation maximizing the acceleration component along $\hat{\boldsymbol{\lambda}}$ is sought. However, when considering both SRP and aerodynamics the set of all possible sail accelerations forms a highly-nonlinear envelope surface whose shape is time variant. Indeed, whereas the SRP-based and aerodynamic-based AE curves presented in Sections 6.3.1 and 6.3.2 are shape-invariant when expressed in the sunlight and velocity reference frames, respectively, the shape of the full dynamics AE surface depends on the relative orientation of the instantaneous $\hat{\boldsymbol{s}}$ and $\hat{\boldsymbol{v}}$ directions, as well as the relative magnitude of the SRP characteristic acceleration, a_c, compared to the maximum aerodynamic acceleration, $a_{Aero,max}$. In addition, the envelope surface can also be self-intersecting, meaning that different sail attitudes can result in the same total acceleration vector. An example of such a surface is given for $\hat{\boldsymbol{s}} \perp \hat{\boldsymbol{v}}$ and $a_c = a_{Aero,max}$ in Fig. 6.7, where the corresponding SRP and aerodynamic AE surfaces are also shown for comparison. Because of the complex, time-variant shape of the AE surface and the fact that, to the best of the author's knowledge, no analytical solution to the optimization problem exists, a numerical approach is proposed in the subsequent subsections.

6.3.3.1. Numerical Approaches to the Optimization Problem

The most straightforward way of solving the full-dynamics optimization problem, is through a grid search approach. This translates into taking a large set of attitude angles, evaluating the corresponding acceleration vectors, $\boldsymbol{a}_{SRP}$ and $\boldsymbol{a}_{Aero}$, using these accelerations to determine the AE surface, and eventually retrieving the orientation that maximizes the acceleration component along the $\hat{\boldsymbol{\lambda}}$ direction. However, since the shape of the AE surface depends on the instantaneous sailcraft state and time, this routine ought to be performed at each propagation time step. As a consequence, although such a technique works in theory and ensures that the global optimal solution is found, in practice a large number of function evaluations is required even for small propagation times, thereby yielding impractical runtimes.

Alternatively, techniques such as the interior-point optimization method (e.g., available in Matlab®'s function *fmincon*) can be applied. Although this optimization technique requires less computational effort than the grid search, it requires an initial guess for the optimal sail orientation. For the first propagation time step such an initial guess can be found by using a grid search, whereas for the subsequent time steps the initial guess can be provided by the optimal attitude found in the previous time step. However, the attitudes found are often sub-optimal because it is only a local optimization method. Indeed, the shape of the AE surface can become highly nonlinear during the propagation, which translates into multiple local optima of the cost function $J(\boldsymbol{u})$. In addition, for some steering laws, the primer direction, $\hat{\boldsymbol{\lambda}}$, can change in a discontinuous manner between adjacent propagation time steps. When using the optimal attitude found in the previous

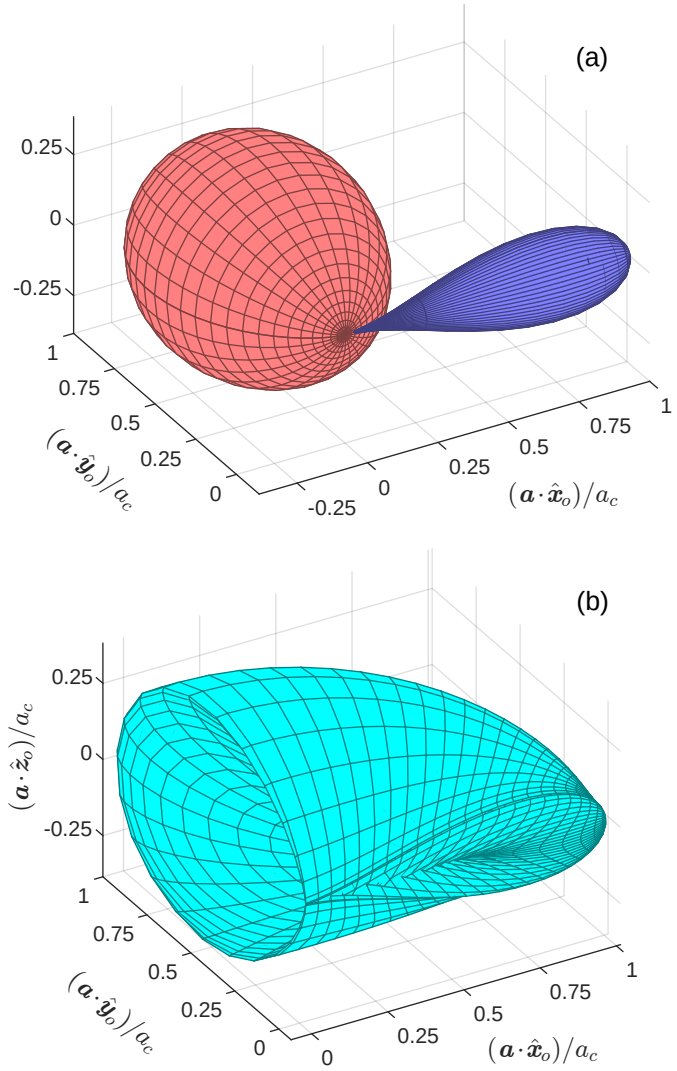


Figure 6.7: Envelope surfaces of a) the SRP acceleration (red), aerodynamic acceleration (blue), and b) total (SRP+aerodynamic) acceleration in frame O_O, for $a_c = a_{Aero,max}$ and $\hat{\boldsymbol{s}} = \hat{\boldsymbol{y}}_b$ (corresponding to $\eta = \pi/2$).

propagation step as initial guess for the current step, this can cause the optimizer to get trapped in a local minimum.

To circumvent the downsides of the techniques mentioned above, this chapter proposes a new optimization approach, whose main advantages are a short runtime for the trajectory propagation and the global validity of the optimal solutions found. The basic idea behind the proposed approach is to first find the global optimal solution of the cost function J(u) for a large variety of scenarios and subsequently interpolate these pre-computed optimal solutions at each time step in the trajectory propagation to retrieve

an interpolated global optimum. In this way, the attitude optimization computation is completely separated from the trajectory propagation, thereby allowing the latter to be performed with small computational effort. Hereinafter this optimization method is referred to as the Pre-run Optimization and in-run INTerpolation (POINT) method. The two phases of the method, the optimization and interpolation phases, are described in detail in Sections 6.3.3.2 and 6.3.3.3.

6.3.3.2. Pre-run Optimization Phase

The pre-run optimization phase of the POINT method aims to solve the optimization problem for a large set of different scenarios, i.e., for a large variety of combinations of AE shapes and $\hat{\boldsymbol{\lambda}}$ directions. To do so, the optimization problem is parametrized through four parameters: $\mathcal{R}$, η, θ, and ϕ.

- The coefficient $\mathcal{R}$ represents the ratio of the maximum SRP acceleration to the maximum aerodynamic acceleration and its value affects the AE shape. This coefficient indicates to what extent the AE shape is similar to the AE shape of the pure SRP acceleration or pure aerodynamic acceleration. For example, for increasing values of $\mathcal{R}$, the SRP acceleration increasingly dominates the aerodynamic acceleration, meaning that the AE shape becomes more similar to the SRP one. On the other hand, for $\mathcal{R}$ values close to zero, the aerodynamic acceleration is dominant so that the AE shape tends to resemble the AE shape of the pure aerodynamic case. By taking into account that the maximum SRP acceleration is equal to the solar-sail characteristic acceleration and that the maximum aerodynamic acceleration is achieved for $\alpha_A = 0$ (i.e., when the sail is perpendicular to the wind flow), $\mathcal{R}$ can be expressed using Eqs. 6.9, 6.12, 6.13, and 6.14 as:

$$\mathcal{R} = \frac{a_c}{a_{Aero,max}} = \frac{S_{TSI}}{c}\frac{2}{\rho v}\frac{1}{[2-\sigma_N(1-V_R)]} \tag{6.27}$$

  Note that since both the SRP and aerodynamic accelerations are inversely proportional to the sail loading parameter σ, $\mathcal{R}$ is independent of σ. This result implies that the AE shape – and thus the entire optimization process – is independent of the sail loading parameter.

- The parameter η determines the relative orientation of the SRP and aerodynamic AE surfaces and its definition is given in Section 6.2.1.4. Together with $\mathcal{R}$, it uniquely defines the AE shape of the full-dynamics case, which results from combining the two separate (i.e., pure SRP and pure aerodynamic) AE surfaces. An example is given in Fig. 6.7, where the combination of the AE surfaces in the Fig. 6.7a plot generates the one in Fig. 6.7b.

- The angles θ and ϕ represent the spherical coordinates of the $\hat{\boldsymbol{\lambda}}$ direction in the O_O frame, see Fig. 6.3b.

Each set $\{\mathcal{R},\eta,\theta,\phi\}$ represents a specific optimization problem which can be solved numerically to find the corresponding optimal sail attitude. To achieve this, a grid search is performed over the angles α_O and δ_O of the sail normal direction in frame O_O, see Fig. 6.3b. To explore the entire parameter space, a four-dimensional grid of discrete values for $\mathcal{R}$, η, θ, and ϕ is created across the following domains: $\mathcal{R} \in [\mathcal{R}_{min},\mathcal{R}_{max}]$,

$\eta \in [0,\pi]$, $\theta \in [0,2\pi]$, and $\phi \in [0,\pi/2]$. $\mathcal{R}_{min}$ and $\mathcal{R}_{max}$ are two threshold parameters whose values are defined in Section 6.4.4 and determine when the full-dynamics optimization should be used instead of the aerodynamic-based optimization ($\mathcal{R} < \mathcal{R}_{min}$) or the SRP-based optimization ($\mathcal{R} > \mathcal{R}_{max}$). Also, it is worth noting that only positive values of ϕ are considered because of the symmetry of the AE surface with respect to the $(\hat{\boldsymbol{x}}_O, \hat{\boldsymbol{y}}_O)$ plane. Due to this symmetry, each pair of angles $\pm\phi$ corresponds to optimal normal directions in the O_O frame, $\hat{\boldsymbol{n}}^*_O$, that differ only in the sign of the component along the $\hat{\boldsymbol{z}}_O$ direction, i.e., $\hat{\boldsymbol{n}}^*_O = [\hat{\boldsymbol{n}}^*_{O,x}, \hat{\boldsymbol{n}}^*_{O,y}, \pm\hat{\boldsymbol{n}}^*_{O,z}]^T$. Therefore, whenever a $\hat{\boldsymbol{\lambda}}$ direction with $\phi < 0$ is encountered during the trajectory propagation, the optimal normal direction $\hat{\boldsymbol{n}}^*_O$ computed for $-\phi$ (> 0) in the pre-run optimization phase is retrieved and the sign of its $\hat{\boldsymbol{n}}^*_{O,z}$-component is changed to obtain the optimal attitude for $\phi < 0$.

The computation of the four-dimensional, pre-optimized grid can require a significant computational effort, particularly because of the large domains for the parameters $\mathcal{R}$, η, θ, and ϕ. One way to overcome this issue is to analyze the problem at hand and determine in advance the range of $\hat{\boldsymbol{\lambda}}$ directions achievable along the trajectory. In this way, the θ and ϕ domains can be shrunk and the number of discrete points to consider in the grid can be reduced, strongly lowering the computational effort. This procedure has been used to create all pre-optimized grids of Sections 6.4 and 6.5, where orbit-raising and inclination-increase steering laws are discussed, for which the $\hat{\boldsymbol{\lambda}}$ direction always points opposite and perpendicular to $\hat{\boldsymbol{x}}_O$, respectively.

6.3.3.3. IN-RUN INTERPOLATION PHASE

To describe the interpolation process adopted in the POINT method, each set of variables $\mathcal{R},\eta,\theta,\phi$ will be represented as a point $\boldsymbol{S} = [S_1, S_2, S_3, S_4]^T = [\mathcal{R},\eta,\theta,\phi]^T$ in a four-dimensional vector space. In this way, each grid point computed in the pre-run optimization phase is represented by $S \in \mathbb{R}^{4x1}$, while the set of all grid points is $\Sigma = \{\boldsymbol{S}_1, \boldsymbol{S}_2, \ldots, \boldsymbol{S}_N\} \in \mathbb{R}^{4xN}$, with N equal to the total number of grid points.

At each time step of the trajectory propagation, specific values for $\mathcal{R}$, η, θ, and ϕ are encountered which identify a target point $\boldsymbol{S}_t = [S_{t,1}, S_{t,2}, S_{t,3}, S_{t,4}]^T$. In general, $\boldsymbol{S}_t$ will be different from any of the points $\boldsymbol{S}$ available in Σ. However, it is always possible to find a subset of neighboring points $\Sigma_{NBH} \subset \Sigma$ close to $\boldsymbol{S}_t$ that enclose the region of space where $\boldsymbol{S}_t$ is located. This region is obtained by considering, for each component $S_{t,k}$, the two closest neighboring values in the pre-optimized grid, $S^-_{t,k}$ and $S^+_{t,k}$, such that $S_{t,k} \in [S^-_{t,k}, S^+_{t,k}]$, with $k = 1, \ldots, 4$. This results in $2^4 = 16$ possible combinations representing the coordinates of the points in $\Sigma_{NBH} \in \mathbb{R}^{4x16}$, i.e.:

$$\Sigma_{NBH} = \left\{ \begin{array}{l} S_{NBH,1} = \left[S^-_{t,1},\ S^-_{t,2},\ S^-_{t,3},\ S^-_{t,4}\right]^T \\ S_{NBH,2} = \left[S^-_{t,1},\ S^-_{t,2},\ S^-_{t,3},\ S^+_{t,4}\right]^T \\ S_{NBH,3} = \left[S^-_{t,1},\ S^-_{t,2},\ S^+_{t,3},\ S^-_{t,4}\right]^T \\ S_{NBH,4} = \left[S^-_{t,1},\ S^-_{t,2},\ S^+_{t,3},\ S^+_{t,4}\right]^T \\ \vdots \\ S_{NBH,16} = \left[S^+_{t,1},\ S^+_{t,2},\ S^+_{t,3},\ S^+_{t,4}\right]^T \end{array} \right\} \tag{6.28}$$

Since each point in Σ_{NBH} corresponds to an optimal sail orientation computed in the pre-run optimization phase, a set $\Gamma_{NBH} \in \mathbb{R}^{3x16}$ of 16 optimal normal directions in frame O_O, $\hat{\boldsymbol{n}}_O^*$, is also given. The interpolation of these normal directions is performed through a normalized Inverse Distance Weighting (IDW) technique [416] and applied to the problem at hand as follows. Before the interpolation is performed, $\boldsymbol{S}_t$ and the points in Σ_{NBH} are normalized[2] to restrict the domain of their four components to $[0,1]$, thus resulting in the normalized target point $\bar{S}_t$ and neighboring set $\bar{\Sigma}_{NBH} = \{\bar{\boldsymbol{S}}_{NBH,1}, \ldots, \bar{\boldsymbol{S}}_{NBH,16}\}$. From these, the vector $\boldsymbol{\varrho} = [\varrho_1, \ldots, \varrho_{16}]^T$ is computed which contains the inverses of the Euclidean distances between $\bar{\boldsymbol{S}}_t$ and $\bar{\boldsymbol{S}}_{NBH,1}, \ldots, \bar{\boldsymbol{S}}_{NBH,16}$. The inverse distance weight vector, $\boldsymbol{w} \in \mathbb{R}^{16x1}$, is also calculated as:

$$\boldsymbol{w} = [w_1, \ldots, w_{16}]^T = \frac{\boldsymbol{\varrho} \circ \boldsymbol{\varrho}}{\boldsymbol{\varrho}^T \cdot \boldsymbol{\varrho}} \tag{6.29}$$

where $\circ$ indicates the element-wise Hadamard product of two vectors [417]. Finally, the optimal normal directions in Γ_{NBH}, i.e., $\hat{\boldsymbol{n}}^*_{O,NBH,1}$, …, $\hat{\boldsymbol{n}}^*_{O,NBH,16}$, are used to define the following matrix $\mathcal{N} \in \mathbb{R}^{3x16}$:

$$\mathcal{N} = \left[\hat{\boldsymbol{n}}^*_{O,NBH,1}, \ldots, \hat{\boldsymbol{n}}^*_{O,NBH,16}\right] \tag{6.30}$$

which is then used to find the final interpolated normal direction, $\hat{\boldsymbol{n}}_O^*$, as:

$$\hat{\boldsymbol{n}}_O^* = \frac{\mathcal{N} \cdot \boldsymbol{w}}{\mathcal{N} \cdot \boldsymbol{w}} \tag{6.31}$$

As the neighboring points $\bar{\boldsymbol{S}}_{NBH,1}$, …, $\bar{\boldsymbol{S}}_{NBH,16}$ consider different values for $\mathcal{R}$, η, θ, and ϕ, they represent optimization problems with slightly different AE shapes and $\hat{\boldsymbol{\lambda}}$ directions. However, due to the high nonlinearity of the problem, in certain cases slightly different AE shapes and directions of the primer vector make the optimal normal directions $\hat{\boldsymbol{n}}^*_{O,NBH,1}$, …, $\hat{\boldsymbol{n}}^*_{O,NBH,16}$ differ substantially. Such scenarios take place when the target point considered, $\boldsymbol{S}_t$, corresponds to an optimization problem with regions of similar degrees of local optimality. These regions contain both the globally optimal solution and other locally optimal solutions. Although all these optimal solutions are associated to similar cost function values, in some cases the corresponding sail normal directions can significantly differ from one another. When this kind of optimization problem is encountered, small variations in the components of $\boldsymbol{S}_t$ yield slight variations in the cost function values of these optimal regions. This in turn can make the global optimum shift from one region to another and the corresponding optimal normal direction suddenly change. For this reason, when dealing with this kind of optimization problems, the optimal normal directions found for the neighboring points $\bar{\boldsymbol{S}}_{NBH,1}$, …, $\bar{\boldsymbol{S}}_{NBH,16}$ strongly differ from each other and, as a consequence, using IDW interpolation yields an interpolated solution $\hat{\boldsymbol{n}}_O^*$ that is less optimal than $\hat{\boldsymbol{n}}^*_{O,NBH,1}$, …, $\hat{\boldsymbol{n}}^*_{O,NBH,16}$.

To avoid the above issue, the POINT method makes use of an algorithm that aims to identify such locally optimal regions before the interpolation. In this way, it is possible to

[2] When performing the normalization, two of the three Cartesian components of the $\hat{\boldsymbol{\lambda}}$ direction are considered instead of the spherical coordinates θ and ϕ to avoid dealing with discontinuous variables in the interpolation process.

consider each region separately in the interpolation phase and compute different optimal solutions $\hat{\boldsymbol{n}}_O^*$, which contains the global optimum. The algorithm is based on the idea that different locally optimal regions of the solution space correspond to locally optimal sail normal vectors pointing in different directions. The angular distances between the optimal normal directions of Γ_{NBH} allow to define clusters of normal directions, which in turn identify the local optimal regions. In this chapter the cluster detection has been performed by means of a hierarchical clustering algorithm with single-linkage criterion [418]. The algorithm computes the norm of the difference of each pair of normal directions in Γ_{NBH}, compares these norms with a threshold value, and determines the number of clusters in Γ_{NBH}. More specifically, in this chapter the Matlab® function *cluster* is employed using a distance-based criterion and a hierarchical cluster tree (defined through the function *linkage*) built with a "shortest Euclidean distance" method. The value used for the threshold is $2\sin(\pi/60)$, corresponding to a minimum angle of 6 deg between normal directions of different clusters. This value was tuned based on the knowledge of the optimization problem under investigation, the number of grid points in Σ, and some trial and error. When the optimization problem is not characterized by multiple locally optimal regions, the algorithm returns one unique cluster that coincides with Γ_{NBH} and therefore the interpolation routine can be performed as explained in the previous section. Conversely, if different clusters are found, for each cluster in Γ_{NBH} the corresponding points in Σ_{NBH} are taken and the normalization and interpolation routines are performed separately on each subset of Σ_{NBH} to find multiple locally optimal solutions $\hat{\boldsymbol{n}}_O^*$. From these, the normal direction corresponding to the largest cost function value is taken as the global optimal solution.

6.4. VALIDATION AND TESTING

In this section, different analyses are presented that aim to tune all parameters regulating the atmospheric density averaging algorithm and the POINT optimization method. In Table 6.1 the simulation settings are given for each of the four tests presented in Sections 6.4.1 to 6.4.4.

All analyses make use of the ACS3 mission as baseline scenario, corresponding to a solar-sail characteristic acceleration of $a_c = 0.05\ \text{mm}\,\text{s}^{-2}$, a simulation start time of July 1st, 2022 (i.e., the expected deployment date of the solar sail at the time of the study), and the following vector of initial Keplerian elements:

$$\left[a_0,\ e_0,\ i_0,\ \Omega_0,\ \omega_0,\ f_0\right]^T = \left[7093.1363\ \text{km},\ 0,\ 98.2490\ \text{deg},\ 10.5029\ \text{deg},\ 0\ \text{deg},\ 0\ \text{deg}\right]^T \tag{6.32}$$

where a is the semi-major axis (SMA), e the eccentricity, i the inclination, Ω the right ascension of the ascending node, ω the argument of perigee, f the true anomaly, and the subscript "0" denotes the initial value of these variables[3]. Note that these Keplerian elements represent a circular, Sun-synchronous orbit with altitude $h_0 = a_0 - R = 715$ km and a local time of the ascending node (LTAN) at 0600 hrs (corresponding to a dawn-dusk orbit). As shown in Table 6.1, the dynamical model used in all tests considers the

[3] ACS3 mission data taken from personal communication with W.K. Wilkie, Principal Investigator of the ACS3 mission, NASA Langley Research Center, September 2021.

Table 6.1: Simulation settings used for the validation and testing in 6.4.

Test/Section	6.4.1	6.4.2	6.4.3	6.4.4
Dynamics	Earth's central gravity, SRP, and aerodynamic accelerations			
a_c	$0.05\ \text{mms}^{-2}$			
Sim. start	July 1st, 2022			
Sim. duration	10 days	1 orb. period		
Initial state	ACS3, with variations in a and i	ACS3		
Integrator	Matlab®'s *ode45*			
Rel./Abs. tol.	10^{-12}	10^{-8}		
Atmospheric model of ref. solution	NRLMSISE-00 model	Avg. NRLMSISE-00 model (ApO : 25, NpA : 4)		Constant density
Optimization method of ref. solution	SRP-based	Full-dynamics, grid search with $\Delta\alpha_\odot = \Delta\delta_\odot = 0.01$ deg		SRP-based or aerodynamic-based
Steering law	a	a and i		
Atmospheric model	Avg. NRLMSISE-00 model (ApO : $2 \div 200$, NpA : $2 \div 20$)	Avg. NRLMSISE-00 model (ApO : 25, NpA : 4)		Constant density
Optimization method	SRP-based	Full-dynamics, POINT		
$\Delta\Lambda$	N/A	1 deg	0.1 – 2 deg	1 deg
$\Delta\mathcal{R}$	N/A	1.21	$1.1^{-1/4} \div 1.1^{4}$	1.21
$\Delta\delta_O$	N/A	$\Delta\Lambda/10$		
$\Delta\alpha_O$	N/A	$\Delta\Lambda/10$		

Earth's central gravitational acceleration, SRP acceleration, and aerodynamic acceleration. On the other hand, the J_2 gravitational acceleration is not considered. This choice is justified by the fact that the parameter tuning is conducted on test cases that consider an increase in SMA or inclination. The J_2 perturbation has no secular effect on these Keplerian elements, only a short-term periodic effect [308]. Therefore, including the J_2 acceleration would only add significant noise to the results. Propagations are performed using Matlab®'s *ode45* integrator for all tests, with absolute and relative tolerances of 10^{-8} or 10^{-12} depending on the simulation duration.

6.4.1. TUNING OF THE ATMOSPHERIC DENSITY MODEL

The parameters affecting the density averaging procedure described in Section 6.2.2.2 are the number of averaging segments per orbit, ApO, and the number of nodes per orbit segment, NpA. By tuning these parameters, a significant reduction in runtime can be achieved at the cost of a decreased accuracy in the results. These two criteria (runtime and accuracy) form the basis of the trade-off described hereinafter.

As shown in Table 6.1, the steering law adopted is an orbit-raising steering law computed using the SRP-based optimization of Section 6.3.1, meaning that aerodynamic drag is not considered in the optimization but only in the propagation of the dynamics. The choice for this steering law is based on the fact that aerodynamic drag negatively affects

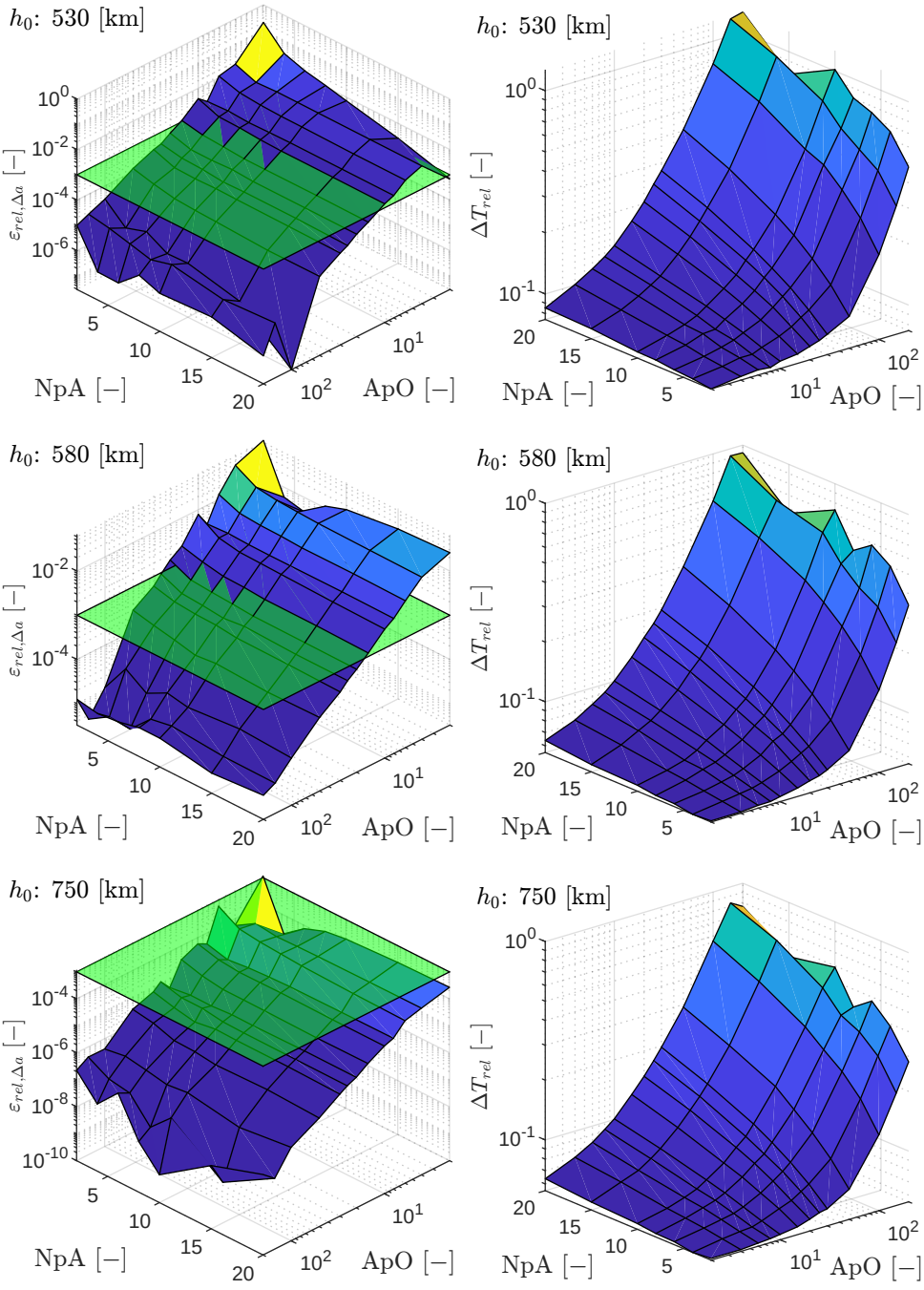


Figure 6.8: $\varepsilon_{rel,\Delta a}$ and ΔT_{rel} as function of the initial altitude, h_0, and tuning parameters *ApO* and *NpA*.

the rate of change of the orbital altitude, enlarging the effect of different averaged density models when aerodynamic drag is not accounted for in the optimization process. The achieved increase in altitude is taken as a metric for the accuracy. More specifically, the relative error, $\varepsilon_{rel,\Delta a}$, defined as:

$$\varepsilon_{rel,\Delta a} = \left| \frac{\Delta a - \Delta a_{ref}}{\Delta a_{ref}} \right| \tag{6.33}$$

is used, where Δa and Δa_{ref} are the increases in SMA achieved with the averaged density model and the full NRLMSISE-00 model, respectively. Similarly, the relative runtime, ΔT_{rel}, is used as a measure of the runtime reduction obtained by using a specific averaged atmospheric density model:

$$\Delta T_{rel} = \left| \frac{\Delta T}{\Delta T_{ref}} \right| \tag{6.34}$$

where ΔT and ΔT_{rel} are the runtimes required by the averaged density model and the full NRLMSISE-00 model for the entire propagation, respectively. In the analyses, the sailcraft characteristics, simulation start time, and orbital parameters correspond to those of the ACS3 mission except for the initial orbital altitude and inclination. Indeed, the metrics $\varepsilon_{rel,\Delta a}$ and ΔT_{rel} are computed for three different initial altitudes to account for the effect of different ranges of acceleration ratios $\mathcal{R}$ on the results. In particular, the altitudes considered are 530 km, 580 km, and 750 km, corresponding to $\mathcal{R} \in [1/23.9797, 1.1656]$ (aerodynamic-dominated case), $\mathcal{R} \in [1/3.2528, 2.4394]$ (intermediate case), and $\mathcal{R} \in [2.7672, 39.7815]$ (SRP-dominated case), respectively. Also, the initial altitudes of 530 km, 580 km, and 750 km correspond to Sun-synchronous inclinations of 97.5158, 97.7090, and 98.3933 deg, respectively.

The resulting values for $\varepsilon_{rel,\Delta a}$ and ΔT_{rel} for each initial altitude, *ApO*, and *NpA* are displayed in Fig. 6.8. The *ApO* values used to generate the surface plots are $\{2, 4, 6, 8, 10, 15, 20, 25, 30, 50, 100, 150, 200\}$, while the *NpA* values considered are $\{2, 4, 6, 8, 10, 15, 20\}$. The plots on the left-hand side of Fig. 6.8 also show a plane corresponding to $\varepsilon_{rel,\Delta a} = 10^{-3}$. This value is chosen as the maximum allowable value for $\varepsilon_{rel,\Delta a}$ in the trade-off between different combinations of *ApO* and *NpA*. Figure 6.8 shows that - for any given altitude - decreasing values of *ApO* and *NpA* yield smaller runtimes at the cost of larger relative errors. However, while the value for *NpA* affects the runtime to some extent, no clear correlation can be determined between *NpA* and the relative error. Based on this, a final value of $NpA = 4$ is chosen for all altitudes and will be considered in the following analysis to determine the value for *ApO*. Unlike *NpA*, the value for *ApO* largely affects both $\varepsilon_{rel,\Delta a}$ and ΔT_{rel} and the extent of the effect depends on the initial altitude:

- $h_0 = 530$ km: In order to achieve the shortest possible runtime while keeping the relative error below the threshold, $\varepsilon_{rel,\Delta a} = 10^{-3}$, a value for $ApO \geq 20$ should be selected.
- $h_0 = 580$ km: By the same logic, $ApO \geq 25$ in order for the relative error constraint to be met.
- $h_0 = 750$ km: In this case, the relative error is considerably below the threshold for any *ApO*.

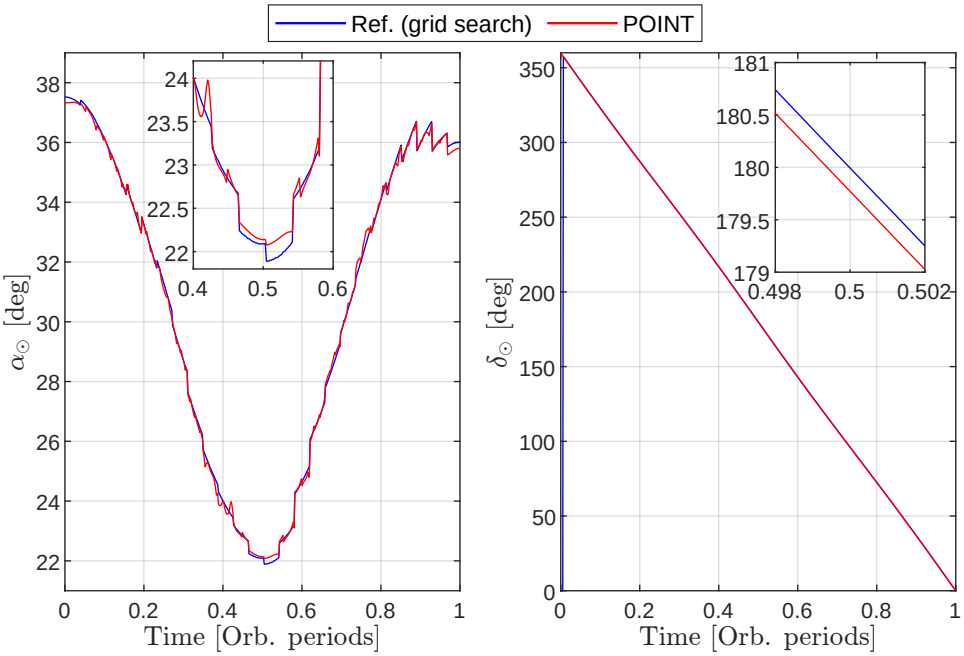


Figure 6.9: Orbit raising: control profile of the reference solution and POINT solution over one orbital period.

Based on the above considerations, a final value of $ApO = 25$ is used for all altitude regimes, corresponding to $\varepsilon_{rel,\Delta a}$ in the range $[7.17026 \cdot 10^{-6}, 5.83754 \cdot 10^{-4}]$ and ΔT_{rel} in the range $[7.76874 \cdot 10^{-2}, 1.07546 \cdot 10^{-1}]$.

6.4.2. VALIDATION OF FULL-DYNAMICS POINT OPTIMIZATION

In this section, two cases are discussed which aim to validate the POINT optimization method and show its accuracy, both for an orbit-raising steering law and an inclination-increase steering law. This is achieved by propagating one single orbit, optimizing its control with the POINT method, and comparing the control profile achieved with a reference solution. Based on the results of Section 6.4.1, the reference solution in this section uses the averaged NRLMSISE-00 atmospheric density model, with $ApO = 25$ and $NpA = 4$. The reference solutions for both steering laws are found by performing a grid search at each propagation time step (as explained in Section 6.3.3.1), with steps equal to $\Delta\alpha_\odot = \Delta\delta_\odot = 0.01$ deg for the pitch and clock angles. Based on the tuning of the pre-run optimization grid that will be discussed in Section 6.4.3, the grid Σ used by the POINT method is defined by using an angular step, $\Delta\Lambda$, of 1 deg for the variables η, θ, and ϕ and a step of $\Delta\mathcal{R} = 1.1^2 = 1.21$ for the acceleration ratio (see Section 6.4.3 for more details on the definition of $\Delta\mathcal{R}$). Finally, the grid search of the pre-run optimization phase of POINT is performed using $\Delta\alpha_O = \Delta\delta_O = \Delta\Lambda/10 = 0.1$ deg as angular steps.

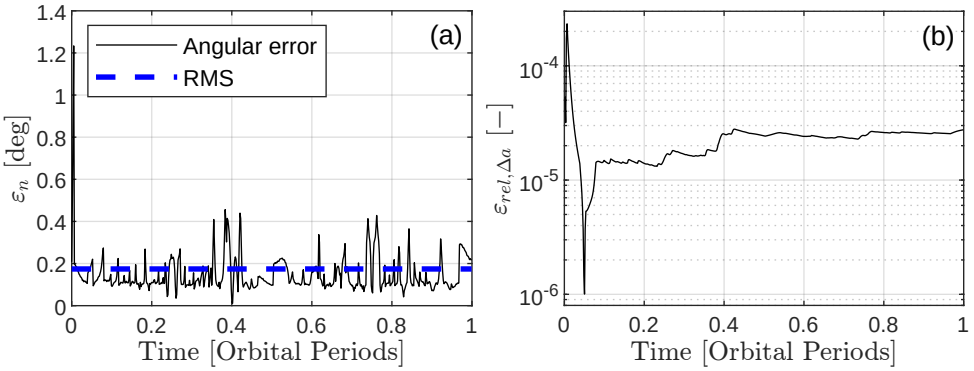


Figure 6.10: Orbit raising: comparison of the reference (grid search) and POINT solutions over one orbital period, showing a) the angular error in the sail normal direction and b) the relative error in Δa.

6.4.2.1. ORBIT RAISING

For the orbit-raising steering law, the control profiles of the reference solution and the POINT solution are given in Fig. 6.9. As can be appreciated from the zoomed-in plots of the pitch and clock angle profiles, the POINT solution (in red) accurately approximates the reference solution (in blue, dashed). Also, from Fig. 6.9 it can be noted that the pitch-angle profile exhibits instantaneous jumps, both in the reference and POINT solutions. This is due to the averaging procedure of the atmospheric density model employed, which yields a step-wise variation in the density along the orbit and, therefore, also in the acceleration ratio, see Fig. 6.4. This in turn affects the control computation procedure, leading to the sudden variations in $\alpha_\odot$ shown in the figure. As a measure of the error in optimal sail normal direction as computed by the POINT method, the angular displacement, ε_n, between the sail normal direction of the POINT method and the reference solution is computed at each time step. The result is displayed in Fig. 6.10a, where the red dashed line indicates the root mean square (RMS) of ε_n, equal to 0.1742 deg. It should be noted that the RMS of ε_n depends on the angular steps $\Delta\Lambda$, $\Delta\delta_O$, and $\Delta\alpha_O$ used in the pre-run optimization phase of POINT and are of comparable magnitudes, as one would expect when performing an interpolation. The relative error of the SMA increase, $\varepsilon_{rel,\Delta a}$, is displayed in Fig. 6.10b. This error is defined as per Eq. 6.33, with Δa and Δa_{ref} the increases in SMA of the POINT and reference solutions, respectively. After a sudden increase in $\varepsilon_{rel,\Delta a}$ at the beginning of the simulation – which coincides with a large value for ε_n – the relative error stabilizes with a final value after one orbit of $\varepsilon_{rel,\Delta a} = 2.7537 \cdot 10^{-5}$. This value is deemed acceptable, also in relation to the relative error threshold of 10^{-3} used for the atmospheric density model tuning of Section 6.4.1.

6.4.2.2. INCLINATION INCREASE

The $\alpha_\odot$ and $\delta_\odot$ angle profiles for the inclination steering laws of the POINT and reference solutions are given in Fig. 6.11. Here, it can be noted that the POINT solution closely resembles the reference solution. Nonetheless, the POINT solution manages to approximate the reference solution better during the first and last quarter of the orbit than in the middle part of the orbital revolution. This becomes even clearer in the zoomed-in

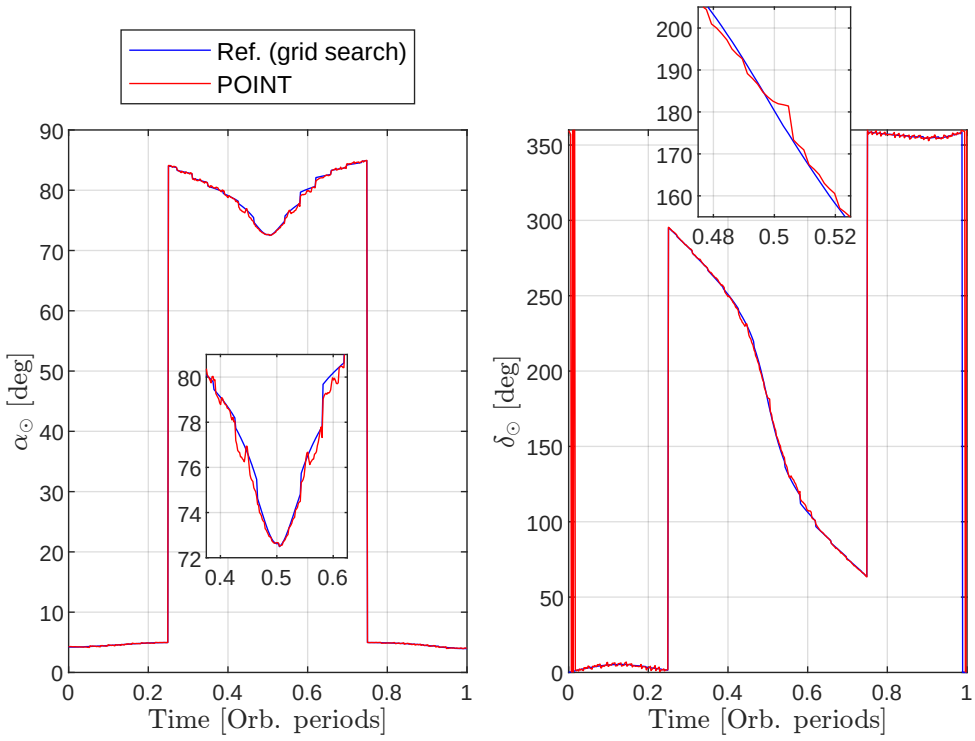


Figure 6.11: Inclination increase: control profile of the reference solution and POINT solution over one orbital period.

plots of Fig. 6.11, as well as in Fig. 6.12a, which displays the evolution of ε_n. In particular, the latter figure shows that the POINT method experiences difficulties in finding the true optimal solution in the middle part of the orbital revolution, leading to displacements in the sail normal direction in the order of some degrees. Consequently, a steep growth in the inclination-increase relative error, $\varepsilon_{rel,\Delta i}$, is also observed during this time, see Fig. 6.12b. Note that this relative error is defined similar to $\varepsilon_{rel,\Delta a}$ as:

$$\varepsilon_{rel,\Delta i} = \left| \frac{\Delta i - \Delta i_{ref}}{\Delta i_{ref}} \right| \tag{6.35}$$

where Δi_{ref} and Δi are the increases in inclination of the reference and POINT solutions, respectively. The errors observed are due to the intrinsic difficulty in increasing the inclination in the middle part of the orbit where every non-zero, out-of-plane solar-sail acceleration points opposite to $\hat{\boldsymbol{\lambda}}$ and would therefore yield a negative Δi. Consequently, the optimal attitude is the one that minimizes the out-of-plane acceleration, resulting in no change in inclination, see Fig. 6.12a. However, multiple sail attitudes lead to a Δi close to zero, hence making the search for the global optimal attitude hard for the POINT method. Despite the errors introduced in this middle part of the orbit, the relative error achieved at the end of the propagation is $\varepsilon_{rel,\Delta i} = 8.4872 \cdot 10^{-6}$, which, again, is deemed

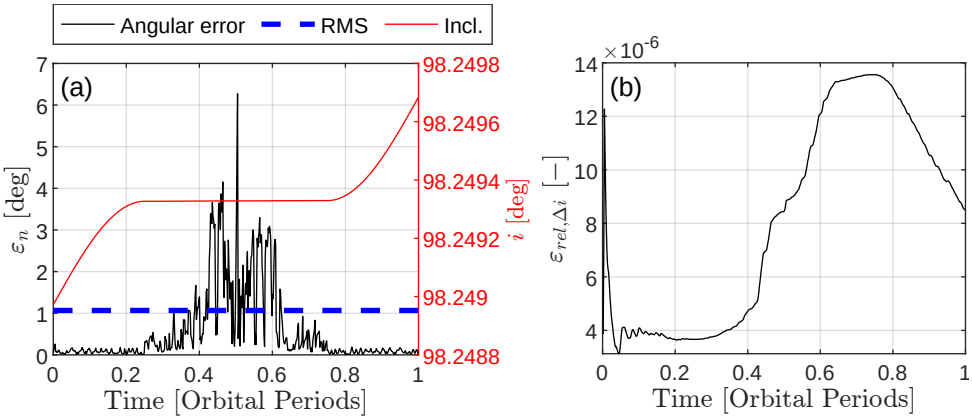


Figure 6.12: Inclination increase: comparison of the reference (grid search) and POINT solutions over one orbital period, showing a) the angular error in the sail normal direction and the variation in inclination of the POINT solution, and b) the relative error in Δi.

acceptable in relation to the threshold of 10^{-3} used for the atmospheric density model tuning of Section 6.4.1.

6

6.4.3. TUNING OF THE PRE-RUN OPTIMIZATION GRID

As described in Section 6.3.3.3, the in-run interpolation phase of the POINT method aims to compute the interpolated optimal sail normal directions based on the grid points $\boldsymbol{S} \in \Sigma$ of the pre-run optimization phase. The way in which these points are chosen and – in particular – the spacing between them, affects the accuracy of the results obtained by the interpolation. In this section, the results for different grids Σ are evaluated to determine the correlation between the accuracy of the optimal solutions found and the spacing of the grid points. Based on this, a final grid Σ is chosen.

Because this chapter only considers steering laws for orbit raising and inclination increase, the grid points' spacing will be evaluated separately for these two steering laws. Since the spacing of the points $\boldsymbol{S} \in \Sigma$ is determined by the step used for each of the points' components (i.e., $\Delta\mathcal{R}$, $\Delta\eta$, $\Delta\theta$, and $\Delta\phi$), a computationally demanding, four-dimensional parametric analysis ought to be performed. To reduce the dimensionality of the parametric analysis, the angular steps of the variables η, θ, and ϕ are set equal to a common value $\Delta\Lambda$, so that $\Delta\Lambda = \Delta\eta = \Delta\theta = \Delta\phi$. The set of values used for $\Delta\Lambda$ in the parametric analysis is $\{0.1, 0.2, 0.5, 1.0, 2.0\}$ deg, while the set for $\Delta\mathcal{R}$ is $\{1.1^{1/4}, 1.1^{1/2}, 1.1, 1.1^2, 1.1^4\}$. It should be noted that, while $\Delta\Lambda$ represents the difference between adjacent angular values of the grid, $\Delta\mathcal{R}$ represents the ratio of consecutive $\mathcal{R}$ values. This means that given a value $\mathcal{R}_k$ of the grid, the adjacent one, $\mathcal{R}_{k+1}$, is found as $\mathcal{R}_{k+1} = \mathcal{R}_k \cdot \Delta\mathcal{R}$. This approach is employed because the change in shape of the AE surface with $\mathcal{R}$ is exponential.

To determine the correlation between the accuracy of the optimal solutions and the spacing of the grid points, the POINT optimization is run with different grids Σ and the final increases in altitude or inclination are computed and compared with a reference

Table 6.2: Relative errors on Δa for each pair of $\Delta\Lambda$ and $\Delta\mathcal{R}$.

$\varepsilon_{rel,\Delta a} \cdot 10^{-5}$		$\Delta\mathcal{R}$ [−]				
		$1.1^{1/4}$	$1.1^{1/2}$	1.1	1.1^2	1.1^4
$\Delta\Lambda$ [deg]	0.1	7.3042	4.9774	3.1956	7.0016	8.2448
	0.2	6.0737	4.1505	2.2168	5.5576	7.9439
	0.5	2.4879	1.8414	1.1708	2.4118	6.6047
	1.0	2.4806	1.8681	2.4475	2.7537	6.4701
	2.0	6.7333	5.4641	4.5604	6.3204	9.7635

optimal solution (the same reference solution as used in Section 6.4.2, see Table 6.1). The differences in final altitude/inclination are a measure of the errors introduced by using different grids Σ (i.e., different combinations of steps $\Delta\Lambda$ and $\Delta\mathcal{R}$).

The parametric analyses are performed using the settings presented in Table 6.1. In particular, the same settings as in Section 6.4.2 are used, with the only difference being the different set of $\Delta\Lambda$ and $\Delta\mathcal{R}$ steps considered.

6.4.3.1. ORBIT RAISING

The results of the analysis for the orbit-raising steering law are given in Table 6.2, where the relative error on the SMA increase achieved after one orbit, $\varepsilon_{rel,\Delta a}$, is displayed for each pair of $\Delta\Lambda$ and $\Delta\mathcal{R}$. The table shows that the largest values for $\varepsilon_{rel,\Delta a}$ are found for $\Delta\Lambda$ = 2 deg and $\Delta\mathcal{R} = 1.1^4$, whereas the smallest $\varepsilon_{rel,\Delta a}$ values are achieved for intermediate values of $\Delta\mathcal{R}$ and $\Delta\Lambda$. Nonetheless, no clear correlation between $\Delta\mathcal{R}$, $\Delta\Lambda$, and $\varepsilon_{rel,\Delta a}$ can be derived from the results. When the relative error of 10^{-3} introduced in the atmospheric density averaging is once again used as threshold, virtually any combination of $\Delta\mathcal{R}$ and $\Delta\Lambda$ can be adopted, including the steps $\Delta\mathcal{R} = 1.1^4$ and $\Delta\Lambda$ = 2 deg for which the least computational runtime is required both in the pre-run optimization and in-run interpolation phases. Nonetheless, since the simulations of Section 6.5 will be performed on Sun-synchronous orbits with values of the altitude, LTAN, and a_c different from the ones of the ACS3 mission, some contingency is considered and $\Delta\mathcal{R} = 1.1^2 = 1.21$ and $\Delta\Lambda$ = 1 deg are selected for which $\varepsilon_{rel,\Delta a} = 2.7537 \cdot 10^{-5}$.

6.4.3.2. INCLINATION INCREASE

The results for the inclination-increase steering law are given in Table 6.3, wherein a clear variation of $\varepsilon_{rel,\Delta i}$ with $\Delta\mathcal{R}$ and $\Delta\Lambda$ can be observed. In particular, it can be noted that an increase in either $\Delta\mathcal{R}$ or $\Delta\Lambda$ (which corresponds to a coarser grid Σ) yields a larger $\varepsilon_{rel,\Delta i}$. Depending on how coarse the grid Σ is, relative errors of different magnitudes can be achieved, ranging between $2.6527 \cdot 10^{-7}$ and $5.2362 \cdot 10^{-5}$. These values are well below the relative error of 10^{-3} introduced in the atmospheric density averaging. Therefore, using the same rationale as in Section 6.4.3.1, $\Delta\mathcal{R} = 1.1^2 = 1.21$ and $\Delta\Lambda$ = 1 deg are once again chosen for which $\varepsilon_{rel,\Delta i} = 8.4872 \cdot 10^{-6}$.

Table 6.3: Relative errors on Δi for each pair of $\Delta\Lambda$ and $\Delta\mathcal{R}$.

$\varepsilon_{rel,\Delta i} \cdot 10^{-7}$		$\Delta\mathcal{R}$ [−]				
		$1.1^{1/4}$	$1.1^{1/2}$	1.1	1.1^{2}	1.1^{4}
$\Delta\Lambda$ [deg]	0.1	4.6549	2.6527	9.2171	23.265	521.70
	0.2	3.9877	3.1171	8.2609	25.585	218.47
	0.5	15.403	17.043	17.518	41.719	159.00
	1.0	54.429	63.226	63.852	84.872	290.93
	2.0	304.84	365.86	290.51	410.91	523.62

6.4.4. Tuning of the Boundaries of the Acceleration Ratio

The boundaries of the acceleration ratio, $\mathcal{R}_{min}$ and $\mathcal{R}_{max}$, define when the full-dynamics optimization ($\mathcal{R}_{min} \leq \mathcal{R} \leq \mathcal{R}_{max}$) is to be performed instead of the aerodynamic-based optimization ($\mathcal{R} < \mathcal{R}_{min}$) or SRP-based optimization ($\mathcal{R} > \mathcal{R}_{max}$). To determine these boundaries, multiple propagations of the ACS3 orbit are performed over one orbital period, using a range of hypothetical constant values of the atmospheric density, ρ. Based on Eq. 6.27 and the fact that the sailcraft inertial velocity, v, remains nearly constant along one orbital revolution, the different densities uniquely determine the values of $\mathcal{R}$. For each acceleration ratio, the relative difference in the final increase of a target orbital element found through the full-dynamics optimization and the aerodynamic/SRP-based optimization is computed. Finally, the values of $\mathcal{R}$ for which such a difference becomes smaller than a predefined threshold are taken as the boundaries $\mathcal{R}_{min}$ and $\mathcal{R}_{max}$.

The above-mentioned analysis is performed for the orbit-raising and inclination-increase steering laws and the corresponding results are discussed in Sections 6.4.4.1 and 6.4.4.2, respectively. The test settings are specified in Table 6.1.

6.4.4.1. Orbit Raising

The relative error between the SMA increase of the full-dynamics optimization and SRP-based optimization, $\varepsilon_{rel,\Delta a}$, as a function of $\mathcal{R}$ is shown in the plot of Fig. 6.13a. $\varepsilon_{rel,\Delta a}$ is defined as in Eq. 6.33, with Δa and Δa_{ref} the increase in SMA achieved by the SRP-based optimization and full-dynamics optimization, respectively. As can be seen, $\varepsilon_{rel,\Delta a}$ rapidly decreases for increasing values of $\mathcal{R}$, indicating that for large acceleration ratios, the SRP AE becomes a valid approximation of the full-dynamics AE. In choosing a suitable threshold value for $\varepsilon_{rel,\Delta a}$, the following should be considered. While the relative errors found in the tuning of the optimization grid in Section 6.4.3 were computed with respect to a reference solution found with a grid search, in this section the relative errors are defined with respect to the full-dynamics solution of the POINT method. Consequently, the relative errors $\varepsilon_{rel,\Delta a}$ computed here build upon the ones found in Section 6.4.3. Taking this into account, and considering that an overall relative error smaller than 10^{-3} is sought, a threshold for $\varepsilon_{rel,\Delta a}$ of 10^{-4} is set. As can be seen from Fig. 6.13a, this threshold is met for $\mathcal{R} = 55$, where $\varepsilon_{rel,\Delta a} = 9.23459 \cdot 10^{-5}$. Consequently, $\mathcal{R}_{max}$ is set to 55.

To determine $\mathcal{R}_{min}$, Fig. 6.13b displays the absolute error, $\varepsilon_{abs,\Delta a} = \left|\Delta a - \Delta a_{ref}\right|$, between the SMA increase obtained by the aerodynamic-based optimization, Δa, and the full-dynamics optimization, Δa_{ref}, as a function of $\mathcal{R}$. In this case, the absolute error

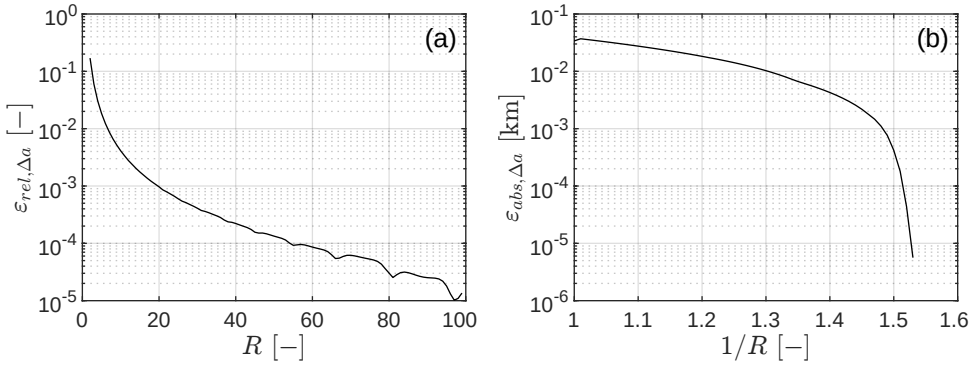


Figure 6.13: Orbit raising: relative and absolute errors on Δa between the full-dynamics solutions and a) the SRP-based optimization solutions, b) the aerodynamic-based optimization solutions.

is preferred as metric for the accuracy because the solution found by the aerodynamic-based optimization constantly orients the sail parallel to the wind flow, thereby yielding no variation in the SMA and a relative error of 1. As can be seen from Fig. 6.13b, the absolute error rapidly decreases for increasing values of $1/\mathcal{R}$, until $1/\mathcal{R} = 1.54$ for which $\varepsilon_{abs,\Delta a} = 0$. For $1/\mathcal{R} \geq 1.54$ the aerodynamic acceleration is so dominant that the solutions found by the full-dynamics optimization and the aerodynamic-based optimization are the same. Based on this value and by including some contingency, $1/\mathcal{R}_{min}$ is set to 4.

6.4.4.2. INCLINATION INCREASE

The approach used to determine $\mathcal{R}_{min}$ and $\mathcal{R}_{max}$ for the inclination-increase steering law is similar to the one used in the previous section. The only difference is that the accuracy is measured through the relative inclination error, $\varepsilon_{rel,\Delta i}$, defined as per Eq. 6.35, where Δi and Δi_{ref} are the increases in inclination achieved by the SRP/aerodynamic-based optimization and full-dynamics optimization, respectively.

As can be seen from Fig. 6.14a, $\varepsilon_{rel,\Delta i}$ rapidly decreases for increasing values of $\mathcal{R}$, thereby demonstrating the convergence of the full-dynamics AE to the SRP AE. By considering once again a maximum relative error of 10^{-4}, the acceleration ratios meeting this condition are found for $\mathcal{R} \geq 30$. Based on this, $\mathcal{R}_{max} = 30$ is chosen.

Figure 6.14b shows that, for decreasing $\mathcal{R}$ values, smaller relative errors between the solutions for the full-dynamics and aerodynamic-based optimizations are obtained. Nonetheless, the values for $\varepsilon_{rel,\Delta i}$ are always well above the threshold of 10^{-4}, even for very small acceleration ratios, e.g., $1/\mathcal{R} = 100$. Without considering even smaller values for $\mathcal{R}$, $1/\mathcal{R}_{min} = 100$ is chosen as acceleration ratio boundary because values of $1/\mathcal{R} > 100$ are highly unlikely for the analyses performed in Section 6.5. Such small acceleration ratios are only found for very low altitudes where the solar sail would deorbit in less than one revolution because of atmospheric drag.

6.5. RESULTS AND ANALYSIS

In this section, the POINT method will be used to compute the control laws to maximize the increase in SMA or inclination starting from different initial Earth-centered orbits and

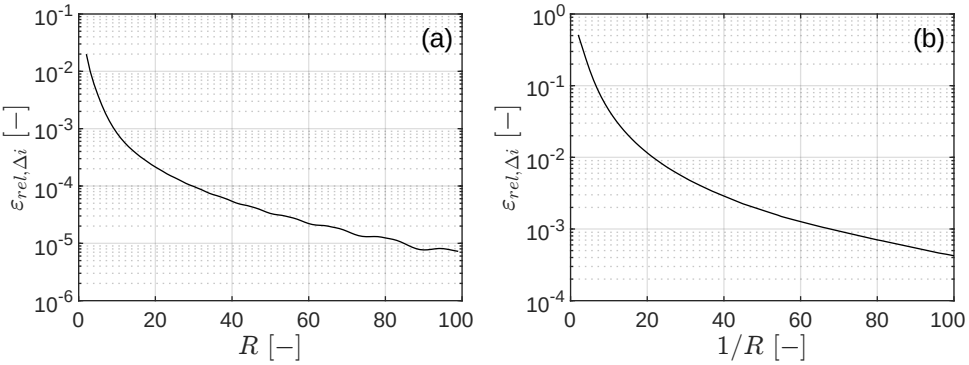


Figure 6.14: Inclination increase: relative error on Δi between the full-dynamics solutions and a) the SRP-based optimization solutions, b) the aerodynamic-based optimization solutions.

for different solar-sail characteristic accelerations and different levels of solar activity. In this way, a wide variety of scenarios is considered and a thorough analysis of the orbit change capabilities of solar sailing for Earth-bound missions is achieved. To consider a broad range of initial conditions representative of orbits commonly used for scientific LEO missions, the analyses are performed for circular, Sun-synchronous orbits with an LTAN at 0600 hrs (dawn/dusk) or 1200 hrs (noon/midnight) and altitudes ranging between 300 km and 1000 km. The characteristic accelerations considered vary between 10^{-2} and 10^{-1} mm s^{-2} in order to represent the current and near-future solar-sail technologies anticipated at the time of writing. For reference, at that time, NASA's ACS3 and NEA Scout missions had yet to be launched and they achieved solar-sail characteristic accelerations of $5.0 \cdot 10^{-2}$ and $6.3 \cdot 10^{-2}$ mm s^{-2}, respectively [107, 177]. Finally, to account for the effect of solar activity on the atmospheric density, two different starting dates are considered: September 23$^{\text{rd}}$, 2023 and September 23$^{\text{rd}}$, 2030, corresponding to epochs of maximum and minimum solar activity, respectively. It should be noted that these dates are chosen somewhat arbitrarily within longer-duration periods of solar maximum and minimum activity and correspond to the autumn equinoxes, for which the Sun "orbits" in the Earth's equatorial plane. Other dates within the periods of solar maximum/minimum can of course be considered, which would then correspond to slightly different orientations of the science orbit with respect to the Sun and, therefore, would lead to slightly different results of the analyses.

For each scenario, an orbit propagation of 10 days is performed using Matlab®'s *ode45* integrator, with absolute and relative tolerances of 10^{-12}. Consistent with the values obtained in 6.4, the averaged NRLMSISE-00 atmospheric density is used with $ApO = 25$ and $NpA = 4$. The POINT optimization method uses an optimized grid Σ found through $\Delta\Lambda = 1$ deg and $\Delta\mathcal{R} = 1.21$. Finally, the acceleration ratio domains considered are $\mathcal{R} \in [1/4, 55]$ and $\mathcal{R} \in [1/100, 30]$ for the orbit-raising and inclination-increase steering laws, respectively.

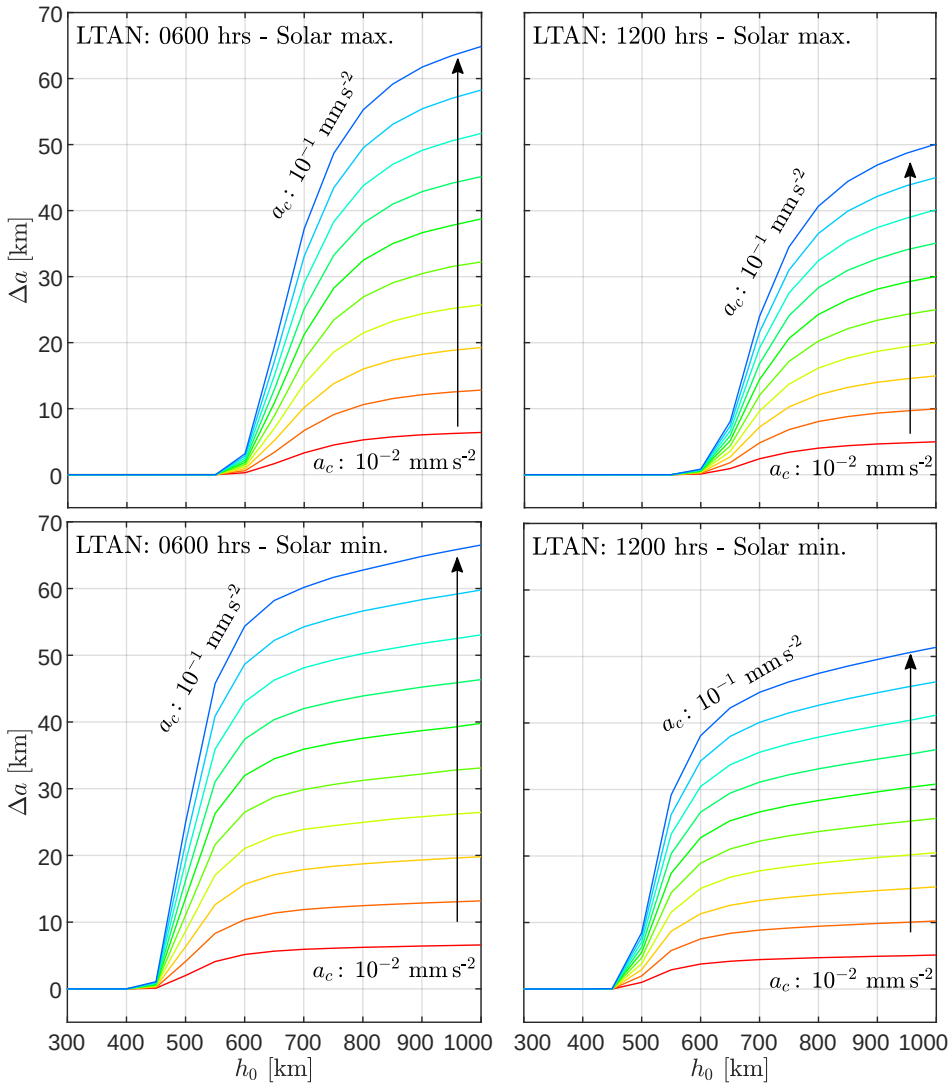


Figure 6.15: Orbit raising: SMA increase as a function of the initial altitude and solar-sail characteristic acceleration for different LTANs and intensities of solar activity. The characteristic acceleration increases in the direction of the arrows from 10^{-2} to 10^{-1} mm s^{-2} with a step size of 10^{-2} mm s^{-2}.

6.5.1. ORBIT RAISING

The results for the parametric analyses performed for the orbit-raising steering law appear in Fig. 6.15. The four plots display the increase in SMA achieved after 10 days for different combinations of LTAN and solar activity. Each plot shows 10 curves for 10 different values of the characteristic acceleration. The figure shows that, independently of the LTAN, the solar activity determines the minimum altitude for which orbit raising is still possible. This

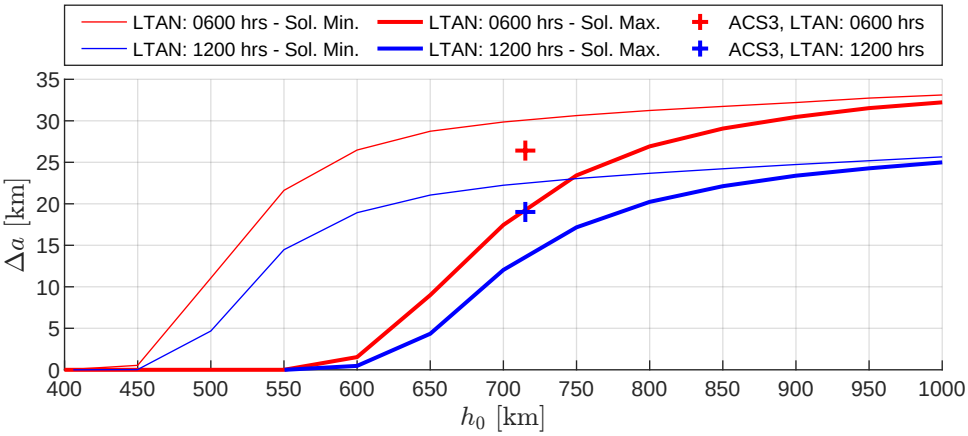


Figure 6.16: Orbit raising: SMA increase for ACS3's characteristic acceleration, $a_c = 5 \cdot 10^{-2}$ mm s^{-2}.

minimum altitude is approximately equal to 450 and 600 km for minimum and maximum solar activity, respectively, and therefore demonstrates the orbit-raising capabilities of solar sails above such altitudes. The plots also show that the effect of a different solar activity on Δa becomes negligible at high altitudes, as the curves asymptotically tend to the same values. At such high altitudes, the aerodynamic drag becomes negligible and similar SMA increases are found even for largely different solar activities. Comparison of the plots for different LTAN values and the same solar activity shows that the effect of changing the LTAN from 0600 hrs (dawn/dusk) to 1200 hrs (noon/midnight) reduces the SMA increase due to the presence of eclipses for a noon/midnight orbit.

The results in Fig. 6.15 for $a_c = 5.0 \cdot 10^{-2}$ mm s^{-2} are combined in Fig. 6.16 to gain further insights in the ranges of achievable SMA increase. For example, if one considers a specific LTAN, the two curves for minimum and maximum solar activity enclose the region of maximum SMA increase for any solar activity. A specific example is given by the two marks that represent the ACS3 mission with a simulation start date of July 1st, 2022. This date corresponds to an intermediate solar activity and, as such, the Δa values achieved for the ACS3 mission lie well within the above-mentioned region. Alternatively, the curves for a fixed solar activity but with different LTANs can be considered. Since LTANs at 0600 hrs and 1200 hrs represent the orbits with the shortest and longest eclipsing time, respectively, any initial orbit with an LTAN different from 0600 hrs or 1200 hrs will show an SMA increase within the region enclosed by these two curves. Figure 6.16 shows that the largest SMA increases are achieved at solar minimum and for an LTAN at 0600 hrs, whereas the smallest values for Δa are achieved at solar maximum and for an LTAN at 1200 hrs. These two curves correspond to the overall best and worst orbit-raising scenarios. For any circular, Sun-synchronous orbit the achievable increase in SMA is always enclosed by these curves.

The results in Figs. 6.15 and 6.16 can be used to conduct the preliminary design of solar-sail LEO missions. In fact, although the results are given only for a propagation time of 10 days, the achievable SMA increase for longer propagation times can be retrieved

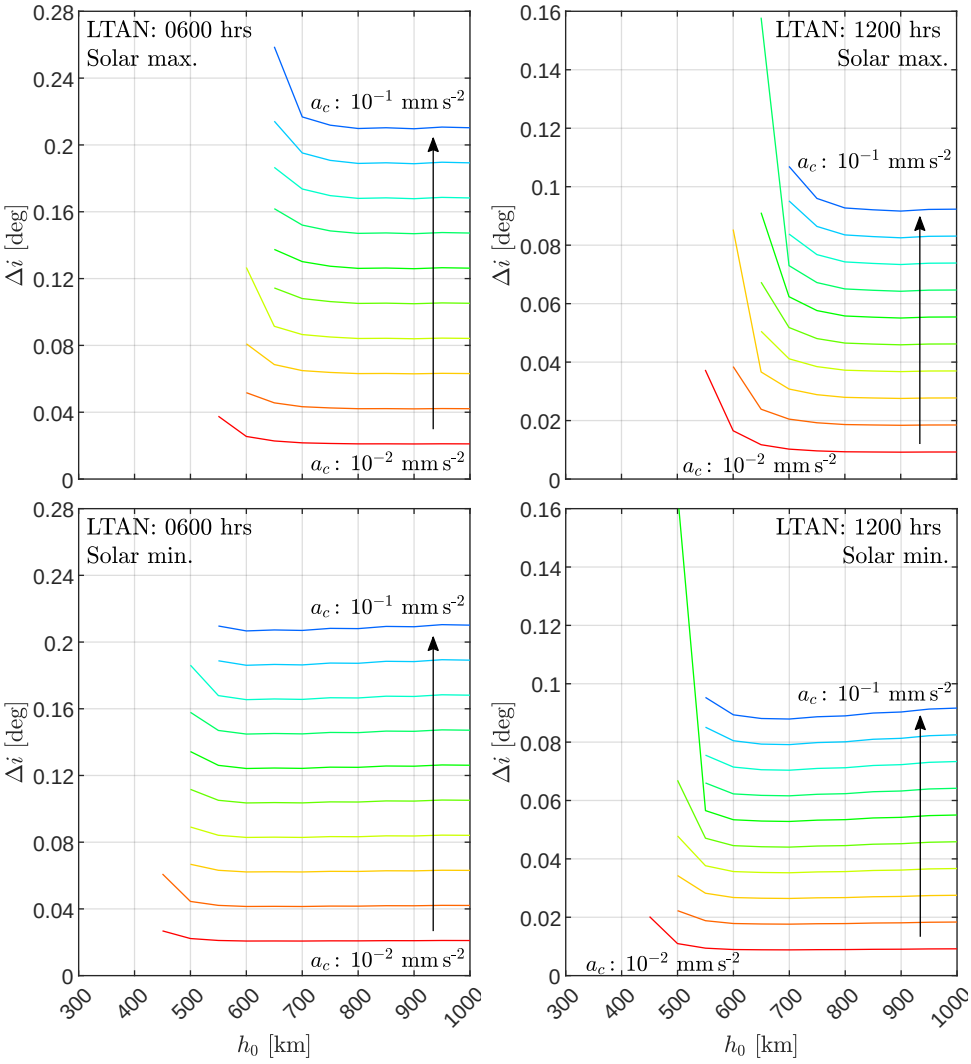


Figure 6.17: Inclination increase: inclination increase as a function of the initial altitude and solar-sail characteristic acceleration for different LTANs and intensities of solar activity. The characteristic acceleration increases in the direction of the arrows from 10^{-2} to 10^{-1} mm s^{-2} with a step size of 10^{-2} mm s^{-2}.

from the same results by consulting the plots in an iterative fashion: consider a given initial altitude, h_0, with an SMA increase Δa_0, then the same plot can be reused starting from a new altitude $h_1 = h_0 + \Delta a_0$ to retrieve Δa_1, which in turn is used to define h_2 and so forth. At each iteration of this process the mission duration increases by 10 days, so that the iterations can be stopped until the desired mission duration is obtained.

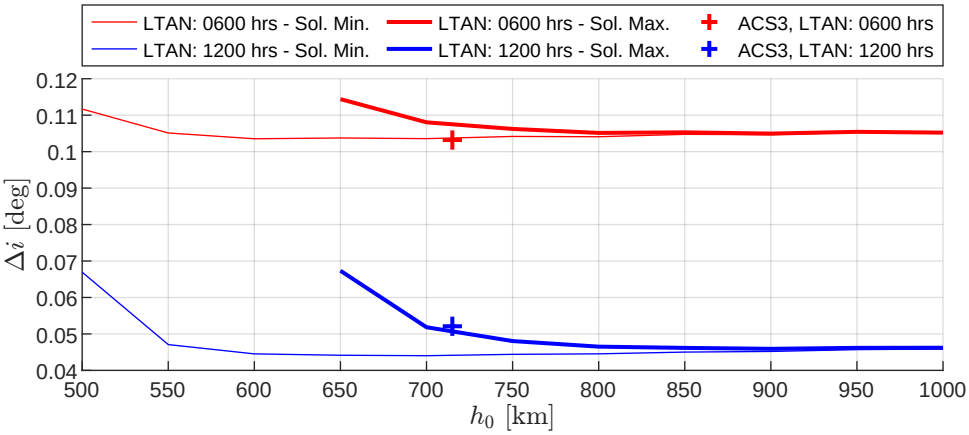


Figure 6.18: Inclination increase: inclination increase for ACS3's characteristic acceleration, $a_c = 5{\cdot}10^{-2}$ mm s^{-2}.

6.5.2. Inclination Increase

The results of the parametric analyses for the inclination-increase steering law appear in Fig. 6.17. The truncation of the curves at low altitude is due to a rapid loss in altitude when increasing the inclination under the effects of atmospheric drag. The orbit propagation is stopped when an altitude lower than 100 km is reached within 10 days. As can be seen, the altitude at which this condition occurs ranges between 400 and 650 km and depends on the characteristic acceleration, solar activity, and LTAN. An interesting trend which can be appreciated in all four plots of Fig. 6.17 is the steep gradient in the inclination increase for decreasing altitudes: when lowering the orbital altitude, not only drag increases, but also the aerodynamic lift, which provides the out-of-plane acceleration used to change the inclination. At higher altitudes, no significant change in the inclination increase as a function of altitude can be observed. Conversely, a strong correlation between the inclination increase and the solar-sail characteristic acceleration can be noted.

Similar to Fig. 6.16 for the orbit-raising case, Fig. 6.18 displays the variation in inclination increase for a characteristic acceleration of $a_c = 5.0 \cdot 10^{-2}$ mm s^{-2}, for minimum and maximum solar activity and LTANs at 0600 hrs and 1200 hrs. For increasing values of h_0, the results for the solar minimum case and solar maximum case converge to the same values. This is because the atmospheric density decreases and the inclination increase is produced solely by the SRP acceleration, which is equal in both cases. Fig. 6.18 also shows the inclination increases achievable by the ACS3 missions at an intermediate solar activity. As can be seen, the values for Δi fall slightly below or above the regions enclosed by the minimum and maximum solar activity. By further analyzing these results, it was found that these differences are due to the simulation start date of July 1st, 2022 which results in a different orientation of the ACS3's initial orbit with respect to the Sun than at the autumn equinox, and hence different values for Δi.

6.6. CONCLUSIONS

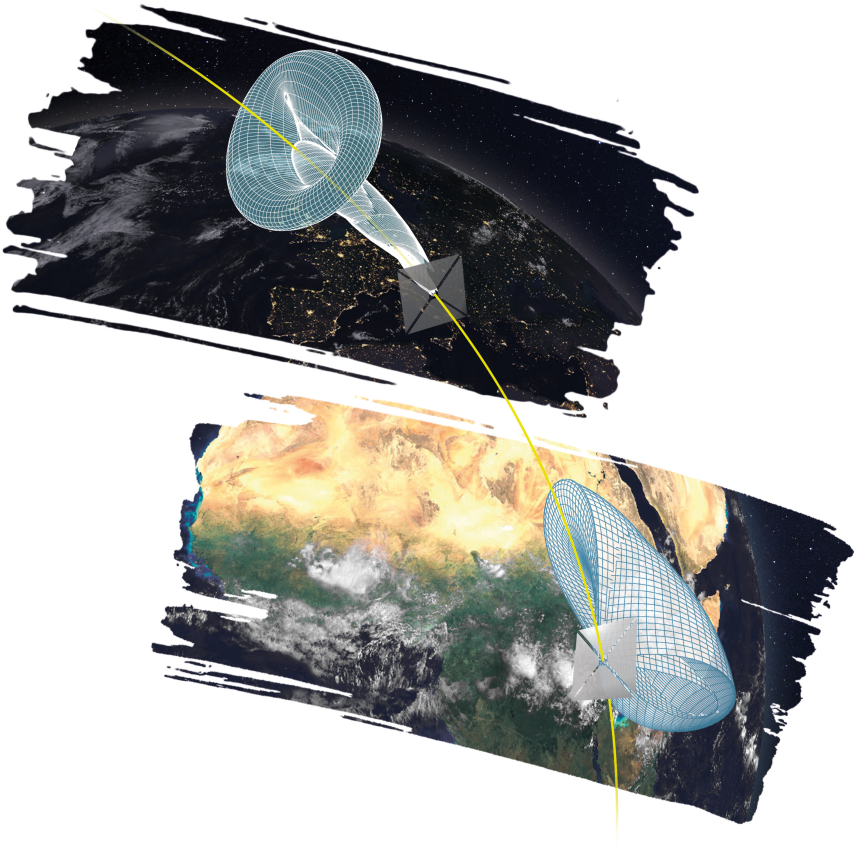
In this chapter a novel method to optimize Earth-bound solar-sail orbits in the presence of atmospheric drag has been presented and employed on a wide variety of scenarios. To reduce the computational effort required, an averaged atmospheric density model has been introduced and its performance has been tested, both with respect to its accuracy and runtime. The optimal control problem has been formulated and thoroughly analyzed for three different dynamical regimes. These are the solar radiation pressure (SRP)-dominated regime, the aerodynamic drag-dominated regime, and the full-dynamics (SRP + drag) regime, for which it has been shown that the optimal control problem is independent of the solar-sail loading parameter. To solve the full-dynamics optimal control problem, the POINT optimization method has been developed, which is based on a pre-run optimization phase and in-run interpolation phase. The pre-run optimization phase takes place before the trajectory propagation and aims to solve the optimal control problem for a broad range of scenarios, in order to store the corresponding optimal sail normal directions. Afterwards, the in-run interpolation of the optimal sail normal directions takes place at each integration time step during the propagation. All parameters used by the POINT method have been tuned and a validation test has been performed to demonstrate the accuracy and global validity of the optimal solutions found. The POINT method has been applied to an orbit-raising steering law and inclination-increase steering law on NASA's ACS3 mission and a range of other circular, Sun-synchronous orbits, differing from each other in the local time of the ascending node, the altitude, and the solar-sail characteristic acceleration. The results of the analyses show that the minimum altitude for which orbit raising is achievable varies between 450 and 600 km and strongly depends on the solar activity, while the local time of the ascending node affects the magnitude of the altitude increase. The inclination-increase steering law proved to be unsuited for orbits with altitudes below $400 \div 650$ km, as the sailcraft tends to de-orbit rapidly. Conversely, at high altitudes, increases in inclination are achievable, with their magnitude depending largely on the solar-sail characteristic acceleration.

ACKNOWLEDGEMENTS

Special thanks go to W. Keats Wilkie and Sarah M. Cook from NASA Langley Research Center, and Andrew Heaton from NASA Marshall Space Flight Center for the several fruitful discussions on the ACS3 mission and the valuable information shared.

7

High-fidelity Characterization of the Maneuvering Capabilities of Earth-bound Solar Sails



ABSTRACT

Solar sailing is a propulsion method that uses solar radiation pressure (SRP) as main source of thrust. However, in close proximity of the Earth, SRP is not the only acceleration governing the sailcraft dynamics, as atmospheric drag and the Earth's planetary radiation pressure (PRP) acceleration are also present. Because of their significant magnitudes relative to the SRP acceleration, these accelerations could potentially be exploited by the sail to maneuver more effectively around the Earth. Nevertheless, the majority of research conducted on Earth-bound solar sailing to date either neglects these accelerations or treats them as uncontrollable sources of perturbation. This hinders accurate prediction of the sailcraft's maneuvering capabilities and, accordingly, the accurate design of future solar-sail missions. In view of this, this chapter presents a high-fidelity trajectory optimization method which is then used to comprehensively characterize the maneuvering capabilities of solar sails in the near-Earth environment. The optimization algorithm is designed to change any orbital element in a locally optimal manner, while accounting for and optimally controlling the SRP, PRP, and aerodynamic accelerations. Following its introduction, the algorithm is exploited to characterize the maneuverability of Earth-bound solar sails, taking NASA's recently-launched ACS3 solar-sail mission as a baseline. Specifically, different sensitivity analyses are conducted to determine ACS3's orbit-raising and inclination-changing capabilities for a large set of orbits, times of the year, solar activities, and sailcraft characteristics. The results of this study not only enhance the understanding of ACS3's performance but also provide valuable insights for the mission design of future Earth-bound solar-sail missions for a variety of mission applications, such as active-debris removal and in-orbit servicing.

The content of this chapter has been accepted for publication in *Acta Astronautica*, see Ref. [419]:
Livio Carzana, Pieter Visser, and Jeannette Heiligers. "Characterization of Solar-sail Maneuvering Capabilities in a High-fidelity Near-Earth Dynamical Environment". In: *Acta Astronautica* (June 2026). DOI: https://doi.org/10.1016/j.actaastro.2026.06.049. Available online, in press.

Cover graphic by Vincenzo Bortone. The illustration shows two examples of full-dynamics acceleration envelope surfaces for a solar sail in low Earth orbit.

7.1. INTRODUCTION

Solar sailing is a propulsion method that takes advantage of solar radiation pressure (SRP) as primary source of thrust [2]. Therefore, solar sails are propellantless by nature, making them a promising alternative to chemical and conventional low-thrust propulsion systems, especially for long-duration mission applications. Due to its mission-enabling potential, solar sailing has drawn increasing attention in the scientific community over the past decades, resulting in several studies investigating its use for a variety of Earth-bound and interplanetary missions [107, 146, 386]. In addition, the increasing interest in solar sailing has also led to the development and launch of the first solar-sail missions, primarily used as technology demonstrators. Although particularly suited for heliocentric flight regimes, only a small number of solar sails have been launched into deep space, with IKAROS by the Japan Aerospace Exploration Agency (JAXA) being the only successful mission of this kind [91]. On the other hand, the vast majority of solar sails launched thus far has remained Earth-bound. Among these are for example NanoSail-D2 by the National Aeronautics and Space Administration (NASA) [103], LightSail 1 and 2 by The Planetary Society [109, 110], Gama's Alpha [124], and, most recently, the Advanced Composite Solar Sail System (ACS3) by NASA, which was launched in April 2024 to demonstrate the deployment and maneuvering capabilities of NASA's solar-sail technology [127].

Similar to ACS3, the majority of future solar-sail missions are expected to be Earth-bound, with the objective to assess or exploit the potential of solar sailing for different mission applications [388]. Compared to interplanetary space, sailcraft orbiting in proximity of the Earth are governed by particularly complex dynamics, which render mission design especially challenging. Indeed, compared to deep space, the near-Earth environment presents several sources of perturbations to the sailcraft dynamics, including those due to the Earth's gravity field, the presence of eclipses, atmospheric drag, and planetary radiation pressure (PRP). As discussed in Chapters 2 and 3, these perturbations can achieve significant magnitudes in the order of – or even larger than – the SRP acceleration. Therefore, taking them into account in the dynamics and sailcraft control is essential to accurately predict the sailcraft's maneuvering capabilities and enable the accurate design of future solar-sail missions. Despite this need, only limited research has been conducted on how to effectively leverage the aforementioned accelerations for the design of Earth-bound solar-sail missions. A number of studies have investigated the effects of atmospheric drag on the sailcraft dynamics, although only treating drag as a perturbation or focusing on its use for drag-sailing applications [212–216]. Outside the context of drag-sailing, research exploring the potential of aerodynamic acceleration as an exploitable means to maneuver solar sails remains limited. Within the available literature, works on the topic include Refs. [218–220], which investigate aerodynamics-based optimal control laws for maneuvering in the atmosphere, and the work presented in Chapter 6 of this dissertation, which provides a first-order analysis of the orbit-raising and inclination-changing capabilities of solar sails in low Earth orbit (LEO). Similarly, research investigating the effects of PRP on the solar-sail dynamics and control is also limited. In particular, Ref. [222] and Chapter 3 and 4 present different models for the PRP acceleration and analyze its perturbing effect on the motion of Earth-bound sailcraft. The only work exploring PRP-based solar-sail control is by Barles [223], who, however, does so by employing a simplistic, low-fidelity dynamical model. In order to properly assess

the maneuvering capabilities of Earth-bound sailcraft, it is essential to incorporate the SRP, PRP, and aerodynamic accelerations in the solar-sail dynamics and trajectory design using high-fidelity models. Accounting for high-fidelity dynamics in solar-sail trajectory design is rendered particularly challenging by the swift variations that the aforementioned accelerations undergo across the sailcraft trajectory. Indeed, these accelerations can vary considerably in magnitude and direction depending on the orbital altitude considered, the orientation of the orbit with respect to the Sun and Earth, the solar activity, time of the year, and sailcraft characteristics. Furthermore, especially in LEO, these accelerations are highly sensitive to the sailcraft orientation, as slight deviations in the solar-sail attitude profile can result in large acceleration variations that strongly affect maneuverability. As a consequence, to effectively leverage these accelerations, the need for trajectory design methods that can handle these rapidly changing dynamics and that are highly robust with respect to a broad range of orbital scenarios arises. To the best of the author's knowledge, no research has been conducted that accounts for the combined effect of the aforementioned accelerations on the sailcraft dynamics and, crucially, sailcraft control. Specifically, there exist no trajectory optimization method for Earth-bound solar sailing that can effectively leverage high-fidelity solar-sail dynamics in the control optimization process. This research gap hinders the detailed design of Earth-bound solar-sail trajectories and, along with it, the investigation into the potential of solar sailing for future Earth-bound mission applications.

In order to address this gap of knowledge, this chapter proposes a solar-sail trajectory optimization method specifically designed for planet-centered solar sailing, and uses it to fully characterize the maneuvering capabilities of Earth-orbiting sailcraft. The novel optimization method forms an extension to the locally optimal steering-law algorithm devised by McInnes [2], though not restricted to the assumption of ideal (perfectly reflecting) solar sails accelerated only by SRP. Indeed, the proposed optimization method accounts for, and exploits, the full high-fidelity sailcraft dynamics, which include (non-ideal) SRP, PRP, aerodynamic acceleration, and gravitational perturbations. Additionally, the optimizer was developed to be robust against several orbital scenarios and capable to generate any desired steering law. Following its description, the newly devised optimizer is employed in several large-scale parametric analyses. These analyses aim to assess the solar-sail orbit-raising and inclination-changing capabilities for a wide range of orbits, considering different Sun-Earth relative geometries, solar activities, and sailcraft characteristics, taking NASA's recently launched ACS3 mission as baseline. The results show that atmospheric drag is particularly dominant at low altitudes, hindering any form of maneuvering for altitudes below 465-655 km, depending on the solar activity and orbit orientation. The orbit orientation relative to the Sun and Earth – which is strictly related to potential presence of eclipses – is also found to affect the maneuvering performance significantly. Furthermore, it is found that PRP is beneficial for sailcraft maneuverability especially for eclipsing orbits, as accounting for PRP in the solar-sail control – as opposed to considering it as an uncontrollable perturbation – enables increases in orbit-raising and inclination-changing performances in the order of 5-10%. Lastly, the analyses also highlight an approximately linear correlation between the mass-to-area ratio of the sailcraft and its maneuvering capabilities, which facilitates the application of the results to a wide range of sailcraft specifics.

The remainder of this chapter is structured as follows. First, the high-fidelity dynamics governing the motion of Earth-bound sailcraft are presented in Section 7.2. Next, Section 7.3 formulates the optimization problem to determine the orbit-raising and inclination-changing steering laws. Thereafter, the newly devised optimization method is fully described and tuning of different optimization settings is discussed. Section 7.4 then presents an analysis to characterize the near-Earth dynamical environment. This analysis supports the discussion of the sensitivity analyses conducted in Section 7.5 to characterize the maneuvering capabilities of Earth-bound solar sails. Finally, Section 7.6 presents the conclusions of the work.

7.2. DYNAMICAL MODEL

The dynamics of a solar sail in proximity of the Earth can be expressed within an Earth-centered pseudo-inertial frame $O_I(\hat{\boldsymbol{x}}, \hat{\boldsymbol{y}}, \hat{\boldsymbol{z}})$ with the $\hat{\boldsymbol{z}}$-axis direction pointing perpendicular to the mean equatorial plane at January 1$^{\text{st}}$, 2000 and towards the North Pole, the $\hat{\boldsymbol{x}}$-axis direction pointing towards the mean vernal equinox of that same epoch, and the $\hat{\boldsymbol{y}}$-axis direction completing the right-handed frame. Within this frame, the equations of motion can be expressed as:

$$\ddot{\boldsymbol{r}} + \frac{\mu}{r^3}\boldsymbol{r} = \boldsymbol{a}_{J2} + \boldsymbol{a}_{SRP} + \boldsymbol{a}_{PRP} + \boldsymbol{a}_{Aero} \tag{7.1}$$

In Eq. 7.1, the dot notation indicates differentiation with respect to time, $\boldsymbol{r} = [x, y, z]^T$ is the sailcraft position vector, with x, y, and z denoting the Cartesian coordinates of the sailcraft, $r = \|\boldsymbol{r}\|$, $\mu = 398600.4415\ \text{km}^3/\text{s}^2$ is the Earth gravitational parameter of the geopotential Joint Gravity Model (JGM) 2 [277, 308], $\boldsymbol{a}_{J2}$ is the acceleration due to the Earth's J_2 spherical harmonics coefficient, and $\boldsymbol{a}_{SRP}$, $\boldsymbol{a}_{PRP}$, and $\boldsymbol{a}_{Aero}$ are the SRP, PRP, and aerodynamic accelerations, respectively. In the following sections, the formal definitions of these accelerations and the reference sailcraft characteristics used throughout the remainder of the chapter are presented.

It should be noted that, while the above dynamics consider the Earth's J_2 gravitational acceleration, they neglect other sources of gravitational perturbations, notably, the gravitational accelerations due to the Sun and the Moon, and the higher-order terms of the Earth's gravity field. These accelerations have been neglected because they are orders of magnitude smaller than the Earth's J_2 gravitational acceleration, and therefore they affect the dynamics only to a very minor extent. Furthermore, the solar and lunar gravitational accelerations induce secular variations in the inclination [308] – an orbital element used in the analyses of this chapter to assess sailcraft maneuverability. Consequently, excluding these accelerations from the dynamics also facilitates a clearer investigation into the effects of the SRP, PRP, and aerodynamic accelerations on the solar-sail maneuvering capabilities.

7.2.1. J_2 GRAVITATIONAL ACCELERATION

The Earth's J_2 gravitational acceleration is defined as:

$$\boldsymbol{a}_{J2} = -\frac{3}{2}\frac{R_\oplus^2}{r^5}\mu J_2\left[\left(x\hat{\boldsymbol{x}} + y\hat{\boldsymbol{y}}\right)\left(1 - 5\frac{z^2}{r^2}\right) + z\hat{\boldsymbol{z}}\left(3 - 5\frac{z^2}{r^2}\right)\right] \tag{7.2}$$

where $R_\oplus = 6378.1363$ km and $J_2 = 1.082626925639 \cdot 10^{-3}$ are the Earth's radius and J_2 gravitational field constant of the JGM 2 model [277, 308], respectively.

7.2.2. SOLAR RADIATION PRESSURE ACCELERATION

The SRP acceleration is modeled using the optical sail model devised by McInnes [2]. This model accounts for the reflection, absorption, and emission properties of the sail, assuming that only the front of the sail is exposed to sunlight. When using this model, the SRP acceleration is given by:

$$\boldsymbol{a}_{SRP} = \boldsymbol{a}_{SRP,n} + \boldsymbol{a}_{SRP,t} \tag{7.3}$$

where $\boldsymbol{a}_{SRP,n}$ and $\boldsymbol{a}_{SRP,t}$ are the acceleration components normal and tangential to the sail plane, respectively. These are defined as:

$$\begin{aligned} \boldsymbol{a}_{SRP,n} = \nu \frac{a_c}{2} \Big[& \left(1 + \hat{r}_f s_f\right) \cos^2(\alpha_\odot) \; + \\ & \left(1 - s_f\right) \hat{r}_f B_f \cos\alpha_\odot \; + \\ & \left(1 - \hat{r}_f\right) \frac{\varepsilon_f B_f - \varepsilon_b B_b}{\varepsilon_f + \varepsilon_b} \cos\alpha_\odot \Big] \hat{\boldsymbol{n}} \end{aligned} \tag{7.4}$$

$$\boldsymbol{a}_{SRP,t} = \nu \frac{a_c}{2} \left(1 - \hat{r}_f s_f\right) \cos\alpha_\odot \sin\alpha_\odot \; \hat{\boldsymbol{t}} \tag{7.5}$$

In Eqs. 7.4 and 7.5, a_c represents the solar-sail characteristic acceleration, that is, the maximum achievable SRP acceleration at 1 AU from the Sun if the sail was perfectly reflecting. Its value provides a measure of the sailcraft thrusting performance and its definition is given by:

$$a_c = \frac{2 S_{TSI}}{c\sigma} \tag{7.6}$$

where $S_{TSI} = 1361$ W/m^2 is the solar flux at Earth [420], $c = 299792.458$ km/s is the speed of light in vacuum [390], and σ is the sailcraft mass-to-area ratio, also referred to as the loading parameter. In Eqs. 7.4 and 7.5, $\nu \in [0,1]$ denotes the shadow factor, which accounts for the effect of eclipses as per the conical shadow model of Ref. [231] and its value ranges from 0 (no sunlight reaches the sail) to 1 (sail completely illuminated). The angle $\alpha_\odot \in [0, \pi/2]$ represents the so-called sunlight pitch angle measured between the instantaneous Sun-to-sailcraft direction, $\hat{\boldsymbol{s}}$ – also referred to as sunlight direction in the following – and the sail normal direction with positive component along $\hat{\boldsymbol{s}}$, $\hat{\boldsymbol{n}}$, see Fig. 7.1a. The direction $\hat{\boldsymbol{t}}$ represents the sail transversal direction defined as:

$$\hat{\boldsymbol{t}} = \hat{\boldsymbol{n}} \times \frac{\hat{\boldsymbol{s}} \times \hat{\boldsymbol{n}}}{\|\hat{\boldsymbol{s}} \times \hat{\boldsymbol{n}}\|} \tag{7.7}$$

Finally, the symbols r, s, B, and ε represent the reflectivity, specular reflection coefficient, non-Lambertian reflection coefficient, and emissivity of the sail, respectively, with the subscripts "f" and "b" indicating whether the optical coefficient refers to the front or back of the sail.

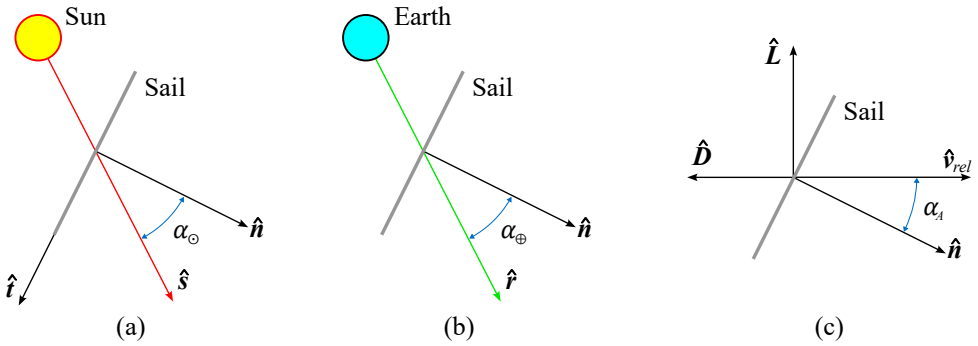


Figure 7.1: Reference directions and pitch angles to compute the (a) SRP acceleration, (b) PRP acceleration, and (c) aerodynamic acceleration.

7.2.3. PLANETARY RADIATION PRESSURE ACCELERATION

The planetary radiation emitted by Earth comprises two components, namely, blackbody radiation and albedo radiation. The former is infrared radiation emitted by the Earth itself to achieve thermal balance, whereas the latter represents the fraction of sunlight reflected by the Earth, emitted in the visible spectrum. These two types of radiation vary across the Earth's surface in a non-uniform manner, as their intensities depend on the geographical location considered and – specifically for albedo radiation – on the illumination condition of said location. Consequently, to accurately represent the distribution of planetary radiation across the Earth and the corresponding PRP acceleration exerted on the sailcraft, a PRP acceleration model that takes into account the above aspects is required. With this in mind, in this chapter the PRP acceleration, $\boldsymbol{a}_{PRP}$, is modeled as per the spherical sinusoidal model presented in Chapter 4, which allows to express the PRP acceleration of optical solar sails analytically and with high accuracy. In order to represent the geographical distribution of the blackbody radiation flux, the model assumes it to vary sinusoidally with latitude, with a maximum at the equator. Similarly, the variation in albedo radiation flux across the Earth's surface is modeled assuming that the albedo coefficient varies sinusoidally with latitude (with maxima at the poles) and, additionally, taking into account the illumination conditions of the Earth's surface through a so-called phase function. This function is maximum at the subsolar point and decreases moving toward the dark side of the Earth, where it attains a value of zero, indicating the complete absence of albedo radiation. Finally, the planetary radiation flux at the sail's location is determined by assuming that the blackbody and albedo radiation fluxes found are uniformly spread over the visible surface of the Earth as seen from the sailcraft. In this way, the Earth is locally approximated as an isotropic radiation source, allowing the PRP acceleration, $\boldsymbol{a}_{PRP}$, to be expressed analytically. As discussed in Section 4.3, this approximation introduces an error, but its impact on sailcraft maneuverability is limited, as relative errors compared to a high-fidelity numerical model are consistently found to be below 1% across several orbital scenarios. While the full mathematical description of the spherical sinusoidal PRP acceleration model is not discussed here for conciseness, the reader is referred to Chapters 3 and 4 for further details.

In the model presented above, the PRP acceleration, $\boldsymbol{a}_{PRP}$, depends only on the sail-

craft altitude, its relative position with respect to the Earth and Sun, and, importantly, its orientation. Similar to the way the SRP acceleration varies with the sunlight pitch angle, the PRP acceleration varies with the so-called planetary pitch angle, $\alpha_{\oplus}$, measured between the radial and sail normal directions, see Fig. 7.1b. In particular, for $\alpha_{\oplus}$ values close to zero, the sail is oriented perpendicular to the radial direction, $\hat{\boldsymbol{r}}$, resulting in the largest magnitude of the $\boldsymbol{a}_{PRP}$ vector. Conversely, for $\alpha_{\oplus}$ values close to 90 deg, the sail is oriented edgewise to the radial direction and both of its sides are exposed to planetary radiation with large incidence angles. As a consequence, the radiation pressures produced on the sides of the sail counteract each other and take on small magnitudes, thus resulting in a small overall PRP acceleration.

Finally, the spherical sinusoidal PRP acceleration model also accounts for the optical properties of the sail, considering distinct optical coefficients to compute the blackbody radiation pressure (BBRP) and albedo radiation pressure (ARP) accelerations. This differentiation is necessary as blackbody radiation is primarily emitted in the infrared range of the electromagnetic spectrum whereas albedo radiation is defined within the visible part of the spectrum, similar to solar radiation. In view of the latter, ARP acceleration is computed using the same optical coefficients as for SRP acceleration, as shown in Section 7.2.5.

7.2.4. AERODYNAMIC ACCELERATION

The sailcraft aerodynamics are modeled assuming the sail to behave as a flat plate in hyperthermal free-molecular flow conditions, in line with Chapter 6 and other works treating drag-perturbed solar-sail dynamics [220, 341]. Under these assumptions, the aerodynamic acceleration is defined as:

$$\boldsymbol{a}_{Aero} = \frac{1}{2}\frac{\rho v_{rel}^2}{\sigma}\left(C_D\hat{\boldsymbol{D}} + C_L\hat{\boldsymbol{L}}\right) \tag{7.8}$$

where ρ is the atmospheric density, v_{rel} is the sailcraft relative velocity with respect to the atmosphere (assumed to be Earth-fixed), C_D and C_L are the drag and lift coefficients, respectively, and $\hat{\boldsymbol{D}}$ and $\hat{\boldsymbol{L}}$ are the drag and lift directions, respectively. In this chapter, the atmospheric density is computed through an averaging method based on the NRLMSISE-00 model [289], as detailed in Section 6.2.2.2. The underlying NRLMSISE-00 model is employed with solar radio flux at 10.7 cm and geomagnetic activity relative to the 50$^{\text{th}}$ percentile, retrieved from the Marshall Space Flight Center's forecast of May 2025 [294]. The drag direction, $\hat{\boldsymbol{D}}$, points anti-parallel to the direction of the sailcraft relative velocity with respect to the atmosphere, $\hat{\boldsymbol{v}}_{rel}$, while the lift direction, $\hat{\boldsymbol{L}}$, points perpendicular to $\hat{\boldsymbol{v}}_{rel}$ and is coplanar with $\hat{\boldsymbol{n}}$ and $\hat{\boldsymbol{v}}_{rel}$, see Fig. 7.1c. The drag and lift coefficients are defined through the formulation by Schaaf and Chambre [348], valid for flat plates in hyperthermal free-molecular flow conditions:

$$C_D = 2\left[\sigma_T + \sigma_N V_R|\cos\alpha_A| + \left(2-\sigma_N-\sigma_T\right)\cos^2(\alpha_A)\right]|\cos\alpha_A| \tag{7.9}$$

$$C_L = 2\left[\sigma_N V_R + \left(2-\sigma_N-\sigma_T\right)|\cos\alpha_A|\right]|\cos\alpha_A|\sin\alpha_A \tag{7.10}$$

where σ_N and σ_T denote the normal and tangential momentum accommodation coefficients, respectively, V_R is the ratio of the average velocity of the atmospheric particles

Table 7.1: ACS3 sailcraft specifics.[1]

Hardware	Mass	16 kg
	Area	80 m^2
	σ	0.2 kg/m^2
	a_c	$4.540 \cdot 10^{-2}$ mm/s^2
Optical properties	$\boldsymbol{oc}_{SW}$	[0.90, 0.82, 0.79, 0.03, 0.43, 0.53, 2/3, 0.60]
	$\boldsymbol{oc}_{LW}$	[0.97, 0.82, 0.79, 0.03, 0.40, 0.53, 2/3, 0.60]
Aerodynamics	σ_N	0.8
	σ_T	0.8
	V_R	0.05

Note: Optical coefficients given as $\left[\hat{r}_f, s_f, B_f, \varepsilon_f, \hat{r}_b, s_b, B_b, \varepsilon_b\right]$.

diffusively reflected by the sail and the sailcraft velocity relative to the atmosphere, and $\alpha_A \in [0, \pi]$ represents the aerodynamic pitch angle between $\hat{\boldsymbol{v}}_{rel}$ and $\hat{\boldsymbol{n}}$, see Fig. 7.1c.

7.2.5. REFERENCE SAILCRAFT SPECIFICS

This chapter makes use of NASA's ACS3 mission as baseline for all analyses. ACS3 was launched on 23 April 2024 in a circular, Sun-synchronous orbit with the local time of the ascending node (LTAN) at 22:30 hrs, and deployed its sail on 29 August 2024. Its specifics are given in Table 7.1 which will be used throughout the remainder of this chapter, unless stated otherwise.[1] In Table 7.1, $\boldsymbol{oc}_{SW}$ and $\boldsymbol{oc}_{LW}$ represent the sets of optical coefficients corresponding to the shortwave range and longwave ranges of the electromagnetic spectrum, respectively, see Section 2.4.4, given in the following order: $\left[\hat{r}_f, s_f, B_f, \varepsilon_f, \hat{r}_b, s_b, B_b, \varepsilon_b\right]$. The coefficients $\boldsymbol{oc}_{SW}$ are used to compute the SRP and ARP accelerations, whereas the coefficients $\boldsymbol{oc}_{LW}$ are used to compute the BBRP acceleration.

7.3. OPTIMAL CONTROL PROBLEM

The formulation of the trajectory optimization problem considered in this chapter draws on the locally optimal control theory developed by McInnes in Ref. [2], which allows to compute steering laws to optimally increase any given orbital element and is valid for perfectly reflecting (ideal) solar sails under the effect of SRP. Similar to Ref. [2], the optimization problem considered in this chapter aims to find the optimal control vector $\boldsymbol{u}(t) = \hat{\boldsymbol{n}}(t)$ that maximizes the cost function $J(\boldsymbol{u}(t)) = \dot{\alpha}(\boldsymbol{u}(t))$ at each moment in time, where α denotes an orbital element of interest. When the Lagrange planetary equations are used to express α, the cost function can be formulated as [2]:

$$J(\boldsymbol{u}(t)) = \dot{\alpha}(\boldsymbol{u}(t)) = \boldsymbol{\lambda} \cdot \boldsymbol{a}(\boldsymbol{u}(t)) \tag{7.11}$$

[1] ACS3 mass, sail area, and optical coefficients taken from personal communication with W.K. Wilkie, Principal Investigator of the ACS3 mission, NASA Langley Research, March 2024.

where $\boldsymbol{a}$ is the sum of all accelerations acting on the sailcraft excluding the acceleration due to central gravity, and $\boldsymbol{\lambda}$ denotes the so-called primer vector, whose direction $\hat{\boldsymbol{\lambda}}$ represents the instantaneous optimal thrust direction to maximize the rate of change of the orbital element of interest, œ. Equation 7.11 highlights that, in order to maximize $\dot{\text{œ}}$, the sailcraft should be oriented in a way that produces the largest acceleration component along $\hat{\boldsymbol{\lambda}}$. Unlike the locally optimal control theory developed by McInnes, for which $\boldsymbol{a}$ is equal to just the ideal SRP acceleration, in this chapter the acceleration $\boldsymbol{a}$ is based on the high-fidelity dynamics introduced in Section 7.2 and corresponds to the right-hand side of Eq. 7.1. As can be noted, $\boldsymbol{a}$ also includes the acceleration due to the Earth's J2 gravitational field, $\boldsymbol{a}_{J2}$. However, because this acceleration – as well as any other gravitational acceleration – do not depend on the sailcraft attitude control $\boldsymbol{u}(t) = \hat{\boldsymbol{n}}(t)$, they do not affect the optimization problem. Therefore, hereinafter $\boldsymbol{a}$ will be considered the sum of only the *attitude-dependent* accelerations acting on the sail – that is, the SRP, PRP, and aerodynamic accelerations – without loss of generality.

While the definition of the optimization problem given above – as well as its characterization and resolution discussed in the Sections 7.3.1 and 7.3.2, respectively – are generally valid for any target orbital element, in the remainder of this chapter discussion will focus only on two orbital elements of interest: the semi-major axis, a, and inclination, i. The corresponding steering laws will be referred to as orbit-raising and deorbit-safe inclination-changing steering laws, respectively. The wording "orbit-raising" stems from the fact that orbital altitude is defined as $h = (a - R_{\oplus})$ in this chapter, and therefore changes in semi-major axis correspond to changes in altitude. On the other hand, "deorbit-safe" indicates that the inclination-changing steering law is designed specifically to prevent altitude losses. Details on the definition of the deorbit-safe inclination-changing steering law are presented in Section 7.3.3. Then, Section 7.3.4 discusses the tuning of the optimization settings employed in the sensitivity analyses in Section 7.5.

7.3.1. CHARACTERIZATION

The complexity of the optimization problem at hand is largely dependent on the dynamics considered, which in turn affect the definition of the attitude-dependent acceleration $\boldsymbol{a}$. As demonstrated by McInnes [2], when considering an ideal solar sail subject only to SRP, $J(\boldsymbol{u}(t))$ takes on a simple form which allows for an analytical resolution of the optimal control problem. Conversely, as shown in Chapter 6, accounting also for the aerodynamics increases the complexity of the optimization problem significantly, therefore allowing only for a numerical solution. Similarly, the solution of the optimization problem in this chapter can also only be achieved through numerical methods. This is due to the high-fidelity dynamics employed, which account for the optical properties of the sail and the combined effect of SRP, PRP, and aerodynamics, as discussed in Section 7.2.

In order to visualize the complexity of the optimization problem associated with these dynamics, Fig. 7.2a displays the so-called acceleration envelopes (AEs) of the SRP, PRP, and aerodynamic accelerations, that is, the sets of all possible SRP, PRP, and aerodynamic accelerations achieved by varying the sailcraft's attitude. The plot illustrates an example scenario in which the sunlight direction, $\hat{\boldsymbol{s}}$, is perpendicular to the drag direction, $\hat{\boldsymbol{D}}$, and anti-parallel to the radial direction, $\hat{\boldsymbol{r}}$. Also, the maximum SRP and aerodynamic accelerations are of the same magnitude, while the maximum PRP acceleration is 25% of

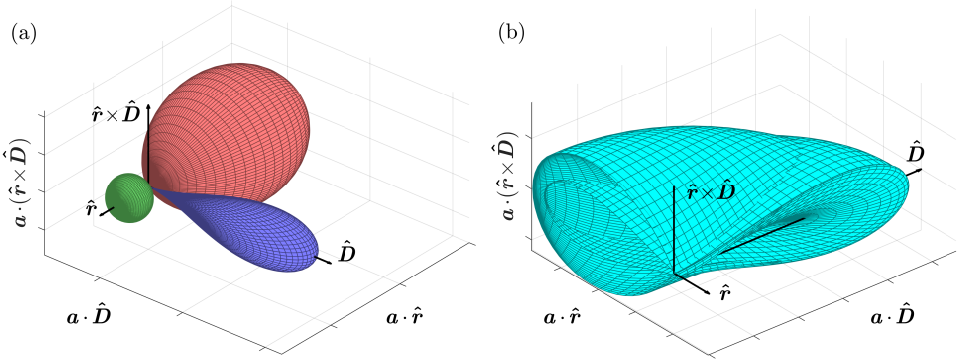


Figure 7.2: Acceleration envelope surfaces of (a) the SRP, PRP, and aerodynamic accelerations (in red, green, and blue, respectively), and (b) the resulting total acceleration.

that magnitude. As will be discussed in Section 7.4, this scenario can occur for sailcraft flying in low Earth orbit, in proximity of the subsolar point. When the SRP, PRP, and aerodynamic accelerations are summed, the resulting AE of the total acceleration $\boldsymbol{a}$ – referred to as full-dynamics AE – takes on the highly nonlinear, self-intersecting shape illustrated in Fig. 7.2b. In the context of the optimization problem at hand, maximizing $J(\boldsymbol{u}(t))$ is equivalent to determining the point of the full-dynamics AE that is tangent to a plane orthogonal to $\hat{\boldsymbol{\lambda}}$. This task is rendered difficult by the non-convex shape of the surface and the fact that it features sharp edges, see Fig. 7.2b. Indeed, due to the non-convex shape of the full-dynamics AE, small variations in the orientation of the above-mentioned plane induce large displacements of the point that is tangent to that plane, whereas the presence of sharp edges renders the tangency problem degenerate. The combination of these two effects therefore makes the optimal attitude very sensitive to the direction $\hat{\boldsymbol{\lambda}}$. Additional complexity is also introduced by the variation of the direction $\hat{\boldsymbol{\lambda}}$ over time with the instantaneous state of the sailcraft. Notably, this variation can even take place discontinuously for some steering laws. Among these is, for example, the inclination-changing steering law, which prescribes $\hat{\boldsymbol{\lambda}}$ to rotate instantly by 180 deg every half orbit [2]. Similarly, also the shape of the full-dynamics AE varies over time and can undergo abrupt changes, particularly when entering or exiting eclipse, where the SRP and ARP acceleration magnitudes vary swiftly.

From an optimization standpoint, the above-described geometrical intricacies of the optimization problem correspond to an extremely complex cost function characterized by a number of properties. The cost function varies over time and, in some scenarios, can do so discontinuously. At each time instant, the cost function is often also characterized by the presence of different local optima, which can be located in non-differentiable regions of the control phase space. These regions correspond to the sharp edges of the full-dynamics AE observed in Fig. 7.2b, which in turn correspond to sail orientations yielding no SRP or aerodynamic accelerations. The sharpness of the full-dynamics AE in these regions also indicates a particularly strong sensitivity of the cost function to the sail

attitude, thereby adding to the overall complexity of the problem.

In view of the above, resolution of the optimization problem requires a robust technique that is effective across all potential (discontinuous) variations in the cost function, can effectively explore the control phase space to avoid convergence to local optima and locate the global optimum, and is capable of handling non-differentiable cost functions. Furthermore, computational efficiency is also paramount, given the need to perform a large number of analyses to characterize the maneuverability of sailcraft in the near-Earth environment, as will be discussed in Section 7.5.

In the literature, a range of optimization methods has been used to address similar solar-sail trajectory optimization problems. In Chapter 6, Earth-bound trajectories of ideal solar sails under the effect of SRP and aerodynamics have been optimized using a so-called Pre-run Optimization and in-run INTerpolation (POINT) method. This method involves a four-dimensional optimization phase performed before propagation of the sailcraft dynamics, followed by an interpolation phase to find the optimal control at each moment in time during propagation. In a first attempt to solve the optimization problem addressed in this chapter, the POINT method was extended to also include the PRP acceleration. Although effective, the newly devised method was found to yield excessively long run times owing to the increased number of dimensions of the pre-run optimization phase, which increased from four to up to eight. Despite efforts to reduce the high-dimensional search space through pruning, the exponential growth in complexity associated with the curse of dimensionality ultimately hindered a time-efficient resolution of the problem. Alternative trajectory optimization methods widely used in the literature include direct and indirect methods [365–367, 369], and methods based on (differential) dynamic programming [373, 374, 421]. All of these methods, however, require the cost function to be time-continuous and generally differentiable – conditions that are not met in the optimization problem under investigation. Furthermore, the effectiveness of these methods often depends on their optimization settings, which need to be appropriately tuned for each optimization scenario at hand. Since the sensitivity analyses in Section 7.5 require performing several trajectory optimizations, the inability to select robust optimization settings effective across all scenarios further limits the applicability of the above-mentioned optimization methods to the analyses in this chapter.

In view of the above, this chapter presents an optimization technique named Memory-based Adaptive Coordinate-searcH Optimization (MACHO) and developed ad-hoc for the optimization problem at hand. As the name suggests, the optimization method uses a derivative-free, coordinate-search algorithm [422] that dynamically adapts the coordinate system of the control phase space in order to handle the non-differentiable regions of the cost function. Because coordinate-search algorithms are local optimization algorithms that require an initial guess, the proposed optimization method also includes an automatic generation of initial guesses. This procedure relies on the memory of the optimum found at a previous time, and on periodic global samplings of the control phase space, thus ensuring that possible time discontinuities in the cost function are accounted for. Consequently, the optimization approach used in MACHO facilitates convergence to the true optimum at every time instant, regardless of the shape of the cost function, time-continuity, differentiability, and/or potential presence of local optima. In addition, the algorithm is robust, as it relies on only three optimization settings which, once tuned,

can be used for a broad range of orbital scenarios, see Section 7.3.4.

7.3.2. OPTIMIZATION ALGORITHM

The MACHO optimization method aims to find the optimum of the cost function at each moment in time by exploring the control phase space at two different resolutions: first globally and then locally. Accordingly, two subsequent stages of the optimization are defined:

- **Global optimization stage**. In this stage, the region of global optimality of the control phase space is identified using two alternative approaches. On the one hand, a grid search can be conducted considering a coarse mesh of points covering the entire phase space, which results in a "coarse" global optimum. On the other hand, the location of the coarse optimum can be assumed to coincide with the location of the optimum at an earlier time during propagation of the dynamics. This second approach allows for a reduced computational burden. However, it can only be used over time spans wherein the cost function retains time continuity.

- **Local optimization stage**. Following the global optimization stage, the local optimization stage uses the coarse global optimum as initial guess to refine the solution. To this aim, a fine mesh of points covering a small region of the phase space around the initial guess is considered. Then, a grid search is performed over the fine mesh, yielding an updated location of the optimum, which is then used as center point of a new fine mesh. Throughout this iterative routine – which represents the coordinate-search algorithm – coordinate transformations of the phase space are performed dynamically. In this way, the fine meshes are defined in the most convenient coordinate system to account for the non-differentiable regions of the phase space, thus allowing convergence to the optimum even when it lies within such regions.

A pseudocode summary of the optimization algorithm is presented in Algorithm 1. The algorithm is called each time the sailcraft dynamics need to be evaluated during the trajectory propagation, assumed to end at time $t = t_f$. As shown in the pseudocode, the algorithm starts by evaluating the optimal thrust direction $\hat{\boldsymbol{\lambda}}$ through the Lagrange planetary equation and – as explained in Section 7.3.3 for the inclination-changing case – through steering laws blending. Thereafter, three different optimization reference frames – that is, the frames within which the coarse and fine meshes will be defined – are introduced. These frames are generally denoted by R, and together they form the set $\mathcal{R}$, see line 3. The frames are defined by selecting a reference direction for their first axis, whereas the directions of the other two axes can be chosen arbitrarily, as they do not affect the optimization. The reference directions are the sunlight direction $\hat{\boldsymbol{s}}$, radial direction $\hat{\boldsymbol{r}}$, and relative-velocity direction $\hat{\boldsymbol{v}}_{rel}$, which correspond to the so-called sunlight, radial, and relative-velocity optimization frames, respectively. To facilitate visualization, Fig. 7.3 shows a generic optimization frame, $R(\hat{\boldsymbol{x}}_o, \hat{\boldsymbol{y}}_o, \hat{\boldsymbol{z}}_o)$, with the $\hat{\boldsymbol{x}}_o$-axis direction pointing along the reference direction, and the $\hat{\boldsymbol{y}}_o$- and $\hat{\boldsymbol{z}}_o$-axis directions pointing along arbitrary directions completing the right-handed frame. Within frame R, the sail normal direction, $\hat{\boldsymbol{n}}$, can be identified by two angles: the pitch angle, α, and clock angle, δ, which form the control phase space $(\alpha, \delta) \in \mathbb{R}^2$. The pitch angle is measured between the $\hat{\boldsymbol{x}}_o$-axis direction

Algorithm 1: Optimization Algorithm

1: **while** $(t < t_f)$ **do**
2: $\hat{\boldsymbol{\lambda}} \leftarrow$ Lagrange Planetary Eqs. (and steering laws blending)
3: $\mathcal{R} \leftarrow$ Set of optimization frames with reference directions $\{\hat{\boldsymbol{s}}, \hat{\boldsymbol{r}}, \hat{\boldsymbol{v}}_{rel}\}$
4: $\mathcal{S} \leftarrow$ Set of critical control regions of the optimization frames in $\mathcal{R}$
5: $\mathcal{A} \leftarrow \{||\boldsymbol{a}_{SRP,max}||, ||\boldsymbol{a}_{PRP,max}||, ||\boldsymbol{a}_{Aero,max}||\}$
6: $(a_{max},\ j) \leftarrow \max(\mathcal{A})$, with j the corresponding index
7: $\mathcal{A}_{rel} \leftarrow \mathcal{A}/a_{max}$
8: Condition $\Theta \leftarrow (\nexists\, \hat{\boldsymbol{n}}_{IG})$ **or** $[(t - t_{IG}) < \tau]$ **or** $[\angle(\hat{\boldsymbol{\lambda}}, \hat{\boldsymbol{\lambda}}_{IG}) \geq 10\,\text{deg}]$ **or** $[\max(|\mathcal{A}_{rel} - \mathcal{A}_{rel,IG}|) \geq 10\%]$
9: **if** condition Θ is true **then**
10: $\{t_{IG}, \hat{\boldsymbol{\lambda}}_{IG}, \mathcal{A}_{rel,IG}\} \leftarrow \{t, \hat{\boldsymbol{\lambda}}, \mathcal{A}_{rel}\}$
11: $\hat{\boldsymbol{n}}^*_c \leftarrow$ Grid search with step H_c in frame R_j
12: $\hat{\boldsymbol{n}}^* \leftarrow$ Grid-search descent from $\hat{\boldsymbol{n}}^*_c$ with step H_f in frame R_j
13: **else**
14: $\hat{\boldsymbol{n}}^*_{IG} \leftarrow$ From last initial guess checkpoint
15: $\hat{\boldsymbol{n}}^* \leftarrow$ Grid-search descent from $\hat{\boldsymbol{n}}^*_{IG}$ with step H_f in frame R_j
16: **end if**
17: **for** any critical control region $S_{k\neq j}$ at a distance $\leq 4H_f$ from $\hat{\boldsymbol{n}}^*$ **do**
18: $\hat{\boldsymbol{n}}^* \leftarrow$ Grid-search descent from $\hat{\boldsymbol{n}}^*$ with step H_f in frame R_k
19: **end for**
20: **if** condition Θ is true **then**
21: $\hat{\boldsymbol{n}}^*_{IG} \leftarrow \hat{\boldsymbol{n}}^*$
22: **end if**
23: Advance time t by propagating the dynamics with control $\boldsymbol{u}^* = \hat{\boldsymbol{n}}^*$
24: **end while**

and $\hat{\boldsymbol{n}}$ and, therefore, it corresponds to either the sunlight pitch angle, $\alpha_\odot$, planetary pitch angle, $\alpha_\oplus$, or aerodynamic pitch angle, α_A, see Figs. 7.1 and 7.3. The clock angle lies between the $\hat{\boldsymbol{z}}_o$-axis direction and the projection of $\hat{\boldsymbol{n}}$ onto the $(\hat{\boldsymbol{y}}_o, \hat{\boldsymbol{z}}_o)$ plane, and it is measured clockwise in this plane, see again Fig. 7.3. Within each optimization frame, a one-dimensional critical control region $(\alpha = 90\,\text{deg}, \delta) \in \mathbb{R}^1$ is then defined. These regions are denoted by S, and together they form the set $\mathcal{S}$, see line 4. The critical regions correspond to curves within the control phase space in proximity to which the SRP, PRP, and aerodynamic accelerations – and thus the cost function – exhibit high sensitivity to the control. In particular, for the critical regions of the sunlight and relative-velocity frames, these curves identify all controls for which no SRP and aerodynamic accelerations are produced, which also correspond to the non-differentiable regions of the phase space. Line 5 computes the set $\mathcal{A}$ of the maximum achievable SRP, PRP, and aerodynamic

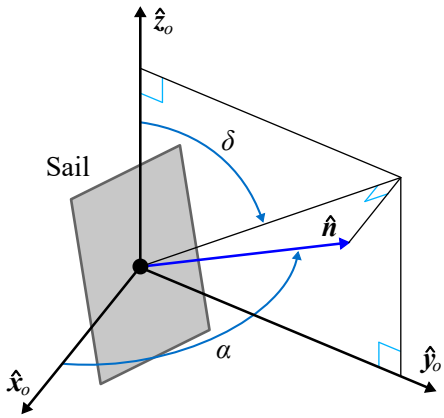


Figure 7.3: Sailcraft normal direction and attitude angles in the optimization reference frame, $R(\hat{x}_o, \hat{y}_o, \hat{z}_o)$.

accelerations, found for $\alpha_\odot = 0$, $\alpha_\oplus = 0$, and $\alpha_A = 0$, respectively. These accelerations are then normalized with respect to the largest one of them, a_{max}, resulting in the set $\mathcal{A}_{rel}$, see lines 6-7. Next, the condition Θ is defined on line 8, which determines whether an initial guess for the optimal normal direction, $\hat{\boldsymbol{n}}^*_{IG}$, ought to be generated through a coarse grid search over the entire phase space. The initial guess is generated in either of the following cases:

- No prior initial guess is available (e.g., at the very beginning of the trajectory propagation).
- The interval between the time when the initial guess was last computed, t_{IG}, and the current time, t, is larger than a user-defined threshold τ. As discussed in Section 7.3.4, this threshold can be tuned to regulate the frequency with which global exploration of the phase space is performed and the corresponding computational cost.
- The optimal thrust directions computed at the current time and time of the initial guess, $\hat{\boldsymbol{\lambda}}$ and $\hat{\boldsymbol{\lambda}}_{IG}$, respectively, form an angle, $\angle(\hat{\boldsymbol{\lambda}}, \hat{\boldsymbol{\lambda}}_{IG})$, larger than a threshold of 10 deg. This condition helps identify discontinuities in the direction $\hat{\boldsymbol{\lambda}}$ over time, as those found in inclination-changing steering laws. Note that the chosen threshold was determined through trial and error, and it does not represent a critical parameter to tune, as any value between 5 and 85 deg was found not to affect the optimization.
- Any of the relative accelerations computed at the current time and time of the initial guess, $\mathcal{A}_{rel}$ and $\mathcal{A}_{rel,IG}$, respectively, differ by more than a threshold of 10%, again chosen through trial and error. This condition helps identify (quasi-)discontinuities in the dynamics, particularly those occurring when sailcraft enter or exit eclipse.

As illustrated in lines 10-12, if the condition Θ is satisfied, the current time t, direction $\hat{\boldsymbol{\lambda}}$, and relative accelerations $\mathcal{A}_{rel}$ are cached as t_{IG}, $\hat{\boldsymbol{\lambda}}_{IG}$, and $\mathcal{A}_{rel,IG}$, respectively. Then, a first-order optimal normal direction, $\hat{\boldsymbol{n}}^*_c$, is found via a coarse grid search over the entire (α, δ) phase space, considering the optimization frame corresponding to the largest

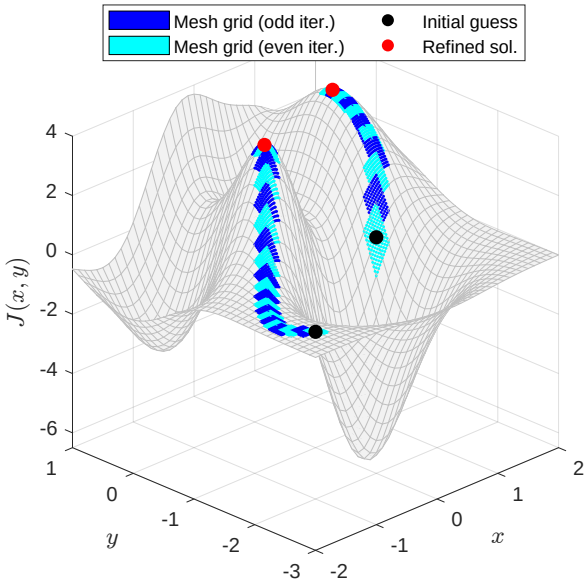


Figure 7.4: Example of coordinate-search routine applied to Matlab®'s "peaks" function.

acceleration among the SRP, PRP, and aerodynamic accelerations, R_j, and using a step of H_c for both α and δ. The coarse optimal solution found, $\hat{\boldsymbol{n}}_c^*$, is then refined through the coordinate-search routine. To this aim, a grid search is first performed over a small square mesh centered in the (α,δ) coordinates of $\hat{\boldsymbol{n}}_c^*$, using a fine step H_f. The coordinates (α,δ) of the refined optimal solution found are then used as center point for a new refinement grid search, again employing the step H_f. By repeating the process iteratively, convergence to a refined optimal solution, $\hat{\boldsymbol{n}}^*$, is eventually achieved. To enhance the reader's visualization of the process, Fig. 7.4 illustrates the coordinate-search iterative routine when applied to Matlab®'s "peaks" function, using two different initial guesses. In the graph, the light and dark blue patches represent the refinement mesh grids of consecutive iterations. As can be seen, the ability of the algorithm to converge to the true optimum strongly depends on the initial guess provided, thus highlighting its locally optimal nature and, consequently, the need for a prior global search of the phase space. After determining the optimum $\hat{\boldsymbol{n}}^*$ in frame R_j, checks are performed to assess if the solution found lies in proximity of any critical control region of the other two optimization frames, $S_{k\neq j}$. For each such case, $\hat{\boldsymbol{n}}^*$ is transformed into the optimization frame of the critical region considered and a coordinate-search routine is employed again to further refine $\hat{\boldsymbol{n}}^*$, see lines 17-19. Finally, assuming again that the condition Θ is satisfied, the optimal solution found, $\hat{\boldsymbol{n}}^*$, is first cached as initial guess for future propagation steps, $\hat{\boldsymbol{n}}_{IG}^*$, and then it is used to propagate the current dynamics, see lines 20-23.

When the condition Θ is not satisfied, the entire optimization process is implemented as described above, though with two differences. First, the coarse grid search is not performed. Instead, the available solution $\hat{\boldsymbol{n}}_{IG}^*$ is used as initial guess for the coordinate-search routine, see lines 14-15. Second, the time, direction $\hat{\boldsymbol{\lambda}}$, relative accelerations, and

optimal solution for the initial guess, t_{IG}, $\hat{\boldsymbol{\lambda}}_{IG}$, $\mathcal{A}_{rel,IG}$, and $\hat{\boldsymbol{n}}^*_{IG}$, respectively, are not updated.

7.3.3. DEORBIT-SAFE INCLINATION-CHANGING STEERING LAW

The Lagrange planetary equations prescribe that the direction $\hat{\boldsymbol{\lambda}}$ for orbit raising always points along the inertial velocity direction. Therefore, by definition, this steering law guarantees that orbital energy increases over time or that, at least, it does not decrease. In contrast, the direction $\hat{\boldsymbol{\lambda}}$ for inclination changing points out of the orbital plane, parallel (or opposite) to the orbital momentum vector. Consequently, inclination changing does not prevent losses in orbital energy. As discussed in Section 6.5.2, such losses occur especially at low altitudes, where aerodynamic drag is particularly strong, thus yielding rapid deorbiting.

To enable inclination changing while maintaining orbital altitude, a "deorbit-safe" adaptation of the inclination-changing steering law is presented hereinafter. This steering law is defined based on the inclination-changing and orbit-raising steering laws by McInnes [2], which are combined following the control blending algorithm of Macdonald and McInnes [204]. More specifically, the directions $\hat{\boldsymbol{\lambda}}$ for orbit raising and inclination changing derived from the Lagrange planetary equations, $\hat{\boldsymbol{\lambda}}_a$ and $\hat{\boldsymbol{\lambda}}_i$, respectively, are blended through the following normalized weighted sum:

$$\hat{\boldsymbol{\lambda}}_{i(a)} = \frac{\sum_k W_k \hat{\boldsymbol{\lambda}}_k}{\left\| \sum_k W_k \hat{\boldsymbol{\lambda}}_k \right\|} \tag{7.12}$$

where W is a blending weight, subscript k indicates the target orbital element of a steering law to be blended (i.e., semi-major axis, a, or inclination, i), and subscript $i(a)$ denotes the resulting blended optimal thrust direction, $\hat{\boldsymbol{\lambda}}$, for deorbit-safe inclination changing. To analyze the inclination-changing capabilities of Earth-orbiting sailcraft, the analyses in Sections 7.3.4 and 7.5 consider several circular orbits at different initial altitudes, h_0. Because orbital altitude, magnitude of atmospheric drag, and deorbiting effects on the sailcraft are strongly correlated, the blending weights should be defined in a way that reflects such correlation. Specifically, the weights should ensure that pure inclination-changing maneuvering is employed only when the sailcraft altitude, h, is above its initial value, h_0. Conversely, when altitude losses are experienced, increasingly more importance should be given to orbit raising, eventually assuming full priority for extremely low altitudes below a lower bound, h_{LB}. Following this rationale, the blended weights are defined as:

$$W_i = \quad 1 \tag{7.13}$$

$$W_a = \begin{cases} +\infty & \text{if } h \leq h_{LB} \\ \dfrac{2\,(h-h_0)^2}{(h_0-h_{LB})\,(h-h_{LB})} & \text{if } h_{LB} < h < h_0 \\ 0 & \text{if } \max(h_{LB}, h_0) \leq h \end{cases} \tag{7.14}$$

The variation of the weights with altitude expressed in Eqs. 7.13 and 7.14 is exemplified in Fig. 7.5a, which was obtained for an ACS3-like sailcraft (see Table 7.1) with an initial

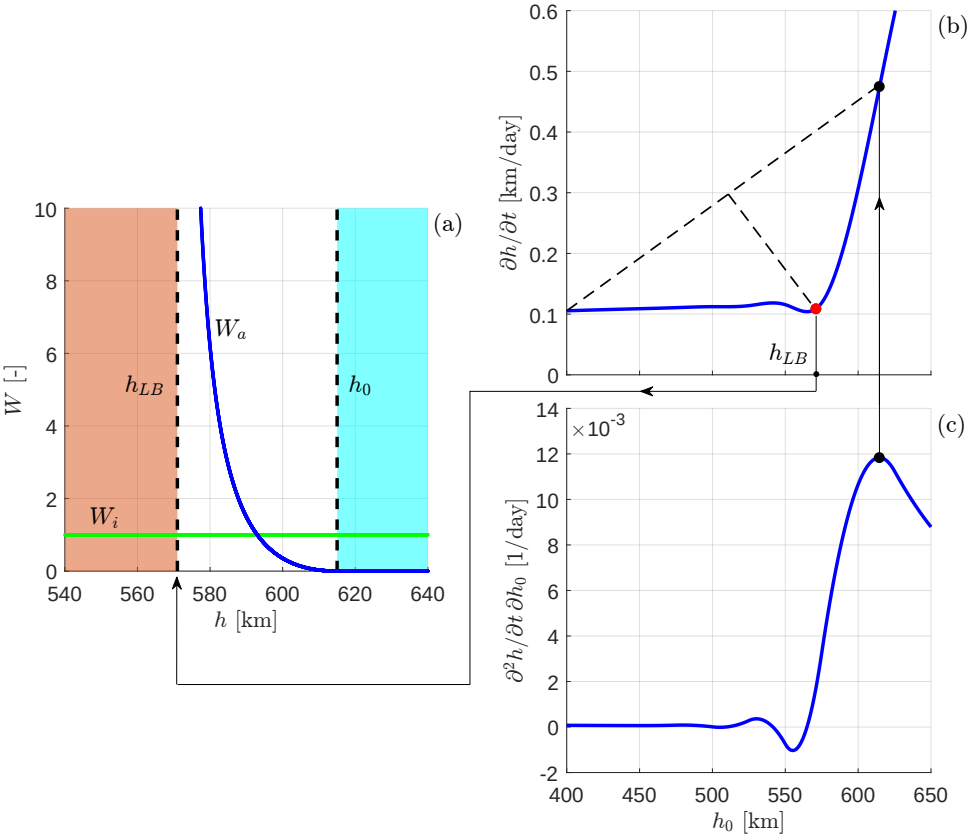


Figure 7.5: Example visualization of a) the W_a and W_i functions, and the altitude ranges corresponding to pure orbit raising (red) and pure inclination changing (light blue), b) $\partial h/\partial t$ for pure orbit raising, the construction lines of the kneedle algorithm (dashed) and the elbow point (red), and c) $\partial^2 h/\partial t \partial h_0$ for pure orbit-raising and its maximum (black).

altitude of $h_0 = 615$ km and LTAN at 22:30 hrs, under intermediate solar activity conditions (found for a simulation date of 20 March 2027). As shown, for $h < h_{LB}$, pure orbit raising is performed, corresponding to $W_a = +\infty$. For altitudes between h_{LB} and h_0, W_a varies from $W_a = +\infty$ to $W_a = 0$ following a continuous, smooth function, chosen such that orbit raising and inclination changing achieve equal priority ($W_a = W_i = 1$) exactly at the midpoint altitude $h = (h_{LB} + h_0)/2$. Ultimately, for altitudes larger than both h_0 and h_{LB}, $W_a = 0$, leading to pure inclination changing.

The lower bound h_{LB} appearing in Eq. 7.14 represents the altitude that, if reached, makes deorbiting inevitable, as recovering altitude becomes practically unfeasible due to the dominating presence of atmospheric drag. In view of this, h_{LB} is determined through prior analysis of the sailcraft orbit-raising capabilities. Specifically, the initial orbital elements corresponding to the orbital scenario under investigation are considered. From there, several other scenarios are defined by varying only the initial altitude, h_0. The

altitude rate of change achieved through the orbit-raising steering law, $\partial h/\partial t$, is then calculated for each of these new scenarios, thus resulting in an altitude rate-of-change profile as the one of Fig. 7.5b. As can be observed, $\partial h/\partial t$ remains almost constant at low altitudes before undergoing a swift rise. The "elbow" point of the curve right before this rise identifies the approximate altitude at which atmospheric drag stops being dominant and orbit raising becomes practically feasible, that is, it identifies the altitude lower bound, h_{LB}. In this chapter, the elbow point of the $\partial h/\partial t$ profile is found through the popular *kneedle* algorithm [423], which identifies the elbow point of a curve as the point having maximum distance from a given reference line. The reference line is defined such that its endpoints lie on the $\partial h/\partial t$ curve at altitudes $h = 400$ km and $h = h^*$, with h^* the altitude corresponding to the point of flex of the $\partial h/\partial t$ curve. To aid visualization, Fig. 7.5b displays the reference line of the kneedle algorithm, the corresponding elbow point, and the distance between the two. It should be noted that the $\partial h/\partial t$ profile is generated considering a limited number of orbit-raising simulations with initial altitudes, h_0, spaced by 25 km, and using cubic-spline interpolation – as per Matlab®'s *spline* function – over the corresponding $\partial h/\partial t$ nodes obtained. The interpolated $\partial h/\partial t$ profile is then numerically differentiated using a finite-difference scheme of order 6 [424]. This way, the profile of the numerical derivative $\partial^2 h/\partial t \partial h_0$ is found and its maximum is used to identify the altitude of the flex point, h^*, as illustrated Fig. 7.5c.

7.3.4. OPTIMIZATION ALGORITHM TUNING

In this section, the tuning of the optimization settings τ, H_c, and H_f is conducted. These settings will be used in Section 7.5 to perform several Earth-bound trajectory optimizations, employing orbit-raising and deorbit-safe inclination-changing steering laws. In view of this, the tuning is conducted by performing several simulations that consider both steering laws, a diverse set of orbital scenarios, and different values for τ, H_c, and H_f. For each simulation, the achieved change in altitude or inclination and the required run time are compared against those of a very accurate solution. In this way, information is gained on the influence of the settings τ, H_c, and H_f on both the optimization accuracy and the required computational effort, thus facilitating their final selection.

Table 7.2 summarizes the settings used for all tuning simulations. For the orbit-raising case, the initial altitudes $h_0 = \{400, 700, 1000\}$ km have been considered in order to account for the effect that different SRP, PRP, and aerodynamic acceleration magnitudes have on the optimization. For the deorbit-safe inclination-changing case, on the other hand, the same initial altitudes as in the orbit-raising case have been considered but with $h_0 = h_{LB} + 5$ km instead of $h_0 = 400$ km. This choice was driven by the fact that $h_0 = 400$ km lies below h_{LB} for all orbital scenarios analyzed, thus yielding pure orbit raising rather than inclination changing, see Eq. 7.14 and Fig. 7.5. Different orbit orientations have also been considered, captured by three initial LTAN values, $\text{LTAN}_0 = \{06{:}00, 09{:}00, 12{:}00\}$ hrs, and three initial inclinations, $i_0 = \{0.5 \text{ deg}, 45 \text{ deg}, i_{SSO}\}$, where i_{SSO} denotes the Sun-synchronous inclination at the given initial altitude, h_0, and initial eccentricity, $e_0 = 0$. For each combination of steering law, altitude, LTAN, and inclination, the sailcraft dynamics in Eq. 7.1 have been propagated for one orbital period using Matlab®'s *ode45* integrator, with absolute and relative tolerances of 10^{-12}. For all simulations, the propagation start date has been set to 20 March 2027, corresponding to solar activity of medium intensity.

Table 7.2: Settings for optimization algorithm tuning.

Initial States and Control				
Target orbital element, œ	a, $i(a)$			
h_0 [km]	$\begin{cases} 400, 700, 1000 & \text{if } \text{œ} = a \\ h_{LB}+5, 700, 1000 & \text{if } \text{œ} = i(a) \end{cases}$			
e_0	0.0			
LTAN_0 [hrs]	06:00, 09:00, 12:00			
i_0	0.5 deg, 45 deg, i_{SSO}			
Sim. start date (solar activity)	20 March 2027 (medium)			
Propagation				
Integrator	Matlab®'s *ode45* integrator			
Duration [orbital periods]	1.0			
Abs. and rel. tolerances	10^{-12}			
Optimization				
τ [orbital periods]	1/10, 1/20, 1/50, 1/100, 1/200			
(H_c, H_f) [deg]	(20, 10)	(20, 5)	(20, 2)	(20, 1)
	(10, 5)	(10, 2)	(10, 1)	(10, 0.5)
	(5, 2.5)	(5, 1)	(5, 0.5)	(5, 0.25)
	(2, 1)	(2, 0.5)	(2, 0.2)	(2, 0.1)
Reference Optimization				
τ_{ref} [orbital periods]	0.0			
$(H_{c,ref}, H_{f,ref})$ [deg]	(1, 0.01)			

The sailcraft control has been computed using the optimization algorithm presented in Section 7.3.2, employing different values of the initial-guess time threshold, τ, as well as different coarse and fine grid-search steps, H_c and H_f, respectively. In particular, for each of the above-mentioned orbital scenario, a trajectory propagation using reference values for τ, H_c, and H_f has been performed, resulting in a reference optimal trajectory. These reference settings (indicated by the subscript "*ref*" in Table 7.2) allow to compute the sailcraft control (attitude) with an accuracy of 0.01 deg without relying on any initial guess (notice $\tau_{ref} = 0$), therefore ensuring global optimality. After having computed the reference optimal trajectory, several other propagations have also been performed using all combinations of τ, H_c, and H_f shown in Table 7.2. In this way, for each orbital scenario, different propagation results are obtained which can be compared in terms of accuracy and required run time. To measure accuracy, the following relative error has

been computed:

$$\varepsilon_{rel} = \frac{\Delta\alpha - \Delta\alpha_{ref}}{\Delta\alpha_{ref}} \tag{7.15}$$

where $\Delta\alpha$ is the gain in altitude (for the orbit-raising steering law) or inclination (for the inclination-changing steering law) achieved for a given triplet of τ, H_c, and H_f values, and $\Delta\alpha_{ref}$ is the same gain obtained using τ_{ref}, $H_{c,ref}$, and $H_{f,ref}$. Similarly, computational efficiency is assessed through the following relative run time:

$$T_{rel} = \frac{\Delta T}{\Delta T_{ref}} \tag{7.16}$$

where ΔT is the run time required when using a given triplet of τ, H_c, and H_f values, and ΔT_{ref} is the run time found using the reference values τ_{ref}, $H_{c,ref}$, and $H_{f,ref}$.

Figure 7.6 shows the mean and maximum values of the distribution of relative errors, ε_{rel}, achieved for all orbital scenarios, for each combination of step-size pair (H_c, H_f) and parameter τ. In addition, a constant relative-error plane is also shown, corresponding to $\varepsilon_{rel} = 0.5\%$. This value is adopted as threshold to ensure a high accuracy, consistent with the sub-1% error levels achieved by the spherical PRP acceleration model presented in Section 7.2.3 and formally defined in Chapter 4. Figure 7.6a provides the results for the orbit-raising steering law. As can be seen, the relative error decreases rapidly for decreasing τ values, thus highlighting the importance of frequent global searches of the control space to avoid local optima and attain a high accuracy. Similarly, the error also decreases for decreasing sizes of the coarse and fine grid-search steps, H_c and H_f, respectively, although less rapidly. Comparison with the 0.5%-error plane shows that, to ensure errors below the specified threshold for any orbital scenario, values of τ equal to 1/100 or 1/200 should be considered in conjunction with a coarse step size of $H_c = 10$ deg or smaller. Figure 7.6b displays the results for the deorbit-safe inclination changing steering law. The mean and maximum relative errors once again decrease for decreasing τ and the grid-search step sizes, similar to the orbit-raising case, see Fig. 7.6a. Compared to the orbit-raising case, however, the sub-0.5% error condition is more easily met, as both mean and maximum relative errors lie well below the threshold for the majority of optimization parameter combinations.

Figure 7.7 shows the mean values of the distribution of relative run times, T_{rel}, achieved for all orbital scenarios, for each combination of optimization settings. The plot displays the dependency of run time on the step sizes along the horizontal axis, whereas the variability of run times with τ is captured by the vertical spread of the colored bands. As can be seen, for both the orbit-raising and deorbit-safe inclination-changing steering laws, τ affects the run time to a much lesser extent compared to the step sizes H_c and H_f. In particular, a pronounced dependency of the run times on H_f is observed, as highlighted by the approximately parabolic trend that the colored bands exhibit for any fixed value of H_c. The step size H_c, on the other hand, affects the run time more weakly, as evidenced by the slight upward trend of the sequence of parabolic arcs moving from left to right, that is, for increasingly smaller H_c values.

The above results indicate that τ values of 1/100 or 1/200 and $H_c \leq 10$ deg should be considered to achieve sub-0.5% errors, for both steering laws. As τ was found to affect the run time only slightly, a value of $\tau = 1/200$ was conservatively chosen. Among the

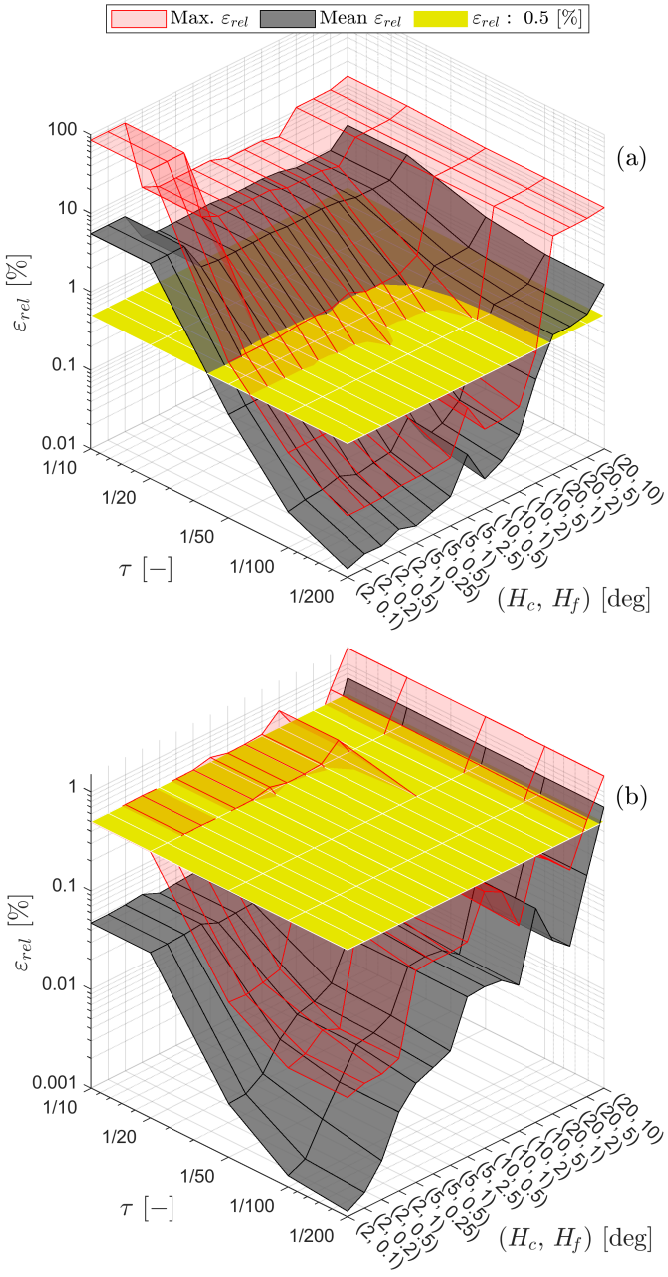


Figure 7.6: Relative errors for the (a) orbit-raising and (b) deorbit-safe inclination changing steering laws.

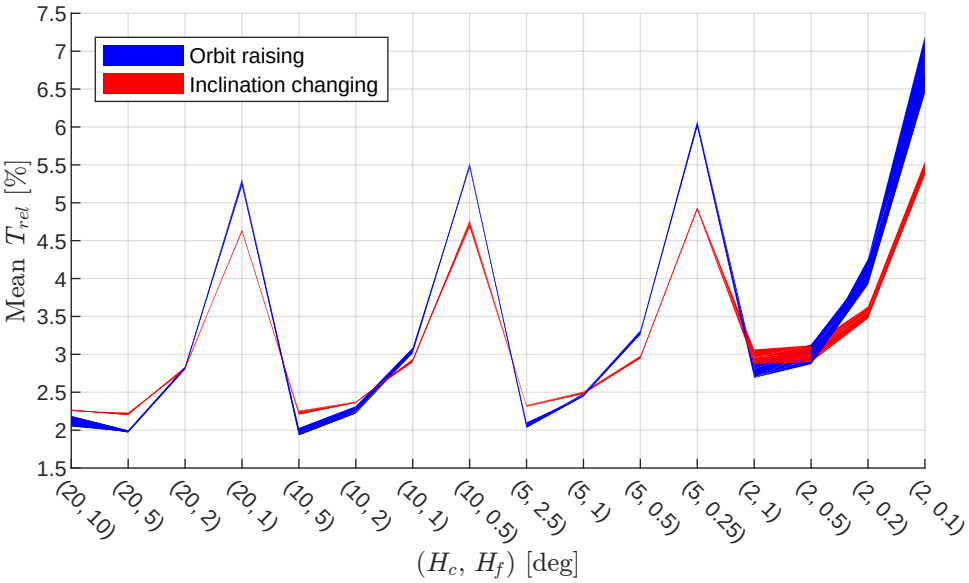


Figure 7.7: Relative run times, T_{rel}, for the orbit-raising and deorbit-safe inclination changing steering laws.

acceptable (H_c, H_f) pairs, the ones yielding the shortest run times are (10, 5) deg and (5, 2.5) deg, achieving mean T_{rel} values of 2-2.5%. Given the minimal deviation in run time and to enhance interpretation of the optimal control profiles and analysis results, the pair (5, 2.5) deg was selected. Finally, to provide a measure of the practical run time involved in the computations, it should be noted that, for the selected τ value and (H_c, H_f) pair, the average run times of the orbit-raising and inclination-changing simulations were of 39.2 s and 36.5 s, respectively. These run times were obtained using a single core of the Intel® Core™ i7-7700HQ processor, with a clock speed of 2.8 GHz.

7.4. NEAR-EARTH DYNAMICAL REGIMES

This section presents a first-order analysis to characterize the dynamical regimes in proximity of the Earth and, therefore, facilitate understanding of the near-Earth dynamical environment. The analysis will also support the discussion of the parametric analyses in Section 7.5, which aim to fully characterize the maneuvering capabilities of Earth-bound solar sails.

Sailcraft controllability in proximity of the Earth strongly depends on the magnitude of the attitude-dependent accelerations. Given the dependency of SRP and ARP on eclipses, the geographical variation of BBRP, and the strong influence of altitude on atmospheric density, these accelerations' magnitudes vary in the near-Earth environment following different trends. Consequently, different so-called dynamical regimes arise, wherein one or more accelerations affect the dynamics (and control) far more significantly than the others.

To visualize the dynamical regimes, an analysis has been conducted in which the max-

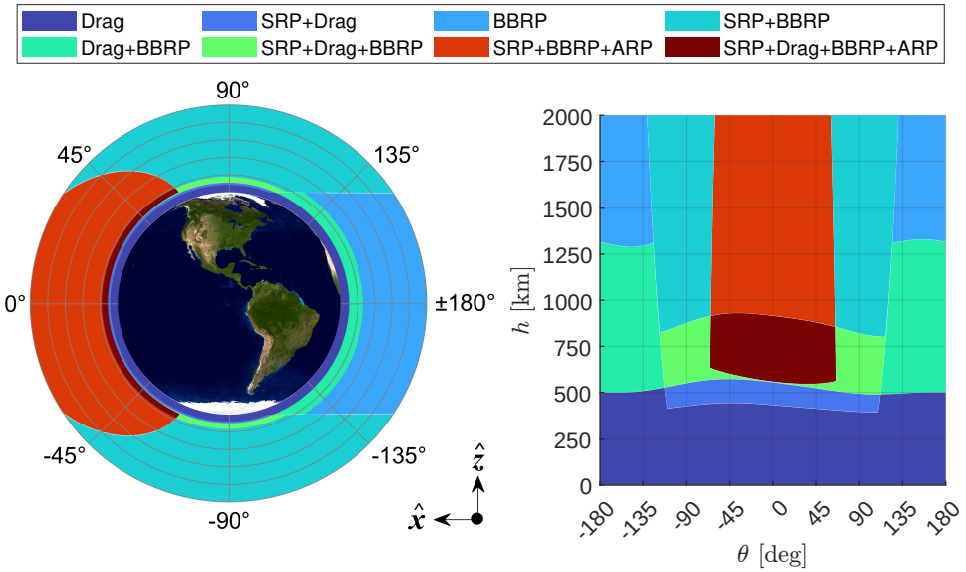


Figure 7.8: Dominating solar-sail accelerations in the near-Earth environment: (a) polar plot and (b) Cartesian plot.

imum achievable SRP, BBRP, ARP, and aerodynamic accelerations have been computed for a wide variety of sailcraft locations around the Earth. The analysis considers the ACS3 sailcraft specifics in Table 7.1 and a simulation start date of 20 March 2027. This date was considered as solar activity of medium intensity is expected in 2027 [294]. Furthermore, this date corresponds to the spring equinox, so that the Earth-to-Sun direction is aligned with the positive $\hat{\boldsymbol{x}}$-axis direction of the $O_I(\hat{\boldsymbol{x}}, \hat{\boldsymbol{y}}, \hat{\boldsymbol{z}})$ frame and the subsolar point lies on the Earth's equator. The sailcraft positions considered lie on the $(\hat{\boldsymbol{x}}, \hat{\boldsymbol{z}})$ plane, at altitudes between zero and 5000 km. The $(\hat{\boldsymbol{x}}, \hat{\boldsymbol{z}})$ plane is coplanar with the plane defined by the Earth's polar axis and the Earth-Sun direction, thereby allowing to easily observe how eclipses and variations in the albedo coefficient and the blackbody radiation flux affect the dynamics. Given the maximum SRP, BBRP, ARP, and aerodynamic accelerations at each sailcraft location, the regions around the Earth wherein different types of accelerations dominate the dynamics are determined. In particular, at each sailcraft location, the largest of the aforementioned accelerations is recorded together with any other acceleration that is at least 5% of this largest acceleration component.

Figure 7.8 shows the dynamical regimes as a function of the sailcraft altitude, h, and polar angle measured from the $\hat{\boldsymbol{x}}$ (Earth-Sun) direction, θ. To enhance visual interpretation of the results, the results are displayed in an Earth-centered polar plot with an altitude grid spacing of 1000 km, see Fig. 7.8a, and a Cartesian plot with maximum altitude restricted to 2000 km, see Fig. 7.8b. The plots show that three macro-regions exist which exhibit different patterns: the sunlit region in proximity of the subsolar point (around $\theta = 0$ deg), the eclipse region (around $\theta = 180$ deg), and the region situated between these two, close to the poles (around $\theta = \pm 90$ deg).

In the eclipse region, the only accelerations present are those from atmospheric drag

and BBRP. Drag is especially strong for altitudes below 500 km, rendering the BBRP acceleration negligible in comparison. However, for increasing altitudes, the acceleration due to drag decreases more rapidly than the acceleration due to BBRP. Therefore, the BBRP acceleration becomes increasingly more relevant, eventually reaching magnitudes comparable to that of drag or even superior to it, particularly for altitudes above 1300 km.

In proximity of the poles, the SRP acceleration significantly affects the dynamics, in particular above 400 km. Similar as for the eclipse region, drag decreases rapidly with altitude, rendering it negligible for altitudes above 800-900 km, where the SRP and BBRP accelerations are the dominating accelerations. Close to the poles, also ARP affects the sailcraft motion. However, because the angle between incoming sunlight and the Earth surface is large, the ARP acceleration magnitude is small, therefore affecting the dynamics only to a negligible extent. It should be noted that, apart from the region in proximity to the poles, a similar change in dynamical regimes with altitude is found at locations closer to the equator, as long as the polar angle θ is close to 90 deg. This result was found by repeating the analysis considering sailcraft positions on the $(\hat{\boldsymbol{y}}, \hat{\boldsymbol{z}})$ plane (orthogonal to the Sun-Earth direction) instead of the $(\hat{\boldsymbol{x}}, \hat{\boldsymbol{z}})$ plane. For the sake of conciseness of the treatment, however, the corresponding plots are not presented.

Lastly, the region in proximity of the subsolar point is the most dynamically complex, as there the ARP acceleration is also of considerable magnitude. The ARP acceleration becomes increasingly relevant, particularly above 500 km. This results in a large region in the altitude range $[550, 925]$ km and θ range $[-65, 65]$ deg where all accelerations significantly affect the dynamics.

The results presented above highlight that Earth-orbiting sailcraft can experience considerable variations in the dynamics across a trajectory. This is the case especially for noon-midnight orbits, for which the orbital plane is approximately parallel to the Sun-Earth direction, with LTANs at 00:00 or 12:00 hrs. Also, a stronger dynamical variability is found for decreasing altitudes, especially below 1000 km. This altitude range corresponds to the region wherein the vast majority of LEO satellites orbit [425]. In view of this, the parametric analyses in Section 7.5 will focus solely on this altitude range. Finally, it should be noted that the high dynamical variability characteristic of the LEO region warrants the robust trajectory optimization routine presented in Section 7.3.2. Indeed, frequent and pronounced variations in the dynamics require an optimization procedure that can effectively determine and exploit the dominant accelerations of each dynamical regime – a requirement that the proposed method was explicitly designed to meet.

7.5. CHARACTERIZATION OF SOLAR-SAIL MANEUVERING CAPABILITIES

This section presents a set of five sensitivity analyses designed to fully characterize the maneuverability of Earth-bound solar sails. Specifically, the analyses explore the effects of the PRP acceleration, solar activity intensity, sailcraft characteristic acceleration, orbital inclination, and Sun-Earth orientation on the orbit-raising and inclination-changing capabilities of Earth-bound sailcraft, for a wide variety of orbits with different altitudes and LTANs.

The common settings used for all sensitivity analyses are detailed in Table 7.3. The

Table 7.3: Common settings to all sensitivity analyses of Section 7.5.

Initial States and Control	
Target orbital element, $\mathfrak{o}$	a, $i(a)$
h_0 [km]	$\begin{cases} 400, 425, ..., 650, 700, ..., 1000 & \text{if } \mathfrak{o} = a \\ h_{LB} - 5, h_{LB} + 5, ..., 950, 1000 & \text{if } \mathfrak{o} = i(a) \end{cases}$
e_0	0.0
LTAN_0 [hrs]	00:00, 01:00, ..., 23:00
Propagation	
Integrator	Matlab®'s *ode45* integrator
Duration [orbital periods]	1.0
Abs. and rel. tolerances	10^{-12}
Optimization	
τ [orbital periods]	1/200
(H_c, H_f) [deg]	(5, 2.5)

7

propagation and optimization settings presented in the table are used to propagate the dynamics in Section 7.2 while employing the MACHO algorithm to perform orbit raising or (deorbit-safe) inclination changing. The analyses consider several initial circular orbits, differing only in their LTANs and altitudes. For the orbit-raising simulations, the initial altitude varies with step sizes of 25 and 50 km for altitudes below and above 650 km, respectively. This discretization was adopted to more accurately identify the minimum altitudes at which maneuvering is feasible, h_{LB}. The altitudes h_{LB} are then used to define the set of initial altitudes for the inclination-changing simulations, which comprises $h_{LB} - 5$ km and $h_{LB} + 5$ km, followed by initial altitudes varying again with a step size of 50 km. In this way, the inclination-changing capabilities are more accurately assessed in proximity of the minimum altitude for maneuvering, that is, in the limit case of almost critical deorbiting conditions.

Table 7.4 presents the specific settings used for each sensitivity analysis. As indicated in the table, depending on the sensitivity analysis, the optimization routine described in Section 7.3.2 has been employed including or excluding the PRP acceleration from the optimization process, that is, including or excluding the contribution of $\boldsymbol{a}_{PRP}$ from the acceleration term of the cost function, $\boldsymbol{a}$, see Eq. 7.11. Depending on the sensitivity analysis, different simulation start dates have been considered as well. Of these, three correspond to spring equinoxes, namely, 20 March 2024, 2027 and 2031, which are associated to solar activities of maximum, medium, and minimum intensity, respectively. Note that because these dates correspond to equinoxes, the Sun is approximately in the Earth's equatorial plane throughout the simulations. In addition, 21 June and 22 December 2027

Table 7.4: Analysis-dependent settings used for the reference scenario and sensitivity analyses of Section 7.5.

Analysis	Reference Scenario	Effect of $\boldsymbol{a}_{PRP}$	Effect of Solar Activity	Effect of Char. Acceleration	Effect of Inclination	Effect of Solar Declination
Section	7.5.1	7.5.2	7.5.3	7.5.4	7.5.5	7.5.6
Opt. $\boldsymbol{a}_{PRP}$	Yes	No	Yes	Yes	Yes	Yes
Sim. Start Date (Solar Activity)	20 Mar 2027 (Mid)	20 Mar 2027 (Mid)	20 Mar 2024, 2027, 2031 (Max, Mid, Min)	20 Mar 2027 (Mid)	20 Mar 2027 (Mid)	21 Jun, 22 Dec 2027 (Mid)
Sailcraft Specifics	ACS3*	ACS3*	ACS3*	ACS3* with a_c equal to $a_c^{ref}/10$, a_c^{ref}, $10\,a_c^{ref}$	ACS3*	ACS3*
i_0	i_{SSO}	i_{SSO}	i_{SSO}	i_{SSO}	0.5 deg, 45 deg, i_{SSO}	i_{SSO}

* See Table 7.1

have been considered, corresponding to summer and winter solstices, respectively, and medium solar activity intensities. The ACS3 solar-sail specifics given in Table 7.1 have been used for all sensitivity analyses, except for the characteristic acceleration, a_c. Indeed, by referring to the characteristic acceleration of ACS3 as a_c^{ref}, characteristic accelerations of either $a_c^{ref}/10$, a_c^{ref}, or $10\,a_c^{ref}$ have been considered. Finally, the sensitivity analyses also consider orbits with different inclinations. Note that, because the Sun-synchronous inclination, i_{SSO}, depends on altitude, its value varies almost linearly between 97.030 deg at 400 km and 99.479 deg at 1000 km.

The sensitivity analyses and their results are discussed in the following sections. For the sake of clarity, the term "parametric analysis" will be used hereinafter to refer to an analysis performed by iterating over the parameters of Table 7.3, that is, when considering different steering laws, initial orbital altitudes and LTANs. In accordance with this terminology, a *sensitivity* analysis consists of a number of *parametric* analyses, each considering a different simulation start date, initial inclination, sailcraft specifics, or optimization specifics, as outlined in Table 7.4.

7.5.1. REFERENCE SCENARIO

The parametric analysis presented in this section aims to assess the maneuvering capabilities of ACS3 under the reference conditions, that is, considering an ACS3-like sailcraft in Sun-synchronous orbit, assuming a medium solar activity intensity, and including PRP in the optimization process, see Table 7.4.

Figure 7.9a displays the results for the orbit-raising case by illustrating the altitude gain rate, $\partial h/\partial t$, as function of the initial orbital altitude and LTAN, h_0 and LTAN_0, respectively. Furthermore, the minimum altitude for which maneuvering is feasible, h_{LB}, see Section 7.3.3, is indicated in red. The graph shows that h_{LB} varies only slightly with the initial LTAN, assuming values between 545 km and 580 km. As evidenced also in Fig. 7.8, this result stems from the dominant effect of aerodynamic drag below such altitudes. Nevertheless, it is interesting to note that even for $h_0 < h_{LB}$, the achieved altitude gain is not exactly zero. The reason for this is that while deorbiting is prevented by orienting the sail edgewise to the incoming wind flow at all times, the optimizer manages to determine the remaining attitude angle such that the SRP and PRP accelerations are optimally exploited. As a consequence, a small altitude increase is still achieved. It should be noted that this result only holds when the optimal control profile is followed precisely. Indeed, because of the significant drag, even slight deviations from the prescribed attitude profile will result in rapid deorbiting. This, therefore, renders orbit raising still unattainable and unreliable at such altitudes in real-life missions. For altitudes above h_{LB}, atmospheric density decreases rapidly and with it also aerodynamic drag. This yields better orbit-raising capabilities and increasingly larger altitude gains, particularly for LTANs close to 06:00 and 18:00 hrs. These LTANs correspond to dawn-dusk orbits, for which the sailcraft does not enter the Earth's eclipse region, allowing the sailcraft to exploit SRP at all times, leading to large altitude gains. On the other hand, for LTANs close to 00:00 and 12:00 hrs, the sailcraft orbits in a noon-midnight orbit and is shadowed by Earth for a prolonged period of time (approximately 33% to 39% of the orbital period, depending on the altitude). Even though this negatively affects the orbit-raising capabilities compared to the dawn-dusk case, the impact on the altitude gain is relatively limited. This stems from the

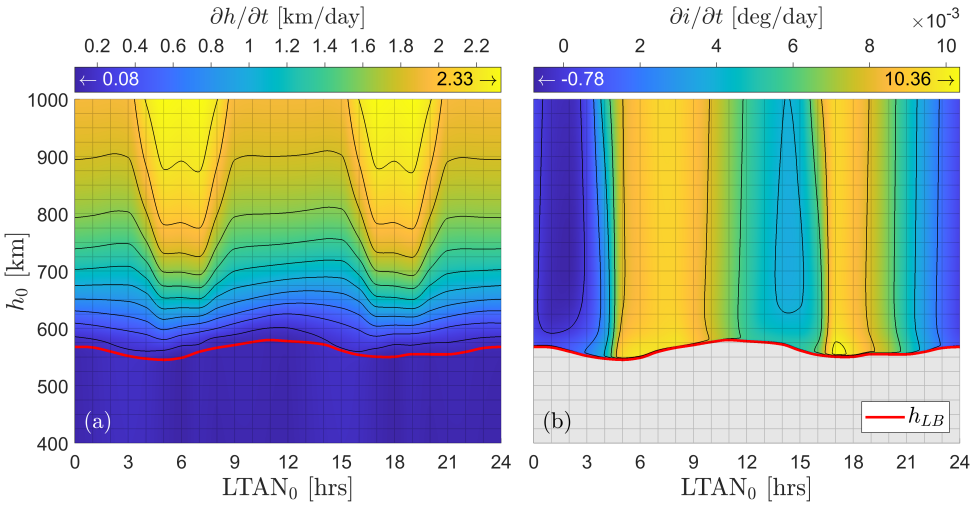


Figure 7.9: Rates of (a) altitude gain and (b) inclination gain obtained for the reference scenario.

fact that, for noon-midnight orbits, the sailcraft passes over the subsolar point once per orbit, where albedo radiation is particularly strong. Consequently, the ARP acceleration can be exploited more effectively, partially counteracting the decrease in performance due to the presence of eclipses.

Similar to Fig. 7.9a, Fig. 7.9b shows the inclination gain rate, $\partial i/\partial t$, when implementing the deorbit-safe inclination-changing steering law of Section 7.3.3 for different combinations of initial altitude and LTAN. The graph displays a shaded region representing the region of infeasibility of inclination changing, found for initial altitudes below h_{LB}, see Eqs. 7.13 and 7.14. Conversely, for initial altitudes above h_{LB}, aerodynamic drag and its deorbiting effects become increasingly less pronounced, resulting in positive inclination gains. Notably, the inclination gains achieved depend only weakly on the initial altitude, h_0, especially beyond $h = 600$ km. Again, this indicates that the aerodynamic acceleration is no longer dominant, see Fig. 7.8, and that inclination gain is therefore achieved by exploiting primarily the SRP and PRP accelerations, which are in fact independent and weakly dependent on altitude, respectively. The major exploitation of SRP for inclination changing above $h = 600$ km is also highlighted by the large inclination gains found for initial LTANs around 06:00 and 18:00 hrs, which reach values up to 0.01 deg. Similar to the orbit-raising case, such large gains are primarily due to the absence of eclipses. Furthermore, they are also due to the favorable relative orientation of the sunlight direction with respect to the orbital plane, which enables the sailcraft to generate larger out-of-plane accelerations.

7.5.2. ANALYSIS OF THE EFFECT OF PLANETARY RADIATION PRESSURE

The parametric analysis presented in this section investigates to what extent the PRP acceleration can be exploited to enhance the solar-sail maneuvering capabilities around Earth. To this aim, the same analysis as in Section 7.5.1 is conducted, although accounting for the PRP acceleration only in the dynamics and not in the optimization process, see

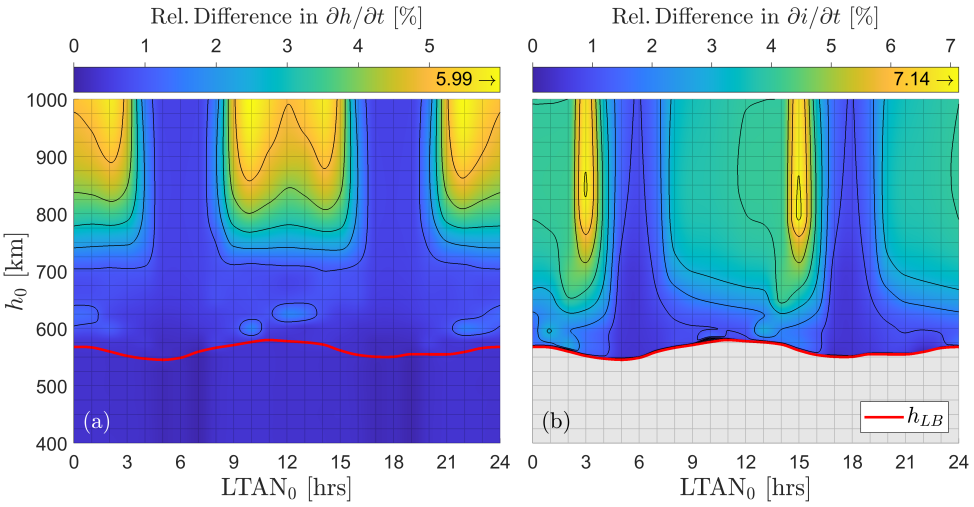


Figure 7.10: Relative differences between the (a) altitude gain rates for the PRP-based and no-PRP optimizations, and between the (b) inclination gain rates for the PRP-based and no-PRP optimizations.

Table 7.4.

Figure 7.10a shows the results for the orbit-raising case, displaying the difference between the altitude gain rates obtained by including and excluding PRP acceleration in the optimization process, normalized by the maximum altitude gain rate found by including PRP acceleration in the optimization process, that is, 2.33 km/day, see Fig. 7.9a. Note that, due to this large normalization factor, the relative difference in displayed in Fig. 7.10a provides a *conservative* measure of the increase in altitude gain rates achieved by optimally leveraging the PRP acceleration. Predictably, the relative difference is always positive, thus indicating that if the PRP acceleration is not accounted for in the optimization, it acts as a perturbation and negatively affects the altitude gain, regardless of the orbit considered. The graph shows that neglecting PRP in the optimization has a minor effect on the altitude increase for LTANs around 06:00 and 18:00 hrs but a significant impact for orbits with LTANs close to 00:00 and 12:00 hrs. Indeed, incorporating the PRP acceleration in the optimization can result in altitude gains of up to 6% larger than those found by the no-PRP optimization. As discussed in Section 7.5.1, the increased orbit-raising capabilities achieved for noon-midnight orbits are a direct consequence of the large ARP acceleration the sailcraft experiences and exploits for maneuvering.

Similar to Fig. 7.10a, Fig. 7.10b illustrates the difference between the inclination gain rates obtained by including and excluding PRP acceleration in the optimization, normalized by the maximum inclination gain rate found by including PRP in the optimization, that is, $10.36{\cdot}10^{-3}$ deg/day, see Fig. 7.9b. The graph shows that the PRP acceleration can be exploited most effectively for altitudes above 700 km and for LTANs in narrow bands around 03:00 and 15:00 hrs. For these LTANs, the sailcraft passes close to the subsolar point, where a large ARP is produced, see Fig. 7.8, and its direction can optimally contribute to the optimal thrust direction, $\hat{\boldsymbol{\lambda}}$. This enables inclination changes of 4% to 7% larger than when PRP is not accounted for in the optimization. The benefit of exploiting

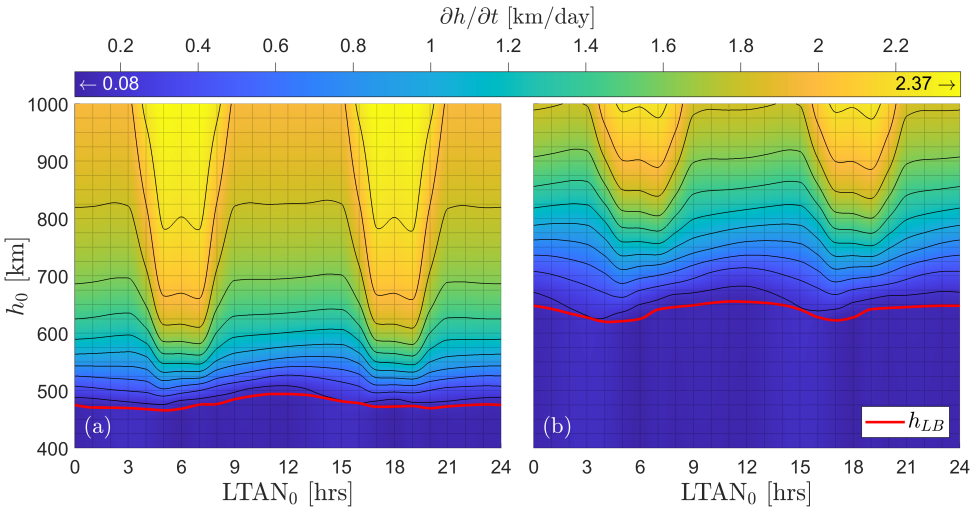


Figure 7.11: Altitude gain rates obtained for solar activities of (a) minimum and (b) maximum intensity.

PRP is lost when slightly larger LTANs at 06:00 and 18:00 hrs are considered. Indeed, these LTANs correspond to dawn-dusk orbits for which the ARP acceleration is almost zero. Finally, the graph also shows that, for LTANs between 08:00 and 14:00 hrs and between 20:00 and 02:00 hrs, PRP can be exploited to some extent and with an almost constant effectiveness.

7.5.3. ANALYSIS OF THE EFFECT OF SOLAR ACTIVITY

To investigate the influence of solar activity on solar-sail maneuverability, the parametric analysis in Section 7.5.1, valid for medium-intensity solar activity, has been repeated using two different simulation start dates that correspond to solar minimum and maximum conditions, see Table 7.4.

Figure 7.11 shows two contour plots illustrating the achievable altitude gain rates for minimum and maximum solar activities. Comparison of these plots highlights that increased solar activity significantly reduces the altitude region wherein maneuvering is feasible, as well as the overall orbit-raising performance, especially at low altitudes. Specifically, a transition from minimum to maximum solar activity intensities causes the minimum altitude for maneuvering, h_{LB}, to rise from the range 465-495 km to the range 620-655 km, in agreement with similar results found in Section 6.5.1. It is of note that the results for the reference scenario with medium-intensity solar activity exhibited a range for h_{LB} of 545-580 km, see Fig. 7.9a. Interestingly, this range lies approximately halfway between those for minimum and maximum solar activity intensities, suggesting an approximately linear relationship. For higher initial orbital altitudes, h_0, atmospheric drag affects the sailcraft dynamics increasingly less and, therefore, the effect of solar activity is less noticeable.

Figure 7.12 provides the results for the inclination-changing case, showing the achievable inclination gain rates, again for minimum and maximum solar activity intensities. Analogous to the orbit-raising case, a stronger solar activity results in stronger drag and

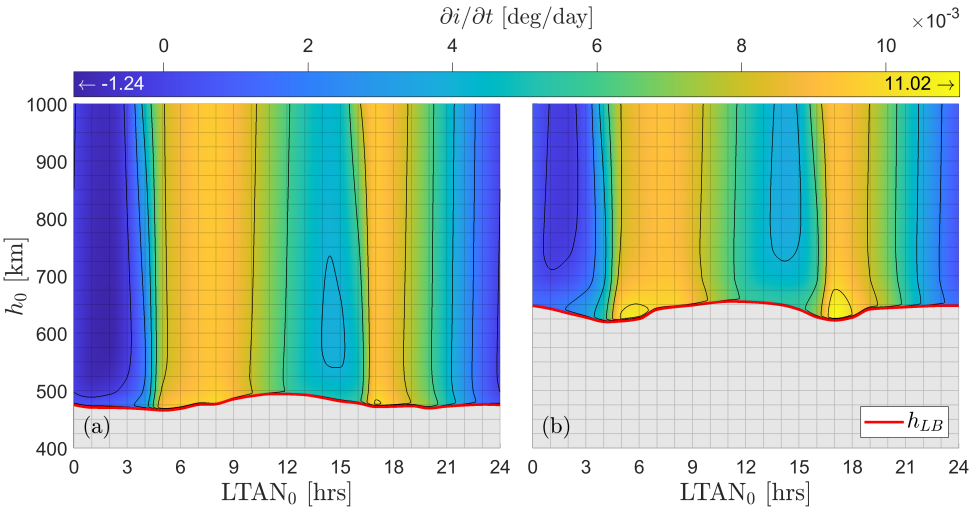


Figure 7.12: Inclination gain rates obtained for solar activities of (a) minimum and (b) maximum intensity.

a higher minimum altitude for which maneuvering is possible, h_{LB}. Notably, the graphs also show that, for altitudes above h_{LB}, the achievable inclination gains become almost independent of the solar activity. This is due to the fact that, outside the high-density region of the atmosphere, inclination change is obtained by exploiting primarily the SRP and PRP accelerations rather than aerodynamic acceleration. Consequently, the results are less affected by the intensity of the solar activity and atmospheric drag.

7

7.5.4. ANALYSIS OF THE EFFECT OF CHARACTERISTIC ACCELERATION

The characteristic acceleration, a_c, is a measure of the achievable thrusting performance of a sailcraft and changes in its value affect the achievable SRP, PRP, and aerodynamic accelerations in a linear manner. To investigate the impact of the characteristic acceleration on the sailcraft maneuverability, the parametric analysis in Section 7.5.1 has been repeated using two different values for a_c equal to either 1/10 or 10 times the characteristic acceleration of ACS3, a_c^{ref}, see Table 7.4.

Figure 7.13 displays the results for the orbit-raising case. As can be observed, the way in which $\partial h/\partial t$ varies with the initial altitude and LTAN, as well as the minimum altitude for maneuvering, h_{LB}, are essentially independent of the characteristic acceleration considered. Comparison with the results obtained for the reference scenario, for which $a_c = a_c^{ref}$, also supports this finding, see Fig. 7.9a. This result highlights that improving the sailcraft characteristic acceleration cannot be used to extend the range of altitudes wherein solar-sail missions can be flown. Furthermore, within this altitude range, the magnitudes of the achievable altitude gains scale in a linear manner with a_c, as can be observed from the different limits of the colorbars in the plots in Fig. 7.13. On the one hand, this result is a consequence of the proportionality of $\boldsymbol{a}_{SRP}$, $\boldsymbol{a}_{PRP}$, and $\boldsymbol{a}_{Aero}$ with a_c. On the other hand, it is also due to the fact that these accelerations are orders of magnitude smaller than the Earth's gravitational accelerations and affect the dynamics to a limited extent. In the frame of linear perturbation theory, this allows to linearly correlate

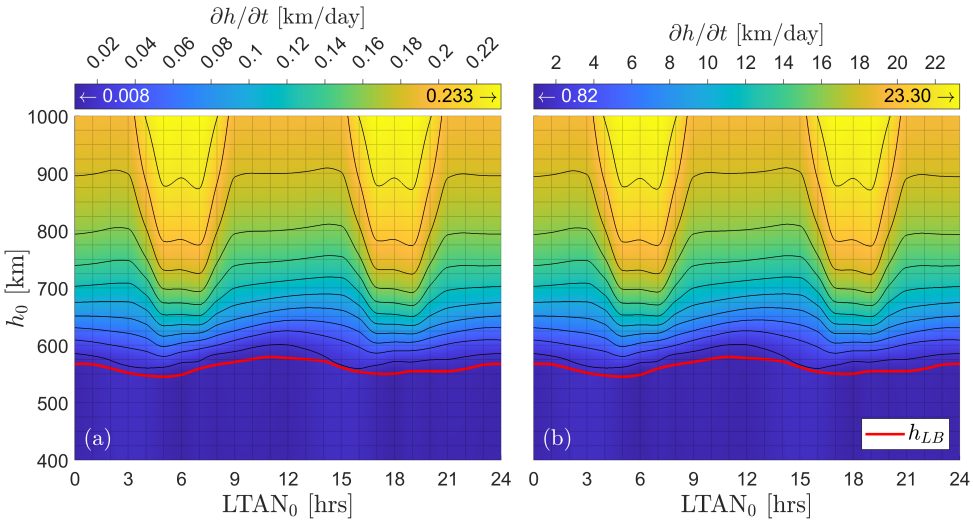


Figure 7.13: Altitude gain rates obtained for characteristic accelerations (a) ten times larger and (b) ten times smaller than that of ACS3.

the magnitude of the SRP, PRP, and aerodynamic accelerations with $\partial h/\partial t$, thus resulting in the linear behavior observed in Fig. 7.13. Importantly, this result allows to infer the orbit-raising performance of solar sails for values of a_c between $a_c^{ref}/10$ and $10\,a_c^{ref}$, that is, for a range of characteristic accelerations representative of a wide spectrum of sailcraft performance, from very limited to futuristic performance. Therefore, interpolation of the results presented in Fig. 7.13 can be conducted to forecast the orbit-raising capabilities of a broad variety of sailcraft, hence proving valuable for the preliminary design of future solar-sail missions.

Similar to Fig. 7.13, Fig. 7.14 illustrates the results for the inclination-changing case. As shown, for $a_c = 10\,a_c^{ref}$, the LTANs corresponding to the best maneuvering performance lie around 06:00 or 18:00 hrs (dawn-dusk orbits), as highlighted by the vertical bands of the contour plot in Fig. 7.14b. This trend is similar to that observed in the reference scenario, valid for $a_c = a_c^{ref}$, see Fig. 7.9b. In line with this observation, the inclination gains are found to scale approximately linearly with a_c between a_c^{ref} and $10\,a_c^{ref}$, particularly within the above-mentioned vertical bands. Fig. 7.14a shows that, for small characteristic accelerations of $a_c = a_c^{ref}/10$, the linear correlation between a_c and $\partial i/\partial t$ no longer holds, as the achieved contour pattern is substantially different from that observed for $a_c \geq a_c^{ref}$. In addition, for LTANs close to 00:00 hrs, negative inclination gains are obtained that have an absolute magnitude comparable to that found for LTANs around 12:00 hrs. Further investigation showed that this particular pattern originates from second-order effects given by the J_2 gravitational acceleration, which become visible because of the extremely small inclination changes achieved. Indeed, excluding the J_2 gravitational acceleration from the dynamics was found to yield a contour pattern similar to those for $a_c \geq a_c^{ref}$.

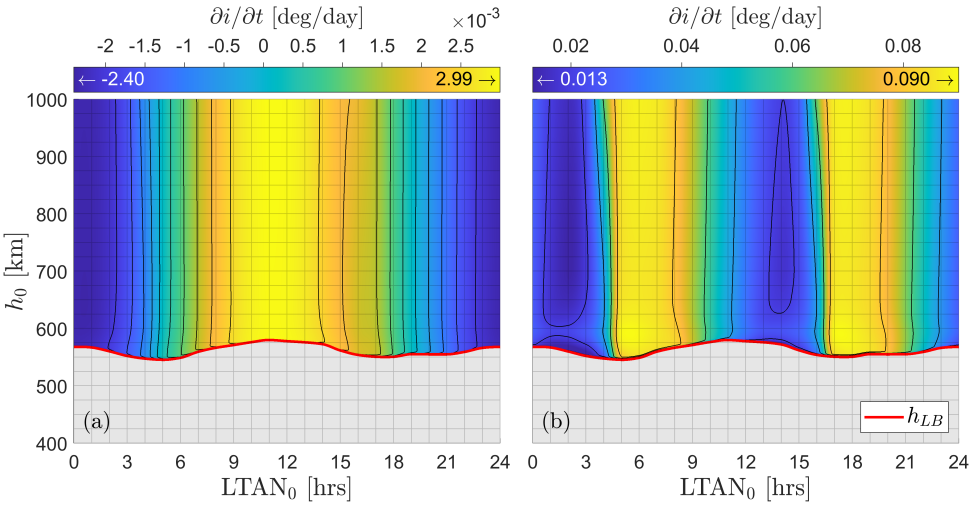


Figure 7.14: Inclination gain rates obtained for characteristic accelerations (a) ten times smaller and (b) ten times larger than that of ACS3.

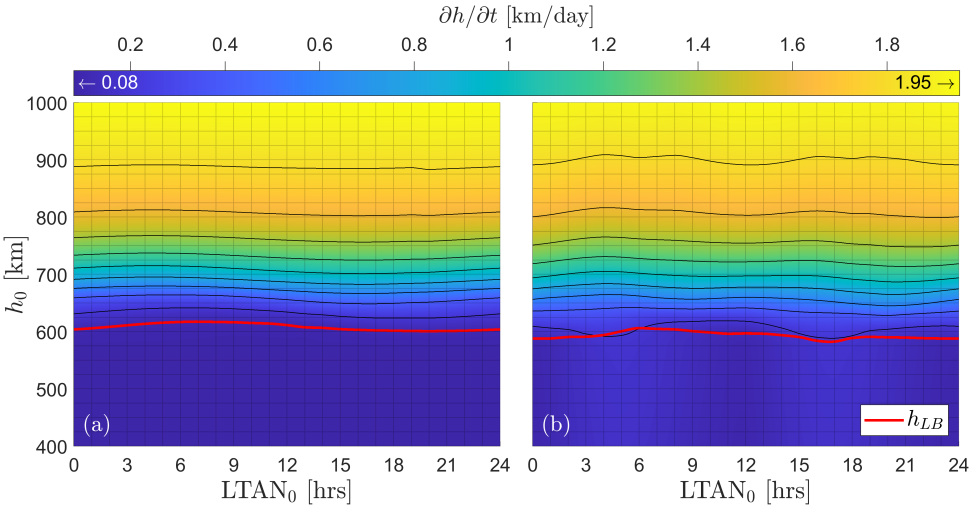


Figure 7.15: Altitude gain rates obtained for inclinations of (a) 0.5 deg and (b) 45 deg.

7.5.5. ANALYSIS OF THE EFFECT OF ORBITAL INCLINATION

To explore how the solar-sail maneuvering capabilities vary with orbital inclination, the parametric analysis in Section 7.5.1 – valid for Sun-synchronous inclinations, i_{SSO} – has been performed again, considering quasi-equatorial and mid-latitude inclinations of 0.5 and 45 deg, see Table 7.4.

Figure 7.15 illustrates the results for the orbit-raising case. Interestingly, the graphs display very similar trends, with $\partial h/\partial t$ only weakly depending on the initial LTAN, LTAN$_0$. These results diverge considerably from those obtained in the Sun-synchronous case, see Fig. 7.9a, which showed a clear variation of $\partial h/\partial t$ with LTAN$_0$. Furthermore, for

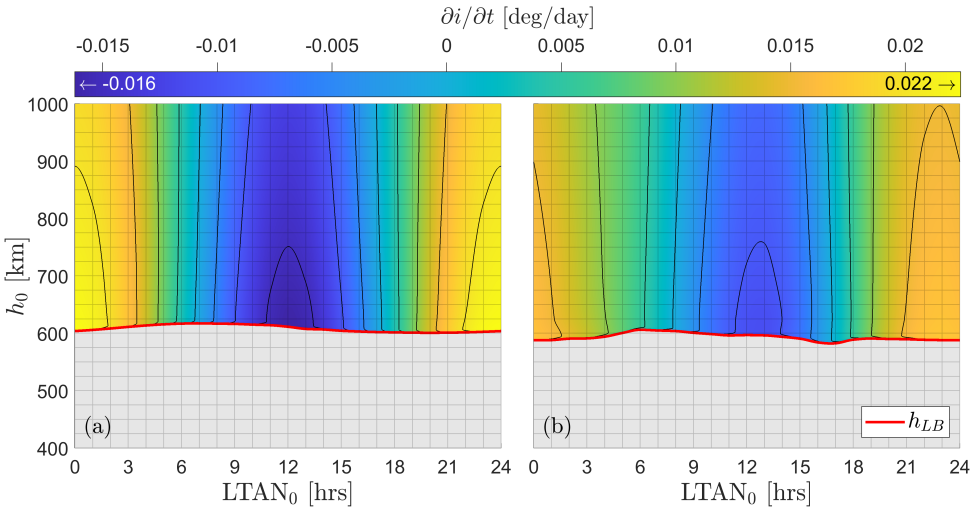


Figure 7.16: Inclination gain rates obtained for inclinations of (a) 0.5 deg and (b) 45 deg.

quasi-equatorial and mid-latitude inclinations, a slightly higher minimum altitude for maneuvering of approximately $h_{LB} = 600$ km is found. The absence of dependency on the LTAN stems from the fact that, unlike in the Sun-synchronous case, eclipses occur for *all* LTANs and with a similar duration. Consequently, regardless of the LTAN, the resulting altitude gains are almost identical to those found for eclipsing Sun-synchronous orbits with LTANs around 00:00 and 12:00 hrs, see again Figs. 7.9a and 7.15.

Figure 7.16 displays the results for the inclination-changing steering law. As can be seen, the $\partial i/\partial t$ contour patterns resemble each other. However, a wider variability with the LTAN is found for quasi-equatorial orbits, as indicated by the more closely spaced contour lines. Notably, while positive inclination gains are achieved for LTANs close to 00:00 hrs, negative gains of comparable (absolute) magnitude are found for LTANs around 12:00 hrs, for both quasi-equatorial and mid-inclination orbits. Similar to the inclination-changing results in Section 7.5.4 for $a_c = a_c^{ref}/10$, this is a consequence of second-order effects given by the J_2 gravitational acceleration, which are visible only when very minor inclination gains are achieved.

7.5.6. ANALYSIS OF THE EFFECT OF SOLAR DECLINATION

In this section, the parametric analysis in Section 7.5.1, which considered a simulation start time at the spring equinox of 2027 corresponding to a solar declination of zero, has been performed again with different start dates. These are the summer and winter solstices of 2027, which correspond to maximum and minimum solar declinations of 23.45 deg and −23.45 deg, respectively, see Table 7.4.

Figure 7.17 displays the results for the orbit-raising case. As can be observed, the two graphs show an almost specular variation of $\partial h/\partial t$ with LTAN$_0$ with respect to the LTAN$_0$ at 12:00 hrs. This result originates from the coupled effect of the fact that the Sun-synchronous orbital inclination is not exactly polar and the non-zero solar declinations. Specifically, at the summer solstice and for LTANs around 18:00 hrs, the orbit is oriented

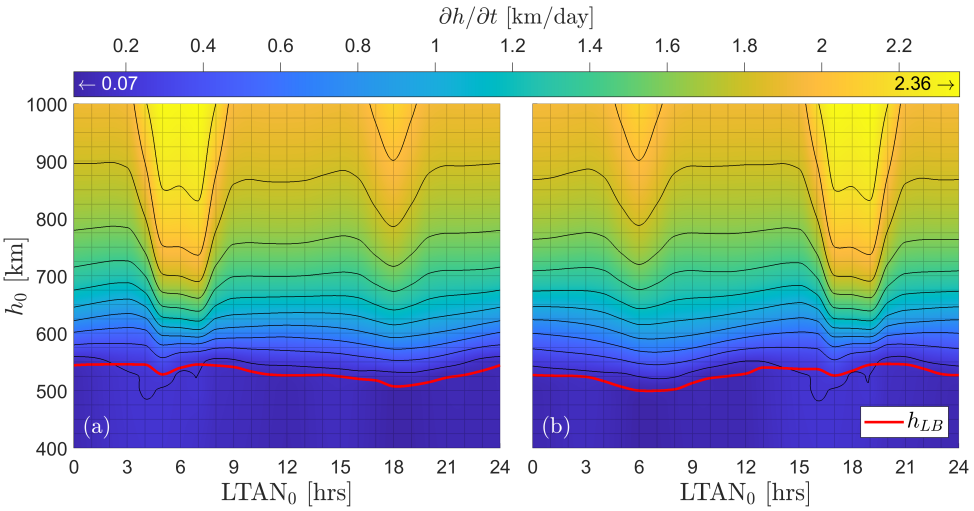


Figure 7.17: Altitude gain rates obtained for (a) summer and (b) winter solstices.

such that the angle between the incoming sunlight and the orbital plane is approximately 57 to 60 deg, depending on altitude. This leads to eclipses and, therefore, reduced orbit-raising capabilities. Conversely, for LTANs around 06:00 hrs, the non-polar inclination and solar declination partially counteract each other, leading to a much larger angle between the sunlight direction and the orbital plane of approximately 74 to 76 deg. This results in eclipses that are either absent or of very short duration, thus yielding larger altitude gains. When considering the winter solstice, the aforementioned geometry is reversed: LTANs around 18:00 hrs correspond to short-term eclipses or their complete absence, while LTANs around 06:00 hrs correspond to long eclipses. As a consequence, the altitude gains achieved are also reversed, though retaining the same magnitude. It should be noted that the above geometric interpretation also holds in the reference scenario. In that case, however, because the solar declination is zero, both LTANs at 06:00 hrs and 12:00 hrs lead to an absence of eclipses and exactly equal orbit-raising capabilities, see Fig. 7.9a. This result suggests that, as the seasons transition from summer to winter and back, the range of LTANs corresponding to the most optimal orbit-raising performance gradually shift from around 06:00 hrs to around 18:00 hrs and back.

Figure 7.18 illustrates the results for the inclination-changing steering law. Similar to the orbit-raising case, the influence of the presence or absence of eclipses on the results is evident: in summer, a better inclination-changing performance is obtained for LTANs at around 06:00 hrs, whereas in winter the same is true for LTANs at approximately 18:00 hrs. Finally, comparison with the reference results in Fig. 7.9a suggests that, over the course of a year, the range of LTANs corresponding to the most optimal inclination-raising performance gradually oscillates between around 06:00 hrs and around 18:00 hrs.

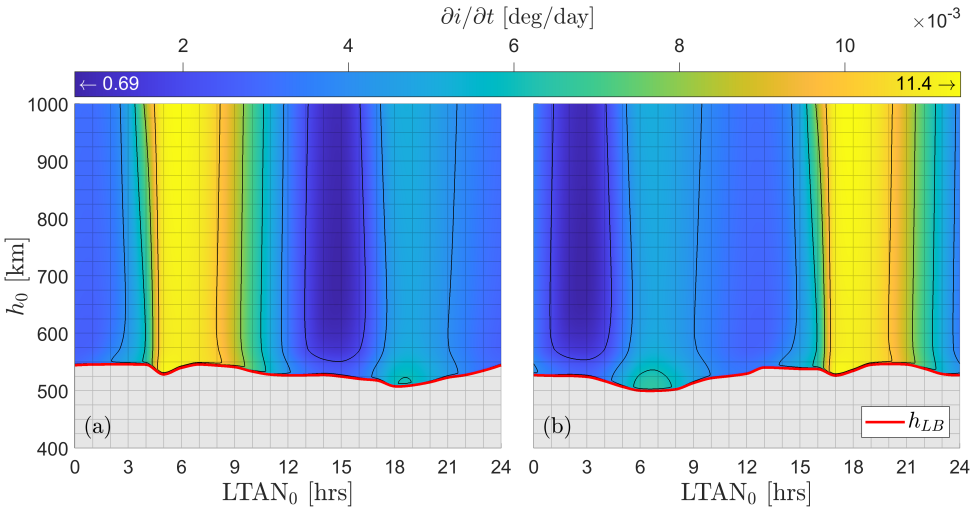


Figure 7.18: Inclination gain rates obtained for (a) summer and (b) winter solstices.

7.6. CONCLUSIONS

This chapter presented a wide set of analyses aimed to thoroughly characterize the maneuvering capabilities of solar sails around the Earth. For this purpose, a trajectory optimization algorithm was developed to locally optimally increase any orbital element of choice, while accounting for and exploiting high-fidelity solar-sail dynamics. The optimization procedure was designed to guarantee robustness against the highly diverse near-Earth dynamical environment – which makes trajectory optimization particularly challenging – while minimizing computational effort. The developed algorithm was employed to compute orbit-raising and deorbit-safe inclination-changing steering laws, that is, inclination-changing control laws explicitly designed to avoid sailcraft deorbiting at low altitudes.

Analysis of the sailcraft maneuvering capabilities in the near-Earth environment was conducted using NASA's ACS3 solar-sail mission as baseline, considering a broad range of orbits with different altitudes, local times of the ascending node (LTANs) and inclinations, for different sailcraft characteristic accelerations, solar activities, and times of the year. The results highlight that solar activity strongly influences the minimum altitude at which maneuvering is feasible without risking deorbiting. When transitioning from minimum to maximum solar activity intensities, this altitude was found to increase by approximately 160 km, from around 465 – 495 km to 620 – 655 km. Outside the high-density region of the atmosphere, the orbit-raising capabilities were found to steadily improve with altitude, reaching values even in the order of 2 km/day for ACS3-like sailcraft. Leveraging planetary radiation pressure (PRP) acceleration to perform orbit raising proved to be particularly beneficial for (quasi-)noon-midnight orbits, as PRP can increase the achievable altitude gains by up to 6%. Nevertheless, the best orbit-raising performance across all scenarios was consistently found for dawn-dusk orbits. This orbital configuration is characterized by minimal presence (or absence) of eclipses, thereby allowing to exploit solar radiation pressure (SRP) for maneuvering for longer. Notably, the orbit-raising capabilities were

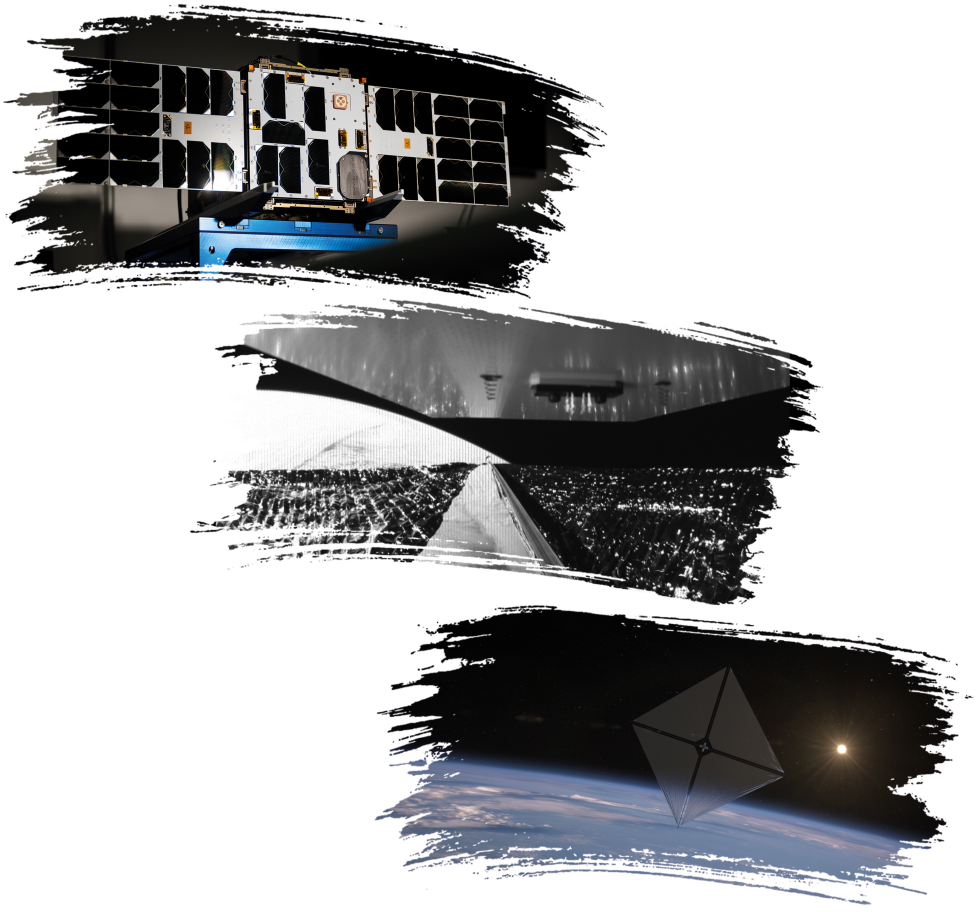
found to change linearly across a wide range of solar-sail characteristic accelerations, ranging from very limited to futuristic sailcraft performance. Therefore, the results presented in this chapter can be effectively used to inform the design of both near-future and long-term solar-sail missions. Similar to the orbit-raising capabilities, the inclination-changing capabilities were observed to scale linearly with the characteristic acceleration, however only for large-enough characteristic accelerations. Furthermore, the achievable inclination changes were found to be almost independent of the altitude, but they vary with the orbit orientation. Finally, it is important to note that the achievable inclination gains across all scenarios considered were found to be minimal, with values in the order of one hundredth of a degree per day for ACS3-like sailcraft. This indicates that achieving meaningful orbital changes through out-of-plane maneuvering can require very long time, potentially rendering such maneuvers impractical for real-life Earth-bound orbital transfers. On the other hand, out-of-plane maneuvering may still prove useful when only minor orbital changes are sought, e.g., for collision avoidance or orbit maintenance.

ACKNOWLEDGEMENTS

The authors thank W. Keats Wilkie from NASA Langley Research Center for several fruitful discussions and for generously sharing information regarding the ACS3 mission.

8

Conclusions and Recommendations



ABSTRACT

This chapter presents the main research findings of the dissertation, building on the investigations conducted in Chapters 2 to 7. In this way, the main research question underlying the entire dissertation and represented hereinafter will be answered:

What are the maneuvering capabilities of present-day and future solar sailcraft within the near-Earth dynamical environment?

To answer the above question, the subquestions introduced in Section 1.4 will be addressed, serving as anchor points guiding the discussion in the chapter. The discussion will first focus on the subquestions concerning the dynamical modeling of Earth-bound solar sails in Section 8.1 and then on the characterization of their maneuvering capabilities, in Section 8.2. In addition to answering the subquestions, these sections will also provide the opportunity to outline recommendations for further research on the topics discussed.

Cover graphic by Vincenzo Bortone. The illustration presents three views of NASA's ACS3 sailcraft: on ground during the final tests before launch (top), photographed from the central bus during in-orbit sail deployment (center), and fully deployed in space (bottom, rendered). Images retrieved from NASA Image and Video Library [426]. Credits: National Aeronautics and Space Administration.

8.1. EARTH-BOUND SOLAR-SAIL DYNAMICAL MODELING

The research aimed at characterizing and further develop the dynamical models for Earth-bound solar sailing is provided in Chapters 2 to 5. Chapter 2 provided a detailed review of the models available in the literature to describe the dynamics of Earth-bound solar sails. To this end, different models to represent the sailcraft shape and properties, the near-Earth dynamical environment, and the accelerations originating from their interaction were discussed, highlighting the accuracy of these models and, in particular, of those employed in the remainder of the dissertation. Motivated by Chapter 2, Chapters 3 and 4 introduced novel models for the planetary radiation pressure (PRP) acceleration for ideal and optical sails, detailing their mathematical derivations and accuracies in a variety of orbital scenarios. Finally, parallel to theoretical modeling, Chapter 5 introduced steering laws to estimate the sailcraft accelerations directly from in-orbit data, in order to enable modeling of the solar-sail dynamics empirically.

8.1.1. RESEARCH FINDINGS

The first research subquestion laid down in Chapter 1 was:

1. *How do the different accelerations characterizing the near-Earth environment contribute to the overall acceleration experienced by solar sails around the Earth?*

This question is primarily addressed in Chapter 2, which provides a review and selection of the most significant accelerations affecting the dynamics of sailcraft in low Earth orbit (LEO), and in Chapters 7, wherein the regions of the near-Earth environment in which different accelerations dominate the dynamics are identified.

As discussed in Section 2.2.1, the gravitational acceleration experienced by Earth-bound sailcraft can be modeled with exceptionally high accuracy and precision by incorporating different contributions, including those arising from the non-spherical gravity field of the Earth, third-body gravity, tides, and relativistic corrections. Among these contributions, the most significant for the analysis and design of Earth-bound solar-sail missions is that due to the Earth's non-spherical gravity and, specifically, its equatorial bulge. The reason is that the corresponding J_2 gravitational acceleration leads the orbit to precess, with potential implications for the presence of eclipses, the illumination conditions of the sailcraft across the orbit, and, therefore, the solar radiation pressure (SRP) and albedo radiation pressure (ARP) accelerations exerted onto the sailcraft. The other contributions to the overall gravitational acceleration experienced by the sailcraft influence the dynamics to a much lesser extent, as these contributions are at least three orders of magnitude smaller than the J_2 acceleration. Therefore, they become relevant only for precise mission design, operations, and applications involving estimation of sailcraft parameters, in line with the treatment in Chapter 5.

For sailcraft in LEO, the SRP, PRP, and aerodynamic accelerations are generally orders of magnitudes smaller than the Earth's central and J_2 gravitational accelerations, see Section 2.2.2. However, their central relevance stem from the fact that they can be controlled through the sailcraft attitude, thereby enabling maneuvering. Although other sources of attitude-dependent accelerations exist – notably, the pressure of solar-wind protons, the Poynting-Robertson effect, and the Lorentz force imparted on the sail – these

have magnitudes more than four orders of magnitude smaller than the SRP, PRP, and aerodynamic accelerations. Therefore, they can be reasonably neglected.

The way the attitude-dependent accelerations contribute to the overall acceleration experienced by the sailcraft strongly depends on the sailcraft position with respect to the Earth and the Sun. As discussed in Section 7.4 and visualized in Fig. 7.8, the solar-sail dynamics are dominated by the aerodynamic acceleration in the lower layer of the atmosphere, typically below 500 km, whereas the SRP and PRP accelerations become increasingly more influential on the dynamics as altitude increases. Notably, the most dynamically complex region – where all three aforementioned accelerations contribute meaningfully to the overall acceleration – is in proximity of the sub-solar point. Conversely, sailcraft located diametrically opposite to that point are in eclipse and, therefore, experience neither SRP nor ARP accelerations.

Following the selection of the most significant accelerations affecting the near-Earth solar-sail dynamics, the second research question addresses the modeling fidelity of these accelerations as follows:

2. *How accurately do solar-sail acceleration models of varying fidelity describe the dynamics of Earth-bound solar sails?*

This question is also addressed in Chapter 2, which provides a comprehensive review of the models available in the literature to represent the SRP, PRP, and aerodynamic accelerations. In addition, after presenting the novel spherical PRP acceleration model, Chapters 3 provides information on the relative difference in PRP acceleration magnitude between said model and state-of-the-art models.

The SRP acceleration may be represented using a variety of models which differ for the underlying assumptions they consider and, correspondingly, the errors they introduce in the acceleration magnitude and direction. As discussed in Section 2.4.3.1, considering a constant Total Solar Irradiance (TSI) introduces only a minimal error in acceleration magnitude at most in the order of 0.1%. In contrast, changes in solar flux due to the eccentricity of the Earth's orbit yield acceleration variations in the order of 3.3%, see Section 2.4.3.2. Section 2.3.2 showed that assuming ideal optical properties – that is, a perfectly reflecting sail – instead of employing an optical sail model can result in errors in the order of 10% in acceleration magnitude and tens of degrees in acceleration direction, especially for large sunlight incidence angles. Similar errors in acceleration magnitude and direction are also obtained when neglecting radiation-induced sail material degradation, although only on long time scales spanning months to years. The data in Fig. 2.6a-b from Ref. [268] highlights that variations in reflectivity and absorptivity with the sunlight incidence angle in the order of 5-10% can be obtained, again, especially for large incidence angles. Finally, among the most important sources of modeling error is the assumption that the sail is perfectly flat. Indeed, the preliminary studies given in Refs. [255–257] and discussed in Section 2.3.1 have shown that, for a static, billowed sail presenting wrinkles and creases, the associated error can be in the order of 10% in magnitude and tens of degrees in direction. Notably, however, the shape of a solar sail, as well as the presence and amount of wrinkles and creases on its surface, generally vary with time, the orbit, and the specific mission considered. Therefore, defining an error interval with confidence is difficult, and errors larger than those predicted by the above studies for the static case may occur.

The influence of PRP acceleration modeling on the solar-sail dynamics had only been explored to a limited extent before the investigation presented in this dissertation. Compared to the SRP acceleration, the PRP acceleration was known to have a more limited impact on the dynamics, as it attains values typically between 10% and 30% of the maximum SRP acceleration in LEO. However, the PRP acceleration was also expected to exhibit larger modeling errors overall. The reason is that, along with the sources of approximation concerning the sail's shape, optical properties, and degradation that also characterize SRP acceleration modeling, PRP acceleration modeling is inherently subject to additional uncertainty stemming from the representation of the Earth's radiative output. Nevertheless, research confirming this expectation was lacking, as literature on PRP-perturbed solar sailing was available to a very limited extent, and it only considered ideal sails and finite-disk representations of the Earth as radiation source. A preliminary analysis of the error introduced by the finite-disk model on the PRP acceleration magnitude was provided in Section 2.5.5, which highlighted that relative errors in the order of 10% can be achieved when radiation is received by only one side of the sail. This result was confirmed and further extended to the case when both sides of the sail are exposed to planetary radiation in Section 3.5.1, showing that even larger errors are found for intermediate planetary pitch angles between 45 and 75 deg, see Fig. 3.9. Furthermore, assuming the flux of albedo radiation to depend on the cosine of the Sun-Earth center-sailcraft angle instead of on the phase function introduces an additional error in the order of $5-7\%$, see Fig. 3.10.

The solar-sail acceleration affected by the largest modeling errors is the aerodynamic acceleration. These errors stem from uncertain knowledge of the atmospheric density, as well as from uncertainty regarding the sail shape and the modalities of Gas-Surface Interaction (GSI), which together govern the drag and lift coefficients. As discussed in Section 2.4.2.1, current state-of-the-art atmospheric density models achieve relative errors in density estimates up to 15-20% for altitudes at 300 km, 30-50% at 500 km, and even larger errors for altitudes between 500 and 1000 km. In the latter altitude range – corresponding to the altitudes of interest for Earth-bound solar sailing – assuming hyperthermal free-molecular flow conditions instead of non-hyperthermal conditions also introduces an error, though of a smaller magnitude, in the order of 5-10%, see Section 2.5.2.2. At LEO altitudes, and especially above 500 km, the nature of GSI remains highly uncertain because it strongly depends on the sail surface properties at the atomic scale and the relative amounts of different species in the atmosphere – two aspects that are extremely difficult to model accurately. As a result, errors in the accommodation coefficients characterizing GSI even in the order of 50% may arise, see again Section 2.5.2.2. The impact of deviations in sail shape from a perfectly flat configuration on the aerodynamic coefficients is more challenging to estimate. As discussed in Section 2.3.1, studies that do not assume free-molecular flow conditions show that even slight billowing can yield extremely large errors in these coefficients, even in the order of 100% [259–261]. Therefore, although these results cannot be directly transposed to free-molecular flow regimes, errors in the the drag and lift coefficients of a similar magnitude can be expected. Finally, the impact of sail material degradation – e.g., induced by interaction with atomic oxygen – on the aerodynamic acceleration is also uncertain, and represents an active field of research [112, 408].

The above discussion highlighted that the aerodynamic and PRP accelerations are associated to particularly large margins of error. This consideration, together with the fact that these accelerations are specific to the near-Earth environment, allows to directly address the third research subquestion, namely:

3. *Among existing solar-sail acceleration models, which are the least mature and require further development to support practical Earth-bound mission planning?*

Although refining SRP acceleration models would certainly benefit the design of Earth-bound solar-sail missions, priority ought to be given to improving existing models for the aerodynamic and PRP accelerations, as these accelerations are associated with larger errors and greater dynamical uncertainties. It is important to note that, while the aerodynamic and PRP accelerations both require an improved fidelity to the actual conditions encountered by sailcraft in LEO, these improvements are constrained in two fundamentally different ways. As discussed in Section 2.4.2.1, higher-fidelity modeling of the aerodynamic acceleration is limited by the need of empirical data, especially for altitudes above 500 km. This is because the most widely used atmospheric density models, including the models from the Jacchia, Drag Temperature Model (DTM), and Mass Spectrometer and Incoherent Scatter (MSIS) series, have been developed leveraging data retrieved by satellites orbiting at altitudes below 500 km, notably, CHAMP, GOCE, and GRACE. Although some recent models such as the NRLMSIS 2.0 account for the presence of anomalous oxygen to improve fidelity above 500 km, also their accuracy degrades rapidly above 600 km. On the other hand, the discussion in Sections 2.5.3 and 2.5.5 showed that the fidelity of PRP acceleration models was limited either by mathematical complexity or by the simplifying assumptions underlying the existing models in the literature, namely, the representation of the Earth as a finite-disk radiation source and the ideal reflection properties of the sail.

With the above in mind, the fourth research subquestion may be answered:

4. *What higher-fidelity solar-sail acceleration models can be developed from the existing state of the art, and how do they improve upon available models?*

Before this dissertation, all works on solar sailing accounting for the PRP acceleration represented this acceleration using the ideal finite-disk model introduced in Section 2.5.3.3, which was regarded as the state of the art. Initially devised by McInnes [2] for the SRP acceleration, this model assumes the sail to have ideal optical properties and the radiation source to have a disk-like shape with a finite angular size. Although this representation of the radiation source enables a higher degree of fidelity than the more commonly employed point-like radiation source model, see Fig. 2.16, it still relies on a simplifying assumption inherited from the point-like model: that radiation reaches the sail in parallel rays. This assumption is reasonably valid at large distances from the radiation source, therefore making it suited for calculating the SRP acceleration, as McInnes originally intended. However, this simplifying assumption introduces significant errors when calculating the PRP acceleration induced by the Earth on LEO sailcraft, due to the large angular size of the planet as seen from the sail. As an alternative to the finite-disk model, other studies have formulated the PRP acceleration for different satellite geometries using integral and series-expansion forms, see Sections 2.4.4 and 2.5.5. These formulations, however, do not lead to closed-form expressions of the PRP acceleration, primarily because of the

mathematical complexity introduced by the dependency of the radiative output of the Earth on the geographical location considered and its illumination conditions.

Despite the simplistic assumptions and mathematical difficulties characterizing the aforementioned models, the available knowledge of the Earth radiation environment and physics of sail-radiation interaction was sufficient to develop higher-fidelity, analytical PRP acceleration models. This was first suggested in Section 2.5.5 and subsequently demonstrated in Chapters 3 and 4, which present the newly developed spherical PRP acceleration models for ideal and optical solar sails, respectively. These models overcome the parallel-ray assumption of the finite-disk PRP acceleration model by considering the Earth to be a spherical radiation source, such that radiation impinges on the sail simultaneously from multiple directions. Furthermore, to express the PRP acceleration in a closed-form, analytical manner, a local surface averaging approach was employed to express the geographical variation of the blackbody radiation flux, albedo coefficient, and the illumination conditions of the Earth as seen from the sailcraft's perspective.

The analyses in Sections 3.5.2 and 4.3 aimed to quantify the increase in fidelity achieved by these models compared to the state of the art through assessment of the sailcraft maneuvering capabilities. The results show that the ideal sinusoidal spherical model developed in this dissertation yields a significant improvement over the ideal finite-disk model, typically reducing the errors in the predicted orbit-raising and inclination-changing capabilities by a factor 5, see Figs. 3.11-3.14. Furthermore, accuracy can be further improved through the optical sinusoidal spherical model also developed in this dissertation, which removes the assumption of ideal reflection. Indeed, when compared to a high-fidelity numerical model, errors are reduced from $5-23\%$ for the ideal model to $1-6\%$ for the optical model, see Fig. 4.6.

Parallel to analytical modeling, improvement of the fidelity of the solar-sail acceleration models may also be pursued by means of an alternative approach relying on in-orbit data. This is the philosophy underlying the calibration steering laws presented in Chapter 5, which were applied therein to solar-sail operational scenarios subject to real flight constraints. These control laws were designed to estimate the empirical accelerations experienced by Earth-orbiting sailcraft, thereby allowing to assess the accuracy of existing acceleration models and enabling their refinement. Chapter 5 highlighted that, in this case, the ability to improve the fidelity of the solar-sail dynamics is primarily limited not by the lack of analytical modeling tools or understanding of the physics underlying the solar-sail accelerations, but rather by the current readiness level of solar-sail technology. As exemplified by NASA's Advanced Composite Solar Sail System (ACS3) mission, the technological capabilities of present-day sailcraft allow only for relatively simple, fixed-pointing steering laws, see Section 5.6.1. Furthermore, these steering laws ought to guarantee power positivity and sufficient communication time with the ground stations – two requirements which were found to be the most constraining for the practical implementation of these steering laws, see Sections 5.6.2 and 5.7.2. In addition, it should be noted that additional requirements concerning the estimation process may also play an important role for the feasibility of the steering laws. This represents an active field of research [406].

8.1.2. RECOMMENDATIONS

As discussed in the previous section, some sources of perturbations affecting solar-sail accelerations are particularly difficult to model accurately, primarily due to incomplete knowledge – or the inherently non-deterministic nature – of the underlying physical processes involved. Examples include the perturbations arising from deviations in predicted atmospheric density and GSI, as well as the irregular variations in TSI, sail deformation, and formation of creases and wrinkles on the sail surface. In view of the uncertainty characterizing these perturbations, modeling the corresponding accelerations using a deterministic approach (as the one adopted in this dissertation) allows improvements in fidelity only to a limited extent, whereas employing a probabilistic approach may be more suited. As discussed in Section 8.2.2, such a probabilistic description of the solar-sail dynamics would enable statistical characterization of the solar-sail maneuvering capabilities, paving the way to uncertainty-aware, robust trajectory design.

The novel spherical PRP acceleration models for ideal and optical sails presented in this dissertation offer significant potential for application and further development. While these models were presented to investigate the potential of Earth-bound solar sailing, they can also be employed to explore solar sailing in proximity of other celestial bodies. A notable example is Venus, whose extremely intense blackbody and albedo radiation make the achievable PRP acceleration often greater than the SRP acceleration [222], effectively rendering the planet – instead of the Sun – the primary source of radiation. Solar sails may therefore prove particularly useful for Venus-centered missions, making the application of accurate PRP acceleration models – such as those presented in this dissertation – paramount to mission design.

Further work on the modeling of the PRP acceleration could focus on extending the spherical PRP acceleration model to account for advanced transmissive and refractive sail materials [357]. In this way, the model could be applied to a broader range of solar-sail designs, expanding its scope of applicability. Furthermore, although developed for solar sails, it is important to note that the spherical PRP acceleration model is applicable to any flat surface impinged on by planetary radiation. Therefore, future work could extend the model to compute the PRP acceleration of spacecraft with arbitrarily complex shapes by approximating the satellite geometry through a set of adjacent flat surfaces – similar to standard box-wing models – and considering only the faces exposed to planetary radiation. Such an extension must, however, account for potential self-shadowing, which is absent when considering flat sails. The same logic may also be employed to extend the spherical PRP acceleration model to billowed solar sails. In this case, the sail can be represented through a mesh of facets, allowing to compute the total PRP acceleration as a sum of the facets' individual contributions. Alternatively, an analytical approach may be pursued instead by adapting the generalized sail model [253] – originally devised for the SRP acceleration – to the PRP acceleration. However, this approach may require significant analytical effort, as the generalized sail model assumes radiation to reach the sail in parallel rays and without any self-shadowing occurring – two conditions that generally do not hold true for planetary radiation illuminating non-planar sails.

As discussed in the previous section, calibration steering laws may be employed to refine current solar-sail acceleration models and, consequently, partially reduce the aforementioned uncertainties. To enable the calibration process, data comprising position

and attitude measurements is required, so as to reconstruct the attitude profile of the sailcraft and the impact of the solar-sail accelerations on the orbit, thereby allowing to estimate these accelerations and their dependencies with the sail attitude. Because orbit and attitude determination capabilities depend on the quantity and quality of the measurements, the calibration process greatly benefits from data collected through precise instruments over extended periods of time. Accordingly, it is preferable to perform the calibration over a dedicated phase of the mission, ideally soon after sail deployment, in order to characterize the in-orbit acceleration capabilities of the sailcraft and be able to inform the planning and execution of maneuvers for subsequent phases of the mission. Furthermore, if feasible, calibration could be repeated later in the mission to acquire insights into the degradation of the sailcraft acceleration performance caused by radiation- and aerodynamic-induced sail material degradation. To maximize the effectiveness of the calibration process, it is generally desirable to employ multiple instruments to measure the sailcraft position and attitude, giving priority to instruments that offer high accuracy and precision. E.g., the use of Global Navigation Satellite System (GNSS) receivers ought to be preferred to ground-based ranging for orbit determination [238, 427], whereas star trackers ought to be preferred to Sun sensors and magnetometers for attitude determination [238]. Importantly, uncertainties in the estimation process can be greatly reduced by coupling position-tracking sensors with onboard accelerometers. Indeed, using accelerometers enables the direct measurement of the non-gravitational, attitude-dependent accelerations of the sailcraft. The use of accelerometers therefore prevents the introduction of noise caused by mismodeling of the gravitational accelerations and, crucially, of the sailcraft's total acceleration when reconstructing these quantities from position measurements.

In addition to the estimation of the solar-sail accelerations from position and attitude measurements, dynamical uncertainties could also be reduced taking advantage of photographic imagery. Recently flown solar-sail missions, including ACS3 and Lightsail-2, have made use of cameras mounted on the central bus of the sailcraft and pointed toward the sail quadrants to assess the structural integrity of the sail and booms throughout the mission lifetime. In addition to inspecting structural integrity, this visual data may be used to characterize sail deformation, as well as the formation of creases and wrinkles over time, thereby enabling more accurate modeling of the temporal evolution of the sail geometry and its optical properties. Furthermore, photos taken from ground or other satellites may be used to determine the overall shape of the sailcraft and attitude change over time, thus providing valuable information to estimate the sailcraft accelerations. This approach was used by the ACS3 mission team, who deduced the pyramidal, in-orbit shape of the sailcraft from pictures taken by Maxar's WorldView-2 satellite, see Fig. 8.1.

As discussed in the previous section, the solar-sail dynamics in the denser regions of the atmosphere are dominated by aerodynamic drag, making orbital altitudes above 500 km the most relevant for Earth-bound solar sailing. Crucially, however, these altitudes also correspond to the region wherein knowledge of the atmosphere is characterized by the largest degree of uncertainty. As a consequence, reliable characterization of the composition and density of the atmosphere at altitudes above 500 km represents the primary challenge to overcome to increase the fidelity of solar-sail aerodynamic models. To this aim, estimation of the atmospheric density and aerodynamic coefficients from

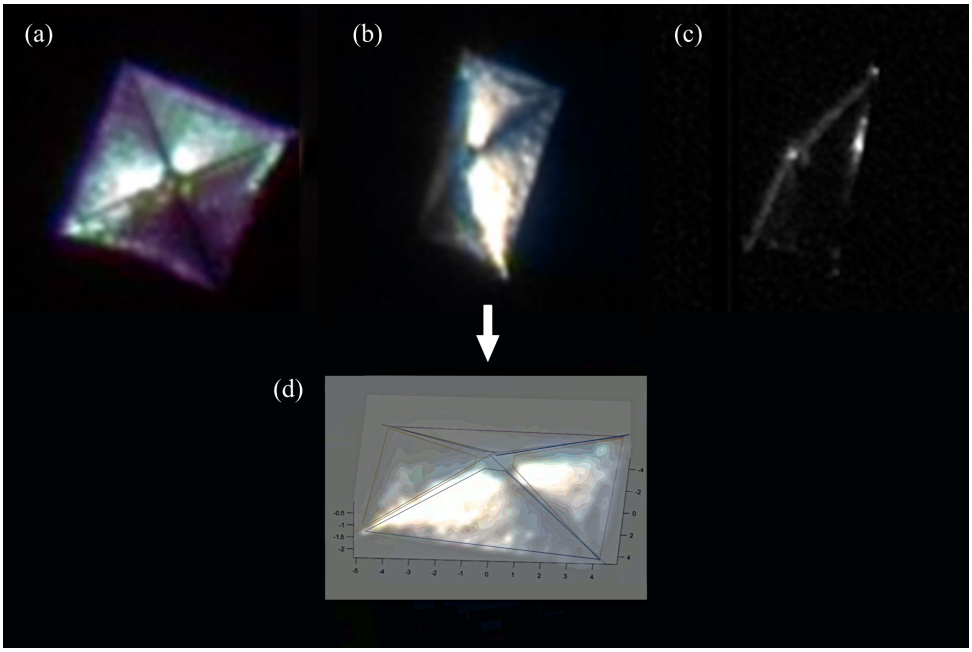


Figure 8.1: a-c) Photos of ACS3 taken by the WorldView-2 satellite on September 11, 2024 at 20-second intervals, and d) reconstruction of the sailcraft pyramidal shape by the ACS3 mission team. Image adapted from Ref. [129]; credits to Maxar.

precise orbit determination of satellites orbiting at these altitudes ought to be pursued increasingly more in the future. Alternatively, the density of the atmosphere and, crucially, of its composition may also be assessed in a more direct manner through the use of accelerometers and mass spectrometers aboard dedicated satellites and sailcraft. The use of several such satellites at different altitudes would help not only deepen knowledge of atmospheric density variability, but also determine the variation of the relative amounts of different atmospheric species and aerodynamic flow conditions with altitude – aspects of crucial importance to characterize the nature of GSI.

8.2. EARTH-BOUND SOLAR-SAIL MANEUVERING CAPABILITIES

The investigation of the maneuvering capabilities of Earth-orbiting sailcraft was conducted in Chapters 6 and 7. In both chapters, in-plane and out-of-plane maneuverability were evaluated for a variety of orbital scenarios, using the altitude and inclination rates of change achieved through locally optimal steering laws as metrics, respectively. Chapter 6 provided a first assessment of the influence of SRP acceleration and, crucially, aerodynamic acceleration on solar-sail maneuverability. To this aim, a novel locally optimal steering-law algorithm accounting for both accelerations in the optimization process was developed. Thereafter, Chapter 7 presented another newly devised locally optimal steering-law algorithm to account not only for the SRP and aerodynamic accelerations, but also the PRP acceleration in the definition of the control profile. Finally, this algorithm

was employed in a range of sensitivity analyses to assess sailcraft maneuverability for a large set of orbits, times of the year, solar activities, and sailcraft characteristics, chosen specifically to reflect realistic configurations of Earth-bound solar-sail missions.

8.2.1. RESEARCH FINDINGS

The fourth research subquestion posed in Chapter 1 was:

5. *To what extent can accelerations specific to Earth-bound solar sails hinder or enhance the in-plane and out-of-plane maneuvering capabilities of sailcraft?*

This question is addressed across Chapters 3, 4, 6, and 7, wherein the individual and combined effects of SRP, PRP, and aerodynamic accelerations on in-plane and out-of-plane maneuverability are assessed through the orbit-raising and inclination-changing capabilities of sailcraft.

The analyses in Section 3.5.2 and Section 4.3 assessed the errors in orbit-raising and inclination-changing capabilities when neglecting the PRP acceleration and including it using different models, relative to a high-fidelity numerical model. The steering laws considered were designed without accounting for the PRP acceleration, which, therefore, acted as a perturbing acceleration. Consequently, the observed relative errors in altitude and inclination gains when neglecting the PRP acceleration provide a direct measure of the detrimental effect of PRP as a source of perturbation. The analyses show that, depending on the orientation and altitude of the orbit, maximum errors in altitude increase between 12% and 17% are incurred assuming a perfectly reflecting solar sail, see Figs. 3.13a and 3.14a, whereas this range shrinks to $10-15\%$ when considering realistic sail optical properties, see Figs. 4.6a and 4.6c. Similarly, maximum errors in inclination in the ranges $27-46\%$ and $31-88\%$ are found for ideal and optical solar sails, respectively, as shown in Figs. 3.13b and 3.14b, and Figs. 4.6b and 4.6d. Importantly, Section 3.6 highlighted that when also the aerodynamic acceleration is left uncontrolled and acts as a perturbing acceleration, decreases in orbit-raising capabilities can be magnified by approximately a factor 2. This result can be observed through comparison of the results in Fig. 3.11 and Table. 3.1, for an orbital altitude of 715 km and orbit orientations corresponding to local times of the ascending node (LTANs) of 0000/1200 hrs. Also, the analyses in Sections 6.5, 7.5.1, and 7.5.3 highlighted the critical impact of aerodynamic drag at even lower altitudes, as below 450 km to 600 km (depending on the solar activity) orbit raising becomes effectively unachievable, whereas inclination changing can be achieved but yields rapid deorbiting, see Figs. 6.15, 6.17, 7.9, 7.11, and 7.13. On the other hand, from a complementary perspective, controlling the aerodynamic acceleration has the major advantage of avoiding loss of altitude, regardless of the steering law adopted, by orienting the sail edgewise with respect to the incoming wind flow. Finally, the analysis in Section 7.5.2 showed that, when controlled, the PRP acceleration can be leveraged to increase the orbit-raising and inclination-changing capabilities by up to $6-7\%$, as shown in Fig. 7.10.

The analyses of the maneuvering capabilities conducted in Sections 6.5 and 7.5 allow to answer also the last two research subquestions, namely:

6. *How do solar-sail in-plane and out-of-plane maneuvering capabilities vary across the near-Earth environment?*

7. *How do solar-sail in-plane and out-of-plane maneuvering capabilities change with increasing sailcraft performance, from present-day to future levels?*

The analyses in the aforementioned sections showed that in-plane maneuverability – measured through the orbit-raising capabilities – steadily increases with altitude for two reasons. Most importantly, atmospheric density decreases and, with it, the detrimental effect of aerodynamic drag. Secondly, the magnitude of the Earth's gravitational acceleration also decreases, therefore increasing the relative magnitude of the attitude-dependent accelerations used for maneuvering. Because these decreases vary exponentially with altitude, maneuverability increases most rapidly at low altitudes – below approximately 700 km to 900 km, from minimum to maximum solar activity – while increases become less pronounced above these altitudes, see Figs. 6.15, 7.9 and 7.11. While aerodynamic drag has a particularly significant influence on in-plane maneuverability, it was found to affect out-of-plane maneuverability – and the corresponding inclination-changing capabilities – considerably less. This result stem from the fact that out-of-plane maneuvering requires the sail to thrust perpendicularly to the direction of drag rather than against it. For this reason, outside the altitude region wherein maneuvering is unfeasible, the inclination-changing capabilities remain almost constant with altitude, see Figs. 6.17, 7.9, and 7.12.

Enhanced maneuverability was also found for dawn-dusk orbits – corresponding to LTANs at 0600/1800 hrs – across all orbital scenarios considered in Sections 6.5 and 7.5, due to the absence (or very short duration) of eclipses. Conversely, typically worse maneuvering capabilities were found for noon-midnight orbits – corresponding to LTANs at 0000/1200 hrs – as eclipses reduce the available time to exploit SRP and ARP by approximately one third. As discussed in Section 7.5.5, changes in orbital inclination were found to significantly affect maneuverability for the same reason: inclinations departing from polar values yield eclipses of longer duration, thus decreasing the ability to leverage SRP and ARP for maneuvering, see Figs. 7.15 and 7.16. Similarly, solar declination was also found to influence eclipse duration and, therefore, maneuverability. Indeed, specifically for dawn-dusk orbits, high solar declinations introduce eclipses in proximity of the Earth poles that can lower the orbit-raising and inclination-changing capabilities by up to 20% and 50%, respectively, see Section 7.5.6 and Figs. 7.17-7.18.

Finally, by considering solar-sail characteristic accelerations ranging from one tenth to ten times that of ACS3 – thereby spanning values representative of very limited to futuristic performances – it was found that the characteristic acceleration affects orbit-raising capability in a quasi-linear manner, see Section 7.5.4 and Fig. 7.13, and Section 6.5.1 and Fig. 6.15. On the other hand, while the inclination-changing capabilities were found to vary quasi-linearly for characteristic accelerations representative of present-day to futuristic performance, linearity is lost for very small characteristic accelerations, see Section 7.5.4 and Fig. 7.14.

8.2.2. RECOMMENDATIONS

By leveraging the probabilistic description of the solar-sail dynamics discussed in Section 8.1.2, the maneuverability of Earth-orbiting sailcraft may also be described probabilistically. This approach would allow not only to estimate the nominal maneuvering capabilities, but also their associated confidence intervals, proving particularly useful to

inform the design of future solar-sail missions. Making use of non-deterministic models for the sailcraft dynamics also paves the way to the design of uncertainty-aware steering laws, leveraging the theory of robust optimal control. Developing robust control strategies would help account for the risks associated with sailcraft controllability and operations in the mission design, thereby allowing to move from theoretical to realistic mission concepts. In the literature, a number of studies have explored solar-sail robust trajectory design focusing on specific sources of uncertainty, e.g., uncertainties in the sail optical properties, solar irradiance, and thrust magnitude and direction [258, 266, 267, 428, 429], and uncertainties arising from sail wrinkling and billowing [250, 258, 262, 267]. On the other hand, only few studies have investigated the impact of attitude determination and control errors [258, 428], whereas the influence of Earth-specific dynamical uncertainties – such as fluctuations in atmospheric density and planetary radiation intensity – remains unexplored to date. The ability to account for uncertainties in the solar-sail dynamics and control would prove particularly beneficial for a range of applications wherein precise maneuvering plays a crucial role, e.g., collision avoidance, station-keeping, formation-flying configuration control, rendezvous, proximity operations, and docking. Furthermore, a probabilistic approach could ultimately provide the basis for a comprehensive framework for solar-sail mission design under uncertainty. As discussed throughout Sections 2.3-2.5 and illustrated by the diagram in Fig. 2.3, the accelerations experienced by a solar sail arise from strongly coupled interactions between the sailcraft and the space environment. Consequently, the uncertainties associated with the underlying environmental, structural, material, and interaction models are themselves inherently coupled. Accounting for these dependencies within a unified framework – while also incorporating uncertainties in the performance of the attitude determination and control system (ADCS), the sail deployment procedure, and the subsequent sail shape – could enable a fully uncertainty-aware concurrent design approach. Ultimately, this would allow to co-optimize sail structures and control systems in the early stages of the mission life cycle.

The analyses conducted in this dissertation focused exclusively on orbit-raising and inclination-changing maneuvers, allowing to identifying the region of the near-Earth environment wherein maneuvering is feasible. Building on the insights developed, other types of maneuvers may be explored in the future, extending the work beyond unconstrained, open-end maneuvers. For example, given the significant impact of the illumination conditions of the sailcraft on its thrust performance, exploring solar-sail orbit raising while constraining the orbit to remain Sun-synchronous is of particular interest. Similarly, investigating the feasibility and performance of Earth-bound solar-sail orbital rendezvous is also of significant interest, as the ability to perform such maneuvers enables a variety of applications, notably, in-orbit servicing and active debris removal.

To investigate the aforementioned types of maneuvers, the trajectory optimization methods developed in this dissertation may be employed by interfacing them with other algorithms. Indeed, both the POINT and MACHO optimization methods allow to determine the optimal sailcraft attitude corresponding to an optimal thrust direction, that is, a desired direction along which thrust should be maximized. When this direction is found using the Lagrange planetary equations, locally optimal control laws – as those presented in this dissertation – are found. Nevertheless, the optimal thrust direction may also be defined through other techniques, allowing for more complex maneuvering. For

example, so-called blending methods can be used to define the optimal thrust direction as a weighted combination of individual optimal thrust directions derived from the Lagrange planetary equations. Notable examples of such methods include the accessibility and deficit method devised by Macdonald and McInnes [201, 382], as well as methods based on Lyapunov feedback control, such as the Q-law algorithm developed by Petropoulos [430–432], whose application to solar sailing has been recently explored [206, 381]. It should be noted that these blending methods only offer sub-optimal solutions to the trajectory optimization problem. Nevertheless, these solutions can serve as strong initial guesses for succeeding, global optimization methods.

Finally, as discussed in Section 1.3, rendering solar sails a potentially viable alternative to fuel-based propulsion systems for Earth-bound missions requires not only advances in the theoretical understanding of solar-sail maneuverability, but also development of more reliable and performant sailcraft attitude control systems. These systems ought to be able to sustain rapid changes of attitude throughout the mission lifetime, to be performed relatively frequently, due to the short orbital period characterizing Earth orbits. Furthermore, miniaturized systems should be considered, in agreement with the increasingly preferred use of CubeSats over large buses.

A

Derivation of Ideal Radiation Pressure Acceleration from Tensor Formulation

This appendix provides the analytical derivation of the radiation pressure acceleration on an ideal, perfectly reflecting sail from the tensor formulation presented in Section 2.5.3.3. As discussed in that section, the radiation pressure acceleration for an ideal, perfectly reflecting sail can be expressed in tensor form as in Eq. 2.37, which is reproduced here for convenience:

$$\boldsymbol{a}_* = \frac{2}{\sigma}\left(\hat{\boldsymbol{n}} \cdot \underline{\underline{\boldsymbol{P}}} \cdot \hat{\boldsymbol{n}}\right)\hat{\boldsymbol{n}} \tag{A.1}$$

with σ the sailcraft mass-to-area ratio – that is, the loading parameter – $\hat{\boldsymbol{n}}$ the sail normal direction forming the smallest angle with the radiation source-to-sailcraft direction, $\hat{\boldsymbol{r}}_*$, see Fig. A.1, $\underline{\underline{\boldsymbol{P}}}$ the radiation pressure tensor, and $\cdot$ denoting tensor contraction. Assuming the radiation source is an isotropic, Lambertian emitter that illuminates only one side of the sail and is fully visible from the sailcraft, the tensor $\underline{\underline{\boldsymbol{P}}}$ can be defined – in line with the discussion in Section 2.5.3.1 – as as follows:

$$\underline{\underline{\boldsymbol{P}}} = \frac{I_*}{c}\int_{\Omega_*} \hat{\boldsymbol{l}} \otimes \hat{\boldsymbol{l}}\, d\Omega \tag{A.2}$$

where I_* is the constant frequency-integrated specific intensity of the radiation source, c is the speed of light in vacuum, Ω_* is the conical solid angle subtended by the radiation source, $d\Omega$ is the solid angle subtending a differential element of surface of the source from the sailcraft's perspective, $\hat{\boldsymbol{l}}$ is the unit vector pointing from said surface element to the sailcraft, see Fig. 2.15, $\hat{\boldsymbol{l}} \otimes \hat{\boldsymbol{l}}$ is a dyadic tensor, and $\otimes$ denotes the tensor product. The unit vector $\hat{\boldsymbol{l}}$ can be expressed within a sailcraft-centered reference frame $O_*\left(\hat{\boldsymbol{x}}_*, \hat{\boldsymbol{y}}_*, \hat{\boldsymbol{z}}_*\right)$ with $\hat{\boldsymbol{x}}_* = \hat{\boldsymbol{r}}_*$, $\hat{\boldsymbol{y}}_*$ with positive component along $\hat{\boldsymbol{n}}$ (or chosen arbitrarily if $\hat{\boldsymbol{n}}$ is parallel to $\hat{\boldsymbol{r}}_*$),

A

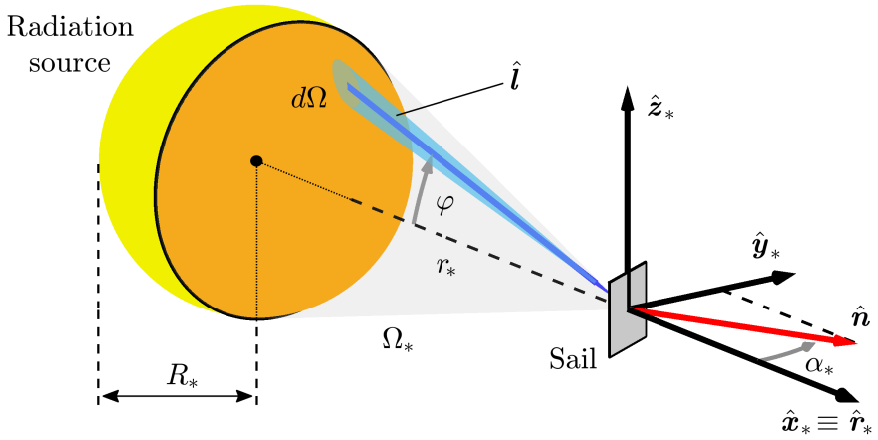


Figure A.1: Geometry of a spherical radiation source illuminating a flat sail.

and $\hat{\boldsymbol{z}}_*$ forming a right-handed frame, see Fig. 2.15. In this frame, $\hat{\boldsymbol{l}}$ is defined as:

$$\hat{\boldsymbol{l}} = \left[\cos\varphi,\ \sin\varphi\cos\psi,\ \sin\varphi\sin\psi\right]^T \tag{A.3}$$

where φ is the angle between $\hat{\boldsymbol{l}}$ and $\hat{\boldsymbol{r}}_*$, see again Fig. 2.15, and ψ is the azimuthal angle measured between $\hat{\boldsymbol{y}}_*$ and the projection of $\hat{\boldsymbol{l}}$ onto the $(\hat{\boldsymbol{x}}_*, \hat{\boldsymbol{y}}_*)$ plane. The dyadic tensor $\hat{\boldsymbol{l}}\otimes\hat{\boldsymbol{l}}$ is therefore found as:

$$\hat{\boldsymbol{l}}\otimes\hat{\boldsymbol{l}} = \hat{\boldsymbol{l}}\hat{\boldsymbol{l}}^T = \begin{bmatrix} \cos^2\varphi & \sin\varphi\cos\varphi\cos\psi & \sin\varphi\cos\varphi\sin\psi \\ \sin\varphi\cos\varphi\cos\psi & \sin^2\varphi\cos^2\psi & \sin^2\varphi\sin\psi\cos\psi \\ \sin\varphi\sin\psi\cos\varphi & \sin^2\varphi\sin\psi\cos\psi & \sin^2\varphi\sin^2\psi \end{bmatrix} \tag{A.4}$$

Furthermore, within frame O_*, the sail normal direction can be expressed as:

$$\hat{\boldsymbol{n}} = \left[\cos\alpha_*,\ \sin\alpha_*,\ 0\right]^T \tag{A.5}$$

and the differential solid angle, $d\Omega$, is given by:

$$d\Omega = \sin\varphi\ d\varphi\, d\psi \tag{A.6}$$

Substituting Eqs. A.4 and A.6 into Eq. A.2, and considering Eq. A.5 for expressing the double tensor contraction, the radiation pressure acceleration in Eq. A.1 can be rewritten as:

$$\boldsymbol{a}_* = \frac{2I_*}{\sigma c}\left(\int_{\varphi_0}^{\varphi_f}\int_{\psi_0}^{\psi_f} L_{nn}\sin\varphi\ d\varphi\, d\psi\right)\hat{\boldsymbol{n}} \tag{A.7}$$

where:

$$L_{nn} = \hat{\boldsymbol{n}} \cdot \left(\hat{\boldsymbol{l}} \otimes \hat{\boldsymbol{l}} \right) \cdot \hat{\boldsymbol{n}} =$$

$$[\cos\alpha_*,\ \sin\alpha_*,\ 0] \begin{bmatrix} \cos^2\varphi & \sin\varphi\cos\varphi\cos\psi & \sin\varphi\cos\varphi\sin\psi \\ \sin\varphi\cos\varphi\cos\psi & \sin^2\varphi\cos^2\psi & \sin^2\varphi\sin\psi\cos\psi \\ \sin\varphi\sin\psi\cos\varphi & \sin^2\varphi\sin\psi\cos\psi & \sin^2\varphi\sin^2\psi \end{bmatrix} \begin{bmatrix} \cos\alpha_* \\ \sin\alpha_* \\ 0 \end{bmatrix} =$$

$$\cos^2\varphi\cos^2\alpha_* + 2\sin\varphi\cos\varphi\cos\psi\sin\alpha_*\cos\alpha_* + \sin^2\varphi\cos^2\psi\sin^2\alpha_* \tag{A.8}$$

and φ_0, φ_f, ψ_0, and ψ_f are the limits of integration identifying the solid-angle region Ω_*, equal to:

$$\begin{cases} \varphi_0 = 0 \\ \varphi_f = \sin^{-1}\left(\dfrac{R_*}{r_*}\right) \\ \psi_0 = 0 \\ \psi_f = 2\pi \end{cases} \tag{A.9}$$

Inserting Eqs. A.8 into Eq A.7, separating the resulting double integrals, and expressing each double integral as the product of single integrals yields:

$$\begin{aligned} \boldsymbol{a}_* = \frac{2I_*}{\sigma c} \Bigg[& \cos^2\alpha_* \int_{\psi_0}^{\psi_f} d\psi \int_{\varphi_0}^{\varphi_f} \cos^2\varphi \sin\varphi d\varphi + \\ & \sin^2\alpha_* \int_{\psi_0}^{\psi_f} \cos^2\psi\ d\psi \int_{\varphi_0}^{\varphi_f} \sin^3\varphi d\varphi + \\ & 2\sin\alpha_*\cos\alpha_* \int_{\psi_0}^{\psi_f} \cos\psi\ d\psi \int_{\varphi_0}^{\varphi_f} \sin^2\varphi\cos\varphi\ d\varphi \Bigg] \hat{\boldsymbol{n}} \end{aligned} \tag{A.10}$$

Substituting the integration limits in Eq. A.9 and solving the integrals then yields:

$$\boldsymbol{a}_* = \frac{4}{3}\frac{\pi I_*}{c\sigma} \left\{ 1 - \left[1 - \left(\frac{R_*}{r_*} \right)^2 \right]^{\frac{3}{2}} \right\} \cos^2\alpha_* \hat{\boldsymbol{n}} + \frac{2}{3}\frac{\pi I_*}{c\sigma} \left\{ 2 - \left[2 + \left(\frac{R_*}{r_*} \right)^2 \right] \sqrt{1 - \left(\frac{R_*}{r_*} \right)^2} \right\} \sin^2\alpha_* \hat{\boldsymbol{n}} \tag{A.11}$$

which, through algebraic and trigonometric manipulation, may also be expressed as:

$$\boldsymbol{a}_* = \frac{4}{3}\frac{\pi I_*}{c\sigma} \left\{ 1 - \left[1 - \left(\frac{R_*}{r_*} \right)^2 \right]^{\frac{3}{2}} - \frac{3}{2} \left(\frac{R_*}{r_*} \right)^2 \sqrt{1 - \left(\frac{R_*}{r_*} \right)^2} \sin^2\alpha_* \right\} \hat{\boldsymbol{n}} \tag{A.12}$$

When the sail normal direction, $\hat{\boldsymbol{n}}$, points along the radiation source-to-sailcraft direction, $\hat{\boldsymbol{r}}_*$, $\alpha_* = 0$ and Eq. A.11 and A.12 reduce to Eq. 2.38. On the other hand, when $\hat{\boldsymbol{n}}$ points away from $\hat{\boldsymbol{r}}_*$, $\alpha_* \neq 0$. In this case, substituting I_*, R_*, r_*, and α_* with the frequency-integrated terrestrial specific intensity, $I_\oplus$, Earth radius, R, geocentric orbital radius, r, and planetary pitch angle, $\alpha_\oplus$, respectively, Eq. 2.57 is found.

B

Derivation of the Geometrical Factors

This appendix provides the analytical derivation of the normal specular and transversal geometrical factors for optical solar sails presented in Chapter 4. The derivation of the normal specular geometrical factor for ideal – that is, perfectly reflecting – sails presented in Chapter 3 is also provided as a special case of the normal specular geometrical factors for optical sails.

B.1. Geometry of the Problem

This section presents the geometry of the problem underlying the definition of the geometrical factors, together with the variables used throughout the remainder of the appendix. The reader is referred to the sketch of the geometrical configuration provided in Fig. B.1 as the main visual reference for the discussion that follows. When needed, the sketches in Fig. B.2 will also be referenced as they provide detailed views of the sail and the Earth, further facilitating visualization of the geometrical parameters of the problem.

As shown in Fig. B.1, the Earth is assumed to be spherical with radius R. The sailcraft lies above the Earth at a distance $r = \|\boldsymbol{r}\|$ from its geometrical center, with $\boldsymbol{r}$ the position vector of the sailcraft. Therefore, from the sailcraft's perspective, the visible part of the Earth surface is a spherical cap, whose area is denoted by A^*. The angle between $-\boldsymbol{r}$ and the horizon as seen from the sailcraft — that is, the edge of the spherical cap – is denoted by φ_m, whereas the angle between $\boldsymbol{r}$ and the edge of the spherical cap as seen from the center of the Earth is denoted by γ_m. By introducing the adimensional inverse orbital radius $H = R/r$ for notational convenience, these angles can be defined as:

$$\varphi_m = \sin^{-1} H \tag{B.1a}$$

$$\gamma_m = \cos^{-1} H \tag{B.1b}$$

and therefore:

$$\sin\varphi_m = \cos\gamma_m = H \tag{B.1c}$$

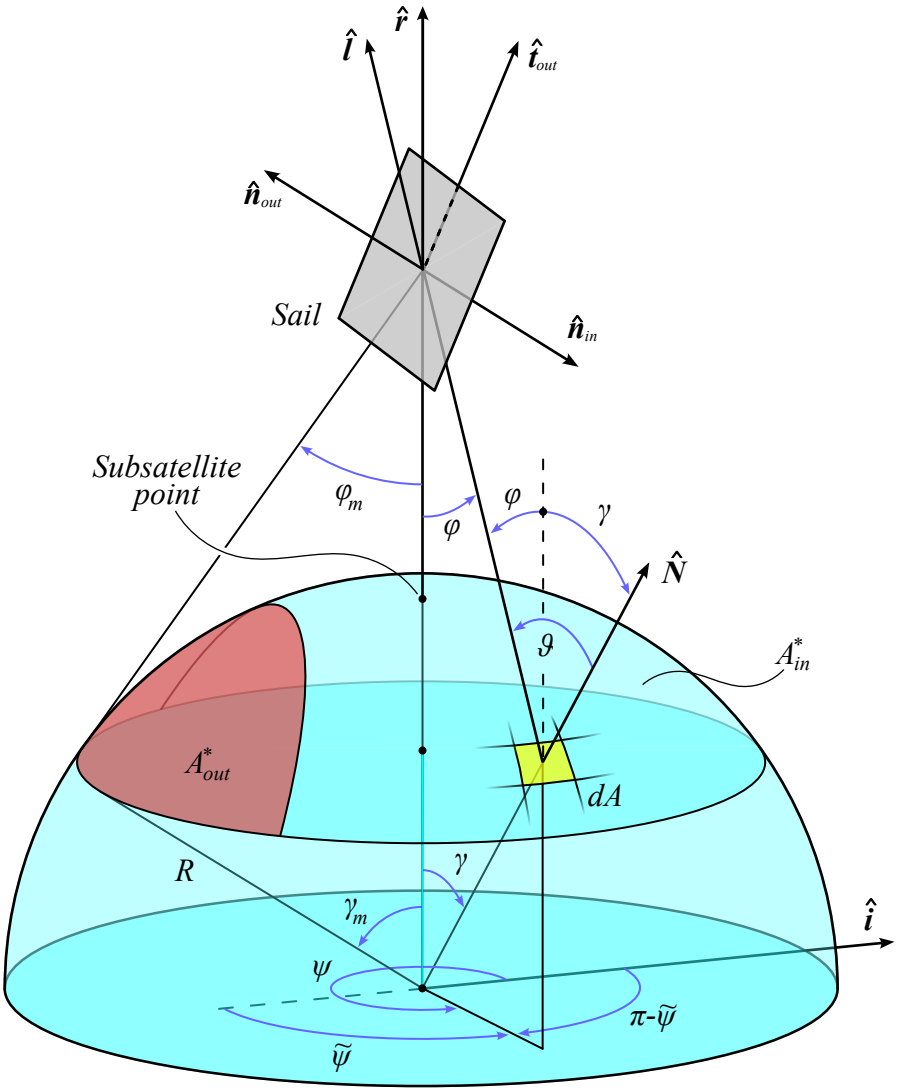


Figure B.1: Geometry of the problem and variables to derive the geometrical factors.

$$\cos\varphi_m = \sin\gamma_m = \sqrt{1-H^2} \tag{B.1d}$$

A differential piece of surface of area dA on the spherical cap is identified through either the Earth-centered polar angle γ or the sailcraft-centered polar angle φ, and through the azimuthal angle ψ, see Figs. B.1 and B.2b. The Earth-centered polar angle, γ, is measured from $\boldsymbol{r}$ to $\hat{\boldsymbol{N}}$, where $\hat{\boldsymbol{N}}$ is the direction pointing from the center of the Earth to dA and, accordingly, it is normal to the surface of the Earth at dA. The sailcraft-centered polar angle φ is measured from $-\boldsymbol{r}$ to $-\boldsymbol{l}$, with $\boldsymbol{l}$ the vector from dA to the sailcraft. The

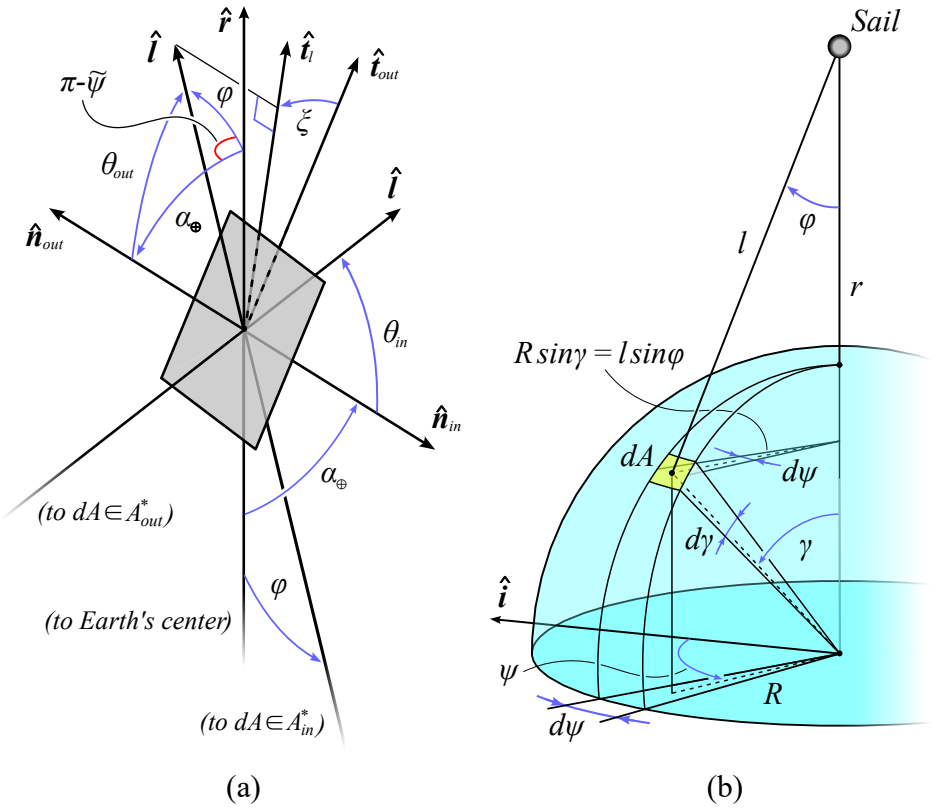


Figure B.2: Directions and angles describing a) the sail orientation with respect to the center of the Earth and the surface element dA, and b) the size and relative position of the surface element dA with respect to the center of the Earth and the sailcraft.

azimuthal angle ψ is defined inside the plane perpendicular to $\boldsymbol{r}$ and passing through the geometrical center of the Earth. This angle is measured between the reference direction $\hat{\boldsymbol{i}}$ and the projection of $\hat{\boldsymbol{N}}$ onto said plane. The direction $\hat{\boldsymbol{i}}$ is defined as:

$$\hat{\boldsymbol{i}} = \hat{\boldsymbol{r}} \times \frac{\hat{\boldsymbol{r}} \times \hat{\boldsymbol{n}}_{out}}{\|\hat{\boldsymbol{r}} \times \hat{\boldsymbol{n}}_{out}\|} \tag{B.2}$$

where $\hat{\boldsymbol{r}} = \boldsymbol{r}/r$ and $\hat{\boldsymbol{n}}_{out}$ is the normal direction of the outward-facing side of the sail, that is, the sail normal direction forming the smallest angle with $\hat{\boldsymbol{r}}$, such that $\hat{\boldsymbol{r}} \cdot \hat{\boldsymbol{n}}_{out} \geq 0$ and $\hat{\boldsymbol{i}} \cdot \hat{\boldsymbol{n}}_{out} \leq 0$. The local zenith angle at dA, ϑ, is measured between $\hat{\boldsymbol{N}}$ and $\hat{\boldsymbol{l}} = \boldsymbol{l}/l$, with $l = \|\boldsymbol{l}\|$. As can be observed in Fig. B.1, $\vartheta = \varphi + \gamma$ and therefore:

$$\cos\vartheta = \cos(\varphi + \gamma) = \cos\varphi\cos\gamma - \sin\varphi\sin\gamma \tag{B.3}$$

It is important to recognize that, because both the angles φ and γ provide information on the angular location of the surface element dA with respect to the radial direction, $\hat{\boldsymbol{r}}$, they are geometrically dependent. As illustrated in Fig. B.2b, these angles are related

through the following relationships:

$$R\sin\gamma = l\sin\varphi \tag{B.4a}$$

$$R\cos\gamma + l\cos\varphi = r \tag{B.4b}$$

which, upon differentiation and rearrangement of the terms, become:

$$dl = \frac{R\cos\gamma\, d\gamma - l\cos\varphi\, d\varphi}{\sin\varphi} \tag{B.5a}$$

$$dl = \frac{l\sin\varphi\, d\varphi + R\sin\gamma\, d\gamma}{\cos\varphi} \tag{B.5b}$$

Equating Eqs. B.5a and B.5b and solving for $d\gamma$ yields:

$$d\gamma = \frac{l}{R}\frac{1}{\left(\cos\varphi\cos\gamma - \sin\varphi\sin\gamma\right)} d\varphi \tag{B.6}$$

so that, using Eq. B.3, the following relationship is found:

$$d\gamma = \frac{l}{R\cos\vartheta} d\varphi \tag{B.7}$$

The above differential relationship can be used to express the differential element of surface area, dA. As can be observed in Fig. B.2b, this is found as:

$$dA = \left(R d\gamma\right)\left(R\sin\gamma d\psi\right) = R^2\sin\gamma\, d\psi\, d\gamma \tag{B.8}$$

which, taking advantage of Eqs. B.4a and B.7, can also be expressed as:

$$dA = l^2\frac{\sin\varphi}{\cos\vartheta}\, d\psi\, d\varphi \tag{B.9}$$

The relative orientation of the sailcraft with respect to the visible spherical cap of the Earth and the differential surface element dA is described by means of different directions and angles. The angle between $\hat{\boldsymbol{r}}$ and $\hat{\boldsymbol{n}}_{out}$ is the planetary pitch angle (PPA), $\alpha_\oplus \in [0, \pi/2]$, which also corresponds to the angle between $-\hat{\boldsymbol{r}}$ and $\hat{\boldsymbol{n}}_{in}$, with $\hat{\boldsymbol{n}}_{in} = -\hat{\boldsymbol{n}}_{out}$ the inward-facing side of the sail, see Fig. B.2a. The local pitch angle, $\theta \in [0, \pi/2]$, is the incidence angle of the radiation emitted by a surface element dA reaching the sail. This angle is measured between $\hat{\boldsymbol{l}}$ and the sail normal direction with positive component along $\hat{\boldsymbol{l}}$, that is:

$$\hat{\boldsymbol{n}}_l = \mathrm{sgn}\left(\hat{\boldsymbol{l}}\cdot\hat{\boldsymbol{n}}_{out}\right)\hat{\boldsymbol{n}}_{out} \tag{B.10}$$

When radiation impinges on the inner-facing side of the sail, θ is measured between $\hat{\boldsymbol{l}}$ and $\hat{\boldsymbol{n}}_l = \hat{\boldsymbol{n}}_{out}$, see Eq. B.10, and will therefore be denoted with the subscript "*out*". As shown in Fig. B.2a, by superimposing the origins of the unit vectors $\hat{\boldsymbol{n}}_{out}$, $\hat{\boldsymbol{r}}$, and $\hat{\boldsymbol{l}}$, a spherical triangle is formed. This geometrical construction allows to use the spherical law of cosines to express the angle θ_{out} as a function of $\alpha_\oplus$, φ, and ψ as [433]:

$$\cos\theta_{out} = \cos\alpha_\oplus\cos\varphi + \sin\alpha_\oplus\sin\varphi\cos\left(\pi - \tilde{\psi}\right) = \cos\alpha_\oplus\cos\varphi + \sin\alpha_\oplus\sin\varphi\cos\psi \tag{B.11}$$

where $\tilde{\psi} = |\pi - \psi|$ is the angle between the direction $-\hat{\boldsymbol{i}}$ and the projection of $\hat{\boldsymbol{N}}$ onto the reference plane through the center of the Earth, see Fig. B.1. When radiation illuminates the outer-facing side of the sail, θ is measured between $\hat{\boldsymbol{l}}$ and $\hat{\boldsymbol{n}}_l = \hat{\boldsymbol{n}}_{in}$, see again Eq. B.10, and therefore it will be denoted with the subscript "*in*". In this case, the spherical triangle formed by $\hat{\boldsymbol{n}}_{in}$, $\hat{\boldsymbol{r}}$, and $\hat{\boldsymbol{l}}$ can be considered, for which the spherical law of cosines yields [433]:

$$\cos\theta_{in} = \cos(\pi - \alpha_\oplus)\cos\varphi + \sin(\pi - \alpha_\oplus)\sin\varphi\cos\tilde{\psi} = -\cos\alpha_\oplus\cos\varphi - \sin\alpha_\oplus\sin\varphi\cos\psi \tag{B.12}$$

Based on Eqs. B.11 and B.12, the following general relationships for the local pitch angle, θ, can therefore be defined:

$$\cos\theta = \mathrm{sgn}\left(\hat{\boldsymbol{l}}\cdot\hat{\boldsymbol{n}}_{out}\right)\cos\theta_{out} \tag{B.13}$$

$$\sin\theta = \sin\theta_{in} = \sin\theta_{out} = \sqrt{1-\cos^2\theta} \tag{B.14}$$

Figure B.2a also displays the outward transversal direction, $\hat{\boldsymbol{t}}_{out}$, the local transversal direction relative to surface element dA, $\hat{\boldsymbol{t}}_l$, and the angle between them, ξ. The direction $\hat{\boldsymbol{t}}_{out}$ is defined as:

$$\hat{\boldsymbol{t}}_{out} = \hat{\boldsymbol{n}}_{out}\times\frac{\hat{\boldsymbol{r}}\times\hat{\boldsymbol{n}}_{out}}{\|\hat{\boldsymbol{r}}\times\hat{\boldsymbol{n}}_{out}\|} = \frac{1}{\sin\alpha_\oplus}\left[\hat{\boldsymbol{n}}_{out}\times(\hat{\boldsymbol{r}}\times\hat{\boldsymbol{n}}_{out})\right] \tag{B.15}$$

and, similarly, $\hat{\boldsymbol{t}}_l$ is given by:

$$\hat{\boldsymbol{t}}_l = \hat{\boldsymbol{n}}_l\times\frac{\hat{\boldsymbol{l}}\times\hat{\boldsymbol{n}}_l}{\left\|\hat{\boldsymbol{l}}\times\hat{\boldsymbol{n}}_l\right\|} = \frac{1}{\sin\theta}\left[\hat{\boldsymbol{n}}_l\times\left(\hat{\boldsymbol{l}}\times\hat{\boldsymbol{n}}_l\right)\right] \tag{B.16}$$

Notably, expanding the double cross products in Eqs. B.15 and B.16 [433], $\hat{\boldsymbol{t}}_{out}$ and $\hat{\boldsymbol{t}}_l$ can also be expressed as:

$$\hat{\boldsymbol{t}}_{out} = \frac{1}{\sin\alpha_\oplus}\left(\hat{\boldsymbol{r}} - \cos\alpha_\oplus\hat{\boldsymbol{n}}_{out}\right) \tag{B.17}$$

$$\hat{\boldsymbol{t}}_l = \frac{1}{\sin\theta}\left(\hat{\boldsymbol{l}} - \cos\theta\hat{\boldsymbol{n}}_l\right) \tag{B.18}$$

Using Eqs. B.17 and B.18, the cosine of the angle between $\hat{\boldsymbol{t}}_{out}$ and $\hat{\boldsymbol{t}}_l$ can be defined as:

$$\cos\xi = \hat{\boldsymbol{t}}_{out}\cdot\hat{\boldsymbol{t}}_l = \frac{1}{\sin\alpha_\oplus\sin\theta}\left(\hat{\boldsymbol{r}} - \cos\alpha_\oplus\hat{\boldsymbol{n}}_{out}\right)\cdot\left(\hat{\boldsymbol{l}} - \cos\theta\hat{\boldsymbol{n}}_l\right) \tag{B.19}$$

Using the following identities:

$$\hat{\boldsymbol{r}}\cdot\hat{\boldsymbol{n}}_l = \mathrm{sgn}\left(\hat{\boldsymbol{l}}\cdot\hat{\boldsymbol{n}}_{out}\right)\cos\alpha_\oplus \tag{B.20a}$$

$$\hat{\boldsymbol{n}}_{out} \cdot \hat{\boldsymbol{l}} = \text{sgn}\left(\hat{\boldsymbol{l}} \cdot \hat{\boldsymbol{n}}_{out}\right) \cos\theta = \cos\theta_{out} \tag{B.20b}$$

$$\hat{\boldsymbol{n}}_{out} \cdot \hat{\boldsymbol{n}}_{l} = \text{sgn}\left(\hat{\boldsymbol{l}} \cdot \hat{\boldsymbol{n}}_{out}\right) \tag{B.20c}$$

$$\hat{\boldsymbol{r}} \cdot \hat{\boldsymbol{l}} = \cos\varphi \tag{B.20d}$$

and expressing $\cos\theta_{out}$ as per Eq. B.11 allows to reduce Eq. B.19 to:

$$\cos\xi = \frac{1}{\sin\theta}\left(\cos\varphi\sin\alpha_{\oplus} - \sin\varphi\cos\psi\cos\alpha_{\oplus}\right) \tag{B.21}$$

where, notably, $\cos\xi$ does not depend on $\text{sgn}\left(\hat{\boldsymbol{l}} \cdot \hat{\boldsymbol{n}}_{out}\right)$, that is, on whether the radiation along $\boldsymbol{l}$ illuminates the inward or outward side of the sail.

B.2. NORMAL SPECULAR GEOMETRICAL FACTORS

The definition of the normal specular geometrical factors is given in Eq. 4.18 and is reported here for convenience:

$$G_{FNS,\diamondsuit} = \frac{3}{2\pi}\int_{A^*_{\diamondsuit}} \frac{\cos\vartheta\cos^2\theta}{l^2}\, dA \tag{B.22}$$

In Eq. B.22, "$\diamondsuit$" is used as placeholder to indicate either "*in*" or "*out*". A^*_{in} denotes the part of the spherical cap's surface, A^*, that is visible from the inward-facing side of the sail – that is, the side visible from the subsatellite point, see Fig. B.1. Conversely, A^*_{out} is the fraction of spherical cap's surface that is visible from the outward-facing side of the sail, which is not visible from the subsatellite point, see again Fig. B.1. Also, note that, in the following, the subscripts "*in*" and "*out*" may be extended with different suffixes to denote sub-regions of the surfaces A^*_{in} and A^*_{out}, respectively, and the corresponding components of the geometrical factors. Substituting Eq. B.9 into Eq. B.22 yields:

$$G_{FNS,\diamondsuit} = \frac{3}{2\pi}\int_{\varphi_0}^{\varphi_f}\int_{\psi_0}^{\psi_f} \cos^2\theta\sin\varphi\, d\psi\, d\varphi \tag{B.23}$$

where the limits of integration φ_0, φ_f, ψ_0, and ψ_f depend on the region of the spherical cap's surface considered and, therefore, on whether the full inward geometrical factor, full outward geometrical factor, or a subcomponent of either is being calculated. Based on Eq. B.13, $\cos^2\theta = \cos^2\theta_{out}$ regardless of whether the inward or outward geometrical factor is considered. Therefore, substituting Eq. B.11 into Eq. B.23 results in:

$$G_{FNS,\diamondsuit} = \frac{3}{2\pi}\int_{\varphi_0}^{\varphi_f}\int_{\psi_0}^{\psi_f} \left(\cos\alpha_{\oplus}\cos\varphi + \sin\alpha_{\oplus}\sin\varphi\cos\psi\right)^2 \sin\varphi\, d\psi\, d\varphi \tag{B.24}$$

and developing the square of binomial and separating the resulting integrals gives:

$$
\begin{aligned}
G_{FNS,\Diamond} = \frac{3}{2\pi}\Bigg[& \cos^2\alpha_\oplus \underbrace{\int_{\varphi_0}^{\varphi_f}\int_{\psi_0}^{\psi_f} \cos^2\varphi \sin\varphi \; d\psi d\varphi}_{\boxed{A}_\Diamond} + \\
& \sin^2\alpha_\oplus \underbrace{\int_{\varphi_0}^{\varphi_f}\int_{\psi_0}^{\psi_f} \sin^3\varphi \cos^2\psi \; d\psi d\varphi}_{\boxed{B}_\Diamond} + \\
& 2\sin\alpha_\oplus \cos\alpha_\oplus \underbrace{\int_{\varphi_0}^{\varphi_f}\int_{\psi_0}^{\psi_f} \sin^2\varphi \cos\varphi \cos\psi \; d\psi d\varphi}_{\boxed{C}_\Diamond} \Bigg] = \\
& \frac{3}{2\pi}\left[\cos^2\alpha_\oplus \boxed{A}_\Diamond + \sin^2\alpha_\oplus \boxed{B}_\Diamond + 2\sin\alpha_\oplus \cos\alpha_\oplus \boxed{C}_\Diamond \right]
\end{aligned}
\tag{B.25}
$$

The above double integrals $\boxed{A}_\Diamond$, $\boxed{B}_\Diamond$, and $\boxed{C}_\Diamond$ will be solved considering different integration domains depending on the geometrical configuration or subcomponent of the geometrical factor considered. Specifically, two geometrical configurations can arise which require distinct approaches, namely:

- The case in which the sail plane does not intersect the Earth, meaning that the surface of the spherical cap is entirely visible from the inward side of the sail. This configuration occurs when $\alpha_\oplus + \varphi_m \leq \pi/2$.
- The case in which the sail plane intersects the Earth – as shown in Fig. B.1 – dividing the surface of the spherical cap into two regions: one visible from the inward side of the sail and one visible from the outward side of the sail. This configuration occurs when $\alpha_\oplus + \varphi_m > \pi/2$.

These above cases are discussed separately in the following subsections.

B.2.1. SAIL PLANE NOT INTERSECTING THE EARTH

In this case, the surface of the spherical cap is entirely visible from the inward side of the sail. Therefore, $A^*_{out} = 0$ and accordingly $G_{FNS,out} = 0$. The surface A^*_{in} corresponds to the entire spherical cap's surface, which is identified by the following domain boundaries:

$$
\begin{cases}
\varphi_0 = 0 \\
\varphi_f = \varphi_m = \sin^{-1} H \\
\psi_0 = 0 \\
\psi_f = 2\pi
\end{cases}
\tag{B.26}
$$

where the expression for φ_m was taken from Eq. B.1a. The above domain boundaries are not functions of φ nor ψ. Therefore, using them as integration limits allows to simplify the double integrals in Eq. B.25 to products of single integrals as:

$$
\boxed{A}_{in} = \int_{\psi_0}^{\psi_f} d\psi \int_{\varphi_0}^{\varphi_f} \cos^2\varphi \sin\varphi \; d\varphi \tag{B.27}
$$

$$\boxed{B}_{in} = \int_{\psi_0}^{\psi_f} \cos^2\psi \, d\psi \int_{\varphi_0}^{\varphi_f} \sin^3\varphi \, d\varphi \tag{B.28}$$

$$\boxed{C}_{in} = \int_{\psi_0}^{\psi_f} \cos\psi \, d\psi \int_{\varphi_0}^{\varphi_f} \sin^2\varphi \cos\varphi \, d\varphi \tag{B.29}$$

Substituting the limits of integration in Eq. B.26 and solving the integrals yields:

$$\boxed{A}_{in} = \left[\psi\right]_0^{2\pi} \left[-\frac{1}{3}\cos^3\varphi\right]_0^{\sin^{-1}H} = \frac{2\pi}{3}\left[1-(1-H^2)^{\frac{3}{2}}\right] \tag{B.30}$$

$$\boxed{B}_{in} = \left[\frac{1}{2}\left(\psi+\sin\psi\cos\psi\right)\right]_0^{2\pi} \left[\cos\varphi\left(\frac{\cos^2\varphi}{3}-1\right)\right]_0^{\sin^{-1}H} = \frac{\pi}{3}\left[2-\left(2+H^2\right)\sqrt{1-H^2}\right] \tag{B.31}$$

$$\boxed{C}_{in} = \left[\sin\psi\right]_0^{2\pi} \left[\frac{1}{3}\sin^3\varphi\right]_0^{\sin^{-1}H} = 0 \tag{B.32}$$

Then, substituting $\boxed{A}_{in}$, $\boxed{B}_{in}$, and $\boxed{C}_{in}$ into Eq. B.25, the geometrical factor for the inward side of the sail is found:

$$G_{FNS,in} = \left[1-(1-H^2)^{\frac{3}{2}}\right]\cos^2\alpha_\oplus + \frac{1}{2}\left[2-\left(2+H^2\right)\sqrt{1-H^2}\right]\sin^2\alpha_\oplus \tag{B.33}$$

Finally, through algebraic and trigonometric manipulation of the right-hand side of Eq. B.33, the definition of the geometrical factor given in Eq. 4.21 is found.

Note that when the expression for $G_{FNS,in}$ given in Eq. B.33 is multiplied by $\hat{\boldsymbol{n}}_{out}$ and $a_{c,PRP}$, see Eq. 3.23, and the radiation flux term, $\bar{S}$, is expressed through Eq 3.9, Eq. 2.57 is found. As Eq. 2.57 was independently derived from the tensor formulation of radiation-pressure acceleration presented in Appendix A, it provides a cross-verification of the derivation of the specular geometrical factor presented above.

B.2.2. SAIL PLANE INTERSECTING THE EARTH

In this case, the surface of the spherical cap is partly visible from the inward side of the sail, and partly from the outward side of the sail. The corresponding surface regions, A^*_{in} and A^*_{out}, are illustrated in Figs. B.1 and B.3, whereas the corresponding geometrical factors, $G_{FNS,in}$ and $G_{FNS,out}$, are derived in the following subsections.

B.2.2.1. GEOMETRICAL FACTOR OF THE INWARD SIDE OF THE SAIL

The surface A^*_{in} can be split into two regions: one having a circular boundary and symmetric with respect to $\hat{\boldsymbol{r}}$, denoted by $A^*_{in,1}$, and the remaining part of the spherical cap's surface, having a more complex boundary and denoted by $A^*_{in,2}$, see Fig. B.3. Accordingly, the geometrical factor of the inward side of the sail, $G_{FNS,in}$, can be expressed as the sum of two components, namely, $G_{FNS,in} = G_{FNS,in,1} + G_{FNS,in,2}$.

As can be observed in Fig. B.3, the region $A^*_{in,1}$ is defined by the following domain boundaries:

$$\begin{cases} \varphi_0 = 0 \\ \varphi_f = \dfrac{\pi}{2} - \alpha_\oplus \\ \psi_0 = 0 \\ \psi_f = 2\pi \end{cases} \tag{B.34}$$

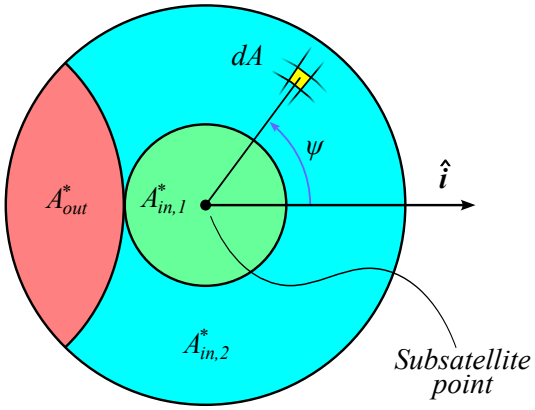


Figure B.3: Top view of the Earth's spherical cap when the sail plane intersects it.

As these domain boundaries do not depend on φ nor ψ, using them as integration limits allows to express the double integrals $\boxed{A}_{in,1}$, $\boxed{B}_{in,1}$, and $\boxed{C}_{in,1}$ in Eq. B.25 as in Eqs. B.27-B.29. Then, substituting the limits of integration in Eq. B.34, the solutions to the double integrals can be computed similarly to Eqs. B.30-B.32:

$$\boxed{A}_{in,1} = \left[\psi\right]_0^{2\pi}\left[-\frac{1}{3}\cos^3\varphi\right]_0^{\frac{\pi}{2}-\alpha_\oplus} = \frac{2\pi}{3}\left(1-\sin^3\alpha_\oplus\right) \tag{B.35}$$

$$\boxed{B}_{in,1} = \left[\frac{1}{2}\left(\psi+\sin\psi\cos\psi\right)\right]_0^{2\pi}\left[\cos\varphi\left(\frac{\cos^2\varphi}{3}-1\right)\right]_0^{\frac{\pi}{2}-\alpha_\oplus} = \frac{\pi}{3}\left(\sin^3\alpha_\oplus-3\sin\alpha_\oplus+2\right) \tag{B.36}$$

$$\boxed{C}_{in,1} = \left[\sin\psi\right]_0^{2\pi}\left[\frac{1}{3}\sin^3\varphi\right]_0^{\frac{\pi}{2}-\alpha_\oplus} = 0 \tag{B.37}$$

Substituting Eqs. B.35-B.37 into Eq. B.25 and simplifying the resulting expression, the component of the geometrical factor relative to the surface region $A^*_{in,1}$, $G_{FNS,in,1}$, is found:

$$G_{FNS,in,1} = \frac{1}{2}\left(3\sin^4\alpha_\oplus-5\sin^3\alpha_\oplus+2\right) \tag{B.38}$$

The region $A^*_{in,2}$, see Fig. B.3, is defined by the following domain boundaries:

$$\begin{cases} \varphi_0 = \dfrac{\pi}{2}-\alpha_\oplus \\ \varphi_f = \varphi_m = \sin^{-1}H \\ \psi_0 = -\cos^{-1}\left(-\dfrac{\cos\alpha_\oplus\cos\varphi}{\sin\alpha_\oplus\sin\varphi}\right) = \cos^{-1}\left(\dfrac{\cos\alpha_\oplus\cos\varphi}{\sin\alpha_\oplus\sin\varphi}\right)-\pi \\ \psi_f = -\psi_0 = \cos^{-1}\left(-\dfrac{\cos\alpha_\oplus\cos\varphi}{\sin\alpha_\oplus\sin\varphi}\right) \end{cases} \tag{B.39}$$

where the definition of φ_m in Eq. B.1a was used. The domain boundaries ψ_0 and ψ_f are found from Eq. B.11 by imposing $\theta_{out} \leq \pi/2$, with $\theta_{out} = \pi/2$ identifying the curve arising from the intersection of the sail plane with the spherical cap's surface. Also, it is of note that $\psi_f = -\psi_0$ because of the symmetry of the domain and integrands with respect to the $\hat{\boldsymbol{i}}$ axis. This symmetry allows to halve the domain of the double integrals in Eq. B.25 as follows:

$$\boxed{A}_{in,2} = \int_{\varphi_0}^{\varphi_f} \cos^2\varphi \sin\varphi \left(\int_{-\psi_f}^{\psi_f} d\psi \right) d\varphi = 2 \int_{\varphi_0}^{\varphi_f} \cos^2\varphi \sin\varphi \left(\int_{0}^{\psi_f} d\psi \right) d\varphi \tag{B.40}$$

$$\boxed{B}_{in,2} = \int_{\varphi_0}^{\varphi_f} \sin^3\varphi \left(\int_{-\psi_f}^{\psi_f} \cos^2\psi \; d\psi \right) d\varphi = 2 \int_{\varphi_0}^{\varphi_f} \sin^3\varphi \left(\int_{0}^{\psi_f} \cos^2\psi \; d\psi \right) d\varphi \tag{B.41}$$

$$\boxed{C}_{in,2} = \int_{\varphi_0}^{\varphi_f} \sin^2\varphi \cos\varphi \left(\int_{-\psi_f}^{\psi_f} \cos\psi \; d\psi \right) d\varphi = 2 \int_{\varphi_0}^{\varphi_f} \sin^2\varphi \cos\varphi \left(\int_{0}^{\psi_f} \cos\psi \; d\psi \right) d\varphi \tag{B.42}$$

Solving the integrals in Eqs. B.40-B.42 with respect to ψ gives:

$$\boxed{A}_{in,2} = 2 \int_{\varphi_0}^{\varphi_f} \cos^2\varphi \sin\varphi \; \psi_f \; d\varphi \tag{B.43}$$

$$\begin{aligned} \boxed{B}_{in,2} &= \int_{\varphi_0}^{\varphi_f} \sin^3\varphi \left(\psi_f + \sin\psi_f \cos\psi_f \right) d\varphi = \\ &\underbrace{\int_{\varphi_0}^{\varphi_f} \sin^3\varphi \; \psi_f \; d\varphi}_{\boxed{B}_{in,2a}} + \underbrace{\int_{\varphi_0}^{\varphi_f} \sin^3\varphi \sin\psi_f \cos\psi_f \; d\varphi}_{\boxed{B}_{in,2b}} = \\ &\boxed{B}_{in,2a} + \boxed{B}_{in,2b} \end{aligned} \tag{B.44}$$

$$\boxed{C}_{in,2} = 2 \int_{\varphi_0}^{\varphi_f} \sin^2\varphi \cos\varphi \sin\psi_f \; d\varphi \tag{B.45}$$

Substituting the limits of integration in Eq. B.39 into $\boxed{A}_{in,2}$, $\boxed{B}_{in,2a}$, $\boxed{B}_{in,2b}$, and $\boxed{C}_{in,2}$ then yields:

$$\boxed{A}_{in,2} = 2 \int_{\frac{\pi}{2}-\alpha_\oplus}^{\sin^{-1}H} \cos^2\varphi \sin\varphi \cos^{-1}\left(-\frac{\cos\alpha_\oplus \cos\varphi}{\sin\alpha_\oplus \sin\varphi} \right) d\varphi \tag{B.46}$$

$$\boxed{B}_{in,2a} = \int_{\frac{\pi}{2}-\alpha_\oplus}^{\sin^{-1}H} \sin^3\varphi \cos^{-1}\left(-\frac{\cos\alpha_\oplus \cos\varphi}{\sin\alpha_\oplus \sin\varphi} \right) d\varphi \tag{B.47}$$

$$\boxed{B}_{in,2b} = -\int_{\frac{\pi}{2}-\alpha_\oplus}^{\sin^{-1}H} \sin^3\varphi \frac{\cos\alpha_\oplus \cos\varphi}{\sin\alpha_\oplus \sin\varphi} \sqrt{1 - \left(\frac{\cos\alpha_\oplus \cos\varphi}{\sin\alpha_\oplus \sin\varphi} \right)^2} \; d\varphi \tag{B.48}$$

$$\boxed{C}_{in,2} = 2\int_{\frac{\pi}{2}-\alpha_\oplus}^{\sin^{-1}H} \sin^2\varphi\cos\varphi\sqrt{1-\left(\frac{\cos\alpha_\oplus\cos\varphi}{\sin\alpha_\oplus\sin\varphi}\right)^2}\,d\varphi \tag{B.49}$$

Solving the integrals on the right-hand sides of Eqs. B.46-B.49 and using Eq. B.44 to express $\boxed{B}_{in,2}$ results in:

$$\boxed{A}_{in,2} = \frac{2}{3}\left[\pi\sin^3\alpha_\oplus + \mathcal{B}\cos^2\alpha_\oplus - \left(1-H^2\right)^{\frac{3}{2}}\cos^{-1}(-\mathcal{A}) - \tan^{-1}\mathcal{B}\right] \tag{B.50}$$

$$\boxed{B}_{in,2a} = \frac{1}{3}\left[\pi\sin\alpha_\oplus\left(3-\sin^2\alpha_\oplus\right) - \sqrt{1-H^2}\left(2+H^2\right)\cos^{-1}(-\mathcal{A}) - 2\tan^{-1}\mathcal{B} - \mathcal{B}\cos^2\alpha_\oplus\right] \tag{B.51}$$

$$\boxed{B}_{in,2b} = -\frac{1}{3}\frac{\cos^4\alpha_\oplus}{\sin^2\alpha_\oplus}\mathcal{B}^3 \tag{B.52}$$

$$\begin{aligned}\boxed{B}_{in,2} = \frac{1}{3}\Bigg[&\pi\sin\alpha_\oplus\left(3-\sin^2\alpha_\oplus\right) - \sqrt{1-H^2}\left(2+H^2\right)\cos^{-1}(-\mathcal{A}) \\ &- 2\tan^{-1}\mathcal{B} - \mathcal{B}\cos^2\alpha_\oplus\left(1+\mathcal{B}^2\frac{\cos^2\alpha_\oplus}{\sin^2\alpha_\oplus}\right)\Bigg]\end{aligned} \tag{B.53}$$

$$\boxed{C}_{in,2} = \frac{2}{3}\frac{\cos^3\alpha_\oplus}{\sin\alpha_\oplus}\mathcal{B}^3 \tag{B.54}$$

where:

$$\mathcal{A} = \frac{\cos\alpha_\oplus}{\sin\alpha_\oplus}\sqrt{\frac{1}{H^2}-1} \qquad \mathcal{B} = \sqrt{\frac{H^2}{\cos^2\alpha_\oplus}-1} \tag{B.55}$$

By inserting Eq. B.50 alongside Eqs. B.53 and B.54 into Eq. B.25 and performing trigonometric simplifications, the final expression for the component of the geometrical factor relative to $A^*_{in,2}$, $G_{FNS,in,2}$, is found:

$$\begin{aligned}G_{FNS,in,2} =& \frac{1}{2}\left(5\sin^3\alpha_\oplus - 3\sin^4\alpha_\oplus\right) \\ &- \frac{1}{\pi}\Bigg\{\frac{1}{2}\sqrt{1-H^2}\left[H^2\left(1-3\cos^2\alpha_\oplus\right)+2\right]\cos^{-1}(-\mathcal{A}) + \tan^{-1}\mathcal{B} \\ &- \frac{1}{2}\mathcal{B}\cos^2\alpha_\oplus\left[3\cos^2\alpha_\oplus\left(1+\mathcal{B}^2\right)-1\right]\Bigg\}\end{aligned} \tag{B.56}$$

Finally, summing Eqs. B.38 and B.56 yields the normal specular geometrical factor of the inward side of the sail provided in Eq. 4.22.

B.2.2.2. GEOMETRICAL FACTOR OF THE OUTWARD SIDE OF THE SAIL

The surface region A^*_{out}, see Fig. B.3, is defined by the following domain boundaries:

$$\begin{cases} \varphi_0 = \dfrac{\pi}{2} - \alpha_\oplus \\ \varphi_f = \varphi_m = \sin^{-1} H \\ \psi_0 = \cos^{-1}\left(-\dfrac{\cos\alpha_\oplus \cos\varphi}{\sin\alpha_\oplus \sin\varphi}\right) = \cos^{-1}\left(\dfrac{\cos\alpha_\oplus \cos\varphi}{\sin\alpha_\oplus \sin\varphi}\right) - \pi \\ \psi_f = 2\pi - \psi_0 = 2\pi - \cos^{-1}\left(-\dfrac{\cos\alpha_\oplus \cos\varphi}{\sin\alpha_\oplus \sin\varphi}\right) \end{cases} \tag{B.57}$$

where the definition of φ_m in Eq. B.1a was used and the domain boundaries ψ_0 and ψ_f were found from Eq. B.11 by imposing $\theta_{out} \geq \pi/2$. Adopting an approach similar to that of Section B.2.2.1, the above domain can be halved by leveraging the symmetry of both the domain itself and the integrands in Eq. B.25 with respect to the $\hat{\boldsymbol{i}}$ axis. Consequently, the double integrals in Eq. B.25 can be expressed as:

$$\boxed{A}_{out} = \int_{\varphi_0}^{\varphi_f} \cos^2\varphi \sin\varphi \left(\int_{\psi_0}^{2\pi-\psi_0} d\psi \right) d\varphi = 2 \int_{\varphi_0}^{\varphi_f} \cos^2\varphi \sin\varphi \left(\int_{\psi_0}^{\pi} d\psi \right) d\varphi \tag{B.58}$$

$$\boxed{B}_{out} = \int_{\varphi_0}^{\varphi_f} \sin^3\varphi \left(\int_{\psi_0}^{2\pi-\psi_0} \cos^2\psi \; d\psi \right) d\varphi = 2 \int_{\varphi_0}^{\varphi_f} \sin^3\varphi \left(\int_{\psi_0}^{\pi} \cos^2\psi \; d\psi \right) d\varphi \tag{B.59}$$

$$\boxed{C}_{out} = \int_{\varphi_0}^{\varphi_f} \sin^2\varphi \cos\varphi \left(\int_{\psi_0}^{2\pi-\psi_0} \cos\psi \; d\psi \right) d\varphi = 2 \int_{\varphi_0}^{\varphi_f} \sin^2\varphi \cos\varphi \left(\int_{\psi_0}^{\pi} \cos\psi \; d\psi \right) d\varphi \tag{B.60}$$

Solving the integrals in Eqs. B.58-B.60 with respect to ψ gives:

$$\begin{aligned} \boxed{A}_{out} =& 2 \int_{\varphi_0}^{\varphi_f} \cos^2\varphi \sin\varphi \left(\pi - \psi_0\right) \; d\varphi = \\ & \underbrace{2\pi \int_{\varphi_0}^{\varphi_f} \cos^2\varphi \sin\varphi \; d\varphi}_{\boxed{A}_{out,a}} - \underbrace{2 \int_{\varphi_0}^{\varphi_f} \cos^2\varphi \sin\varphi \; \psi_0 \; d\varphi}_{\boxed{A}_{out,b}} = \\ & \boxed{A}_{out,a} - \boxed{A}_{out,b} \end{aligned} \tag{B.61}$$

$$\begin{aligned} \boxed{B}_{out} =& \int_{\varphi_0}^{\varphi_f} \sin^3\varphi \left(\pi - \psi_0 - \sin\psi_0 \cos\psi_0\right) d\varphi = \\ & \underbrace{\pi \int_{\varphi_0}^{\varphi_f} \sin^3\varphi d\varphi}_{\boxed{B}_{out,a}} - \underbrace{\int_{\varphi_0}^{\varphi_f} \sin^3\varphi \; \psi_0 d\varphi}_{\boxed{B}_{out,b}} - \underbrace{\int_{\varphi_0}^{\varphi_f} \sin^3\varphi \sin\psi_0 \cos\psi_0 \; d\varphi}_{\boxed{B}_{out,c}} = \\ & \boxed{B}_{out,a} - \boxed{B}_{out,b} - \boxed{B}_{out,c} \end{aligned} \tag{B.62}$$

$$\boxed{C}_{out} = -2\int_{\varphi_0}^{\varphi_f} \sin^2\varphi\cos\varphi\sin\psi_0\, d\varphi \tag{B.63}$$

Substituting the limits of integration in Eq. B.57 into $\boxed{A}_{out,a}$, $\boxed{A}_{out,b}$, $\boxed{B}_{out,a}$, $\boxed{B}_{out,b}$, $\boxed{B}_{out,c}$, and $\boxed{C}_{out}$ yields:

$$\boxed{A}_{out,a} = 2\pi\int_{\frac{\pi}{2}-\alpha_\oplus}^{\sin^{-1}H} \cos^2\varphi\sin\varphi\, d\varphi \tag{B.64}$$

$$\boxed{A}_{out,b} = 2\int_{\frac{\pi}{2}-\alpha_\oplus}^{\sin^{-1}H} \cos^2\varphi\sin\varphi\cos^{-1}\left(-\frac{\cos\alpha_\oplus\cos\varphi}{\sin\alpha_\oplus\sin\varphi}\right) d\varphi = \boxed{A}_{in,2} \tag{B.65}$$

$$\boxed{B}_{out,a} = \pi\int_{\frac{\pi}{2}-\alpha_\oplus}^{\sin^{-1}H} \sin^3\varphi\, d\varphi \tag{B.66}$$

$$\boxed{B}_{out,b} = \int_{\frac{\pi}{2}-\alpha_\oplus}^{\sin^{-1}H} \sin^3\varphi\cos^{-1}\left(-\frac{\cos\alpha_\oplus\cos\varphi}{\sin\alpha_\oplus\sin\varphi}\right) d\varphi = \boxed{B}_{in,2a} \tag{B.67}$$

$$\boxed{B}_{out,c} = -\int_{\frac{\pi}{2}-\alpha_\oplus}^{\sin^{-1}H} \sin^3\varphi\frac{\cos\alpha_\oplus\cos\varphi}{\sin\alpha_\oplus\sin\varphi}\sqrt{1-\left(\frac{\cos\alpha_\oplus\cos\varphi}{\sin\alpha_\oplus\sin\varphi}\right)^2}\, d\varphi = \boxed{B}_{in,2b} \tag{B.68}$$

$$\boxed{C}_{out} = -2\int_{\frac{\pi}{2}-\alpha_\oplus}^{\sin^{-1}H} \sin^2\varphi\cos\varphi\sqrt{1-\left(\frac{\cos\alpha_\oplus\cos\varphi}{\sin\alpha_\oplus\sin\varphi}\right)^2}\, d\varphi = -\boxed{C}_{in,2} \tag{B.69}$$

Notably, the solutions to the integrals in Eqs. B.65 and B.67-B.69 were already found in Eqs. B.50, B.51, B.52, and B.54. Therefore, only the integrals in Eqs. B.64 and B.66 need to be solved, which yields:

$$\boxed{A}_{out,a} = \frac{2\pi}{3}\left[\sin^3\alpha_\oplus - \left(1-H^2\right)^{\frac{3}{2}}\right] \tag{B.70}$$

$$\boxed{B}_{out,a} = \frac{\pi}{3}\left[\sin\alpha_\oplus\left(3-\sin^2\alpha_\oplus\right) - \sqrt{1-H^2}\left(2+H^2\right)\right] \tag{B.71}$$

Therefore, inserting Eqs. B.70 and B.50 into Eq. B.61, and Eq. B.71, B.51, and B.52 into Eq. B.62 yields:

$$\boxed{A}_{out} = \frac{2}{3}\left[\tan^{-1}\mathcal{B} - \mathcal{B}\cos^2\alpha_\oplus - \left(1-H^2\right)^{\frac{3}{2}}\cos^{-1}\mathcal{A}\right] \tag{B.72}$$

$$\boxed{B}_{out} = \frac{1}{3}\left[2\tan^{-1}\mathcal{B} + \mathcal{B}\cos^2\alpha_\oplus\left(2-\frac{1-H^2}{\sin^2\alpha_\oplus}\right) - \left(2+H^2\right)\sqrt{1-H^2}\cos^{-1}\mathcal{A}\right] \tag{B.73}$$

By expressing $\boxed{C}_{out}$ as the negative of Eq. B.54 (as per Eq. B.69), inserting it alongside Eqs. B.72 and B.73 in Eq. B.25, and simplifying, the final expression for the geometrical factor of the outward-facing sail side, $G_{FNS,out}$, provided in Eq. 4.23 is found.

B.2.3. REDUCED FORM FOR IDEAL SAILS

When a double-coated perfectly reflecting – i.e., ideal – sail is considered, the geometrical factors of the inward-facing and outward-facing sides of the sail can be used to define a single overall specular geometrical factor, namely:

$$G_{FNS} = G_{FNS,in} - G_{FNS,out} \tag{B.74}$$

If the Earth's spherical cap is visible only from the inward side of the sail, then $G_{FNS,out} = 0$ and, therefore, $G_{FNS} = G_{FNS,in}$, as highlighted by the equivalence of Eqs. 3.20 and 4.21. On the other hand, if the spherical cap is visible from both sides of the sail, Eqs. 4.22 and 4.23 can be substituted into Eq. B.74, which, upon simplification, yields the geometrical factor given in Eq. 3.21.

B.3. TRANSVERSAL GEOMETRICAL FACTORS

The transversal geometrical factors are defined in Eq. 4.20 and are reported here for convenience.

$$G_{FT,\Diamond} = \frac{3}{2}\int_{A^*_\Diamond} \frac{\cos\vartheta\cos\theta\sin\theta}{l^2}\cos\xi\, dA \tag{B.75}$$

Substituting Eqs. B.13, B.11, B.21, and B.9 into Eq. B.75 gives:

$$\begin{aligned} G_{FT,\Diamond} = &\frac{3}{2}\mathrm{sgn}\left(\hat{\boldsymbol{l}}\cdot\hat{\boldsymbol{n}}_{out}\right)\Bigg[\left(\sin^2\alpha_\oplus - \cos^2\alpha_\oplus\right)\underbrace{\int_{\varphi_0}^{\varphi_f}\int_{\psi_0}^{\psi_f}\sin^2\varphi\cos\varphi\cos\psi\; d\psi\, d\gamma}_{\boxed{C}_\Diamond} + \\ &\sin\alpha_\oplus\cos\alpha_\oplus\left(\underbrace{\int_{\varphi_0}^{\varphi_f}\int_{\psi_0}^{\psi_f}\cos^2\varphi\sin\varphi\; d\psi\, d\gamma}_{\boxed{A}_\Diamond} - \underbrace{\int_{\varphi_0}^{\varphi_f}\int_{\psi_0}^{\psi_f}\sin^3\varphi\cos^2\psi\; d\psi\, d\gamma}_{\boxed{B}_\Diamond}\right)\Bigg] = \\ &\frac{3}{2}\mathrm{sgn}\left(\hat{\boldsymbol{l}}\cdot\hat{\boldsymbol{n}}_{out}\right)\left[\left(\sin^2\alpha_\oplus - \cos^2\alpha_\oplus\right)\boxed{C}_\Diamond + \sin\alpha_\oplus\cos\alpha_\oplus\left(\boxed{A}_\Diamond - \boxed{B}_\Diamond\right)\right] \end{aligned} \tag{B.76}$$

where $\boxed{A}_\Diamond$, $\boxed{B}_\Diamond$, and $\boxed{C}_\Diamond$ are defined in Eq. B.25. The fact that the integrals in Eq. B.76 coincide with those in Eq. B.25 allows to reuse the solutions to the integrals found in Section B.2, greatly facilitating the derivation of the transversal geometrical factors. As discussed in that section, the limits of integration of the integrals $\boxed{A}_\Diamond$, $\boxed{B}_\Diamond$, and $\boxed{C}_\Diamond$ depend on the geometrical configuration considered, namely, whether the sail plane intersects the visible spherical cap of the Earth or not. The transversal geometrical factors relative to these two cases are derived separately in the following subsections.

B.3.1. SAIL PLANE NOT INTERSECTING THE EARTH

Because the surface of the spherical cap is entirely visible from the inward side of the sail, $A^*_{out} = G_{FT,out} = 0$ and $\mathrm{sgn}\left(\hat{\boldsymbol{l}}\cdot\hat{\boldsymbol{n}}_{out}\right) = 1$ in Eq. B.76. The surface A^*_{in} corresponds to the entire surface of the spherical cap, which is identified by the domain boundaries in Eq. B.26. The solutions to the integrals $\boxed{A}_{in}$, $\boxed{B}_{in}$, and $\boxed{C}_{in}$ are given in Eqs. B.30-B.32.

Substituting them into Eq. B.76 and simplifying the resulting expressions, the transversal geometrical factor for the inward side of the sail given in Eq. 4.28 is found.

B.3.2. SAIL PLANE INTERSECTING THE EARTH

In this case, the surface of the spherical cap is separated into two regions, A^*_{in} and A^*_{out}, visible from the inward and outward sides of the sail, respectively, see Figs. B.1 and B.3. The corresponding geometrical factors, $G_{FT,in}$ and $G_{FT,out}$, are derived in the following subsections.

B.3.2.1. GEOMETRICAL FACTOR OF THE INWARD SIDE OF THE SAIL

The radiation from the surface region A^*_{in} impinges only on the inward-facing side of the sail, therefore implying $\text{sgn}\left(\hat{\boldsymbol{l}}\cdot\hat{\boldsymbol{n}}_{out}\right)=1$ in Eq. B.76. Using the same approach as in Section B.2.2.1, the surface A^*_{in} is split into one region having a circular boundary and symmetric with respect to $\hat{\boldsymbol{r}}$, denoted by $A^*_{in,1}$, and the remaining part of the spherical cap's surface, denoted by $A^*_{in,2}$, see Fig. B.3. Accordingly, the geometrical factor $G_{FT,in}$ can be expressed as the sum of two components as $G_{FT,in}=G_{FT,in,1}+G_{FT,in,2}$.

The region $A^*_{in,1}$ is defined by the domain boundaries given in Eq. B.34. The solutions to the integrals $\boxed{A}_{in,1}$, $\boxed{B}_{in,1}$, and $\boxed{C}_{in,1}$ – which use these domain boundaries as limits of integration – are given in Eqs. B.35-B.37. Substituting Eqs. B.35-B.37 into Eq. B.76, considering $\text{sgn}\left(\hat{\boldsymbol{l}}\cdot\hat{\boldsymbol{n}}_{out}\right)=1$, and simplifying yields:

$$G_{FT,in,1}=\frac{3\pi}{2}\sin^2\alpha_\oplus\cos^3\alpha_\oplus \tag{B.77}$$

The region $A^*_{in,2}$ is defined by the domain boundaries in Eq. B.39. When using these boundaries as integration limits, the integrals $\boxed{A}_{in,2}$, $\boxed{B}_{in,2}$, and $\boxed{C}_{in,2}$ are found, with solutions given by Eqs. B.50, B.53, and B.54. Substituting these solutions into Eq. B.76 again with $\text{sgn}\left(\hat{\boldsymbol{l}}\cdot\hat{\boldsymbol{n}}_{out}\right)=1$ and simplifying yields:

$$\begin{aligned}G_{FT,in,2}=\frac{1}{2}\Bigg\{&\mathcal{B}\left[2\sin\alpha_\oplus\cos^3\alpha_\oplus\left(\mathcal{B}^2+2+\frac{\cos^2\alpha_\oplus}{\sin^2\alpha_\oplus}\right)-\left(1+H^2\right)\frac{\cos^3\alpha_\oplus}{\sin\alpha_\oplus}\right]\\&+3H^2\sqrt{1-H^2}\sin\alpha_\oplus\cos\alpha_\oplus\cos^{-1}(-\mathcal{A})-3\pi\sin^2\alpha_\oplus\cos^3\alpha_\oplus\Bigg\}\end{aligned} \tag{B.78}$$

Finally, summing Eqs. B.77 and B.78 yields the transversal geometrical factor of the inward side of the sail provided in Eq. 4.29.

B.3.2.2. GEOMETRICAL FACTOR OF THE OUTWARD SIDE OF THE SAIL

The radiation emitted by the surface region A^*_{out}, see Fig. B.3, only illuminates the outward-facing side of the sail and, therefore, $\text{sgn}\left(\hat{\boldsymbol{l}}\cdot\hat{\boldsymbol{n}}_{out}\right)=-1$ in Eq. B.76. This surface region is defined by the domain boundaries in Eq. B.57. Using these boundaries as limits of integration, the integrals $\boxed{A}_{out}$, $\boxed{B}_{out}$, and $\boxed{C}_{out}$ are found, with solutions given by Eqs. B.72, B.73, and the negative of Eq. B.54. Substituting these solutions into Eq. B.76 with $\text{sgn}\left(\hat{\boldsymbol{l}}\cdot\hat{\boldsymbol{n}}_{out}\right)=-1$ yields the transversal geometrical factor of the outward side of the sail provided in Eq. 4.30.

C

Derivation of the Latitudinal Factor

This appendix provides the analytical derivation of the latitudinal factor presented in Chapter 3 to compute the surface-averaged blackbody radiation flux and albedo coefficient.

C.1. Geometry of the Problem

This section presents the geometry of the problem underlying the definition of the latitudinal factor, together with the variables used throughout the remainder of the appendix. The reader is referred to the sketch of the geometrical configuration provided in Fig. C.1 as the main visual reference for the discussion that follows.

As shown in Fig. C.1, the Earth is assumed to be spherical with radius R. The sailcraft lies above the Earth at a distance $r = \|\boldsymbol{r}\|$ from its geometrical center, with $\boldsymbol{r}$ the position vector of the sailcraft. Therefore, from the sailcraft's perspective, the visible part of the Earth surface is a spherical cap, whose area is denoted by A^*. The angle between $-\boldsymbol{r}$ and the horizon as seen from the sailcraft — that is, the edge of the spherical cap – is denoted by φ_m, whereas the angle between $\boldsymbol{r}$ and the edge of the spherical cap as seen from the center of the Earth is denoted by γ_m. By introducing the adimensional inverse orbital radius $H = R/r$ for notational convenience, these angles can be defined as:

$$\varphi_m = \sin^{-1} H \tag{C.1a}$$

$$\gamma_m = \cos^{-1} H \tag{C.1b}$$

and therefore:

$$\sin\varphi_m = \cos\gamma_m = H \tag{C.1c}$$

$$\cos\varphi_m = \sin\gamma_m = \sqrt{1-H^2} \tag{C.1d}$$

A differential piece of surface dA on the spherical cap is identified through the Earth-centered polar angle γ and the azimuthal angle ψ, see Fig. C.1. The Earth-centered polar

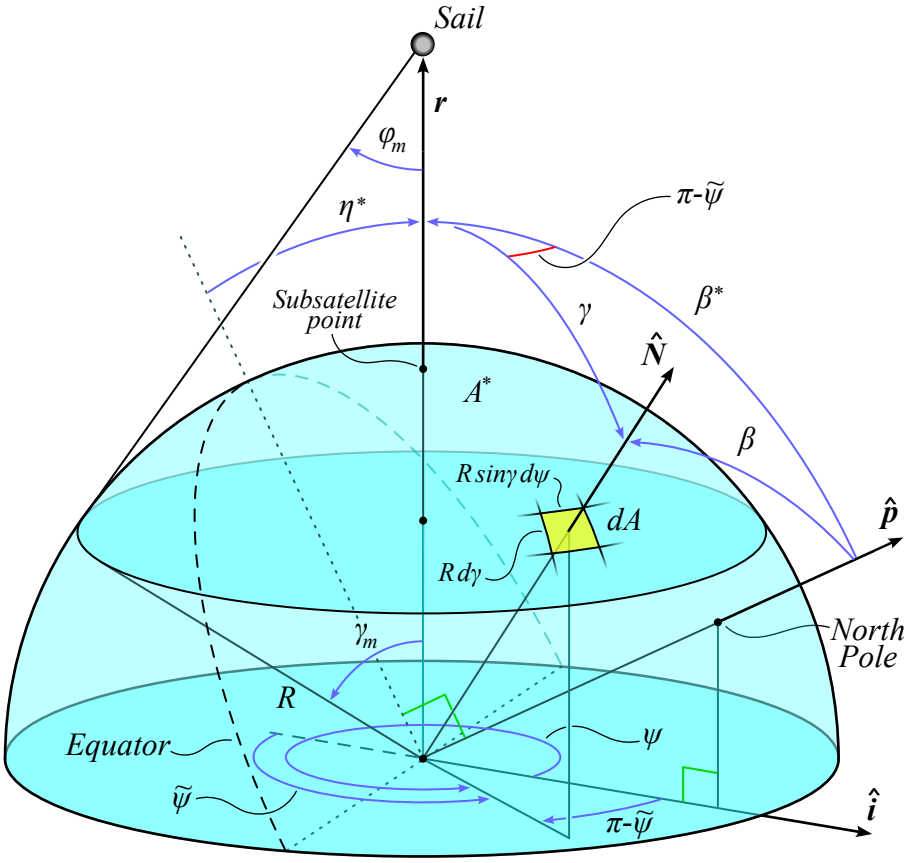


Figure C.1: Geometry of the problem and variables to derive the latitudinal factor.

angle, γ, is measured from $\boldsymbol{r}$ to $\hat{\boldsymbol{N}}$, where $\hat{\boldsymbol{N}}$ is the direction pointing from the center of the Earth to dA and, accordingly, it is normal to the surface of the Earth at dA. The azimuthal angle ψ is defined inside the plane perpendicular to $\boldsymbol{r}$ and passing through the geometrical center of the Earth. This angle is measured between the reference direction $\hat{\boldsymbol{i}}$ and the projection of $\hat{\boldsymbol{N}}$ onto said plane. The direction $\hat{\boldsymbol{i}}$ is defined as:

$$\hat{\boldsymbol{i}} = \hat{\boldsymbol{r}} \times \frac{\hat{\boldsymbol{p}} \times \hat{\boldsymbol{r}}}{\left\| \hat{\boldsymbol{p}} \times \hat{\boldsymbol{r}} \right\|} \tag{C.2}$$

where $\hat{\boldsymbol{r}} = \boldsymbol{r}/r$ and $\hat{\boldsymbol{p}}$ is the direction pointing from the center of the Earth to the North Pole, such that $\hat{\boldsymbol{i}} \cdot \hat{\boldsymbol{p}} \geq 0$. As can be observed in Fig. C.1, the differential element of surface area, dA, can be expressed through the angles γ and ψ as:

$$dA = \left(R d\gamma\right)\left(R \sin\gamma d\psi\right) = R^2 \sin\gamma \, d\psi \, d\gamma \tag{C.3}$$

The relative positions of the visible spherical cap of the Earth, the surface element dA, the equator, and North Pole are defined through different angles. The location of

the surface element dA is identified by its latitude, $\eta \in [-\pi/2, \pi/2]$, measured from the Earth's equatorial plane to $\hat{\boldsymbol{N}}$, and its colatitude, $\beta \in [0, \pi]$, measured between $\hat{\boldsymbol{p}}$ and $\hat{\boldsymbol{N}}$. Similarly, the latitude of the surface element dA, $\eta^* \in [-\pi/2, \pi/2]$, is the angle between the equatorial plane and $\hat{\boldsymbol{r}}$, whereas the colatitude of the sailcraft, $\beta^* \in [0, \pi]$, is measured between $\hat{\boldsymbol{p}}$ and $\hat{\boldsymbol{r}}$. Notably, latitude and colatitude angles are complementary. Therefore, the following relationships hold true:

$$\beta = \frac{\pi}{2} - \eta \quad \Longrightarrow \quad \begin{cases} \sin\eta = \cos\beta \\ \cos\eta = \sin\beta \end{cases} \tag{C.4a}$$

$$\beta^* = \frac{\pi}{2} - \eta^* \quad \Longrightarrow \quad \begin{cases} \sin\eta^* = \cos\beta^* \\ \cos\eta^* = \sin\beta^* \end{cases} \tag{C.4b}$$

As shown in Fig. C.1, the unit vectors $\hat{\boldsymbol{r}}$, $\hat{\boldsymbol{N}}$, and $\hat{\boldsymbol{p}}$ form a spherical triangle. This geometrical construction allows to use the spherical law of cosines to express the colatitude of the differential surface element, β, as a function of the angles γ and β^* as [433]:

$$\cos\beta = \cos\gamma\cos\beta^* + \sin\gamma\sin\beta^*\cos\left(\pi - \tilde{\psi}\right) = \cos\gamma\cos\beta^* + \sin\gamma\sin\beta^*\cos\psi \tag{C.5}$$

where $\tilde{\psi} = |\pi - \psi|$ is the angle between the direction $-\hat{\boldsymbol{i}}$ and the projection of $\hat{\boldsymbol{N}}$ onto the reference plane through the center of the Earth, see Fig. C.1.

C.2. INTEGRAL FORMULATION

The latitudinal factor is defined in Eq. 3.26 and is reported here for convenience:

$$L_F = \frac{\int_{A^*} \sin^2\eta \, dA}{\int_{A^*} dA} \tag{C.6}$$

The denominator on the right-hand side of Eq. C.6 corresponds to the entire surface area of the spherical cap, A^*, which is found as [433]:

$$A^* = \int_{A^*} dA = 2\pi R^2 \left(1 - \cos\gamma_m\right) = 2\pi R^2 \left(1 - H\right) \tag{C.7}$$

where Eq. C.1c was used. Substituting Eq. C.7 into Eq. C.6 and applying the identity $\sin\eta = \cos\beta$, see Eq. C.4a, the latitudinal factor can then be rewritten as:

$$L_F = \frac{1}{2\pi R^2 \left(1 - H\right)} \int_{A^*} \cos^2\beta \, dA \tag{C.8}$$

which, upon substituting Eqs. C.3 and C.5, becomes:

$$L_F = \frac{1}{2\pi\left(1 - H\right)} \int_{\gamma_0}^{\gamma_f} \int_{\psi_0}^{\psi_f} \left(\cos\gamma\cos\beta^* + \sin\gamma\sin\beta^*\cos\psi\right)^2 \sin\gamma \, d\psi \, d\gamma \tag{C.9}$$

where γ_0, γ_f, ψ_0, and ψ_f identify the domain boundaries of the surface of the visible spherical cap, A^*. Developing the square of binomial in Eq. C.9 and separating the resulting integrals finally yields:

$$\begin{aligned} L_F = \frac{1}{2\pi(1-H)} \Bigg[\cos^2\beta^* \underbrace{\int_{\gamma_0}^{\gamma_f}\int_{\psi_0}^{\psi_f} \cos^2\gamma \sin\gamma \, d\psi d\gamma}_{\boxed{A}} + \\ \sin^2\beta^* \underbrace{\int_{\gamma_0}^{\gamma_f}\int_{\psi_0}^{\psi_f} \sin^3\gamma \cos^2\psi \, d\psi d\gamma}_{\boxed{B}} + \\ 2\sin\beta^*\cos\beta^* \underbrace{\int_{\gamma_0}^{\gamma_f}\int_{\psi_0}^{\psi_f} \sin^2\gamma \cos\gamma \cos\psi \, d\psi d\gamma}_{\boxed{C}} \Bigg] = \\ \frac{1}{2\pi(1-H)} \Big[\cos^2\beta^* \boxed{A} + \sin^2\beta^* \boxed{B} + 2\sin\beta^*\cos\beta^* \boxed{C} \Big] \end{aligned} \tag{C.10}$$

The above double integrals $\boxed{A}$, $\boxed{B}$, and $\boxed{C}$ will be solved in the next section, allowing to express the latitudinal factor, L_F, analytically.

C.3. ANALYTICAL EVALUATION

The domain boundaries appearing in Eq. C.10 identify the surface of the visible spherical cap, A^*, and are given by:

$$\begin{cases} \gamma_0 = 0 \\ \gamma_f = \gamma_m = \cos^{-1} H \\ \psi_0 = 0 \\ \psi_f = 2\pi \end{cases} \tag{C.11}$$

where the expression for γ_m was taken from Eq. C.1b. As can be observed, these domain boundaries are not functions of γ nor ψ. Therefore, using them as integration limits allows to simplify the double integrals in Eq. C.10 to products of single integrals as:

$$\boxed{A} = \int_{\psi_0}^{\psi_f} d\psi \int_{\gamma_0}^{\gamma_f} \cos^2\gamma \sin\gamma \, d\gamma \tag{C.12}$$

$$\boxed{B} = \int_{\psi_0}^{\psi_f} \cos^2\psi \, d\psi \int_{\gamma_0}^{\gamma_f} \sin^3\gamma \, d\gamma \tag{C.13}$$

$$\boxed{C} = \int_{\psi_0}^{\psi_f} \cos\psi \, d\psi \int_{\gamma_0}^{\gamma_f} \sin^2\gamma \cos\gamma \, d\gamma \tag{C.14}$$

Substituting the limits of integration in Eq. C.11 and solving the integrals then yields:

$$\boxed{A} = [\psi]_0^{2\pi} \left[-\frac{1}{3}\cos^3\gamma \right]_0^{\cos^{-1}H} = \frac{2\pi}{3}\left(1 - H^3\right) \tag{C.15}$$

$$\boxed{B} = \left[\frac{1}{2}\left(\psi - \sin\psi\cos\psi\right) \right]_0^{2\pi} \left[\frac{1}{3}\cos\gamma\left(\cos^2\gamma - 1\right) \right]_0^{\cos^{-1}H} = \frac{\pi}{3}(1-H)^2(2+H) \tag{C.16}$$

$$\boxed{C} = [\sin\psi]_0^{2\pi} \left[\frac{1}{3}\sin^3\gamma \right]_0^{\cos^{-1}H} = 0 \tag{C.17}$$

Finally, by substituting $\boxed{A}$, $\boxed{B}$, and $\boxed{C}$ into Eq. C.10, applying the identities in Eq. C.4a, and manipulating the resulting expression algebraically, the definition of the latitudinal factor given in Eq. 3.27 is found.

D

Derivation of the Albedo Phase Function

This appendix provides the analytical derivation of the phase function presented in Chapter 3 to compute the albedo radiation flux.

D.1. Geometry of the Problem

This section presents the geometry of the problem underlying the definition of the albedo phase function, together with the variables used throughout the remainder of the appendix. The reader is referred to the sketch of the geometrical configuration provided in Fig. D.1 as the main visual reference for the discussion that follows.

As shown in Fig. D.1, the Earth is assumed to be spherical with radius R. The sailcraft lies above the Earth at a distance $r = \|\boldsymbol{r}\|$ from its geometrical center, with $\boldsymbol{r}$ the position vector of the sailcraft. Therefore, from the sailcraft's perspective, the visible part of the Earth surface is a spherical cap, whose area is denoted by A^*. The angle between $-\boldsymbol{r}$ and the horizon as seen from the sailcraft — that is, the edge of the spherical cap – is denoted by φ_m, whereas the angle between $\boldsymbol{r}$ and the edge of the spherical cap as seen from the center of the Earth is denoted by γ_m. By introducing the adimensional inverse orbital radius $H = R/r$ for notational convenience, these angles can be defined as:

$$\varphi_m = \sin^{-1} H \tag{D.1a}$$

$$\gamma_m = \cos^{-1} H \tag{D.1b}$$

and therefore:

$$\sin\varphi_m = \cos\gamma_m = H \tag{D.1c}$$

$$\cos\varphi_m = \sin\gamma_m = \sqrt{1-H^2} \tag{D.1d}$$

A differential piece of surface dA on the spherical cap is identified through the Earth-centered polar angle γ and the azimuthal angle ψ, see Fig. D.1. The Earth-centered polar

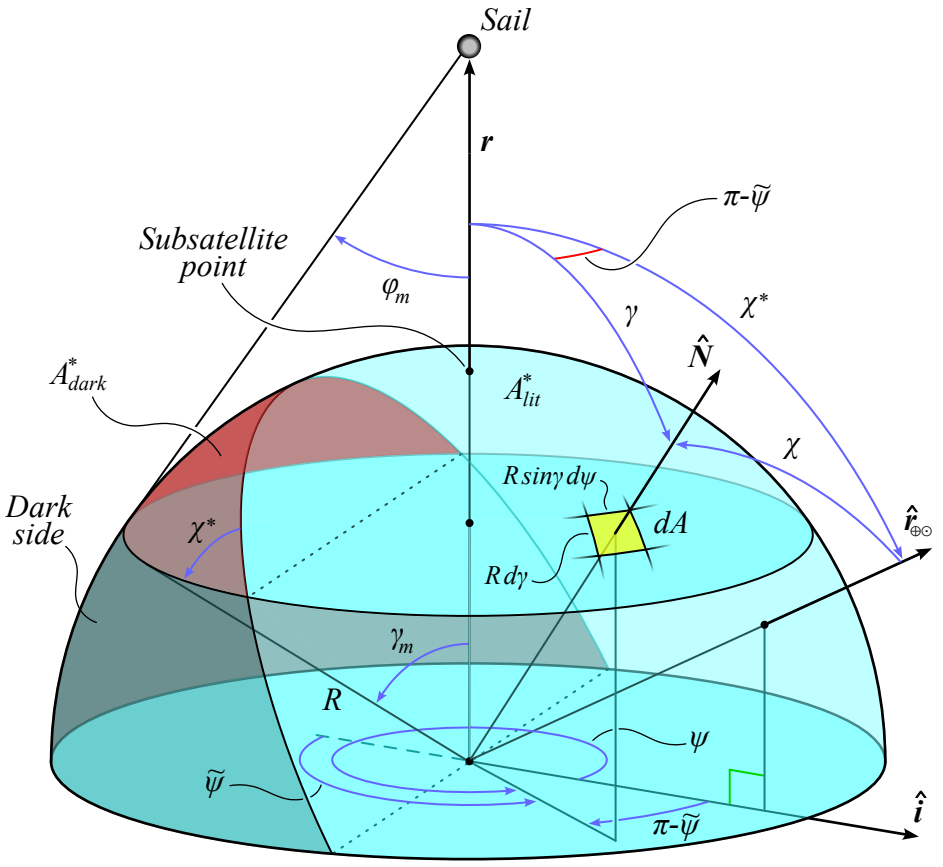


Figure D.1: Geometry of the problem and variables to derive the phase function.

angle, γ, is measured from $\boldsymbol{r}$ to $\hat{\boldsymbol{N}}$, where $\hat{\boldsymbol{N}}$ is the direction pointing from the center of the Earth to dA and, accordingly, it is normal to the surface of the Earth at dA. The azimuthal angle ψ is defined inside the plane perpendicular to $\boldsymbol{r}$ and passing through the geometrical center of the Earth. This angle is measured between the reference direction $\hat{\boldsymbol{i}}$ and the projection of $\hat{\boldsymbol{N}}$ onto said plane. The direction $\hat{\boldsymbol{i}}$ is defined as:

$$\hat{\boldsymbol{i}} = \hat{\boldsymbol{r}} \times \frac{\hat{\boldsymbol{r}}_{\odot\oplus} \times \hat{\boldsymbol{r}}}{\| \hat{\boldsymbol{r}}_{\odot\oplus} \times \hat{\boldsymbol{r}} \|} \tag{D.2}$$

where $\hat{\boldsymbol{r}} = \boldsymbol{r}/r$ and $\hat{\boldsymbol{r}}_{\odot\oplus}$ is the Earth-to-Sun direction, such that $\hat{\boldsymbol{i}} \cdot \hat{\boldsymbol{r}}_{\odot\oplus} \geq 0$. Note that, in Chapter 3 and 4, $\hat{\boldsymbol{r}}_{\odot\oplus}$ is assumed equal to the sailcraft-to-Sun direction, $-\hat{\boldsymbol{s}}$, as the angular difference between the two is negligible for Earth-orbiting sailcraft. E.g., this difference is less than 0.017 deg at geostationary altitudes, and less than 0.003 deg at an altitude of 1000 km. As can be observed in Fig. D.1, the differential element of surface area, dA, can be expressed through the angles γ and ψ as:

$$dA = \left(R d\gamma\right)\left(R \sin\gamma d\psi\right) = R^2 \sin\gamma \, d\psi \, d\gamma \tag{D.3}$$

The relative position of the Sun with respect to the visible spherical cap of the Earth and the surface element dA is described by means of different angles. The angle between $\hat{\boldsymbol{r}}$ and $\hat{\boldsymbol{r}}_{\odot\oplus}$ is the phase angle, $\chi^* \in [0,\pi]$, whereas the solar zenith angle at dA, χ, is measured between $\hat{\boldsymbol{N}}$ and $\hat{\boldsymbol{r}}_{\odot\oplus}$. As shown in Fig. D.1, the unit vectors $\hat{\boldsymbol{r}}$, $\hat{\boldsymbol{N}}$, and $\hat{\boldsymbol{r}}_{\odot\oplus}$ form a spherical triangle. This geometrical construction allows to use the spherical law of cosines to express the solar zenith angle, χ, as a function of the angles γ and χ^* as [433]:

$$\cos\chi = \cos\gamma\cos\chi^* + \sin\gamma\sin\chi^*\cos\left(\pi-\tilde{\psi}\right) = \cos\gamma\cos\chi^* + \sin\gamma\sin\chi^*\cos\psi \tag{D.4}$$

where $\tilde{\psi} = |\pi - \psi|$ is the angle between the direction $-\hat{\boldsymbol{i}}$ and the projection of $\hat{\boldsymbol{N}}$ onto the reference plane through the center of the Earth, see Fig. D.1.

D.2. INTEGRAL FORMULATION

The phase function is defined in Eq. 3.33 and is reported here for convenience:

$$\Phi = \frac{\displaystyle\int_{A^*} \max(0,\cos\chi)\,dA}{\displaystyle\int_{A^*} dA} \tag{D.5}$$

The denominator on the right-hand side of Eq. D.5 corresponds to the entire surface area of the spherical cap, A^*, which is found as [433]:

$$A^* = \int_{A^*} dA = 2\pi R^2\left(1-\cos\gamma_m\right) = 2\pi R^2\left(1-H\right) \tag{D.6}$$

where Eq. D.1c was used. In the right-hand side of Eq. D.5, the "max" function in the numerator restricts the integral to the fraction of the spherical cap's surface that is illuminated by sunlight, denoted by A^*_{lit}, see Fig. D.1. Mathematically, this surface region corresponds to the region for which $\chi < \pi/2$. Accordingly, the complementary fraction of the spherical cap's surface for which $\chi > \pi/2$ identifies the surface region not receiving sunlight, denoted by A^*_{dark}, whereas the curve found for $\chi = \pi/2$ identifies the day-night terminator, see again Fig. D.1. Taking advantage of Eq. D.5 and the above definitions of the illuminated surface region, A^*_{lit}, Eq. D.5 can be rewritten as:

$$\Phi = \frac{1}{2\pi R^2\left(1-H\right)}\int_{A^*_{lit}} \cos\chi\,dA \tag{D.7}$$

which, upon substituting Eq. D.3, becomes:

$$\Phi = \frac{1}{2\pi\left(1-H\right)}\int_{\gamma_0}^{\gamma_f}\int_{\psi_0}^{\psi_f} \cos\chi\,\sin\gamma\,d\psi\,d\gamma \tag{D.8}$$

where the limits of integration γ_0, γ_f, ψ_0, and ψ_f depend on the shape of the illuminated surface region of the spherical cap, A^*_{lit}. Substituting Eq. D.4 into Eq. D.8 yields:

$$\Phi = \frac{1}{2\pi\left(1-H\right)}\int_{\gamma_0}^{\gamma_f}\int_{\psi_0}^{\psi_f} \left(\cos\gamma\cos\chi^* + \sin\gamma\sin\chi^*\cos\psi\right)\sin\gamma\,d\psi\,d\gamma \tag{D.9}$$

and separating the resulting integrals results in:

$$\Phi = \frac{1}{2\pi(1-H)}\left[\cos\chi^* \underbrace{\int_{\gamma_0}^{\gamma_f}\int_{\psi_0}^{\psi_f}\cos\gamma\,\sin\gamma\,d\psi\,d\gamma}_{\boxed{A}} + \sin\chi^* \underbrace{\int_{\gamma_0}^{\gamma_f}\int_{\psi_0}^{\psi_f}\sin^2\gamma\cos\psi\,d\psi\,d\gamma}_{\boxed{B}}\right] =$$

$$\frac{1}{2\pi(1-H)}\left[\cos\chi^*\boxed{A} + \sin\chi^*\boxed{B}\right] \tag{D.10}$$

The above double integrals $\boxed{A}$ and $\boxed{B}$ will be solved in the next sections considering different integration domains, which depend on the illumination conditions of the spherical cap and, therefore, on the Sun-Earth-sailcraft geometrical configuration.

D

D.3. ANALYTICAL EVALUATION

Deriving the analytical expression of the phase function from its integral representation in Eq. D.10 requires distinct approaches depending on the Sun-Earth-sailcraft geometric configuration at hand. Specifically, four cases can be distinguished:

- The case in which the surface of the spherical cap is completely illuminated and, therefore, $A^*_{lit} = A^*$. This configuration occurs when $\chi^* \leq \varphi_m$.

- The case in which the surface of the spherical cap is partially illuminated, with the illuminated fraction exceeding half of the total surface. In this case – shown in Fig. D.1 – the day-night terminator lies over the surface of the spherical cap and, together with the edge of the spherical cap, it delimitates the illuminated surface region, A^*_{lit}. This configuration occurs when $\varphi_m < \chi^* \leq \pi/2$.

- The case in which the surface of the spherical cap is partially illuminated, with the illuminated fraction covering less than half of the total surface. As in the previous case, the day-night terminator crosses the surface of the spherical cap, and together with the edge of the cap, it delineates the boundary of the illuminated surface region, A^*_{lit}. This configuration occurs when $\pi/2 < \chi^* < \pi - \varphi_m$.

- The case in which the surface of the spherical cap is completely dark, meaning that the surface domain A^*_{lit} is nonexistent, yielding $\Phi = 0$, see Eq. D.7. This configuration occurs when $\pi - \varphi_m \leq \chi^*$.

The analytical expressions for the phase function in the first three cases listed above – namely, when the spherical cap is completely illuminated, predominantly illuminated, or predominantly dark – are derived separately in the following subsections.

D.3.1. VISIBLE SURFACE COMPLETELY ILLUMINATED

When the surface of the spherical cap is completely illuminated, the boundary of the illuminated region, A^*_{lit}, coincides with the edge of the spherical cap, which corresponds to the following domain boundaries:

$$\begin{cases} \gamma_0 &= 0 \\ \gamma_f &= \gamma_m = \cos^{-1} H \\ \psi_0 &= 0 \\ \psi_f &= 2\pi \end{cases} \tag{D.11}$$

where the expression for γ_m was taken from Eq. D.1b. The above domain boundaries are not functions of γ nor ψ. Therefore, using them as integration limits allows to simplify the double integrals in Eq. D.10 to products of single integrals as:

$$\boxed{A} = \int_{\psi_0}^{\psi_f} d\psi \int_{\gamma_0}^{\gamma_f} \cos\gamma \sin\gamma \, d\gamma \tag{D.12}$$

$$\boxed{B} = \int_{\psi_0}^{\psi_f} \cos\psi \, d\psi \int_{\gamma_0}^{\gamma_f} \sin^2\gamma \, d\gamma \tag{D.13}$$

Substituting the limits of integration in Eq. D.11 and solving the integrals yields:

$$\boxed{A} = \left[\psi\right]_0^{2\pi} \left[-\frac{1}{2}\cos^2\gamma\right]_0^{\cos^{-1}H} = \pi\left(1 - H^2\right) \tag{D.14}$$

$$\boxed{B} = \left[\sin\psi\right]_0^{2\pi} \left[\frac{1}{2}\left(\gamma - \sin\gamma\cos\gamma\right)\right]_0^{\cos^{-1}H} = 0 \tag{D.15}$$

Finally, substituting $\boxed{A}$ and $\boxed{B}$ into Eq. D.10 and simplifying the resulting expression, the definition of the phase function for a fully illuminated spherical cap given in Eq. 3.34 is found.

D.3.2. VISIBLE SURFACE PREDOMINANTLY ILLUMINATED

In this case, the illuminated surface, A^*_{lit}, covers more than half – but not the entirety – of the total surface of the spherical cap, A^*. Therefore, the surface region A^*_{lit} is delimited by the edge of the spherical cap and the day-night terminator. Importantly, the region A^*_{lit} can be split into two subregions: one having a circular boundary and symmetric with respect to $\hat{\boldsymbol{r}}$, denoted by $A^*_{lit,1}$, and the remaining part of the spherical cap's surface, having a more complex boundary and denoted by $A^*_{lit,2}$, see Fig. D.2a. The phase function, Φ, can therefore be expressed as the sum of two components, Φ_1 and Φ_2, respectively. Each of these components is defined similarly to Eq. D.10 as:

$$\Phi_\diamondsuit = \frac{1}{2\pi(1-H)}\left[\cos\chi^* \boxed{A}_\diamondsuit + \sin\chi^* \boxed{B}_\diamondsuit\right] \tag{D.16}$$

where $\diamondsuit$ is a placeholder for either "1" or "2", and $\boxed{A}_\diamondsuit$ and $\boxed{B}_\diamondsuit$ represent the double integrals $\boxed{A}$ and $\boxed{B}$ from Eq. D.10, evaluated over the surface region $A^*_{lit,\diamondsuit}$.

As can be observed in Fig. D.2a, the region $A^*_{lit,1}$ is defined by the following domain boundaries:

$$\begin{cases} \gamma_0 &= 0 \\ \gamma_f &= \dfrac{\pi}{2} - \chi^* \\ \psi_0 &= 0 \\ \psi_f &= 2\pi \end{cases} \tag{D.17}$$

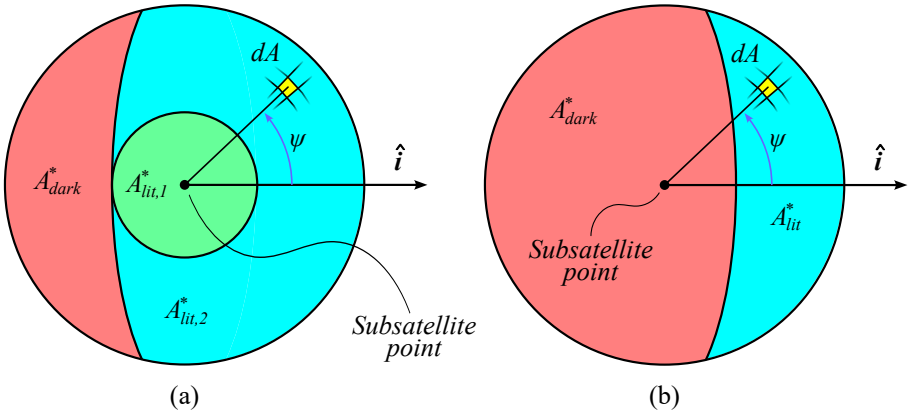


Figure D.2: Top view of the Earth's spherical cap when it is predominantly a) illuminated and b) in shadow.

As these domain boundaries do not depend on γ nor ψ, using them as integration limits allows to express the double integrals $\boxed{A}_1$ and $\boxed{B}_1$ as in the right-hand side of Eqs. D.12-D.13. Then, substituting the limits of integration in Eq. D.17, the solutions to these integrals can be computed similarly to Eqs. D.14-D.15:

$$\boxed{A}_1 = [\psi]_0^{2\pi}\left[-\frac{1}{2}\cos^2\gamma\right]_0^{\frac{\pi}{2}-\chi^*} = \pi\cos^2\chi^* \tag{D.18}$$

$$\boxed{B}_1 = [\sin\psi]_0^{2\pi}\left[\frac{1}{2}(\psi-\sin\psi\cos\psi)\right]_0^{\frac{\pi}{2}-\chi^*} = 0 \tag{D.19}$$

Then, substituting $\boxed{A}_1$ and $\boxed{B}_1$ into Eq. D.16, the component of the phase function relative to the surface region $A^*_{lit,1}$ is found:

$$\Phi_1 = \frac{1}{2}\frac{\cos^3\chi^*}{(1-H)} \tag{D.20}$$

The region $A^*_{lit,2}$, see Fig. D.2a, is defined by the following domain boundaries:

$$\begin{cases} \gamma_0 = \dfrac{\pi}{2}-\chi^* \\ \gamma_f = \gamma_m = \cos^{-1}H \\ \psi_0 = -\cos^{-1}\left(-\dfrac{\cos\chi^*\cos\gamma}{\sin\chi^*\sin\gamma}\right) = \cos^{-1}\left(\dfrac{\cos\chi^*\cos\gamma}{\sin\chi^*\sin\gamma}\right)-\pi \\ \psi_f = -\psi_0 = \cos^{-1}\left(-\dfrac{\cos\chi^*\cos\gamma}{\sin\chi^*\sin\gamma}\right) \end{cases} \tag{D.21}$$

where the definition of γ_m in Eq. D.1b was used. The domain boundaries ψ_0 and ψ_f are found from Eq. D.4 by imposing $\chi \leq \pi/2$, with $\chi = \pi/2$ identifying the day-night terminator

lying over the surface of the spherical cap. Also, it is of note that $\psi_f = -\psi_0$ because of the symmetry of the domain and integrands with respect to the $\hat{\boldsymbol{i}}$ axis. This symmetry allows to halve the domain of the double integrals $\boxed{A}_2$ and $\boxed{B}_2$ appearing in Eq. D.16 and defined in Eq. D.10 as follows:

$$\boxed{A}_2 = \int_{\gamma_0}^{\gamma_f} \cos\gamma \sin\gamma \left(\int_{-\psi_f}^{\psi_f} d\psi \right) d\gamma = 2 \int_{\gamma_0}^{\gamma_f} \cos\gamma \sin\gamma \left(\int_{0}^{\psi_f} d\psi \right) d\gamma \tag{D.22}$$

$$\boxed{B}_2 = \int_{\gamma_0}^{\gamma_f} \sin^2\gamma \left(\int_{-\psi_f}^{\psi_f} \cos\psi \; d\psi \right) d\gamma = 2 \int_{\gamma_0}^{\gamma_f} \sin^2\gamma \left(\int_{0}^{\psi_f} \cos\psi \; d\psi \right) d\gamma \tag{D.23}$$

Solving the integrals in Eqs. D.22 and D.23 with respect to ψ and substituting the limits of integration given in Eq. D.21 then yields:

$$\boxed{A}_2 = 2 \int_{\gamma_0}^{\gamma_f} \cos\gamma \sin\gamma \; \psi_f \; d\gamma = 2 \int_{\frac{\pi}{2}-\chi^*}^{\cos^{-1}H} \cos\gamma \sin\gamma \; \cos^{-1}\left(-\frac{\cos\chi^* \cos\gamma}{\sin\chi^* \sin\gamma} \right) d\gamma \tag{D.24}$$

$$\boxed{B}_2 = 2 \int_{\gamma_0}^{\gamma_f} \sin^2\gamma \; \sin\psi_f \; d\gamma = 2 \int_{\frac{\pi}{2}-\chi^*}^{\cos^{-1}H} \sin^2\gamma \sqrt{1 - \left(\frac{\cos\chi^* \cos\gamma}{\sin\chi^* \sin\gamma} \right)^2} \; d\gamma \tag{D.25}$$

Solving the integrals on the right-hand sides of Eqs. D.24 and D.25 results in:

$$\boxed{A}_2 = \left(1 - H^2\right) \cos^{-1}\left(-\frac{\cos\chi^*}{\sin\chi^*} \frac{H}{\sqrt{1-H^2}} \right) + \cos\chi^* \cos^{-1}\left(\frac{H}{\sin\chi^*} \right) - \pi \cos^2\chi^* \tag{D.26}$$

$$\boxed{B}_2 = \sin\chi^* \cos^{-1}\left(\frac{H}{\sin\chi^*} \right) - H\sqrt{1 - \frac{H^2}{\sin^2\chi^*}} \tag{D.27}$$

By substituting Eqs. D.26 and D.27 into Eq. D.16 and simplifying, the final expression for the component of the phase function relative to the surface region $A^*_{lit,2}$ is found:

$$\begin{aligned} \Phi_2 = \frac{1}{2\pi(1-H)} \Bigg[& \cos^{-1}\left(\frac{H}{\sin\chi^*} \right) - H\sqrt{\sin^2\chi^* - H^2} \\ & + \left(1 - H^2\right) \cos\chi^* \cos^{-1}\left(-\frac{\cos\chi^* \cos\gamma}{\sin\chi^* \sin\gamma} \right) - \pi \cos^3\chi^* \Bigg] \end{aligned} \tag{D.28}$$

Finally, summing Eqs. D.20 and D.28 yields the phase function for a predominantly illuminated spherical cap provided in Eq. 3.35.

D.3.3. VISIBLE SURFACE PREDOMINANTLY DARK

In this case, the illuminated surface, A^*_{lit}, covers less than half of the total surface of the spherical cap, A^*. The surface region A^*_{lit} is delimited by the edge of the spherical cap and the day-night terminator, see Fig. D.2b, corresponding to the following domain

boundaries:

$$\begin{cases} \gamma_0 = \chi^* - \dfrac{\pi}{2} \\ \gamma_f = \gamma_m = \cos^{-1} H \\ \psi_0 = -\cos^{-1}\left(-\dfrac{\cos\chi^*\cos\gamma}{\sin\chi^*\sin\gamma}\right) = \cos^{-1}\left(\dfrac{\cos\chi^*\cos\gamma}{\sin\chi^*\sin\gamma}\right) - \pi \\ \psi_f = -\psi_0 = \cos^{-1}\left(-\dfrac{\cos\chi^*\cos\gamma}{\sin\chi^*\sin\gamma}\right) \end{cases} \tag{D.29}$$

where, similar to Section D.3.2, the definition of γ_m in Eq. D.1b was used, and the domain boundaries ψ_0 and ψ_f were found from Eq. D.4 by imposing $\chi \leq \pi/2$. Note that the domain boundaries in Eq. D.29 are the same as those in Eq. D.21, with the exception of γ_0, which takes the opposite sign. Adopting an approach similar to that of Section D.3.2, the domain of A^*_{lit} can be halved by leveraging the symmetry of both the domain itself and the integrands in Eq. D.10 with respect to the $\hat{\boldsymbol{\imath}}$ axis. The double integrals $\boxed{A}$ and $\boxed{B}$ in Eq. D.10 can then be expressed as in the right-hand sides of Eqs. D.22 and D.23, respectively. Then, solving the integrals appearing on the right-hand side of Eqs. D.22 and D.23 with respect to ψ and substituting the limits of integration given in Eq. D.29 yields:

$$\boxed{A} = 2\int_{\gamma_0}^{\gamma_f} \cos\gamma\sin\gamma\,\psi_f\,d\gamma = 2\int_{\chi^*-\frac{\pi}{2}}^{\cos^{-1}H} \cos\gamma\sin\gamma\,\cos^{-1}\left(-\frac{\cos\chi^*\cos\gamma}{\sin\chi^*\sin\gamma}\right)d\gamma \tag{D.30}$$

$$\boxed{B} = 2\int_{\gamma_0}^{\gamma_f} \sin^2\gamma\,\sin\psi_f\,d\gamma = 2\int_{\chi^*-\frac{\pi}{2}}^{\cos^{-1}H} \sin^2\gamma\sqrt{1-\left(\frac{\cos\chi^*\cos\gamma}{\sin\chi^*\sin\gamma}\right)^2}\,d\gamma \tag{D.31}$$

Solving the integrals on the right-hand sides of Eqs. D.30 and D.31 results in:

$$\boxed{A} = \left(1-H^2\right)\cos^{-1}\left(-\frac{\cos\chi^*}{\sin\chi^*}\frac{H}{\sqrt{1-H^2}}\right) + \cos\chi^*\cos^{-1}\left(\frac{H}{\sin\chi^*}\right) = \boxed{A}_1 + \boxed{A}_2 \tag{D.32}$$

$$\boxed{B} = \sin\chi^*\cos^{-1}\left(\frac{H}{\sin\chi^*}\right) - H\sqrt{1-\frac{H^2}{\sin^2\chi^*}} = \boxed{B}_2 \tag{D.33}$$

where $\boxed{A}_1$, $\boxed{A}_2$, and $\boxed{B}_2$ are given in Eqs. D.18, D.26, and D.27, respectively. Finally, substituting Eqs. D.32 and D.33 into Eq. D.10 and simplifying yields the phase function for a predominantly dark spherical cap, whose expression coincides with that derived in Section D.3.2 for a predominantly illuminated cap. Therefore, the phase function for a predominantly dark spherical cap is also given by Eq. 3.35.

BIBLIOGRAPHY

[1] Konstantin E. Tsiolkovsky. “The Spread of Man in Space / Rasprostraneniye Cheloveka v Kosmose”. Archive of the Russian Academy of Sciences, Collection 555, Inventory 1, File 246 / Arkhiv Rossiyskoy Akademii Nauk, Fond 555, Opis’ 1, Delo 246. Sept. 1921. Digitally available (accessed on August 12, 2026).

[2] Colin R. McInnes. *Solar Sailing: Technology, Dynamics and Mission Applications*. Van Godewijckstraat 30, 3311 GX Dordrecht, The Netherlands: Springer Science & Business Media, 1999. ISBN: 978-1-4471-3992-8. DOI: https://doi.org/10.1007/978-1-4471-3992-8.

[3] Johannes Kepler. *Dissertatio cum Nuncio Sidereo*. Frankfurt am Main, Germany: Francofurti: Apud Zachariam Palthenium, 1611, p. 43. Digitally available (accessed on August 12, 2026).

[4] Johannes Kepler. *Astronomiae Pars Optica*. Frankfurt am Main, Germany: Francofurti: Apud Claudium Marnium & Hæredes Ioannis Aubrii, 1604. Chap. VI, IX, pp. 264, 324. Digitally available (accessed on August 12, 2026).

[5] William H. Donahue. *Johannes Kepler: Optics, Paralipomena to Witelo & Optical Part of Astronomy*. 1611 Camino Cruz Blanca, Santa Fe, New Mexico, 87501: Green Lion Press, 2000. ISBN: 978-1-888009-12-5. Digitally available (accessed on August 12, 2026).

[6] Johannes Kepler. *De Cometis Libelli Tres*. Augsburg, Germany: Andrea Apergeri, sumptibus Sebastiani Mylii Bibliopole Augustani, 1619. Digitally available (accessed on August 12, 2026).

[7] Jean le Rond d’Alembert. “Recherches sur la courbe que forme une corde tenduë mise en vibration”. In: *Histoire de l’Académie Royale des Sciences et Belles-Lettres* 3 (1746), pp. 214–219. Digitally available (accessed on August 12, 2026).

[8] Leonhard Euler. “Recherches Physiques sur la cause de la queüe des cometes, de la lumiere boreale, et de la lumiere zodiacale”. In: *Histoire de l’Académie Royale des Sciences et Belles-Lettres* 2 (1746), p. 121. Digitally available (accessed on August 12, 2026).

[9] Dortous de Mairan. *Traité Physique et Historique de l’Aurore Boréale*. Vol. 4. Galeries du Louvre, Paris, France: De l’Imprimerie Royale, 1754. Chap. Eclaircis VIII, pp. 357–358. Digitally available (accessed on August 12, 2026).

[10] Ernest Fox Nichols and Gordon Ferrie Hull. “The Pressure due to Radiation”. In: *Proceedings of the American Academy of Arts and Sciences*. Vol. 38. 20. 1903, pp. 559–599. DOI: https://doi.org/10.2307/20021808.

[11] Meghnad Saha and S. Chakraborty. “On the Pressure of Light”. In: *Journal of the Asiatic Society of Bengal* 14.425 (1918), pp. 6–9.

[12] Abraham Bennet. “A new Suspension of the Magnetic Needle, intended for the Discovery of minute Quantities of Magnetic Attraction also an Air Vane of great Sensibility; with new Experiments on the Magnetism of Iron Filings and Brass”. In: *Philosophical Transactions of the Royal Society of London* 82 (1792), pp. 81–98. DOI: https://doi.org/10.1098/rstl.1792.0008.

[13] Augustin-Jean Fresnel. “Note sur la Répulsion que des corps échauffés exercent les uns sur les autres à des distances sensibles”. In: *Annales de Chimie et de Physique* XXIX (1825), pp. 57–62. Digitally available (accessed on August 12, 2026).

[14] Augustin-Jean Fresnel. “Observation à ajouter à la Note sur les Répulsion des corps échauffés”. In: *Annales de Chimie et de Physique* XXIX (1825), pp. 107–108. Digitally available (accessed on August 12, 2026).

[15] James Clerk Maxwell. *A Treatise on Electricity and Magnetism*. Vol. 1. Great Clarendon Street, Oxford OX2 6DP, United Kingdom: Clarendon Press, 1873.

[16] Adolfo Bartoli. “Il Calorico Raggiante e il Secondo Principio di Termodinamica”. In: *Il Nuovo Cimento (1877-1894)* 15 (1884), pp. 193–202. DOI: https://doi.org/10.1007/BF02737234.

[17] Jules Verne. *De la Terre à la Lune*. 18, rue Jacob, Paris, France: Pierre-Jules Hetzel, 1865.

[18] Georges Le Faure and Henri de Graffigny. *Les Aventures Extraordinaires d’un Savant Russe, Vol. II: Le Soleil et les Petites Planètes*. Paris, France: Edinger, 1889.

[19] William Crookes. “On Attraction and Repulsion resulting from Radiation”. In: *Philosophical Transactions of the Royal Society of London* 164 (1874), pp. 501–527. DOI: https://doi.org/10.1098/rstl.1874.0015.

[20] Arthur Schuster. “On the Nature of the Force producing the Motion of a Body exposed to Rays of Heat and Light”. In: *Proceedings of the Royal Society of London* 24.164-170 (1876), pp. 391–392. DOI: https://doi.org/10.1098/rspl.1875.0052.

[21] Osborne Reynolds. “On certain Dimensional Properties of Matter in the Gaseous State”. In: *Philosophical Transactions of the Royal Society of London* 170 (1879), pp. 727–845. DOI: https://doi.org/10.1098/rstl.1879.0078.

[22] John Worrall. “The Pressure of Light: The Strange Case of the Vacillating ‘Crucial Experiment’”. In: *Studies in History and Philosophy of Science* 13.2 (1982), pp. 133–171. DOI: https://doi.org/10.1016/0039-3681(82)90023-1.

[23] Friedrich Zöllner. “Untersuchungen über die Bewegungen Strahlender und Bestrahlter Körper”. In: *Annalen der Physik und Chemie* CLX.160 (1877), pp. 154–169, 296–317, 459–466. Digitally available (accessed on August 12, 2026).

[24] Peter Lebedew. “Untersuchungen über die Druckkräfte des Lichtes”. In: *Annalen der Physik* 311.11 (1901), pp. 433–458. DOI: https://doi.org/10.1002/andp.19013111102.

[25] Mary Bell and S. E. Green. “On Radiometer Action and the Pressure of Radiation”. In: *Proceedings of the Physical Society* 45.2 (1933), pp. 320–357. DOI: https://doi.org/10.1088/0959-5309/45/2/315.

[26] Leo Graetz. “Radiometer”. In: *Handbuch der Physik* 2.2 (1896), pp. 262–264. Digitally available (accessed on August 12, 2026).

[27] V.N. Sokolsky. “The Life and Work of Konstantin E. Tsiolkovsky”. In: *K.E. Tsiolkovsky: Selected Works*. Institute of History of Science and Technology, Russian Academy of Sciences, 2006, pp. 305–331. Digitally available (accessed on August 12, 2026).

[28] Mgr. Urbanczyk. *Solar Sails – A Realistic Propulsion for Spacecraft*. Tech. rep. RSIC-694. Redstone Scientific Information Center, U.S. Army Missile Command, 1967. Digitally available (accessed on August 12, 2026).

[29] F. A. Tsander. *From a Scientific Heritage*. Tech. rep. TT F-541. NASA, 1969. Digitally available (accessed on August 12, 2026).

[30] F. A. Tsander. “The Use of Light Pressure for Flight in Interplanetary Space”. In: *Problems of Flight by Jet Propulsion*. Israel Program for Scientific Translations, 1924, pp. 303–321. Digitally available (accessed on August 12, 2026).

[31] John Burdon Sanderson Haldane. *The Last Judgment: A Scientist's Vision of the Future of Man*. 195 Broadway, New York, New York 10007, USA: Harper & Brothers, 1927. Digitally available (accessed on August 12, 2026).

[32] John Desmond Bernal. *The World, the Flesh and the Devil: An Enquiry into the Future of the Three Enemies of the Rational Soul*. Paternoster House, Charing Cross Road, London, England: Kegan Paul, Trench, Trubner & Co., Ltd., 1929. Digitally available (accessed on August 12, 2026).

[33] Olaf Stapledon. *Last and First Men*. 36 Essex Street, Strand, London, W.C.2., United Kingdom: Methuen & Co. Ltd., London, 1930. Digitally available (accessed on August 12, 2026).

[34] Carl Atwood Wiley (writing as Russell Saunders). “Clipper Ships of Space”. In: *Astounding Science Fiction* (May 1951), pp. 136–143. Digitally available (accessed on August 12, 2026).

[35] Richard L. Garwin. “Solar Sailing – A Practical Method of Propulsion Within the Solar System”. In: *Jet Propulsion* 28.123 (1958), pp. 188–190. Digitally available (accessed on August 12, 2026).

[36] Gregory L. Matloff. “Appendix: Photon Sail History, Engineering and Mission Analysis”. In: *Deep-Space Probes: To the Outer Solar System and Beyond*. Heidelberger Platz 3, 14197 Berlin, Germany: Springer Berlin Heidelberg, 2005, pp. 185–221. ISBN: 978-3-540-27340-0. DOI: https://doi.org/10.1007/3-540-27340-9_15.

[37] Malcolm Macdonald. “Solar Sailing: Applications and Technology Advancement”. In: *Advances in Spacecraft Technologies*. 32 London Bridge Street, London, Greater London, SE1 9SG, United Kingdom: InTechOpen, 2011. Chap. 2, pp. 35–60. ISBN: 978-953-307-551-8. DOI: https://doi.org/10.5772/13614.

[38] R. B. Powers and V. L. Coverstone. “Optimal Solar Sail Orbit Transfers to Synchronous Orbits”. In: *The Journal of the Astronautical Sciences* 49 (2001), pp. 269–281. DOI: https://doi.org/10.1007/BF03546322.

[39] Melvin Birnbaum. *Minimum Time Earth/Mars trajectory for a Solar Sail*. Tech. rep. GGC/EE/68-3 AD836734. Air Force Institute of Technology, 1968.

[40] Ralph Hoyt Bacon. "Logarithmic Spiral: An Ideal Trajectory for the Interplanetary Vehicle with Engines of Low Sustained Thrust". In: *American Journal of Physics* 27.3 (Mar. 1959), pp. 164–165. DOI: https://doi.org/10.1119/1.1934788.

[41] Theodore P. Cotter. *Solar Sailing*. Tech. rep. SCR-78. Sandia Corporation, Research Colloquium, Apr. 1959. Digitally available (accessed on August 12, 2026).

[42] T. C. Tsu. "Interplanetary Travel by Solar Sail". In: *American Rocket Society Journal* 29.6 (Oct. 1959), pp. 422–427. DOI: https://doi.org/10.2514/8.4791.

[43] Henry J. Kelley. "Gradient Theory of Optimal Flight Paths". In: *American Rocket Society Journal* 30.10 (1960), pp. 947–954. DOI: https://doi.org/10.2514/8.5282.

[44] H. S. London. "Some Exact Solutions of the Equations of Motion of a Solar Sail with a Constant Setting". In: *American Rocket Society Journal* 30.2 (Feb. 1960), pp. 198–200.

[45] Bruce Joel Gordon. "A Study of Interplanetary Travel by Solar Sail". MSc. thesis. Wright-Patterson Air Force Base, Ohio: Air Force University, USAF, Aug. 1961.

[46] Normal Sands. "Escape from Planetary Gravitational Fields by Use of Solar Sails". In: *American Rocket Society Journal* 31.4 (Apr. 1961), pp. 527–531. DOI: https://doi.org/10.2514/8.5547.

[47] William R. Fimple. "Generalized Three-Dimensional Trajectroy Analysis of Planetary Escape by Solar Sail". In: *American Rocket Society Journal* 32.6 (1962), pp. 883–887. DOI: https://doi.org/10.2514/8.6163.

[48] Carlos R. Cavoti. *Numerical Solutions on the Astronautical Problem of Thrust Vector Control for Optimum Solar Sail Transfer*. Tech. rep. paper number 2627-62. General Electric Co., Philadelphia, PA. Missile and Space Division, Nov. 1962, pp. 13–18. Digitally available (accessed on November 4, 2025).

[49] A. N. Zhukov and V. N. Lebedev. "Variational Problem of Transfer between Heliocentric Orbits by means of a Solar Sail". In: *Kosmicheskie Issledovaniya (Cosmic Research)* 2 (Jan. 1964), pp. 45–50.

[50] Philip C. Norem. "Interstellar Travel: A Round Trip Propulsion System with Relativistic Velocity Capabilities". In: *Proceedings of the American Astronautical Society (AAS) Conference*. 69-388. June 1969.

[51] Mike E. Lippman. *In-space Fabrication of Thin-film Structures*. Tech. rep. NASA CR-1969. Astro Research Corporation, Feb. 1972. Digitally available (accessed on August 12, 2026).

[52] Peter R. Preiswerk and Mike E. Lippman. *Physical Properties of Thin Films*. Tech. rep. NASA CR-1972. Astro Research Corporation, Feb. 1972. Digitally available (accessed on August 12, 2026).

[53] Peter R. Preiswerk and Mike E. Lippman. *Fabrication of Carbon Film Composites for High-strength Structures*. Tech. rep. CR-4972. NASA, Aug. 1972. Digitally available (accessed on August 12, 2026).

[54] Theodore P. Cotter. *An Encomium on Solar Sailing*. Tech. rep. LA-5231-MS. Los Alamos Scientific Laboratory, University of California, 1973. Digitally available (accessed on August 12, 2026).

[55] L. K. Grinevitskaia and E. N. Polyakhova. *Postroenie Priblizhennogo Resheniya Uravnenii Geotsentricheskogo Dvizheniya Kosmicheskogo Apparata s Solnechnym Parusom (Derivation of an Approximate Solution to the Equation of Geocentric Motion of a Space Vehicle with a Solar Sail)*. Vol. 7. Series 1: Mathematics, Mechanics, Astronomy. 6th Line V.O., 11, Saint Petersburg, 199004, Russia: Vestnik Leningradskogo Universiteta (Vestnik Leningrad University), 1973, pp. 134–143.

[56] Richard H. MacNeal. *The Heliogyro: An Interplanetary Flying Machine*. Tech. rep. NASA ARC-R-249. Astro Research Corporation, Mar. 1967. Digitally available (accessed on August 12, 2026).

[57] John M. Hedgepeth and Max D. Benton. *Analysis of Planetary Flyby using the Heliogyro Solar Sailer*. Tech. rep. NASA ARC-R-296. Astro Research Corporation, Aug. 1968. Digitally available (accessed on August 12, 2026).

[58] Richard H. MacNeal, John M. Hedgepeth, and Hans U. Schuerch. *Heliogyro Solar Sailer: Summary Report*. Tech. rep. NASA CR-1329. Astro Research Corporation, June 1969. Digitally available (accessed on August 12, 2026).

[59] Richard H. MacNeal. *Structural Dynamics of the Heliogyro*. Tech. rep. NASA CR-1745. MacNeal-Schwendler Corporation, May 1971. Digitally available (accessed on August 12, 2026).

[60] Jerome L. Wright. *Solar Sailing: Evaluation of Concept and Potential*. Tech. rep. BMI-NLVP-TM-74-3. Battelle Memorial Institute, Nov. 1974.

[61] Chauncy W. Uphoff. *Solar Sailing: Potential for Future Missions*. Tech. rep. 760-164. NASA Jet Propulsion Laboratory, Jan. 1977.

[62] Jerome L. Wright and Janice M. Warmke. "Solar Sail Mission Applications". In: *Astrodynamics Conference*. 76-808. Aug. 1976. DOI: https://doi.org/10.2514/6.1976-808.

[63] L. Friedman et al. "Solar Sailing - The Concept Made Realistic". In: *16th Aerospace Sciences Meeting*. AIAA-78-82. Jan. 1978. DOI: https://doi.org/10.2514/6.1978-82.

[64] John M. Logsdon. "Missing Halley's Comet: The Politics of Big Science". In: *Isis* 80.2 (1989), pp. 254–280. DOI: https://doi.org/10.1086/355011.

[65] Guy Pignolet. "Making the High Frontier Highly Visible with a Solar Sail Race to the Moon". In: *Advances in Astronautical Sciences* 53 (1983), pp. 249–257.

[66] Jean-Yves Prado, Alain Perret, and Ignazio Ozcariz. "Solar Sail on the Track". In: *Acta Astronautica* 24 (1991), pp. 309–313. DOI: https://doi.org/10.1016/0094-5765(91)90179-9.

[67] Koryo Miura, Jean-Yves Prado, and R. Staehle. "Report on SSU, U3P and Foundation Solar Sail Activities for the Earth-Moon Race". In: *42nd International Astronautical Congress (IAC) Proceedings*. IAF 91-513. International Astronautical Federation (IAF). Oct. 1991.

[68] Klaus P. Heiss. “The Columbus 500 Space Sail Cup: Sails of Exploration”. 2004. Unpublished memoir.

[69] Marco C. Bernasconi and Arthur R. Woods. “Lights in the Sky: Membrane Structures for Art in Space”. In: *International Conference on Textile Composites and Inflatable Structures*. 2009. Digitally available (accessed on August 12, 2026).

[70] Elena Nikolaevna Polyakhova. *Kosmicheskiy Polet Solnechnym Parusom: Problemy i Perspektivy (Space Flight Using a Solar Sail – The Problems and Prospects)*. Shubinskiy Lane, 6, Building 1, Moscow 121099, Russia: Nauka, Russia, 1986.

[71] Louis Friedman. *Starsailing: Solar Sails and Interstellar Travel*. 111 River Street Hoboken, New Jersey 07030, USA: Wiley, 1988. ISBN: 978-0-471-62593-3. Digitally available (accessed on August 12, 2026).

[72] Eugene E. Mallove and Gregory L. Matloff. *The Starflight Handbook: A Pioneer's Guide to Interstellar Travel*. 111 River Street Hoboken, New Jersey 07030, USA: Wiley, 1989. ISBN: 978-0-471-61912-3.

[73] Jerome L. Wright. *Space Sailing*. 38 Langham Street, London W1W 7AR, United Kingdom: Gordon and Breach Science Publishers, 1992. ISBN: 978-2-88124-842-9. Digitally available (accessed on August 12, 2026).

[74] V. A. Koshelev and V. M. Melnikov. *Large Space Structures Formed by Centrifugal Forces*. 1st. 5 Howick Place, 2nd Floor, London, SW1P 1WG, United Kingdom: CRC Press, 1998. ISBN: 978-1-003-07820-3. DOI: https://doi.org/10.1201/9781003078203.

[75] L. Herbeck et al. “Development and Test of Deployable Ultra-lightweight CFRP-booms for a Solar Sail”. In: *Spacecraft Structures, Materials and Mechanical Testing* 468 (2001), pp. 107–112.

[76] M. Leipold et al. “Solar Sail Technology Development and Demonstration”. In: *Acta Astronautica* 52.2 (2003). Selected Proceedings of the 4th IAA International Conference on Low Cost Planetary Missions, pp. 317–326. DOI: https://doi.org/10.1016/S0094-5765(02)00171-6.

[77] Roy Young, Edward Montgomery, and Charles Adams. “TRL Assessment of Solar Sail Technology Development following the 20-meter System Ground Demonstrator Hardware Testing”. In: *48th AIAA/ASME/ASCE/AHS/ASC Structures, Structural Dynamics, and Materials Conference*. Apr. 2007, p. 2248. DOI: https://doi.org/10.2514/6.2007-2248.

[78] David M. Murphy, Brian Macy, and James Gaspar. “Demonstration of a 10-m Solar Sail System”. In: *40th Joint Propulsion Conference*. 200-1576. July 2004. Digitally available (accessed on August 12, 2026).

[79] Greg Laue, David Case, and Jim Moore. “Fabrication and Deployment Testing of Solar Sail Quadrants for a 20-meter Solar Sail Ground Test System Demonstration”. In: *41st AIAA/ASME/SAE/ASEE Joint Propulsion Conference & Exhibit*. 3930. July 2005. DOI: https://doi.org/10.2514/6.2005-3930.

[80] David M. Murphy et al. “Demonstration of a 20-m Solar Sail System”. In: *46th AIAA/ASME/ASCE/AHS/ASC Structures, Structural Dynamics and Materials Conference*. 2126. 2005. DOI: https://doi.org/10.2514/6.2005-2126.

[81] Jim L. Gaspar et al. “Testing of a 20-meter Solar Sail System”. In: *Spacecraft Propulsion Subcommittee Joint Meeting*. 2005. Digitally available (accessed on August 12, 2026).

[82] David M. Murphy. “Validation of a Scalable Solar Sailcraft System”. In: *Journal of Spacecraft and Rockets* 44.4 (July 2007), pp. 797–808. DOI: ttps://doi.org/10.2514/1.23024.

[83] David Lichodziejewski et al. “Bringing an Effective Solar Sail Design to TRL 6”. In: *39th AIAA/ASME/SAE/ASEE Joint Propulsion Conference and Exhibit*. 4659. July 2003. DOI: https://doi.org/10.2514/6.2003-4659.

[84] David Lichodziejewski et al. “Vacuum Deployment And Testing Of a 4-Quadrant Scalable Inflatable Rigidizable Solar Sail System”. In: *46th AIAA/ASME/ASCE/AHS/ASC Structures, Structural Dynamics and Materials Conference*. 2122. Apr. 2005. DOI: https://doi.org/10.2514/6.2005-2122.

[85] David Sleight et al. “Structural Analysis and Test Comparison of a 20-meter Inflation-Deployed Solar Sail”. In: *47th AIAA/ASME/ASCE/AHS/ASC Structures, Structural Dynamics, and Materials Conference*. 1706. May 2006. DOI: https://doi.org/10.2514/6.2006-1706.

[86] Troy Mann et al. “Ground Testing a 20-meter Inflation Deployed Solar Sail”. In: *47th AIAA/ASME/ASCE/AHS/ASC Structures, Structural Dynamics, and Materials Conference*. 1707. May 2006. DOI: https://doi.org/10.2514/6.2006-1707.

[87] David Lichodziejewski et al. “Vaccum Deployment and Testing of a 20M Solar Sail System”. In: *47th AIAA/ASME/ASCE/AHS/ASC Structures, Structural Dynamics, and Materials Conference*. 1705. May 2006. DOI: https://doi.org/10.2514/6.2006-1705.

[88] Louis Friedman. *Human Spaceflight: from Mars to the Stars*. 1510 East University Boulevard, Tucson, Arizona 85721, USA: University of Arizona Press, 2015. ISBN: 978-0-8165-3146-2.

[89] Osamu Mori et al. “First Solar Power Sail Demonstration by IKAROS”. In: *Transactions of the Japan Society for Aeronautical and Space Sciences (JSASS), Aerospace Technology Japan* 8.ists27 (2010), pp. 4.25–4.31. DOI: https://doi.org/10.2322/tastj.8.To_4_25.

[90] Osamu Mori et al. “Overview of IKAROS Mission”. In: *Advances in Solar Sailing*. Ed. by Malcolm Macdonald. Heidelberger Platz 3, D-14197 Berlin, Germany: Springer Berlin Heidelberg, 2014. Chap. 1, pp. 25–43. ISBN: 978-3-642-34907-2. DOI: https://doi.org/10.1007/978-3-642-34907-2_3.

[91] Yuichi Tsuda et al. “Achievement of IKAROS – Japanese Deep Space Solar Sail Demonstration Mission”. In: *Acta Astronautica* 82.2 (2013), pp. 183–188. ISSN: 0094-5765. DOI: https://doi.org/10.1016/j.actaastro.2012.03.032.

[92] Hirotaka Sawada et al. “Deployable Camera (DCAM3) System for Observation of Hayabusa2 Impact Experiment”. In: *Space Science Reviews* 208.1–4 (Feb. 2017), pp. 143–164. DOI: https://doi.org/10.1007/s11214-017-0337-9.

[93] AKATSUKI Special Site. *Mission Photo, Movie*. Japan Aerospace Exploration Agency (JAXA). URL: https://www.jaxa.jp/countdown/f17/live/missionphoto_e.html. Accessed on January 24, 2026.

[94] “The 3-step DLR–ESA Gossamer Road to Solar Sailing”. In: *Advances in Space Research* 48.11 (Sept. 2011), pp. 1695–1701. DOI: https://doi.org/10.1016/j.asr.2010.09.016.

[95] Marco Straubel et al. “The Design and Test of the GOSSAMER-1 Boom Deployment Mechanisms Engineering Model”. In: *Proceedings of the 2nd AIAA Spacecraft Structures Conference*. American Institute of Aeronautics and Astronautics (AIAA), Jan. 2015. DOI: https://doi.org/10.2514/6.2015-1837.

[96] Tom Spröwitz et al. “Design of the Gossamer-1 Deployment Demonstrator”. In: *Proceedings of the 4th International Symposium on Solar Sailing*. 2017. Digitally available (accessed on August 12, 2026).

[97] Patric Seefeldt et al. “Gossamer-1: Mission Concept and Technology for a Controlled Deployment of Gossamer Spacecraft”. In: *Advances in Space Research* 59.1 (Jan. 2017), pp. 434–456. DOI: https://doi.org/10.1016/j.asr.2016.09.022.

[98] Tom Spröwitz et al. “Membrane Deployment Technology Development at DLR for Solar Sails and Large-Scale Photovoltaics”. In: *Proceedings of 2019 IEEE Aerospace Conference*. 2019, pp. 1–20. DOI: https://doi.org/10.1109/AERO.2019.8741630.

[99] Mark Whorton et al. “Nanosail-D: The First Flight Demonstration of Solar Sails for Nanosatellites”. In: *22nd Annual AIAA/USU Conference on Small Satellites*. SSC08-X-1. 2008. Digitally available (accessed on August 12, 2026).

[100] Les Johnson et al. “NanoSail-D: A Solar Sail Demonstration Mission”. In: *Acta Astronautica* 68.5 (2011), pp. 571–575. DOI: https://doi.org/10.1016/j.actaastro.2010.02.008.

[101] Dean Alhorn et al. “Nanosail-D: The Small Satellite That Could!” In: *25th Annual AIAA/USU Conference on Small Satellites*. SSC11-VI-1. 2011. Digitally available (accessed on August 12, 2026).

[102] Chelsea Katan. “NASA’s Next Solar Sail: Lessons Learned from NanoSail-D2”. In: *26th Annual AIAA/USU Conference on Small Satellites*. M12-1762. 2012. Digitally available (accessed on August 12, 2026).

[103] Giovanni Vulpetti, Les Johnson, and Gregory L. Matloff. “The NanoSail-D2 NASA Mission”. In: *Solar Sails: A Novel Approach to Interplanetary Travel*. One New York Plaza, Suite 4600, New York, New York 10004-1562, USA: Springer New York, Sept. 2014. Chap. IV “Breakthroughs in Space”, pp. 173–178. ISBN: 978-1-4939-0941-4. DOI: https://doi.org/10.1007/978-1-4939-0941-4_16.

[104] Arthur Charles Clarke. “Sunjammer”. In: *Boys’ Life* (Mar. 1964). Digitally available (accessed on August 12, 2026).

[105] Nathan C. Barnes et al. “Sunjammer: A Solar Sail Demonstration”. In: *Advances in Solar Sailing*. Ed. by Malcolm Macdonald. Berlin, Heidelberg: Springer, 2014. Chap. I, pp. 115–126. ISBN: 978-3-642-34907-2. DOI: https://doi.org/10.1007/978-3-642-34907-2_8.

[106] Jeannette Heiligers et al. “Sunjammer: Preliminary End-to-End Mission Design”. In: *AIAA/AAS Astrodynamics Specialist Conference*. San Diego, California, USA, Aug. 2014. DOI: https://doi.org/10.2514/6.2014-4127.

[107] David A. Spencer, Les Johnson, and Alexandra C. Long. “Solar Sailing Technology Challenges”. In: *Aerospace Science and Technology* 93 (2019), p.105276. DOI: https://doi.org/10.1016/j.ast.2019.07.009.

[108] Rex W. Ridenoure et al. “Testing the Lightsail Program: Advancing Solar Sailing Technology using a Cubesat Platform”. In: *Journal of Small Satellites* 5.2 (2016), pp. 531–550. Digitally available (accessed on August 12, 2026).

[109] Bruce Betts et al. “Lightsail 1 Mission Results and Public Outreach Strategies”. In: *The 4th International Symposium on Solar Sailing, Kyoto Research Park, Kyoto, Japan*. 2017, pp. 17–20. Digitally available (accessed on August 12, 2026).

[110] David A. Spencer et al. “The LightSail 2 Solar Sailing Technology Demonstration”. In: *Advances in Space Research* 67.9 (2021), pp. 2878–2889. DOI: https://doi.org/10.1016/j.asr.2020.06.029.

[111] Justin R. Mansell et al. “LightSail 2 Solar Sail Control and Orbit Evolution”. In: *Aerospace* 10.579 (7 2023). DOI: https://doi.org/10.3390/aerospace10070579.

[112] Bruce Betts. *LightSail 2 Image-Based Engineering Assessment*. Presentation at the 6th International Symposium on Space Sailing. New York City College of Technology, New York, USA, June 2023. Digitally available (accessed on August 12, 2026).

[113] The Bruce Murray Space Image Library. *LightSail 2 High-Resolution Deployment Sequence, Camera 2*. The Planetary Society. URL: https://www.planetary.org/space-images/lightsail-2-high-res-deploy-cam-2. Accessed on January 29, 2026.

[114] Vaios Lappas et al. “CubeSail: A Low-cost CubeSat-based Solar Sail Demonstration Mission”. In: *Advances in Space Research* 48.11 (2011), pp. 1890–1901. DOI: https://doi.org/10.1016/j.asr.2011.05.033.

[115] V. Lappas et al. “DEORBITSAIL: De-orbiting of Satellites Using Solar Sails”. In: *2011 2nd International Conference on Space Technology*. IEEE, Sept. 2011, pp. 1–3. DOI: https://doi.org/10.1109/icspt.2011.6064667.

[116] Olive R. Stohlman and Vaios Lappas. “Deorbitsail: a Deployable Sail for De-orbiting”. In: *54th AIAA/ASME/ASCE/AHS/ASC Structures, Structural Dynamics, and Materials Conference*. American Institute of Aeronautics and Astronautics (AIAA), Apr. 2013. DOI: https://doi.org/10.2514/6.2013-1806.

[117] Olive R. Stohlman and Vaios Lappas. “Development of the Deorbitsail Flight Model”. In: *Spacecraft Structures Conference*. American Institute of Aeronautics and Astronautics (AIAA), Jan. 2014. DOI: https://doi.org/10.2514/6.2014-1509.

[118] Andrew Pukniel et al. “The Dynamics and Control of the CubeSail Mission: A Solar Sailing Demonstration”. In: *Advances in Space Research* 48.11 (2011), pp. 1902–1910. DOI: https://doi.org/10.1016/j.asr.2011.07.014.

[119] Rodney Burton et al. “UltraSail – Ultra-Lightweight Solar Sail Concept”. In: *41st AIAA/ASME/SAE/ASEE Joint Propulsion Conference & Exhibit*. DOI: https://doi.org/10.2514/6.2005-4117.

[120] Rodney Burton et al. “Initial Development of the CubeSail/Ultrasail Spacecraft”. In: *Joint Army Navy NASA Air Force (JANNAF) Spacecraft Propulsion Subcommittee Meeting*. 2010. Digitally available (accessed on August 12, 2026).

[121] Tiffany Russell Lockett et al. “Near-Earth Asteroid Scout Flight Mission”. In: *IEEE Aerospace and Electronic Systems Magazine* 35.3 (2020), pp. 20–29. DOI: https://doi.org/10.1109/MAES.2019.2958729.

[122] Les Johnson et al. “Near Earth Asteroid Scout – Mission Update”. In: *36th Annual Small Satellite Conference*. 2022. Digitally available (accessed on August 12, 2026).

[123] Gregory Lantoine et al. “Trajectory & Maneuver Design of the NEA Scout Solar Sail Mission”. In: *Acta Astronautica* 225 (2024), pp. 77–98. DOI: https://doi.org/10.1016/j.actaastro.2024.08.039.

[124] Elena Ancona and Roman Ya. Kezerashvili. “Recent Advances in Space Sailing Missions and Technology: Review of the 6th International Symposium on Space Sailing (ISSS 2023)”. In: *Aeronautics and Aerospace Open Access Journal* 9.1 (2025), pp. 62–73. DOI: https://doi.org/10.15406/aaoaj.2025.09.00221.

[125] Andrew Nutter. *Objectives, Design, and Initial Test Results of the Upcoming GAMA-Beta Solar Sail In-Orbit Demonstration*. Presentation at the 6th International Symposium on Space Sailing. New York City College of Technology, New York, USA, June 2023. Digitally available (accessed on August 12, 2026).

[126] Andrew Nutter. *Gama: Status Update*. Presentation at the 7th International Symposium on Space Sailing. Delft University of Technology, Delft, The Netherlands, July 2025.

[127] William Keats Wilkie. “Overview of the NASA Advanced Composite Solar Sail System (ACS3) Technology Demonstration Project”. In: *AIAA SciTech 2021 Forum*. 2021, p. 1260. Digitally available (accessed on August 12, 2026).

[128] William Keats Wilkie and Johnny Fernandez. *Advanced Composite Solar Sail System (ACS3) Mission Update*. Presentation at the 6th International Symposium on Space Sailing. New York City College of Technology, New York, USA, June 2023. Digitally available (accessed on August 12, 2026).

[129] William Keats Wilkie et al. *Lessons Learned from the Advanced Composite Solar Sail System (ACS3) Mission – Volume I*. Keynote presentation at the 7th International Symposium on Space Sailing. Delft University of Technology, Delft, The Netherlands, June 2025.

[130] NASA. *NASA’s ACS3 Satellite, Built by NanoAvionics, Successfully Deploys Solar Sail*. NanoAvionics. URL: https://nanoavionics.com/news/nasas-acs3-satellite-built-by-nanoavionics-successfully-deploys-solar-sail/. Accessed on February 3, 2026.

[131] Maximilien Berthet et al. “Space Sails for Achieving Major Space Exploration Goals: Historical Review and Future Outlook”. In: *Progress in Aerospace Sciences* 150 (Oct. 2024), p. 101047. DOI: https://doi.org/10.1016/j.paerosci.2024.101047.

[132] Tony Reichhardt. “Setting Sail for History”. In: *Nature* 433.7027 (Feb. 2005), pp. 678–679. DOI: https://doi.org/10.1038/433678a.

[133] V. Lappas et al. “Demonstrator Flight Missions at the Surrey Space Centre Involving Gossamer Sails”. In: *Advances in Solar Sailing*. Heidelberger Platz 3, 14197 Berlin, Germany: Springer Berlin Heidelberg, 2014. Chap. I, pp. 153–167. ISBN: 978-3-642-34907-2. DOI: https://doi.org/10.1007/978-3-642-34907-2_11.

[134] Wolfgang Seboldt and Bernd Dachwald. “Solar Sails for Near-Term Advanced Scientific Deep Space Missions”. In: *Rocket Propulsion: Present and Future (Edited Proceedings of the 8th International Workshop on Combustion and Propulsion)*. Ed. by Luigi T. De Luca. Milano, Italy: Politecnico di Milano, 2003. Digitally available (accessed on August 12, 2026).

[135] Wolfgang Seboldt. “Solar Spacecraft of First Generation”. In: *54th International Astronautical Congress of the International Astronautical Federation, the International Academy of Astronautics, and the International Institute of Space Law*. American Institute of Aeronautics and Astronautics (AIAA), Sept. 2003. DOI: https://doi.org/10.2514/6.IAC-03-S.6.03.

[136] Les Johnson et al. “Status of Solar Sail Technology Within NASA”. In: *2nd International Symposium on Solar Sailing (ISSS 2010)*. New York, New York, USA, July 2010. Digitally available (accessed on August 12, 2026).

[137] Amir Alexander and Louis D. Friedman. *The Planetary Report – Cosmos 1: Our Solar Sail*. Ed. by Charlene M. Anderson. 65 North Catalina Avenue, Pasadena, California, USA, Nov. 2004. Digitally available (accessed on August 12, 2026).

[138] Martin E. Zander et al. “Mechanical Testing of Deployable Thin Shell CFRP Booms in Ideal and Realistic Interfaces for the Solar Sail Demonstrator Gossamer-1”. In: *14th European Conference on Spacecraft Structures, Materials and Environmental Testing (ECSSMET) 2016*. Toulouse, France, Sept. 2016. Digitally available (accessed on November 24, 2025).

[139] Alexander R. Sobey and Tiffany Russell Lockett. “Design and Development of NEA Scout Solar Sail Deployer Mechanism”. In: *43rd Aerospace Mechanisms Symposium*. Moffett Field, California, USA, May 2016. Digitally available (accessed on August 12, 2026).

[140] National Aeronautics and Space Administration. *NASA Facts – NanoSail-D*. Tech. rep. FS-2010-09-150-MSFC 8-479695. Huntsville, Alabama, USA: George C. Marshall Space Flight Center, Sept. 2010. Digitally available (accessed on August 12, 2026).

[141] Rikio YOKOTA, Masahiko MIYAUCHI, and Yuichi ISHIDA. “Novel Asymmetric Aromatic Polyimide Having Excellent Space Environmental Stability and Application for Solar Sail “IKAROS” Membrane”. In: *International Journal of the Society of Materials Engineering for Resources* 20.1 (2014), pp. 65–70. DOI: https://doi.org/10.5188/ijsmer.20.65.

[142] Jin Ho Kang et al. “Durability Characterization of Mechanical Interfaces in Solar Sail Membrane Structures”. In: *Advances in Space Research* 67.9 (May 2021), pp. 2643–2654. DOI: https://doi.org/10.1016/j.asr.2020.08.015.

[143] Robert G. Bryant et al. “Selection and Manufacturing of Membrane Materials for Solar Sails”. In: *Advances in Solar Sailing*. Heidelberger Platz 3, 14197 Berlin, Germany: Springer Berlin Heidelberg, 2014. Chap. III, pp. 525–540. ISBN: 978-3-642-34907-2. DOI: https://doi.org/10.1007/978-3-642-34907-2_33.

[144] Eve Wooldridge et al. “Effects of Manufacturing and Deployment on Thin Films for the NGST Sunshade”. In: *19th AIAA Applied Aerodynamics Conference*. American Institute of Aeronautics and Astronautics (AIAA), June 2001. DOI: https://doi.org/10.2514/6.2001-1349.

[145] Shengping Gong and Malcolm Macdonald. “Review on Solar Sail Technology”. In: *Astrodynamics* 3.2 (Mar. 2019), pp. 93–125. DOI: https://doi.org/10.1007/s42064-019-0038-x.

[146] Pengyuan Zhao, Chenchen Wu, and Yangmin Li. “Design and Application of Solar Sailing: A Review on Key Technologies”. In: *Chinese Journal of Aeronautics* 36.5 (2023), pp. 125–144. DOI: https://doi.org/10.1016/j.cja.2022.11.002.

[147] Colin R. McInnes. “Near-term, Low Cost Missions for Solar Sails”. In: *Journal of the British Interplanetary Society* 53 (2000), pp. 48–61. Digitally available (accessed on August 12, 2026).

[148] Gareth W. Hughes et al. “Sample Return from Mercury and Other Terrestrial Planets Using Solar Sail Propulsion”. In: *Journal of Spacecraft and Rockets* 43.4 (July 2006), pp. 828–835. DOI: https://doi.org/10.2514/1.15889.

[149] Pamela Anderson, Malcolm Macdonald, and Chen-wan Yen. “Novel Orbits of Mercury, Venus and Mars Enabled Using Low-thrust Propulsion”. In: *Acta Astronautica* 94.2 (Feb. 2014), pp. 634–645. DOI: https://doi.org/10.1016/j.actaastro.2013.08.018.

[150] Merel Vergaaij and Jeannette Heiligers. “Time-optimal Solar Sail Heteroclinic-like Connections for an Earth-Mars Cycler”. In: *Acta Astronautica* 152 (Nov. 2018), pp. 474–485. DOI: https://doi.org/10.1016/j.actaastro.2018.08.008.

[151] Mehmet Eşit, Leticia Barros, and Koju Hiraki. “Comparative Study on Trajectory Optimization for Solar Sail Mercury Mission”. In: *34th International Symposium on Space Technology and Science*. June 2023. Digitally available (accessed on May 14, 2026).

[152] Dan Thomas et al. “Solar Polar Imager Concept”. In: *ASCEND 2020*. American Institute of Aeronautics and Astronautics (AIAA), Nov. 2020. DOI: https://doi.org/10.2514/6.2020-4060.

[153] Bernd Dachwald, Andreas Ohndorf, and Bong Wie. “Solar Sail Trajectory Optimization for the Solar Polar Imager (SPI) Mission”. In: *AIAA/AAS Astrodynamics Specialist Conference and Exhibit*. Keystone, Colorado, USA: American Institute of Aeronautics and Astronautics (AIAA), June 2006. DOI: https://doi.org/10.2514/6.2006-6177.

[154] Bernd Dachwald. "Optimal Solar Sail Trajectories for Missions to the Outer Solar System". In: *Journal of Guidance, Control, and Dynamics* 28.6 (2005), pp. 1187–1193. DOI: https://doi.org/10.2514/1.13301.

[155] Malcolm Macdonald, Colin McInnes, and Gareth Hughes. "Technology Requirements of Exploration Beyond Neptune by Solar Sail Propulsion". In: *Journal of Spacecraft and Rockets* 47.3 (May 2010), pp. 472–483. DOI: https://doi.org/10.2514/1.46657.

[156] Deepti N. Sharma and D. J. Scheeres. "Solar System Escape Trajectories Using Solar Sails". In: *Journal of Spacecraft and Rockets* 41.4 (July 2004), pp. 684–687. DOI: https://doi.org/10.2514/1.2354.

[157] M. Leipold et al. "Heliopause Explorer – A Sailcraft Mission to the Outer Boundaries of the Solar System". In: *Acta Astronautica* 59.8–11 (Oct. 2006), pp. 785–796. DOI: https://doi.org/10.1016/j.actaastro.2005.07.024.

[158] Giovanni Vulpetti. "Sailcraft at High Speed by Orbital Angular Momentum Reversal". In: *Acta Astronautica* 40.10 (May 1997), pp. 733–758. DOI: https://doi.org/10.1016/s0094-5765(97)00153-7.

[159] Carl Sauer. "Solar Sail Trajectories for Solar Polar and Interstellar Probe Missions". In: *AIAA/AAS Astrodynamics Specialist Conference*. JPL Open Repository, Aug. 1999. Digitally available (accessed on December 3, 2025).

[160] Giovanni Mengali et al. "H2-reversal Trajectory: A New Mission Application for High-performance Solar Sails". In: *Advances in Space Research* 48.11 (Dec. 2011), pp. 1763–1777. DOI: https://doi.org/10.1016/j.asr.2010.11.037.

[161] Jeannette Heiligers, Merel Vergaaij, and Matteo Ceriotti. "End-to-end Trajectory Design for a Solar-sail-only Pole-sitter at Venus, Earth, and Mars". In: *Advances in Space Research* 67.9 (May 2021), pp. 2995–3011. DOI: https://doi.org/10.1016/j.asr.2020.06.011.

[162] Jeannette Heiligers et al. "Design of Optimal Earth Pole-sitter Transfers Using Low-thrust Propulsion". In: *Acta Astronautica* 79 (Oct. 2012), pp. 253–268. DOI: https://doi.org/10.1016/j.actaastro.2012.04.025.

[163] Jeannette Heiligers et al. "Mission Analysis and Systems Design of a Near-term and Far-term Pole-sitter Mission". In: *Acta Astronautica* 94.1 (Jan. 2014), pp. 455–469. DOI: https://doi.org/10.1016/j.actaastro.2012.12.015.

[164] Colin R McInnes. "Solar Sail Mission Applications for Non-Keplerian Orbits". In: *Acta Astronautica* 45.4–9 (Aug. 1999), pp. 567–575. DOI: https://doi.org/10.1016/s0094-5765(99)00177-0.

[165] John L. West. "The Geostorm Warning Mission: Enhanced Opportunities based on New Technology". In: *14th AAS/AIAA Space Flight Mechanics Conference*. Maui, Hawaii, USA: JPL Open Repository, Feb. 2004. Digitally available (accessed on December 3, 2025).

[166] Jeannette Heiligers and Colin R. McInnes. "Solar Sail Heliocentric Earth-Following Orbits". In: *Journal of Guidance, Control, and Dynamics* 38.5 (May 2015), pp. 937–944. DOI: https://doi.org/10.2514/1.G000579.

[167] Hexi Baoyin and Colin R. McInnes. “Solar Sail Orbits at Artificial Sun-Earth Libration Points”. In: *Journal of Guidance, Control, and Dynamics* 28.6 (Nov. 2005), pp. 1328–1331. DOI: https://doi.org/10.2514/1.14598.

[168] Hexi Baoyin and Colin R. McInnes. “Solar Sail Equilibria in the Elliptical Restricted Three-Body Problem”. In: *Journal of Guidance, Control, and Dynamics* 29.3 (May 2006), pp. 538–543. DOI: https://doi.org/10.2514/1.15596.

[169] Thomas J. Waters and Colin R. McInnes. “Periodic Orbits Above the Ecliptic in the Solar-Sail Restricted Three-Body Problem”. In: *Journal of Guidance, Control, and Dynamics* 30.3 (May 2007), pp. 687–693. DOI: https://doi.org/10.2514/1.26232.

[170] Ariadna Farrés and Àngel Jorba. “Periodic and Quasi-periodic Motions of a Solar Sail Close to SL 1 in the Earth–Sun System”. In: *Celestial Mechanics and Dynamical Astronomy* 107.1–2 (Mar. 2010), pp. 233–253. DOI: https://doi.org/10.1007/s10569-010-9268-4.

[171] A. Farrés and À. Jorba. “Dynamics of a Solar Sail near a Halo Orbit”. In: *Acta Astronautica* 67.7–8 (Oct. 2010), pp. 979–990. DOI: https://doi.org/10.1016/j.actaastro.2010.05.022.

[172] Alvaro Fernandez Mora and Jeannette Heiligers. “Solar-Sail Quasi-Periodic Orbits in the Sun–Earth System”. In: *Journal of Guidance, Control, and Dynamics* 43.9 (Sept. 2020), pp. 1740–1749. DOI: https://doi.org/10.2514/1.g005021.

[173] Alessandro Peloni, Bernd Dachwald, and Matteo Ceriotti. “Multiple Near-earth Asteroid Rendezvous Mission: Solar-sailing Options”. In: *Advances in Space Research* 62.8 (Oct. 2018), pp. 2084–2098. DOI: https://doi.org/10.1016/j.asr.2017.10.017.

[174] Yu Song and Shengping Gong. “Solar Sail Trajectory Optimization of Multi-asteroid Rendezvous Mission”. In: *Acta Astronautica* 157 (Apr. 2019), pp. 111–122. DOI: https://doi.org/10.1016/j.actaastro.2018.12.016.

[175] Giuseppe Cataldi and Salvo Marcuccio. “Design of 3-D Trajectory Sequences for Multiple Asteroid Flyby Missions”. In: *Aerospace Systems* 5.4 (Oct. 2022), pp. 531–544. DOI: https://doi.org/10.1007/s42401-022-00166-6.

[176] Gonzalo Zamora-Caballero, Rafael Vazquez, and Francesco Topputo. “Solar Sail Trajectory Optimization for Asteroid Flyby and Rendezvous”. In: *Journal of Guidance, Control, and Dynamics* 48.10 (Oct. 2025), pp. 2257–2271. DOI: https://doi.org/10.2514/1.g008632.

[177] James Pezent, Rohan Sood, and Andrew Heaton. “High-fidelity Contingency Trajectory Design and Analysis for NASA’s Near-earth Asteroid (NEA) Scout Solar Sail Mission”. In: *Acta Astronautica* 159 (June 2019), pp. 385–396. DOI: https://doi.org/10.1016/j.actaastro.2019.03.050.

[178] Alessandro A. Quarta, Karim Abu Salem, and Giuseppe Palaia. “Solar Sail Transfer Trajectory Design for Comet 29P/Schwassmann–Wachmann 1 Rendezvous”. In: *Applied Sciences* 13.17 (Aug. 2023), p. 9590. DOI: https://doi.org/10.3390/app13179590.

[179] Gareth W. Hughes and Colin R. McInnes. “Small-Body Encounters Using Solar Sail Propulsion”. In: *Journal of Spacecraft and Rockets* 41.1 (Jan. 2004), pp. 140–150. DOI: https://doi.org/10.2514/1.9277.

[180] Colin R. McInnes. “Solar Sail Trajectories at the Lunar L2 Lagrange Point”. In: *Journal of Spacecraft and Rockets* 30.6 (Nov. 1993), pp. 782–784. DOI: https://doi.org/10.2514/3.26393.

[181] Jeannette Heiligers et al. “Solar Sail Lyapunov and Halo Orbits in the Earth–Moon Three-body Problem”. In: *Acta Astronautica* 116 (Nov. 2015), pp. 25–35. DOI: https://doi.org/10.1016/j.actaastro.2015.05.034.

[182] Shengping Gong, Junfeng Li, and Jules Simo. “Orbital Motions of a Solar Sail Around the L2 Earth–Moon Libration Point”. In: *Journal of Guidance, Control, and Dynamics* 37.4 (July 2014), pp. 1349–1356. DOI: https://doi.org/10.2514/1.g000063.

[183] Jeannette Heiligers, Malcolm Macdonald, and Jeffrey S. Parker. “Extension of Earth-Moon Libration Point Orbits with Solar Sail Propulsion”. In: *Astrophysics and Space Science* 361.7 (June 2016). DOI: https://doi.org/10.1007/s10509-016-2783-3.

[184] Toshihiro Chujo. “Quasi-periodic Orbits of Small Solar Sails with Time-varying Attitude Around Earth–Moon Libration Points”. In: *Astrodynamics* 8.1 (Feb. 2024), pp. 161–174. DOI: https://doi.org/10.1007/s42064-023-0186-0.

[185] Jeannette Heiligers. “Homo- and Heteroclinic Connections in the Planar Solar-Sail Earth-Moon Three-Body Problem”. In: *Frontiers in Applied Mathematics and Statistics* 4 (Oct. 2018). DOI: https://doi.org/10.3389/fams.2018.00042.

[186] Xun Duan et al. “A Picture of Solar-sail Heteroclinic Enhanced Connections Between Lissajous Libration Point Orbits”. In: *Communications in Nonlinear Science and Numerical Simulation* 85 (June 2020), p. 105252. DOI: https://doi.org/10.1016/j.cnsns.2020.105252.

[187] Megan Estrada et al. “Solar Sail Orbits in Cislunar Space for Lunar Surface Surveying”. In: *AAS/AIAA Astrodynamics Specialist Conference*. Boston, Massachusetts, USA, Aug. 2025. Digitally available (accessed on August 12, 2026).

[188] Jeannette Heiligers, Jeffrey S. Parker, and Malcolm Macdonald. “Novel Solar-Sail Mission Concepts for High-Latitude Earth and Lunar Observation”. In: *Journal of Guidance, Control, and Dynamics* 41.1 (Jan. 2018), pp. 212–230. DOI: https://doi.org/10.2514/1.g002919.

[189] Toshihiro Chujo. “Near-Optimal Lunar-Orbit Control Using Solar Sails”. In: *AIAA SciTech 2024 Forum*. American Institute of Aeronautics and Astronautics (AIAA), Jan. 2024. DOI: https://doi.org/10.2514/6.2024-0840.

[190] M. T. Ozimek, D. J. Grebow, and K. C. Howell. “Design of Solar Sail Trajectories with Applications to Lunar South Pole Coverage”. In: *Journal of Guidance, Control, and Dynamics* 32.6 (Nov. 2009), pp. 1884–1897. DOI: https://doi.org/10.2514/1.41963.

[191] Martin T. Ozimek. “A Collocation Approach for Computing Solar Sail Lunar Pole-Sitter Orbits”. In: *The Open Aerospace Engineering Journal* 3.1 (Oct. 2010), pp. 65–75. DOI: https://doi.org/10.2174/1874146001003010065.

[192] Jules Simo and Colin R. McInnes. “Designing Displaced Lunar Orbits Using Low-Thrust Propulsion”. In: *Journal of Guidance, Control, and Dynamics* 33.1 (Jan. 2010), pp. 259–265. DOI: https://doi.org/10.2514/1.45305.

[193] Geoffrey G. Wawrzyniak and Kathleen C. Howell. “Generating Solar Sail Trajectories in the Earth-Moon System Using Augmented Finite-Difference Methods”. In: *International Journal of Aerospace Engineering* 2011 (2011), pp. 1–13. DOI: https://doi.org/10.1155/2011/476197.

[194] Geoffrey G. Wawrzyniak and Kathleen C. Howell. “Numerical Techniques for Generating and Refining Solar Sail Trajectories”. In: *Advances in Space Research* 48.11 (Dec. 2011), pp. 1848–1857. DOI: https://doi.org/10.1016/j.asr.2011.04.012.

[195] Fernando Gámez Losada and Jeannette Heiligers. “New Solar-Sail Orbits for Polar Observation of the Earth and Moon”. In: *Journal of Guidance, Control, and Dynamics* 44.12 (Dec. 2021), pp. 2155–2171. DOI: https://doi.org/10.2514/1.g005955.

[196] Gregory L. Matloff. “The Solar Photon Thruster As a Terrestrial Pole Sitter”. In: *Annals of the New York Academy of Sciences* 1017.1 (May 2004), pp. 468–474. DOI: https://doi.org/10.1196/annals.1311.028.

[197] Merel Vergaaij and Jeannette Heiligers. “Solar-Sail Trajectory Design to Planetary Pole Sitters”. In: *Journal of Guidance, Control, and Dynamics* 42.6 (June 2019), pp. 1402–1412. DOI: https://doi.org/10.2514/1.g003952.

[198] Matteo Ceriotti and Colin R. McInnes. “Generation of Optimal Trajectories for Earth Hybrid Pole Sitters”. In: *Journal of Guidance, Control, and Dynamics* 34.3 (May 2011), pp. 847–859. DOI: https://doi.org/10.2514/1.50935.

[199] Colin R. McInnes and John F. L. Simmons. “Solar Sail Halo Orbits Part II - Geocentric Case”. In: *Journal of Spacecraft and Rockets* 29.4 (July 1992), pp. 472–479. DOI: https://doi.org/10.2514/3.55639.

[200] Colin R. McInnes et al. “GEOSAIL: Exploring the Geomagnetic Tail Using a Small Solar Sail”. In: *Journal of Spacecraft and Rockets* 38.4 (July 2001), pp. 622–629. DOI: https://doi.org/10.2514/2.3727.

[201] Malcolm Macdonald et al. “GeoSail: Exploring the Magnetosphere Using a Low-cost Solar Sail”. In: *Acta Astronautica* 59.8–11 (Oct. 2006), pp. 757–767. DOI: https://doi.org/10.1016/j.actaastro.2005.07.023.

[202] Victoria L. Coverstone and John E. Prussing. “Technique for Escape from Geosynchronous Transfer Orbit Using a Solar Sail”. In: *Journal of Guidance, Control, and Dynamics* 26.4 (July 2003), pp. 628–634. DOI: https://doi.org/10.2514/2.5091.

[203] Giovanni Mengali and Alessandro A. Quarta. “Earth Escape by Ideal Sail and Solar-Photon Thrustor Spacecraft”. In: *Journal of Guidance, Control, and Dynamics* 27.6 (Nov. 2004), pp. 1105–1108. DOI: https://doi.org/10.2514/1.10637.

[204] Malcolm Macdonald and Colin R. McInnes. “Realistic Earth Escape Strategies for Solar Sailing”. In: *Journal of Guidance, Control, and Dynamics* 28.2 (Mar. 2005), pp. 315–323. DOI: https://doi.org/10.2514/1.5165.

[205] Riley M. Fitzgerald. “Characterizing Minimum-Time Solar Sail Geostationary Orbit Transfers Using Pseudospectral Optimal Control”. In: *Journal of Spacecraft and Rockets* 58.4 (July 2021), pp. 997–1009. DOI: https://doi.org/10.2514/1.a34950.

[206] Kenshiro Oguri et al. “Solar Sailing Q-Law for Planetocentric, Many-Revolution Sail Orbit Transfers”. In: *Journal of Guidance, Control, and Dynamics* 46.10 (Oct. 2023), pp. 2005–2014. DOI: https://doi.org/10.2514/1.g007103.

[207] Fernando Gámez Losada, Pieter Visser, and Jeannette Heiligers. “Fundamentals of Circular-to-circular Solar-sail Transfers Around Planetary Bodies”. In: *Advances in Space Research* (Feb. 2026). DOI: https://doi.org/10.1016/j.asr.2026.02.049.

[208] Fernando Gámez Losada, Pieter Visser, and Jeannette Heiligers. “Estimating the Performance of Patched Multirevolution Solar-Sail Transfers Around Planets”. In: *Journal of Guidance, Control, and Dynamics* 49.1 (Jan. 2026), pp. 149–160. DOI: https://doi.org/10.2514/1.G009233.

[209] Jeannette Heiligers et al. “Displaced Geostationary Orbit Design Using Hybrid Sail Propulsion”. In: *Journal of Guidance, Control, and Dynamics* 34.6 (Nov. 2011), pp. 1852–1866. DOI: https://doi.org/10.2514/1.53807.

[210] Christian Circi. “Simple Strategy for Geostationary Stationkeeping Maneuvers Using Solar Sail”. In: *Journal of Guidance, Control, and Dynamics* 28.2 (Mar. 2005), pp. 249–253. DOI: https://doi.org/10.2514/1.6797.

[211] Patrick Kelly and Riccardo Bevilacqua. “An Optimized Analytical Solution for Geostationary Debris Removal Using Solar Sails”. In: *Acta Astronautica* 162 (Sept. 2019), pp. 72–86. DOI: https://doi.org/10.1016/j.actaastro.2019.05.055.

[212] Narcís Miguel, Camilla Colombo, et al. “Planar Orbit and Attitude Dynamics of an Earth-orbiting Solar Sail under J2 and Atmospheric Drag Effects”. In: *Advances in the Astronautical Sciences* 167 (2018), pp. 299–319. Digitally available (accessed on August 12, 2026).

[213] Narcís Miguel and Camilla Colombo. “Deorbiting Spacecraft with Passively Stabilised Attitude using a Simplified Quasi-rhombic-pyramid Sail”. In: *Advances in Space Research* 67.9 (2021). Solar Sailing: Concepts, Technology, and Missions II, pp. 2561–2576. DOI: https://doi.org/10.1016/j.asr.2020.03.028.

[214] Camilla Colombo et al. “Drag and Solar Sail Deorbiting: Re-entry Time versus Cumulative Collision Probability”. In: *68^{th} International Astronautical Congress (IAC) Proceedings*. International Astronautical Federation (IAF). 2017, pp. 3535–3553. Digitally available (accessed on August 12, 2026).

[215] Alexandru Ionel. “Deorbiting Upper-stages in LEO at EOM using Solar Sails”. In: *INCAS Bulletin* 9.2 (2017), pp. 117–132. Digitally available (accessed on August 12, 2026).

[216] Peter C. E. Roberts and Patrick G. Harkness. “Drag Sail for End-of-life Disposal from Low Earth Orbit”. In: *Journal of Spacecraft and Rockets* 44.6 (2007), pp. 1195–1203. DOI: https://doi.org/10.2514/1.28626.

[217] Lourens Visagie and Theodoros Theodorou. *HybridSail: Hybrid Solar Sails for Active Debris Removal – Final Report*. Tech. rep. 10-6411b. Keplerlaan 1, 2201 AZ, Noordwijk, The Netherlands: European Space Agency, June 2011. Digitally available (accessed on August 12, 2026).

[218] T. O. Morgan. "The Inclination Change for Solar Sails and Low Earth Orbit". In: *Advances in Astronautical Sciences* (1979), pp. 559–573.

[219] Giovanni Mengali and Alessandro A. Quarta. "Near-Optimal Solar-Sail Orbit-Raising from Low Earth Orbit". In: *Journal of Spacecraft and Rockets* 42.5 (Sept. 2005), pp. 954–958. DOI: https://doi.org/10.2514/1.14184.

[220] Valentin Stolbunov et al. "Optimal Law for Inclination Change in an Atmosphere Through Solar Sailing". In: *Journal of Guidance, Control, and Dynamics* 36.5 (2013), pp. 1310–1323. DOI: https://doi.org/10.2514/1.59931.

[221] Paul D. Fieseler. "A Method for Solar Sailing in a Low Earth Orbit". In: *Acta Astronautica* 43.9 (1998), pp. 531–541. DOI: https://doi.org/10.1016/S0094-5765(98)00175-1.

[222] Alessia De Iuliis et al. "Sailing with Solar and Planetary Radiation Pressure". In: *Advances in Space Research* 67.9 (2021), pp. 2795–2811. DOI: https://doi.org/10.1016/j.asr.2019.11.036.

[223] Anaïs Barles et al. "An Optimal Steering Law for Sailing with Solar and Planetary Radiation Pressure". In: *Aerospace Science and Technology* 118 (2021), p.107051. DOI: https://doi.org/10.1016/j.ast.2021.107051.

[224] Andrea Minervino Amodio, Pieter Visser, and Jeannette Heiligers. "Dynamical Modelling of NASA's ACS3 Solar Sail Mission". In: *Aerospace Science and Technology* 161 (June 2025), p. 110146. DOI: https://doi.org/10.1016/j.ast.2025.110146.

[225] NASA Space Technology Mission Directorate. *GO: Advanced Propulsion*. Apr. 2024. Digitally available (accessed on August 12, 2026).

[226] Onur Çelik et al. "Enhancing Terrestrial Solar Power Using Orbiting Solar Reflectors". In: *Acta Astronautica* 195 (June 2022), pp. 276–286. DOI: https://doi.org/10.1016/j.actaastro.2022.03.015.

[227] Onur Çelik and Colin R. McInnes. "A Constellation Design for Orbiting Solar Reflectors to Enhance Terrestrial Solar Energy". In: *Acta Astronautica* 217 (Apr. 2024), pp. 145–161. DOI: https://doi.org/10.1016/j.actaastro.2024.01.031.

[228] Andrea Viale et al. "A Reference Architecture for Orbiting Solar Reflectors to Enhance Terrestrial Solar Power Plant Output". In: *Advances in Space Research* 72.4 (Aug. 2023), pp. 1304–1348. DOI: https://doi.org/10.1016/j.asr.2023.05.037.

[229] CelesTrak. *Satellite Catalog (SATCAT)*. URL: https://celestrak.org/satcat/search.php. Accessed on December 1, 2025.

[230] Ulrich Walter. "Orbit Perturbations". In: *Astronautics: The Physics of Space Flight*. Third edition. Gewerbestrasse 11, Cham 6330, Switzerland: Springer International Publishing, 2018. Chap. 12, pp. 555–660. ISBN: 978-3-319-74373-8. DOI: http://doi.org/10.1007/978-3-319-74373-8_12.

[231] O. Montenbruck and E. Gill. *Satellite Orbits: Models, Methods and Applications*. 1st. Heidelberger Platz 3, D-14197 Berlin, Germany: Springer-Verlag, 2000. ISBN: 978-3-540-67280-7. DOI: https://doi.org/10.1007/978-3-642-58351-3.

[232] Karel Franciscus Wakker. *Fundamentals of Astrodynamics*. Kluyverweg 1, 2629 HS, Delft, The Netherlands: Delft University of Technology, 2015. ISBN: 978-94-6186-419-2. Digitally available (accessed on August 12, 2026).

[233] Hanspeter Schaub and John L. Junkins. "Appendix F: First-Order Mapping Between Mean and Osculating Orbit Elements". In: *Analytical Mechanics of Space Systems*. Fourth edition. 12700 Sunrise Valley Drive, Suite 200, Reston, Virginia 20191-5807, USA: American Institute of Aeronautics and Astronautics (AIAA), 2018, pp. 883–886. ISBN: 978-1-62410-521-0. DOI: http://doi.org/10.2514/5.9781624105210.0883.0886.

[234] James Richard Wertz et al. *Orbit & Constellation Design & Management*. Second printing. 4940 West 147th Street, Hawthorne 90250, California, USA and One New York Plaza, Suite 4600, New York, New York 10004-1562, USA: Microcosm, Inc. and Springer, 2009. ISBN: 978-1-88188-307-4.

[235] Kyoung-Min Roh, Sergei M. Kopeikin, and Jung-Ho Cho. "Numerical Simulation of the Post-Newtonian Equations of Motion for the Near Earth Satellite with an Application to the LARES Satellite". In: *Advances in Space Research* 58.11 (2016), pp. 2255–2268. DOI: https://doi.org/10.1016/j.asr.2016.08.009.

[236] Mateusz Matyszewski et al. "Satellite Laser Ranging Technique As a Tool for the Determination of the Schwarzschild, De Sitter and Lense-Thirring Effects". In: *Reports on Geodesy and Geoinformatics* 116.1 (Dec. 2023), pp. 77–84. DOI: https://doi.org/10.2478/rgg-2023-0013.

[237] P. Knocke, J. Ries, and B. Tapley. "Earth Radiation Pressure Effects on Satellites". In: *Astrodynamics Conference*. American Institute of Aeronautics and Astronautics (AIAA), Aug. 1988. DOI: http://doi.org/10.2514/6.1988-4292.

[238] *State-of-the-Art: Small Spacecraft Technology*. Tech. rep. NASA/TP-20250000142. National Aeronautics and Space Administration, Jan. 2025. Digitally available (accessed on August 12, 2026).

[239] Jamie Chin et al. *CubeSat 101: Basic Concepts and Processes for First-Time CubeSat Developers*. Tech. rep. National Aeronautics and Space Administration, Oct. 2017. Digitally available (accessed on August 12, 2026).

[240] WIlliam H. Ailor. *Large Constellation Disposal Hazards*. Tech. rep. OTR201901097. National Aeronautics and Space Administration, Jan. 2020. Digitally available (accessed on August 12, 2026).

[241] Joseph A. Burns, Philippe L. Lamy, and Steven Soter. "Radiation Forces on Small Particles in the Solar System". In: *Icarus* 40.1 (1979), pp. 1–48. DOI: https://doi.org/10.1016/0019-1035(79)90050-2.

[242] F.A. Abd El-Salam. "The Effects of Poynting–Robertson Drag on Solar Sails". In: *Results in Physics* 9 (2018), pp. 897–903. ISSN: 2211–3797. DOI: https://doi.org/10.1016/j.rinp.2018.03.057.

[243] Kento Hosh, Hirotsugu Kojima, and Hiroshi Yamakawa. “Numerical Analysis of Potential Structure around Electric Solar Wind Sail Tethers”. In: *Transactions of the Japan Society for Aeronautical and Space Sciences, Aerospace Technology Japan* 14.ists30 (2016), Pb_83–Pb_89. DOI: https://doi.org/10.2322/tastj.14.Pb_83.

[244] Howard J. Wintle. “The Capacitance of the Cube and Square Plate by Random Walk Methods”. In: *Journal of Electrostatics* 62.1 (2004), pp. 51–62. DOI: https://doi.org/10.1016/j.elstat.2004.04.005.

[245] C. C. Finlay et al. “International Geomagnetic Reference Field: The Eleventh Generation”. In: *Geophysical Journal International* 183.3 (Dec. 2010), pp. 1216–1230. DOI: https://doi.org/10.1111/j.1365-246X.2010.04804.x.

[246] Luisa Boni, Alessandro A. Quarta, and Giovanni Mengali. “Thermal-structural Analysis of a Square Solar Sail”. In: *Acta Astronautica* 154 (Jan. 2019), pp. 268–277. DOI: https://doi.org/10.1016/j.actaastro.2018.03.037.

[247] Benjamin M. Gauvain and Daniel A. Tyler. “A Solar Sail Shape Modeling Approach for Attitude Control Design and Analysis”. In: *Proceedings of the 6th International Symposium on Space Sailing*. New York City College of Technology, New York, USA, June 2023, pp. 66–72. Digitally available (accessed on August 12, 2026).

[248] Feng Zhang et al. “Solar Sail Attitude Control Using Shape Variation of Booms”. In: *Chinese Journal of Aeronautics* 35.10 (Oct. 2022), pp. 326–336. DOI: https://doi.org/10.1016/j.cja.2021.10.036.

[249] Hiraku Sakamoto, K. C. Park, and Yasuyuki Miyazaki. “Effect of Static and Dynamic Solar Sail Deformation on Center of Pressure and Thrust Forces”. In: *AIAA Guidance, Navigation, and Control Conference and Exhibit*. American Institute of Aeronautics and Astronautics (AIAA), June 2006. DOI: https://doi.org/10.2514/6.2006-6184.

[250] Xiyao Huang et al. “Analysis of the Solar Sail Deformation Based on the Point Cloud Method”. In: *Advances in Space Research* 67.9 (May 2021), pp. 2613–2627. DOI: https://doi.org/10.1016/j.asr.2020.05.008.

[251] Daniel Tyler et al. “Attitude Control Approach for Solar Cruiser, a Large, Deep Space Solar Sail”. In: *45th Annual AAS Guidance, Navigation and Control (GN&C) Conference*. Breckenridge, Colorado, USA, Feb. 2023. Digitally available (accessed on August 12, 2026).

[252] Luisa Boni, Giovanni Mengali, and Alessandro A Quarta. “Finite Element Analysis of Solar Sail Force Model with Mission Application”. In: *Proceedings of the Institution of Mechanical Engineers, Part G: Journal of Aerospace Engineering* 233.5 (Mar. 2018), pp. 1838–1846. DOI: https://doi.org/10.1177/0954410018764183.

[253] Leonel Rios-Reyes. “Solar Sails: Modeling, Estimation, and Trajectory Control”. PhD thesis. The University of Michigan, 2006. Digitally available (accessed on August 12, 2026).

[254] Nobuhiro Funabiki et al. “Accurate Aerodynamic Model of Membranes in Free-Molecular Flow for Deorbit Device Design”. In: *Transactions of the Japan Society for Aeronautical and Space Sciences, Aerospace Technology Japan* 17.2 (2019), pp. 189–196. DOI: https://doi.org/10.2322/tastj.17.189.

[255] Bruce A. Campbell and Stephanie J. Thomas. “Realistic Solar Sail Thrust”. In: *Advances in Solar Sailing*. Heidelberger Platz 3, 14197 Berlin, Germany: Springer Berlin Heidelberg, 2014. Chap. III, pp. 407–436. ISBN: 978-3-642-34907-2. DOI: https://doi.org/10.1007/978-3-642-34907-2_27.

[256] Anthony Ewing. “Solar Sail Propulsion Sensitivity to Membrane Shape and Optical Properties using the Solar Vectoring Evaluation Tool (SVET)”. In: *53rd oint Army Navy Nasa Air Force (JANNAF) Propulsion Meeting*. Monterey, California, USA, 2005. Digitally available (accessed on August 12, 2026).

[257] Anthony Ewing and Jim Moore. “Propulsion Sensitivity Study on NASA’s Proposed ST9 Evolved Design Solar Sail Using the Solar Vectoring Evaluation Tool (SVET)”. In: *48th AIAA/ASME/ASCE/AHS/ASC Structures, Structural Dynamics, and Materials Conference*. American Institute of Aeronautics and Astronautics (AIAA), Apr. 2007. DOI: https://doi.org/10.2514/6.2007-1825.

[258] Juan Garcia Bonilla, Livio Carzana, and Jeannette Heiligers. “Uncertainty Quantification for Solar Sails in the Near-Earth Environment”. In: *Proceedings of the 6th International Symposium on Space Sailing*. New York City College of Technology, New York, USA, June 2023, pp. 119–126. Digitally available (accessed on August 12, 2026).

[259] Esztella Balla and János Vad. “An Empirical Model to Determine Lift and Drag Coefficients of Cambered Plates at Moderate Reynolds Numbers”. In: *Proceedings of the Institution of Mechanical Engineers, Part A: Journal of Power and Energy* 235.2 (Apr. 2020), pp. 202–210. DOI: https://doi.org/10.1177/0957650920915317.

[260] Esztella Balla and János Vad. “Models for Estimation of Lift and Drag Coefficients for Low-Reynolds-Number Cambered Plates”. In: *AIAA Journal* 60.12 (Dec. 2022), pp. 6620–6632. DOI: https://doi.org/10.2514/1.J061579.

[261] A. Bruining. *Aerodynamic Characteristics of a Curved Plate Airfoil Section at Reynolds Numbers 60.000 and 100.000 and Angles of Attack from -10 to +90 Degrees*. Tech. rep. Report LR-281. Delft, The Netherlands: Delft University of Technology, May 1979. Digitally available (accessed on August 12, 2026).

[262] Tommaso Pino, Christian Circi, and Giovanni Vulpetti. “Wrinkling Analysis for Small Solar-photon Sails: An Experimental and Analytic Approach for Trajectory Design”. In: *Advances in Space Research* 63.11 (June 2019), pp. 3675–3690. DOI: https://doi.org/10.1016/j.asr.2019.02.016.

[263] Giovanni Vulpetti et al. “Wrinkling Analysis of Solar-photon Sails”. In: *Advances in Space Research* 67.9 (May 2021), pp. 2669–2687. DOI: https://doi.org/10.1016/j.asr.2020.07.016.

[264] Jie Zou et al. “Experimental Study of Measuring the Wrinkle of Solar Sails”. In: *Aerospace* 9.6 (May 2022), p. 289. DOI: https://doi.org/10.3390/aerospace9060289.

[265] Jie Wang et al. “Uncertainty characterization of solar sail thrust with a multiscale modeling method”. In: *Advances in Space Research* 75.7 (2025), pp. 5640–5655. DOI: https://doi.org/10.1016/j.asr.2025.01.026.

[266] Lorenzo Niccolai et al. “Effects of Optical Parameter Measurement Uncertainties and Solar Irradiance Fluctuations on Solar Sailing”. In: *Advances in Space Research* 67.9 (May 2021), pp. 2784–2794. DOI: https://doi.org/10.1016/j.asr.2019.11.037.

[267] Christian Bianchi, Lorenzo Niccolai, and Giovanni Mengali. “Solar Sail Transfers under Uncertainties: A Deep Reinforcement Learning Approach”. In: *Space: Science & Technology* 5 (Jan. 2025). DOI: https://doi.org/10.34133/space.0297.

[268] G. Vulpetti and S. Scaglione. “The Aurora Project: Estimation of the Optical Sail Parameters”. In: *Acta Astronautica* 44.2–4 (Jan. 1999), pp. 123–132. DOI: https://doi.org/10.1016/S0094-5765(99)00038-7.

[269] D. Y. Smith, E. Shiles, and M. Inokuti. *The Optical Properties and Complex Dielectric Function of Metallic Aluminum from 0.04 to 10^4 eV*. Tech. rep. ANL-83-34. 9700 South Cass Avenue, Argonne, Illinois, USA: Argonne National Laboratory, Mar. 1983. Digitally available (accessed on August 12, 2026).

[270] Giovanni Mengali et al. “Refined Solar Sail Force Model with Mission Application”. In: *Journal of Guidance, Control, and Dynamics* 30.2 (2007), pp. 512–520. DOI: https://doi.org/10.2514/1.24779.

[271] Bernd Dachwald et al. “Potential Solar Sail Degradation Effects on Trajectory and Attitude Control”. In: *AIAA Guidance, Navigation, and Control Conference and Exhibit*. San Francisco, California, USA, Aug. 2005. DOI: http://doi.org/10.2514/6.2005-6172.

[272] Bernd Dachwald et al. “Parametric Model and Optimal Control of Solar Sails with Optical Degradation”. In: *Journal of Guidance, Control, and Dynamics* 29.5 (2006), pp. 1170–1178. DOI: https://doi.org/10.2514/1.20313.

[273] Bernd Dachwald et al. “Impact of Optical Degradation on Solar Sail Mission Performance”. In: *Journal of Spacecraft and Rockets* 44.4 (2007), pp. 740–749. DOI: https://doi.org/10.2514/1.21432.

[274] Marco Bassetto et al. “Trajectory Analysis of a Sun-Facing Solar Sail with Optical Degradation”. In: *Journal of Guidance, Control, and Dynamics* 43.9 (2020), pp. 1727–1732. DOI: https://doi.org/10.2514/1.G005214.

[275] Lorenzo Niccolai, Alessandro A. Quarta, and Giovanni Mengali. “Trajectory Approximation of a Solar Sail With Constant Pitch Angle and Optical Degradation”. In: *IEEE Transactions on Aerospace and Electronic Systems* 58.4 (2022), pp. 3643–3649. DOI: http://doi.org/10.1109/TAES.2021.3124867.

[276] Erik M. Klein et al. “Solar Sail Propulsion Limitations Due to Hydrogen Blistering: Progression of Reflectance Decrease”. In: *Advances in Space Research* (Dec. 2025). DOI: https://doi.org/10.1016/j.asr.2025.12.061.

[277] R. S. Nerem et al. “Gravity model development for TOPEX/POSEIDON: Joint Gravity Models 1 and 2”. In: *Journal of Geophysical Research: Oceans* 99.C12 (1994), pp. 24421–24447. DOI: https://doi.org/10.1029/94JC01376.

[278] B. D. Tapley et al. “The Joint Gravity Model 3”. In: *Journal of Geophysical Research: Solid Earth* 101.B12 (1996), pp. 28029–28049. DOI: https://doi.org/10.1029/96JB01645.

[279] Nikolaos K. Pavlis et al. “The Development and Evaluation of the Earth Gravitational Model 2008 (EGM2008)”. In: *Journal of Geophysical Research: Solid Earth* 117.B4 (2012). DOI: https://doi.org/10.1029/2011JB008916.

[280] Christoph Förste et al. “EIGEN-6C4 – The Latest Combined Global Gravity Field Model including GOCE Data up to Degree and Order 2190 of GFZ Potsdam and GRGS Toulouse”. In: *Geophysical Research Abstracts*. Vol. 16. EGU2014-3707. Vienna, Austria: GFZ Data Services, 2014. DOI: https://doi.org/10.5880/ICGEM.2015.1.

[281] Thomas Fecher, Roland Pail, and Thomas Gruber. “GOCO05c: A New Combined Gravity Field Model Based on Full Normal Equations and Regionally Varying Weighting”. In: *Surveys in Geophysics* 38.3 (Jan. 2017), pp. 571–590. DOI: http://doi.org/10.1007/s10712-016-9406-y.

[282] Shaylah Mutschler et al. “A Survey of Current Operations-Ready Thermospheric Density Models for Drag Modeling in LEO Operations”. In: *Advanced Maui Optical and Space Surveillance Technologies Conference (AMOS)*. 2023. Digitally available (accessed on August 12, 2026).

[283] Eelco Doornbos. *Thermospheric Density and Wind Determination from Satellite Dynamics*. Heidelberger Platz 3, 14197 Berlin, Germany: Springer Berlin Heidelberg, 2012. ISBN: 978-3-642-25128-3. DOI: http://doi.org/10.1007/978-3-642-25129-0.

[284] S. C. Chapman and T. Dudok de Wit. “A Solar Cycle Clock for Extreme Space Weather”. In: *Scientific Reports* 14.1 (Apr. 2024). DOI: https://doi.org/10.1038/s41598-024-58960-5.

[285] Jeffrey P. Thayer et al. “Thermospheric Density Oscillations Due to Periodic Solar Wind High-speed Streams”. In: *Journal of Geophysical Research: Space Physics* 113.A6 (June 2008). DOI: https://doi.org/10.1029/2008JA013190.

[286] David A. Vallado and David Finkleman. “A Critical Assessment of Satellite Drag and Atmospheric Density Modeling”. In: *Acta Astronautica* 95 (Feb. 2014), pp. 141–165. DOI: https://doi.org/10.1016/j.actaastro.2013.10.005.

[287] Sean Bruinsma and Claude Boniface. “The Operational and Research DTM-2020 Thermosphere Models”. In: *Journal of Space Weather and Space Climate* 11 (2021), p. 47. DOI: https://doi.org/10.1051/swsc/2021032.

[288] Bruce Bowman et al. “A New Empirical Thermospheric Density Model JB2008 Using New Solar and Geomagnetic Indices”. In: *AIAA/AAS Astrodynamics Specialist Conference and Exhibit*. Honululu, Hawaii, USA: American Institute of Aeronautics and Astronautics (AIAA), June 2008. DOI: https://doi.org/10.2514/6.2008-6438.

[289] J. M. Picone et al. “NRLMSISE-00 Empirical Model of the Atmosphere: Statistical Comparisons and Scientific Issues”. In: *Journal of Geophysical Research: Space Physics* 107.A12 (2002), SIA15-1–SIA15-16. DOI: https://doi.org/10.1029/2002JA009430.

[290] J. T. Emmert et al. “NRLMSIS 2.0: A Whole-Atmosphere Empirical Model of Temperature and Neutral Species Densities”. In: *Earth and Space Science* 8.3 (Mar. 2021). DOI: https://doi.org/10.1029/2020EA001321.

[291] Frank Marcos, Bruce Bowman, and Robert Sheehan. “Accuracy of Earth’s Thermospheric Neutral Density Models”. In: *AIAA/AAS Astrodynamics Specialist Conference and Exhibit*. Keystone, Colorado, USA: American Institute of Aeronautics and Astronautics (AIAA), June 2006. DOI: https://doi.org/10.2514/6.2006-6167.

[292] C. Pardini, K. Moe, and L. Anselmo. “Thermospheric Density Model Biases at the 23rd Sunspot Maximum”. In: *Planetary and Space Science* 67.1 (July 2012), pp. 130–146. DOI: https://doi.org/10.1016/j.pss.2012.03.004.

[293] Lirong Yin et al. “Evaluation of Empirical Atmospheric Models Using Swarm-C Satellite Data”. In: *Atmosphere* 13.2 (Feb. 2022), p. 294. DOI: https://doi.org/10.3390/atmos13020294.

[294] NASA Marshall Space Flight Center. *Marshall Solar Cycle Forecast*. URL: https://www.nasa.gov/solar-cycle-progression-and-forecast/archived-forecast. Accessed on December 1, 2025.

[295] D.G. King-Hele and R.R. Allan. “The Rotational Speed of the Upper Atmosphere”. In: *Space Science Reviews* 6.2 (Nov. 1966). DOI: https://doi.org/10.1007/BF00222595.

[296] H. Rishbeth. “Superrotation of the Upper Atmosphere”. In: *Reviews of Geophysics* 10.3 (Aug. 1972), pp. 799–819. DOI: https://doi.org/10.1029/RG010i003p00799.

[297] P.W. Blum and I. Harris. “Some New Aspects on the Superrotation of the Thermosphere”. In: *Journal of Atmospheric and Terrestrial Physics* 36.6 (June 1974), pp. 967–978. DOI: https://doi.org/10.1016/0021-9169(74)90006-3.

[298] D.G. King-hele and Doreen M.C. Walker. “Upper-atmosphere Zonal Winds from Satellite Orbit Analysis”. In: *Planetary and Space Science* 31.5 (May 1983), pp. 509–535. DOI: https://doi.org/10.1016/0032-0633(83)90042-9.

[299] D.G. King-Hele and Doreen M.C. Walker. “Upper-atmosphere Zonal Winds from Satellite Orbit Analysis: An Update”. In: *Planetary and Space Science* 36.11 (Nov. 1988), pp. 1085–1093. DOI: https://doi.org/10.1016/0032-0633(88)90062-1.

[300] Siti Syazwani Nasuha et al. “Thermospheric Neutral Wind Studies over the Equatorial Region: A Review”. In: *Earth and Planetary Physics* 9.1 (2025), pp. 81–100. DOI: https://doi.org/10.26464/epp2024074.

[301] D. P. Drob et al. “An Empirical Model of the Earth’s Horizontal Wind Fields: HWM07”. In: *Journal of Geophysical Research: Space Physics* 113.A12 (Dec. 2008). DOI: https://doi.org/10.1029/2008JA013668.

[302] Douglas P. Drob et al. “An Update to the Horizontal Wind Model (HWM): The Quiet Time Thermosphere”. In: *Earth and Space Science* 2.7 (July 2015), pp. 301–319. DOI: https://doi.org/10.1002/2014EA000089.

[303] Yihui Cai et al. “Altitude Extension of the NCAR-TIEGCM (TIEGCM-X) and Evaluation”. In: *Space Weather* 20.11 (Nov. 2022). DOI: https://doi.org/10.1029/2022SW003227.

[304] Greg Kopp. “Solar Irradiance Measurements”. In: *Living Reviews in Solar Physics* 22.1 (July 2025). DOI: https://doi.org/10.1007/s41116-025-00040-5.

[305] Claus Fröhlich. “Total Solar Irradiance Observations”. In: *Surveys in Geophysics* 33.3–4 (Dec. 2011), pp. 453–473. DOI: https://doi.org/10.1007/s10712-011-9168-5.

[306] I. Ermolli et al. “Recent Variability of the Solar Spectral Irradiance and Its Impact on Climate Modelling”. In: *Atmospheric Chemistry and Physics* 13.8 (Apr. 2013), pp. 3945–3977. DOI: https://doi.org/10.5194/acp-13-3945-2013.

[307] Thierry Dudok de Wit et al. “Methodology to Create a New Total Solar Irradiance Record: Making a Composite Out of Multiple Data Records”. In: *Geophysical Research Letters* 44.3 (Feb. 2017), pp. 1196–1203. DOI: https://doi.org/10.1002/2016GL071866.

[308] James Richard Wertz and Wiley J. Larson. *Space Mission Analysis and Design*. Third edition, Seventh printing. 2377 Crenshaw Boulevard, Suite 350, Torrance, California 90501, USA and P.O. Box 17, 3300 AA Dordrecht, The Netherlands: Microcosm Press and Kluwer Academic Publishers, 2005. ISBN: 978-1-881883-10-4.

[309] D. Vokrouhlicky, P. Farinella, and F. Mignard. “Solar Radiation Pressure Perturbations for Earth Satellites – IV. Effects of the Earth’s Polar Flattening on the Shadow Structure and the Penumbra Transitions”. In: *Astronomy and Astrophysics* 307 (Mar. 1996), pp. 635–644. Digitally available (accessed on August 12, 2026).

[310] Sima Adhya et al. “Oblate Earth Eclipse State Algorithm for Low-Earth-Orbiting Satellites”. In: *Journal of Spacecraft and Rockets* 41.1 (Jan. 2004), pp. 157–159. DOI: https://doi.org/10.2514/1.1485.

[311] Marco Nugnes and Camilla Colombo. “Analytical Determination of Eclipse Entry and Exit Points Considering a Conical Shadow and Oblate Earth”. In: *Acta Astronautica* 211 (Oct. 2023), pp. 795–807. DOI: https://doi.org/10.1016/j.actaastro.2023.07.007.

[312] D. Vokrouhlicky, P. Farinella, and F. Mignard. “Solar Radiation Pressure Perturbations for Earth Satellites – I. A Complete Theory Including Penumbra Transitions”. In: *Astronomy and Astrophysics* 280 (Dec. 1993), pp. 295–312. Digitally available (accessed on August 12, 2026).

[313] D. Vokrouhlicky, P. Farinella, and F. Mignard. “Solar Radiation Pressure Perturbations for Earth Satellites – III. Global Atmospheric Phenomena and the Albedo Effect”. In: *Astronomy and Astrophysics* 290 (Oct. 1994), pp. 324–334. Digitally available (accessed on August 12, 2026).

[314] Sung Hwan Lee and Siyul Lee. “Illuminance During a Solar Eclipse with Limb Darkening: A Mathematical Model”. In: *Journal of The Korean Astronomical Society* 45.5 (Oct. 2012), pp. 111–116. DOI: https://doi.org/10.5303/JKAS.2012.45.5.111.

[315] Charles H. Acton. “Ancillary Data Services of NASA’s Navigation and Ancillary Information Facility”. In: *Planetary and Space Science* 44.1 (Jan. 1996), pp. 65–70. DOI: https://doi.org/10.1016/0032-0633(95)00107-7.

[316] Ryan S. Park et al. “The JPL Planetary and Lunar Ephemerides DE440 and DE441”. In: *The Astronomical Journal* 161.3 (Feb. 2021), p. 105. DOI: https://doi.org/10.3847/1538-3881/abd414.

[317] PaGMO Development Team. *Pl_Eph_An.cpp: Analytical planetary ephemerides source code*. Advanced Concepts Team (ACT), European Space Agency (ESA). 2015. URL: https://github.com/esa/pagmo/blob/master/src/AstroToolbox/Pl_Eph_An.cpp. Accessed on April 20, 2026. Last changed in commit “fe6ec2a” on March 24, 2015.

[318] U.S. Naval Observatory Nautical Almanac Office and Her Majesty’s Nautical Almanac Office. *The Astronomical Almanac for the Year 2010*. 732 North Capitol Street Northwest, Washington, D.C. 20401, USA: U.S. Government Printing Office, 2008. ISBN: 978-0-7077-40829. Digitally available (accessed on August 12, 2026).

[319] Kuo-Nan Liou. “Absorption and Scattering of Solar Radiation in the Atmosphere”. In: *An Introduction to Atmospheric Radiation*. Vol. 84. International Geophysics. Academic Press, 2002. Chap. 3, pp. 65–115. DOI: https://doi.org/10.1016/S0074-6142(02)80018-3.

[320] David A. Glenar et al. “Earthshine As an Illumination Source at the Moon”. In: *Icarus* 321 (Mar. 2019), pp. 841–856. DOI: https://doi.org/10.1016/j.icarus.2018.12.025.

[321] CERES Science Team. *The Best of CERES: Images*. NASA Langley Research Center. URL: https://ceres.larc.nasa.gov/resources/images/. Accessed on December 11, 2025.

[322] Bruce R. Barkstrom. “The Earth Radiation Budget Experiment (ERBE)”. In: *Bulletin of the American Meteorological Society* 65.11 (Nov. 1984), pp. 1170–1185. DOI: https://doi.org/10.1175/1520-0477(1984)065<1170:TERBE>2.0.CO;2.

[323] Bruce A. Wielicki et al. “Clouds and the Earth’s Radiant Energy System (CERES): An Earth Observing System Experiment”. In: *Bulletin of the American Meteorological Society* 77.5 (May 1996), pp. 853–868. DOI: https://doi.org/10.1175/1520-0477(1996)077<0853:CATERE>2.0.CO;2.

[324] E. LEVIN. “Reflected Radiation Received by an Earth Satellite”. In: *ARS Journal* 32.9 (Sept. 1962), pp. 1328–1331. DOI: https://doi.org/10.2514/8.6278.

[325] F. G. Cunningham. “Earth Albedo Input to Flat Plates”. In: *AIAA Journal* 1.6 (June 1963), pp. 1434–1435. DOI: https://doi.org/10.2514/3.1823.

[326] D. A. Lautman. “Perturbations of a Close-Earth Satellite Due to Sunlight Diffusely Reflected from the Earth: I: Uniform Albedo”. In: *Celestial Mechanics* 15.4 (Aug. 1977), pp. 387–420. DOI: https://doi.org/10.1007/BF01228609.

[327] Nicole Borderies and Pierre-yves Longaretti. “A New Treatment of the Albedo Radiation Pressure in the Case of a Uniform Albedo and of a Spherical Satellite”. In: *CELESTIAL MECHANICS AND DYNAMICAL ASTRONOMY* 49.1 (1990), pp. 69–98. DOI: https://doi.org/10.1007/BF00048582.

[328] D. A. Lautman. “Perturbations of a Close-earth Satellite Due to Sunlight Diffusely Reflected from the Earth: II. Variable Albedo”. In: *Celestial Mechanics* 16.1 (Sept. 1977), pp. 3–25. DOI: https://doi.org/10.1007/BF01235724.

[329] L. Sehnal. “Effects of the Terrestrial Infrared Radiation Pressure on the Motion of an Artificial Satellite”. In: *Celestial Mechanics* 25.2 (Oct. 1981), pp. 169–179. DOI: https://doi.org/10.1007/BF01230517.

[330] T. Dale Bess, Richard N. Green, and G. Louis Smith. “Deconvolution of Wide Field-of-View Radiometer Measurements of Earth-Emitted Radiation Part II: Analysis of First Year of Nimbus 6 ERB Data”. In: *Journal of the Atmospheric Sciences* 38.3 (Mar. 1981), pp. 474–488. DOI: https://doi.org/10.1175/1520-0469(1981)038<0474:DOWFOV>2.0.CO;2.

[331] Richard N. Green. *Comparison of Data Inversion Techniques for Remotely Sensed Wide-angle Observations of Earth Emitted Radiation*. Tech. rep. NASA TP-1924. Hampton, Virginia, USA: NASA Langley Research Center, Dec. 1981. Digitally available (accessed on August 12, 2026).

[332] T. Dale Bess and G. Louis Smith. *Atlas of Wide-field-of-view Outgoing Longwave Radiation Derived from Nimbus 7 Earth Radiation Budget Data Set – November 1978 to October 1985*. Tech. rep. NASA RP-1186. Hampton, Virginia, USA: NASA Langley Research Center, Aug. 1987. Digitally available (accessed on August 12, 2026).

[333] Jake J. Gristey et al. “Determination of Global Earth Outgoing Radiation at High Temporal Resolution Using a Theoretical Constellation of Satellites”. In: *Journal of Geophysical Research: Atmospheres* 122.2 (Jan. 2017), pp. 1114–1131. DOI: https://doi.org/10.1002/2016JD025514.

[334] Robert M. L. Baker. “Radiation on a Satellite in the Presence of Partly Diffuse and Partly Specular Reflecting Body”. In: *Trajectories of Artificial Celestial Bodies as Determined from Observations / Trajectoires des Corps Celestes Artificiels Déterminées D'après les Observations*. Heidelberger Platz 3, 14197 Berlin, Germany: Springer Berlin Heidelberg, 1966, pp. 85–150. ISBN: 978-3-642-49326-3. DOI: https://doi.org/10.1007/978-3-642-49326-3_14.

[335] Nicole Borderies. “A General Model of the Planetary Radiation Pressure on a Satellite with a Complex Shape”. In: *CELESTIAL MECHANICS AND DYNAMICAL ASTRONOMY* 49.1 (1990), pp. 99–110. DOI: https://doi.org/10.1007/BF00048583.

[336] David Parry Rubincam and Nelson R. Weiss. “Earth Albedo and the Orbit of Lageos”. In: *Celestial Mechanics* 38.3 (Mar. 1986), pp. 233–296. DOI: https://doi.org/10.1007/BF01231110.

[337] The Open Group and IEEE. *The Open Group Base Specifications, Issue 8: IEEE Std 1003.1-2024 (POSIX.1-2024)*. URL: https://pubs.opengroup.org/onlinepubs/9799919799/. Accessed on December 19, 2025.

[338] Brandon A. Jones. “Efficient Models for the Evaluation and Estimation of the Gravity Field”. PhD thesis. 2010. Digitally available (accessed on August 12, 2026).

[339] International Center for Global Gravity Field Models (ICGEM). *Global Gravity Field Models*. Helmholtz Centre Potsdam, GFZ German Research Centre for Geosciences. URL: https://icgem.gfz.de/tom_longtime. Accessed on January 9, 2026.

[340] David A. Vallado. “Coordinate and Time Systems”. In: *Fundamentals of Astrodynamics and Applications*. Fourth edition. 4940 West 147th Street, Hawthorne, California 90250-6708, USA: Microcosm Press, 2013. Chap. 3, pp. 129–239. ISBN: 978-1-881883-18-0.

[341] J. A. Storch. *Aerodynamic Disturbances on Spacecraft in Free-molecular Flow*. Tech. rep. SMC-TR-03-06, TR-2003(3397)-1. 2430 E. El Segundo Boulevard, Los Angeles Air Force Base, CA 90245: Vehicle Systems Division, Space and Missile Systems Center, Air Force Space Command, Oct. 2002. Digitally available (accessed on August 12, 2026).

[342] Sabrina Livadiotti et al. “A Review of Gas-surface Interaction Models for Orbital Aerodynamics Applications”. In: *Progress in Aerospace Sciences* 119 (Nov. 2020), p. 100675. DOI: https://doi.org/10.1016/j.paerosci.2020.100675.

[343] Jiaheng Chen et al. “Aerodynamic Analysis of Deorbit Drag Sail for CubeSat Using DSMC Method”. In: *Aerospace* 11.4 (Apr. 2024), p. 315. DOI: https://doi.org/10.3390/aerospace11040315.

[344] Andrew Walker, Piyush Mehta, and Josef Koller. “Drag Coefficient Model Using the Cercignani–Lampis–Lord Gas–Surface Interaction Model”. In: *Journal of Spacecraft and Rockets* 51.5 (Sept. 2014), pp. 1544–1563. DOI: https://doi.org/10.2514/1.A32677.

[345] Sabin-Viorel Anton et al. “A Wave Scattering Approach to Modelling Surface Roughness in Orbital Aerodynamics”. In: *Advances in Space Research* 76.2 (July 2025), pp. 811–864. DOI: https://doi.org/10.1016/j.asr.2025.05.069.

[346] Lee H. Sentman. *Free Molecule Flow Theory and its Applicaton to the Determination of Aerodynamic Forces*. Tech. rep. AD265409. Lockheed Missiles & Space Company, Lockheed Aircraft Corporation, Oct. 1961. Digitally available (accessed on August 12, 2026).

[347] Andrew Walker, Piyush Mehta, and Josef Koller. “Different Implementations of Diffuse Reflection with Incomplete Accommodation for Drag Coefficient Modeling”. In: *Journal of Spacecraft and Rockets* 51.5 (Sept. 2014), pp. 1522–1532. DOI: https://doi.org/10.2514/1.A32668.

[348] Paul A. Chambre and Samuel A. Schaaf. *Flow of Rarefied Gases*. 41 William Street, Princeton, New Jersey 08540, USA: Princeton University Press, Dec. 1961. ISBN: 978-1-4008-8580-0. DOI: https://doi.org/10.1515/9781400885800.

[349] Justin A. Atchison and Mason A. Peck. “Length Scaling in Spacecraft Dynamics”. In: *Journal of Guidance, Control, and Dynamics* 34.1 (Jan. 2011), pp. 231–246. DOI: https://doi.org/10.2514/1.49383.

[350] C. Cercignani and M. Lampis. “Kinetic Models for Gas-surface Interactions”. In: *Transport Theory and Statistical Physics* 1.2 (Jan. 1971), pp. 101–114. DOI: https://doi.org/10.1080/00411457108231440.

[351] Jeffrey P. Thayer et al. “Remaining Issues in Upper Atmosphere Satellite Drag”. In: *Space Weather Effects and Applications*. 111 River Street Hoboken, New Jersey 07030, USA: American Geophysical Union and Wiley, 2021. Chap. 5, pp. 111–140. ISBN: 9781119507574. DOI: https://doi.org/10.1002/9781119815570.ch5.

[352] Valerie Bernstein and Marcin Pilinski. “Drag Coefficient Constraints for Space Weather Observations in the Upper Thermosphere”. In: *Space Weather* 20.5 (May 2022). DOI: https://doi.org/10.1029/2021SW002977.

[353] Piyush M. Mehta et al. “Satellite Drag Coefficient Modeling for Thermosphere Science and Mission Operations”. In: *Advances in Space Research* 72.12 (Dec. 2023), pp. 5443–5459. DOI: https://doi.org/10.1016/j.asr.2022.05.064.

[354] Andrew C. Walker, Piyush Mehta, and Josef Koller. “The Effect of Different Adsorption Models on Satellite Drag Coefficients”. In: *Advances in the Astronautical Sciences*. Vol. 150. Aug. 2013, pp. 675–686.

[355] Peter C. Hughes. *Spacecraft Attitude Dynamics*. Dover edition. Mineola, New York: Dover Publications, Inc., 2004. ISBN: 978-0-486-43925-9.

[356] Lorenzo Niccolai and Giovanni Mengali. “Performance Estimate of a Spin-Stabilized Drag Sail for Spacecraft Deorbiting”. In: *Applied Sciences* 14.2 (Jan. 2024), p. 612. DOI: https://doi.org/10.3390/app14020612.

[357] Samuel M. Thompson, Nishanth Pushparaj, and Chantal Cappelletti. “Reflective and Transmissive Solar Sails: Dynamics, Flight Regimes and Applications”. In: *Acta Astronautica* 220 (July 2024), pp. 478–494. DOI: https://doi.org/10.1016/j.actaastro.2024.04.032.

[358] Christian Bianchi et al. “Preliminary Design of a Space Debris Removal Mission in LEO Using a Solar Sail”. In: *Advances in Space Research* 73.8 (Apr. 2024), pp. 4254–4268. DOI: https://doi.org/10.1016/j.asr.2024.01.024.

[359] Kiduck Kim. “Preliminary Trajectory Design for Mitigating Debris Utilizing Solar Sailing and Conventional Propulsion”. In: *International Journal of Aeronautical and Space Sciences* 26.3 (Sept. 2024), pp. 1246–1257. DOI: https://doi.org/10.1007/s42405-024-00833-2.

[360] S. J. Arnold and J. M. Dow. *Models for Spacecraft Acceleration due to Earth Albedo and Infrared Radiation*. Tech. rep. OAD WP 265. Darmstadt, Germany: European Space Operations Centre (ESOC), 1984.

[361] B. Putney et al. “Precision Orbit Determination at the NASA Goddard Space Flight Center”. In: *Advances in Space Research* 10.3–4 (Jan. 1990), pp. 197–203. DOI: https://doi.org/10.1016/0273-1177(90)90350-9.

[362] F. Gini, M. Bardella, and S. Casotto. “Precise Non-gravitational Forces Modeling for GOCE”. In: *Advances in the Astronautical Sciences* 152 (2014), pp. 3141–3157.

[363] E. Doornbos et al. *GOCE+ theme 3: Air Density and Wind Retrieval using GOCE Data - Algorithm Theoretical Basis Document*. Tech. rep. ESA AO/1-6367/10/NL/AF - ESA contract 4000102847/NL/EL. European Space Agency, June 2013. Digitally available (accessed on August 12, 2026).

[364] James M. Longuski, José J. Guzm'an, and John E. Prussing. *Optimal Control with Aerospace Applications*. One New York Plaza, Suite 4600, New York, New York 10004-1562, USA: Springer New York, 2014. ISBN: 978-1-4614-8944-3. DOI: https://doi.org/10.1007/978-1-4614-8945-0.

[365] Sean Matthew Nolan. "Practical Numerical Trajectory Optimization via Indirect Methods". PhD thesis. Purdue University, 2023. DOI: https://doi.org/10.25394/PGS.23528169.v1.

[366] David Morante, Manuel Sanjurjo Rivo, and Manuel Soler. "A Survey on Low-Thrust Trajectory Optimization Approaches". In: *Aerospace* 8.3 (2021). DOI: https://doi.org/10.3390/aerospace8030088.

[367] Oskar Von Stryk and Roland Bulirsch. "Direct and Indirect Methods for Trajectory Optimization". In: *Annals of Operations Research* 37.1 (1992), pp. 357–373. DOI: https://doi.org/10.1007/BF02071065.

[368] John T. Betts. *Practical Methods for Optimal Control and Estimation Using Nonlinear Programming*. 3600 Market Street, 6th Floor, Philadelphia, Pennsylvania 19104-2688, USA: Society for Industrial and Applied Mathematics, Jan. 2010. ISBN: 978-0-89871-857-7. DOI: https://doi.org/10.1137/1.9780898718577.

[369] F. Topputo and C. Zhang. "Survey of Direct Transcription for Low-Thrust Space Trajectory Optimization with Applications". In: *Abstract and Applied Analysis* 2014.1 (2014), p. 851720. DOI: https://doi.org/10.1155/2014/851720.

[370] Fariba Fahroo and I. Michael Ross. "Advances in Pseudospectral Methods for Optimal Control". In: *AIAA Guidance, Navigation and Control Conference and Exhibit*. American Institute of Aeronautics and Astronautics (AIAA), June 2008. DOI: https://doi.org/10.2514/6.2008-7309.

[371] Anil V. Rao. "A Survey of Numerical Methods for Optimal Control". In: *Advances in the Astronautical Sciences* 135.1 (2009), pp. 497–528. Digitally available (accessed on August 12, 2026).

[372] Michael A. Patterson and Anil V. Rao. "GPOPS-II: A MATLAB Software for Solving Multiple-Phase Optimal Control Problems Using Hp-Adaptive Gaussian Quadrature Collocation Methods and Sparse Nonlinear Programming". In: *ACM Transactions on Mathematical Software* 41.1 (Oct. 2014), pp. 1–37. DOI: https://doi.org/10.1145/2558904.

[373] David Q. Mayne. "Differential Dynamic Programming – A Unified Approach to the Optimization of Dynamic Systems". In: *Control and Dynamic Systems*. Radarweg 29, 1043 NX Amsterdam, The Netherlands: Elsevier B.V., 1973, pp. 179–254. DOI: https://doi.org/10.1016/B978-0-12-012710-8.50010-8.

[374] Gregory Lantoine and Ryan P. Russell. "A Hybrid Differential Dynamic Programming Algorithm for Constrained Optimal Control Problems. Part 1: Theory". In: *Journal of Optimization Theory and Applications* 154.2 (Apr. 2012), pp. 382–417. DOI: https://doi.org/10.1007/s10957-012-0039-0.

[375] Marco Nugnes. "Robust Design of Low-thrust Trajectories through Differential Dynamic Programming Enhancing the Effects of Orbital Perturbations". PhD thesis. Politecnico di Milano, Milan, Italy, 2023. Digitally available (accessed on August 12, 2026).

[376] A. E. Eiben and J. E. Smith. *Introduction to Evolutionary Computing*. Heidelberger Platz 3, 14197 Berlin, Germany: Springer Berlin Heidelberg, 2015. ISBN: 978-3-662-44873-1. DOI: https://doi.org/10.1007/978-3-662-44874-8.

[377] Andrea Caruso et al. "Shape-based Approach for Solar Sail Trajectory Optimization". In: *Aerospace Science and Technology* 107 (Dec. 2020), p. 106363. DOI: https://doi.org/10.1016/j.ast.2020.106363.

[378] Alessandro Peloni, Anil V. Rao, and Matteo Ceriotti. "Automated Trajectory Optimizer for Solar Sailing (ATOSS)". In: *Aerospace Science and Technology* 72 (Jan. 2018), pp. 465–475. DOI: https://doi.org/10.1016/j.ast.2017.11.025.

[379] Jeannette Heiligers et al. "Trajectory Design for a Solar-sail Mission to Asteroid 2016 HO3". In: *Astrodynamics* 3.3 (Sept. 2019), pp. 231–246. DOI: https://doi.org/10.1007/s42064-019-0061-1.

[380] Bernd Dachwald. "Low-Thrust Trajectory Optimization and Interplanetary Mission Analysis Using Evolutionary Neurocontrol". PhD thesis. Universität der Bundeswehr München, Munchen, Germany, 2004. Digitally available (accessed on August 12, 2026).

[381] Lorenzo Niccolai, Alessandro A. Quarta, and Giovanni Mengali. "Solar Sail Heliocentric Transfers with a Q-law". In: *Acta Astronautica* 188 (Nov. 2021), pp. 352–361. DOI: https://doi.org/10.1016/j.actaastro.2021.07.037.

[382] Malcolm Macdonald and Colin R. McInnes. "Analytical Control Laws for Planet-Centered Solar Sailing". In: *Journal of Guidance, Control, and Dynamics* 28.5 (Sept. 2005), pp. 1038–1048. DOI: https://doi.org/10.2514/1.11400.

[383] Gijs Leemans, Livio Carzana, and Jeannette Heiligers. "Many-Revolution Earth-Centred Solar-Sail Trajectory Optimisation Using Differential Dynamic Programming". In: *AIAA SciTech 2022 Forum*. American Institute of Aeronautics and Astronautics (AIAA), Jan. 2022. DOI: https://doi.org/10.2514/6.2022-1776.

[384] Livio Carzana, Pieter Visser, and Jeannette Heiligers. "A New Model for the Planetary Radiation Pressure Acceleration for Solar Sails". In: *Journal of Guidance, Control, and Dynamics* 47.8 (Aug. 2024), pp. 1674–1687. DOI: https://doi.org/10.2514/1.G007668.

[385] Livio Carzana, Pieter Visser, and Jeannette Heiligers. *Data underlying the publication: "A New Model for the Planetary Radiation Pressure Acceleration for Solar Sails"*. 4TU.ResearchData, Dataset version 1, Apr. 2026. DOI: https://doi.org/10.4121/b87209ec-b247-428c-a62c-fb50fe218d5c.v1.

[386] Malcolm Macdonald and Colin McInnes. “Solar Sail Science Mission Applications and Advancement”. In: *Advances in Space Research* 48.11 (2011), pp. 1702–1716. DOI: https://doi.org/10.1016/j.asr.2011.03.018.

[387] Giovanni Mengali and Alessandro A. Quarta. “Optimal Three-Dimensional Interplanetary Rendezvous Using Non-Ideal Solar Sail”. In: *Journal of Guidance, Control, and Dynamics* 28.1 (Jan. 2005), pp. 173–177. DOI: https://doi.org/10.2514/1.8325.

[388] Malcolm Macdonald. *Advances in Solar Sailing*. Heidelberger Platz 3, 14197 Berlin, Germany: Springer Berlin Heidelberg, 2014. ISBN: 978-3-642-34906-5. DOI: https://doi.org/10.1007/978-3-642-34907-2.

[389] F.A. Abd El-Salam and L. Sehnal. “The Effects of the Terrestrial Infrared Radiation Pressure on the Earth’s Artificial Satellite Dynamics”. In: *Applied Mathematics and Computation* 162.3 (Mar. 2005), pp. 1431–1451. DOI: https://doi.org/10.1016/j.amc.2004.03.019.

[390] Eite Tiesinga et al. “CODATA Recommended Values of the Fundamental Physical Constants: 2018”. In: *Journal of Physical and Chemical Reference Data* 50.3 (2021). DOI: https://doi.org/10.1103/RevModPhys.93.025010.

[391] Bradley W. Carroll and Dale A. Ostlie. *An Introduction to Modern Astrophysics*. The Triangle Building, Shaftesbury Road, Cambridge, CB2 8EA, United Kingdom: Cambridge University Press, Sept. 2017. ISBN: 978-1-108-38098-0. DOI: https://doi.org/10.1017/9781108380980.

[392] Jack J. Lissauer and Imke de Pater. *Fundamental Planetary Science: Physics, Chemistry and Habitability*. The Triangle Building, Shaftesbury Road, Cambridge, CB2 8EA, United Kingdom: Cambridge University Press, Sept. 2013. ISBN: 978-1-139-05046-3. DOI: https://doi.org/10.1017/CBO9781139050463.

[393] F. G. Cunningham. *Power Input to a Small Flat Plate from a Diffusely Radiating Sphere, with Application to Earth Satellites*. Tech. rep. D-710. Washington D.C., USA: National Aeronautics and Space Administration, Aug. 1961. Digitally available (accessed on August 12, 2026).

[394] B. Fritsche et al. *Radiation Pressure Forces on Complex Spacecraft*. Tech. rep. HTG Final Report 98-8. Katlenburg-Lindau, Germany: Hyperschall Technologie Göttingen GmbH, 1998.

[395] E. Doornbos et al. “Improved Modelling of Surface Forces in the Orbit Determination of ERS and ENVISAT”. In: *Canadian Journal of Remote Sensing* 28.4 (Jan. 2002), pp. 535–543. DOI: https://doi.org/10.5589/m02-055.

[396] Earl A. Thornton. *Thermal Structures for Aerospace Applications*. 12700 Sunrise Valley Drive, Suite 200, Reston, Virginia 20191-5807, USA: American Institute of Aeronautics and Astronautics (AIAA), Jan. 1996. ISBN: 978-1-60086-254-0. DOI: https://doi.org/10.2514/4.862540.

[397] Livio Carzana, Pieter Visser, and Jeannette Heiligers. “Extending the Spherical Planetary Radiation Pressure Acceleration Model to Optical Solar Sails”. In: *Journal of Guidance, Control, and Dynamics* 48.7 (July 2025), pp. 1662–1669. DOI: https://doi.org/10.2514/1.G008940.

[398] Livio Carzana, Pieter Visser, and Jeannette Heiligers. *Data underlying the publication: “Extending the Spherical Planetary Radiation Pressure Acceleration Model to Optical Solar Sails”*. 4TU.ResearchData, Dataset version 1, Apr. 2026. DOI: https://doi.org/10.4121/8a606add-36f7-438a-85b4-31271d336c6a.v1.

[399] Slava G. Turyshev et al. “Science Opportunities with Solar Sailing Smallsats”. In: *Planetary and Space Science* 235 (Oct. 2023), p. 105744. DOI: https://doi.org/10.1016/j.pss.2023.105744.

[400] Patrick W. Kelly et al. “TugSat: Removing Space Debris from Geostationary Orbits Using Solar Sails”. In: *Journal of Spacecraft and Rockets* 55.2 (Mar. 2018), pp. 437–450. DOI: https://doi.org/10.2514/1.A33872.

[401] Patrick Kelly and Riccardo Bevilacqua. “Geostationary Debris Mitigation Using Minimum Time Solar Sail Trajectories with Eclipse Constraints”. In: *Optimal Control Applications and Methods* 42.1 (Sept. 2020), pp. 279–304. DOI: https://doi.org/10.1002/oca.2676.

[402] J. P. S. Carvalho et al. “A Single-Averaged Model for the Solar Radiation Pressure Applied to Space Debris Mitigation Using a Solar Sail”. In: *Symmetry* 15.5 (May 2023), p. 1107. DOI: https://doi.org/10.3390/sym15051107.

[403] J. J. McCarthy and T. V. Martin. *A Computer Efficient Model of Earth Albedo Satellite Effects*. Tech. rep. 012-77. 8800 Greenbelt Road, Greenbelt, Maryland, USA: NASA Goddard Space Flight Center, Planetary Sciences Department, June 1977.

[404] Andres Dono, Ted Hendriks, and W. Keats Wilkie. “Navigation for the ACS3 Solar Sail Mission”. In: *Proceedings of the 4S Symposium (Small Satellites Systems and Services Symposium)*. European Space Agency (ESA) and Centre National d’Études Spatiales (CNES). Palma de Mallorca, Spain, May 2024. Digitally available (accessed on August 12, 2026).

[405] Livio Carzana et al. “Solar-sail Steering Laws to Calibrate the Accelerations from Solar Radiation Pressure, Planetary Radiation Pressure, and Aerodynamic Drag”. In: *Proceedings of the 6th International Symposium on Space Sailing*. New York City College of Technology, New York, USA, June 2023, pp. 58–65. Digitally available (accessed on August 12, 2026).

[406] Andrea Minervino Amodio et al. “Covariance-Based Estimation Performance for In-Flight Calibration of NASA’s ACS3 Solar Sail”. In: *Advances in Space Research* (2025). DOI: https://doi.org/10.1016/j.asr.2025.10.090.

[407] Bong Wie. “Solar Sail Attitude Control and Dynamics, Part 1”. In: *Journal of Guidance, Control, and Dynamics* 27.4 (July 2004), pp. 526–535. DOI: https://doi.org/10.2514/1.11134.

[408] Jin Ho Kang et al. *Space Environmental Damage Assessment on Sail/Deorbit Materials in Low Earth Orbit*. Presentation at the 6th International Symposium on Space Sailing. New York City College of Technology, New York, USA, June 2023. Digitally available (accessed on August 12, 2026).

[409] Livio Carzana, Pieter Visser, and Jeannette Heiligers. "Locally Optimal Control Laws for Earth-bound Solar Sailing with Atmospheric Drag". In: *Aerospace Science and Technology* 127 (Aug. 2022), p. 107666. DOI: https://doi.org/10.1016/j.ast.2022.107666.

[410] Livio Carzana, Pieter Visser, and Jeannette Heiligers. *Data underlying the publication: "Locally Optimal Control Laws for Earth-bound Solar Sailing with Atmospheric Drag"*. 4TU.ResearchData, Dataset version 1, Apr. 2026. DOI: https://doi.org/10.4121/5c1d3263-3267-44c4-9560-50872e9c90b3.v1.

[411] Lorenzo Niccolai, Alessandro A. Quarta, and Giovanni Mengali. "Analytical Solution of the Optimal Steering Law for Non-ideal Solar Sail". In: *Aerospace Science and Technology* 62 (2017), pp. 11–18. DOI: https://doi.org/10.1016/j.ast.2016.11.031.

[412] Giovanni Mengali and Alessandro A. Quarta. "Solar Sail Trajectories with Piecewise-constant Steering Laws". In: *Aerospace Science and Technology* 13.8 (Dec. 2009), pp. 431–441. DOI: https://doi.org/10.1016/j.ast.2009.06.007.

[413] Shahin Firuzi and Shengping Gong. "Refractive Sail and Its Applications in Solar Sailing". In: *Aerospace Science and Technology* 77 (June 2018), pp. 362–372. DOI: https://doi.org/10.1016/j.ast.2018.03.016.

[414] Shahin Firuzi, Yu Song, and Shengping Gong. "Gradient-index Solar Sail and Its Optimal Orbital Control". In: *Aerospace Science and Technology* 119 (Dec. 2021), p. 107103. DOI: https://doi.org/10.1016/j.ast.2021.107103.

[415] Christian Bianchi et al. "Collinear Artificial Equilibrium Point Maintenance with a Wrinkled Solar Sail". In: *Aerospace Science and Technology* 119 (Dec. 2021), p. 107150. DOI: https://doi.org/10.1016/j.ast.2021.107150.

[416] Donald Shepard. "A Two-dimensional Interpolation Function for Irregularly-spaced Data". In: *Proceedings of the 1968 23rd ACM national conference on* -. ACM Press, 1968, pp. 517–524. DOI: https://doi.org/10.1145/800186.810616.

[417] George P.H. Styan. "Hadamard Products and Multivariate Statistical Analysis". In: *Linear Algebra and its Applications* 6 (1973), pp. 217–240. DOI: https://doi.org/10.1016/0024-3795(73)90023-2.

[418] Frank Nielsen. "Hierarchical Clustering". In: *Introduction to HPC with MPI for Data Science*. Gewerbestrasse 11, 6330 Cham, Switzerland: Springer International Publishing, 2016. Chap. 8, pp. 195–211. ISBN: 978-3-319-21903-5. DOI: https://doi.org/10.1007/978-3-319-21903-5_8.

[419] Livio Carzana, Pieter Visser, and Jeannette Heiligers. "Characterization of Solar-sail Maneuvering Capabilities in a High-fidelity Near-Earth Dynamical Environment". In: *Acta Astronautica* (June 2026). DOI: https://doi.org/10.1016/j.actaastro.2026.06.049. Available online, in press.

[420] KL Yeo, NA Krivova, and SK Solanki. “Solar Cycle Variation in Solar Irradiance”. In: *Space Science Reviews* 186 (2014), pp. 137–167. DOI: https://doi.org/10.1007/s11214-014-0061-7.

[421] Dimitri Bertsekas. *Dynamic Programming and Optimal Control: Volume I*. Fourth edition. 1 Chestnut Street, Suite 222, Nashua, New Hampshire 03060, USA: Athena Scientific, 2012. Chap. 1, pp. 2–51. ISBN: 978-1-886529-43-4. Digitally available (accessed on August 12, 2026).

[422] Charles Audet and Warren Hare. “The Beginnings of Derivative-free Optimization Algorithms”. In: *Derivative-Free and Blackbox Optimization*. Gewerbestrasse 11, 6330 Cham, Switzerland: Springer, 2017. Chap. 3, pp. 33–54. ISBN: 978-3-319-68913-5. DOI: https://doi.org/10.1007/978-3-319-68913-5_3.

[423] Ville Satopää et al. “Finding a “Kneedle” in a Haystack: Detecting Knee Points in System Behavior”. In: *31st International Conference on Distributed Computing Systems Workshops*. IEEE. June 2011, pp. 166–171. DOI: https://doi.org/10.1109/ICDCSW.2011.20.

[424] Bengt Fornberg. “Generation of Finite Difference Formulas on Arbitrarily Spaced Grids”. In: *Mathematics of Computation* 51.184 (1988), pp. 699–706. DOI: https://doi.org/10.1090/s0025-5718-1988-0935077-0.

[425] Carmen Pardini and Luciano Anselmo. “Evaluating the Impact of Space Activities in Low Earth Orbit”. In: *Acta Astronautica* 184 (2021), pp. 11–22. DOI: https://doi.org/10.1016/j.actaastro.2021.03.030.

[426] *NASA Image and Video Library*. NASA. URL: https://images.nasa.gov/. Accessed on April 13, 2026.

[427] Kannan Selvan et al. “Precise Orbit Determination of LEO Satellites: a Systematic Review”. In: *GPS Solutions* 27.4 (Aug. 2023). DOI: https://doi.org/10.1007/s10291-023-01520-7.

[428] Kenshiro Oguri, Gregory Lantoine, and Theodore H. Sweetser. “Robust Solar Sail Trajectory Design under Uncertainty with Application to NEA Scout Mission”. In: *AIAA SciTech 2022 Forum*. American Institute of Aeronautics and Astronautics (AIAA), Jan. 2022. DOI: https://doi.org/10.2514/6.2022-1627.

[429] Lorenzo Niccolai, Marco Bassetto, and Giovanni Mengali. “Robust NMPC Strategy for Solar Sail Trajectory Control in Uncertain Environments”. In: *Aerospace Science and Technology* 165 (Oct. 2025), p. 110490. DOI: https://doi.org/10.1016/j.ast.2025.110490.

[430] Anastassios Petropoulos. “A Simple Control Law for Low-thrust Orbit Transfers”. In: *AIAA/AAS Astrodynamics Specialist Conference*. Big Sky, Montana, USA: JPL Open Repository, Aug. 2003. Digitally available (accessed on December 12, 2025).

[431] Anastassios Petropoulos. “Low-Thrust Orbit Transfers Using Candidate Lyapunov Functions with a Mechanism for Coasting”. In: *AIAA/AAS Astrodynamics Specialist Conference and Exhibit*. Providence, Rhode Island, USA: American Institute of Aeronautics and Astronautics (AIAA), June 2004. DOI: https://doi.org/10.2514/6.2004-5089.

[432] Anastassios Petropoulos. “Refinements to the Q-law for the Low-thrust Orbit Transfers”. In: *15th AAS/AIAA Space Flight Mechanics Conference*. Copper Mountain, Colorado, USA: JPL Open Repository, Jan. 2005. Digitally available (accessed on December 12, 2025).

[433] Daniel Zwillinger. *CRC Standard Mathematical Tables and Formulae*. 6000 Broken Sound Parkway Northwest, Suite 300, Boca Raton, Florida 33487, USA: Chapman and Hall/CRC, Nov. 2002. ISBN: 978-1-4200-3534-6. DOI: https://doi.org/10.1201/9781420035346.

List of Publications

Journal Articles

6. **Livio Carzana**, Pieter Visser, and Jeannette Heiligers. "Characterization of Solar-sail Maneuvering Capabilities in a High-fidelity Near-Earth Dynamical Environment". In: *Acta Astronautica* (June 2026). DOI: https://doi.org/10.1016/j.actaastro.2026.06.049. Available online, in press.

5. Oliver Hetherington, **Livio Carzana**, Erik Klein, Pieter Visser, Patric Seefeldt, and Jeannette Heiligers. "Effects of Radiation Induced Optical Degradation on Earth Bound Solar Sail Manoeuvring Capabilities". In: *Advances in Space Research* (April 2026). DOI: https://doi.org/10.1016/j.asr.2026.04.057. Available online, in press.

4. Andrea Minervino Amodio, **Livio Carzana**, Dominic Dirkx, and Jeannette Heiligers. "Covariance-based Estimation Performance for In-flight Calibration of NASA's ACS3 Solar Sail". In: *Advances in Space Research* (in press, available online, October 2025). DOI: https://doi.org/10.1016/j.asr.2025.10.090.

3. **Livio Carzana**, Pieter Visser, and Jeannette Heiligers. "Extending the Spherical Planetary Radiation Pressure Acceleration Model to Optical Solar Sails". In: *Journal of Guidance, Control, and Dynamics* 48.7 (July 2025), pp.1662–1669. DOI: https://doi.org/10.2514/1.G008940.

2. **Livio Carzana**, Pieter Visser, and Jeannette Heiligers. "A New Model for the Planetary Radiation Pressure Acceleration for Solar Sails". In: *Journal of Guidance, Control, and Dynamics* 47.8 (August 2024), pp.1674–1687. DOI: https://doi.org/10.2514/1.G007668.

1. **Livio Carzana**, Pieter Visser, and Jeannette Heiligers. "Locally Optimal Control Laws for Earth-bound Solar Sailing with Atmospheric Drag". In: *Aerospace Science and Technology* 127 (August 2022), p.107666. DOI: https://doi.org/10.1016/j.ast.2022.107666.

Selected Conference Publications

6. **Livio Carzana**, Pieter Visser, and Jeannette Heiligers. "High-fidelity Optimal Control Laws to Characterize the Maneuvering Capabilities of Earth-bound Solar Sails". In: *75^{th} International Astronautical Congress (IAC) Proceedings*. International Astronautical Federation (IAF). Milan, Italy, October 2024. Digitally available (accessed on August 12, 2026).

5. **Livio Carzana**, Andrea Minervino Amodio, Pieter Visser, William Keats Wilkie, and Jeannette Heiligers. "Calibration Steering Laws to Estimate the Optical Properties of NASA's ACS3 Solar Sail". In: *Proceedings of the 29^{th} International Symposium on Space Flight Dynamics*. European Space Operations Centre (ESOC) and EUMETSAT. Darmstadt, Germany, April 2024. Digitally available (accessed on August 12, 2026).

4. **Livio Carzana**, Pieter Visser, and Jeannette Heiligers. "Solar-sail Steering Laws to Calibrate the Accelerations from Solar Radiation Pressure, Planetary Radiation Pressure, and Aerodynamic Drag". In: *Proceedings of the 6th International Symposium on Space Sailing*. New York City College of Technology, New York, USA, June 2023, pp.58—65. Digitally available (accessed on August 12, 2026).

3. Juan Garcia Bonilla, **Livio Carzana**, and Jeannette Heiligers. "Uncertainty Quantification for Solar Sails in the Near-Earth Environment". In: *Proceedings of the 6th International Symposium on Space Sailing*. New York City College of Technology, New York, USA, June 2023, pp.119—126. Digitally available (accessed on August 12, 2026).

2. Gijs Leemans, **Livio Carzana**, and Jeannette Heiligers. "Many-revolution Earth-centred Solar-sail Trajectory Optimisation Using Differential Dynamic Programming". In: *AIAA SCITECH 2022 Forum*. American Institute of Aeronautics and Astronautics (AIAA). San Diego, California, USA, January 2022. DOI: https://doi.org/10.2514/6.2022-1776.

1. **Livio Carzana**, Bernd Dachwald, and Ron Noomen. "Model and Trajectory Optimization for an Ideal Laser-enhanced Solar Sail". In: *68th International Astronautical Congress (IAC) Proceedings*. International Astronautical Federation (IAF). Adelaide, Australia, October 2017. Digitally available (accessed on August 12, 2026).

CURRICULUM VITÆ

Livio CARZANA

December 3, 1993 — Born in Santa Maria Capua Vetere, Italy.

EDUCATION

2008–2012 — Secondary Education
Liceo Statale “Salvatore Pizzi”, Capua, Italy

2012–2015 — Bachelor of Science in Aerospace Engineering
University of Naples “Federico II”, Naples, Italy

2015–2017 — Master of Science in Aerospace Engineering
Delft University of Technology, Delft, The Netherlands
Thesis: Laser-Enhanced Solar Sailing: Modeling and Trajectory Optimization for Interplanetary Missions

2018–2020 — Earth Observation Mission Analysis Engineer
Deimos Space, Tres Cantos, Spain

2020–2026 — PhD in Aerospace Engineering
Delft University of Technology, Delft, The Netherlands
Thesis: Sailing on Sunlight in Earth’s Embrace: Dynamical Modeling and Maneuvering Capabilities of Earth-bound Solar Sails

ACKNOWLEDGMENTS

As I have often been reminded over the past years, the goal of a PhD is to become an independent researcher. In many ways, this journey is therefore shaped by ambition, perseverance, curiosity, and a fair amount of individual effort. Yet, becoming an independent researcher does not mean getting there alone, hidden away and working like a hermit for four years.[1] If anything, this PhD has reminded me how much even the most individual journeys depend on the people around us, as I have had so many who made this experience better in more ways than I can say. To those who guided me, challenged my views, shared the joy of the good moments, and helped me through the difficult ones, whether in Delft or from afar: these final words of this dissertation are dedicated to all of you, to thank you for everything you did to make this possible.

I would first like to thank my copromotor and promotor for their support over the past years, as well as the many others who contributed to my growth as a researcher. Jeannette, thank you for your supervision, dedication, and effort throughout these years, especially during the early stages of my PhD, which coincided with the pandemic. I have always greatly appreciated how, through our frequent meetings, you made me feel like the PhD was not a solitary endeavor at a time when the entire world was suffering from a lack of social interaction. I am also grateful for your confidence in my potential as a researcher, and for giving me the freedom to pursue research directions I found interesting, without constraining my curiosity. Furthermore, thank you for introducing me to aspects of academic life beyond the research contained in this dissertation. Among others, the opportunities you gave me to supervise several students, contribute to NASA's ACS3 mission, and help organize the 7th International Symposium on Space Sailing have been great sources of professional and personal satisfaction. Thank you, Pieter, for your availability, reliability, and timeliness in providing feedback on my research. I hope my work has sparked your interest in solar sailing over these past few years. Thank you, Dominic, for your valuable feedback on this dissertation, which definitely contributed to improving its quality. Also, my sincere thanks go to the ACS3 mission team and, in particular, to Keats Wilkie. Our first meeting took place just three days into my PhD, and in the countless ones that followed, you helped me learn an incredible amount about the technical aspects of a real-life solar-sail mission. Working with you and the entire mission team has been a real pleasure.

Un altro enorme grazie va alla mia famiglia, più o meno allargata, per il sostegno che non mi avete mai fatto mancare, nonostante la distanza che ci separa. Grazie mamma, papà e Francesca per le lunghe chiacchierate al telefono durante i miei giri in bici o, peggio ancora, ad orari improponibili quando mi trovavo dall'altra parte del mondo, come se non ci fossero diversi fusi orari a separarci. Ho sempre apprezzato il modo in cui mi ascoltavate fingendo di capire qualsiasi cosa anche solo vagamente tecnica di cui

[1] ...even though, during some sleepless working nights, it certainly felt that way.

parlassi, il vostro genuino interesse per ciò che mangiavo a colazione, pranzo e cena e, naturalmente, gli innumerevoli "pacchi da giù" che mi avete mandato negli anni. Ma soprattutto, vi ringrazio per avermi fatto sentire a casa ogni volta che rientravo in Italia, indipendentemente dalla mia permanenza, dalle circostanze o dalla vita sempre più nomade che ho condotto negli ultimi anni. Angelina e Pasqualino, grazie per la leggerezza e l'allegria che avete portato con voi ogni volta che ci siamo visti, sempre rigorosamente intorno ad una tavola imbandita con quantità di cibo poco raccomandabili. Grazie Riccardo per capire cosa significhi mettere radici lontano da casa e per aver seguito, anche a distanza, questo mio lungo *camino*, e grazie Matteo per essere qui a condividerne il traguardo. Grazie Andrea (*fratm*) per il tuo supporto, la tua immancabile positività che mi hai trasmesso tutte le volte che ci siamo sentiti e per avermi fatto conoscere Delft circa tredici anni fa. Senza rendertene conto, hai in qualche modo aperto la strada ai due periodi "olandesi" della mia vita, che mi hanno più di tutti formato come persona. Grazie Federica per aver saputo capire gli sforzi, le difficoltà e le soddisfazioni che accompagnano un PhD. E a te, Aurorina, grazie semplicemente per esserci (e per le ore passate a far finta di cucinare con pentole di plastica).

Delft would not have meant nearly as much without the people who filled it. Over the years, I was lucky enough to find flatmates who became friends, friends who became like siblings, colleagues that became trusted companions in the PhD journey, and a small, chosen group of people who made Delft feel like home. For all that you have meant to me, I could spend pages thanking you and still not do you justice, but I will do my best.

Un grazie di cuore a tutte le persone con cui ho vissuto a Doelenplein, che è diventata ben presto molto più di un semplice tetto sopra la testa. Ritrovarsi chiusi tra quelle mura durante la pandemia ci ha subito trasformati da coinquilini in una sorta di famiglia disfunzionale, tenuta insieme in modo tanto precario quanto Pippo teneva in piedi la nostra casa. Alcuni dei miei ricordi più belli di Delft appartengono a quel luogo, a quel periodo e a tutti voi. Giuppa, grazie per le tue perle di saggezza, per le nostre schedules completamente diverse che in un qualche modo si overlappavano sempre alle due di notte, per le tue cene da stella Michelin, per i tanti *shock termici* e i tuoi corsi di cucina (completamente sprecati su uno come me). Isa, grazie per essere un vulcano di energia difficile da arginare, per esser riuscita sempre a trovare una scusa per invitare un'infinità di gente a casa e per averci coinvolto in ognuna delle tue fissazioni. Tra i vari progetti DIY, la tua carriera da DJ, l'ossessione per Bloodborne ed Elden Ring, i cruciverba impossibili del Bartezzaghi, le sessioni di *boulderini* e le campagne di D&D, ogni giorno era diverso dal precedente. Sai bene che tenere il passo col tuo ritmo è stato, talvolta, piuttosto impegnativo. Ma la verità è che con te, e grazie a te, ho vissuto i due anni più belli della mia vita. Te ne sarò sempre grato. Grazie Giulione per esserti inserito con tanta facilità in quella casa semplicemente saltando da una finestra e attraversando un terrazzo, per le serate trascorse insieme, la musica dei tuoi vinili, le tue doti da *chef* e l'inevitabile clima da derby che hai portato in quella casa. Marione, gracias por haber sido no solo un compañero de piso o un colega, sino uno de mis mejores amigos durante estos años en Holanda. Eres una de las personas más inteligentes, positivas y generosas que he conocido nunca, y me ha hecho muchísima ilusión ver cómo nuestra amistad ha crecido año tras año. Llevaré siempre conmigo todas nuestras charlas sobre la vida, la teoría cuántica de campos, la astrodinámica y la parafernalia que es la academia. Gracias, de

corazón, por tu apoyo constante y por haber sido el mejor compañero que podría haber deseado para compartir toda esta aventura.

My thanks also go out to everyone I met in and around Delft, with whom I shared so many incredible nights, experiences, and lasting friendships. Lara e Dani, voi meritereste ben più di un paio di righe di ringraziamento (anche perché lo so, Lara, che le conterai). Siete stati una costante in questi anni e il bene che vi voglio lo sanno solo le lacrime che ho cacciato a Sutri. Lara, grazie per le dosi di drama che porti sempre con te, il tuo OCD per la pulizia, il tuo pragmatismo e l'innata arte di saperti godere la vita. Grazie per il tuo modo di vivere i rapporti, in cui aiutarsi e condividere tutto è semplicemente la normalità, e per la tua assurda capacità di stringere amicizia con chiunque, incluso un noleggiatore d'auto che fino a un minuto prima ci stava scammando. Ma soprattutto, grazie per esser una persona tanto spontanea, diretta e autentica quanto capace di dare il cuore come poche altre ho visto in vita mia. Mi hai fatto rialzare nel momento in cui ne avevo più bisogno ed è qualcosa per cui ti ringrazierò a vita. Sappi che questo traguardo porta dentro anche la tua presenza e la forza che mi hai saputo dare. Dani, grazie per la tua (solo apparente) tranquillità, per la tua pazienza infinita, per il modo in cui in certi aspetti mi ricordi me stesso e, forse anche per questo, per essere stato un punto di riferimento in questi anni. Grazie per le lezioni di bouldering, per le sofferenze e le gioie condivise con l'Inter, per i tuoi DJ set, e per aver sopportato che io dessi a Lucio porzioni di cibo partenopee, col serio rischio di renderlo obeso. La tua presenza ha reso questi anni più leggeri e facili da affrontare. Biscottone, grazie per la tua costante positività, per la quantità infinita di date stories e aneddoti che ci hai regalato, per il tuo talento nel creare giochi di carte, e per la tenacia con cui continui a sostenere di essere allergico al vino (lo sappiamo che sono solo scuse). Edo, sei tra le persone più dolci che abbia mai conosciuto. Grazie per la tua sensibilità e simpatia, capaci davvero di curare ogni male. Grazie ai malesseri, Federica, Sofia, K, Djdj, Gemma, e Zana, per tutti i momenti condivisi in un posto o un altro dell'Olanda. Many thanks also go to Gianluca (con *pz8* sempre pronto all'occorrenza), Paula, Irene, Benji, Jack, Rochi, Zofi, Cisco, Jenna and everyone whose paths I crossed along the way, for making these years so memorable.

This journey was also made infinitely better by everyone I met in the corridors of our department, who, more than anybody else, could understand the joys and difficulties of academic life. Grazie Andrea (*bro*) per essere diventato in così poco tempo il mio PhD buddy e una presenza costante in questi anni. L'onestà intellettuale e la lucidità con cui hai affrontato qualsiasi discussione abbiamo avuto, dalla ricerca alle questioni personali, mi hanno aiutato più di quanto tu possa immaginare. Più di molti altri, hai saputo capire davvero cosa significasse vivere questo percorso e le sue sfide dall'interno, e spero di averti restituito almeno una parte del supporto che mi hai dato. Detto ciò, sappi che non dimenticherò facilmente il tuo attentato alla mia vita facendomi scalare il Monte Sanitas. Sam and Rania, thank you for sharing this journey with me from the very beginning to the very end, including the endless COVID times, when having our little PhD bubble made all the difference. Fernando, gracias por tu actitud y por ser una de las personas más random y chill que he conocido nunca. Kevin, thank you for always finding the time to catch up over a coffee or a beer, talking about your next trip to Italy and life in general. My thanks also go to Oliver (I'm still dreaming about your eggs Benedict), Natalia, Miguel (should I buy you some more peaches?), Riccardo, Leonardo, Sabin, Linh, Gitte, Şevket, Rens,

Joshua (please appreciate that I still thank you despite the culinary trauma you inflicted on me), and everyone else in our department who shared a coffee, a laugh, or a deadline with me.

Voglio ringraziare anche i miei *sfravcated mates* e tutti voi che, tra SMCV e Milano, avete sempre continuato a esserci: Pietro, Feffa, Vinz, Manuel, Mariomacc, Federica B., Debora, Peppe, Maurizio, Fabiano, e Antonella. Grazie per il modo in cui, nonostante il tempo e la distanza, ogni volta che ci rivediamo sembra sia passato solo un attimo dall'ultima volta. E a te, Vinz, grazie in particolar modo per le grafiche di questa tesi, in cui hai dato forma a "fatti spaziali" di cui ignoravi felicemente l'esistenza (sia messo agli atti che l'armistizio del borsone è ufficialmente sancito).

Last but definitely not least, grazie Maria per esser stata spesso il mio "vento in faccia" in questi anni, facendomi vedere me stesso e il mondo con occhi diversi. Questo PhD mi ha insegnato tanto. Eppure, le cose davvero importanti le ho capite grazie alle tue parole. Le porterò con me a lungo.



Solar sails navigate the cosmos pushed by sunlight, like sailboats driven by the wind.

Close to our planet, however, additional sources of acceleration affect sailcraft dynamics.

This dissertation investigates these dynamics, their modeling, and impact on solar-sail maneuverability, revealing the limits and potential of Earth-bound solar sailing.

